INSTABILITY SATURATION AND TURBULENT DYNAMOS IN SHEAR FLOWS

By

BINDESH TRIPATHI

A dissertation submitted in partial fulfillment of

the requirements for the degree of

Doctor of Philosophy

(Physics)

at the

UNIVERSITY OF WISCONSIN–MADISON

2025

Date of final oral examination: 11/11/2025

The dissertation is approved by the following members of the Final Oral Committee:

Paul W. Terry, Professor, Physics

Ellen G. Zweibel, Professor, Astronomy, Physics

M.J. Pueschel, Senior Scientist, Dutch Institute for Fundamental Energy Research

Chris C. Hegna, Professor, Engineering Physics

to my loving mother and other mothers.

ABSTRACT

Instabilities in nature drive turbulence, which impedes fusion-energy gain in reactors and impacts cosmic observables such as magnetic fields and multi-messenger-astronomy signals. To understand the underlying turbulent processes, this thesis investigates two central questions: How instabilities may saturate, and how turbulence may generate astrophysical magnetic fields at large scales—a process called the dynamo. Previous efforts to address the former have relied on an energy cascade to microphysical scales and thus missed critical elements of instability-scale mode-couplings. Dynamo efforts have been frustrated because large-scale magnetic-field generation is suppressed via Alfvénization—a robust magnetohydrodynamic process that aligns fluctuations in the fluid velocity $\mathbf{u}$ with those in the magnetic field $\mathbf{b}$, i.e., $\mathbf{u} \,||\, \pm \mathbf{b}$. Addressing these challenges, this thesis develops fundamental principles of instability saturation and applies them to demonstrate a novel mechanism where Alfvénization *generates* magnetic fields, instead of suppressing the fields. These findings, organized in three parts, apply to shear flows driven unstable by their velocity gradients.

Part I of this thesis demonstrates the new paradigm of instability saturation via stable eigenmodes. These modes spatially resemble the instability but decay exponentially in time. However, the stable modes are nonlinearly excited to significant amplitudes via mode-couplings to instability. Hence, most of the energy injected by the instability is transferred to the stable modes, which then return energy to the large-scale unstable flow, thus reducing the energy available to cascade to small scales. The stable modes sequester magnetic fields at large scales by reducing the rate-of-strain and field-line distortion. Nonlinear simulations in two dimensions without the stable modes display a splitting of otherwise merging large-scale vortices, a spreading of turbulence, and a surging of visco-resistive dissipation and momentum transport.

Part II confirms the findings of Part I by considering three-dimensional turbulence. The three-dimensional (3D) stable modes are found to be more effective than the two-dimensional (2D) stable modes in transporting momentum in the direction of the large-scale flow gradient. Moreover, vortex stretching—a 3D process—is countered by the stable modes, thus transforming thin, long cylinders of vortices to thick, short cylinders. In three dimensions, the stable modes receive energy via inherently 3D zonal jets; these jets are fluctuating 3D flows that propagate in, while remaining invariant along, the direction of the large-scale 2D shear flow. In a jet-dominated system, numerical simulations validate an analytic turbulence closure model that predicts stellar spin-down rates, relevant for the solar tachocline.

Part III, using 3D magnetohydrodynamic turbulence, reports the generation of magnetic fields via Alfvénization—the suppressor of the traditional dynamos. The large-scale vorticity, which traditional dynamo theories ignore, contributes here to the large-scale electromotive force. A working physical mechanism of this effect is identified, where the 3D zonal jets described in Part II interact with Alfvénized magnetic fluctuations, thereby generating large-scale, quasi-cyclic magnetic fields, consistent with astrophysical observations. This large-scale vorticity effect produces seed large-scale magnetic field, parallel to the large-scale flow, purely from small-scale flow-field correlation. Then, the large-scale cross-helicity — alignment between large-scale flow and magnetic field — is transferred by turbulent stress to small scales, in a way analogous to the forward transfer of momentum and energy. Thus, the two dynamo steps cyclically reinforce each other, spontaneously magnetizing the fluid. The new dynamo mechanism explains confounding measurements of a laboratory experiment. This mechanism is also predicted to operate in binary neutron star mergers on time scales of microseconds, which in millisecond mergers can generate some of the strongest magnetic fields in the Universe.

ACKNOWLEDGMENTS

Words fail to convey my gratitude to my dear Ph.D. advisors, Profs. Paul W. Terry and Ellen G. Zweibel, who kindly taught, guided, gave freedom, and cared for me beyond what one can dream about. Among the endless list of characters I appreciate about them are their availabilities even when surrounded by a mountain of work, precision in communication, unpretentious humility, empathizing hearts, and graceful mentorship style.

It would be unfair if I did not mention Dr. M.J. Pueschel and Dr. Adrian Fraser, because much of what has been accomplished in this thesis are the products of scientific discussions among the 5 minds for five and a half years, which were continuous except for the Christmas. Many thanks to M.J. for teaching elegant writing style, notably the minutiae (e.g., using mathrm in subscript of variables and using $\sim$ after a dot in a TeX file to control the spacing between characters), which once learnt I cannot resist the urge to fuss with. All four mentors have been a constant source of pleasure, knowledge, and ideas.

I would like to thank Prof. Chris C. Hegna for teaching me the wonderful courses *waves and instabilities* and *magnetohydrodynamics*, in addition to providing feedback throughout the graduate program. Thanks are due also to members of research groups of Paul, MJ, and Ellen for lively weekly engagements, feedback, and sharing of broader research results. These groups are responsible for what I know about saturation of the ion-temperature-gradient-driven turbulence, GENE gyrokinetic code, Dimits shift, fusion reactors, cosmic rays, and particle acceleration. In particular, I am delighted to acknowledge countless interactions and fruitful conversations with Roark Habegger, Taweesak Jitsuk, Augustus Azelis, Braden Buck, Sanket Patil, Jack Schroeder, Daniel Humprey, and Michael J. Gerard. I have been very fortunate to have the opportunity

to mentor two undergraduate students during my graduate program: Christopher Fan (University of Wisconsin–Madison) and Tim de Hoogen (Eindhoven University, The Netherlands), who helped with several aspects of linear eigenvalue problems and 3D Paraview visualizations, respectively.

I owe thanks to several researchers inside and outside of my home institution as interacting with them greatly benefited my research program. Specifically, I must thank V. Zhdankin, J. Sarff, C.R. Sovinec, J.R. Beattie, A. Bhattacharjee, D. Lecoanet, K.J. Burns, F. Ebrahimi, E.R. Most, and A. Beloborodov. Special thanks to B. Ripperda and the friendly people here at the Canadian Institute of Theoretical Astrophysics, Toronto, which has freely provided caffeine and warmth to write this part of the thesis.

I thank Prof. A.J. Barker, Dr. D. Mitra, and Prof. D. Nandy for the four side projects and papers I worked on and published during my graduate program in Madison. Heartfelt thanks to Prof. L. Everett who engagingly taught quantum mechanics and the Van Vleck Fellowship that enabled me early in my graduate program to work on, and publish results from, resuming the Wentzel–Kramers–Brioullin series to all orders. As in any field, roots of a visible tree can always be traced, and hence I offer thanks to all the instructors and teachers, including my family, who all helped give shape to my academic and personal journey.

Journal Articles

The following peer-reviewed journal articles were published or appeared during the PhD program 2019–25.

B. Tripathi, A.E. Fraser, P.W. Terry, E.G. Zweibel, and M.J. Pueschel, Spontaneous Generation of Magnetic Fields via Turbulent Cross-Helicity Instability in Shear Flows, *Ready for submission to Phys. Rev. Lett.*

B. Tripathi, A.E. Fraser, P.W. Terry, E.G. Zweibel, and M.J. Pueschel, The Life-Cycle of the Jet-Driven Shear-Flow Dynamo, *Under revision after review for publication in Phys. Plasmas.*

B. Tripathi, A.E. Fraser, P.W. Terry, E.G. Zweibel, M.J. Pueschel, and R. Fan, Large-Scale Dynamos Driven by Shear-Flow-Induced Jets, *Accepted for publication in* ***Nature*** (2025).

B. Tripathi, A.J. Barker, A.E. Fraser, P.W. Terry, and E.G. Zweibel, Predicting the slowing of stellar differential rotation by instability-driven turbulence, *Astrophys. J.* **966**, 195 (2024).

B. Tripathi and D. Mitra, Anisotropic Magnetized Asteroseismic Waves, *Astrophys. J.* **976**, 57 (2024).

R. Gaur, I.G. Abel, **B. Tripathi**, and E. Koleman, Effect of insulator end cap thickness on time-dependent Hartmann flow in a supersonic mirror, *J. Plasma Phys. (Letter)* **90**, 175900603 (2024).

B. Tripathi, P.W. Terry, A.E. Fraser, E.G. Zweibel, and M.J. Pueschel, Three-dimensional shear-flow instability saturation via stable modes, *Phys. Fluids* **35**, 105151 (2023).

B. Tripathi, A.E. Fraser, P.W. Terry, E.G. Zweibel, M.J. Pueschel, and E.H. Anders, Nonlinear mode coupling and energetics of driven magnetized shear-flow turbulence, *Phys. Plasmas* **30**, 072107 (2023).

B. Tripathi, A.E. Fraser, P.W. Terry, E.G. Zweibel, and M.J. Pueschel, Near-cancellation of up- and down-gradient momentum transport in forced magnetized shear-flow turbulence, *Phys. Plasmas* **29**, 092301 (2022).

B. Tripathi and D. Mitra, Exact analytical solutions in inhomogeneous magnetic fields for linear asteroseismic waves, *Astrophys. J.* **934**, 61 (2022).

B. Tripathi, A.E. Fraser, P.W. Terry, E.G. Zweibel, and M.J. Pueschel, Mechanism for sequestering magnetic energy at large scales in shear-flow turbulence, *Phys. Plasmas (Letter)* **29**, 070701 (2022).

B. Tripathi, Resummed Wentzel–Kramers–Brillouin series: Quantization and physical interpretation, *Phys. Rev. D.* **105**, 036010 (2022).

B. Tripathi, D. Nandy, and S. Banerjee, Stellar mid-life crisis: subcritical magnetic dynamos of solar-like stars and the breakdown of gyrochronology, *Mon. Not. R. Astron. Soc.: Lett.* **506**, L50 (2021).

CONTENTS

LIST OF TABLES

LIST OF FIGURES

1 INTRODUCTION

The concepts presented in this chapter are fundamental to understanding themes and novel findings detailed in this thesis. The chief findings of the thesis, while related, can be categorized into two classes, Secs. 1.1 and 1.2. The first challenges the traditional paradigm of nonlinear saturation of unstable systems. Key elements from the first are employed in the second. The latter builds a new foundation for understanding the origin of astrophysical magnetic fields.

1.1 Instability Saturation

A. Instability and Eigenmodes

A system is unstable if an infinitesimal disturbance grows. For example, a spark in a dry forest can cause fire to grow uncontained. When milk, a heavier fluid, is poured in a cup of coffee or tea composed of a lighter fluid, the heavier fluid sinks continuously in the lighter fluid, causing the disturbance in the cup to grow. This behavior is because the cup with milk above water has extra potential energy—a free energy—which is used for mixing. Following the laws of thermodynamics, mixing maximizes disorderedness and thus decreases free energy stored in the system's ordered behavior. Free energy exists in nature often in the form of gradients of density, flow velocity, temperature, etc. Free energy provides the source for instabilities, which abound from sub-atomic scales to nuclear fusion laboratory experiments to all branches of physics, astronomy, and sciences. Modeling instability and its saturation are, thus, critical to control instabilities in fusion reactors, to harness fusion energy, and to better understand physical processes that determine the evolution of astrophysical environments.

Stability of a system is examined by perturbing it slightly. Introducing small-amplitude perturbations around a background state—the equilibrium state—one keeps physical effects that are linear in perturbations. The linearized governing equations generally admit multiple solutions, also called the normal modes [10] or eigenmodes[1]. The normal mode that grows in time is the instability. If a normal mode does not grow, that mode is labeled stable eigenmode. If a stable eigenmode decays at nearly the same rate as the instability growth rate, that eigenmode is referred to as conjugate-stable eigenmode.

B. Mode-Coupling and Traditional Saturation Theory

When the amplitudes of the normal modes are large (either due to the instability or their initial excitation levels), the linear theory must be modified to include nonlinearity. The nonlinear coupling transfers energy among the normal modes. When normal modes at different spatial and temporal scales are coupled nonlinearly, the system often displays a seemingly random but self-similar behavior across a range of physical and temporal scales. This phenomenon, called turbulence, transfers energy from a scale where energy is externally supplied to a scale where energy is dissipated in the form of heat via microphysical effects, e.g., molecular collisions, or other dissipation mechanisms [11, 12].

When an instability at large scale drives turbulence, the energy supplied by the instability at large scale is widely assumed to be cascaded in its entirety to small scales for dissipation [12]. This idea, originally due to A. N. Kolmogorov[2] [14], is expressed

[1]Throughout this thesis, the word "mode" represents eigenmode at a given physical scale. This usage distinguishes eigenmode perturbation from wavenumber perturbation—the former is one of the many solutions of the linearized equations at a given wavenumber, whereas the latter sums over all the solutions at the given wavenumber.

[2]The problem of modeling nonlinear saturation of fluid instability was also investigated by

as

$$\text{Energy given by instability } (Q_1) = \text{Energy dissipated at small scales } (\epsilon). \quad (1.1)$$

This Kolmogorov theory, Eq. (1.1), is widely used to model nonlinear saturation of instability as the theory appears reasonable. However, this theory misses a critical component of saturation and has profound observable consequences, which are shown in this thesis for a natural instability that is ubiquitous and fundamental.

C. Saturation via Stable Eigenmodes

The Kolmogorov theory breaks down because the theory only considers nonlinear coupling between unstable eigenmodes (instability) and small scales[3] — and because the theory ignores nonlinear coupling among unstable eigenmodes and stable eigenmodes, both existing at large scales [15]. The latter coupling is often significant. This is because the spatial structures of these eigenmodes are often similar, if not identical[4].

When nonlinear mode-coupling among large-scale unstable eigenmodes and large-scale stable eigenmodes is significant, most of the free energy extracted by the instability from the large-scale gradient is transferred to the large-scale stable eigenmodes[5] [15, 17]. The latter then transfers energy back to the large-scale gradient, building up the available free energy and damping the energy in turbulence [17]. This time-reversed process (stable eigenmodes) is nonlinearly driven and can be as effective as, and

L. D. Landau, who analyzed amplitude of the unstable eigenmode [13].

[3]Small-scale fluctuations are, in general, linearly stable. In this thesis, the word "stable mode" refers to large-scale stable eigenmodes and not the small-scale fluctuations. The latter are visco-resistively damped, whereas the former has direct connections to the large-scale instability.

[4]The spatial structures of the unstable and stable eigenmodes are complex conjugates to each other in systems where space-time-reversal symmetry is preserved [16].

[5]This transfer occurs even in freely-evolving systems where the unstable gradient relaxes to a stable configuration—a process called quasilinear flattening.

at times more effective than, the time-forward process (unstable eigenmodes) [18]. This seeming reversal of the arrow of time, however, does not violate the laws of thermodynamics, as over a longer time, the time-reversed process is slightly weaker than the time-forward process. The symmetry between the time-forward and time-reversed processes is broken by microphysical dissipation. The foregoing saturation mechanism replaces the Kolmogorov theory with

$$\begin{aligned}\text{Energy given by instability } (Q_1) - \text{Energy taken by stable eigenmodes } (Q_2) \\ = \text{Energy dissipated at small scales } (\epsilon).\end{aligned} \tag{1.2}$$

This thesis shows that Q_2 is often 90–99% of Q_1, and ϵ is only 1–10% of Q_1 [19]. Thus, the small-scale dissipation (ϵ) is reduced by up to 2 orders of magnitude, which impacts laboratory and astrophysical observations.

D. Shear-Flow Instability

In liquids, gases, and plasmas, some regions move faster than others. Take, for example, water flowing in a pipe where the flow near the pipe boundaries hardly moves, whereas the flow at the middle of the pipe moves fast. Such a flow with a gradient in velocity is called a shear flow. Examples of shear flows are found in fluids of electrons moving in metals approximated by electron-hydrodynamics [20], in everyday lives including our blood vessels where fluids are driven by the pumping heart, in water faucets in the kitchen, in the evening air breeze, in nuclear fusion devices [21], in tornadoes and tsunamis, in geophysics and astrophysics [22], and even at cosmological scales [23].

A beautiful example of shear flow is observed in the atmosphere, as shown in Fig. 1.1. In this photograph, air at a lower altitude is denser and thus moves slowly, as opposed to at a higher altitude, where the air is lighter and thus moves quickly.

Figure 1.1: A motorcycle crashing against a car illustrates the underlying mechanism behind the Kelvin–Helmholtz instability. The instability is driven by the difference in fluid velocity. The background scene was spotted at Smith Mountain Lake, Virginia, on the evening of June 18, 2019 by Amy Christie Hunter (Facebook), which shows public excitement about the topic investigated in this thesis.

This differential velocity of air is analogous to a motorcyclist colliding against a car; there, the lower portion of the motorcyclist is at rest whereas the upper portion is in motion. These two systems are equivalent if one applies the Galilean transformation to use the frame of reference affixed to the center point of the motorcyclist, around which their body is rotated, due to the unfortunate collision. This analogy between the rotating body and the sheared atmospheric flow explains the observed pattern of waves. The amplitudes of these waves grow over time after which they saturate.

The unstable waves also appear routinely in the sea and the ocean, where wind blowing over the water gives rise to a velocity gradient (the wind near the surface of the water has zero velocity). This phenomenon of growing waves at the water-wind interface was speculated to be related to the water-wind velocity-difference by Kelvin and Helmholtz [10]. Thus, these unstable waves have come to be known as the Kelvin–Helmholtz (KH) instability.

E. Nonlinear Saturation and Quasilinear Theory

It remains a challenge to address the question: What are the dominant nonlinear mode-couplings that saturate the KH instability? Although the KH instability has been numerically simulated since the 1960s [24], numerical simulations—similar to satellite observations—merely generate data. These raw data are the initial numerical input to develop final theoretical conclusions. Such conclusions and theory are to be tested under critical conditions and, if needed, revised to make them general and robust. Historically, however, it has been assumed that, by performing numerical simulations in a limited parameter range, one gains an understanding of the general physical theory. This situation shares similarity with the naïve claim that experimental data of a room's temperature explains *why* the room has a specific thermal state. Variables to examine are the adjacent spaces and windows, which may couple the room to other channels via which energy is transferred. A physical theory of saturation of the KH instability requires an analysis of the coupling of the instability to other types of fluctuations, namely large-scale stable eigenmodes and small-scale fluctuations. A central achievement of this thesis is the development of a general theory for the KH-instability saturation; additionally, observable consequences of the novel saturation mechanism are demonstrated for both hydrodynamics and magnetohydrodynamics, in two dimensions and three dimensions [1, 17–19].

The KH instability saturates by transferring most of its energy to the stable eigenmodes at the same physical scale where the instability exists [17]. This thesis shows that the energy cascaded to small scales is a minute fraction ($\sim$0.01–0.2) of what the instability supplies for turbulence [19]. This effect is more pronounced in three dimensions than in two dimensions [1]. The stable eigenmode is significantly excited because its eigenmode structure is nearly identical to that of the unstable

eigenmode, as shown in Fig. 1.2. This similarity has profound consequences for nonlinear properties of instability-driven turbulence [1].

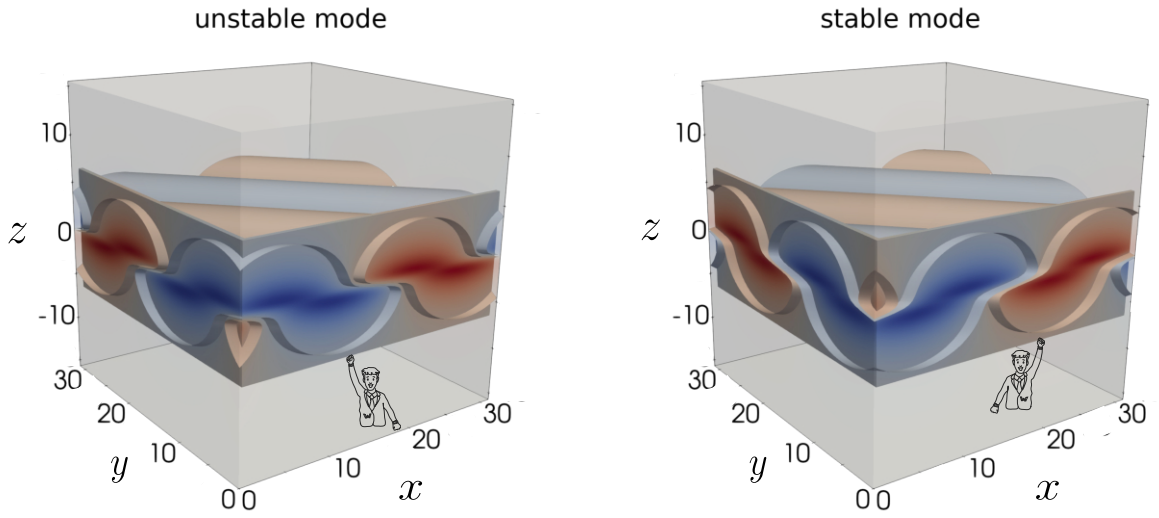

Figure 1.2: Three-dimensional rendering of vertical velocity u_z of unstable and stable eigenmodes [1]. The two modes are identical except in their orientations—a result of complex-conjugate symmetry (or equivalently, the parity-time-reversal symmetry of the inviscid KH instability). The KH-unstable large-scale shear flow is directed along x and reversed in z. The isocontours and the surface rendering highlight a symmetry that is illustrated with a cartoon.

Brute-force numerical simulations of turbulence driven by shear flows in astrophysics, geophysics, and laboratory are challenging because of the vast range of scales and extreme parameters. On the other hand, these nonlinear systems resist analytic solutions. These limitations force researchers to seek refuge in the middle ground between simple analytic solutions and comprehensive numerical simulations. This is where hybrid understanding of turbulence is critical as it allows one to develop simpler and predictive models of turbulence, A widely used hybrid approach to modeling turbulence is called quasilinear modeling. Quasilinear models provide insights into turbulent transport of momentum and heat, particle mixing, pattern formation, and magnetic field generation, which all impact astrophysical observations [25].

A common quasilinear model of instability-driven turbulence assumes that the rate

of energy cascade to small scales is equal to the rate of free-energy extraction by the unstable eigenmodes from the large-scale driving gradient [26–29]. This model assumes that, at the instability-scale, only the unstable eigenmodes at different wavenumbers couple together — only outside of the instability-scale do unstable eigenmodes couple to stable modes at small scales. However, when stable eigenmodes that exist at the same scale as the instability are excited to large amplitudes, they interfere with the cascade process [17]. This thesis shows that, when stable eigenmodes are artificially removed in numerical simulations of KH instability-driven turbulence, turbulence is drastically different [17]. First, the eddies that form due to the KH instability violently split apart instead of being merged. Second, turbulence spreads in physical space and displays disordered, destructive motions. Third, small scales of flow and magnetic fields are amplified by more than an order of magnitude, causing a corresponding increase in microphysical dissipation. All these behaviors point to a shortcoming of traditional theories relying on an inertial cascade.

Other consequences of stable modes include the near-cancellation of momentum transport across the shear flow [18]: While the instability attempts to transport the large-scale momentum in the direction of decreasing flow-gradient, the stable eigenmodes transport the large-scale momentum in the direction of increasing flow-gradient. Mixing of fluid due to turbulence is also reduced by stable eigenmodes [17].

F. Instability-Induced Zonal Jets

Instability and turbulence are generally different in two and three dimensions. One may, therefore, suspect that the significant excitation of stable eigenmodes at large scales may be connected to turbulence that is two-dimensional. Thus, it is essential

to also examine the saturation of the KH instability in three dimensions. Separate analyses using hydrodynamic and magnetohydrodynamic models are necessary, as magnetic fields can impact turbulence fundamentally.

In three dimensions, where a large-scale shear flow $U_x(z)$ is directed along x and varies along z, a special family of perturbations exists. These perturbations vary along y but do not vary along x. These perturbations are special because they are not subject to the KH instability, as they have no variation along the direction of the mean flow [10]. Hence, these special x-invariant perturbations have zero growth rates [10] in the ideal magnetohydrodynamic (MHD) limit. Since these perturbations are not necessarily eigenmodes of the system, they can be generically called *stable perturbations*. Perturbations that are x-directed and x-invariant are exact solutions to the governing nonlinear equations. These perturbations are analogous to banded equatorial flows in planetary atmospheres and zonal flows in fusion plasmas [30], and to Elsässer fields in MHD turbulence [31]. Hence, these are labeled zonal flows or zonal jets throughout this thesis. Their magnetic counterparts are zonal magnetic fields. Although these special perturbations (generally) have zero growth rates and zero frequencies, they can be significantly excited nonlinearly, in a way similar to how stable eigenmodes are excited nonlinearly. The timescale of zonal-flow excitation, however, can be longer than that of stable-mode excitation.

When large-scale zonal flows are prominent in a turbulent system, they often dominate nonlinear interactions. The three-wave couplings are, therefore, approximated well by coupling between two general fluctuations and one zonal fluctuation [32]. This approximation allows one to develop an analytically soluble model of turbulence closure [32]; a closure is a scheme that truncates the hierarchy of correlations between fluctuations, where the n^{th} order correlator depends on the $(n+1)^{\text{th}}$ order correlator [32–34]. The closure model can predict the saturated amplitude of turbulence and the

rates of turbulent transport of momentum across the shear flow.

As a direct application to astronomy and astrophysics, this thesis also considers slowing down of stellar spins due to angular momentum transport via instability-driven turbulence [35]. Instability naturally arises in differentially rotating stars. Such differential velocity can be linearly unstable; however, strong stellar stratification (a density gradient) tends to suppress the instability. On the other hand, to explain the observed slowing down of stellar spins, instability needs to exist. Instability is likely reinstated when thermal diffusion weakens the stabilizing force of buoyancy, thus making the stellar differential rotation unstable again [36–38]. The free energy for this instability resides in the unstable angular momentum gradient and is made accessible by thermal diffusion. Hence, this so-called the Goldreich–Schubert–Fricke (GSF) instability is a diffusive instability. A nonlinear saturation theory of this instability is built in this thesis using a zonal-flow-coupled turbulence closure model [35]. The theory agrees with numerical simulations and makes predictions for time scales of the spin down of stars and the solar tachocline[6] — a thin region in the Sun at around 0.7 of the solar radius, where the gradient in the solar rotation is strong.

The large-excitation of zonal jets in three-dimensional (3D) shear-flow turbulence is noteworthy because zonal jets—the long-lived 3D coherent structures—have the potential to generate and sustain magnetic fields in three dimensions [1]. Such self-consistently-generated magnetic fields are of primary importance in astrophysics. Thus, this thesis seeks to understand the roles of turbulence and shear flows in stellar magnetism, particularly as they relate to dynamos.

[6] In Greek, *tákhos*: speed and *klínō*: to slope.

1.2 Dynamos

Why is our Universe magnetized? This question remains a fundamental challenge to address, given that magnetic fields exist everywhere in the Universe. Examples are found in the Earth's dipole magnetic field, sunspots, stars, interstellar medium, galaxies, and cosmic voids [8, 39–43]. Magnetic fields impact the formation of stars, affect the evolution of astrophysical objects, influence the transport of cosmic rays and momentum, and produce multi-messenger signals [44], among others.

A. Dynamo Action

The generation of magnetic fields and their maintenance against resistive dissipation is called dynamo action [45]. Initial studies of dynamo action until the middle of the 20^{th} century presented continuous frustrations because they were confronted by several mathematical proofs, known as anti-dynamo theorems [46, 47]. The essence of these theorems is that the dynamo action is impossible in systems that lack three-dimensionality [45].

Only in the 1950s and 1970s, the first few examples of a successful dynamo action were reported [48–50]. These studies, however, assumed flows to be laminar, prescribed, and steady, rather than allowing them to be turbulent, self-consistently generated, and time-evolving. When the Lorentz feedback on the flow is ignored, the resulting dynamo is often called a kinematic dynamo [45], and was the focus of studies until the beginning of the current century, when powerful computing systems enabled nonlinear, self-consistent studies of dynamos. Such advanced simulations produce data that can be used to test mathematical dynamo theories [45].

B. Mean-Field Theory

A mathematical formulation of dynamo action is given by the so-called mean-field theory [45]. This theory models coarse-grained correlations between small-scale fluctuations to derive an effective evolution equation for large-scale magnetic fields (also called mean magnetic fields). The first coarse-grained dynamo model was visualized by Eugene Parker in 1955 [51], when he argued from a pictorial representation how three-dimensional turbulence can be parameterized to incorporate its effects in a simple, one-dimensional, coarse-grained, mean-field model of the dynamo. The chief objective of any mean-field dynamo theory is to predict how the correlation between turbulent fluid motions $\widetilde{\mathbf{u}}$ and turbulent magnetic fields $\widetilde{\mathbf{b}}$ — which is called the turbulent electromotive force $\widetilde{\mathbf{u}} \times \widetilde{\mathbf{b}}$ — depends on the properties of the mean magnetic field. Note that the turbulent electromotive force (or equivalently, the turbulent electric field $\widetilde{\mathbf{u}} \times \widetilde{\mathbf{b}}$) is orthogonal to $\widetilde{\mathbf{b}}$ in standard electrodynamics. Parker's visual interpretation, nevertheless, suggested that when correlations between fluctuations are averaged (over certain scales, represented by a suitable averaging operation $\langle \cdot \rangle$), the *mean* turbulent electromotive force $\mathcal{E} = \langle \widetilde{\mathbf{u}} \times \widetilde{\mathbf{b}} \rangle$ has a component parallel to the *mean* magnetic field $\mathbf{B}$, given by $\mathcal{E} \propto \mathbf{B}$ [51].

Parker's visualization, shown in Fig. 1.3, was later put on a firm mathematical foundation in 1966 when a mathematical dynamo model was built using the separation of two physical scales—large and small [52]. The model assumes that the mean turbulent EMF $\mathcal{E}$ depends only on the mean magnetic field $\mathbf{B}$ and its spatial derivatives; the mean flow is assumed to be zero [45, 52]. This mean-field model showed that Parker's proportionality constant α between the mean EMF $\mathcal{E}$ and mean magnetic field $\mathbf{B}$ measures the turbulent kinetic helicity [51, 52]. This helicity measures the alignment between turbulent velocity $\widetilde{\mathbf{u}}$ and turbulent vorticity $\nabla \times \widetilde{\mathbf{u}}$. The coefficient

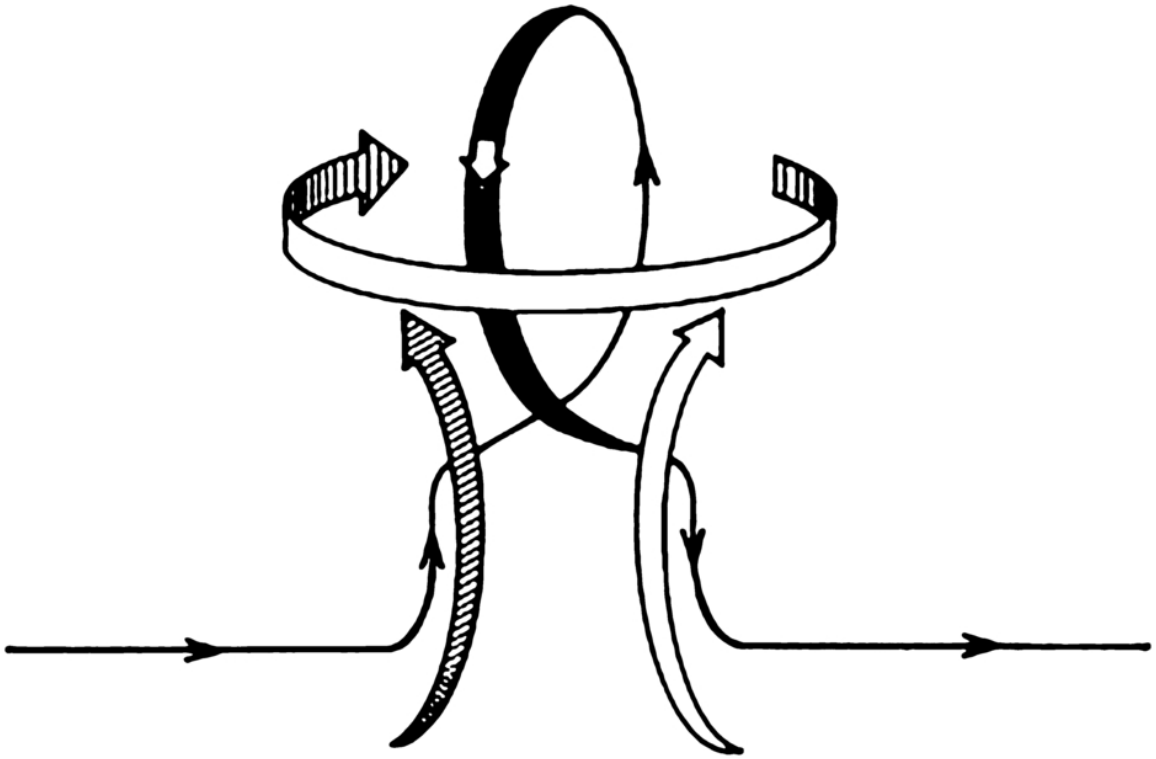

Figure 1.3: Pictorial representation of the α-effect. An initially horizontal magnetic field is perturbed upward by a turbulent flow and subsequently rotated by turbulent vorticity around a vertical line that passes through the middle of the page. The α-effect requires alignment between velocity and vorticity, measured by kinetic helicity. Figure 1 in Parker (1970) [2].

α is a measure of the lack of reflection symmetry in turbulent fluid motions. A larger α means more helical motion of fluid, with a preferential handedness in the system—either left- or right-handed helical motions. This mean-field theory gives an expression for the mean turbulent EMF [52]

$$\mathcal{E} = \alpha \mathbf{B} - \beta \nabla \times \mathbf{B}, \tag{1.3}$$

where the β-effect, related to turbulent energy, acts as turbulent resistivity and is a dynamo sink, as the curl of the mean EMF ($\nabla \times \mathcal{E}$), appearing in the magnetic induction equation, produces the diffusion term $\beta \nabla^2 \mathbf{B}$. Here, the α-term is Parker's

dynamo source.

The mean-field framework of the 1960s served as the foundation of the dynamo theory [52]. From the late 1960s to the early 1990s, the mean-field framework provided explanations for several long-standing problems of solar and astrophysical magnetism [45, 53].

C. Nonlinear Suppression of Dynamo via Alfvénization

Around the 1990s, however, limitations of the α-dynamo became apparent [5–9]. One of these is the Lorentz feedback: Small-scale magnetic fields grow rapidly and, via their Lorentz feedback, reduce the growth rate of large-scale magnetic fields to near zero before the large-scale magnetic fields can attain large amplitudes [5–8]. Although this nonlinear Lorentz feedback was mathematically indicated in 1976 using an MHD turbulence closure calculation [4], this effect remained unappreciated until the 1990s [5–7].

To illustrate, the kinematic expression (without the Lorentz feedback) for the α-effect is [45, 52]

$$\alpha = -\frac{\tau}{3}\langle \widetilde{\mathbf{u}} \cdot \nabla \times \widetilde{\mathbf{u}} \rangle, \tag{1.4}$$

where τ is a turbulence correlation time. The expression for the α-effect *with* the Lorentz feedback is [4]

$$\alpha = -\frac{\tau}{3}\left[\langle \widetilde{\mathbf{u}} \cdot \nabla \times \widetilde{\mathbf{u}} \rangle - \langle \widetilde{\mathbf{b}} \cdot \nabla \times \widetilde{\mathbf{b}} \rangle \right], \tag{1.5}$$

where the second term $\langle \widetilde{\mathbf{b}} \cdot \nabla \times \widetilde{\mathbf{b}} \rangle$, the current helicity, is the magnetic correction

[4, 8].

To understand how the α-effect is dramatically reduced, note that small-scale magnetohydrodynamic fluctuations rapidly produce equipartition of kinetic and magnetic energies via a process called Alfvénization—a fundamental MHD process that tends to create fluctuations of velocity $\widetilde{\mathbf{u}}$ and magnetic fields $\widetilde{\mathbf{b}}$ that are equipartitioned and aligned [31, 54–57]. Energy-equipartition gives $|\widetilde{\mathbf{u}}|^2 \approx |\widetilde{\mathbf{b}}|^2$. Alignment gives $\widetilde{\mathbf{u}} \propto \pm\widetilde{\mathbf{b}}$ [31]. So, α of Eq. (1.5) is reduced to near zero. When $\alpha \to 0$, the growth of the large-scale dynamo is severely stunted before the dynamo is able to produce appreciable large-scale magnetic fields [4]. It is the *exponential growth* of the large-scale dynamo that is severely reduced by the nonlinear feedback from quickly saturated small scales. Hence, the time required to attain the saturation of the large-scale dynamo is increasingly long (smaller growth rate) with quicker feedback from small scales [9]. Moreover, the small scales saturate and become Alfvénized[7] more quickly with increasing magnetic Reynolds number Rm, a dimensionless coefficient that measures the inverse of electric resistivity. Hence, the α-effect is reduced increasingly with increasing Rm, due to increasingly fast Alfvénization. It is strongly emphasized that the root cause of the α-quenching (severe reduction of α) is Alfvénization [4].

Alfvénization can be understood, in simple terms, as the result of perturbing a magnetic field along which Alfvén waves traverse [58]. The magnetic field here does not need to be a global mean magnetic field, but locally, in every small region, some turbulent magnetic field can serve as a time-evolving local background field along which local Alfvén waves propagate. Thus, Alfvénization occurs even in homogeneous incompressible MHD turbulence [59]. If a large-scale shear flow is absent, ideal MHD demands that there should be a conservation of volume-averaged turbulent cross-

[7]The pure Alfvénic states feature $\widetilde{\mathbf{u}} \,||\, \pm\, \widetilde{\mathbf{b}}$.

helicity[8] $\widetilde{\mathbf{u}} \cdot \widetilde{\mathbf{b}}$ [60]. The turbulent cross-helicity measures alignment between turbulent flow $\widetilde{\mathbf{u}}$ and turbulent magnetic field $\widetilde{\mathbf{b}}$. Although the global average of correlation between turbulent flow and turbulent magnetic field is zero (or a constant depending on the initial conditions) in a homogeneous system, the turbulent flow and turbulent magnetic field become locally aligned everywhere in the system. This local alignment rapidly develops even from a random, uncorrelated initial condition. This process can be understood in the following way: Pure Alfvénic states ($\widetilde{\mathbf{u}} \,||\, \pm \widetilde{\mathbf{b}}$) are exact solutions of the ideal incompressible MHD equations; hence, these states are the natural, asymptotically relaxed states of MHD turbulence [31, 59, 60]. Alfvénization is found to operate even in systems with compressibility [61]. Therefore, Alfvénization is a robust process, which plays a chief role in astrophysical turbulence from the solar wind to the interstellar medium to galaxies [55–57, 61, 62]. Since Alfvénization reduces the α-effect to near zero, it has frustrated efforts to understand the creation of astrophysical magnetic fields using traditional helical dynamos. Hence, **Alfvénization is commonly known as a dynamo suppressor** [4].

D. Alfvénization with Shear Flow as a Dynamo Enabler

Alfvénization, however, can also act as a *dynamo enabler*, which this thesis confirms [63–65]. This idea, which contrasts with conventional belief, had its early roots in a turbulence closure [66]. The closure generalizes the conventional mean-field dynamo theory [52] by incorporating the effect of a large-scale shear flow $\mathbf{U}$. The

[8]The word *cross-helicity* represents helicity between two independent variables, flow and magnetic field, and hence the word *cross*. Self-helicity of a vector $\mathbf{V}$ measures the degree of knottedness between the 3D vector lines of $\mathbf{V}$ and 3D vector lines of $\nabla \times \mathbf{V}$. So, $\mathbf{u} \cdot \nabla \times \mathbf{u}$ is kinetic (self-)helicity, $\mathbf{A} \cdot \nabla \times \mathbf{A}$ is magnetic (self-)helicity, and $\mathbf{b} \cdot \nabla \times \mathbf{b}$ is current (self-)helicity.

generalized closure expresses the mean EMF $\mathcal{E}$ as [66]

$$\boxed{\mathcal{E} = \underbrace{\alpha \mathbf{B}}_{\substack{\text{Suppressed by} \\ \text{Alfvénization}}} - \beta \nabla \times \mathbf{B} + \underbrace{\Upsilon \nabla \times \mathbf{U}}_{\substack{\text{Enabled by} \\ \text{Alfvénization}}},} \tag{1.6}$$

where the last term is the new dynamo source, arising from the vorticity of the large-scale shear flow. The Upsilon term $\Upsilon = \tau \langle \widetilde{\mathbf{u}} \cdot \widetilde{\mathbf{b}} \rangle / 3$ measures the alignment between the turbulent flow $\widetilde{\mathbf{u}}$ and turbulent magnetic field $\widetilde{\mathbf{b}}$ — which is the turbulent *cross-helicity*.

The unconventional idea that Alfvénization enables a dynamo, instead of suppressing it, was briefly entertained in the late 1990s [67–69]. However, this idea was quickly abandoned based on the reasoning that, this thesis proves, is inconsistent and incomplete [64]. Yoshizawa postulated Eq. (1.6), but it was only later when it was realized that the Υ-dynamo source could act as the generator of the large-scale magnetic field even from zero initial large-scale magnetic field [67–69].

Since a dynamo based on the α-effect requires an initial large-scale field to cause the large-scale field to grow exponentially, it was predicted that the α-effect would not be able to generate a substantial-amplitude large-scale field in young galaxies if the initial seed large-scale field is taken to be very small and the time allowed for exponential growth is taken to be the limited time scale on which the galaxies could form [68]. Hence, it was proposed that the Υ-dynamo might create some initial large-scale field acting as a seed. Yet, the seed large-scale field was claimed to be created only linearly in time [67–69]. This slow growth was claimed because—similar to the constant kinematic coefficients, $\alpha = -\tau \langle \widetilde{\mathbf{u}} \cdot \nabla \times \widetilde{\mathbf{u}} \rangle / 3$ and $\beta = \tau \langle \widetilde{\mathbf{u}} \cdot \widetilde{\mathbf{u}} \rangle / 3$, which depend only on turbulent flow—it was assumed that the Υ-coefficient was also a constant in the kinematic growth phase of the dynamo [67–69]. When Υ is assumed

to be a constant in Eq. (1.6) (and the α-effect is neglected), the magnetic induction equation $(\partial_t - \eta\nabla^2)\mathbf{B} = \nabla \times \mathcal{E}$ has a source term on its right-hand side, which does not depend on $\mathbf{B}$, but rather on the time-constant $\nabla \times (\Upsilon\nabla \times \mathbf{U})$. Thus, it was claimed that the Υ-effect cannot produce exponential growth of magnetic fields, and it could at best produce only linear-in-time growth [67–69]. Such slow growth may provide a seed large-scale field for the α-effect to operate on, as it was argued [67–69]. However, the α-effect suffers from nonlinear suppression via Alfvénization; see Sec. 1.2 C. Hence, the progress promised by considering the Υ-effect in Eq. (1.6) seemed limited.

E. A Self-Consistent Alfvénic Dynamo Theory

There is a fundamental difference between traditional dynamo effects (e.g., the α-effect) and the Υ-effect: $\Upsilon = \tau\langle\widetilde{\mathbf{u}} \cdot \widetilde{\mathbf{b}}\rangle/3$ depends on the strength of the fluctuating magnetic field $\widetilde{\mathbf{b}}$, whereas $\alpha = -\tau\langle\widetilde{\mathbf{u}} \cdot \nabla \times \widetilde{\mathbf{u}}\rangle/3$ depends only on the fluctuating flow $\widetilde{\mathbf{u}}$. The fluctuating field $\widetilde{\mathbf{b}}$ is inevitably coupled to the mean magnetic field $\mathbf{B}$. Hence, this thesis claims and shows that, as $\mathbf{B}$ grows, Υ also grows, thereby suggesting the possibility of an exponential growth. Indeed, this possibility is made manifest using an analytical theory in this thesis [64], which shows how $\widetilde{\mathbf{b}}$ (or, equivalently Υ) evolves with $\mathbf{B}$, and how $\mathbf{B}$ evolves as a result of Υ. This feedback dynamo loop is confirmed using numerical simulations. This self-consistent Alfvénic dynamo, operating in the presence of a shear flow, provides a model that is free from the suppressive effect of Alfvénization. Furthermore, the novel mechanism offers a new paradigm, allowing *unmagnetized fluids to become spontaneously magnetized*.

This thesis additionally shows that even when there is no initial large-scale magnetic field, Alfvénization becomes dominant over time; and the fluctuations in velocity and magnetic fields tend to become equipartitioned and aligned. This effect occurs not

only locally but also globally (in a volume-averaged sense), when a large-scale shear flow is present, but still with no initial large-scale magnetic field. In such a case with a large-scale shear flow, the volume-averaged cross-helicity in MHD *fluctuations* grows exponentially, due to the exchange of cross-helicity between the large-scale and fluctuations. This finding is shown in this thesis both analytically and numerically. In a system with no large-scale shear flow, the volume-averaged cross-helicity in *fluctuations* (turbulent cross-helicity) can never grow: Turbulent cross-helicity remains conserved in ideal MHD, and hence it is either steady in time or decays slowly due to micro-physical dissipation. Thus, a large-scale shear flow promotes large-scale Alfvénic states, consequently generating large-scale magnetic fields. There exists, however, a specific requirement for the shear-flow topology, which is discussed in the next section.

1.3 Necessity of Shear-Flow Instability in Alfvénic Dynamo

An analytic theory shows that the Υ-dynamo exponentially creates magnetic fields when two simple requirements are met [64]: The flow must have an inflection point; and the turbulent transport of momentum across the shear flow must be non-zero. These two conditions reduce to one condition: The shear flow should be Kelvin–Helmholtz-unstable [10]. The instability is then naturally subject to the laws of thermodynamics, which demand that there must be a non-zero momentum transport across the unstable flow-gradient.

This thesis in Figure 3 of Ref. [63] presents a pictorial representation of the Υ-effect, which has correspondence to Parker's pictorial representation of the α-effect [51]. This correspondence is due to the isomorphism of magnetic field lines and vorticity. It is

found that the Υ-effect operates via the formation of zonal jets described in Sec. 1.1 F, where 3D hydrodynamic instability saturation was discussed in relation to the formation of strong zonal jets.

This thesis naturally connects the three chief elements described until now: nonlinear saturation of shear-flow instability, zonal jets, and dynamos, all of which play crucial roles in plasma physics and astrophysics. This overarching connection is illustrated in Fig. 1.4, where the findings of this work are illustrated exemplarily in the context of binary neutron star mergers [63].

1.4 Thesis Overview: From Instability to Jets to Dynamo

The chief findings of this thesis are categorized into two major classes: instability saturation and dynamos. The first pertains to the nonlinear saturation of instability (Part I, Chs. 2–5) and zonal jets (Part II, Chs. 6–7). These pave the path to turbulent dynamos (Part III, Chs. 8–10). This division of three parts of the thesis carries physical meaning because the instability quickly saturates by exciting stable eigenmodes (Part I); the saturated instability then slowly excites the zero-frequency zonal jets (Part II); and the zonal jets even more slowly generate large-scale magnetic fields, which are global in scale (Part III). Thus, a temporal separation of scales—fast, intermediate, and slow—provides a natural division to the thesis findings. The said parts of the thesis also reflect increasing complexity of the physics involved. For example, the dimensionality of turbulence increases from 2D MHD to 3D hydrodynamics to 3D MHD. Hence, computational resources and post-processing analyses required for each part increase in size and sophistication. Overall, the three parts of the thesis—all

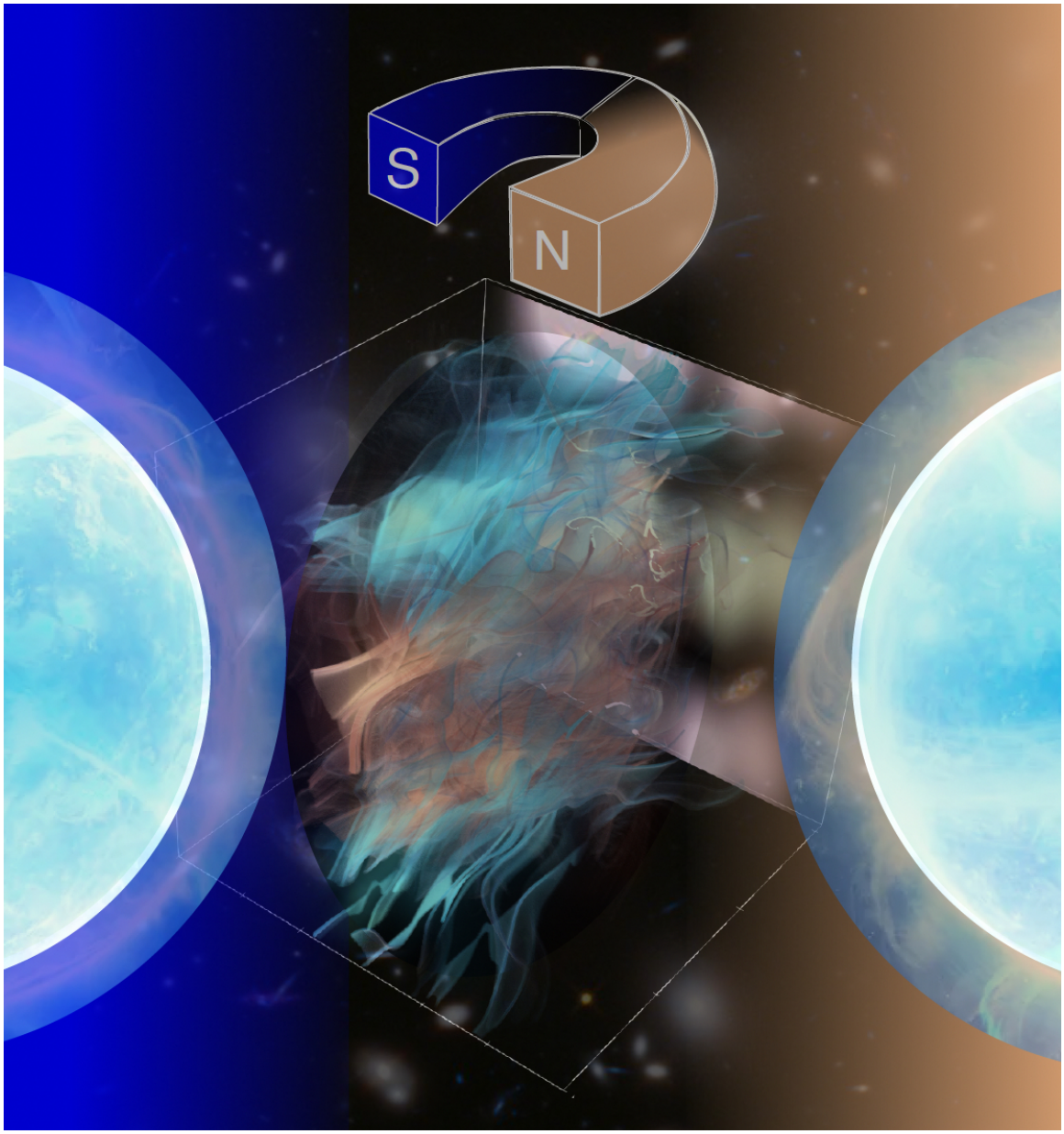

Figure 1.4: Generation of magnetic fields in a stellar collision. This thesis shows that the KH instability, active in between the merging neutron stars, generates zonal jets (shown at the center of the image, using a dynamo simulation of this thesis). The jets then create ultra-strong magnetic fields. The large-scale dipolar fields (blue-orange, prominent on the left and right margins) are first created at the middle, where the zonal jets are the strongest; the fields then diffuse outward. The astrophysical dynamo context is indicated by two neutron stars [Image credit: Tobias Roetsch] and the Pandora's galaxy cluster in the background [Image credit: NASA, ESA, and J. Lotz, M. Mountain, A. Koekemoer, and the HFF Team (STScI)].

related to shear flows—present a holistic view of fundamentally new mechanisms that saturate the instability and then drive dynamos. These results apply to shear-driven systems from laboratory plasmas to astrophysical observations.

An introduction to instability saturation via stable modes is presented in Sec. 1.1 using descriptive words. Chapter 2 provides a minimal mathematical model of the novel mechanism of instability saturation. The model—a mechanical analogy of a general unstable system—considers a block of mass that lies at the top of a large hemisphere, where a slight perturbation causes the block to slide downhill; this instability is designed to saturate via a nonlinear process arising from the strong stretching of a spring that tries to prevent the block from further sliding downhill. Interestingly, this simple mechanical analog captures essential details of instability-saturation via stable modes in turbulent fluids and plasmas.

Chapter 3 deals with the problem of modeling turbulent transport of momentum in two-dimensional magnetized shear flows. This chapter shows that, while instability of a shear flow transports momentum across the direction of the shear and down the flow-gradient, nonlinearly excited stable eigenmodes transport momentum up the flow-gradient. The up- and down-gradient momentum transport contributions nearly cancel out, leaving only around 1% to 10% of the transport related to the instability.

Chapter 4 deals with the long-standing issue of preserving magnetic fields at large scales, given that studies of turbulence with shear flows show rapid generation of small scales due to robust shear-flow straining [21, 70, 71]. The results of this chapter are significant because it is shown here for the first time that stable eigenmodes counteract the straining of magnetic fields by unstable eigenmodes (instability). Hence, when stable eigenmodes are deleted in high-resolution MHD simulations, the uninhibited instability rapidly folds magnetic fields into small-scale structures. Large-scale coherency is then lost. Small-scale current sheets and vorticity dominate in the absence of stable

modes. When stable modes remain untouched, magnetic fields are sequestered at large scales.

Chapter 5 addresses the questions related to how stable eigenmodes are excited and what nonlinear mode-coupling channels enable the excitation. This chapter first uses wavenumber-decomposition to understand energy cascades in MHD turbulence, and then generalizes the traditional energy cascade diagnostics by decomposing fluctuations in a non-periodic eigenbasis at every wavenumber. Detailed analyses of energetics confirm that the stable eigenmodes are not a product of the inverse cascade of energy, but rather of nonlinear mode-coupling among fluctuations at the large scale where instability exists. This work shows that, with the strong excitation of stable modes, the energy cascade to small scales is severely reduced. The direction of the energy cascade, however, is unaltered. That is, both kinetic energy and magnetic energy cascade to small scales; this process replaces the oft-invoked inverse cascade mechanism. Additionally, this work surgically removes large-scale stable eigenmodes from MHD equations and simulates the resulting equations without stable modes. This novel simulation technique shows that vortices formed from the saturation of the Kelvin–Helmholtz instability split apart and move ballistically father away, spreading turbulence all over the available domain. This result challenges the widespread beliefs that the Kelvin–Helmholtz vortices merge due to the instability and that turbulence is confined near the shear layer (where the flow reverses). This analysis suggests that vortices repel in the absence of stable modes; vortices attract in the presence of stable modes. Such behavior is potentially also applicable to the tearing instability, where the reversed flow is replaced with a reversed magnetic field [25].

Chapter 6 presents the first three-dimensional study of hydrodynamic shear-flow-instability saturation via stable modes, where stable modes are shown to be excited via a wholly new channel that is inherently 3D. This new 3D channel involves zonal

flows (jets), which do not vary along the x-direction of the large-scale flow $U_x(z)$, but vary in the y-direction orthogonal to the plane of the large-scale flow. While one may have argued that stable modes might be related to 2D nature of turbulence, here it is shown that stable modes are not only excited in 3D, but are more effective in 3D than in 2D. All of pertinent results reported above in 2D are recovered here in 3D. This includes decreased cascade of energy to small scales, decreased microphysical dissipation, and reduced turbulent transport of momentum across the shear flow. Additionally, this chapter presents new observable effects of 3D stable modes. It is first shown that 3D unstable modes support vortex stretching, which makes the vortices filamentary—an inherently 3D process that cascades energy to small scales. Conversely, 3D stable modes counteract vortex stretching and instead scrunch the vortices, turning filamentary vortices into fattened vortices. Thus, the small-scale cascade, though present in 3D, is severely reduced.

Chapter 7 develops a turbulence closure model coupling zonal flows arising from an instability in stars where their angular momentum gradients, related to their differential rotation, have unstable profiles. The density stratification in stars is generally large, which thus suppresses perturbations that could otherwise grow by feeding on the unstable angular momentum gradient. However, when thermal diffusion is substantial—a case widely applicable in stars including the solar tachocline—displaced fluid parcels can quickly equilibrate with the surrounding fluid and thus expand or contract rapidly. Hence, the stabilizing buoyancy force arising from density stratification is weakened, and the instability of the stellar angular momentum gradient is reinstated [36–38]. This diffusive instability, whose free energy resides in the shear flow, saturates by nonlinearly exciting zonal flows. These zonal flows dominate triadic interactions. Under such zonal-flow dominance, this chapter shows that an eddy-damped quasi-normal Markovian turbulence closure [32, 33] yields a set of equations that become

linear, thus enabling an analytic solution. The closure predictions of the rates at which stars slow down agree with numerical simulations in the scanned parameter range; this agreement is better than a previous quasilinear model [38]. The closure also provides predictions for extreme parameter regimes, which simulations cannot probe at present. The diffusive instability is bound to affect the long-term evolution of the solar tachocline (where the ratio between viscosity and thermal diffusivity is 10^{-6}).

Chapter 8 reports perhaps the most surprising finding of this thesis: Alfvénization coupled with large-scale vorticity gives rise to a large-scale dynamo, instead of suppressing the dynamo. This effect operates, as reported in *Nature*, via the inherently 3D zonal jets [63]. These are the same jets (reported in Ch. 6), which arise from the shear-flow instability (reported in Chs. 3–5). The jet-driven shear dynamo is robust to variations in key MHD parameters and operates in both periodic and non-periodic domains. This work confirms a non-traditional dynamo mechanism involving Alfvénization [66]. The confirmation is given by a new analytic theory and advanced numerical simulations of 3D MHD turbulence driven by a shear-flow instability, for which this thesis uses up to $4096 \times 4096 \times 8192$ grid points (and more than 90 million CPU-hours). It is demonstrated here that quasi-periodic, large-scale magnetic fields are generated via the mean-vorticity effect, even when initial large-scale magnetic field is absent and turbulence is non-helical. This work, introducing the effect of jets, contributes to the development of dynamo theory. 70 years ago, Parker discovered dynamos driven by helical turbulent motions [51], which however faced significant challenge due to dynamo suppression via Alfvénization [4–9]. 35 years ago, Yoshizawa assumed the potential role of large-scale vorticity in dynamos, which had remained unconfirmed, and whose working mechanism has remained unknown [66]. This chapter resolves such issues and implicates zonal jets as a novel and robust mechanism via which the

dynamo generates magnetic fields in laboratory and astrophysics. The dynamo theory presented here provides a consistent explanation for unresolved issues related to an unusual orientation of magnetic field, current density, and EMF, which were measured for the first time in a dynamo laboratory experiment [72]. An example of the dynamo application for astrophysical magnetic fields includes dynamos in binary neutron star mergers where the approaching neutron stars create a substantial KH-unstable velocity gradient at the merge interface [73]. This dynamo is predicted in this chapter to likely operate on microsecond time scale, producing in milliseconds some of the strongest magnetic fields in the Universe [74], which help produce detectable signals for multi-messenger astronomy [44].

Chapter 9 analyzes the dynamo of chapter 8 using extensive energy transfer diagnostics to identify the essential dynamo steps. These steps transfer energy from the large-scale shear flow to various turbulent components, eventually depositing the turbulent energy in the large-scale magnetic field. This chapter provides a mechanistic viewpoint and presents comprehensive analysis of turbulence and dynamo arising from a KH-unstable shear flow.

Chapter 10, building on Chs. 8 and 9, challenges traditional dynamo assumptions and derives a self-consistent analytic theory of the kinematic dynamo, where Alfvénization coupled with large-scale vorticity produces an exponential growth of magnetic fields. This chapter addresses limitations in previous theories, where it was claimed that a dynamo driven by Alfvénization coupled with large-scale vorticity cannot produce exponential growth of magnetic fields and can only lead to slow linear growth [67–69]. The new analytic theory of the kinematic dynamo also explains the feedback loop that gives the exponential growth. It is shown that an infinitesimal cross-helicity in *fluctuations* generates infinitesimally weak magnetic fields at large scales when a large-scale shear flow is present; this generation occurs via the mean-vorticity effect.

The thus-generated large-scale magnetic field is aligned with the large-scale shear flow. This cross-helicity at the large scales is transferred to small scales by the Reynolds stress, in a way analogous to how the Reynolds stress transfers momentum and energy from large scales to small scales. Hence, cross-helicity in fluctuations increases. This then reinvigorates the generation of the large-scale magnetic field aligned with the large-scale flow. The feedback loop operates until the large-scale field is approximately on the same order of magnitude as the large-scale flow. These analytic predictions are confirmed using numerical simulations.

Chapter 11 presents concluding remarks, summarizes wider implications of the thesis findings, and suggests potential future directions.

***Significance, novelty, and impact of the thesis*:**

The new dynamo mechanism presented in this thesis constitutes a breakthrough result for several reasons: First, a large-scale unstable shear flow produces an exponential dynamo growth from an infinitesimally weak fluctuation of magnetic fields, with no additional ingredient — no large-scale magnetic field. Second and most importantly, the dynamo growth is surprisingly *enabled* by magnetic fluctuations formed via Alfvénization (flow–field alignment effect); these Alfvénic fluctuations have long been known to suppress traditional dynamos. Third, these magnetic fluctuations correlate with flow fluctuations that appear in the form of zonal flows. The latter exist only in 3D shear flows and strongly couple to stable eigenmodes, conjugate to the shear-flow instability. The stable eigenmodes are demonstrated to saturate the shear-flow instability, in both 2D and 3D, with observable consequences for turbulence, transport, mixing, and pattern formation in laboratory and astrophysical environments.

Part I

Instability Saturation via Stable Modes

2 A MECHANICAL ANALOG OF INSTABILITY-SATURATION VIA STABLE MODES

An idea for this chapter was conceived while writing chapter 1.

2.1 A mathematical introduction

Consider a simple harmonic oscillator

$$\partial_t^2 x = \gamma_0^2 x, \tag{2.1}$$

where x represents a time-varying quantity, and γ_0^2 is a real number. When γ_0^2 is negative, x oscillates in time t, with degenerate frequencies $\pm\sqrt{-\gamma_0^2}$.

Now imagine that γ_0^2 is increased from a negative value to zero and then made positive. When γ_0^2 is positive, the two degenerate oscillatory modes become distinct: one grows (instability) and the other (stable mode) decays, at a rate γ_0.

The unstable system requires a nonlinearity to saturate. The simplest nonlinearity incorporated in Eq. (2.1) is

$$\partial_t^2 x = \gamma_0^2 x - cx^2, \tag{2.2}$$

where c is a nonlinear coupling constant. Note that this toy nonlinear model of instability is physically meaningful, as Eq. (2.2) is derived from an oscillator turned unstable and captures two eigenmodes: unstable and stable when γ_0^2 is a positive number.

To be read with caution, another model of instability that is often considered is

$$\partial_t x = \gamma_0 x - cx^2. \tag{2.3}$$

However, **this model is unphysical**, because it assumes from the onset that the stable mode is not important for nonlinear dynamics. Most natural systems feature a mode-pair, arising from, for example, a time-oscillating stable system that becomes unstable when a control parameter is varied.

Linear eigenmodes

Equation (2.1) can be written as a set of first-order time-differentials

$$\partial_t x = v, \tag{2.4a}$$

$$\partial_t v = \gamma_0^2 x, \tag{2.4b}$$

which has two linear eigenmodes satisfying

$$x : v = 1 : \pm\gamma_0, \tag{2.5}$$

where the $-(+)$ sign corresponds to the (un)stable mode.

When Eqs. (2.4a) and (2.4b) are written in the eigenbasis,

$$\partial_t \beta_\pm = \pm\gamma_0 \beta_\pm, \tag{2.6}$$

where $\beta_\pm$ is the amplitude of the eigenmodes ($+$ for instability, and $-$ for the stable mode).

Nonlinear evolution

Similarly, when the nonlinear equation (2.2) is written in the eigenbasis,

$$\partial_t \beta_\pm = \pm\gamma_0 \beta_\pm \mp \frac{c}{2\gamma_0}(\beta_+ + \beta_-)^2. \tag{2.7}$$

Equation (2.7) explains how the stable mode is excited nonlinearly (via the coupling to the unstable mode).

Equation (2.2) admits analytic solutions for x and v in terms of the Elliptic integrals.

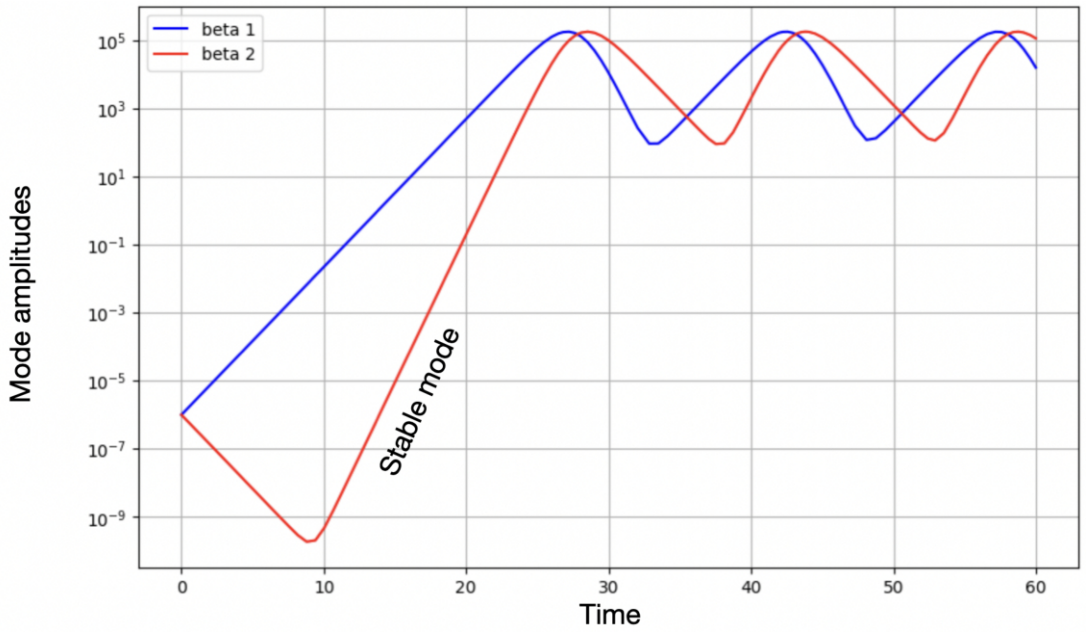

Figure 2.1: Eigenmode-amplitudes obtained by solving Eq. (2.2). $\beta_+ = \text{beta}\,1$ and $\beta_- = \text{beta}\,2$ are the amplitudes of unstable and stable modes, respectively.

These two solutions can be decomposed into the two eigenmodes presented in Eq. (2.5). This decomposition provides the time-varying amplitudes of the eigenmodes, displayed in Fig. 2.1.

2.2 A mechanical analog

Up until here, the presentation has been purely mathematical. We now present a mechanical analog described by Eq. (2.2).

Model

Consider a block of mass m placed on a horizontal surface and connected to a wall by a spring of length x_0 and spring constant k, as shown in Fig. 2.2. This system displays only oscillatory modes.

Figure 2.2: A block clamped against a wall displays harmonic oscillations—a stable system.

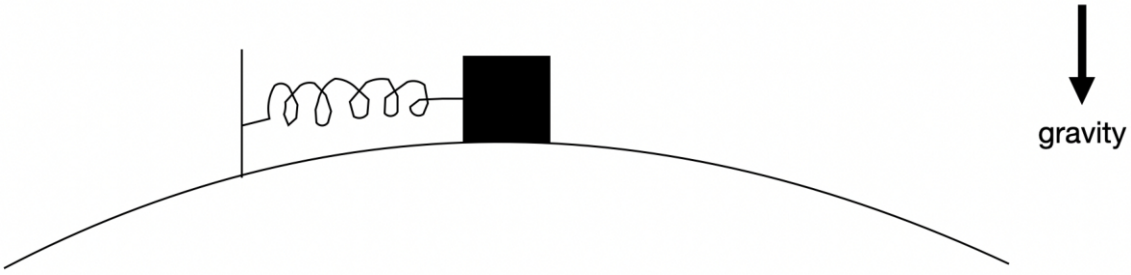

Figure 2.3: A block clamped against a wall and placed on a hemisphere is unstable when $(mg/R - k) > 0$ and stable when $(mg/R - k) < 0$, as predicted by Eq. (2.10). Gravity points vertically downward.

To obtain an instability, we make the surface curved—imagine the surface being part of a hemisphere, as shown in Fig. 2.3.

The equation of motion for the block when displaced by x on the surface (Fig. 2.4) is

$$F = mg\sin\theta - F_{\text{spring}}, \tag{2.8}$$

where, if $x/R \ll 1$ (very large hemisphere), $\sin\theta = \theta$ gives

$$F = mgx/R - F_{\text{spring}}. \tag{2.9}$$

In Eq. (2.9), F_{spring} is the spring force, which depends on the extension x, relative to x_0. If x/x_0 is small, Hooke's linear law prescribes $F_{\text{spring}} = kx$. Considering this

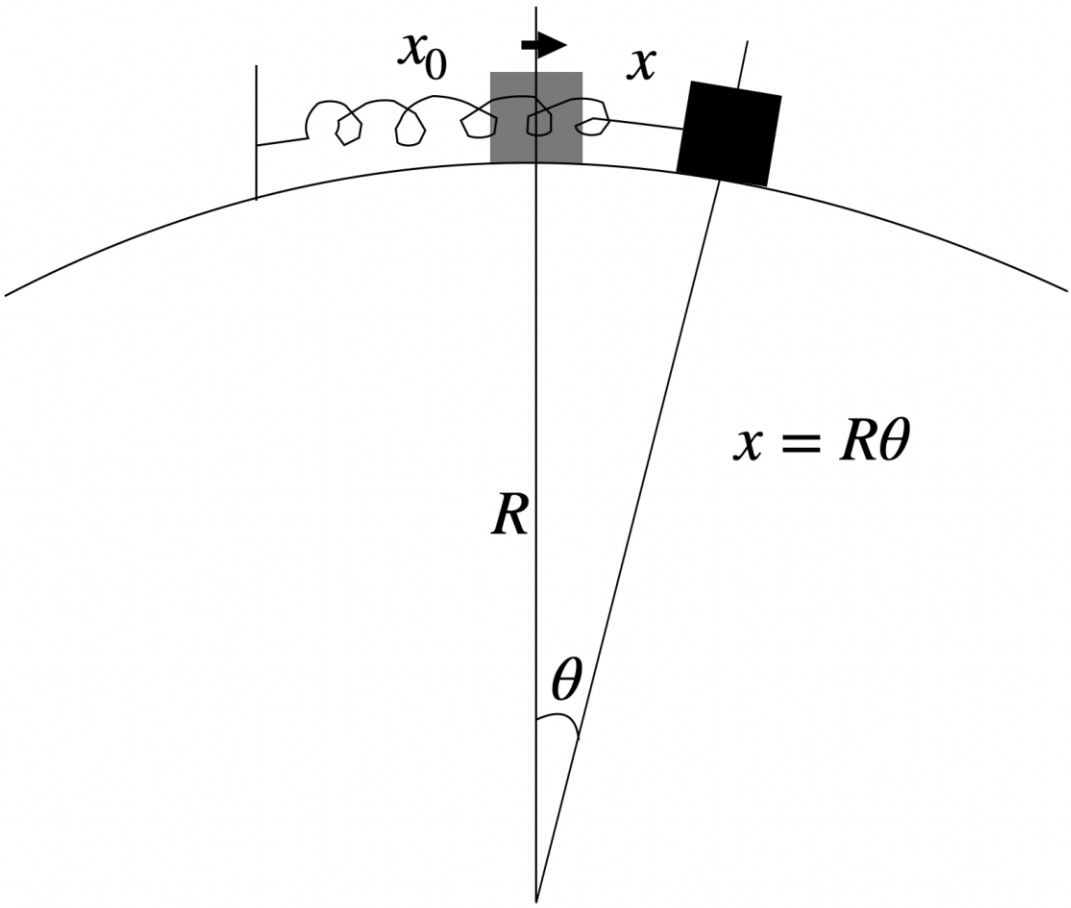

Figure 2.4: The block mentioned in Fig. 2.3 is slightly perturbed. The initial length of the spring is x_0, and the displacement of the block is x.

linearity, we re-write Eq. (2.9)

$$m\partial_t^2 x = (mg/R - k)x, \tag{2.10}$$

where $(mg/R - k) \equiv \gamma_0^2$ defined in the previous section. Depending on the sign of $(mg/R - k)$, the block can display oscillatory modes or can become unstable. Note that if $(mg/R - k) > 0$, the block continues to slide downhill and never goes uphill, because both the gravitational pull and spring force are considered linear, and the former continuously dominates when $(mg/R - k) > 0$.

When the system is unstable, x continuously grows and becomes comparable to x_0 at some point. Then, the Hooke's linear law no longer holds true (we are still considering $x/R \ll 1$, a very large hemisphere, but $x/x_0 \sim 1$). In such a case of $x/x_0 \sim 1$, the linear Hooke's law is replaced by a non-ideal spring force (applicable to thick laboratory metal springs) given by

$$m\partial_t^2 x = (mg/R - k)x - cx^2, \tag{2.11}$$

where c is a constant arising from the overstretching of the non-ideal spring.

Physical interpretation

Equation (2.11) is equivalent to Eq. (2.2), whose solution is presented in Fig. 2.5. The annotations show when the block physically slides uphill and downhill.

The physical interpretation of the solutions to Eq. (2.11) is summarized in Fig. 2.6. The block lying at the top of the hemisphere represents an unstable equilibrium. The free energy, which is the gravitational potential energy of the block, decreases as the block slides away from the top position. Hence, an instability is favored to minimize the free energy. This instability causes the block to continuously slide down the hill. While the block is sliding downhill, the stable mode is already excited nonlinearly, as shown in Fig. 2.5. Since the unstable mode amplitude is initially large, the block continues to go downhill, until the nonlinearly excited stable mode pushes the block uphill. Since Eq. (2.10) or (2.2) represents an ideal system, with no dissipation, both eigemodes are exactly of equal magnitudes in the nonlinear phase, when time-averaged. With a slight dissipation, e.g., friction, the stable mode is still excited to significant amplitude but has slightly weaker amplitude than the unstable mode.

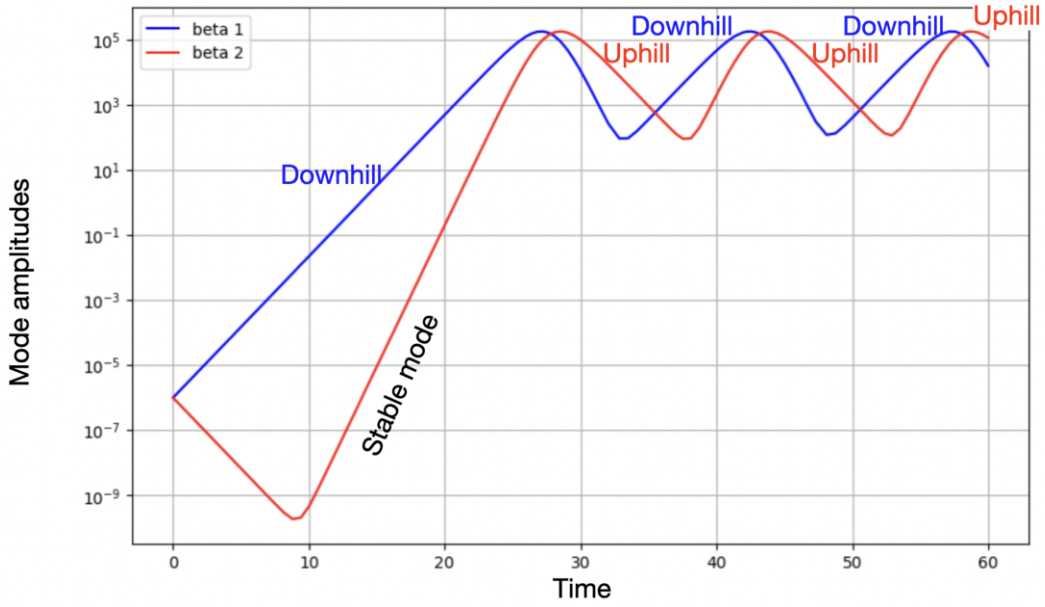

Figure 2.5: When the amplitude of the unstable mode is larger than the stable mode, the block slides downhill. However, when the amplitude of the unstable mode is lower than that of the stable mode, the block physically slides uphill! This sliding up is *not* due to the linear spring force but due to the nonlinear effect; see Eq. (2.10) and consider $(mg/R - k) > 0$.

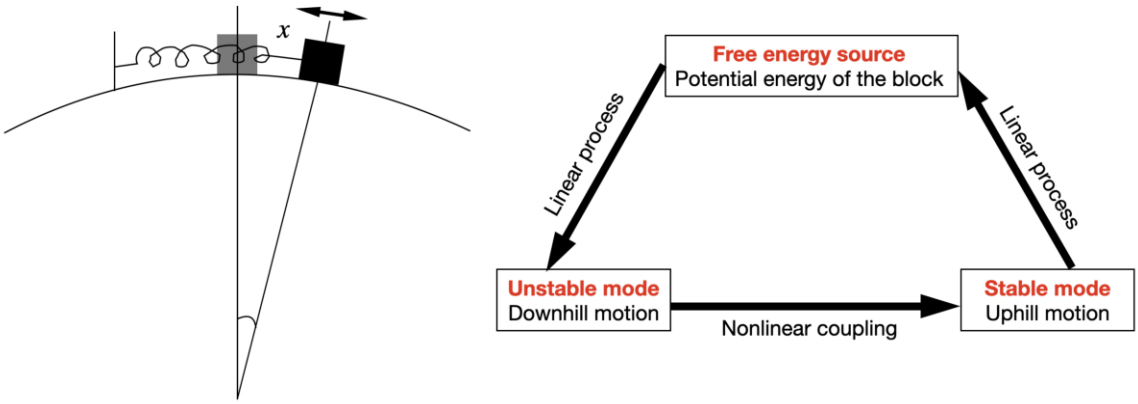

Figure 2.6: A physical interpretation of free-energy (gravitational potential energy), instability (downhill motion), and stable mode (uphill motion). The instability reduces the free energy; the stable mode builds up the free energy.

How does the instability saturate without the stable mode?

To demonstrate instability saturation without the stable mode, we consider Eq. (2.10), cast it in the eigenbasis to obtain Eq. (2.7), reproduced below for convenience,

$$\partial_t \beta_\pm = \pm\gamma_0 \beta_\pm \mp \frac{c}{2\gamma_0}(\beta_+ + \beta_-)^2, \tag{2.12}$$

and then forcefully set $\beta_- = 0$ by hand to arrive at

$$\partial_t \beta_+ = \gamma_0 \beta_+ - \frac{c}{2\gamma_0}\beta_+^2. \tag{2.13}$$

Note that Eq. (2.13) is the unphysical model of instability-saturation alluded to earlier in Eq. (2.3).

The solution to Eq. (2.13) is

$$\beta_+ = \frac{A}{1 + Be^{-\gamma_0 t}}, \tag{2.14}$$

where A and B are constants of the problem. For small t, β_+ grows exponentially. For large t, β_+ reaches a completely stationary value. Physically, this process represents, as shown in Fig. 2.7, a block sliding downhill and staying at the maximal location of displacement—with no uphill motion, at all, because the stable mode is forced to be zero.

It is strongly emphasized that the uphill motion is not related to the linear property of the spring, because the considered linear spring force is always weaker than the linear gravitational pull, regardless of the displacement x, as confirmed by Eq. (2.10)**. It is the nonlinear effect that excites the stable eigenmode, which then pushes the block uphill.**

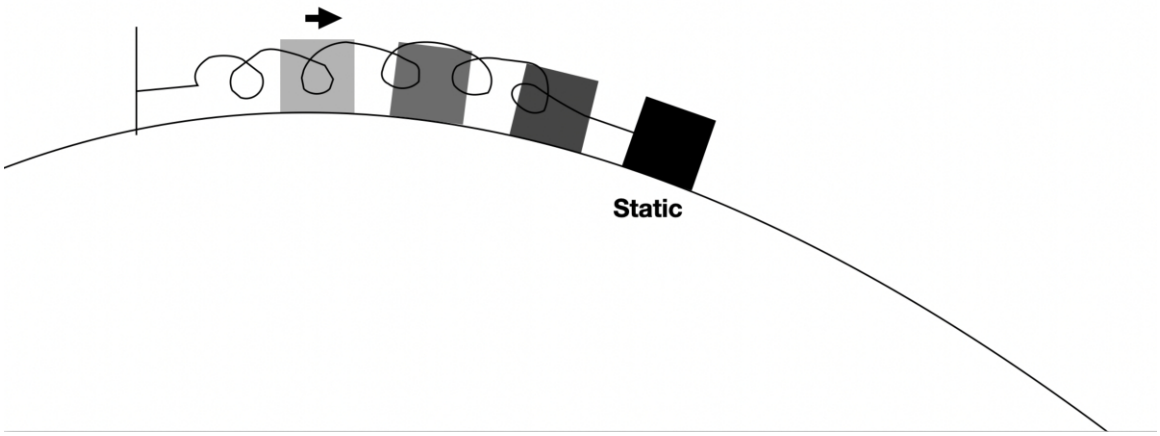

Figure 2.7: A sliding block reaches a *static* final state when the stable mode is artificially zeroed. See Eq. (2.14). This artificial system never displays any uphill motion (because the stable mode is artifically zeroed). The uphill motion is not due to the linear spring force, but due to the nonlinearly excited stable mode.

The foregoing mechanical analog of instability-saturation via stable mode can be a simple table-top experiment to detect for the first time the excitation of stable in a laboratory experiment.

In the remaining chapters, this general saturation paradigm of instability via stable mode is demonstrated in comprehensive numerical simulations of 2D and 3D instabilities in fluids and plasmas.

3 **PAPER A**: NEAR-CANCELLATION OF UP- AND DOWN-GRADIENT MOMENTUM TRANSPORT IN FORCED MAGNETIZED SHEAR-FLOW TURBULENCE

A version of this chapter was published in Phys. Plasmas 29, 092301 (2022).

ABSTRACT

Visco-resistive magnetohydrodynamic turbulence, driven by a two-dimensional unstable shear layer that is maintained by an imposed body force, is examined by decomposing it into dissipationless linear eigenmodes of the initial profiles. The down-gradient momentum flux, as expected, originates from the large-scale instability. However, continual up-gradient momentum transport by large-scale linearly stable but nonlinearly excited eigenmodes is identified, and found to nearly cancel the down-gradient transport by unstable modes. The stable modes effectuate this by depleting the large-scale turbulent fluctuations via energy transfer to the mean flow. This establishes a physical mechanism underlying the long-known observation that coherent vortices formed from nonlinear saturation of the instability reduce turbulent transport and fluctuations, as such vortices are composed of both the stable and unstable modes, which are nearly equal in their amplitudes. The impact of magnetic fields on the nonlinearly excited stable modes is then quantified. Even when imposing a strong magnetic field that almost completely suppresses the instability, the up-gradient transport by the stable modes is at least two-thirds of the down-gradient transport by the unstable modes, whereas for weaker fields, this fraction reaches up to 98%. These effects are persistent with variations in magnetic Prandtl number and forcing strength. Finally, continuum modes are shown to be energetically less important, but essential for capturing the magnetic fluctuations and Maxwell stress. A simple analytical scaling law is derived for their saturated turbulent amplitudes. It predicts the fall-off rate as the inverse of the Fourier wavenumber, a property which is confirmed in numerical simulations.

3.1 Introduction

Owing to their ubiquity in laboratory,[75] geophysical,[76, 77] and astrophysical environments,[26–28, 78–80] shear layers have been extensively studied. [81, 82] Observations and analyses from experiments and direct numerical simulations have offered insights into the connection between large-scale vortical structures formed from the instability of a shear layer and turbulent transport across the layer.[83–85] Properties like shape and scale of the nonlinearly saturated vortices, which dominate the transport, are generally attributed to the linearly-unstable eigenmodes or closely related nonlinear fluctuations. [86, 87] The nonlinear saturation of the instability, however, can be more complex than just the finite-amplitude modifications of unstable modes, as emerging understanding in fusion plasma instability demonstrates.[15, 32, 88–99]

Already in the late 1960s, using one of the early numerical simulations of shear instability,[24] it was hinted that the nonlinear saturation of Kelvin-Helmholtz instability involves, contrary to finite-amplitude modifications of unstable modes, quasi-periodic oscillations in the fluctuations. Later, an intuitive understanding of how such a phenomenon occurs in sheared fluids[100] has been reported by invoking vortex nutation:[86] Fluctuation-amplitude oscillations correlate with oscillations in the mean flow energy and lead to vortex nutation. Fluctuations, however, are usually not decomposed into the complete set of linear eigenmodes, and are commonly assumed[86] to be due to unstable mode structures. But since unstable modes always drive a down-gradient momentum transport, they cannot explain the increase of kinetic energy in the mean flow.

Notably, occasional up-gradient momentum transport has been observed in several experimental and numerical studies where an unstable shear layer drives the

turbulence.[101–105] Analyses of these transient events [83, 106–109] do not address the underlying conditions producing this dynamics—whether the transient up-gradient transport is a part of an ongoing subdominant process with occasional breakthroughs, or simply spontaneous fluctuations. The laboratory and prior numerical experiments alone are not sufficient to definitively answer this question. One way to expose the underlying process is to examine the turbulent fluctuations using a complete eigenmode decomposition, and assign roles and activities to each mode in the transport phenomena. Indeed there can be modes other than the unstable modes that are important in the turbulent phase, as an insightful study hints: the dominant vortex in a turbulent background orients quasi-periodically against (or towards) the mean flow and drives the down-gradient (or up-gradient) momentum transport.[83] To understand such behaviors in detail, it is instructive to also analyse how the instability saturates, a question that has long been of interest[13] but for which understanding remains incomplete.

When turbulence is sustained via continuous energy injection from a large-scale instability, there exist two primary candidates for instability saturation. A common (but not necessarily justified) assumption is that energy injected by the instability is transferred conservatively to increasingly smaller scales in a forward, Kolmogorov-like cascade, where nonlinear interactions move energy between linearly unstable or marginal modes until a dissipation range is reached at small scales.[26] An alternative process involves linearly stable eigenmodes at the large injection scales, which absorb and remove significant energy from scales that launch the inertial cascade. In several studies of microturbulence in fusion plasmas, linearly stable modes have been found to be excited to significant levels via nonlinear interactions and to drastically affect the saturated amplitudes and transport characteristics of the system.[15, 32, 88–93, 97–99]

Stable modes in shear flow turbulence, however, have been studied only recently[110–

112] and more remains to be understood, e.g., their role in mixing and magnetic field evolution and how they might affect reduced models of turbulence and transport. It was predicted in Ref. [110] that the Kelvin-Helmholtz instability in its nonlinear evolution excites a linearly-stable conjugate-root[113] of the inviscid instability, which affects the instability saturation even when viscosity is finite. This was later verified in numerical simulations of freely evolving shear layers. [111] However, the rapid relaxation of the layer towards a stable profile on a time scale similar to that of stable-mode excitation prevented general conclusions from being reached, regarding how the turbulence and transport are affected by the stable modes. The issue is aggravated by the addition of a flow-aligned magnetic field, which causes the layer to relax even more rapidly. To circumvent this challenge, one may drive the mean flow towards the unstable profile and thus achieve a thorough statistical quantification of the stable modes. Note that driven profiles are quite common in astrophysical shear flows, with forces like gravity providing free energy for the drive. For these reasons, driven shear flow is studied here.

The principal result of this study is that significant up-gradient momentum transport is driven by nonlinearly excited (linearly-)stable modes, cancelling a substantial portion of the down-gradient transport by unstable modes, and notably this transport is present not just during turbulent momentum flux reversals, but is continuously at work at a slightly lower level than that of the unstable modes. This finding is robust even for variations of orders of magnitude in background magnetic field strength, magnetic Prandtl number (or resistivity), and forcing strength of the mean flow. Note that the stronger background magnetic field tends to suppress the instability [113] and disrupt the large-scale vortices, [114] while larger magnetic Prandtl number (weaker resistivity for a fixed viscosity) extends the scale range of magnetic fluctuations, compared to the flow fluctuations. [115] We also show, for astrophysical applications,

that a turbulent viscosity can be defined, with the addition of stable modes, that can reliably capture the Reynolds stress: Without stable modes, however, the stresses are greatly over-predicted by the unstable modes.

This article is organized in the following manner. Section 5.2 entails the magnetohydrodynamic (MHD) model of the shear flow and details the system set-up. In Sec. 5.3, the complete linear eigenspectrum is presented, along with a discussion on the roles of different eigenmodes. Section 5.4 shows the full nonlinear evolution of MHD Kelvin-Helmholtz instability using direct numerical simulations. A decomposition of the turbulent fluctuations onto linear eigenmodes is performed in Sec. 5.5, where a detailed study of imprints of stable modes in turbulence and transport is presented. Section 5.5 summarizes the findings of this work.

3.2 Model and simulation set-up

An incompressible magneto-fluid is considered in this study, and standard MHD equations are adopted:

$$\nabla \cdot \mathbf{u} = 0, \tag{3.1a}$$

$$\partial_t \mathbf{u} + \mathbf{u} \cdot \nabla \mathbf{u} = -\frac{\nabla P}{\rho} + \frac{(\nabla \times \mathbf{B}) \times \mathbf{B}}{4\pi\rho} + \nu \nabla^2 \mathbf{u} + \mathbf{f}, \tag{3.1b}$$

$$\nabla \cdot \mathbf{B} = 0, \tag{3.1c}$$

$$\partial_t \mathbf{B} = \nabla \times (\mathbf{u} \times \mathbf{B}) + \eta \nabla^2 \mathbf{B}, \tag{3.1d}$$

where $\mathbf{u}$, $\mathbf{B}$, P, ρ, ν, η, and $\mathbf{f}$ respectively denote the fluid velocity, magnetic field, pressure, fluid density, viscosity, ohmic diffusivity, and externally supplied acceleration to the magneto-fluid.

Background flow, magnetic field, and forcing

A shear layer is examined on a two-dimensional (x, z) plane with the initial fluid velocity given by $\mathbf{u}(x, z, t = 0) = U_0 \tanh(z/a)\hat{\mathbf{x}}$ and a flow-aligned magnetic field, initially uniform, as $\mathbf{B}(x, z, t = 0) = B_0\hat{\mathbf{x}}$. The parameters $a, U_0,$ and B_0 signify the half-width of the flow-shear, maximum initial fluid velocity, and initial magnetic field, respectively. These parameters are exploited to non-dimensionalize all the variables henceforth. Length, time, and energy (per unit mass) are hereafter measured in units of a, a/U_0, and U_0^2, respectively. Thus the initial (or reference) flow and magnetic field are represented by $U_{\rm ref}(z) = \tanh(z)$ and $B_{\rm ref}(z) = 1$ in the rest of this article. The ratio of the maximum fluid speed U_0 to the AlfvÃ©n speed can be written as the AlfvÃ©nic Mach number $M_{\rm A} = U_0\sqrt{4\pi\rho}/B_0$. The viscosity and resistivity are quantified via fluid Reynolds number $Re = U_0 a/\nu$ and magnetic Reynolds number $Rm = U_0 a/\eta$, respectively.

In two dimensions, a more convenient formalism is available, using the streamfunction ϕ and flux function ψ. Defining $\mathbf{u} = \hat{\mathbf{y}} \times \nabla\phi$ and $\mathbf{B} = \hat{\mathbf{y}} \times \nabla\psi$, the vorticity and the current become $\nabla^2\phi\hat{\mathbf{y}}$ and $\nabla^2\psi\hat{\mathbf{y}}$, respectively. Taking the curl of Eq. (5.1a), and rewriting Eq. (5.1b) in terms of the stream- and flux-functions yields [25]

$$\partial_t\nabla^2\phi + \{\nabla^2\phi, \phi\} = M_{\rm A}^{-2}\{\nabla^2\psi, \psi\} + Re^{-1}\nabla^4\phi + \partial_z f(k_x{=}0, z, t), \tag{3.2a}$$

$$\partial_t\psi = \{\phi, \psi\} + Rm^{-1}\nabla^2\psi, \tag{3.2b}$$

where the Poisson bracket is $\{P, Q\} = \partial_x P \cdot \partial_z Q - \partial_z P \cdot \partial_x Q$; e.g., $\{\phi, \psi\} = -\mathbf{u} \cdot \nabla\psi$. Here, k_x is the Fourier wavenumber along the x-axis. The parameters $Re = Rm = 500$ are chosen for all simulations unless mentioned otherwise (where Rm is changed to 50 and 5 000 in different simulations). It should be emphasized that these Reynolds

numbers are defined using the initial scale a of the sharpest gradient in the flow as the characteristic length scale; however, as the system evolves nonlinearly via vortex merging, despite the forced mean flow, eddies of the size of the simulation box appear, which may be considered as the characteristic length scale of motion.[82] When choosing this normalization, non-dimensional numbers should be scaled accordingly, e.g., $Rm = 5\,000$ becomes $Rm = 5\,000 \times L_x \approx 1.5 \times 10^5$, where L_x represents the box-size along the mean flow direction. The external body force, $\mathbf{f} = f(k_x{=}0, z, t)\hat{\mathbf{x}}$, is applied to the mean flow only, which is highlighted in Eq. 4.4a using the explicit mention of $k_x{=}0$. As in a recent study,[112] the forcing drives the instantaneous mean flow towards the initial unstable profile $U_{\mathrm{ref}}(z)$. A similar forcing mechanism exists for geo- and astrophysical flows where gravitation[116] tends to build shear layers. We assume here such a force, represented as a Krook operator, [117–119] as

$$f = D_{\mathrm{Krook}}\left[U_{\mathrm{ref}}(z) - \langle U(x,z,t)\rangle_x\right] + F_0, \tag{3.3}$$

where D_{Krook}, sometimes also referred to as the profile relaxation rate,[120] measures the forcing strength (in units of U_0/a); and $\langle U(x,z,t)\rangle_x$ represents the instantaneous x-averaged flow. If $D_{\mathrm{Krook}} = 0$, the shear layer evolves freely and decaying turbulence is realized as a result of the Kelvin-Helmholtz instability and the turbulence it generates.

The time-independent force F_0 is implemented only to balance the viscous diffusion of the initial shear layer: $Re^{-1}\nabla^2 U_{\mathrm{ref}}(z) + F_0 = 0$ ensures an initial equilibrium state to which small-amplitude perturbations are added before the system is evolved.

Initial and boundary conditions

As in the unforced study, [111] a simulation box of $L_x = 10\pi$ is considered, but double the size along the z-axis ($L_z = 20\pi$), given that the quasi-stationary turbulence

simulated herein is run for much longer time, which tends to create fully developed turbulent features that are larger in size. Thus we adopt a larger domain to minimize their potential interactions with the boundaries in the z-axis. Note the forcing applied to the mean flow prevents profile relaxation and the turbulence remains mostly in the vicinity of the shear layer. The numerical code Dedalus, [121] a pseudospectral solver, is used in this study. Fourier modes along the x-axis and Chebyshev polynomials along the z-axis are employed with $(N_x, N_z) = (2048, 2048)$ spectral modes. We confirmed that the spectral energy density and dissipation are converged at this resolution. Note also that these high resolutions benefit the eigenmode projection of nonlinear data in the post-processing analysis. Only for the simulation with magnetic Prandtl number of 10, the box size was changed to $(L_x, L_z) = (6\pi, 8\pi)$ and the resolution was increased to $(N_x, N_z) = (4096, 4096)$; the same simulation was repeated with $(N_x, N_z) = (4096, 8192)$, but only for early times due to computational cost, and found to reproduce, among others, the energy evolution. All simulations use 3/2 dealiasing rule, additionally. The boundary conditions used in all simulations are periodic along the x-axis; and perfectly conducting, no-slip, co-moving (with the initial flow) at the top and bottom boundaries, $z = \pm L_z/2$.[111, 112]

The initial equilibrium state is seeded with small-amplitude perturbations $(\widetilde{\phi}, \widetilde{\psi})$ at all Fourier wavenumbers, as[111]

$$\widetilde{\phi}(x, z, t = 0) = A_\phi \sum_{k_x \neq 0} k_x^a e^{i r_\phi(k_x)} e^{-z^2/\sigma^2} e^{i k_x x}, \tag{3.4}$$

and

$$\widetilde{\psi}(x, z, t = 0) = A_\psi \sum_{k_x \neq 0} k_x^a e^{i r_\psi(k_x)} e^{-z^2/\sigma^2} e^{i k_x x}. \tag{3.5}$$

Here, A_ϕ and A_ψ set the overall amplitudes of the perturbations that have a Gaussian

width controlled by σ and the rate at which they fall-off with the wavenumbers given by a. The random phases $r_\phi(k_x)$ and $r_\psi(k_x)$, forming a uniform distribution in $[0, 2\pi)$, are issued for each different k_x using a pseudo-random number generator. Different choices of these initial conditions were investigated in Ref. [111], motivating the choice here: $a = -1$, $\sigma = 2$, and $A_\phi = A_\psi = 10^{-3}$. This set of parameters offers distinct linear and nonlinear phases of evolution.

3.3 Linear eigenmodes

Aiming to understand the nonlinear excitation of linear eigenmodes in the turbulent phase, first the nonlinear initial-value problem is solved to collect high-fidelity turbulent data. Afterward, a separate eigenvalue problem is solved to obtain a complete linear eigenspectrum and eigenmodes, which are used to expand the nonlinear data on this basis to track the amplitude of each eigenmode. Such a basis is obtained by linearizing the governing equations around the initial flow and magnetic field profiles, by dropping the dissipative terms. The eigenmodes thus obtained are of a dissipationless linear operator. Of course, the meaning and utility of this linear basis is *a priori* unknown. Nevertheless, when a basis forms a *complete* set, one can always expand an arbitrary fluctuation on that basis. As the non-dissipative equations of motion preserve Parity-Time (PT-)reversal symmetry, such a system is theoretically guaranteed to yield a complete basis as established recently in PT-symmetric quantum mechanics.[122] Previous studies in gyrokinetic and MHD plasmas have also revealed the usefulness of dissipationless linear eigenmodes in interpreting dissipative nonlinear systems. [97, 111, 123]

Complete eigenspectrum

With the intent of obtaining dissipationless linear eigenmodes, the variables (ϕ, ψ) in Eqs. (4.4a) and (4.4b) are decomposed into background and perturbations, $(\phi, \psi) = (\phi_{\rm ref}, \psi_{\rm ref}) + (\widetilde{\phi}, \widetilde{\psi})$. The linearized dissipationless equations for the evolution of perturbations are

$$\partial_t \nabla^2 \widetilde{\phi} = -\left[U_{\rm ref}\partial_x \nabla^2 - (\partial_z^2 U_{\rm ref})\cdot\partial_x\right]\widetilde{\phi} + \frac{1}{M_{\rm A}^2}\left[B_{\rm ref}\partial_x\nabla^2 - (\partial_z^2 B_{\rm ref})\cdot\partial_x\right]\widetilde{\psi}, \quad (3.6a)$$

$$\partial_t \widetilde{\psi} = -U_{\rm ref}\partial_x\widetilde{\psi} + B_{\rm ref}\partial_x\widetilde{\phi}. \quad (3.6b)$$

Fourier transforming along the x-axis and assuming time variation at each Fourier wavenumber takes the form $\hat{\phi}(k_x, z, \omega)e^{i\omega(k_x)t}$, Eqs. (3.6a)-(3.6b) become

$$\omega\left(\partial_z^2 - k_x^2\right)\hat{\phi} = -k_x\left[U_{\rm ref}\left(\partial_z^2 - k_x^2\right) - (\partial_z^2 U_{\rm ref})\right]\hat{\phi} + \frac{1}{M_{\rm A}^2}k_x\left[B_{\rm ref}\left(\partial_z^2 - k_x^2\right) - (\partial_z^2 B_{\rm ref})\right]\hat{\psi}, \quad (3.7a)$$

$$\omega\hat{\psi} = -U_{\rm ref}k_x\hat{\psi} + B_{\rm ref}k_x\hat{\phi}. \quad (3.7b)$$

Solving Eqs. (3.7a)-(3.7b), the eigenvalues ω are found to be real except when $0 < |k_x| < 1$, where two of the real eigenvalues coalesce to produce imaginary eigenvalues, [16] as complex conjugate to each other. These are the growth rates of the unstable eigenmode and its conjugate stable eigenmode, which evolve in time as $\mathrm{e}^{\gamma(k_x)t}$ and $\mathrm{e}^{-\gamma(k_x)t}$, respectively. This mode-pair is shown, for the first Fourier wavenumber $k_x = 2\pi/L_x = 0.2$, in Fig. 3.1(a), along with all the purely real eigenvalues. The latter constitute the eigenmode continuum [124] and are theoretically infinite in number, although numerical discretization always yields a finite but very large number of modes ($> 3,000$ for each wavenumber in this study). These eigenvalues are given by the

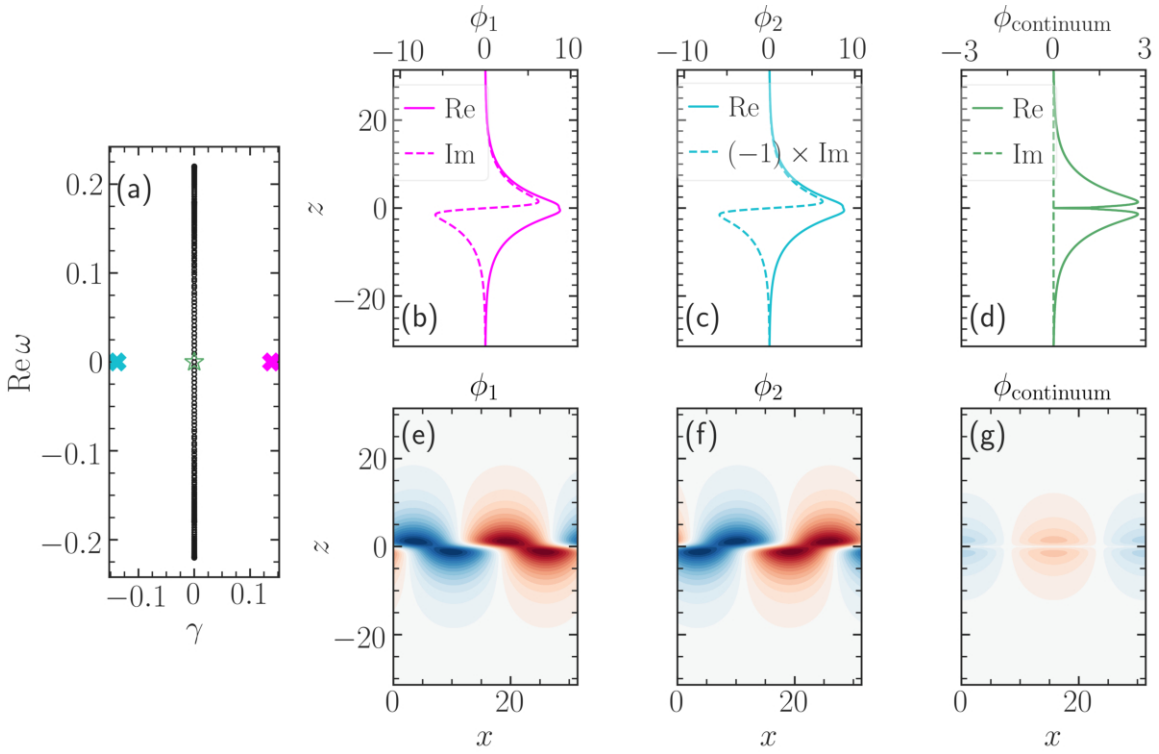

Figure 3.1: (a) Linear eigenspectrum of the MHD shear-flow system (at $k_x = 0.2$ with $M_A = 10$). The unstable and stable modes are shown with thick (colored) crosses. Among the continuum modes that form a vertical line, a zero-frequency continuum mode is displayed with a green-colored star. (b)–(d) Eigenfunctions in z-space, with real (Re) and imaginary (Im) parts, for unstable (ϕ_1), stable (ϕ_2), and one continuum ($\omega = 0$) mode. (e)–(g) Corresponding eigenmode structures in (x, z) space. Note that the eigenmodes ϕ_1 and ϕ_2 are complex conjugate to each other. Imaginary parts in their eigenfunctions induce relative tilt between them in (x, z) space, which will be consequential for momentum transport in Sec. 3.3. Each eigenmode is normalized to have unit total energy [following which the maximum values of ϕ in (b)–(g) are chosen.

relation $\omega/k_x + U_{\rm ref}(z) \pm v_{\rm A,ref}(z) = 0$, where $v_{\rm A,ref}(z)$ is the AlfvÃ©n speed along the reference magnetic field at the vertical coordinate z.

The eigenfunctions, normalized to have unit total energy, are also shown in Fig. 3.1: along the z-axis, see Figs. 3.1(b)–(d), and in (x, z) space, see Figs. 3.1(e)–(g). Note that complex conjugation transforms the unstable mode $\phi_1(k_x, z)$ into the stable mode $\phi_2(k_x, z)$ and vice-versa. This is a direct consequence of spontaneous PT-symmetry breaking in the ideal shear-flow instability. [16] (The spontaneous symmetry breaking does not imply that the equation of motion or the associated Hamiltonian breaks PT-symmetry; it is rather some of the eigenfunctions of such a PT-symmetry-preserving Hamiltonian that break PT-symmetry.)

A representative eigenfunction of a continuum mode, shown in Fig. 3.1(d), exhibits sharp and narrow structure. To what physics each type of eigenmode structure contributes will be explored in this article.

Competing roles of unstable and stable modes

Shown in Fig. 3.2 is a schematic diagram, illustrating how the relative tilts in the eddies can transport momentum in opposite directions across the shear layer.[85] It can be qualitatively observed from Figs. 3.1(e) and (f) that the unstable and stable modes, drive down- and up-gradient momentum transport, respectively. Precise quantative measures will be built and computed later in Sec. 3.5.

Since the unstable and stable modes compete with each other to transport momentum in opposing directions, the excitation levels of these modes are crucial. In the linear phase of instability evolution, the transport by the unstable modes dominates over the transport by the stable modes. However, this need not be the case in the nonlinear phase, as nonlinear processes can excite the stable modes to appreciable

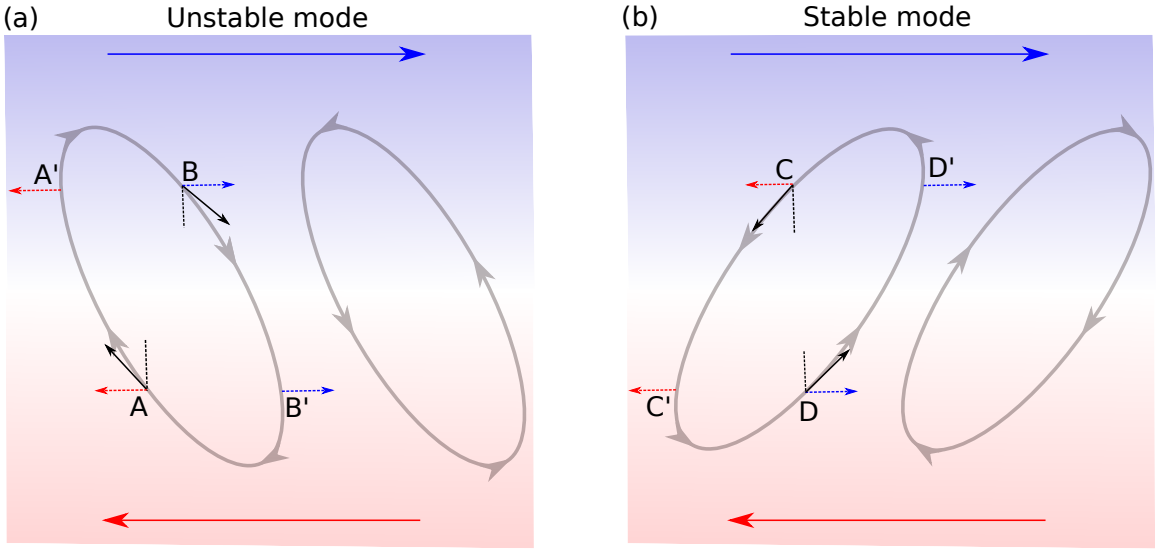

Figure 3.2: (a) The unstable mode of the flow transport momentum in the down-gradient direction: $-x$-directed momentum at A is carried to A' and $+x$-directed momentum at B is carried to B'. Fluxes A→A' and B→B' act to relax the mean flow gradient (shown with the long horizontal arrows). (b) Oppositely tilted eddies, which correspond to a stable mode, transport momentum in the up-gradient direction: $-x$-directed momentum at C is carried to C' and $+x$-directed momentum at D is carried to D'. Both of these fluxes replenish the mean flow. The direction of the streamlines (shown with grey arrows on the elliptic eddies) does not alter these properties, but the tilt does.

levels. Whenever the stable modes surpass the unstable modes in amplitudes, net momentum is transported in the up-gradient direction. [111, 125] In extremely simplified models of transport, such as eddy viscosity models, this contributes to negative eddy viscosity. Computing the amplitude of each eigenmode in the nonlinear phase can thus be helpful to build improved reduced transport models. A recent investigation also demonstrated that this kind of competition between the two large-scale eigenmodes alters the magnetic cascade substantially. [112]

3.4 Nonlinear evolution

Having provided a description of linear eigenmodes, we now turn to properties of the nonlinear system, before discussing how expressions of linear modes may be identified in turbulent fluctuations.

Finte-amplitude Kelvin-Helmholtz instability

Small-amplitude perturbations in the flow and magnetic field evolve exponentially fast in the linear regime of the instability, giving rise to a chain of spiral vortices, as evident in Figs. 3.3(a) and (d). These structures then interact nonlinearly with nearby vortices to yield even larger turbulent structures as in Figs. 3.3(b) and (c). A contrast is to be made between forced and unforced simulations. In the latter, the gradient of the mean flow flattens out as the instability extracts energy. Decaying turbulence then ensues. Forcing the mean flow, however, leads to a quasi-stationary turbulence, as the energy in the gradient is replenished with the instability drawing on its energy. In the saturated stage, energy input through the unstable modes is balanced by energy removal via stable modes as well as dissipative channels.

Momentum transport

It is now timely to discuss the turbulent transport of momentum in nonlinear simulations. To derive the turbulent stresses, the evolution equation of the mean flow can be written by x-averaging the momentum equation,

$$\frac{\partial}{\partial t}\langle U\rangle_x = -\frac{\partial}{\partial z}\left(\tau_u + \tau_b\right) + D_{\rm Krook}\left[U_{\rm ref}(z) - \langle U\rangle_x\right] + \frac{1}{Re}\frac{\partial^2}{\partial z^2}\left[\langle U\rangle_x - U_{\rm ref}(z)\right], \quad (3.8)$$

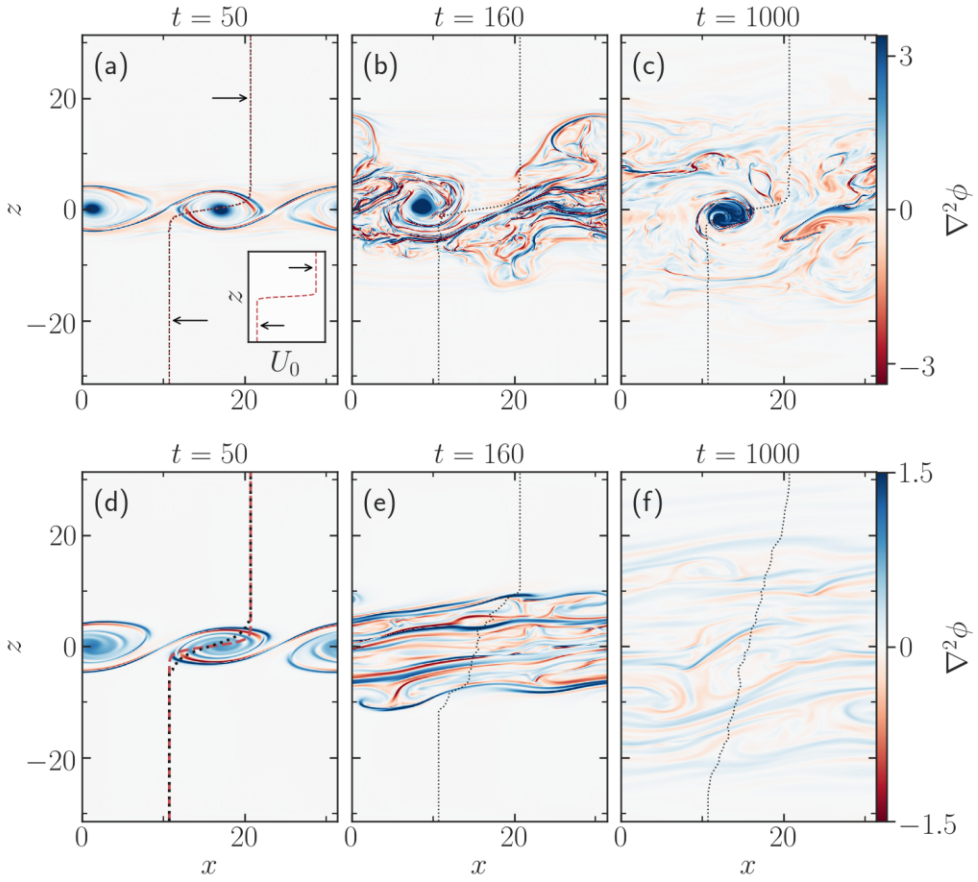

Figure 3.3: Time evolution of vorticity in (a)–(c) in a simulation with a forced background flow, $D_{\mathrm{Krook}} = 2$; and (d)–(f) in a simulation with a freely evolving shear layer, $D_{\mathrm{Krook}} = 0$; both for $M_{\mathrm{A}} = 10$. Panels (a)–(c) share the same colorbar, and (d)–(f) share another colorbar. The instantaneous mean flow profile in each of the subplots is shown with a black dotted curve, where the vertical axis represents the z-coordinate and the horizontal direction corresponds to the x-velocity $U_0(z,t)$, as exemplified in the inset of (a). Two arrows pointing in opposite directions show the direction of the flow in the regions $z > 0$ and $z < 0$. The initial flow profile $U_0(z, t = 0) = \tanh(z)$ is shown with a red dashed curve in (a) and (d). Rapid profile flattening is evident in (d). While the instability dies out in the unforced case, quasi-stationary turbulence is realized in the forced case in (c).

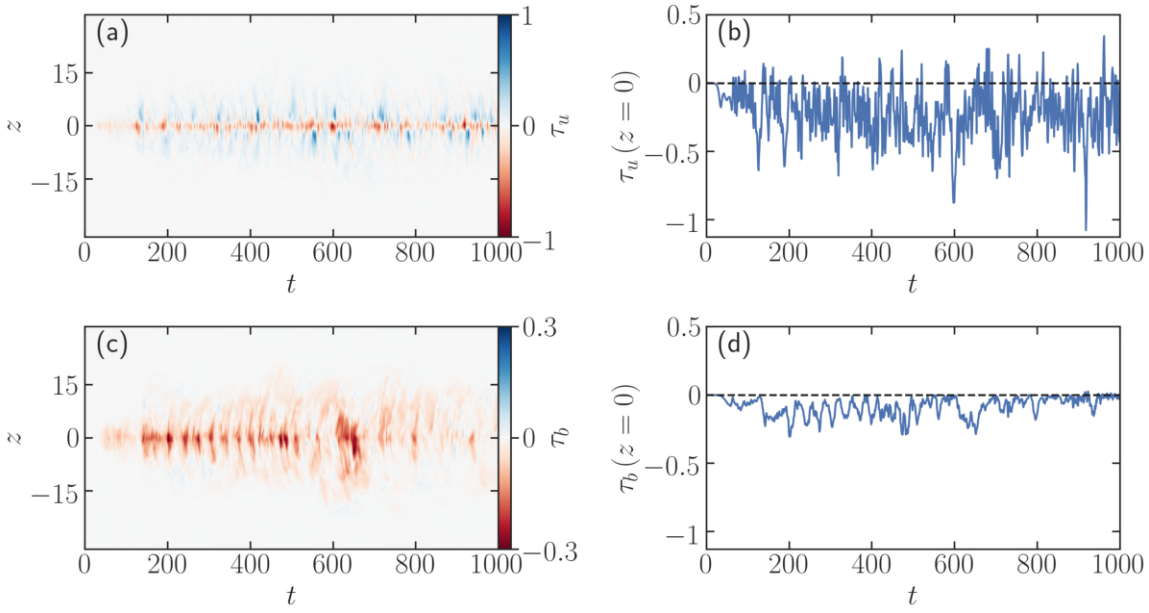

Figure 3.4: Time evolution of MHD stresses. (a) Reynolds stress $\tau_u(t,z)$. (b) Reynolds stress $\tau_u(t,z=0)$ at the middle of the layer, $z=0$. (c) Maxwell stress $\tau_b(z,t)$. (d) Maxwell stress $\tau_b(t,z=0)$ at $z=0$. All data shown are for a single simulation with $M_\mathrm{A}=10$, $D_\mathrm{Krook}=2$. The Reynolds stress in (b) reverses several times, in contrast to the Maxwell stress in (d), which is almost always down-gradient.

where $U = U(x,z,t)$ represents the instantaneous flow, $\langle\cdot\rangle_x$ signifies x-averaging operation, and τ_u and τ_b are the Reynolds and Maxwell stresses, arising from the correlations of turbulent fluctuations of the flow and the magnetic fields, respectively. Note that in Fraser *et al.*[111], a negative sign was typographically missed in front of the first term on the right-hand side of Eq. (3.8). With the sign displayed in Eq. (3.8) above, the turbulent stresses are given by

$$\tau_u = \langle \widetilde{u}_x \widetilde{u}_z \rangle_x = -\langle \partial_z \widetilde{\phi} \cdot \partial_x \widetilde{\phi} \rangle_x, \tag{3.9a}$$

$$\tau_b = -\frac{1}{M_\mathrm{A}^2} \langle \widetilde{b}_x \widetilde{b}_z \rangle_x = \frac{1}{M_\mathrm{A}^2} \langle \partial_z \widetilde{\psi} \cdot \partial_x \widetilde{\psi} \rangle_x. \tag{3.9b}$$

These stresses are evaluated from nonlinear simulations and shown in Fig. 3.4. Fluctuations of Reynolds stress are concentrated in the shear layer, near $z \approx 0$. Time

histories of the Reynolds and Maxwell stresses, at $z = 0$, where they are largest in magnitude, are compared in Figs. 3.4(b) and 3.4(d). Note the recurring dominant up-gradient transport via the Reynolds stress. The Maxwell stress, however, is almost always down-gradient. Figures 3.4(a) and 3.4(c) also convey that the Maxwell stress is generally broader along the z-axis than the Reynolds stress, which is more localized near the shear layer.

3.5 Decomposition of nonlinear simulation onto linear modes

To probe the nonlinear simulation data, the turbulent fluctuations are expanded on the linear eigenmode basis described in Sec. 5.3. Consider an arbitrary turbulent fluctuation $\widetilde{\chi}_{\text{turb}} = (\widetilde{\phi}_{\text{turb}}, \widetilde{\psi}_{\text{turb}})$, which is expanded as

$$\widetilde{\chi}_{\text{turb}}(x, z, t) = \sum_{k_x \neq 0} \mathrm{e}^{ik_x x} \sum_j \beta_j(k_x, t) \chi_j(k_x, z) \tag{3.10}$$

where the eigenmode basis $\chi_j(k_x, z)$ is employed along the z-axis at each wavenumber k_x to decompose the fluctuations. The complex mode-amplitude $\beta_j(k_x, t)$, defined for each eigenmode j, can then be computed using properties of the linear operator, described in the Appendix A, even when the eigenmodes of the operator are non-orthogonal, as is the case here.

Following earlier studies, [97, 99, 110–112] $j = 1, 2$ will be used to represent unstable and stable modes, respectively. The computations herein resolve as many as 3109 eigenmodes at a particular k_x.

Nonlinear excitation of stable modes

The amplitudes of the unstable and stable modes are tracked in the nonlinear simulations, and their time series are plotted in Fig. 3.5(a). As expected, the unstable mode grows and the stable mode decays exponentially in the early phase. However, as the fluctuations increase due to the growth of the unstable modes, nonlinear interactions among them begin exciting the linearly stable mode,[15] causing it to rise to almost the same level as the unstable mode at that wavenumber, see Fig. 3.5(a). Later, in the fully nonlinear stage, all eigenmodes can participate in the energy redistribution.

The energy in individual eigenmodes $|\beta_j|^2$, averaged over a turbulent state ($t =$ 150–1000), is displayed in Fig. 3.5(b). It is evident that the unstable and stable eigenmode pair contains a majority ($> 70\%$) of the energy in the system. The remaining eigenmodes share a wide spectrum of the remaining energy. This suggests that the turbulent system at hand may be amenable to a substantial dimensionality reduction.[90, 97] For the cases of the weaker magnetic fields, this finding is more prominent, as evidenced in the Appendix B. In addition, the weaker fields support more coherent amplitude-oscillations, unlike the large excursions in the amplitudes observed with the stronger fields, e.g., $M_{\rm A} = 10$ in Fig. 3.5(a). In the latter case, the stronger Lorentz back-reaction acting on the large-scale turbulent flow cause strong oscillations in the eigenmode amplitudes.

Reduced representation of the turbulent flow

To obtain a better understanding of turbulent dynamics, it is of interest to compare different components of eigenmodes in the turbulent flow. An approximate (reduced) representation of the turbulent flow $\widetilde{\phi}_{\rm approx}$ can be constructed from a class of eigenmodes at each wavenumber, e.g., $\widetilde{\phi}_{\rm approx}(x, z, t)$ can be written as a sum of an

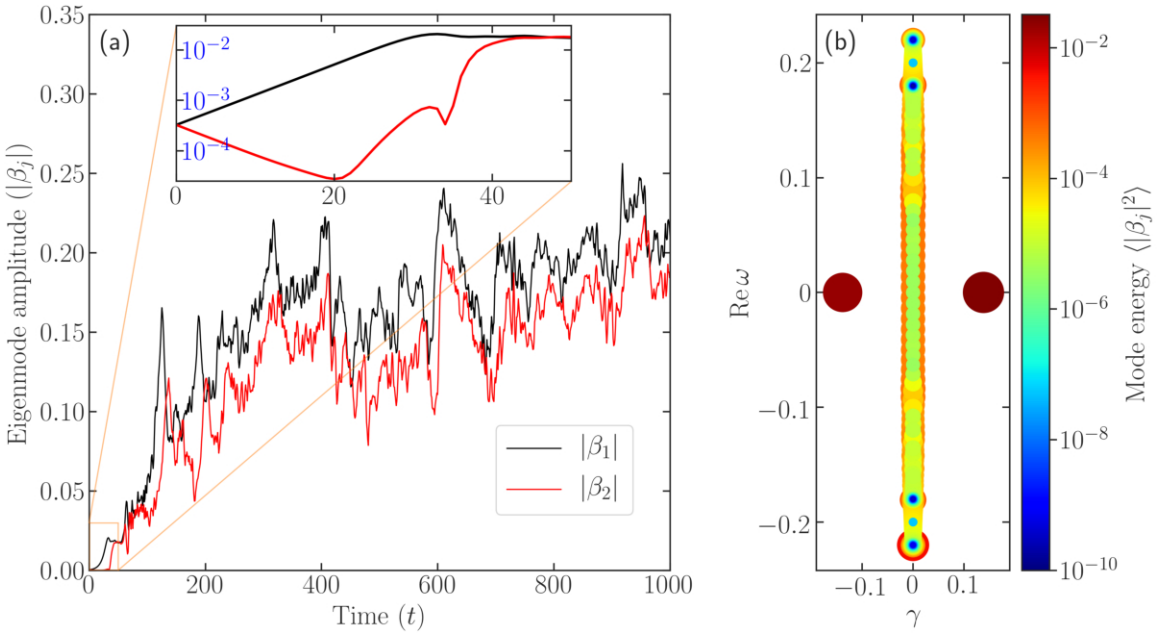

Figure 3.5: (a) Time traces of the eigenmode amplitudes are shown for $k_x = 0.2$ for a simulation with $M_\mathrm{A} = 10$ and $D_\mathrm{Krook} = 2$. Note, in the inset, the nonlinear excitation of linearly stable mode ($|\beta_2|$) in instability saturation ($|\beta_1|$ is the unstable mode amplitude). (b) All 3109 eigenmodes at $k_x = 0.2$ are plotted with their squared excitation levels in the nonlinearly saturated phase, which represent the energy in each eigenmode. The diameter of each circle shown corresponds to the energy in each eigenmode, and modes with lower energy are plotted on top of more highly excited modes, such that all data points are (partially) visible. Note that the total fluctuation energy is composed of both the modal and non-modal energy because of the non-orthogonal modes. Evaluating total energy at a wavenumber, $E = \int dz\,[|\mathbf{u}|^2 + |\mathbf{B}|^2/M_\mathrm{A}^2]\,/2 = \int dz\,[(\sum_m \beta_m \mathbf{u}_m)\cdot(\sum_n \beta_n \mathbf{u}_n)^* + (\sum_m \beta_m \mathbf{B}_m)\cdot(\sum_n \beta_n \mathbf{B}_n)^*/M_\mathrm{A}^2]\,/2$, taking the form $E = \sum_{m,n} E_{mn}$, where $(\mathbf{u}_m, \mathbf{B}_m)$ represents the m-th eigenmode. When m and n belong to discrete (d) modes, E_dd is, upon time-averaging (t = 150–1000), around 72% of the total energy, whereas when m and n belong to continuum (c) modes, E_cc is $\approx 22\%$; E_dc is $\approx 6\%$.

unstable mode per wavenumber $\sum_{k_x} \mathrm{e}^{ik_x x}\beta_1(k_x,t)\phi_1(k_x,z)$, or as a sum of an unstable and a stable mode per wavenumber $\sum_{k_x} \mathrm{e}^{ik_x x}\left[\beta_1(k_x,t)\phi_1(k_x,z)+\beta_2(k_x,t)\phi_2(k_x,z)\right]$. Respective short-hand notations $\beta_1\phi_1$ and $\beta_1\phi_1+\beta_2\phi_2$ will be used hereafter, i.e.,

$$\beta_1\phi_1 \equiv \sum_{0<|k_x|<1} \mathrm{e}^{ik_x x}\beta_1(k_x,t)\phi_1(k_x,z), \tag{3.11a}$$

$$\beta_1\phi_1+\beta_2\phi_2 \equiv \sum_{0<|k_x|<1} \mathrm{e}^{ik_x x}\left[\beta_1(k_x,t)\phi_1(k_x,z)+\beta_2(k_x,t)\phi_2(k_x,z)\right]. \tag{3.11b}$$

The nonlinear fluctuations of the flow are compared in Fig. 3.6, viewed at different levels of truncation in the eigenmode expansion. The leftmost panel, Fig. 3.6(a), shows the full turbulent fluctuations in the Kelvin-Helmholtz (KH-)unstable wavenumbers $k_x = 0.2, 0.4, 0.6, 0.8$, which appear similar to the full turbulent fluctuations that include all wavenumbers in the nonlinear simulation (not shown); Fig. 3.6(b) displays the sum of unstable eigenmodes at each of these KH-unstable wavenumbers; and Fig. 3.6(c) presents the sum of unstable and stable eigenmodes at the same wavenumbers, while omitting all continuum modes. Adding stable modes produces a substantial improvement in the reconstruction. Note that such a reconstruction was found to deteriorate quickly over time (i.e., a few instability e-folding times where one e-folding time for the fastest growing mode $k_x = 0.4$ is $\gamma^{-1} \approx 5$) in the study of unforced shear layers, [111] as the rapid relaxation of the layer towards a stable profile rendered the unstable and stable eigenmodes of the system to be less representative of the decaying turbulence. The turbulent fluctuation shown in Fig. 3.6 is at $t = 702$, which lies well within the nonlinear phase (the linear phase ends around $t \approx 30$). In this respect, the forced shear layer is markedly different from the freely evolving layer.

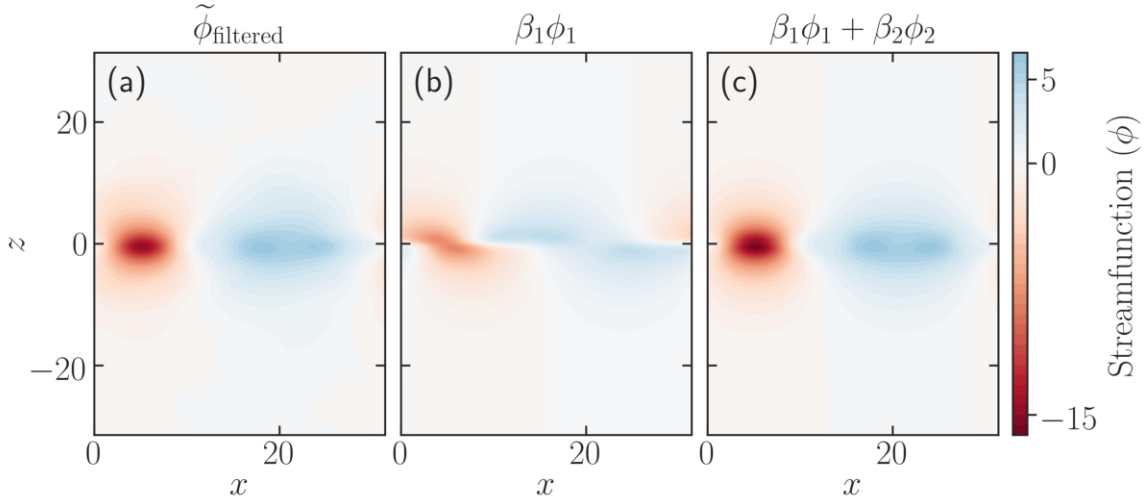

Figure 3.6: (a) Full turbulent fluctuations in streamfunction in the Kelvin-Helmholtz-unstable wavenumbers $0 < |k_x| < 1$ (thus called $\widetilde{\phi}_{\text{filtered}}$), observed in nonlinear simulations with $M_{\text{A}} = 30$, $D_{\text{Krook}} = 2$. The shown plot of fluctuations includes all types of eigenmodes—the unstable, stable and continuum modes. (b) Reconstruction of the turbulent fluctuations by summing only the unstable modes at the same wavenumber range. (c) Reconstruction by adding stable and unstable modes, while omitting all continuum modes. The reconstruction in (c) is clearly much alike the turbulent fluctuations in (a), in contrast to the reconstruction in (b). Saturation theory of instability that considers the unstable modes only, at best, can produce (b), but with inclusion of the stable modes, substantial improvement can be achieved.

Performance of reduced representations

While the qualitative analysis of the turbulent-flow reconstruction in Sec. 3.5 is instructive, a quantitative measurement is desirable. To this end, following Ref. [111], the reconstructive capability of reduced representations is quantified, at each time step in the simulation, using the standard energy norm that measures the fraction of kinetic energy lost when the eigenmode basis is truncated, compared to the kinetic energy in the full turbulent flow data—see the definition in Eq. (3.12). The energy norm is well-suited for studying large-scale structures. Small-scale phenomena, however, may not be amenable to such analysis, although one may be able to find ties between the small- and large-scale pheonomena in some cases. This measure is also called a

"truncation error." Note that this error arises not in the nonlinear simulations but merely in the reduced representations of turbulent fluctuations, when truncating the eigenmode basis in post-processing analyses.

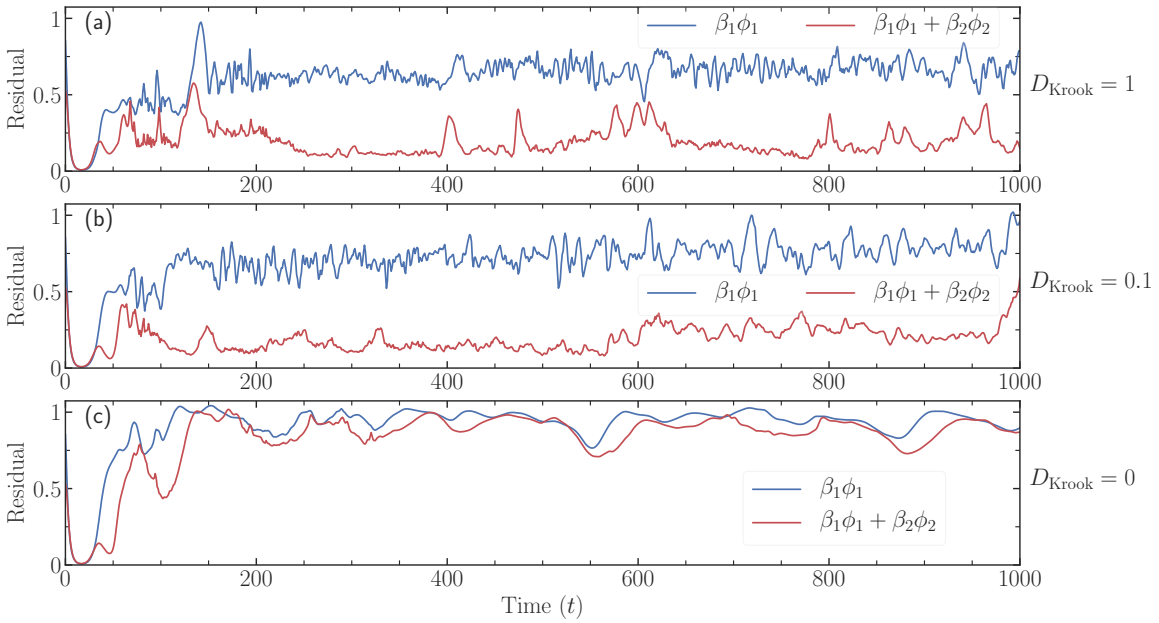

Figure 3.7: Time traces of residuals, i.e., the fraction of energy missed in truncated bases, normalized to the total energy in the turbulent flow at each time step. The reconstruction uses truncated bases with unstable modes alone, and unstable and stable modes together. The forcing strength is varied in three different simulations with $M_{\mathrm{A}} = 10$: (a) $D_{\mathrm{Krook}} = 1$, (b) $D_{\mathrm{Krook}} = 0.1$, and (c) $D_{\mathrm{Krook}} = 0$. The unforced shear layer in (c) rapidly flattens out, and thus instability no longer drives the turbulence. As long as the turbulence is driven by the instability, the unstable and stable modes together can reconstruct a large fraction of the turbulent flow features in (a) and (b).

Using the energy norm, we define the relative truncation error, which may also be called a normalized residual, in the following manner:

$$\text{Residual} = \frac{||\widetilde{\phi}_{\mathrm{exact}} - \widetilde{\phi}_{\mathrm{approx}}||^2_{\mathrm{KE}}}{||\widetilde{\phi}_{\mathrm{exact}}||^2_{\mathrm{KE}}} = \frac{||\widetilde{\phi}_{\mathrm{diff}}||^2_{\mathrm{KE}}}{||\widetilde{\phi}_{\mathrm{exact}}||^2_{\mathrm{KE}}} = \frac{\int dxdz \left[\left(\partial_x \widetilde{\phi}_{\mathrm{diff}}\right)^2 + \left(\partial_z \widetilde{\phi}_{\mathrm{diff}}\right)^2\right]}{\int dxdz \left[\left(\partial_x \widetilde{\phi}_{\mathrm{exact}}\right)^2 + \left(\partial_z \widetilde{\phi}_{\mathrm{exact}}\right)^2\right]}, \tag{3.12}$$

where $(\partial_x \phi)^2$ and $(\partial_z \phi)^2$ are the squared z- and x-components of velocities; $\widetilde{\phi}_{\mathrm{diff}} =$

$\widetilde{\phi}_{\text{exact}} - \widetilde{\phi}_{\text{approx}}$ with $\widetilde{\phi}_{\text{exact}}$ and $\widetilde{\phi}_{\text{approx}}$ representing respectively the turbulent stream-function from nonlinear simulation and its reduced representation—either a summation over the unstable modes alone or over the unstable and stable modes together—both spanning fluctuations over a range of wavenumbers. Here, this range, taken to be the same for both, is considered to be $0 < |k_x| < 1$, which corresponds to the wavenumber range of the instability. If the residual is less than unity, the truncation in the eigen-mode expansion may be considered as a representative of the full system and thus a candidate for reduced-order model building. On the contrary, the residual being around unity or more signfies the failure of the reduced representation in effectively capturing the overall nonlinear fluctuations.

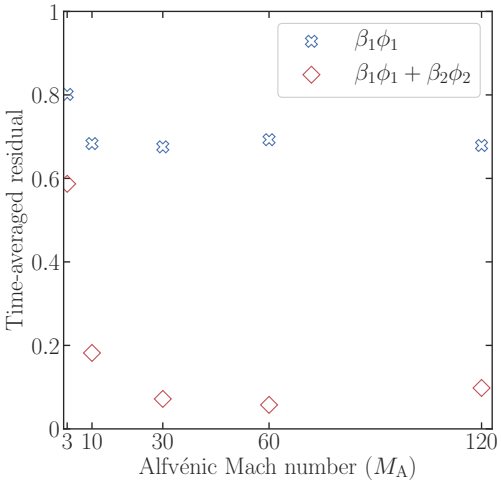

Figure 3.8: Shown are the time-averaged residuals for simulations different M_{A}. Note the residuals are the fractions of energy missed in the truncated bases, compared to the total energy in the instantaneous full turbulent flow. Time-averaging is performed over a quasi-stationary state of turbulence ($t = 600$–1000). The reconstruction uses truncated bases with unstable modes alone, and unstable and stable modes together, leaving all the continuum modes. All simulations use $D_{\text{Krook}} = 2$. Note the dramatic improvement with the inclusion of the stable modes. For $M_{\text{A}} = 3$, the improvement is modest, as the stronger Lorentz force back-reacts on the large-scale turbulent flow, producing more fluctuations in the continuum modes.

The time evolution of the residuals is compared in Fig. 3.7 for varying forcing strengths. As expected, the unstable modes entirely capture the fluctuations in the linear phase (i.e., $t \lesssim 30$). In the nonlinear phase, however, the unstable modes capture only a rather limited fraction of the turbulent fluctuations. This is greatly improved when the stable modes are added. This suggests that the success of quasilinear models in capturing key properties of the turbulence can crucially depend on whether stable modes are considered when constructing such models.

It is also interesting to note that the turbulence in the unforced shear layer, see Fig. 3.7(c), is different from the forced cases. In the former, the shear layer quickly flattens out and nearly shuts off the instability, leading to a decaying turbulence. Regardless of whether the unstable and/or stable modes are considered, the corresponding reconstructions fail to model the turbulence with any degree of accuracy. By contrast, when the shear layer is forced, a reduced representation of the turbulent flow with two modes (per wavenumber) is found to perform well, recovering a substantial fraction of the full nonlinear system.

A similar reconstruction is shown for various strengths of magnetic fields M_A in Fig. 3.8, where residuals are time-averaged over a quasi-stationary state of turbulence. With stronger magnetic fields (lower M_A), the vortices begin disrupting due to stronger Lorentz force and consequently generate more fluctuations at scales beyond the Kelvin-Helmholtz-instability (KHI) range. [114] This accounts for an increase of the residual for low M_A, although it remains below 0.2 for $M_\mathrm{A} = 10$. For $M_\mathrm{A} = 3$, the improvement with the inclusion of the stable modes is modest. Momentum transport by large-scale structures, formed from the unstable and stable modes, within the KHI range, however, may still dominate over the transport contributed by much smaller scales or the remaining continuum modes; hence, a quantitative analysis of transport will be conducted next.

Competing up- and down-gradient momentum transport and their reduced models

The Reynolds stress can be expressed in terms of the contribution from each wavenumber, which can further be decomposed into the contribution from each eigenmode. At a wavenumber k_x, the Reynolds stress from all the fluctuations $\hat{\phi}_{k_x}$ read

$$\tau_u(\text{all modes}) = 2\ \text{Im}[k_x \hat{\phi}_{k_x} \cdot \partial_z \hat{\phi}^*_{k_x}], \tag{3.13}$$

whereas the contribution from an unstable mode alone, and from an unstable and a stable mode alone, at that wavenumber are respectively given as

$$\begin{aligned} \tau_u(\text{unstable}) &= 2\ \text{Im}[k_x(\beta_1 \phi_{1,k_x}) \cdot \partial_z(\beta_1 \phi_{1,k_x})^*] \\ &= 2|\beta_1|^2\ \text{Im}[k_x \phi_{1,k_x} \cdot \partial_z \phi^*_{1,k_x}], \end{aligned} \tag{3.14}$$

and

$$\begin{aligned} \tau_u(\text{stable}) &= 2|\beta_2|^2\ \text{Im}[k_x \phi_{2,k_x} \cdot \partial_z \phi^*_{2,k_x}] \\ &= 2|\beta_2|^2\ \text{Im}[k_x \phi^*_{1,k_x} \cdot \partial_z \phi_{1,k_x}] \\ &= -2|\beta_2|^2\ \text{Im}[k_x \phi_{1,k_x} \cdot \partial_z \phi^*_{1,k_x}], \end{aligned} \tag{3.15}$$

where $\hat{\phi}_{k_x}$ is the Fourier transform of the streamfunction at wavenumber k_x and ϕ_{j,k_x} represents the z-dependent j-th complex eigenmode: $j = 1, 2$ for unstable and stable modes, respectively. The conjugate symmetry of unstable and stable modes, as shown in Figs. 3.1(b) and 3.1(c), is used in Eq. (3.15), i.e., $\phi_{2,k_x}(z) = \phi^*_{1,k_x}(z)$. The negative sign of the last expression in Eq. (3.15) corresponds to the up-gradient nature of momentum transport by stable modes, which was physically analyzed in Sec. 3.3 and visually demonstrated in Fig. 3.2.

The summed contributions of unstable and stable modes in transport, however, can have cross-terms—quadratic correlations between unstable and stable modes—that do not appear in Eqs. (3.14) and (3.15) where contribution from individual modes are shown. But the cross-terms vanish when the unstable and stable modes are *exactly* complex conjugates of each other, as is the case for the ideal Kelvin-Helmholtz instability (when this conjugate symmetry is broken, e.g., in resistive tearing instability or in ion-temperature-gradient instability,[125] the cross-terms can have non-zero contribution):

$$\begin{aligned}\tau_u(\text{unstable } + \text{ stable}) &= 2\ \mathrm{Im}[k_x(\beta_1\phi_{1,k_x} + \beta_2\phi_{2,k_x}) \cdot \partial_z(\beta_1\phi_{1,k_x} + \beta_2\phi_{2,k_x})^*] \\ &= 2\left(|\beta_1|^2 - |\beta_2|^2\right)\ \mathrm{Im}[k_x\phi_{1,k_x} \cdot \partial_z\phi^*_{1,k_x}] + \text{cross-terms}, \quad (3.16)\end{aligned}$$

where

$$\begin{aligned}\text{cross-terms} &= 2\ \mathrm{Im}[k_x(\beta_1\phi_{1,k_x}) \cdot \partial_z(\beta_2\phi_{2,k_x})^*] + 2\ \mathrm{Im}[k_x(\beta_2\phi_{2,k_x}) \cdot \partial_z(\beta_1\phi_{1,k_x})^*] \\ &= 2\ \mathrm{Im}[\beta_1\beta_2^* k_x\phi_{1,k_x} \cdot \partial_z\phi^*_{2,k_x}] + 2\ \mathrm{Im}[\beta_2\beta_1^* k_x\phi_{2,k_x} \cdot \partial_z\phi^*_{1,k_x}] \\ &= 2\ \mathrm{Im}[\beta_1\beta_2^* k_x\phi_{1,k_x} \cdot \partial_z\phi^*_{2,k_x}] + 2\ \mathrm{Im}[\beta_2\beta_1^* k_x\phi^*_{1,k_x} \cdot \partial_z\phi_{2,k_x}] \\ &= 2\ \mathrm{Im}[\beta_1\beta_2^* k_x\phi_{1,k_x} \cdot \partial_z\phi^*_{2,k_x}] + 2\ \mathrm{Im}[\left(\beta_1\beta_2^* k_x\phi_{1,k_x} \cdot \partial_z\phi^*_{2,k_x}\right)^*] \\ &= 0.\end{aligned} \quad (3.17)$$

Thus we obtain

$$\begin{aligned}\tau_u(\text{unstable } + \text{ stable}) &= 2\left(|\beta_1|^2 - |\beta_2|^2\right)\ \mathrm{Im}[k_x\phi_{1,k_x} \cdot \partial_z\phi^*_{1,k_x}] \\ &= \tau_u(\text{unstable}) + \tau_u(\text{stable}). \quad (3.18)\end{aligned}$$

These relations inform us about the z-profile of the Reynolds stress, contributed

by each wavenumber and each eigenmode. As largest momentum transport happens in the region with the largest flow-gradient, it is instructive to compute, in the forced shear layers, the turbulent stresses at the middle of the layer at $z = 0$, and compare the stress contributions from different eigenmodes at various wavenumbers.

The total Reynolds stress from all modes and all wavenumbers in the simulations is compared in Fig. 3.9 with the stress contributions from the wavenumber range $0 < |k_x| < 1$, which is decomposed further into eigenmodes to assess the contribution of the unstable modes, stable modes, and their sum. The subplots demonstrate that the stable modes are highly efficient in transporting momentum in the up-gradient direction, as compared to the down-gradient transport by the unstable modes. Even for the strongest magnetic field $M_{\rm A} = 3$, close to the instability threshold, the stable modes contribute significantly to a *continuous* reduction of the turbulent momentum flux. In addition, the occasional breakthroughs in stable-mode activity cause reversals of the transport direction. This reversal can be observed when the total Reynolds stress in the system is computed, without decomposing the stress into contributions by each eigenmode. However, when the stable modes are not overtaking the unstable modes in transport, the resulting down-gradient transport observed in simulations or experiments is difficult to interpret, in regards to the contributions of stable modes in subdominantly reducing the transport. An eigenmode decomposition of turbulent fluctuations, however, uncovers a complete picture, as is shown here.

Similar variations of momentum transport across the middle of the shear layer are compared in Fig. 3.10 for different forcing strengths. Note the unforced case differs from the forced cases, as the nearly-flattened shear layer has less momentum to be transported across the layer. As reported in Ref. [111], despite the profile relaxation, the two eigenmodes per wavenumber describe well the temporal variation of the Reynolds stress across the shear layer, although the stress itself is very low

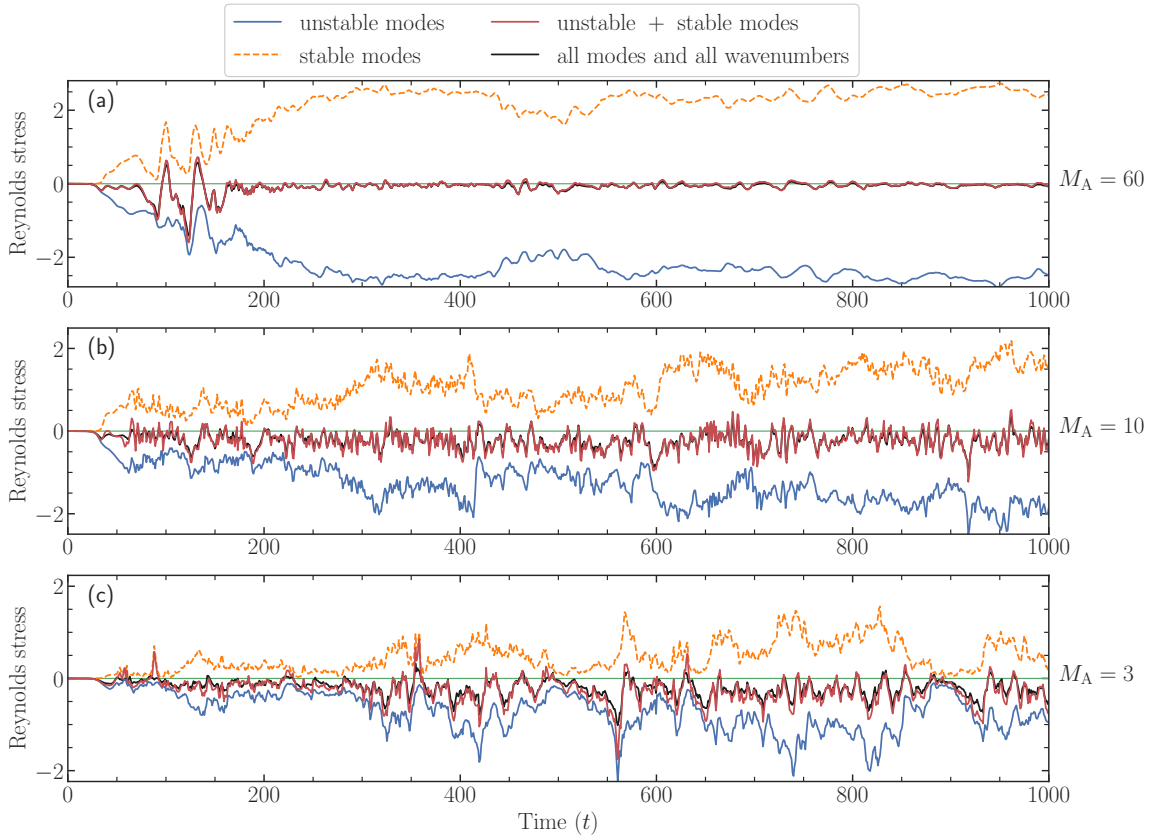

Figure 3.9: Time variations of Reynolds stress at the middle of the shear layer, $z = 0$. The stress contributions from unstable modes (blue), stable modes (orange), their sum (red), and full nonlinear fluctuations, i.e., all modes and all wavenumbers in the simulations (black), are compared, for varying strengths of magnetic fields: (a) $M_A = 60$, (b) $M_A = 10$, and (c) $M_A = 3$. Thin green lines represent the zero level. All simulations use $D_{Krook} = 2$. Although, with stronger magnetic fields, the up-gradient momentum transport by stable modes are reduced, the up- and down-gradient transport nearly cancel each other throughout all cases.

(note its vertical scale). In all cases, the stress captured via the sum of unstable and stable modes almost completely follows the total stress from all modes.

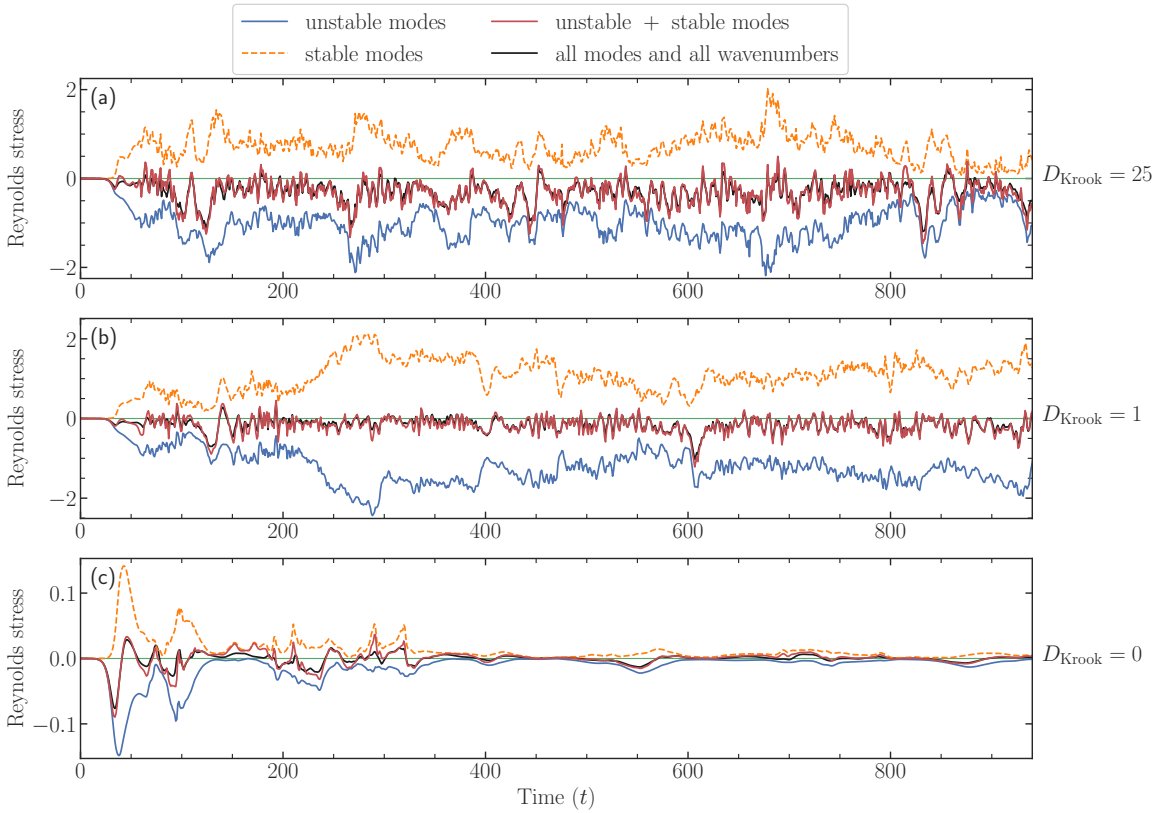

Figure 3.10: Time variations of Reynolds stress at the middle of the shear layer, $z = 0$. The stress contributions from unstable modes (blue), stable modes (orange), their sum (red), and full nonlinear fluctuations, i.e., all modes and all wavenumbers in the simulations (black), are compared, for varying forcing strengths: (a) $D_{\mathrm{Krook}} = 25$, (b) $D_{\mathrm{Krook}} = 1$, and (c) $D_{\mathrm{Krook}} = 0$. All simulations use $M_{\mathrm{A}} = 10$. Thin green lines represent the zero level. Qualitative differences can be observed in unforced ($D_{\mathrm{Krook}} = 0$) and forced cases ($D_{\mathrm{Krook}} \neq 0$): as instability extracts energy from the mean flow, the profile relaxation in the unforced layer leads to a decaying turbulence, and the transport rates become very small [note the vertical axis labels in (c)]. However, in all cases, the summed stable modes producing up-gradient transport nearly cancel the down-gradient transport by unstable modes. The addition of these two contributions produces a stress that is almost identical to the stress from all modes.

In Fig. 3.11, the momentum transport by the unstable and stable modes is presented as a function of magnetic Prandtl number $Pm = Rm/Re$. All simulations until this

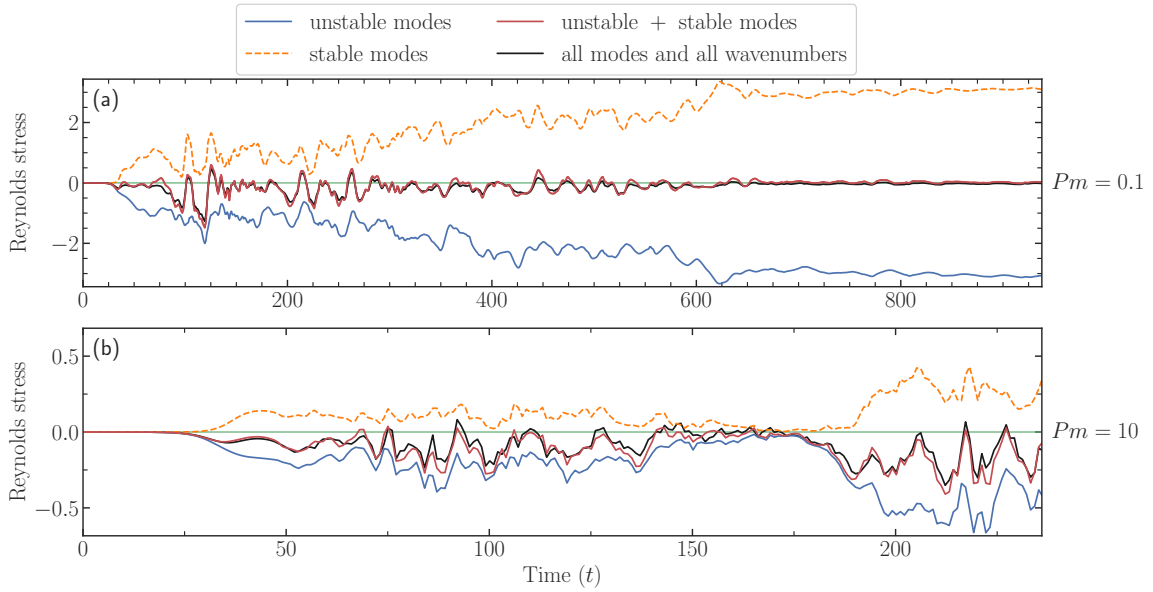

Figure 3.11: Time variations of Reynolds stress at the middle of the shear layer, $z = 0$. The stress contributions from unstable modes (blue), stable modes (orange), their sum (red), and full nonlinear fluctuations, i.e., all modes and all wavenumbers in the simulations (black), are compared, for varying magnetic Prandtl numbers (resistivities): (a) $Pm = 0.1$ and (b) $Pm = 10$. All simulations use $M_{\rm A} = 10$, $D_{\rm Krook} = 2$, and $Re = 500$. Thin green lines represent the zero level. It can be observed that the stable modes begin driving up-gradient momentum transport at around $t \approx 30$ when the nonlinear phase of evolution begins. By varying Pm by two orders of magnitude, around *unity*, the stable modes are found to substantially reduce the down-gradient transport; note the case of $Pm = 1$ is shown in Fig. 3.9(b).

point used $Rm = 500$, which is now changed to $Rm = 50$ and $Rm = 5\,000$. In both cases of $Pm = 0.1$ and $Pm = 10$, the stable modes still substantially offset the turbulent momentum transport of the unstable modes. The shorter time trace for $Pm = 10$ is due to the higher simulation cost. It should be noted that the quasi-stationary state in this simulation is still undergoing changes, unlike in the case of $Pm = 0.1$ in Fig. 3.11(a) or $Pm = 1$ in Fig. 3.9(b), all with the same $M_{\rm A} = 10$, $D_{\rm Krook} = 2$ and $Re = 500$.

The efficiency of time-averaged up-gradient momentum transport due to stable modes is compared in Fig. 3.12 with the time-averaged down-gradient transport due

to unstable modes, via a measure, defined below:

$$\text{Transport reduction efficiency} = \frac{\langle \text{Up-gradient transport by stable modes} \rangle_t}{\langle \text{Down-gradient transport by unstable modes} \rangle_t}, \tag{3.19}$$

where $\langle A \rangle_t$ represents a time-averaging operation on A.

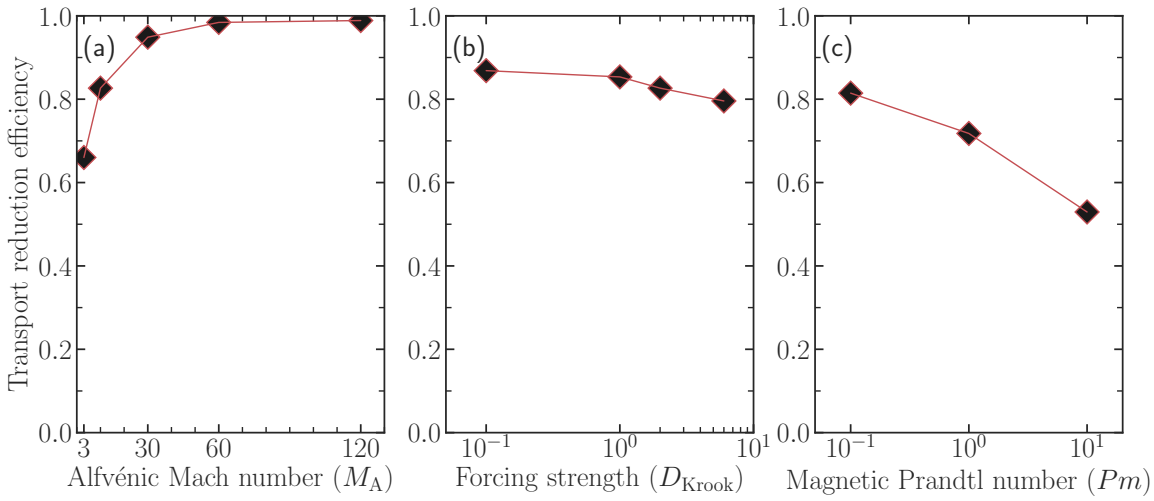

Figure 3.12: Parameter dependence of transport reduction efficiency, which is defined as the ratio of time-averaged up-gradient Reynolds stress due to stable modes and time-averaged down-gradient Reynolds stress due to unstable modes. The stress is measured at the middle of the shear layer, $z = 0$, where the momentum transport is at its maximum. (a) Variations in $M_A = 3, 10, 30, 60, 120$ with $D_{Krook} = 2$, $Pm = 1$, and linear x-scale. (b) Variations in $D_{Krook} = 0.1, 1, 2, 6$ with $M_A = 10$, $Pm = 1$, and logarithmic x-scale. (c) Variations in Pm $= 0.1, 1, 10$ (or, equivalent changes in resistivities) with $M_A = 10$, $D_{Krook} = 2$, and logarithmic x-scale. All plots have the same y-axis. The time-average for (a) and (b) is taken over a long quasi-stationary state of turbulence $t = 350$–900, while for (c), it is $t = 137$–237 where the quasi-stationary state is still undergoing changes. In all cases, substantial reduction of transport by stable modes is evident, which cancel, via their up-gradient transport, more than half of the down-gradient transport by unstable modes, and this fraction reaches up to 98%, see (a), for $M_A = 60$ and $M_A = 120$.

Variations in magnetic field strength, forcing strength, and magnetic Prandtl number all demonstrate that the stable modes cancel an appreciable amount of the turbulent momentum flux associated with the unstable modes. On average, around

80% of the down-gradient flux is offset in this manner.

A remark should be made now regarding the use of unstable and stable modes for building a reliable reduced mode of transport for geo- and astro-physical problems. One approach would be to relate the activity of these two modes with a coefficient of diffusive flux (although the unstable and stable modes offer spatial profiles of transport as well, with both diffusive and non-diffusive fluxes, because they do not rely on an ad-hoc eddy-viscosity model, which is an explicit diffusive-flux-based model). In the middle of the shear layer, the diffusive flux, however, dominates because of the maximum in the flow-gradient. The ad-hoc turbulent viscosity can thus be defined [97], more importantly without a "free-parameter," using Eq. (3.18) as

$$\nu_{\text{turb}} = \frac{\tau_u(\text{unstable } + \text{ stable})}{(dU_0/dz)\Big|_{z=0}} = \sum_{0<k_x<1} 2\left(|\beta_1|^2 - |\beta_2|^2\right)\ \text{Im}[k_x\phi_{1,k_x}\cdot\partial_z\phi^*_{1,k_x}]\Big|_{z=0}. \tag{3.20}$$

Note that the denominator is unity for the shear-flow that has a linear profile in the vicinity of $z = 0$. To assess the importance of stable modes in this construct, $|\beta_1|^2 - |\beta_2|^2$ can be written as $|\beta_1|^2\left(1 - |\beta_2|^2/|\beta_1|^2\right)$. Since $|\beta_2|^2$ has been found to on the same order of $|\beta_1|^2$, e.g., see Fig. 3.12, where $|\beta_2|^2/|\beta_1|^2$ can range from ≈ 0.8 to ≈ 0.95, yielding $(1 - |\beta_2|^2/|\beta_1|^2) \approx 0.05$ to 0.2. Therefore, neglecting stable modes can overestimate the transport by a factor of 5 to 20.

Reynolds vs. Maxwell stresses

With the above successful low-order representation of Reynolds stress above, we now examine the fluctuations in the magnetic field that give rise of Maxwell stress. The

stress can be quantified as

$$\tau_b(\text{all modes}) = -\frac{2}{M_\text{A}^2}\ \text{Im}[k_x\hat{\psi}_{k_x}\cdot\partial_z\hat{\psi}^*_{k_x}], \tag{3.21}$$

$$\tau_b(\text{unstable}\ +\ \text{stable}) = -\frac{2}{M_\text{A}^2}\left(|\beta_1|^2-\beta_2|^2\right)\ \text{Im}[k_x\psi_{1,k_x}\cdot\partial_z\psi^*_{1,k_x}], \tag{3.22}$$

where $\hat{\psi}_{k_x}$ is the Fourier transform of the flux function at a wavenumber k_x and ψ_{j,k_x} represents the z-dependent j-th complex eigenmode ($j = 1, 2$ for unstable and stable modes, respectively). Again, cross-terms arising from the correlation between the unstable and modes can be shown to vanish, exactly as it was shown for the Reynolds stress in Eq. (3.17).

As can be seen in Fig. 3.13, the Reynolds stress is dominated by large scales while the Maxwell stress involves a large number of different scales. Figure 3.13(a), using axes with linear scales, shows the dominance of Reynolds stress in the entire system, which the two-eigenmodes-per-wavenumber decomposition (unstable and stable modes) captures, not only qualitatively, but also quantitatively with great accuracy. In Fig. 3.13(b), a logarithmic scale is used to expose the range of small scales that contribute significantly to the magnetic fluctuations. Wavenumbers $k_x \lesssim 10$ have major contributions, as opposed to $k_x < 1$ for the fluctuations of the flow. The fact that a large amount of flow energy resides at large scales suggests that the shear-flow turbulence may be amenable to some form of quasilinear modeling. Homogeneous isotropic turbulence, on the other hand, would not be reliably captured with such models, as no scale separation exists therein. Recent studies have highlighted that improved quasilinear models such as the generalized quasilinear approximation are

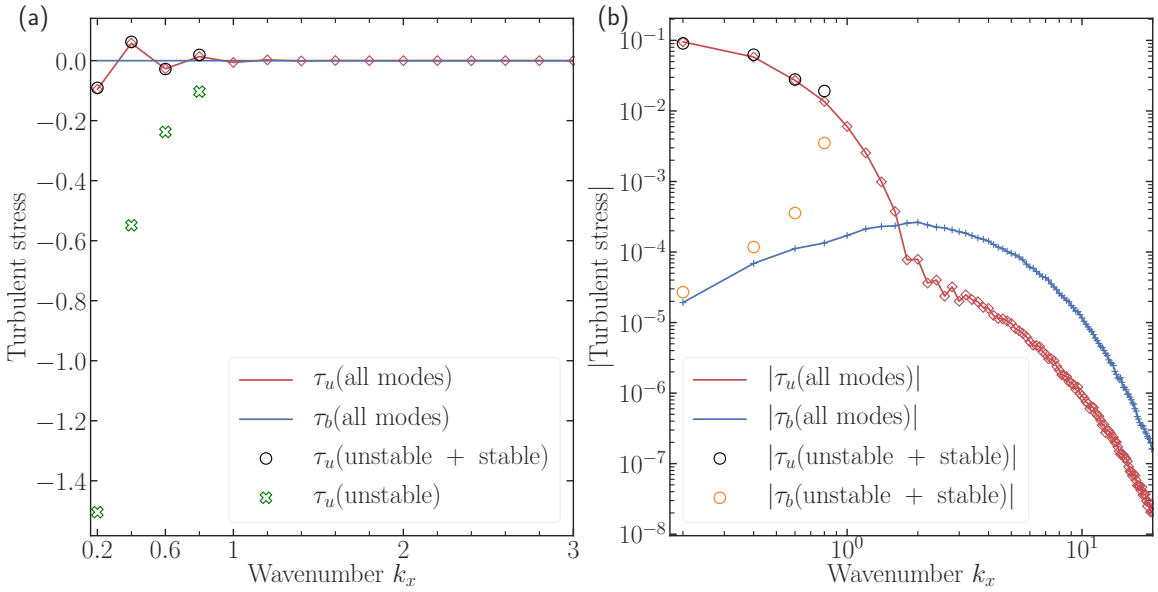

Figure 3.13: Time-averaged turbulent stresses split into their contributions from different wavenumbers. (a) Stresses on a linear scale. (b) Log-log representation of the absolute value of the stresses. Note that only the wavenumbers $k_x < 1$ are Kelvin-Helmholtz-unstable. The simulation parameters are $M_{\rm A} = 60$ and $D_{\rm Krook} = 2$; the time-average is taken over a quasi-stationary state of turbulence, $t = 350$–1000. The total turbulent stress is dominated by the range $|k_x| < 1$, which is captured by the unstable and stable modes at those wavenumbers to a high precision. The small amount of stresses that are contributed by smaller scales of fluctuations span a broad range of wavenumbers, due to the smaller scales in magnetic fields generated via straining by the flow.

realizable in systems with length- or time-scale separation. [126]

The magnetic fluctuations, on the other hand, span a broad range of scales. This can be physically interpreted as a result of the straining of the magnetic fields by the turbulent flow, which generates small scales in the magnetic fields.[70, 71, 115, 127] The straining process by the large-scale turbulent eddies converts the large-scale kinetic energy into the intermediate-scale magnetic energy. [128] Magnetic fluctuations at such scales can then, via Lorentz force, feed back on the flow, although mostly at smaller scales. A comprehensive analysis of energy transfer for the present system will be reported in a forthcoming publication where nonlinear mode-coupling and

energy transfer between fluctuations of discrete and continuum modes of velocity and magnetic fields are also analyzed.

To model any aspect of magnetic fluctuations, one must thus rely on tools such as statistical theories to obtain scaling laws that can offer insights into these fluctuations. One such approach is detailed next.

Scaling law for continuum modes

Until this point, the discrete modes—unstable and stable modes—which describe the turbulent flow well, have been our focus. The magnetic fluctuations, on the other hand, result from the straining of field lines by the flow, exciting the remaining continuum modes. Hence these modes are necessary for a successful reconstruction of the magnetic fluctuations. Thus, we seek a simple scaling law for the saturated turbulent amplitudes of the continuum modes.

Analytical prediction for continuum mode amplitudes

It is instructive to write the nonlinear MHD equations in the eigenmode basis, arriving at what is also referred to as the mode-amplitude evolution equation[15, 110, 112, 129, 130]

$$\partial_t \beta_j(k_x) = i\omega_j(k_x)\beta_j(k_x) + \sum_{\substack{k'_x,k''_x,m,n \\ k'_x+k''_x=k_x}} C_{jmn}(k_x,k'_x)\beta_m(k'_x)\beta_n(k''_x), \tag{3.23}$$

where $\beta_j(k_x)$ represents the complex amplitude of an eigenmode j at wavenumber k_x with ω_j the associated mode-frequency; the nonlinear mode coupling coefficient C_{jmn} measures the three-wave overlap, which dictates the strength of nonlinear beating between an eigenmode m at wavenumber k'_x and an eigenmode n at wavenumber k''_x, driving an eigenmode j at wavenumber k_x (with the constraint $k'_x + k''_x = k_x$).

For the continuum modes, as was mentioned in Sec. 3.3, their frequencies depend linearly on the wavenumber k_x as [124] $\omega/k_x + U_{\rm ref}(z) \pm v_{\rm A,ref}(z) = 0$. This implies $\omega_j = \omega \propto k_x$.

Heuristically, the scaling of the nonlinear mode coupling coefficient with wavenumber can be obtained in the following manner: In Eqs. (4.4a) and (4.4b), the separation of linear and nonlinear terms arises in Poisson brackets. Consider a prototype equation,

$$\begin{aligned} \partial_t \widetilde{P} &= \{P, Q\} + ... \\ &= \{\widetilde{P}, \widetilde{Q}\} + \{\widetilde{P}, Q_0\} + \{P_0, \widetilde{Q}\} + ..., \end{aligned} \tag{3.24}$$

where $P = P_0 + \widetilde{P}$ and $Q = Q_0 + \widetilde{Q}$ represent two fields (e.g., $\nabla^2\phi$ or ψ for the present problem), with P_0 representing the x-averaged mean component of P, and $\widetilde{P}$ standing for perturbations. The linear term, e.g., $ik_x\hat{P}\cdot\partial_z Q_0$ which is in spectral space, contains only one perturbed field, whereas the nonlinear term, e.g., $ik'_x\hat{P}'\cdot\partial_z\hat{Q}''$, has two perturbed fields, with $\hat{P}'$ and $\hat{Q}''$ representing the Fourier-transformed quantities at wavenumbers k'_x and k''_x, respectively. It may be supposed that the derivative ∂_z on the perturbed quantities is roughly on the scale of $|\partial_z| \sim k_x$. (This can be shown analytically for all the eigenmodes, where the background flow is approximately uniform, see Ref.[110].) Notice, however, that this argument applies only to the perturbations: the operator ∂_z acting on Q_0 clearly does not produce a factor of k_x, which is zero for the mean component Q_0. We now use this distinction to make a prediction for the amplitudes of perturbations, in particular the continuum mode-amplitudes. The linear and nonlinear terms thus assume the forms $ik_x\hat{P}\cdot\partial_z Q_0$ and $ik'_x\hat{P}'\cdot ik''_x\hat{Q}''$, respectively.

In Eq. 3.24, expanding the perturbations in the eigenmode basis, e.g., $\hat{P} = \sum_l \beta_l \hat{P}_l$ with $\hat{P}_l$ representing the l-th eigenmode, and diagonalizing the linear terms (operator),

one finds an equation of the form given in Eq. 4.11. We can now attempt to understand the behavior of the nonlinear mode coupling coefficients that drive the continuum modes. Assuming nonlinear interactions between the continuum modes are local in spectral space—interaction of three wavenumbers of similar scales—the nonlinear term in Eq. 3.24 simplifies, e.g., $ik_x'\hat{P}' \cdot ik_x''\hat{Q}''$ becomes $-k_x^2\hat{P}\hat{Q}$; note the linear term has the form $ik_x\hat{P} \cdot \partial_z Q_0$.

In assuming local interaction between the continuum modes spectral space in k_x, the involvement of unstable and stable modes in nonlinear interactions is ignored, which otherwise could bring in non-local effects. This may be a valid assumption for continuum modes at scales much above the Kelvin-Helmholtz-unstable wavenumber range, i.e., $k_x > 1$, as the wavenumber convolution constraint of $k_x = k_x' + k_x''$ does not allow two (un-)stable modes to beat together to drive a continuum mode at large k_x, e.g., $k_x > 2$.

Continuing with the above assumption, the nonlinear term $-k_x^2\hat{P}\hat{Q}$ has one extra k_x compared to the linear term $ik_x\hat{P} \cdot \partial_z Q_0$. This implies that, for the continuum modes, the nonlinear mode coupling coefficients C are expected to scale as

$$C \propto k_x^2, \tag{3.25}$$

because the linear term for the continuum modes in Eq. 4.11 has the eigenfrequency that depends linearly on k_x, i.e.,

$$\omega \propto k_x. \tag{3.26}$$

Such a property of nonlinear coupling coefficient is common in other turbulence calculations, as well. [32]

In order to obtain a phenomenological scaling law, we now make no distinction

between different continuum modes, and thus balance the linear and nonlinear terms of Eq. 4.11 in the quasi-stationary state as $\omega\beta \sim C\beta^2$. Inserting their asymptotic dependences on k_x, the amplitudes of continuum modes is found to follow

$$\beta \sim k_x^{-1}. \tag{3.27}$$

Note that the assumptions made in arriving at this simple scaling law are crude. The next step will be to determine from nonlinear simulations whether this scaling can be recovered or whether a number of assumptions made above render the result inapplicable.

Numerical verification

Time-averaged eigenmode amplitudes from nonlinear simulations, after multiplying with k_x, are plotted in Fig. 3.14(a) as functions of k_x and eigenmode index j, arranged in order of increasing real frequency of the eigenmodes. The appearance of vertical near-equicontour lines signifies that eigenmodes are excited in a similar pattern across a large range of scales.

The eigenmodes that lie within the yellow bands are localized in space (z-axis), but the band spans a range of heights, outside the shear layer $|z| < 1$. Empirically, we note that the center of the rightmost [leftmost] band corresponds to $\omega/k_x = U_{00}$ [$\omega/k_x = -U_{00}$] where $U_{00} = 1$. These thick bands represent all eigenmodes that have phase speeds $\omega/k_x = U_{00} + cv_{\mathrm{A},0}$ [$\omega/k_x = -U_{00} + cv_{\mathrm{A},0}$] where $-1 < c < 1$ and $v_{\mathrm{A},0} = 1/M_{\mathrm{A}}$; note that $|c| = 1$ is not included in these bands. All of these eigenmodes have peaks and oscillations in their eigenfunctions outside of the shear layer. In the layer, the unstable and stable modes maintain their dominance and thus these two discrete modes alone almost completely regulate the momentum transport across the

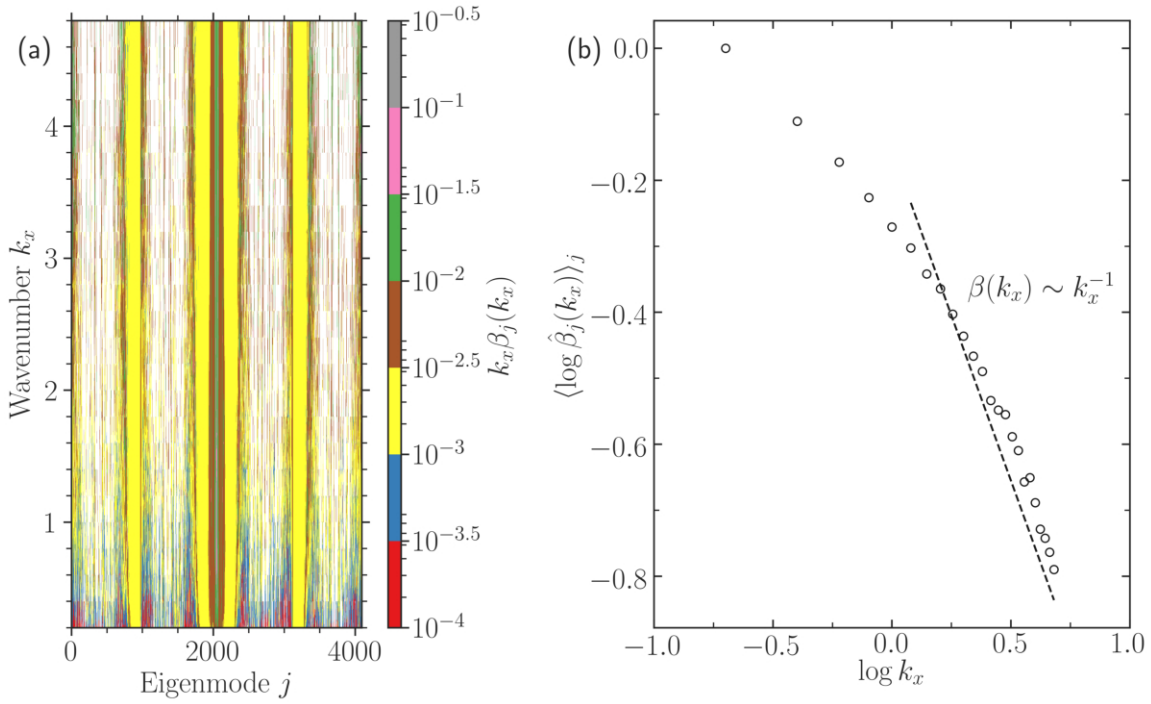

Figure 3.14: (a) Dependence of time-averaged eigenmode amplitudes on k_x. The indices js of the eigenmodes are arranged in increasing order of their real frequencies. Vertical lines signify the self-similar cascade of energy to small scales in k_x. Mode amplitudes are averaged over a quasi-stationary state of turbulence $t = 400$–800 for a simulation with $M_{\rm A} = 120$ and $D_{\rm Krook} = 2$. (b) k_x spectra of mode amplitudes in a nonlinear simulation (shown with empty circles) in a $\log_{10} - \log_{10}$ plot. Shown with a solid line is the analytical prediction, made for the wavenumbers that lie beyond the Kelvin-Helmholtz-unstable range, i.e., for $k_x > 1$. The spectral index, predicted based upon a number of simple assumptions, can be seen to fit the data reasonably well.

layer, as was noted in Sec. 3.5.

It is of interest now to compute from numerical simulation data how the amplitude of each eigenmode j falls off with k_x and construct a j-averaged spectral index. To this end, we note the amplitude $\beta_j(k_x = 0.2)$ for each mode j at $k_x = 0.2$ (the first wavenumber in the simulation) and compute a scaled mode-amplitude $\hat{\beta}_j(k_x)$ as

$$\hat{\beta}_j(k_x) = \frac{\beta_j(k_x)}{\beta_j(k_x{=}0.2)}, \tag{3.28}$$

which is expected to fall-off with k_x as $\sim k_x^{\alpha}$. In principle, the spectral index α can depend on the eigenmode index j, but a j-averaged spectral index is sought now, following the procedure

$$\begin{aligned} \hat{\beta}_j(k_x) &\propto (k_x/0.2)^{\alpha}, \\ \log \hat{\beta}_j(k_x) &\propto \alpha \log k_x, \\ \langle \log \hat{\beta}_j(k_x) \rangle_j &\propto \langle \alpha \rangle_j \log k_x. \end{aligned} \tag{3.29}$$

This j-averaged spectral distribution of the mode-amplitudes informs how, on average, each eigenmode amplitude depend on k_x.

A plot of $\langle \log \hat{\beta}_j(k_x) \rangle_j$ vs. $\log k_x$ is shown in Fig. 3.14(b), along with the analytical prediction of inverse-in-wavenumber fall-off of the mode amplitudes, at scales above the Kelvin-Helmholtz-unstable wavenumber range. It should be highlighted that the computation of all the eigenmode amplitudes at each wavenumber at each simulation time is computationally demanding, as the process requires the computation of modified left eigenmodes for each right eigenmode at each wavenumber, apart from the mode projection calculation at each time step. Therefore, only the first 24 Fourier modes in k_x are shown in Fig. 3.14.

A finding in Fig. 3.14 is the identification of self-similar cascade of energy to smaller scales (larger k_x) in *eigenmode space*. This result also hints that the interaction involving the continuum modes may be reasonably simplified, and potentially be valuable in estimating the amplitudes of unstable and stable modes, using closure theories (see Ref.[32] for a recent example).

3.6 Conclusions

We have investigated MHD turbulence in two-dimensions, driven by a forced unstable shear flow, using a complete eigenmode decomposition of fluctuations in nonlinear simulations, which exposes the nonlinearly saturated excitation level of each eigenmode and its role. Intrinsic to linear instability, the unstable modes derive fluctuation energy from the mean flow gradient. The linearly-decaying stable modes, however, contain almost the same amount of energy as the unstable mode, which they receive via nonlinear excitation. This truncated basis of two eigenmodes per wavenumber is found to reconstruct essential large-scale features of turbulent flow and the associated momentum transport via Reynolds stress. Quantifying transport due to unstable modes alone shows an overestimation up to an order of magnitude higher relative to the actual flux. The reduction in the flux is identified to be due to the continuous up-gradient transport by the stable modes, which causes a near-cancellation of down-gradient transport driven by unstable modes.

The continuum modes, on the other hand, describe small-scale fluctuations of the flow and magnetic field, where the above large-scale unstable and stable modes manifest themselves as a quasi-coherent vortex. To predict the mode amplitudes of the continuum, a simple scaling law is derived from the governing nonlinear equations and the predicted inverse-in-wavenumber fall-off rate is found reasonably agree with the simulation data.

Although both the momentum transport and fluctuation energy are largely described by the discrete modes, the former is more efficiently captured [Figs. 3.9–3.13] as almost all the momentum transport occurs near $z = 0$, which is the region where the discrete modes dominate [Figs. 3.1(b) and 3.1(c)]. The fluctuation energy, on the other hand, is related to fluctuations that are scattered in and around the large-scale

eddies; a portion of this energy is claimed by the continuum modes, although a large fraction still belongs to the discrete modes [Figs. 3.5(b), 3.6–3.8].

Transport reduction by stable modes can also be used to improve phenomenological constructs like eddy viscosity, which are generally agnostic as to the nonlinear excitation of stable modes. By predicting the turbulent amplitudes of the unstable and stable modes, for astrophysically relevant parameters, e.g., very large Rm, Re, Pm compared to unity, the simple relation between turbulent viscosity and eigenmode amplitudes [in Eq.(3.20)] can be exploited to reliably model transport processes in astrophysical objects, which otherwise cannot be solved using current state-of-the-art direct numerical simulations. It should be noted that such a prediction for the mode amplitudes $|\beta_1|$ and $|\beta_2|$ was recently made for ion-temperature-gradient-driven fusion plasma turbulence [88] using statistical closure theory. [33] Undertaking such a task for the present system is interesting, but beyond the purview of this work and will thus be left for future investigations.

The reduced representation of turbulent flow and transport presented here is also useful for building sub-grid-scale models, which can allow performing nonlinear simulations at extreme parameters with less-intensive computational demands. Progress can thus be made in seeking models that reduce the number of degrees of freedom while capturing essential features of the turbulent system. Techniques like proper orthogonal decomposition, dynamic mode decomposition, etc., also exist for such purposes, [131] but they operate on output from nonlinear simulations, and it can be difficult to assign intuitive physical meaning to the characteristic mode structures. Here, the truncated eigenmode basis, composed of the unstable and stable modes, has been demonstrated to reconstruct nonlinear fluctuations to an appreciable degree, thus suggesting that they can be leveraged as a physically-motivated basis for extreme parameter studies, without having to first perform a direct numerical simulation. These modes may

also be useful for generating, via their nonlinear interactions with continuum modes, fluctuations associated with the continuum modes. Such a test could be performed to analyze magnetic fluctuations. The reduced basis, composed of unstable and stable mode alone, can also serve in direct statistical simulations, [120] which have shown promises towards simulating the slowly-evolving turbulent statistics, e.g., two-point two-time correlations, three-point correlations between fluctuating fields, etc., rather than the fast-evolving field variables themselves, e.g., flow velocities. Other improved forms of quasilinear models like the generalized quasilinear approximation[126] may also benefit from using this truncated basis. This possibility will be explored in a separate publication.

In the future, procedures similar to that employed here can be used to examine the properties of other forms of instability-driven turbulence, such as magneto-rotational-instability-driven [27] and stratified-shear-flow-driven turbulence.[29] Building nonlinear energy transfer diagnostics in shear-flow turbulence to study the physical processes and scales that impact the difference in unstable- and stable-mode amplitudes is another possible avenue. Such investigations constitute steps towards deployment in service to one-dimensional stellar transport models. [26] Central to improved predictiveness are the stable modes, whose properties will similarly require additional studies.

Appendix A: Orthogonality of right eigenmode and modified left eigenmode

Due to the non-normality of the linear operator of the shear-flow instability, the eigenmodes are not orthogonal. This presents a significant challenge in the computation

of mode amplitudes. An additional challenge is the generalized eigenvalue nature of the problem at hand, when written in vorticity formalism, as in Eq. (3.6a). This differs from the standard eigenvalue problem, $L\xi_j = \lambda_j \xi_j$, where L is a linear operator whose j-th eigenmode is ξ_j with eigenvalue λ_j. The generalized eigenvalue problem that we encounter here is

$$LX_j = \omega_j M X_j, \tag{A1}$$

where L is a linear operator, M is another linear operator containing the Laplacian operation for our problem, X_j is the j-th (right) eigenmode with corresponding (right) eigenvalue ω_j. [Often times, the distinction between left and right eigenmodes of a linear operator is not made as they happen to be the same; however this is not the case here for the non-normal operator.] The right eigenmodes, although non-orthogonal to each other, can be made orthogonal with an appropriate weight factor to the left eigenmodes, which are solutions to another eigenvalue problem: [129, 130]

$$Y_j^{\mathrm{T}} L = \sigma_j Y_j^{\mathrm{T}} M. \tag{A2}$$

Here, Y_j^{T} is the transpose of the left eigenmode with its left eigenvalue σ_j. A slight reformulation is possible to this equation by taking Hermitian-transpose:

$$L^\dagger Y_j^* = \sigma_j^* M^\dagger Y_j^*. \tag{A3}$$

In the eigenvalue solver in Dedalus, the matrices $L^\dagger$ and $M^\dagger$ for each wavenumber are passed, and their eigenmodes Y_j^* and eigenvalues σ_j^* are found. It can be shown that the eigenvalues σ_j and ω_j are the same (i.e., $\sigma_j = \omega_j$), by analyzing Eqs. (9.21) and (9.22). A modified orthogonality relation between the left and right eigenmodes can

now be derived: [129, 130]

$$
\begin{aligned}
& (Y_j^{\mathrm{T}} L) X_i = Y_j^{\mathrm{T}} (L X_i) = Y_j^{\mathrm{T}} (\omega_i M X_i) \\
\implies & (\sigma_j Y_j^{\mathrm{T}} M) X_i = Y_j^{\mathrm{T}} (\omega_i M X_i) \\
\implies & Y_j^{\mathrm{T}} M X_i (\sigma_j - \omega_i) = 0 \\
\implies & Y_j^{\mathrm{T}} M X_i \propto \delta_{i,j}, \qquad \text{(A4)}
\end{aligned}
$$

which means the left and right eigenmodes are orthogonal to each other with a weight factor M, as long as their eigenvalues differ ($\sigma_j \neq \omega_i$). For numerical computation, it is convenient to define $Y_j^{\mathrm{T}} M = (M^{\mathrm{T}} Y_j)^{\mathrm{T}} = Z_j^{\mathrm{T}}$ where Z_j is the *modified* left eigenmode, which is—by construct—orthogonal to the right eigenmode without any weight factor: $Z_j^{\mathrm{T}} X_i \propto \delta_{i,j}$. Using this relation the eigenmode coefficients $\beta_j(k_x, t)$ in the eigenmode expansion of turbulent fluctuations are computed at each wavenumber and at each time.

Appendix B: Cyclic oscillations in mode-amplitudes for weak magnetic fields

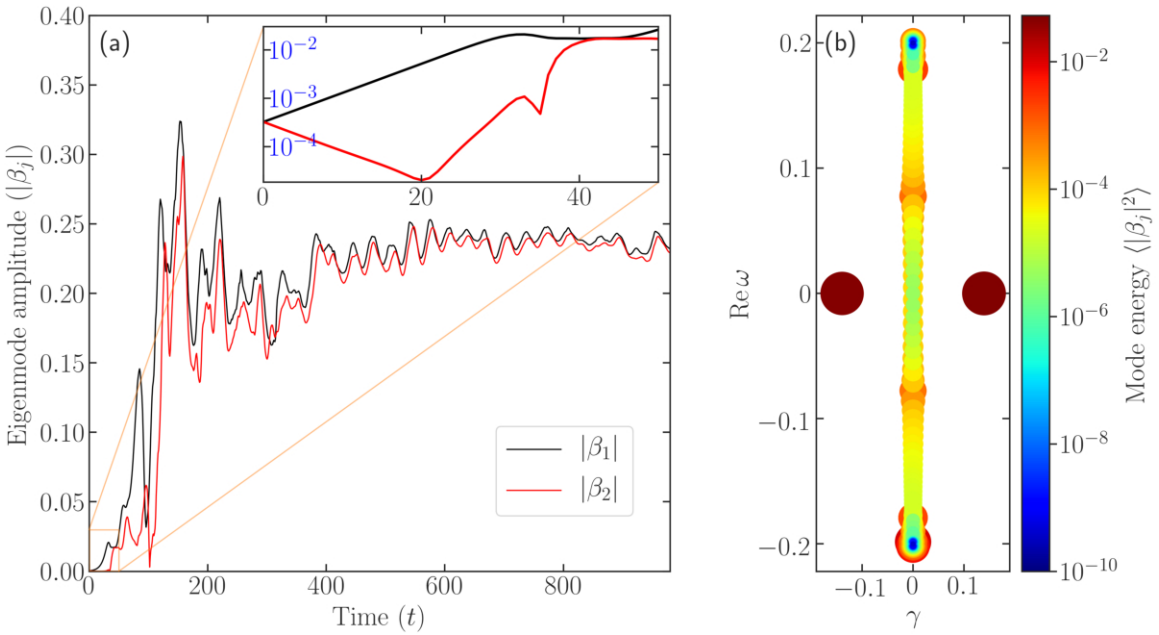

Figure B1: Same as in Fig. 3.5, but for $M_{\rm A} = 120$. The amplitude of the nonlinearly excited stable mode is almost exactly the same as that of the unstable mode. The nature of their oscillations is also similar, although the oscillations in the stable-mode-amplitude lags behind that of the unstable mode. The lag is likely an outcome of a time-delay in energy transfer from the unstable to the stable mode at the same wavenumber, which thus requires a series of nonlinear interactions with fluctuations at other wavenumbers.

4 **PAPER B**: MECHANISM FOR SEQUESTERING MAGNETIC ENERGY AT LARGE SCALES IN SHEAR-FLOW TURBULENCE

A version of this chapter was published in Phys. Plasmas (Letter) 29, 070701 (2022).

ABSTRACT

Straining of magnetic fields by large-scale shear flow, generally assumed to lead to intensification and generation of small scales, is re-examined in light of the persistent observation of large-scale magnetic fields in astrophysics. It is shown that, in magnetohydrodynamic turbulence, unstable shear flows have the unexpected effect of sequestering magnetic energy at large scales, due to counteracting straining motion of nonlinearly excited large-scale stable eigenmodes. This effect is quantified via dissipation rates, energy transfer rates, and visualizations of magnetic field evolution by artificially removing the stable modes. These analyses show that predictions based upon physics of the linear instability alone miss substantial dynamics, including those of magnetic fluctuations.

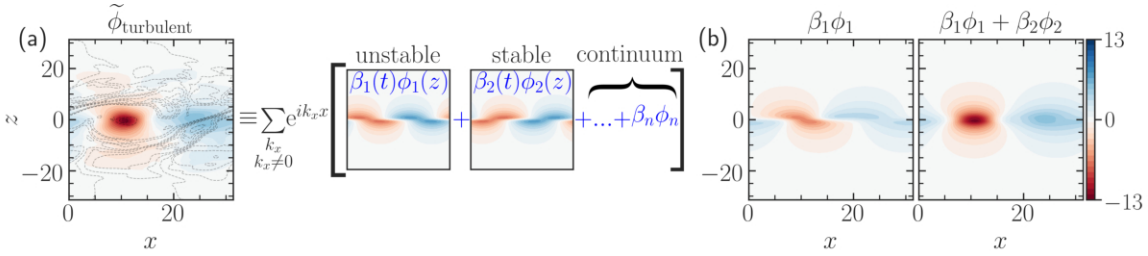

Figure 4.1: (a) Eigenmode decomposition of a characteristic snapshot of the turbulent flow, represented by the solid- and colored-contour lines of the stream function $\widetilde{\phi}_{\text{turbulent}}$ at time $t = 625$, with $M_{\text{A}} = 10$. The decomposition is based on a complete set: unstable, stable, and continuum eigenmodes. The eigenmodes plotted are for the flow fluctuations at the first Fourier wavenumber. The black dashed-contour lines overplotted on the first image show the turbulent magnetic flux function $\widetilde{\psi}_{\text{turbulent}}$, whose distortion near the center of the eddy, $(x, z) \approx (10, 0)$, is significantly impeded. (b) Reconstruction of the turbulent flow: (left) sum of unstable eigenmodes at each Kelvin-Helmholtz-unstable wavenumber; (right) improvement by adding their conjugate stable eigenmodes. Compare these with full $\widetilde{\phi}_{\text{turbulent}}$ in (a). The difference between the plots (a) and (b) are shown in the supplementary material. All panels here share the same colorbar.

Turbulence is a fundamentally multiscale process in which nonlinear dynamical motions carry energy across scales [132]. One of the most robust and extensively studied mechanisms for cross-scale energy transfer is straining by shear flow [70, 127], long recognized for its role in cascades to small scale [71]. This process is especially active in magnetohydrodynamic (MHD) turbulence [133]. The stretching, squeezing, and folding of magnetic field lines by shear flow is readily discernible in visualizations, and leads to, for example, the enhancement of small-scale resistive dissipation and the intensification of magnetic energy at small scales beyond the viscous cutoff in turbulence with magnetic Prandtl number greater than unity [115, 133]. The ubiquity of turbulence and turbulent straining is at odds with the well-established observations of magnetic fields at large scales in the universe (stellar, galactic, and beyond) [39, 134] and part of a conundrum as to how magnetic fields exist at such large scales [8, 42, 43].

In this Letter we report the first observations that magnetic energy is, to a

considerable degree, counterintuitively sequestered at large scales in straining by a paradigmatic turbulent shear flow. The result applies to a Kelvin-Helmholtz- (KH-)unstable flow maintained by an external force with a uniform magnetic field that is initially flow-aligned and therefore optimally configured to promote small-scale generation.

The process that counteracts the small scale generation of magnetic energy, which is quantified in this Letter, can be traced to the nonlinear excitation of large-scale stable linear eigenmodes [93]. The dispersion relation that is associated with the shear-flow instability present in this study has a stable (damped) root, which acts to return energy and momentum to the mean profile, and which is excited to a high level by the nonlinearity [110, 111]. The nonlinear excitation of stable modes and its effect on turbulence levels and transport have been studied previously, particularly in the context of fusion-relevant gyroradius-scale turbulence [15, 32, 89–93, 97–99]. Recent studies have shown that stable modes are excited in macroscopic shear-flow driven turbulence also and transiently affect momentum transport [110, 111]. However, critical features of counteracting straining motion of the stable modes, essential for large-scale sequestering of magnetic energy, have only come to light in the study described here.

To whit, stable-mode effects have been linked to small-scale dissipation [92], suggesting that they affect turbulence only if there is an increase in entropy. However, we show here that the reversible process by which stable modes return energy to the mean flow, in opposition to extraction by the instability, is quite effective at blunting the energy cascade to small scales. Stable modes have been connected to the shear-layer contraction (i.e., build up of mean flow) [111], but only as a transient process. Here we demonstrate that for a driven flow profile, the return of fluctuation energy to the mean profile occurs continuously at a rate that nearly matches the rate

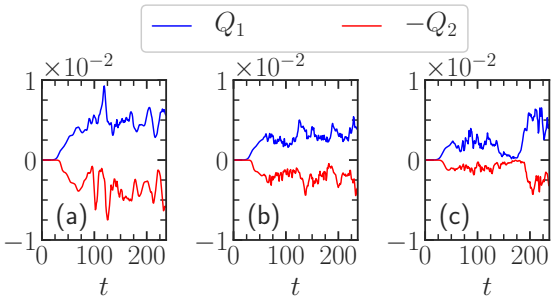

Figure 4.2: Time trace of Q_1 (blue) vs. $-Q_2$ (red) for (a) $Pm = 0.1$, $Rm = 50$; (b) $Pm = 1$, $Rm = 500$; (c) $Pm = 10$, $Rm = 5\,000$. Compare the lower (red) with upper (blue) curves within *each* subplot. To illustrate similar variation of Q_1 and Q_2, and to make the variations maximally visible, we plot $-Q_2$, which physically refers to the energy transfer rate from the fluctuations to the mean profiles. Computationally demanding simulation for (c) was stopped at $t = 237$. All simulations use $M_\mathrm{A} = 10$. Nonlinear phase begins at $t \sim 30$. Energy available for cascading to small scales is significantly impeded by stable modes in all cases.

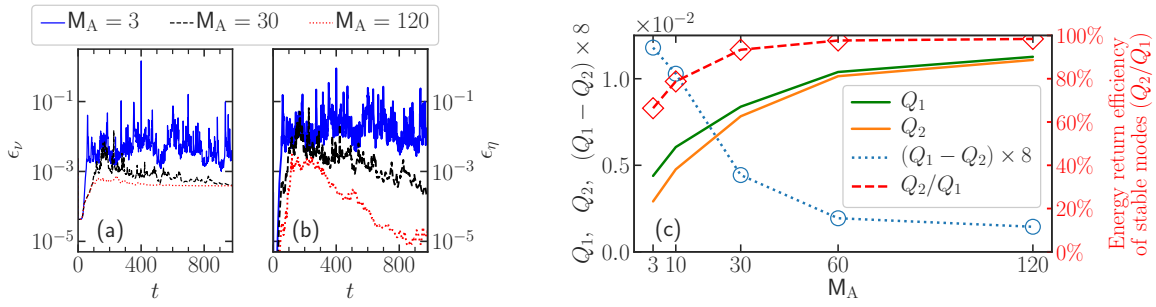

Figure 4.3: Time traces of (a) viscous dissipation rates, ϵ_ν, and (b) resistive dissipation rates, ϵ_η, for different strengths of magnetic fields. Stronger fields enhance both. (c) Impact of magnetic fields on the (time-averaged) energy transfer rates between the background profile ($k_x = 0$) and the large-scale fluctuations ($k_x = 0.2$–0.8) by the unstable eigenmodes Q_1 and by the stable eigenmodes Q_2. Note that the magnetic fields impact Q_2 more than Q_1, but Q_2/Q_1 is still $\gtrsim 60\%$ even for the strongest field.

at which unstable modes attempt to flatten the flow profile.

The principal result of this Letter is that, in driven shear-flow MHD turbulence, the nonlinearly excited large-scale stable eigenmodes efficiently strain the magnetic fields, in a way that counteracts the effect of unstable modes, and thus greatly weakens the magnetic energy cascade to small scales.

We study an incompressible, two-dimensional (2D) system with the initial fluid

velocity given as $\mathbf{v}(x, z, t = 0) = U_{\rm ref}(z)\hat{\mathbf{x}} = U_0 \tanh(z/a)\hat{\mathbf{x}}$ and an initially uniform flow-aligned magnetic field as $\mathbf{B}(x, z, t = 0) = B_0\hat{\mathbf{x}}$. The parameters $a, U_0,$ and B_0 represent the half-width of the flow-shear, the maximum fluid velocity, and the magnetic field strength, respectively, which are used to non-dimensionalize all the variables henceforth. Consequently, time and energy (per unit mass) have units of a/U_0 and U_0^2. We describe the flow and the magnetic field by a stream function ϕ and a flux function ψ, where $\mathbf{v} = \hat{\mathbf{y}} \times \nabla\phi$ and $\mathbf{B} = \hat{\mathbf{y}} \times \nabla\psi$. We study their evolution using the momentum and induction equations of the standard MHD [25**?**]

$$\partial_t \nabla^2\phi = -\{\nabla^2\phi, \phi\} + M_{\rm A}^{-2}\{\nabla^2\psi, \psi\} + Re^{-1}\nabla^4\phi + \partial_z f(k_x{=}0, z, t), \tag{4.1a}$$

$$\partial_t \psi = \{\phi, \psi\} + Rm^{-1}\nabla^2\psi, \tag{4.1b}$$

where $\nabla^2\phi$ and $\nabla^2\psi$ are the vorticity and the current density; Poisson bracket $\{P, Q\} \equiv \partial_x P \cdot \partial_z Q - \partial_x Q \cdot \partial_z P$; the Alfvénic Mach number is $M_{\rm A} \propto U_0/B_0$; the fluid and magnetic Reynolds numbers are defined as $Re = U_0 a/\nu$ and $Rm = U_0 a/\eta$. In this study, we take $Re = 500$. Except for simulations where $Rm = 50$ and $Rm = 5\ 000$ (which will be stated explicitly), all others have $Rm = 500$. In Eq. (4.4a), f represents a body force that continuously regenerates the mean-flow shear. The expression $k_x{=}0$ in it indicates that the force acts only on the (x-averaged) mean flow, where k_x is the Fourier wavenumber. The forcing thus prevents gradual flattening of the mean flow as the instability extracts energy from it. A similar process occurs in astrophysical flows, where forces like gravitation replenish continually the shear profile, e.g., shear layers in accretion disks, stars, and planetary atmospheres. We represent this force by a

Krook-like operator [117–119], sometimes referred to as a profile relaxation term [120],

$$f = D_{\rm Krook}[U_{\rm ref}(z) - \langle U(x,z,t)\rangle_x] + F_0, \tag{4.2}$$

where $D_{\rm Krook}$ represents the rate at which the mean flow is forced towards the reference flow profile. We choose $D_{\rm Krook} = 2$. Detailed analyses of a complete scan of different parameters will be reported elsewhere. The force F_0 balances the viscous diffusion of the mean shear layer, $Re^{-1}\nabla^2 U_{\rm ref}(z) + F_0 = 0$, in Eq. (4.4a), to ensure an initial equilibrium state.

We add small-amplitude perturbations to the flow and the magnetic field [111**?**] and perform time-integration of the above set of equations using the pseudospectral code Dedalus [121] for long times ($t > 1000$; the e-folding growth time of the instability is ≈ 6). Apart from the simulation of $Pm = 10$ that uses spectral resolution of 4096 Fourier (Chebyshev) modes along the x-(z-)axis for the box size of $(L_x, L_z) = (6\pi, 8\pi)$, all other simulations are performed at 2048×2048 spectral resolution for the box size of $(L_x, L_z) = (10\pi, 20\pi)$, while convergence checks utilize resolutions as high as 8192×8192, with no substantial impact on dissipation rates and spectral energy densities. (All simulations additionally use 3/2 dealiasing rule [121]).

We also perform a corresponding eigenvalue calculation of the non-dissipative equations, derived from Eqs. (4.4a) & (4.4b), by linearizing about the initial flow and magnetic field profiles [111]. *A priori*, one does not know whether such an eigenmode basis is useful to understand turbulent features. Nevertheless, since the eigenmodes of this linear operator form a complete (albeit non-orthogonal) basis [122**?**], we can expand the time-evolving state space of nonlinear simulations in this basis after determining amplitude $\beta_j(k_x, t)$ of each eigenmode j at each k_x as a function of time, $\widetilde{\chi}_{\rm turbulent}(x,z,t) = \sum_{k_x:k_x\neq 0} e^{ik_x x}\left[\sum_j \beta_j(k_x,t)\chi_j(k_x,z)\right]$, where

$\widetilde{\chi}_{\rm turbulent} = (\widetilde{\phi}_{\rm turbulent}, \widetilde{\psi}_{\rm turbulent})$ captures the turbulent state space and χ_j is the $j^{\rm th}$ eigenmode [111, 135**? ?**]. This procedure is illustrated in Fig. 10.1(a) where the eigenmodes of the flow fluctuations are shown. (The magnetic fluctuations have eigenmodes [111] and parity [136, 137] related to those of the flow fluctuations.)

At each wavenumber k_x, linearly unstable to perturbations (i.e., $0 < k_x < 1$ for the present shear-flow instability), there is an unstable eigenmode ϕ_1 and its conjugate stable eigenmode ϕ_2, with eigenvalues complex conjugate to each other [110, 113]. All the remaining eigenmodes have purely real eigenfrequencies [135], belong to the continuum [124], and have narrow structures along the z-axis.

Tracking the time evolution of each eigenmode amplitude $\beta_j(k_x, t)$ in the nonlinear simulations, the initially exponentially decaying mode has been found to be nonlinearly excited to almost the same level as the unstable mode [111]. The driving mechanism for this excitation is, at early times, the nonlinear interaction between the unstable modes, see, e.g., Refs. [15, 98, 111]. In the fully nonlinear phase, however, all modes that have large energy interact dominantly.

For a given KH-unstable wavenumber, it is found, in Fig. 10.1(b), that a combination of two eigenmodes from the above basis reconstructs the large-scale turbulent flow at that wavenumber. Figure 10.1(b) shows a reconstruction of the turbulent flow features using unstable eigenmodes at each unstable wavenumber (left column) and with their conjugate stable eigenmodes added (right column). Simply adding one additional mode drastically decreases the difference between the true stream function and its reduced representation compared to what is achieved with a reduced representation based on the unstable modes alone (such as those predicted by quasilinear models) [**?**].

Note that the stable and unstable eigenmodes of the KH linear operator, employed above, are related to one another by a space-time-reversal symmetry operation [16, 122].

Thus the unstable and stable eigenmodes transfer energy in opposite directions—the former from the mean flow to the fluctuations, while the latter in the reverse direction. The energy that is available to cascade to small scales thus depends on this competition. The magnitude of the energy transfer rates between the background shear-flow $U_{\rm ref}$ and the fluctuation scale $k_x \neq 0$ by the unstable and stable eigenmodes can be derived from the MHD equations [**?**]: $Q_1(k_x) = \Gamma(k_x)|\beta_1(k_x)|^2$ and $Q_2(k_x) = \Gamma(k_x)|\beta_2(k_x)|^2$ where $\Gamma(k_x)$ is the linear growth rate of the unstable mode at that wavenumber k_x.

Shown in Fig. 10.2 are the time traces of Q_1 and Q_2 for different Pm (resistivity) over a challenging two orders of magnitude. Summation over the KH-unstable wavenumbers, $0 < k_x < 1$, is used in determining Q_1 and Q_2. Within each subplot, it is observed that Q_1 and Q_2 are nearly in equipartition in the nonlinear phase.

Stable-mode-excitation process may also be impacted by magnetic fields. To analyze such, we first observe the visco-resistive dissipation with varying field strengths in Figs. 10.3(a) and (b). The small-scale dissipation—a proxy of small-scale cascade—enhances with stronger fields, despite the fields reducing the linear growth rate of the instability, which sometimes is argued to lead to subdued turbulent fluctuations as the energy extraction rate by the unstable mode becomes lower.

To understand such enhanced dissipation rate, it may be instructive to compute the energy transfer rates between the background flow and the fluctuations due to both the unstable and stable eigenmodes. As seen in Fig. 10.3(c), the (time-averaged) energy injection rate by the instability, Q_1, decreases with stronger magnetic fields, as anticipated. However, the energy return rate by the stable modes, Q_2, is impacted more by the stronger fields, allowing larger energy cascade to small scales ($\propto Q_1 - Q_2$) that manifests as enhanced dissipation rate at such scales [**?**]. Thus a stronger magnetic field, until it nearly stabilizes the system, allows more net energy extraction from the free-energy source in the *non*linear state. This questions models that assume

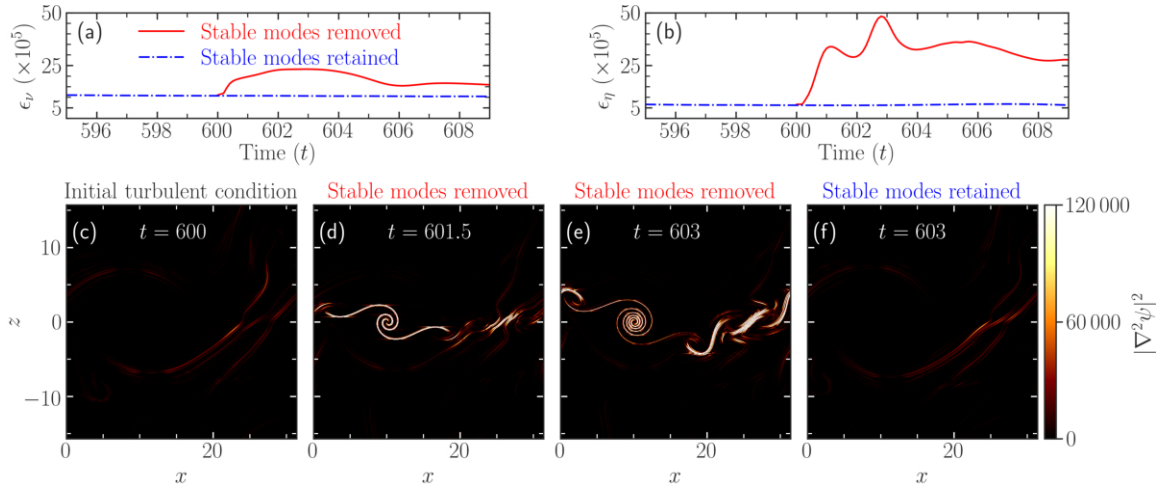

Figure 4.4: (a) Enhancement of the viscous dissipation rate, after removing the large-scale stable eigenmodes at an instant of time $t = 600$ in a simulation with $M_\mathrm{A} = 120$. (b) Similar enhancement of the resistive dissipation. (c) The state when the simulation is paused. Shown is the squared current density at smaller scales, $|k_x| > 1$, focusing on the region near the shear layer, $-5\pi \leq z \leq 5\pi$. At this instant, the large-scale stable modes belonging to $|k_x| < 1$ are deleted to observe their influence on the small-scale magnetic cascade. (d)–(e) Subsequent evolution of the small-scale current density when large-scale stable eigenmodes are removed at $t = 600$. The characteristic enfolding of magnetic fields by the eddies of unstable modes is evident, which generates small-scale magnetic features. (f) Small-scale current density in another simulation where stable eigenmodes are kept intact. The rapid straining of magnetic fields mentioned just before does not occur. For this simulation, the state at $t = 601.5$ (not shown) is almost identical to that at $t = 603$. (Multimedia view)

the linear growth rate of an instability as a surrogate for the cascade rate or a proxy for nonlinear time, see, e.g., [26–29]. Predictions based upon conventional wisdom of instability-saturation are thus challenged.

The ratio Q_2/Q_1 of the stable-eigenmode efficiency to the unstable-eigenmode efficiency in transferring energy between the fluctuations and the background flow is more than 60% even for the strongest magnetic fields in Fig. 10.3(c), see the red dashed line. Such a strong Lorentz back-reaction is most potent in disrupting the vortex [114] and creating more small scales, leading to more reduced Q_2 than the corresponding reduction in Q_1.

We now show visualizations of highly effective role of stable modes in structuring the magnetic fields. After carrying out an initial-value simulation up to a time when the dynamics are nonlinear and turbulent, we perform two distinct simulation continuations—one unchanged with the stable modes untouched, and another with the stable modes removed. For the latter, we set only the large-scale ($0 < |k_x| < 1$) stable-eigenmode amplitudes to zero at the instant when the simulation is restarted. The differences immediately afterward are significant: Removing stable eigenmodes rapidly enhances dissipation rates, see Figs. 10.4(a) and (b); (Multimedia view). To understand this rise in the dissipation, we plot the squared current density $|\nabla^2\psi|^2$ at small scales ($|k_x| > 1$) in Figs. 10.4(c)–(f). Observe in Figs. 10.4(d) and (e) that the magnetic fields get rapidly distorted by the unstable modes of the flow, creating spirals as the counter-straining motion of the stable modes is removed. Note that the (un)stable modes have the largest strain around $(x, z) \approx (10, 0)$ for the shown time, as can also be seen in the figure in the supplementary material. The stable modes here are deleted only at the instant when the simulation is paused; they are quickly nonlinearly driven back. In another simulation where the stable modes are untouched (retained), the spirals do not appear, however, and the time evolution immediately afterward remains almost identical to the initial stage [cf. Figs. 10.4(f) and Fig. 10.4(c)]. This exercise of instantaneous deletion of stable modes exposes the true nonlinear impact of the stable modes on magnetic field evolution, which remained hidden in Fig. 10.1(a).

This numerical experiment illustrates that the energy injected by the unstable modes into the large-scale fluctuations ($|k_x| < 1$) via mean-fluctuation interactions, *in the absence of stable modes*, cascades in its entirety to smaller scales nonlinearly where it dissipates visco-resistively. This is a statement of the classical small-scale cascade by the advective nonlinearity, $(\mathbf{v} \cdot \nabla)\psi$, as commonly understood. When $\mathbf{v}$ is composed

of comparable unstable and stable mode-amplitudes, though, the cascade is weakened by a factor of up to ten [Figs. 10.2, 10.3(c), and 10.4(b)]. Such a finding informs and can be used to improve reduced models of geo- and astrophysical instability-driven turbulence [26, 106], where all the energy injected by the instability is assumed to pass through an inertial cascade, e.g., Refs. [26–29].

It may be noted that, although 2D and 3D turbulence have different conserved quantities and corresponding cascade processes, the stable modes of this study are the conjugate roots of the KH-instability, which exist in both 2D and 3D [113]. Our preliminary studies of 3D turbulence have indeed shown that virtually identical stable mode excitation and its impact in turbulence occur in 3D as well. Details of such an investigation will be left for a future publication [138].

This Letter demonstrates, for the first time, that stable modes via their counteracting straining motion of the flow, sequester magnetic energy at large scales, despite the conventional association of shear-flow with intensification and generation of small scales in MHD turbulence. Our analyses show that the stable modes greatly weaken the magnetic energy cascade to small scales and hence can thwart the magnetic-energy accumulation at sub-viscous scales in the high-magnetic-Prandtl-number regime, typically encountered in diffuse astrophysical plasmas; thus possibly allowing operation of a dynamo with magnetic fields concentrated at large scales, in accord with astrophysical observations [42, 115]. This work opens a new direction towards such studies.

Supplementary Material

See the supplementary material for the details of (I) simulation set-up, (II) modal energy evolution equation, (III) energy transfer rates between the background flow and the fluctuations, and (IV) residuals in low-order representation of the turbulent

flow in Fig. 10.1(b). A simulation movie supplements Fig. 10.4 of this Letter.

This document provides supplemental information related to the article "Mechanism for Sequestering Magnetic Energy at Large Scales in Shear-Flow Turbulence." Section I details the simulation set-up. Section II presents the evolution equation for the modal energy, whenceforth an expression for the energy transfer between the background flow and the fluctuations is derived in Sec. III, which is numerically computed and plotted in Figs. 2 and 3 of the main article. In Sec. IV, residuals in low-order representation of the turbulent flow are compared.

I. Simulation set-up and details

We consider standard incompressible magnetohydrodynamic (MHD) equations

$$\nabla \cdot \mathbf{u} = 0, \tag{4.3a}$$

$$\partial_t \mathbf{u} + \mathbf{u} \cdot \nabla \mathbf{u} = -\frac{\nabla P}{\rho} + \frac{(\nabla \times \mathbf{B}) \times \mathbf{B}}{4\pi\rho} + \nu \nabla^2 \mathbf{u} + \mathbf{f}, \tag{4.3b}$$

$$\nabla \cdot \mathbf{B} = 0, \tag{4.3c}$$

$$\partial_t \mathbf{B} = \nabla \times (\mathbf{u} \times \mathbf{B}) + \eta \nabla^2 \mathbf{B}, \tag{4.3d}$$

where $\mathbf{u}$, $\mathbf{B}$, P, ρ, ν, η, $\mathbf{f}$ represent the fluid velocity, magnetic field, pressure, fluid density, viscosity, resistivity, and force per unit mass of the magneto-fluid respectively. Henceforth, we confine ourselves to a two-dimensional (x, z) system with the initial fluid velocity given as $\mathbf{v}(x, z, t = 0) = U_{\text{ref}}(z)\hat{\mathbf{x}} = U_0 \tanh(z/a)\hat{\mathbf{x}}$ and an initially-uniform flow-aligned magnetic field as $\mathbf{B}(x, z, t = 0) = B_0\hat{\mathbf{x}}$. The parameters $a, U_0,$ and B_0 represent the half-width of the flow-shear, maximum fluid velocity, and magnetic field, respectively. These parameters are utilized to non-dimensionalize all the variables and

calculations henceforward.

The two-dimensional system allows us to employ a more convenient and economical formalism, using stream function (ϕ) and flux function (ψ). Define $\mathbf{u} = \hat{\mathbf{y}} \times \nabla\phi$ and $\mathbf{B} = \hat{\mathbf{y}} \times \nabla\psi$ so that the vorticity is $\nabla^2\phi$ and the current density is $\nabla^2\psi$. Taking the curl of Eq. (5.1a) and rewriting Eq. (5.1b) in terms of the flux function, we arrive at (with all quantities non-dimensionalized with respect to U_0, a, $M_\mathrm{A} \propto U_0/B_0$)

$$\partial_t \nabla^2\phi + \{\nabla^2\phi, \phi\} = M_\mathrm{A}^{-2}\{\nabla^2\psi, \psi\} + Re^{-1}\nabla^4\phi + \partial_z f(k_x{=}0, z, t), \tag{4.4a}$$

$$\partial_t \psi = \{\phi, \psi\} + Rm^{-1}\nabla^2\psi, \tag{4.4b}$$

where the external body force is considered to be $\mathbf{f} = f(k_x{=}0, z, t)\ \hat{\mathbf{x}}$, which acts on the instantaneous mean flow and is directed along the x-axis. Here, k_x stands for the Fourier wavenumber.

These equations are solved using the pseudospectral code Dedalus, with dealiasing according to the standard 3/2 rule. Explicit viscosity and resistivity are used throughout all simulations. The fluid and magnetic Reynolds numbers are defined as $Re = U_0 a/\nu$ and $Rm = U_0 a/\eta$, with shear-width a as the characteristic length scale. Throughout this study, we consider $Re = Rm = 500$, except for two cases where Rm is changed to $Rm = 50$ and $Rm = 5\,000$, which are explicitly mentioned in Fig. 2 of the main article.

The simulation box is of size $(L_x, L_z) = (10\pi, 20\pi)$, unlike $(10\pi, 10\pi)$ in a previous study [111]. The box is considered taller along the z-axis to keep any potential effect of the boundary on turbulent dynamics as minimal as possible. The vortices in the simulations are observed to be located near the shear layer and thus far from the boundaries. The simulations are then performed using the least spectral modes/resolution of $(N_x, N_z) = (2048, 2048)$. Note that Dedalus uses spectral basis

to solve the nonlinear partial differential equations [121]. We employ Fourier modes along the x-axis and Chebyshev polynomials along the z-axis. The smallest Fourier wavenumber in our simulations is $k_x = 2\pi/L_x = 0.2$. The boundary conditions used are periodic in x and for the z-axis, perfectly conducting, no slip, co-moving [with the initial fluid flow, $\mathbf{v}(z, t = 0)$] walls at $z = \pm L_z/2$ are used as in Ref. [111].

We use the following forms of the initial perturbations to start the simulations, by exciting all Fourier wavenumbers as a generalization [111] to many routinely studied form of initial perturbations that excite only a particular or a few Fourier wavenumbers

$$\phi(x, z, t = 0) = A_\phi \sum_{k_x \neq 0} k_x^a e^{i r_\phi(k_x)} e^{-z^2/\sigma^2} e^{i k_x x}, \tag{4.5}$$

and

$$\psi(x, z, t = 0) = A_\psi \sum_{k_x \neq 0} k_x^a e^{i r_\psi(k_x)} e^{-z^2/\sigma^2} e^{i k_x x}. \tag{4.6}$$

Here, A_ϕ and A_ψ set the overall amplitude of the perturbations for the stream function (ϕ) and flux function (ψ); a dictates the steepness of the energy spectrum in the initial perturbations; σ determines the width of the Gaussian profile of the perturbation in the z-axis; $r_\phi(k_x)$ and $r_\psi(k_x)$, defined at each Fourier wavenumber k_x, are different random phases, selected from a pesudo-random number generator, which are uniformly distributed between $[0, 2\pi)$. For the simulations reported here, $a = -1$, $\sigma = 2$, and $A_\phi = A_\psi = 10^{-3}$ were considered, allowing a markedly defined linear evolution phase of the instability.

II. Modal energy evolution equations

Here, we derive rates at which *each eigenmode* gains or gives away energy at any instant in time. Denoting this energy transfer rate by $\dot{E}_j(k_x)$ where j represents an

arbitrary eigenmode at the Fourier wavenumber k_x, we may write an expression for the energy evolution rate (the energy spectrum is symmetric across $k_x = 0$ and hence the $-k_x$ and $+k_x$ have the same energy)

$$\begin{aligned}\dot{E}_j(k_x) &= \frac{dE_j^{\text{Kinetic+Magnetic}}(k_x)}{dt} \\ &= \frac{1}{2}\frac{d}{dt}\left[\frac{1}{L_z}\int dz\left(\frac{|\mathbf{u}_j(k_x)|^2}{2} + \frac{|\mathbf{B}_j(k_x)|^2}{2M_{\text{A}}^2}\right)\right] \\ &= \frac{1}{4L_z}\frac{d}{dt}\left[\int dz\left\{|\beta_j i k_x \phi_j|^2 + |\beta_j \partial_z \phi_j|^2 + \frac{1}{M_{\text{A}}^2}\left(|\beta_j i k_x \psi_j|^2 + |\beta_j \partial_z \psi_j|^2\right)\right\}\right],\end{aligned} \tag{4.7}$$

where $\beta_j = \beta_j(k_x)$ is the amplitude of the j^{th} eigenmode, i.e., $[\phi_j, \psi_j] = [\phi_j(k_x), \psi_j(k_x)]$ at the Fourier wavenumber k_x. The last equality of Eq. (4.7) can be rewritten in a more insightful way as

$$\dot{E}_j(k_x) = \frac{1}{2}\frac{d|\beta_j(k_x)|^2}{dt} n_j, \tag{4.8}$$

with

$$n_j = \frac{1}{2L_z}\int dz\left\{|k_x \phi_j|^2 + |\partial_z \phi_j|^2 + \frac{1}{M_{\text{A}}^2}\left(|k_x \psi_j|^2 + |\partial_z \psi_j|^2\right)\right\}. \tag{4.9}$$

Here, n_j represents the amount of total energy residing in each normalized eigenmode (or eigenfunction). If the energy norm is taken to normalize the eigenmodes, this quantity is automatically **unity**. So,

$$n_j = 1. \tag{4.10}$$

If another norm like L_2 is employed, this quantity has to be evaluated separately. Note, however, that the energy transfer rate, $Q_j(k_x)$, is independent of the choice of the norm. This is because one can switch from an arbitrary norm to the energy norm by dividing the eigenfunctions by the ratio, $r = \sqrt{n_j \text{ in arbitrary norm}/n_j \text{ in energy norm}} =$

$\sqrt{n_j \text{ in arbitrary norm}}$ and multiplying the eigenmode amplitudes in the eigenmode expansion by the same ratio. For example, the eigenmode expansion, defined in a basis, $\chi_j = (\phi_j, \psi_j)$, with an arbitrary norm can be written as $\chi_{\text{any fluctuation}} = \beta_1\chi_1 + \beta_2\chi_2 + ... = 2\beta_1(\chi_1/2) + 2\beta_2(\chi_2/2) + ... = 3\beta_1(\chi_1/3) + 3\beta_2(\chi_2/3) + ... = r\beta_1(\chi_1/r) + r\beta_2(\chi_2/r) + ...$ where r was defined just before and the last expansion, $\chi_{\text{any fluctuation}} = r\beta_1(\chi_1/r) + r\beta_2(\chi_2/r) + ...$, is the one that we encounter in the eigenmode expansion with the energy norm. Alternatively, χ_j in the energy norm = χ_j in an arbitrary norm/r, and β_j in the energy norm = $r \times \beta_j$ in an arbitrary norm. In Eq. (4.8) above, the normalization factor r, however, cancels out as the physical transfer of energy should be independent of the normalization used. Equation (4.8) requires a knowledge of how the eigenmode amplitude $|\beta_j|$ evolves with time. This portion will be achieved in the next section.

III. Energy transfer rates between the background flow and the fluctuations

The governing nonlinear partial differential equations, which are the MHD equations for our case, can be cast onto their linear eigenmode basis from the physical (x, z)-space. This is a mere change of basis and one, therefore, obtains an equivalent set of dynamical equations. Details on how to do so in simplified problems can be found in Refs. [15, 32, 110]. This same procedure has been much utilized in many problems of homogeneous turbulence including homogeneous MHD turbulence where Elsasser variables are realized as linear eigenmodes of the system. Techniques similar to this were also applied in nonlinear tidal instabilities [139]. For quadratic nonlinearity with inhomogeneity along the z-axis, the evolution equation for the eigenmode amplitude,

$\beta_j(k_x)$, assumes the following general form

$$\partial_t \beta_j(k_x) = i\omega_j(k_x)\beta_j(k_x) + \sum_l D_{jl}(k_x)\beta_l(k_x) + \sum_{\substack{k'_x,k''_x,l,m \\ k_x-k'_x-k''_x=0}} C_{jlm}(k_x,k'_x)\beta_l(k'_x)\beta_m(k''_x), \tag{4.11}$$

where $k_x - k'_x - k''_x = 0$ is the selection rule for the three Fourier wavenumber interaction; $\omega_j(k_x)$ is the linear eigenfrequency for eigenmode j at Fourier wavenumber k_x, or in other words, the coupling of the fluctuation with the initial mean profile. Since the instantaneous mean profiles are not exactly the same as the initial mean profiles, despite the flow being forced, a tiny linear coupling $D_{jl}(k_x)$ arises between the eigenmodes j and l at wavenumber k_x via the interaction with the fluctuating component of the mean profiles. The effect of the viscous and the resistive dissipation are also captured by this small linear coupling, as the eigenmodes used here are the eigenmodes of the non-dissipative linear operator. Despite this linear coupling, we have computed and found that its contribution in the energy transfer is small compared to the coupling via the initial mean profiles, represented by $\omega_j(k_x)$. Next, the nonlinear coupling strength of fluctuations is represented by $C_{jlm}(k_x, k'_x)$. This coupling allows two eigenmodes (l, m) at two different Fourier wavenumbers (k'_x, k''_x) to beat together to drive an eigenmode (j) at another Fourier wavenumber (k_x). We have computed the contribution from this nonlinear mode-coupling also, and found, as expected, that the time-averaged nonlinear energy transfer rate to any wavenumber k_x is equal, but opposite in sign, to the time-averaged linear injection rate to the same wavenumber k_x.

Multiplying Eq. (4.11) with $\beta^*_j(k_x)$, the complex conjugate of $\beta_j(k_x)$, and summing the resulting equation with its complex conjugate, an equation for the time evolution

of $|\beta_j(k_x)|^2$ is obtained. This equation is then substituted in Eq. (4.8) as shown below, with $n_j = 1$ [99]

$$\begin{aligned}
\dot{E}_j(k_x) &= \frac{1}{2}\left[\beta_j^* \partial_t \beta_j + \beta_j \partial_t \beta_j^*\right] \\
&= \mathrm{Re}\left[\beta_j^* \partial_t \beta_j\right] \\
&= \mathrm{Re}\left[\beta_j^* i\omega_j \beta_j + \beta_j^* \sum_l D_{jl}(k_x)\beta_l + \beta_j^* \sum_{\substack{k_x', k_x'', l, m \\ k_x - k_x' - k_x'' = 0}} C_{jlm}(k_x, k_x')\beta_l' \beta_m''\right] \\
&= \mathrm{Re}\left[\Gamma_j |\beta_j|^2 + \sum_l D_{jl}(k_x)\beta_j^* \beta_l + \sum_{\substack{k_x', k_x'', l, m \\ k_x - k_x' - k_x'' = 0}} C_{jlm}(k_x, k_x')\beta_l' \beta_m'' \beta_j^*\right] \\
&= \Gamma_j |\beta_j|^2 + \mathrm{Re}\left[\sum_l D_{jl}(k_x)\beta_j^* \beta_l + \sum_{\substack{k_x', k_x'', l, m \\ k_x - k_x' - k_x'' = 0}} C_{jlm}(k_x, k_x')\beta_l' \beta_m'' \beta_j^*\right], \quad (4.12)
\end{aligned}$$

where β_l' and β_m'' represent $\beta_l(k_x')$ and $\beta_m(k_x'')$ respectively. Unprimed quantities are to be evaluated at k_x. The quantity $i\omega_j$ has been replaced by Γ_j as it is the growth rate for the unstable or stable eigenmode (i.e., $e^{i\omega_j t} = e^{\Gamma_j t}$). It may be noted that each of the terms in Eq. (4.12) has been evaluated. A detailed analysis of those energy transfer channels and mechanisms will be reported in a separate forthcoming publication.

Since the free energy source is the background shear flow in this study, the first term on the right hand side of the last equality in Eq. (4.12) is of interest to compute the direct energy transfer rate between the background and the fluctuations. This term informs us about how much energy can cascade down to small scales from the free energy source at any instant in time.

The equation

$$Q_j(k_x) = \Gamma_j |\beta_j|^2, \quad (4.13)$$

is precisely the one that is presented in the main article. Note that $Q_j(k_x)$ represents the energy transfer rate between the background profiles and the fluctuations due to the j^{th} eigenmode at the wavenumber k_x, unlike $\dot{E}_j(k_x)$ that adds up all the effect of the transfer from the background to the fluctuations, the re-distribution among the fluctuation scales via three-wave interactions, and the visco-resistive dissipation [99]. Since the quantity $Q_j(k_x)$ measures the rate at which the energy gets depleted from the background flow and cascades to small scales, this quantity is numerically evaluated during post-processing of the direct numerical simulation data, and their time-averages (for the turbulent phase $t = 350$–800) are plotted in Fig. 3(c) of the main article.

IV. Residuals in low-order representation of the turbulent flow

It can be insightful to analyze the residuals in Fig. 1(b) of the main article, in order to learn about the turbulent features that are captured by the unstable modes alone and by the sum of the unstable and stable modes. Such an analysis is shown here in Fig. 1.

Figure 1 here also helps understand why spirals form in Fig. 4 of the main article. The stable mode structure observed in Fig. 1(b) here, when removed, loses the ability to counteract the unstable mode in straining the magnetic fields. Thus the ensuing straining and folding of the field by the unbridled eddy motion of the unstable mode gives rise to spirals, beginning at around $(x, z) \approx (10, 0)$—the center or “eye" of the stable-mode-eddy. (Note that the location of this center evolves over a longer time.)

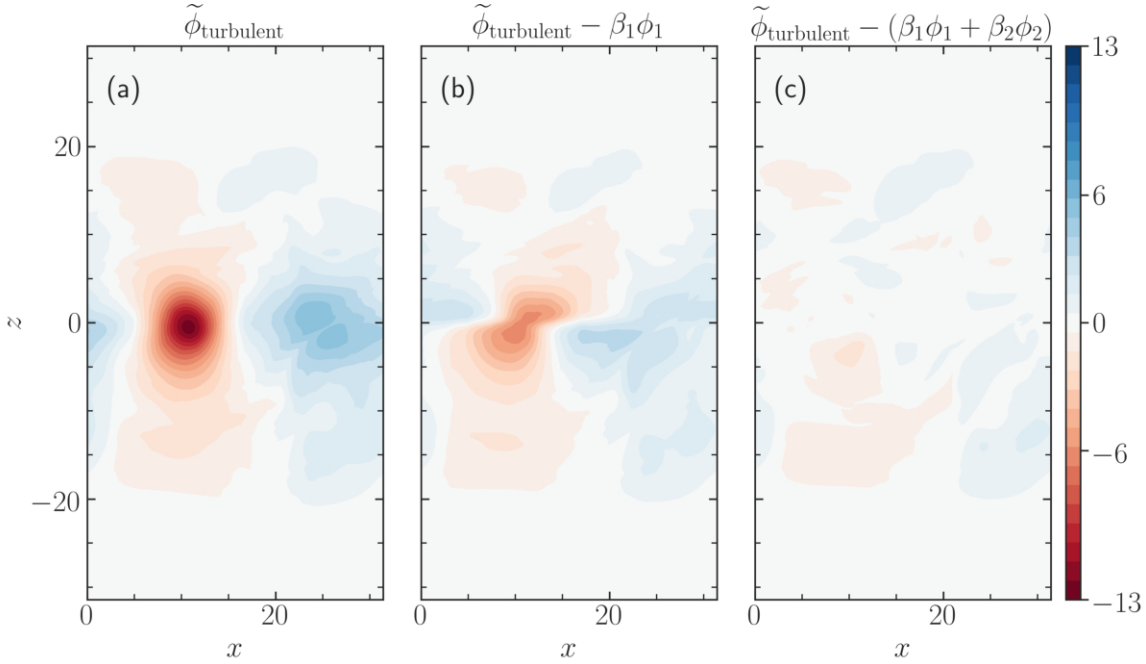

Figure 4.5: (a) Full turbulent fluctuations $\widetilde{\phi}_{\text{turbulent}}$, as shown in Fig. 1(a) of the main article. The aspect ratio of the figure is restored here so that the actual box of the simulation and the turbulent features therein can be seen in their true sizes. (b) The residual $\widetilde{\phi}_{\text{turbulent}} - \beta_1\phi_1$ after subtracting the fluctuations due to unstable eigenmodes. It can be seen that the this plot appears very similar to the stable mode, shown in Fig. 1(a) of the main article. (c) Dramatic reduction in the residual $\widetilde{\phi}_{\text{turbulent}} - (\beta_1\phi_1 + \beta_2\phi_2)$ by adding a conjugate stable mode to its unstable mode at each Kelvin-Helmholtz-unstable wavenumber. The small residual observed in this plot belongs to a large number of continuum eigenmodes, which have their mode structures somewhat afar from the shear layer $|z| \lesssim 1$. All panels share the same colorbar.

5 **PAPER C**: NONLINEAR MODE COUPLING AND ENERGETICS OF DRIVEN MAGNETIZED SHEAR-FLOW TURBULENCE

A version of this chapter was published in Phys. Plasmas 30, 072107 (2023) and was selected by the editors as a Featured article.

ABSTRACT

To comprehensively understand saturation of two-dimensional (2D) magnetized Kelvin-Helmholtz-instability-driven turbulence, energy transfer analysis is extended from the traditional interaction between scales to include eigenmode interactions, by using the nonlinear couplings of linear eigenmodes of the ideal instability. While both kinetic and magnetic energies cascade to small scales, a significant fraction of turbulent energy deposited by unstable modes in the fluctuation spectrum is shown to be re-routed to the conjugate-stable modes at the instability scale. They remove energy from the forward cascade at its inception. The remaining cascading energy flux is shown to attenuate exponentially at a small scale, dictated by the large-scale stable modes. Guided by a widely used instability-saturation assumption, a general quasilinear model of instability is tested by retaining all nonlinear interactions except those that couple to the large-scale stable modes. These complex interactions are analytically removed from the magnetohydrodynamic equations using a novel technique. Observations are: an explosive large-scale vortex separation instead of the well-known merger of 2D, a dramatic enhancement in turbulence level and spectral energy fluxes, and a reduced small-scale dissipation length-scale. These show critical role of the stable modes in instability saturation. Possible reduced-order turbulence models are proposed for fusion and astrophysical plasmas, based on eigenmode-expanded energy transfer analyses.

5.1 Introduction

Instability-driven turbulence, commonly found in nature, has traditionally been regarded as similar to externally stirred turbulence, with instability replacing external stirring and nonlinear behavior remaining comparable.[26–29, 38] However, insights from studies of instability-driven fusion microturbulence have shown that the two kinds of turbulence are different in many essential regards.[15, 32, 88, 89, 91, 93, 95, 98, 140, 141] When turbulence is excited by external forcing at a certain scale, nonlinear interactions between different scales transfer all the injected energy to other scales through an inertial-range energy cascade. In contrast, when an instability taps the free energy of background gradients to drive turbulence, nonlinear interactions quickly become more complex because the nonlinearity excites, at the same instability-scale, other roots of the dispersion relation. This crucially includes linearly stable eigenmodes.[15, 32, 88, 89, 91, 93, 95, 98, 140, 141] Such instability-scale, or large-scale, stable modes are entirely absent in externally stirred turbulence. The stable modes, when present, can be excited to a significant level, such that they return turbulent energy from the instability scale to the background gradients, countering the unstable modes that transfer energy in the opposite direction. This landscape of sources and sinks, mediating the trade of energy between the background gradients and the instability-scale, can have a consequential impact on how small-scale turbulence deals with the energy supplied to it via nonlinear cascades. Despite these critical differences between instability-driven and externally-stirred turbulence, it remains the norm to assume that the stable modes do not impact the energetics in magnetohydrodynamic (MHD)[142] and fluid turbulence.[119] A careful analysis to test such an assumption is missing.

Stable modes in instability-driven fusion microturbulence mediate the energy in-

jected by the instability at the largest scales excited. They set the overall fluctuation level and the rates of transport. Energy is cascaded to small scales, but the amount relative to the energy injected by the instability and removed by the stable modes is so small that it has a negligible effect on transport and fluctuation levels. Analysis of saturation of instability-driven microturbulence by stable modes has enabled predictive reduced calculations of transport levels that agree with observations made in comprehensive numerical simulations and experiment,[32] including absolute levels,[88, 141] the scalings with key parameters,[95] and for situations where transport is suppressed above a linear-instability operational-threshold.[88, 89] Because small-scale cascades are usually of secondary importance for driving turbulent transport—a large-scale aspect, the effect of stable modes on cascades has not been systematically investigated.

Recently, stable modes have been examined in hydrodynamic and magnetized shear-flow-driven turbulence. It has been established that stable modes are nonlinearly excited,[97, 110] that they reach levels comparable to those of the linearly unstable modes in saturation, and that they have significant effects on transport.[111] In MHD, a critical consideration is the effect of the magnetic field on stable-mode physics in shear-flow-driven turbulence. The large-scale unstable flow is very efficient at straining magnetic fields aligned with the flow, thus producing a cascade of magnetic energy to small scale. If the field is sufficiently strong to act back on the flow, and thus on the large-scale stable mode, the smaller scales of the field may blunt the effect of the stable mode. This effect, which is parameterized by the Alfvénic Mach number and which is active somewhat above the instability operational-threshold (i.e., at small Alfvénic Mach number),[114] has motivated careful investigation[143] of parametric dependencies of stable-mode excitation. At low Alfvénic Mach number, stable modes are impacted, but not to a significant degree. Despite consequential excitation of stable modes at all strengths of magnetic field, how the small-scale fluctuations, developed

via cascades, interact with large-scale stable modes, and how such stable modes set the small-scale fluctuation levels and Kolmogorov dissipative length scales are unknown. These questions of feedback of large- and small-scales are particularly important as investigating them directly informs if a low-order model of turbulence is feasible.

Here we undertake a systematic investigation of the effect of stable modes on nonlinear energy transfer in two-dimensional shear-flow-driven MHD turbulence. The investigation necessarily involves connecting the eigenmodes of the Kelvin-Helmholtz (KH) instability with the distinct nonlinearities of MHD—which include the advection of vorticity, the Lorentz force, the advection of field by the flow, and the advection of flow by the field. The eigenmodes of the ideal KH instability are comprised of an unstable mode and a conjugate stable mode (together labeled as discrete modes henceforth) at a given wavenumber in the unstable range, in addition to a set of neutrally stable modes that form a continuum in frequency.[111, 124, 143] The eigenmodes of the ideal MHD operator are useful as a (complete) set of basis functions because they capture the evolution of turbulence driven by an unstable flow profile and offer physical intuition, e.g., the countering behavior of unstable and stable modes in momentum transport.[144] Because the discrete modes exist only at large scales, while the continuum modes extend to small scales, the connection between the MHD nonlinearities and the KH eigenmodes is sensitive to scale. The flow is, however, chiefly concentrated at large scales, while the magnetic field spans a broad range of scales. The locality or nonlocality of energy transfer is also examined because it further impacts the connections between nonlinearities and eigenmodes. Analyses of the above effects provide a detailed picture of the relation of stable eigenmodes to cascade directions and different kinds of nonlinear energy transfer functions.

To quantitatively describe the processes indicated in the previous paragraph, nonlinear energy transfer between fluctuations of non-zero wavenumbers requires

detailed study. The interactions, mediating energy transfer between fluctuations at three wavenumbers (k, k', k''), obey the selection rule $k = k' + k''$. The nonlinearities of energy evolution equations then dictate the transfer, which we write generically as $T(k|k', k'')$. This function represents the energy transferred to k from k' and k'', collectively. But it is not trivial to identify how the transfer is partitioned among k' and k''. Recently,[145] a decomposition of $T(k|k', k'')$ has been learnt, leading to two rates, $S(k|k')$ and $S(k|k'')$; the former (latter) S-transfer-function uniquely represents signed energy transfer rate to k from k' (k'') via the intermediary k'' (k'). We apply this transfer analysis to MHD shear-flow turbulence, and importantly, render the nonlinear energy transfer in an eigenmode-resolved form to learn about the impact of individual eigenmodes, in particular the stable modes, in MHD cascade processes and instability saturation.

The novel transfer analysis of this paper identifies dominant energy transfer channels from sources of fluctuation energy (unstable modes) to turbulent sinks (stable modes), both lying at large scales. It reveals whether the saturation-mediating energy transfer is restricted to a subclass of interactions. This in turn informs, as in the stellarator context,[34] the important question of whether predictive reduced-order models of the turbulence can be constructed.

This paper is organized as follows. Section 5.2 details the methods of energy transfer analysis first in wavenumber space and then in eigenmode space. In Sec. 5.3, the details of the system set-up are presented. Section 5.4 shows the numerical analysis of energetic coupling of scales in Kelvin-Helmholtz turbulence. In Sec. 5.5, energetic coupling of eigenmodes is analyzed in detail. Findings are related to the interaction of the linear eigenmodes with the evolving profiles of the mean flow and the magnetic field, as well as the nonlinear eigenmode coupling coefficients and nonlinear transfer of energy between the eigenmodes. Section 5.5 presents a general quasilinear theory

of instability saturation and then tests it with a numerical solver, informed by a set of newly derived MHD equations where the large-scale stable modes are analytically removed. Discussion is offered in Sec. 5.6.

5.2 Machinery for energy transfer analyses

An incompressible magneto-fluid evolves according to the standard MHD equations[25] as

$$\partial_t \mathbf{u} = -\mathbf{u}\cdot\nabla\mathbf{u} + \mathbf{B}\cdot\nabla\mathbf{B} - \nabla\left(P + |\mathbf{B}|^2/2\right) + \nu\nabla^2\mathbf{u} + \mathbf{f}, \tag{5.1a}$$

$$\partial_t \mathbf{B} = -\mathbf{u}\cdot\nabla\mathbf{B} + \mathbf{B}\cdot\nabla\mathbf{u} + \eta\nabla^2\mathbf{B}, \tag{5.1b}$$

$$\nabla\cdot\mathbf{u} = 0, \tag{5.1c}$$

$$\nabla\cdot\mathbf{B} = 0, \tag{5.1d}$$

where $\mathbf{u}$, $\mathbf{B}$, P, ν, η, and $\mathbf{f}$ respectively stand for the fluid velocity, magnetic field, fluid pressure, viscosity, Ohmic diffusivity, and externally imposed acceleration to the fluid. The factor $4\pi\rho$, with ρ as the fluid density, has been absorbed in the definition of the magnetic field $\mathbf{B}$.

A list of important symbols used in this paper is given in Tab. 5.1 on page 114.

In what follows we shall consider a two-dimensional system (x, z) with z as an inhomogeneous direction. Thus, the x-averaged background profiles of the flow and magnetic fields can have z-dependent structures. We shall consider an unstable mean shear flow $\mathbf{u} = U_{\rm ref}(z)\hat{\mathbf{e}}_x$ with a flow-aligned uniform magnetic field $\mathbf{B} = B_0\hat{\mathbf{e}}_x$. In Sec. 5.2, we show the method of studying nonlinear scale-interactions between the velocity and magnetic fields when the system is arbitrarily inhomogeneous, by integrating energies along the z-axis. Then, in Sec. 5.2, we probe further by

Symbol	Meaning
$T_{\mathbf{u}}(k_x\|k'_x,k''_x)$	Energy transfer rate to $\mathbf{u}(k_x)$ from k'_x and k''_x
$T_{\mathbf{B}}(k_x\|k'_x,k''_x)$	Energy transfer rate to $\mathbf{B}(k_x)$ from k'_x and k''_x
$S^{\mathbf{u}}_{\mathbf{u}}(k_x\|k''_x)$	Energy transfer rate to $\mathbf{u}(k_x)$ from $\mathbf{u}(k''_x)$
$S^{\mathbf{B}}_{\mathbf{u}}(k_x\|k''_x)$	Energy transfer rate to $\mathbf{u}(k_x)$ from $\mathbf{B}(k''_x)$
$S^{\mathbf{u}}_{\mathbf{B}}(k_x\|k''_x)$	Energy transfer rate to $\mathbf{B}(k_x)$ from $\mathbf{u}(k''_x)$
$S^{\mathbf{B}}_{\mathbf{B}}(k_x\|k''_x)$	Energy transfer rate to $\mathbf{B}(k_x)$ from $\mathbf{B}(k''_x)$
$\mathbf{u}<$	Wavenumbers of $\mathbf{u}$, lesser than or equal to k_0
$\mathbf{u}>$	Wavenumbers of $\mathbf{u}$, greater than k_0
$\mathbf{B}<$	Wavenumbers of $\mathbf{B}$, lesser than or equal to k_0
$\mathbf{B}>$	Wavenumbers of $\mathbf{B}$, greater than k_0
$\Pi^{\mathbf{u}<}_{\mathbf{u}>}(k_0)$	Energy flux from $\mathbf{u}<$ to $\mathbf{u}>$ at k_0
$\Pi^{\mathbf{u}<}_{\mathbf{B}>}(k_0)$	Energy flux from $\mathbf{u}<$ to $\mathbf{B}>$ at k_0
$\Pi^{\mathbf{B}<}_{\mathbf{u}>}(k_0)$	Energy flux from $\mathbf{B}<$ to $\mathbf{u}>$ at k_0
$\Pi^{\mathbf{B}<}_{\mathbf{B}>}(k_0)$	Energy flux from $\mathbf{B}<$ to $\mathbf{B}>$ at k_0
$\beta_j(k_x)$	Amplitude of the j^{th} eigenmode at k_x
$\gamma_j(k_x)$	Growth rate of the j^{th} eigenmode at k_x
$C_{jmn}(k_x,k'_x)$	Non-linear mode-coupling coefficient
$Q_j(k_x)$	Energy transfer from MHD fields at $k_x=0, t=0$
$R_j(k_x)$	Energy transfer from time-deviations in MHD fields
$Q_{\mathbf{u}}(k_x)$	Linear energy drive at k_x of flow field
$Q_{\mathbf{B}}(k_x)$	Linear energy drive at k_x of magnetic field

Table 5.1: List of symbols used in this chapter.

decomposing the fluctuations along the z-axis in a complete basis of eigenmodes of the linear operator, corresponding to the initial mean flow and magnetic field.

Nonlinear scale-interaction analysis

We may compose evolution equations for both the kinetic and magnetic energies, by first writing an evolution equation for $\mathbf{u}(k_x)$ and multiplying it with $\mathbf{u}^*(k_x)$, and then adding a complex conjugate to the resulting equation (and likewise for the magnetic

field) to arrive at

$$\partial_t E_{\mathbf{u}}(k_x) = Q_{\mathbf{u}}(k_x) + \sum_{\substack{k'_x+k''_x=k_x \\ :k'_x\neq 0 \text{ or } k''_x\neq 0}} T_{\mathbf{u}}(k_x|k'_x,k''_x) + \epsilon_f(k_x), \tag{5.2a}$$

$$\partial_t E_{\mathbf{B}}(k_x) = Q_{\mathbf{B}}(k_x) + \sum_{\substack{k'_x+k''_x=k_x \\ :k'_x\neq 0 \text{ or } k''_x\neq 0}} T_{\mathbf{B}}(k_x|k'_x,k''_x), \tag{5.2b}$$

with $E_{\mathbf{u}}(k_x) = E_{\mathbf{u}}(-k_x) = \langle|\mathbf{u}(k_x)|^2\rangle_z/2$ and $E_{\mathbf{B}}(k_x) = E_{\mathbf{B}}(-k_x) = \langle|\mathbf{B}(k_x)|^2\rangle_z/2$ as z-integrated energies. Here,

$$\langle A\rangle_z = \int_0^{L_z} \frac{dz}{L_z}\, A(z) \tag{5.3}$$

and

$$Q_{\mathbf{u}}(k_x) = T_{\mathbf{u}}(k_x|0,k_x) + T_{\mathbf{u}}(k_x|k_x,0) + \nu\,\mathbb{R}\mathrm{e}\Big\{\langle \mathbf{u}^*(k_x)\cdot\nabla^2\mathbf{u}(k_x)\rangle_z\Big\}, \tag{5.4}$$

with

$$T_{\mathbf{u}}(k_x|k'_x,k''_x) = \mathbb{R}\mathrm{e}\left\{\Big\langle \mathbf{u}^*(k_x)\cdot\Big[-\mathbf{u}(k'_x)\cdot\nabla''\mathbf{u}(k''_x) + \mathbf{B}(k'_x)\cdot\nabla''\mathbf{B}(k''_x)\Big]\Big\rangle_z\right\}. \tag{5.5}$$

The signed transfer function $T_{\mathbf{u}}(k_x|k'_x,k''_x)$ represents the net energy transfer (positive or negative) to a wavenumber k_x from k'_x and k''_x [similarly for $T_{\mathbf{B}}(k_x|k'_x,k''_x)$], akin to the net energy transfer in hydrodynamics.[146]

Because the velocity is a real observable in physical space (x,z), Hermiticity imposes a symmetry in the energy transfer function: the energy transfer to the velocity field at k_x from k'_x and k''_x via the triad (k_x,k'_x,k''_x) with $k_x = k'_x + k''_x$ is equal to the energy transfer to the velocity field at $-k_x$ from $-k'_x$ and $-k''_x$ via the triad

$(-k_x, -k'_x, -k''_x)$ with $-k_x = -k'_x - k''_x$, mathematically written as

$$T_{\mathbf{u}}(k_x|k'_x, k''_x) = \mathbb{R}\mathrm{e}\left\{\left\langle u_i\Big[- u'^*_j \nabla''^*_j u''^*_i + B'^*_j \nabla''^*_j B''^*_i\Big]\right\rangle_z\right\} = T_{\mathbf{u}}(-k_x|-k'_x, -k''_x). \quad (5.6)$$

It is straightforward to show that the Fourier transform of the gradient of the effective pressure term $\nabla\left(P + |\mathbf{B}|^2/2\right)$ in Eq. (5.1a), when dotted with the $-k_x$ component of the velocity and integrated along the z-axis, yields zero in the evolution of the total kinetic energy at any wavenumber k_x. This is a consequence of the incompressibility of the flow.

The linear and nonlinear energy transfer rates related to magnetic energy are

$$Q_{\mathbf{B}}(k_x) = T_{\mathbf{B}}(k_x|0, k_x) + T_{\mathbf{B}}(k_x|k_x, 0) + \eta\,\mathbb{R}\mathrm{e}\left\{\langle \mathbf{B}^*(k_x)\cdot\nabla^2\mathbf{B}(k_x)\rangle_z\right\} \quad (5.7)$$

and

$$T_{\mathbf{B}}(k_x|k'_x, k''_x) = \mathbb{R}\mathrm{e}\left\{\left\langle \mathbf{B}^*(k_x)\cdot\Big[- \mathbf{u}(k'_x)\cdot\nabla''\mathbf{B}(k''_x) + \mathbf{B}(k'_x)\cdot\nabla''\mathbf{u}(k''_x)\Big]\right\rangle_z\right\}. \quad (5.8)$$

A relation similar to Eq. (5.6) can be derived for the magnetic energy, yielding $T_{\mathbf{B}}(k_x|k'_x, k''_x) = T_{\mathbf{B}}(-k_x|-k'_x, -k''_x)$.

If any three vector fields $\mathbf{A}, \mathbf{B}$, and $\mathbf{C}$—each representing either a velocity field or a magnetic field—at wavenumbers k_x, k'_x, and k''_x, respectively, interact to drive the field $\mathbf{A}(k_x)$ via the nonlinear term $\mathbf{B}(k'_x)\cdot\nabla''\mathbf{C}(k''_x) + \mathbf{C}(k''_x)\cdot\nabla'\mathbf{B}(k'_x)$, where ∇' and ∇'' serve as reminders to evaluate the gradients at k'_x and k''_x, respectively, then the net energy transfer to $\mathbf{A}(k_x)$ from $\mathbf{B}(k'_x)$ and $\mathbf{C}(k''_x)$ is given as

$$T_{\mathbf{A}}(k_x|k'_x, k''_x) = \mathbb{R}\mathrm{e}\left\{\left\langle \mathbf{A}^*(k_x)\cdot\Big[\mathbf{B}(k'_x)\cdot\nabla''\mathbf{C}(k''_x)\Big] + \mathbf{A}^*(k_x)\cdot\Big[\mathbf{C}(k''_x)\cdot\nabla'\mathbf{B}(k'_x)\Big]\right\rangle_z\right\}. \quad (5.9)$$

Note that this transfer function does not identify the amount of energy transferred to $\mathbf{A}(k_x)$ from $\mathbf{C}(k_x'')$ with $\mathbf{B}(k_x')$ acting purely as an intermediary, or the amount of energy transferred to $\mathbf{A}(k_x)$ from $\mathbf{B}(k_x')$ with $\mathbf{C}(k_x'')$ acting purely as an intermediary. In order to identify such a wavenumber-to-wavenumber transfer, a few additional transfer functions are useful to define. They will offer convenience in analyzing the energy exchange between different Fourier modes of the velocity and the magnetic fields. We first present a general expression, a priori as a purely mathematical construct,

$$S_{\mathbf{A}}^{\mathbf{C}}(k_x|k_x'') = \mathbb{R}\mathrm{e}\left\{\left\langle \mathbf{A}^*(k_x)\cdot\left[\mathbf{B}(k_x')\cdot\nabla''\mathbf{C}(k_x'')\right]\right\rangle_z\right\}. \tag{5.10}$$

The subscript and superscript of $S_{\mathbf{A}}^{\mathbf{C}}(k_x|k_x'')$ denote $\mathbf{A}$ at k_x and $\mathbf{C}$ at k_x''. When the fields $\mathbf{A},\mathbf{B},\mathbf{C}$ all are divergenceless, $S_{\mathbf{A}}^{\mathbf{C}}(k_x|k_x'')$ satisfies:[145, 147–152]

$$S_{\mathbf{A}}^{\mathbf{C}}(k_x|k_x'') = -S_{\mathbf{C}}^{\mathbf{A}}(k_x''|k_x), \tag{5.11a}$$

$$T_{\mathbf{A}}(k_x|k_x',k_x'') = S_{\mathbf{A}}^{\mathbf{C}}(k_x|k_x'') + S_{\mathbf{A}}^{\mathbf{B}}(k_x|k_x'), \tag{5.11b}$$

where

$$S_{\mathbf{A}}^{\mathbf{B}}(k_x|k_x') = \mathbb{R}\mathrm{e}\left\{\left\langle \mathbf{A}^*(k_x)\cdot\left[\mathbf{C}(k_x'')\cdot\nabla'\mathbf{B}(k_x')\right]\right\rangle_z\right\}. \tag{5.12}$$

The proof of Eq. (5.11a) is given in Appendix, and Eq. (5.11b) follows from Eq. (5.9).

Because (a) the sum of S-transfer-functions yields the net energy transfer function T [see Eq. (5.11b)], and, most emphatically, (b) the S-transfer-function has the *anti*-symmetry property that the fields $\mathbf{A}$ and $\mathbf{C}$, along with their wavenumbers, can be swapped to gain an overall negative sign [see Eq. (5.11a)], the decomposition of T-function into the two S-functions has a physical meaning, as has been invoked previously.[128, 145, 147–153] The transfer $S_{\mathbf{A}}^{\mathbf{C}}(k_x|k_x'')$ physically represents the energy transfer rate to the field $\mathbf{A}$ at k_x from the field $\mathbf{C}$ at k_x'', with $\mathbf{B}$ at k_x' acting solely as

an intermediary.

Below, we define wavenumber-to-wavenumber S-transfer-functions in the context of MHD turbulence[128, 145, 147–153]

$$S^{\mathbf{u}}_{\mathbf{u}}(k_x|k''_x) = \mathbb{R}\mathrm{e}\left\{\left\langle \mathbf{u}^*(k_x)\cdot\Big[-\mathbf{u}(k'_x)\cdot\nabla''\mathbf{u}(k''_x)\Big]\right\rangle_z\right\}, \tag{5.13a}$$

$$S^{\mathbf{B}}_{\mathbf{u}}(k_x|k''_x) = \mathbb{R}\mathrm{e}\left\{\left\langle \mathbf{u}^*(k_x)\cdot\Big[+\mathbf{B}(k'_x)\cdot\nabla''\mathbf{B}(k''_x)\Big]\right\rangle_z\right\}, \tag{5.13b}$$

$$S^{\mathbf{u}}_{\mathbf{B}}(k_x|k''_x) = \mathbb{R}\mathrm{e}\left\{\left\langle \mathbf{B}^*(k_x)\cdot\Big[+\mathbf{B}(k'_x)\cdot\nabla''\mathbf{u}(k''_x)\Big]\right\rangle_z\right\}, \tag{5.13c}$$

$$S^{\mathbf{B}}_{\mathbf{B}}(k_x|k''_x) = \mathbb{R}\mathrm{e}\left\{\left\langle \mathbf{B}^*(k_x)\cdot\Big[-\mathbf{u}(k'_x)\cdot\nabla''\mathbf{B}(k''_x)\Big]\right\rangle_z\right\}. \tag{5.13d}$$

We now identify that in a special triad $(\mathbf{u}(k_x), \mathbf{B}(k'_x), \mathbf{B}(k''_x))$ the two transfer functions $S^{\mathbf{B}}_{\mathbf{u}}(k_x|k''_x)$ and $S^{\mathbf{u}}_{\mathbf{B}}(k''_x|k_x)$ represent the energy exchange between the velocity at wavenumber k_x and the magnetic field at wavenumber k''_x. Since the triad is the same, these two transfer functions are equal in magnitude but of opposite sign, $S^{\mathbf{B}}_{\mathbf{u}}(k_x|k''_x) = -S^{\mathbf{u}}_{\mathbf{B}}(k''_x|k_x)$.

Using the above S-transfer-functions in MHD turbulence, the cross-scale (signed) energy fluxes passing through a wavenumber k_0 are [145, 148–152]

$$\Pi^{\mathbf{u}<}_{\mathbf{u}>}(k_0) = \sum_{|k''_x|\le k_0}\sum_{|k_x|>k_0} S^{\mathbf{u}}_{\mathbf{u}}(k_x|k''_x), \tag{5.14a}$$

$$\Pi^{\mathbf{u}<}_{\mathbf{B}>}(k_0) = \sum_{|k''_x|\le k_0}\sum_{|k_x|>k_0} S^{\mathbf{u}}_{\mathbf{B}}(k_x|k''_x), \tag{5.14b}$$

$$\Pi^{\mathbf{B}<}_{\mathbf{u}>}(k_0) = \sum_{|k''_x|\le k_0}\sum_{|k_x|>k_0} S^{\mathbf{B}}_{\mathbf{u}}(k_x|k''_x), \tag{5.14c}$$

$$\Pi^{\mathbf{B}<}_{\mathbf{B}>}(k_0) = \sum_{|k''_x|\le k_0}\sum_{|k_x|>k_0} S^{\mathbf{B}}_{\mathbf{B}}(k_x|k''_x), \tag{5.14d}$$

where $\mathbf{u}<$ and $\mathbf{B}<$ represent velocity and magnetic fields at wavenumbers smaller than or equal to k_0; similarly, $\mathbf{u}>$ and $\mathbf{B}>$ represent respective fields at wavenumbers greater than k_0 (Fig. 10.1). Each flux represents energy flowing in spectral space through k_0 from the superscripted index to the subscripted index, e.g., $\Pi^{\mathbf{u}<}_{\mathbf{u}>}(k_0)$ measures the energy flowing through k_0 when the velocity field at wavenumbers less than or equal to k_0 transfers energy to the velocity field at wavenumbers greater than k_0. Thus, a positive sign of this flux at k_0 represents low wavenumbers giving energy to high wavenumbers, i.e., a forward cascade at k_0. However, if sign of the flux is found to be negative, it signifies an inverse cascade at k_0.

We note that this z-integrated formalism alone, while informative with regard to the energy cascade processes in wavenumber space, cannot inform if there are any dominant structures in the fluctuations along the z-axis. Analyzing energy transfer between those structures can directly guide reduced-order models of Kelvin-Helmholtz turbulence. Hence, we next develop a set of novel tools to examine energy transfer between the structures in the fluctuations along the z-axis, by decomposing the turbulent fluctuations in a complete basis of the eigenmodes of the linear operator.

Nonlinear eigenmode-interaction analysis

To distill the nonlinear interaction between the eigenmodes of the 2D MHD Kelvin-Helmholtz-instability-driven turbulence, it is advantageous to reduce the number of variables using the streamfunction ϕ and flux function ψ. Here, $\mathbf{u} = \hat{\mathbf{e}}_y \times \nabla\phi$ and $\mathbf{B} = \hat{\mathbf{e}}_y \times \nabla\psi$. The governing equations of MHD, presented in Eqs. (5.1a)–(5.1d), then can be written as[25]

$$\partial_t \begin{bmatrix} \nabla^2 & 0 \\ 0 & 1 \end{bmatrix} \begin{bmatrix} \phi \\ \psi \end{bmatrix} = \begin{bmatrix} -\{\nabla^2\phi, \phi\} + \{\nabla^2\psi, \psi\} + \nu\nabla^4\phi + \partial_z f \\ \{\phi, \psi\} + \eta\nabla^2\psi \end{bmatrix}, \tag{5.15}$$

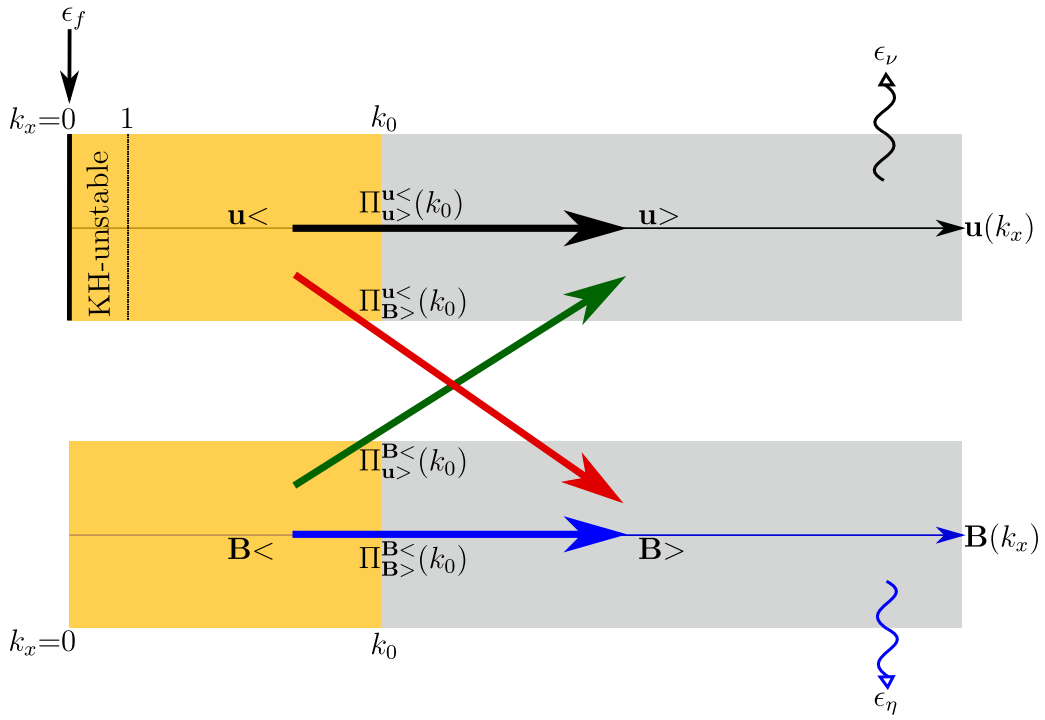

Figure 5.1: Fourier representation of energy dynamics and cross-scale energy fluxes of MHD turbulence. The top one-dimensional box shows different Fourier modes of the flow $\mathbf{u}(k_x)$, whereas the bottom box shows different Fourier modes of the magnetic field $\mathbf{B}(k_x)$. The arrows represent energy transfer between different $\mathbf{u}(k_x)$ and $\mathbf{B}(k_x)$. The arrows need not be in the same directions as shown. If any of the signed energy fluxes in a physical system is negative, the corresponding arrow direction is reversed, because of the energy conservation, e.g., $-\Pi^{\mathbf{u}<}_{\mathbf{u}>}(k_0) = \Pi^{\mathbf{u}>}_{\mathbf{u}<}(k_0)$, where $\mathbf{u}<$ are Fourier modes with wavenumber $k_x \le k_0$ (yellow colored region). The external forcing ϵ_f is applied to prevent the relaxation of the mean shear flow, i.e., $\mathbf{u}(k_x{=}0)$. The wavenumber range $0 < |k_x| < 1$ represents the large-scale KH instability of the flow, which drives the turbulence. Small-scale viscous and resistive dissipation are represented by ϵ_ν and ϵ_η, respectively.

where the Poisson bracket is $\{P,Q\} = \partial_x P \cdot \partial_z Q - \partial_z P \cdot \partial_x Q$, e.g., $\{\phi,\psi\} = -\mathbf{u}\cdot\nabla\psi$.

We now decompose the streamfunction and magnetic flux function into their mean profiles $[\phi_0,\psi_0]$ at $t=0$, profiles $[\widetilde{\phi_0},\widetilde{\psi_0}]$ corresponding to deviation of the instantaneous mean from the initial mean, and their fluctuation spectra $[\widetilde{\phi},\widetilde{\psi}]$ at $k_x \neq 0$. Thus, we write a complete decomposition $\phi = \phi_0(k_x{=}0,t{=}0) + \widetilde{\phi_0}(k_x{=}0,t) + \widetilde{\phi}(k_x \neq 0,t) = \phi_0 + \widetilde{\phi_0} + \widetilde{\phi}$, and likewise for ψ. Equation (5.15) may now be structurally written, at a fluctuation scale where forcing is not applied, as

$$\partial_t M\widetilde{X} = L_0\widetilde{X} + \widetilde{L}\widetilde{X} + L_{\text{diss}}\widetilde{X} + N(\widetilde{X},\widetilde{X}), \tag{5.16}$$

where $\widetilde{X} = [\widetilde{\phi},\widetilde{\psi}]^{\mathrm{T}}$ is the state vector representing the fluctuation spectrum ($k_x \neq 0$); M is a linear operator from Eq. (5.15), given as

$$M = \begin{bmatrix} \nabla^2 & 0 \\ 0 & 1 \end{bmatrix}; \tag{5.17}$$

L_0 represents the dissipationless linear operator[111] based on the background profiles prescribed at $t{=}0$, and acts on the $\widetilde{X}$ as

$$L_0\widetilde{X} = \begin{bmatrix} -\{\nabla^2\phi_0,\widetilde{\phi}\} - \{\nabla^2\widetilde{\phi},\phi_0\} + \{\nabla^2\psi_0,\widetilde{\psi}\} + \{\nabla^2\widetilde{\psi},\psi_0\} \\ \{\phi_0,\widetilde{\psi}\} + \{\widetilde{\phi},\psi_0\} \end{bmatrix}; \tag{5.18}$$

$\widetilde{L}$ stands for the linear operator formed from the time-fluctuating background profiles ($k_x = 0$), and is written as

$$\widetilde{L}_0\widetilde{X} = \begin{bmatrix} -\{\nabla^2\widetilde{\phi_0},\widetilde{\phi}\} - \{\nabla^2\widetilde{\phi},\widetilde{\phi_0}\} + \{\nabla^2\widetilde{\psi_0},\widetilde{\psi}\} + \{\nabla^2\widetilde{\psi},\widetilde{\psi_0}\} \\ \{\widetilde{\phi_0},\widetilde{\psi}\} + \{\widetilde{\phi},\widetilde{\psi_0}\} \end{bmatrix}; \tag{5.19}$$

L_{diss} arises from the visco-resistive dissipative terms

$$L_{\text{diss}}\widetilde{X} = \begin{bmatrix} \nu\nabla^4\widetilde{\phi} \\ \eta\nabla^2\widetilde{\psi} \end{bmatrix}; \tag{5.20}$$

and $N(\widetilde{X},\widetilde{X})$ is a quadratic nonlinear operator (allowing interaction between non-zero Fourier modes)

$$N(\widetilde{X},\widetilde{X}) = \begin{bmatrix} -\{\nabla^2\widetilde{\phi},\widetilde{\phi}\} + \{\nabla^2\widetilde{\psi},\widetilde{\psi}\} \\ \{\widetilde{\phi},\widetilde{\psi}\} \end{bmatrix}. \tag{5.21}$$

Since the eigenmodes of the linear operator L_0 at hand form a complete basis[144], we may expand at a wavenumber k_x an arbitrary Fourier-transformed state vector $\hat{X}(k_x,z)$ as

$$\hat{X}(k_x,z) = \sum_m \beta_m(k_x) X_m(k_x,z). \tag{5.22}$$

Here, $\hat{X}$ is a Fourier amplitude of $\widetilde{X}$, i.e., $\widetilde{X} = \sum_{k_x\neq 0}\hat{X}(k_x,z)\exp(ik_x x)$, and $X_m(k_x,z)$ is the m^{th} eigenmode structure with its complex mode amplitude β_m, evaluated at k_x. We numerically compute well-resolved vertical structures[144] of eigenmodes $X_m(k_x,z)$ using 2048 Chebyshev polynomials for each variable in an eigenvalue solver, implemented in Dedalus. Note that the eigenmodes $X_m(k_x,z)$ here are non-orthogonal.

We Fourier-transform Eq. (5.16) and substitute the above eigenmode decomposition for the fluctuations at that wavenumber k_x. Then, we multiply the resulting equation with the j^{th} left eigenmode Y_j at the same wavenumber. Left eigenmodes are used here because they form a biorthogonal basis with the set of the right eigenmodes X_m in the manner, $\langle Y_j, MX_m\rangle = \delta_{j,m}$. Thus we arrive at

$$\left\langle Y_j, \partial_t M \sum_m \beta_m X_m \right\rangle = \left\langle Y_j, \left[L_0 \sum_m \beta_m X_m + \widetilde{L}\hat{X} + L_{\text{diss}}\hat{X} \right] \right\rangle + \sum_{\substack{k'_x, k''_x \\ :k'_x + k''_x = k_x}} \left\langle Y_j, \hat{N}(\hat{X}', \hat{X}'') \right\rangle, \tag{5.23}$$

which leads us to

$$\partial_t \beta_j = \sum_m \beta_m \langle Y_j, L_0 X_m \rangle + \left\langle Y_j, \left[\widetilde{L}\hat{X} + L_{\text{diss}}\hat{X} \right] \right\rangle + \sum_{k'_x} \left\langle Y_j, \hat{N}(\hat{X}', \hat{X}'') \right\rangle. \tag{5.24}$$

Here, $\hat{X}'$ and $\hat{X}''$ stand for state vectors at k'_x and k''_x (with a constraint $k'_x + k''_x = k_x$).

As the eigenmodes are obtained for the linear opearator L_0, the identity $L_0 X_m = \gamma_m M X_m$ may be used, where γ_m is complex eigenvalue corresponding to the m^{th} right eigenmode at wavenumber k_x. Equation (5.23) can thus be simplified, using the orthogonality of the left and the right eigenmodes, to

$$\partial_t \beta_j(k_x) = \gamma_j(k_x)\beta_j(k_x) + \left\langle Y_j, \left[\widetilde{L}\hat{X} + L_{\text{diss}}\hat{X} \right] \right\rangle + \sum_{k'_x} \left\langle Y_j, \hat{N}(\hat{X}', \hat{X}'') \right\rangle. \tag{5.25}$$

At this stage, the arbitrary state vector $\hat{X}(k_x, z)$ at wavenumber k_x may be decomposed into a complete set of eigenmodes at that wavenumber. Without loss of generality, in an unstable wavenumber range $|k_x| < 1$, we can decompose an arbitrary fluctuation into an unstable X_1 eigenmode and a conjugate-stable X_2 eigenmode, in addition to the remaining summed fluctuations that encompass the sea of continuum modes X_{c}. [144] This yields

$$\hat{X}(k_x, z) = \left[\sum_{j=1}^{2} \beta_j(k_x) X_j(k_x, z) \right] + X_{\text{c}} = X_{\text{d}} + X_{\text{c}}. \tag{5.26}$$

The fluctuations corresponding to the unstable and stable modes are the discrete eigenmodes $X_{\rm d}$. Substituting Eq. (5.26) in the nonlinearity of Eq. (5.25) yields

$$\partial_t \beta_j(k_x) = \gamma_j(k_x)\beta_j(k_x) + \left\langle Y_j, \widetilde{L}\hat{X} \right\rangle + \left\langle Y_j, L_{\rm diss}\hat{X} \right\rangle + \sum_{k_x'} \left\langle Y_j, \left[\hat{N}(X_{\rm d}', X_{\rm d}'') + \hat{N}(X_{\rm d}', X_{\rm c}'') + \hat{N}(X_{\rm c}', X_{\rm d}'') + \hat{N}(X_{\rm c}', X_{\rm c}'') \right] \right\rangle . \quad (5.27)$$

The nonlinear interaction $\hat{N}(X_{\rm d}', X_{\rm d}'')$ between the two discrete eigenmodes at wavenumbers k_x' and k_x'', driving the mode-amplitude $\beta_j(k_x)$, may be further decomposed into individual eigenmode interactions in terms of the unstable and stable modes. This substitution of $X_{\rm d}' = \sum_{m=1}^{2} \beta_m' X_m'$ and $X_{\rm d}'' = \sum_{n=1}^{2} \beta_n'' X_n''$ leads to

$$\begin{aligned} \partial_t \beta_j(k_x) = {} & \gamma_j(k_x)\beta_j(k_x) + \left\langle Y_j, \widetilde{L}\hat{X} \right\rangle + \left\langle Y_j, L_{\rm diss}\hat{X} \right\rangle \\ & + \sum_{k_x'} \sum_{m=1}^{2} \sum_{n=1}^{2} C_{jmn}(k_x, k_x')\beta_m'\beta_n'' \\ & + \sum_{k_x'} \left\langle Y_j, \left[\hat{N}(X_{\rm d}', X_{\rm c}'') + \hat{N}(X_{\rm c}', X_{\rm d}'') + \hat{N}(X_{\rm c}', X_{\rm c}'') \right] \right\rangle , \end{aligned} \quad (5.28)$$

where the appearance of the nonlinear mode-coupling coefficient $C_{jmn}(k_x, k_x') = \left\langle Y_j, \hat{N}(X_{\rm m}', X_{\rm n}'') \right\rangle$ has been made explicit. The mode-coupling coefficient has five indices—j, m, n, k_x and k_x'—denoting the eigenmode m at k_x' interacts with the eigenmode n at k_x'' to drive the eigenmode j at k_x. This coefficient measures the strength of a given three-mode overlap.[110]

It is now straightforward to derive the eigenmode-energy evolution equation. We multiply Eq. (5.28) with β_j^* and add the complex conjugate of the resulting equation to find

$$\partial_t |\beta_j|^2 = Q_j + R_j + D_j + T_{j\rm dd} + T_{j\rm dc} + T_{j\rm cc}, \quad (5.29)$$

where

$$Q_j = 2\gamma_j |\beta_j|^2, \tag{5.30a}$$

$$R_j = 2\mathrm{Re}\left[\left\langle Y_j, \widetilde{L}\hat{X}\right\rangle \beta_j^*\right], \tag{5.30b}$$

$$D_j = 2\mathrm{Re}\left[\left\langle Y_j, L_{\mathrm{diss}}\hat{X}\right\rangle \beta_j^*\right], \tag{5.30c}$$

$$T_{jmn}(k_x, k_x') = 2\mathrm{Re}\left[C_{jmn}(k_x, k_x')\beta_m'\beta_n''\beta_j^*\right], \tag{5.30d}$$

$$T_{j\mathrm{dd}} = \sum_{k_x'}\sum_{m=1}^{2}\sum_{n=1}^{2} T_{jmn}(k_x, k_x'), \tag{5.30e}$$

$$T_{j\mathrm{dc}} = 2\mathrm{Re}\left[\sum_{k_x'}\left\langle Y_j, \left\{\hat{N}(X_{\mathrm{d}}', X_{\mathrm{c}}'') + \hat{N}(X_{\mathrm{c}}', X_{\mathrm{d}}'')\right\}\right\rangle \beta_j^*\right], \tag{5.30f}$$

$$T_{j\mathrm{cc}} = 2\mathrm{Re}\left[\sum_{k_x'}\left\langle Y_j, \hat{N}(X_{\mathrm{c}}', X_{\mathrm{c}}'')\right\rangle \beta_j^*\right]. \tag{5.30g}$$

Here, Q_j refers to a source or sink (arising from the linear operator based on the mean profiles at $t = 0$); R_j is the response term due to deviation of the instantaneous mean profiles from the initial profiles; D_j is the visco-resistive dissipation term at k_x associated with the j^{th} eigenmode; $T_{jmn}(k_x, k_x')$ is the nonlinear energy transfer to mode j at k_x from the interaction between modes m and n at k_x' and k_x'', respectively; $T_{j\mathrm{dd}}$ is the energy transfer to mode j at k_x from all the possible nonlinear interactions between the discrete modes, i.e., unstable and stable modes; $T_{j\mathrm{dc}}$ is the energy transfer to mode j at k_x from the all possible nonlinear interactions between the discrete and the continuum eigenmodes; and $T_{j\mathrm{cc}}$ similarly arises from all possible continuum-continuum mode interactions. Because discrete modes of the Kelvin-Helmholtz linear operator exist only at large scales, $|k_x| < 1$, the quantity $T_{j\mathrm{cc}}$ captures the feedback of small-scale ($|k_x| >> 1$) fluctuations on the j^{th} eigenmode, when $j = 1$ or $j = 2$.

5.3 Simulation set-up

Background profiles and forcing

We initialize the system with a mean shear flow $\mathbf{u} = U_{\rm ref}(z)\hat{\mathbf{e}}_x = U_0 \tanh(z/a)\hat{\mathbf{e}}_x$ and a mean magnetic field $\mathbf{B} = B_0\hat{\mathbf{e}}_x$, where U_0 and a represent the amplitude and the half-width of the shear flow, respectively. Fluctuation spectra ($k_x \neq 0$) are then excited with low-amplitude, random perturbations such that the energy spectrum in wavenumber space is flat, i.e., no preferential Fourier-mode excitation (for more details, see Section 2 of Ref. [144]). The perturbed system is then evolved according to Eq. (5.15). With no drive, the system quickly relaxes the mean-flow profile toward a stable configuration. The ensuing turbulence is thus decaying.[111] To obtain a quasi-stationary state of sustained turbulence, we force the mean flow ($k_x = 0$) continuously toward the initial unstable profile with a Krook forcing[119] $\mathbf{f} = f(z)\hat{\mathbf{e}}_x\delta_{k_x,0}$, where

$$f(z) = D_{\rm Krook}\left[U_{\rm ref}(z) - \langle u_x(x,z,t)\rangle_x\right] + F_0, \tag{5.31}$$

where $D_{\rm Krook}$ is the profile relaxation rate [118, 120] that controls the forcing strength, and $\langle u_x(x,z,t)\rangle_x$ is the instantaneous x-averaged flow. The time-independent force F_0 is imposed only to balance the pure viscous diffusion of the initial shear flow, $\nu\nabla^2 U_{\rm ref}(z) + F_0 = 0$, ensuring that, at $t = 0$, we realize an initial equilibrium state, about which small-amplitude initial perturbations evolve.[144]

Non-dimensionalization

We non-dimensionalize all variables with length scale a and flow speed U_0. Thus, time is measured in units of a/U_0, energy (per unit mass) has units of U_0^2, and $D_{\rm Krook}$ is specified in terms of U_0/a. The mean flow then becomes $U_{\rm ref}(z) = \tanh(z)$. The

magnetic field strength is quantified by the Alfvénic Mach number $M_{\rm A} = U_0/B_0$. The effects of the viscosity and resistivity are measured by the fluid Reynolds number $Re = aU_0/\nu$ and the magnetic Reynolds number $Rm = aU_0/\eta$, respectively. The magnetic Prandtl number is defined as $Pm = Rm/Re$.

All simulations use a box size of $(L_x, L_z) = (10\pi, 20\pi)$, $Re = 500$ (unless stated otherwise), and a high spectral resolution of 2048 Fourier modes along the x-axis and 2048 Chebyshev polynomials along the z-axis to obtain well-converged results.[144] Additionally, we dealias the quadratic nonlinearities of the system using 3/2 times the mentioned spectral modes. We employ a pseudospectral numerical solver Dedalus.[82, 121]

Boundary conditions used are, along the x-axis, periodic, and, along the z-axis, perfectly conducting, no-slip walls, co-moving with the initial flow at the top ($z = L_z/2$) and bottom ($z = -L_z/2$) layers.[144]

5.4 Energetic coupling of scales

Before we present the saturation properties of the Kelvin-Helmholtz-instability-driven turbulence in terms of the nonlinear interaction between the linear eigenmodes, we analyze the interaction between scales associated with the velocity and magnetic fields. The scale-interaction[145] is usually applied to homogeneous turbulence. Here we modify it for inhomogeneous turbulence.

Scale-interaction of velocity and magnetic fields

Because the flow and the magnetic field have mean profiles, it is useful to compare the linear and nonlinear processes in the energy dynamics. The linear energy injection or removal of energy at each scale is shown in Fig. 10.2(a), where the presented $Q_{\mathbf{u}}$

and $Q_{\mathbf{B}}$ are time-averaged over a long quasi-stationary state. As expected, the energy is injected only at scales that lie within the Kelvin-Helmholtz-unstable wavenumber range $0 < |k_x| < 1$, whereas energy from the fluctuation spectrum is removed via linear process at scales beyond the KH-unstable range. It is also observed, somewhat surprisingly, that the energy is linearly removed from wavenumbers $k_x = 0.4$ and $k_x = 0.8$ (the second and the fourth Fourier modes). We note that $k_x = 0.4$ is the wavenumber that is most unstable linearly. The reason behind this energy removal will later be explained by analyzing the energy transfer at each scale, decomposing the fluctuation into different eigenmodes instead of integrating the fluctuation spectrum along the z-axis, as we have done here.

In Fig. 10.2(b), the nonlinear processes that deposit or remove energy at each scale balance the linear processes. This suggests that the forced turbulence at hand is quasi-stationary in nature. The nonlinear transfer term combines contributions from all scales in all possible triads that collectively give or take energy away from each scale k_x. It does not distinguish whether the energy at k_x comes from the velocity or magnetic field at other wavenumbers of the triad. To identify and quantify such detailed contributions, we compute the wavenumber-to-wavenumber energy transfer functions between and among the velocity and magnetic fields, represented by the four transfer functions $S^{\mathbf{u}}_{\mathbf{u}}(k_x|k''_x)$, $S^{\mathbf{B}}_{\mathbf{B}}(k_x|k''_x)$, $S^{\mathbf{u}}_{\mathbf{B}}(k_x|k''_x)$, and $S^{\mathbf{B}}_{\mathbf{u}}(k_x|k''_x)$. Recalling that $S^{\mathbf{u}}_{\mathbf{B}}(k_x|k''_x) = -S^{\mathbf{B}}_{\mathbf{u}}(k''_x|k_x)$, there are only three unique transfer functions. These unique transfer functions are displayed in Figs. 10.3–10.5.

In Fig. 10.3(a), it is seen that, outside the KH-unstable range (shown as a dashed black box in the bottom left corner), the **u**-to-**u** transfer is almost negligible. Only on using a logarithmic scale of the transfer, an interesting feature is observed—a nonlocal triad, with a local energy transfer. This aspect is much more active and prominent in **B**-to-**B** energy transfer in Fig. 10.4, where a linear scale of energy transfer alone shows

such a behavior. The magnetic energy is dominantly transferred to smaller scales from larger scales in an iterative manner. The iteration occurs in such a way that a Fourier mode number n receives magnetic energy from the mode $n-1$ and gives magnetic energy to $n+1$—as evidenced in the bidiagonal structure in the transfer function in Fig. 10.4. This also implies that the **B**-to-**B** energy transfer is local, but the triad involved is highly nonlocal for large n.

We observe yet another different feature in the third transfer function in Fig. 10.5: the flow **u** at low wavenumbers $|k_x''| \sim 0$–0.5 significantly injects energy into the magnetic reservoir at a wide range of wavenumbers.

The transfer functions are sensitive to the strength of the magnetic field. When it is very strong ($M_\mathrm{A} \lesssim 10$), a noticeable change is observed in $S^{\mathbf{u}}_{\mathbf{B}}(k_x|k_x'')$—the emergence of a diagonal in Fig. 9.6. Since **u**-to-**B** transfer is governed by $\mathbb{R}\mathrm{e}\left\{\left\langle \mathbf{B}^*(k_x)\cdot\left[\mathbf{B}(k_x')\cdot\nabla''\mathbf{u}(k_x'')\right]\right\rangle_z\right\}$, and the diagonal of Figure 9.6(c) implies the transfer occurs from $\mathbf{u}(k_x'')$ to $\mathbf{B}(k_x)$ with $k_x = k_x''$, it is the mediator field $\mathbf{B}(k_x'=0)$ that is responsible for the emergence of the diagonal. The diagonal gets amplified with a stronger magnetic field, and becomes prominent when $M_\mathrm{A} \lesssim 10$. Physically, this effect can be interpreted as the stretching of the stronger mean magnetic-field ($k_x'=0$) by the turbulent flow (k_x'') at a wide range of scales, generating larger-amplitude magnetic fluctuations at such scales ($k_x = k_x''$).

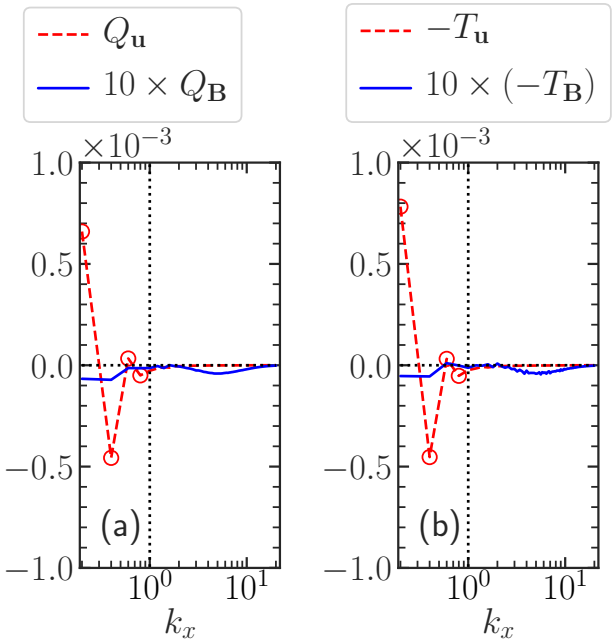

Figure 5.2: Time-averaged (a) linear and (b) nonlinear energy transfer rates in velocity and magnetic fields. The wavenumbers $|k_x| < 1$, to the left of the dotted vertical lines, are Kelvin-Helmholtz-unstable. The time-averaged rates of linear and nonlinear transfers are almost equal and opposite. Note the negative linear energy injection in the flow $Q_{\mathbf{u}}$ at $k_x = 0.4$, despite this being the wavenumber where perturbations linearly grow the fastest. The simulation parameters used are $M_{\mathrm{A}} = 30$, $D_{\mathrm{Krook}} = 2$, and $Pm = 1$.

Cross-scale energy fluxes: Forward or inverse cascade?

The **B**-to-**B** transfer in Fig. 10.4 is consistent with a forward cascade of magnetic energy. This is further confirmed from the cross-scale energy fluxes through a fixed wavenumber k_0. Using Eqs. (5.14a)–(5.14d), which quantify the energy passing through k_0, energy transfer from low wavenumbers $|k_x| \leq k_0$ to high wavenumbers $|k_x| > k_0$ can be measured. In Fig. 9.7, except at the lowest wavenumbers $|k_0| \lesssim 2$, near the KH-instability range, all energy fluxes are robustly in the forward direction—along the arrows shown in Fig. 10.1. The forward cascades of energies are clearly observed in Fig. 9.7(b). Note that, at most of the scales, $\Pi^{\mathbf{B}<}_{\mathbf{B}>}$ is larger than $\Pi^{\mathbf{u}<}_{\mathbf{B}>}$, which is in turn

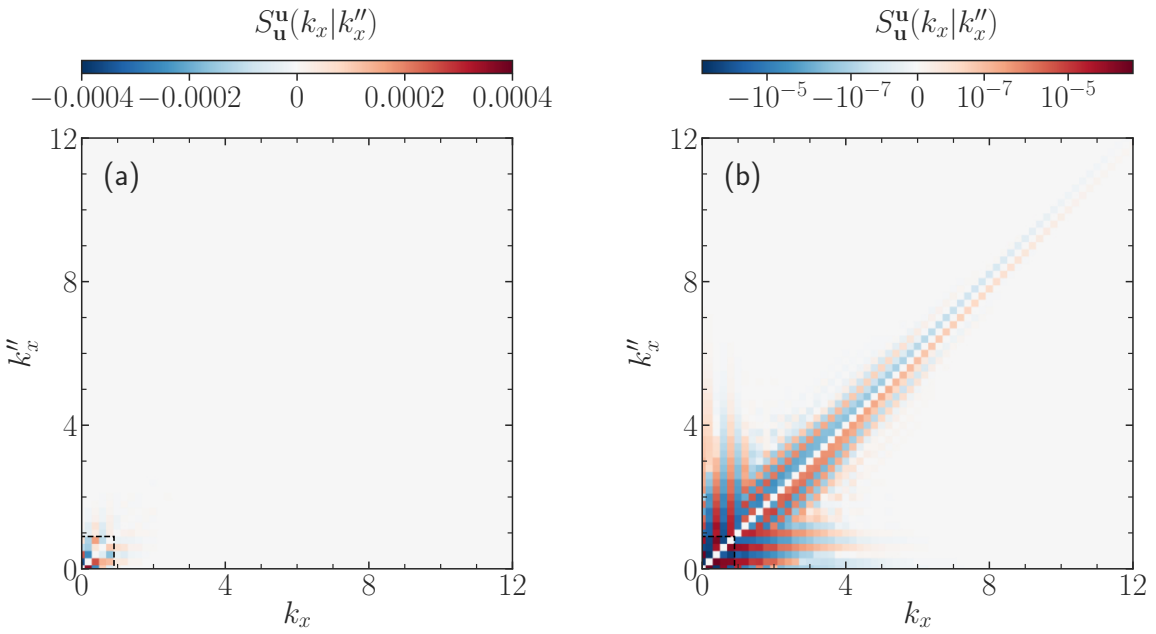

Figure 5.3: Time-averaged wavenumber-to-wavenumber energy transfer rates among the velocity fields. (a) The transfer is almost entirely localized within the Kelvin-Helmholtz instability range, shown with a black dashed box near the lower leftmost end of each subplot. (b) Logarithmic spectrum of the energy transfer reveals nonlocal triads, but local energy transfer, enabled by the box-sized Kelvin-Helmholtz eddy, i.e., the first non-zero Fourier mode number. The simulation parameters used are $M_{\mathrm{A}} = 120$, $D_{\mathrm{Krook}} = 2$, and $Pm = 1$.

larger than $\Pi^{\mathbf{u}<}_{\mathbf{u}>}$, in agreement with the energy transfer in every triad pair shown in Figs. 10.3–10.5. The forward cascade of energy (magnetic and kinetic) is expected for 2D MHD [25], and is intrinsic to the fluxes of Eqs. (5.14a)–(5.14d), which are based on energy transfer rates.

Inverse cascading in 2D homogeneous MHD applies only to the mean-squared magnetic-flux-function, $\int \psi^2 d^2x$, whose corresponding nonlinear transfer carries fewer spatial derivatives than the nonlinear transfer of energy. In this paper, we are expressly interested in the energetics of the inhomogeneous-flow-driven turbulence.

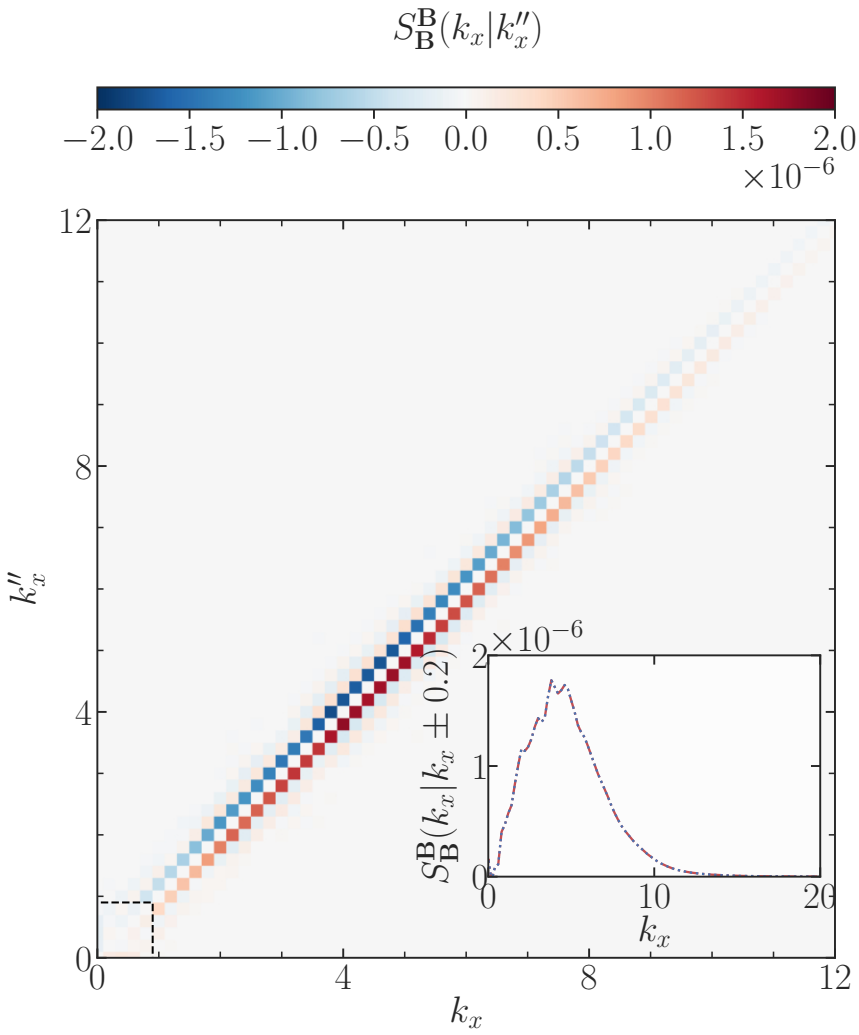

Figure 5.4: Time-averaged wavenumber-to-wavenumber energy transfer rates among the magnetic fields. The transfer is dominant outside the Kelvin-Helmholtz instability range, shown with a black dashed box near the lower leftmost end of the plot. The transfer **B**-to-**B** involves nonlocal triads but energy is locally transferred—from a high wavenumber to another high wavenumber. Shown in the inset are one-dimensional spectra of the transfer function, following the two diagonals, $k''_x - k_x = \pm 2\pi/L_x$. The two curves, red and black, are identical, although one is positive and another negative in sign, which is a consequence of energy conservation in a triad. The simulation parameters used are $M_{\mathrm{A}} = 120$, $D_{\mathrm{Krook}} = 2$, and $Pm = 1$.

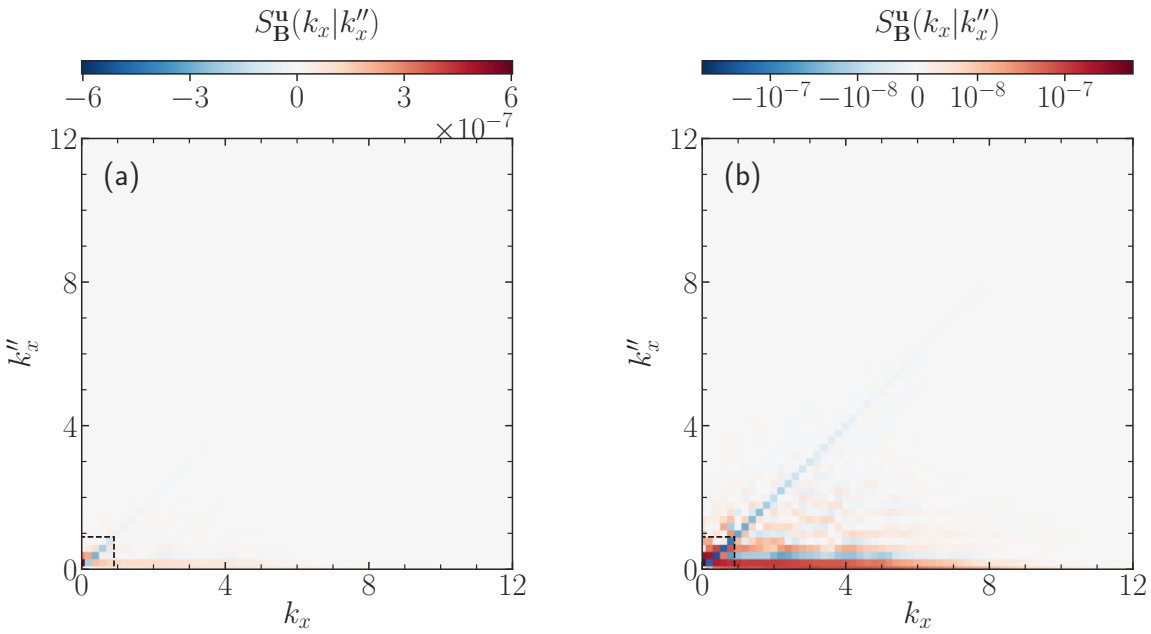

Figure 5.5: Time-averaged wavenumber-to-wavenumber energy transfer rates between the velocity and magnetic fields. (a) The transfer involves nonlocal triads; the energy transfer is also nonlocal. In particular, the first few Fourier modes (up to around 4) of the flow, shown with k''_x, generate significant energy in the magnetic fields even at wavenumbers k_x ranging up to a value, as high as $k_x \sim 8$–12, evidenced in panel (b), using a logarithmic colorbar. The simulation parameters used are $M_{\rm A} = 120$, $D_{\rm Krook} = 2$, and $Pm = 1$.

5.5 Energetic coupling of eigenmodes

Eigenmode interaction with evolving mean profiles

Insights into instability saturation can be obtained by tracing the interaction of the unstable and stable eigenmodes with the mean profiles. Since the instantaneous mean flow profile, although forced, deviates from the initial mean-flow, there is, in general, some linear coupling between the linear eigenmodes of the initial mean profile. Whether this (quasi-)linear coupling is comparable to the linear growth rate of the eigenmodes of the initial profile is an important question. If the energy exchange rate R_j between the fluctuations and the time-deviation of the mean profiles via this

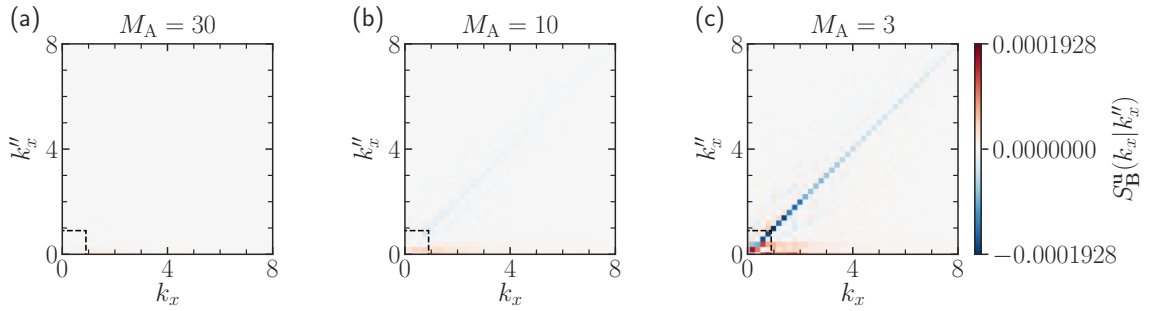

Figure 5.6: Similar to Fig. 10.5, but for differing magnetic field strengths. Here, (a) $M_A = 30$, (b) $M_A = 10$, (c) $M_A = 3$. The single diagonal $k_x = k_x''$ appears distinctly in subplot (c), and to a lesser degree in (b). This emerges from $S^{\mathbf{u}}_{\mathbf{B}}(k_x|k_x'') = \mathbb{R}\mathrm{e}\left\{\left\langle \mathbf{B}^*(k_x)\cdot\left[\mathbf{B}(k_x'=0)\cdot\nabla''\mathbf{u}(k_x''=k_x)\right]\right\rangle_z\right\}$, signifying a larger amount of work the small-scales ($|k_x''| \gg 1$) of the velocity fluctuations do, while attempting to bend the mean magnetic-field $\mathbf{B}(k_x'{=}0)$. Nonlinearly, the first few (up to around 4) Fourier modes of the flow significantly inject energy into the magnetic fields, even into higher wavenumbers, as discussed in Fig. 3(c). Other simulation parameters used are $D_{\mathrm{Krook}} = 2$ and $Pm = 1$.

(quasi-)linear coupling is small compared to the energy exchange rate Q_j between the initial mean profiles and the fluctuations, then using the eigenmodes of the initial mean profiles is justifiable for understanding energy dynamics and nonlinear coupling. To assess this exchange, we first compute the expressions in Eqs. (5.30a) and (5.30b) and compare them as time evoles for both the unstable ($j = 1$) and stable ($j = 2$) eigenmodes.

The rate at which the external forcing replenishes the mean flow can control the deviations of the instantaneous mean profiles from the initial profiles. We investigate this aspect in Fig. 9.8. Both cases of forcing strengths show that the effect of the linear coupling between the eigenmodes—quantified by R_j—is considerably smaller than Q_j. The ratio of R_j to Q_j gets further lowered when the mean flow is replenished faster (i.e., larger D_{Krook}). This means that the evolved shear-flow profile is closer to the initial unstable flow-profile. This detailed analysis provides justification for using eigenmodes of the initial profile as a fluctuation basis.

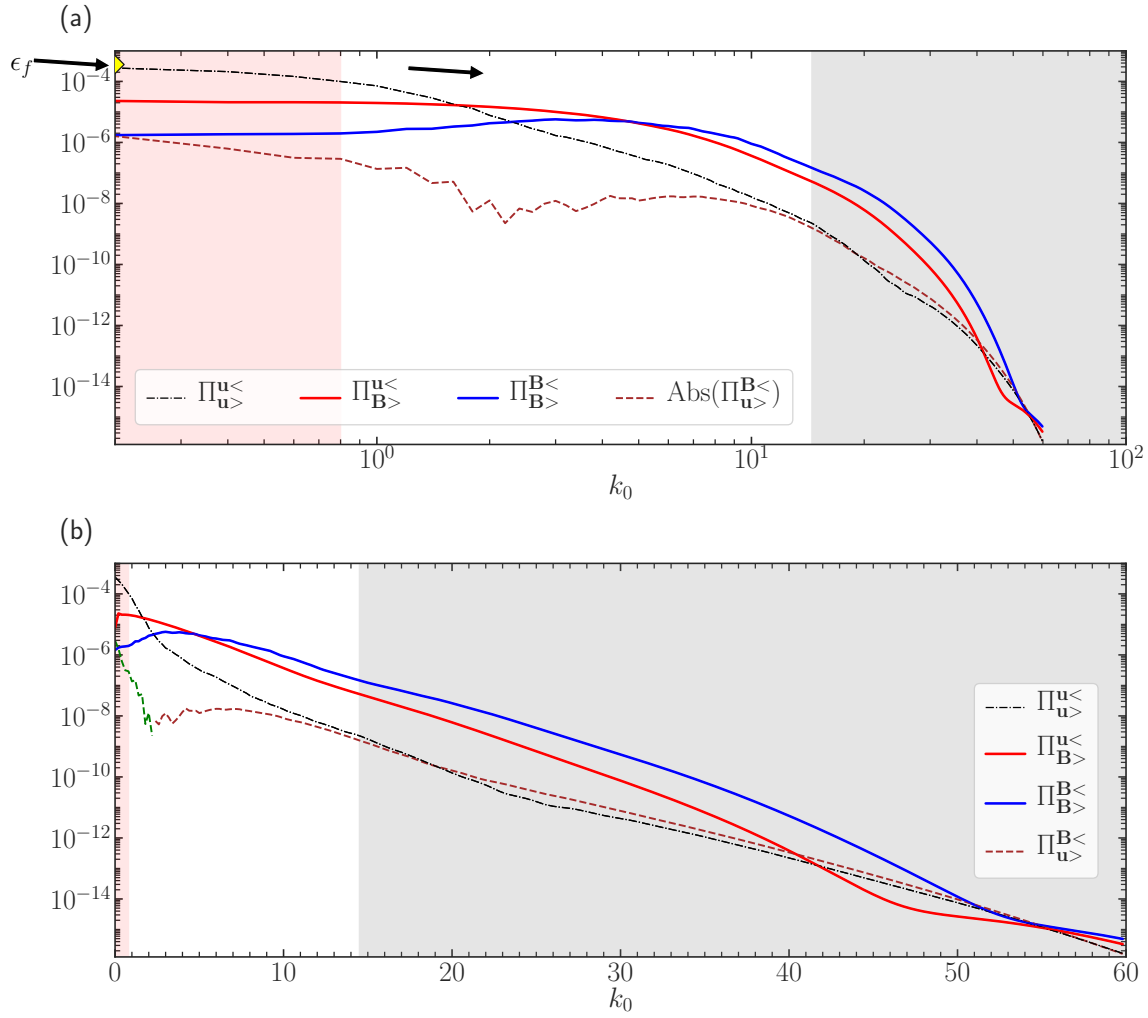

Figure 5.7: Positive Π implies transfer along the arrows of Fig. 10.1. In the 2D turbulence here, cross-scale MHD energy fluxes move from large to small scales. (a) The kinetic and magnetic energies both are robustly cascaded forward at every scale, as evidenced by the black and the blue curves, respectively. The kinetic energy flux $\Pi^{\mathbf{u}<}_{\mathbf{u}>}$ is dominant at the largest scales, and at $k_0 = 0$ (shown with the yellow diamond on the left axis), the flux agrees with the energy $\epsilon_f = 0.0004$ externally supplied by the Krook forcing to the mean flow. (b) The fluxes develop a noticeable exponential envelope at around $k_0 = 15$, after which the exponential fall-off continues with increasing wavenumber. The simulation resolves the dissipation range, as k_0 in the simulation ranges up to 205. The flux $\Pi^{\mathbf{B}<}_{\mathbf{u}>}$ for $k_0 \leq 2.2$ (shown with a green dashed curve) is negative. The grey-shaded region corresponds to the dominant dissipation scales, starting around $k_0 = (\epsilon_f\, Re^3)^{1/4} = 15$; the light-red shaded region is the instability range. Parameters used here are $M_{\rm A} = 120$, $D_{\rm Krook} = 2$, $Re = 500$, and $Pm = 1$.

We note that the energy transfer Q_2 is appreciable whenever the stable modes are excited to large amplitudes. Their excitation at early stage is caused by the nonlinear interaction between the unstable modes at different wavenumbers.[15] So, whenever there are at least a few Kelvin-Helmholtz unstable wavenumbers,[110] stable modes are universally, significantly excited; Q_2 then becomes comparable to Q_1.

Now, we use the eigenmode decomposition to investigate why some wavenumbers, despite lying in the KH-unstable wavenumber range (in Fig. 10.2), withdraw energy from the fluctuation spectrum instead of depositing. In Fig. 9.9, we show the energy transfer via linear processes, decomposing it into the contribution from unstable and stable modes. To show how well the sum of the contributions from unstable and stable modes captures the total z-integrated transfer, we overlay the data from Fig. 10.2. There, contributions from the continuum eigenmodes are also included. At $k_x = 0.2$, it is clearly observed that the stable mode transfers energy at a slightly greater rate than the unstable modes, thus depleting the overall fluctuation energy at that wavenumber. The quantity $Q_1 + Q_2$ captures reasonably well the total energy transfer $Q_{\mathbf{u}} + Q_{\mathbf{B}}$. Any discrepancy is attributed to the contributions from the sum of all the continuum modes, which dominates over the small visco-resistive dissipation of the unstable and stable modes at these large length scales.

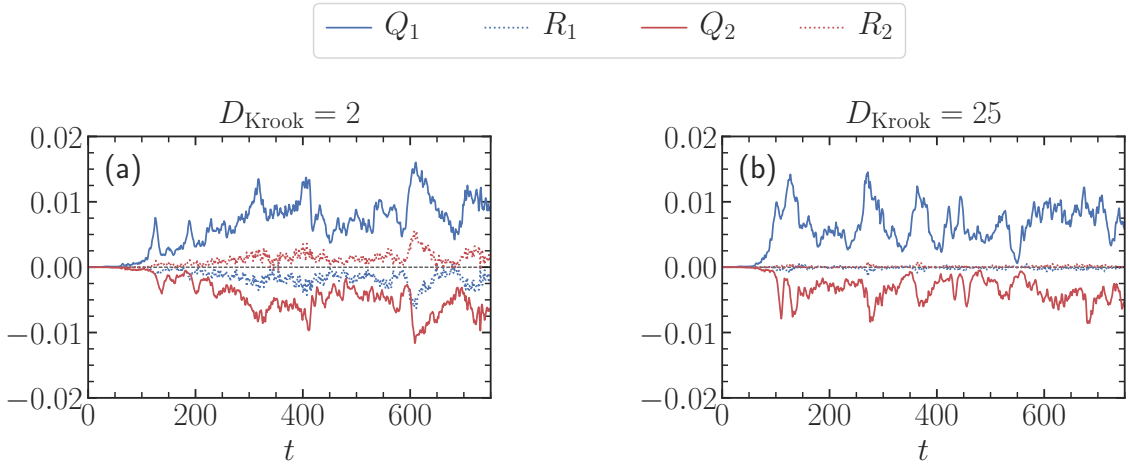

Figure 5.8: Linear processes of energy transfer due to unstable ($j = 1$) and stable ($j = 2$) eigenmodes. Shown are the linear injection or withdrawal rates Q_j using the profiles at $t = 0$, and the rate R_j using deviations of the instantaneous mean profiles of the flow and the magnetic field from their initial profiles. The wavenumber of the fluctuation chosen is $k_x = 0.2$, which is the loweest non-zero wavenumber in the simulation, where both the linear drive rate as well as the fluctuation energy spectrum peak. Comparing (a) $D_{\mathrm{Krook}} = 2$ with (b) $D_{\mathrm{Krook}} = 25$ shows that the higher rate (i.e., the larger D_{Krook}) of replenishment of the mean flow via Krook forcing removes almost all linear coupling—the term R_j—that is induced due to instantaneous fluctuations in the mean profiles. The simulation parameters used are $M_{\mathrm{A}} = 10$ and $Pm = 1$.

Channels of energy transfer between eigenmodes

We now analyze the nonlinear excitation and saturation processes for stable and unstable modes. Figure 9.10 shows the terms that saturate (take away energy from) the unstable modes T_1 and drive (feed energy into) the stable modes T_2. Near-equal levels of T_1 and T_2 are observed. These transfer terms are further probed in Fig. 9.10(b), where three sub-classes of triadic interactions are shown—$T_{j\mathrm{dd}}, T_{j\mathrm{dc}}$, and $T_{j\mathrm{cc}}$, representing the nonlinear interactions among the discrete modes, between the discrete and continuum modes, and among the continuum modes, respectively. These three terms capture all the nonlinear terms appearing on the right-hand side of the evolution equation of the j^{th} mode, with $j = 1$ and $j = 2$ representing the unstable and stable modes, respectively. We compute these three nonlinear terms following

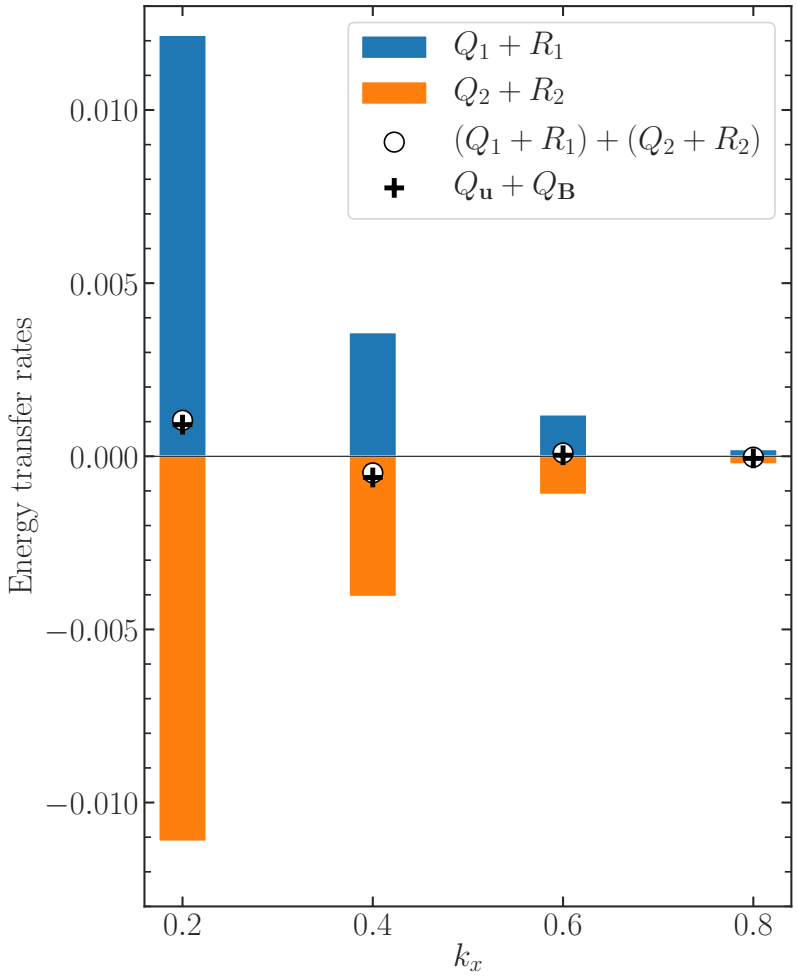

Figure 5.9: Comparison of time-averaged energy transfer rates $Q_j + R_j$ from the instantaneous mean profiles of the flow and the magnetic fields for the unstable ($j = 1$) with that for the stable ($j = 2$) modes. These rates are then summed to predict the total energy transfer rates via linear processes, which also include the contributions from the continuum eigenmodes and the small visco-resistive dissipation occurring at these large scales. The predictions, shown with black circles, are in excellent agreement with the total linear energy transfers, depicted with black plus signs.

the expressions in Eqs. (5.30e)–(5.30g). We find that $T_{j\mathrm{cc}}$ is appreciably smaller than $T_{j\mathrm{dd}}$ and $T_{j\mathrm{dc}}$, which are of similar magnitude but of opposite sign. To be precise, $|T_{j\mathrm{cc}}| \ll |T_{j\mathrm{dc}}| \lesssim |T_{j\mathrm{dd}}|$.

We now investigate whether the above apportionment of the three kinds of nonlinear transfer is intrinsic to a particular simulation-parameter regime or whether magnetic fields and magnetic Prandtl number (the ratio of viscosity to resistivity) affect these channels. We plot time-averaged transfer rates, both linear and nonlinear, in a single diagram. In Fig. 9.11(a), we first show the schematic diagram and then annotate it with numerical time-averaged transfer rates in Fig. 9.11(b), where $Pm = 0.1$. Indeed, $T_{j\mathrm{cc}}$ is negligibly small compared to $T_{j\mathrm{dc}}$, which is only a little smaller than $T_{j\mathrm{dd}}$, even for $Pm = 1$ in Fig. 9.12(a). Weakening the magnetic field strength in Fig. 9.12(b) does not alter $T_{j\mathrm{cc}}$ dramatically, but $T_{j\mathrm{dc}}$ does become appreciably smaller than $T_{j\mathrm{dd}}$. We interpret this as a result of the lower level of fluctuations of the continuum modes, which have been found to capture the magnetic fluctuations[144]; the magnetic fluctuations are weaker when the mean magnetic field is weak. In this case, the discrete modes of the flow assume a dominant role in nonlinearly driving the stable modes.

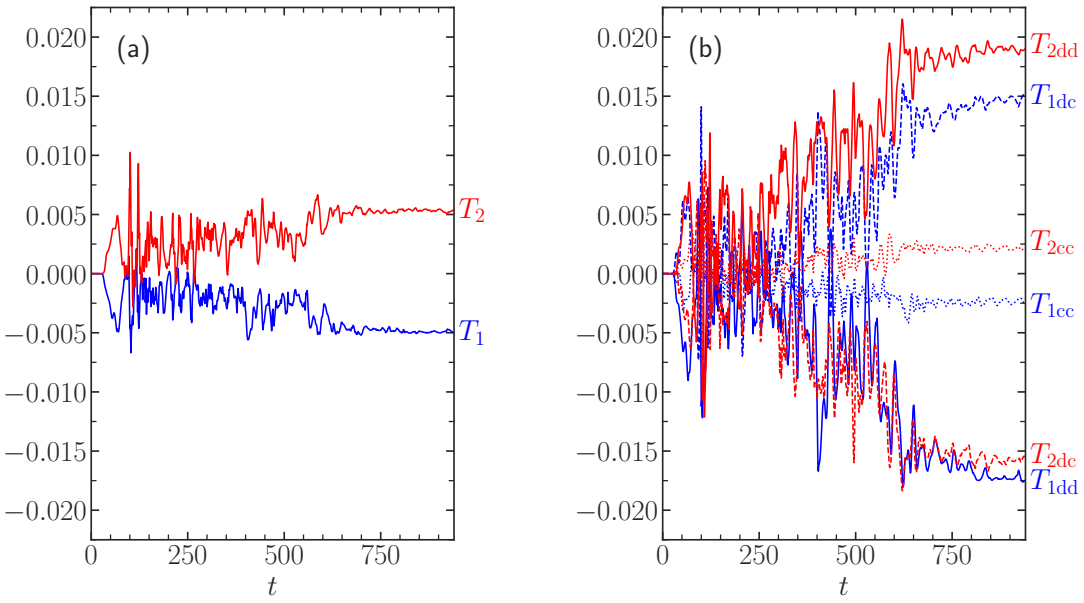

Figure 5.10: (a) Nonlinear energy transfer $T_1(k_x)$ that saturates unstable modes and $T_2(k_x)$ that excites stable modes. (b) These rates are then decomposed into three classes of triadic interactions, where the beating modes are discrete-discrete ($T_{j\mathrm{dd}}$), or discrete-continuum ($T_{j\mathrm{dc}}$), or continuum-continuum ($T_{j\mathrm{cc}}$). The $T_{j\mathrm{cc}}$ are negligibly small. The simulation parameters are $Pm = 0.1, M_\mathrm{A} = 10$, and $D_\mathrm{Krook} = 2$, and the chosen wavenumber is $k_x = 0.4$, which is the linearly fastest growing wavenumber.

Predicting energy transfer from mode-coupling coefficients

Statistical closure theories of turbulence[32, 33] predict that the mode-coupling coefficient is a key factor, although not necessarily the only factor; mode energy levels and the three-wave correlation time also enter the formula for the nonlinear energy transfer rate. [99]

To learn if the nonlinear mode-coupling coefficients are predictive of nonlinear energy transfer between eigenmodes in the quasi-stationary state of turbulence, we now separate the nonlinear energy transfer $T_{j\mathrm{dd}}$ further into individual components T_{jmn} by decomposing the discrete modes into unstable and stable modes: $T_{j\mathrm{dd}} = \sum_{m=1}^{2}\sum_{n=1}^{2} T_{jmn}$, where $m = 1$ stands for unstable modes and $m = 2$ represents stable modes, and likewise for n. The nonlinear mode-coupling coeffi-

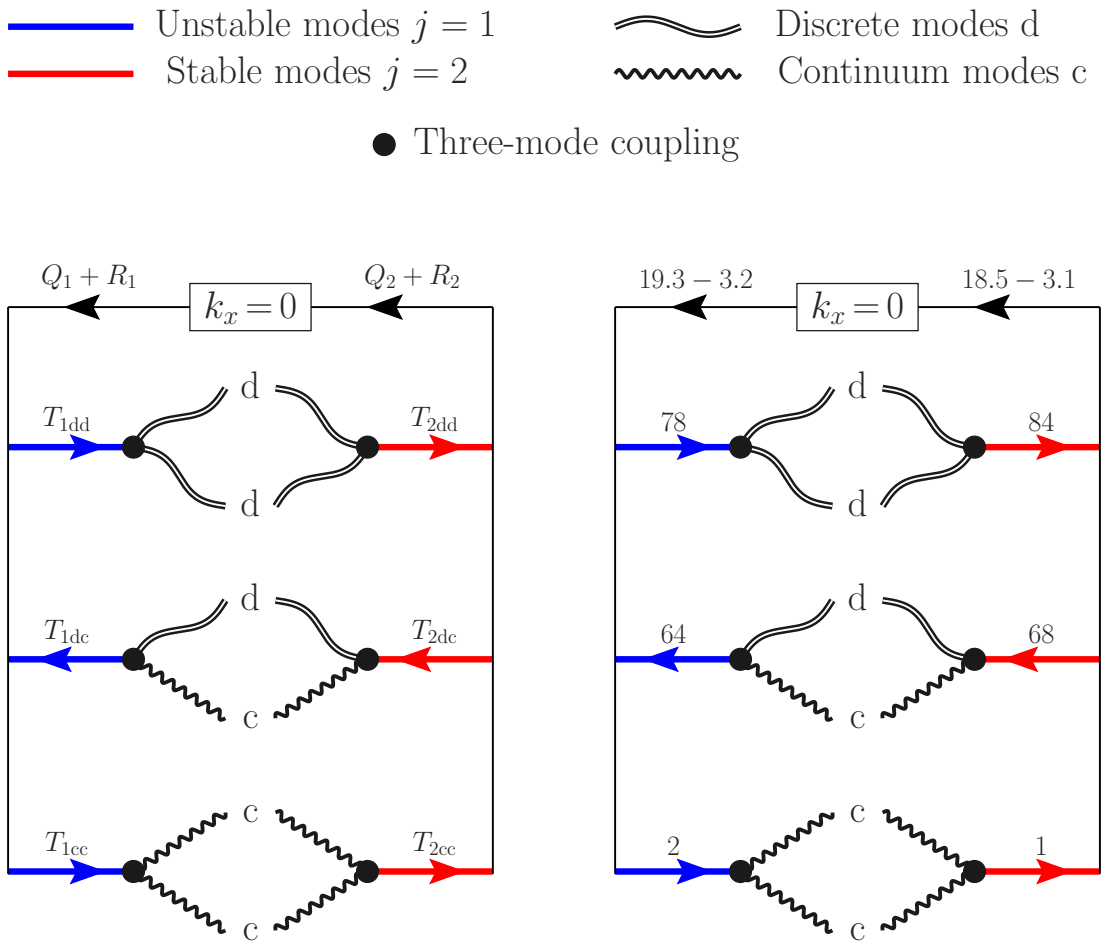

Figure 5.11: (Left) A schematic diagram that shows the terms corresponding to both the linear and nonlinear energy transfer processes that drive and saturate the unstable and stable modes. Since $Q_j, R_j, T_{j\mathrm{dd}}, T_{j\mathrm{dc}}$, and $T_{j\mathrm{c}}$ all appear on the right hand-side of Eq. (5.29), it is expected, on time-averaging, that $|Q_j + R_j| \approx |T_{j\mathrm{dd}} + T_{j\mathrm{dc}} + T_{j\mathrm{c}}|$ for both $j = 1$ and $j = 2$, individually. (Right) The energy transfer terms of the left-hand schematic diagram is quantified in units of $10^{-3}U_0^3/a$, for a simulation with parameters $Pm = 0.1, M_\mathrm{A} = 10$, and $D_\mathrm{Krook} = 2$. The difference between $Q_1 + R_1$ and $Q_2 + R_2$ represents the rate of energy that is supplied by the Krook forcing to the mean flow, attempting to restore the original flow-profile.

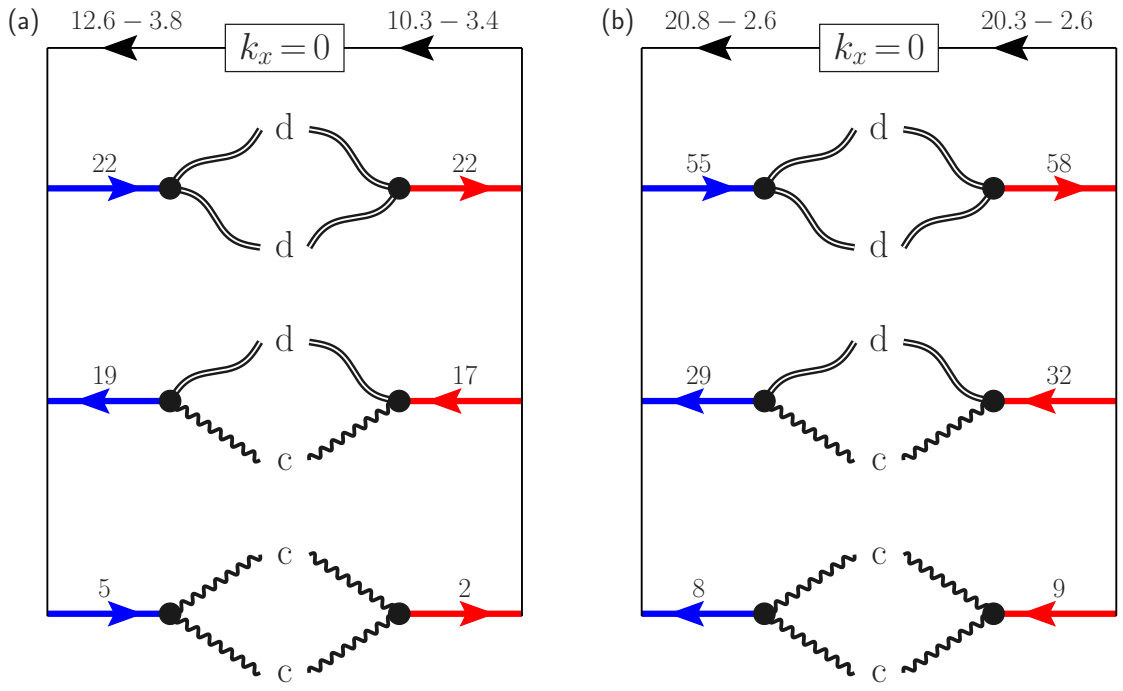

Figure 5.12: Same as the right-hand panel in Fig. 9.11, but now with varying magnetic field strength—the magnetic Prandlt number is also changed to $Pm = 1$. The parameters used are (a) $M_{\rm A} = 10$ and (b) $M_{\rm A} = 120$, both with the forcing strength $D_{\rm Krook} = 2$. Energy transfer rates are measured in units of $10^{-3}U_0^3/a$. With weaker magnetic field, Lorentz feedback on the flow of unstable and stable modes is weakened, and hence discrete-discrete interaction dominates over the discrete-continuum interaction.

cients $C_{jmn}(k_x, k'_x)$ of a mode j at k_x, nonlinearly coupled with a mode m at k'_x and n at $k''_x = k_x - k'_x$, can be computed. Since the mode-coupling coefficient $C_{jmn}(k_x, k'_x)$ is a complex-valued quantity, we compare their absolute values and predict the energy transfer levels $|T_{jmn}(k_x, k'_x)|$. To reduce the number of possible nonlinear mode-coupling terms, we now compose a symmetrized coupling coefficient $\bar{C}_{jmn}(k_x, k'_x)$ and a symmetrized nonlinear energy transfer $\bar{T}_{jmn}(k_x, k'_x)$, and display them in Fig. 5.13 — where $\bar{C}_{jmn}(k_x, k'_x) = C_{jmn}(k_x, k'_x) + C_{jnm}(k_x, k''_x)$ and $\bar{T}_{jmn}(k_x, k'_x) = T_{jmn}(k_x, k'_x) + T_{jnm}(k_x, k''_x)$.

Strong correlation between the coupling coefficient and the energy transfer suggests

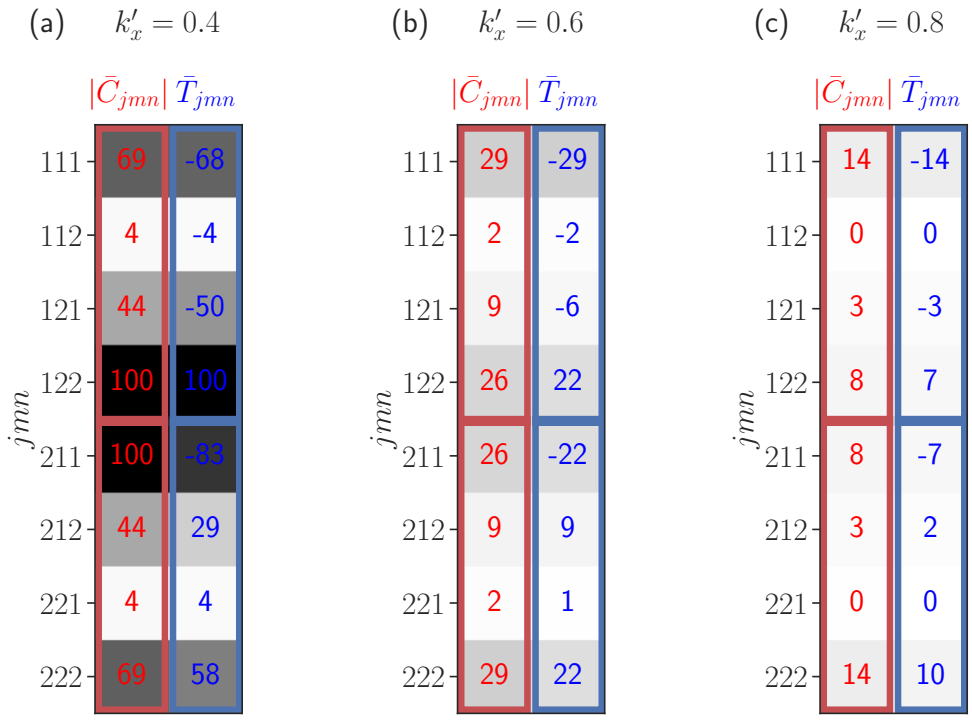

Figure 5.13: Comparison of the symmetrized nonlinear mode-coupling coefficient $\bar{C}_{jmn}(k_x, k'_x)$ and the symmetrized nonlinear energy transfer $\bar{T}_{jmn}(k_x, k'_x)$. The transfer term represents energy being pumped into an eigenmode j at wavenumber $k_x = 0.2$ due to nonlinear interaction between eigenmodes m at k'_x and n at $k''_x = k_x - k'_x$. The largest nonlinear drive is at $k_x = 0.2$ (the first Fourier mode). In the chart, all 48 possible discrete-discrete interactions, decomposed by individual unstable and stable modes and labeled by jmn, are shown, for (a) $k'_x = 0.4$, (b) $k'_x = 0.6$, and (c) $k'_x = 0.8$. In each subplot, the coupling coefficients have been scaled by the same factor. The transfer rates are measured in units of $10^{-3}U_0^3/a$. Positive (negative) transfer feeds (withdraws) energy in (from) an eigenmode j at $k_x = 0.2$. The simulation parameters used are $M_\mathrm{A} = 10$ and $D_\mathrm{Krook} = 2$. Note the symmetry reflected in the upper and lower 4 rows within each subplot, and the strong correlation between the coupling coefficient and the energy transfer.

that the coupling coefficients are critical elements in setting the energy transfer. This property may enable the construction of reduced-order models for nonlinear saturation based on these coupling coefficients.

5.6 Testing a general quasilinear theory of instability saturation

At the heart of all quasilinear theories, one presumes that only a particular family of eigenmodes, most often the unstable mode branch, interacts among itself at different scales leading to an instability saturation. Various approximations then are taken to derive simpler forms of quasilinear theories. Without using any approximation, we wish to test here a general quasilinear model of Kelvin-Helmholtz-instability-driven turbulence where Eqs. (5.1a)–(5.1d) will be kept fully intact, except that the system will be conditioned not to couple with the large-scale ($|k_x| < 1$) conjugate-stable modes. Noting the prevailing notion of instability saturation,[26–29] one may assume that the instability-driven nonlinear system, devoid of the stable modes, would produce essentially the same results as one obtains from a standard numerical solution of Eqs. (5.1a)–(5.1d). Is that really true?

To answer and test such a general model of instability saturation, Eqs. (5.1a)–(5.1d) can be transformed to the eigenmode basis of the linear operator. To do so, we follow the same method as described earlier in arriving at Eq. (5.28) from Eq. (5.16). Note that the eigenmodes of the non-dissipative linear operator of the shear-flow instability has an unstable, a stable, and a (theoretically infinite) number of continuum modes at each wavenumber in the range $0 < |k_x| < 1$. For $|k_x| \geq 1$, only continuum modes exist. Since the continuum modes are numerous and they are not the ideal choice for a basis function to implement in a numerical solver, we develop here a novel method to time-evolve the sum of all continuum-mode-associated fluctuations. First, we decompose an instantaneous state vector $X = [\phi, \psi]$ into an x-averaged mean

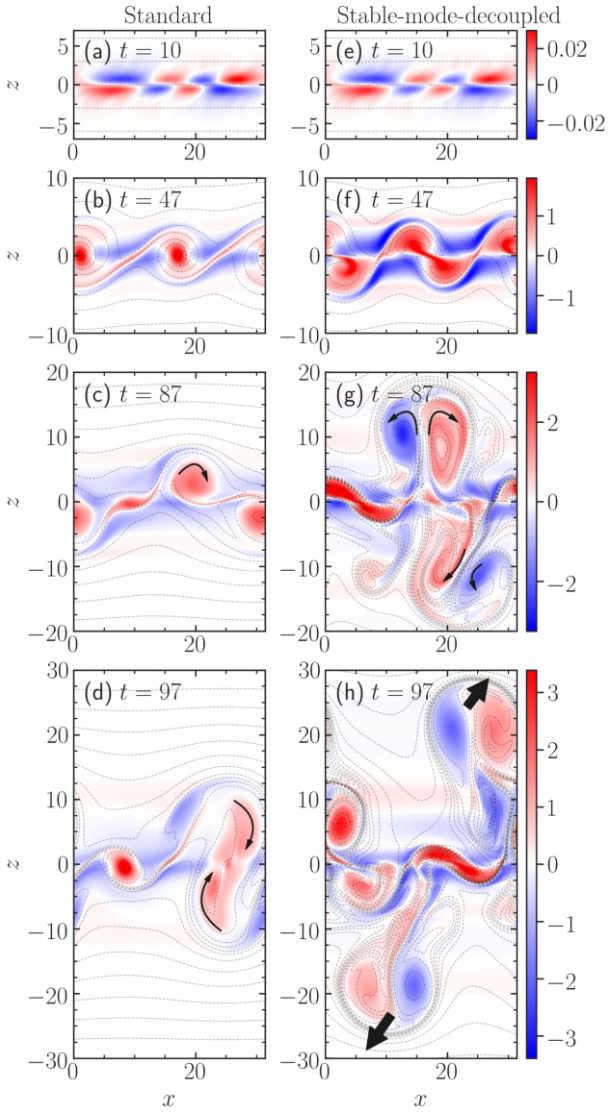

Figure 5.14: Time evolution of vorticity (filled contour) in two different simulations: (a)–(d) “Standard," and (e)–(h) “Stable-mode-decoupled." The grey, dashed contours show the total magnetic flux function ψ, along which the magnetic field lines are aligned. The fields are initially oriented along the positive x-axis. In all panels, same number of contours is shown. Unstable modes dominate at the early stage; even in the nonlinear phase, the unstable modes are qualitatively seen in (f)–(h), conspicuously in (f). Thin curved arrows illustrate eddy motions in (c), (d), and (g). Vortices merge in (d), whereas they separate in (h) with a violent ejection of eddies away from the shear layer, shown with thick straight arrows. In (a)–(d), however, stable modes confine the turbulence near the shear layer. Magnetic structures in (g) and (h) are highly folded. (Multimedia view)

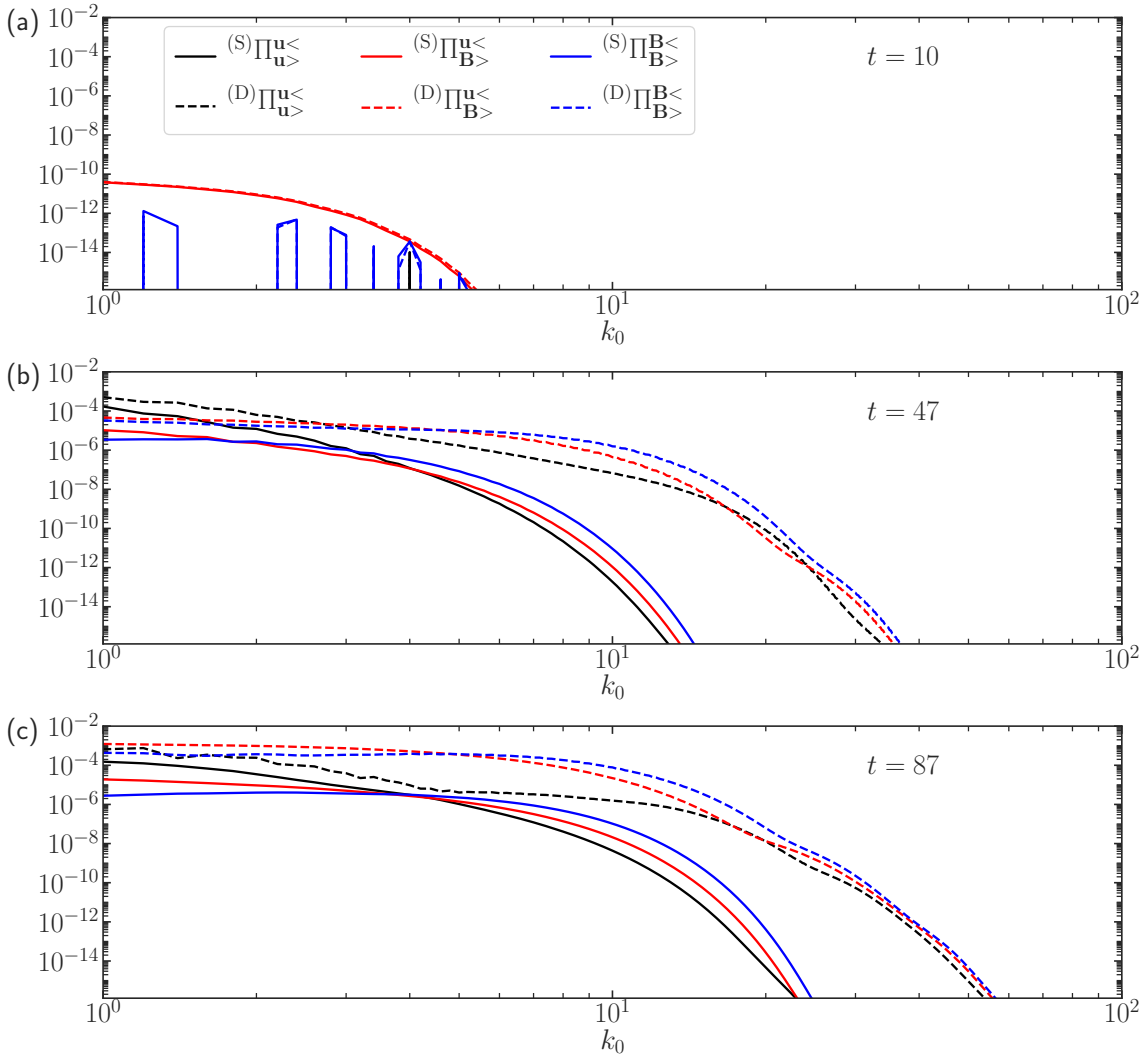

Figure 5.15: Energy flux shown at wavenumbers, beyond the instability scale $0 < k_0 < 1$. The left-handed superscripts "(S)" and "(D)" represent the energy fluxes in a *s*tandard simulation and in a stable-mode-*d*ecoupled simulation, respectively. Both simulations use identical parameters: $M_{\rm A} = 60$, $D_{\rm Krook} = 2$, and $Pm = 1$. At the first few time steps, the flux spectra are alike, but soon evolve differently, c.f. (a) with (b). Positive fluxes mean nonlinear energy cascade to small scales. The flux spectra at $t = 97$ are similar to that in (c). When uninhibited by stable modes, the energy fluxes are larger by order of magnitude, and the dissipation length scale is pushed to larger k_0.

$X(k_x = 0)$ and fluctuations $\widetilde{X}(x, z)$. The fluctuations are then decomposed as

$$\widetilde{X}(x,z) = \sum_{0<|k_x|<1} \sum_{j=1}^{2} \beta_j(k_x) X_j(k_x, z) \mathrm{e}^{ik_x x} + X_{\mathrm{c}}(x,z), \tag{5.32}$$

where the first term on the right-hand side is a sum of the unstable ($j = 1$) and stable modes ($j = 2$) throughout the Kelvin-Helmholtz-unstable wavenumber range; and the second term $X_{\mathrm{c}}(x, z)$ stands for all remaining fluctuations, composed of continuum modes, whose evolution equation can be derived with the help of Eq. (5.32) and is given by

$$\begin{aligned} \partial_t M X_{\mathrm{c}}(x,z) &= \partial_t M \left[\widetilde{X}(x,z) - \sum_{0<|k_x|<1} \sum_{j=1}^{2} \beta_j(k_x) X_j(k_x,z) \mathrm{e}^{ik_x x} \right] \\ &= \partial_t M \widetilde{X}(x,z) - M \sum_{0<|k_x|<1} \sum_{j=1}^{2} \partial_t \beta_j(k_x) X_j(k_x,z) \mathrm{e}^{ik_x x}, \end{aligned} \tag{5.33}$$

where the linear operator M is defined in Eq. (5.17).

The second equality of Eq. (5.33) can be explicitly expressed using Eq. (5.16) as

$$\partial_t M X_{\mathrm{c}}(x,z) = L_0 \widetilde{X} + \widetilde{L} \widetilde{X} + L_{\mathrm{diss}} \widetilde{X} + N(\widetilde{X}, \widetilde{X}) - M \sum_{0<|k_x|<1} \sum_{j=1}^{2} \partial_t \beta_j(k_x) X_j(k_x,z) \mathrm{e}^{ik_x x}, \tag{5.34}$$

and $\partial_t \beta_j$ in Eq. (5.34) can be replaced with the right-hand side of Eq. (5.25), which is repeated below for convenience,

$$\partial_t \beta_j(k_x) = \gamma_j(k_x) \beta_j(k_x) + \left\langle Y_j, \left[\widetilde{L} \hat{X} + L_{\mathrm{diss}} \hat{X} \right] \right\rangle + \sum_{k_x'} \left\langle Y_j, \hat{N}(\hat{X}', \hat{X}'') \right\rangle \quad \text{for } j = 1, 2. \tag{5.35}$$

In a numerical simulation, termed “Standard", we evolve $k_x = 0$ mode in Eq. (5.15). This equation, however, couples with the fluctuations; hence, Eq. (5.25), with $j = 1, 2$,

and Eq. (5.34) are solved in conjunction. Such a solution reproduces the solution obtained from the usual direct numerical simulation of Eq. (5.15) to machine precision. This is anticipated, as Eq. (5.25) is obtained from merely a change of basis.

In another simulation, termed “Stable-mode-decoupled," two changes are made to the “Standard" system. First, Eq. (5.25) with $j = 2$ is erased. Second, from the entire system, all terms containing β_2 are removed—that is, coupling to the stable modes is analytically removed from the nonlinear system. Removing a family of eigenmodes in such a careful way by hand, rather than numerically zeroing them out at each time step of evolution, is unconventional, but has been applied in a few other cases, e.g., removal of a family of helical modes in isotropic and homogeneous turbulence. [154] Since the modes are completely removed from the system, they neither receive nor donate energy in a triadic interaction, and hence the mode-removed equations conserve the ideal invariants of the full standard nonlinear system.

The solutions of vorticity from the above two numerical simulations are visualized in Fig. 5.14 (Multimedia view). Both simulations have identical parameters $M_{\mathrm{A}} = 60$, $D_{\mathrm{Krook}} = 2$, and $Re = Rm = 50$. When the stable modes are analytically removed, the figure shows that the turbulence reaches higher amplitudes and becomes violent. In this case, the unstable modes can saturate only by passing on their energy to the small-scale cascade, which involves the generation of extended secondary flow structures. When stable modes are kept intact in the equations, they confine the turbulence near the shear layer, and thus lead to vortex merging events, as opposed to vortex separation that happens when the system is conditioned not to couple to the stable modes. With no stable modes, the x-directed, initial magnetic fields are highly folded by the violent and energetic eddies.

This brute force numerical experiment provides a visual display that confirms the comprehensive and technical analysis presented earlier in this paper: vortex mergers,

energetics, and cascades are all drastically different when the stable modes are not available to the system.

A further quantitative analysis of the standard and stable-mode-decoupled simulations is presented in Fig. 5.15. In the latter simulation, the energy fluxes show enhancement in their levels by orders of magnitude, compared to the standard simulation, despite both evolving from identical flux spectra at the early stage. The small-scale dissipation length-scale is also pushed to further smaller scales because of larger turbulent energy in the absence of stable modes.

5.7 General implications

Now we assess the detailed energetics shown in the preceding sections in relation to broader understanding and implications.

Imprints of instability-scale flow at small scales

A key aspect of the magnetic energy transfer is its nonlocality, in contrast to homogeneous isotropic turbulence, represented, for example, by the Kolmogorov spectrum. Figures 10.4 and 10.3(b) have a pronounced diagonal feature indicative of a nonlocal interaction. For each pair of red and blue cells across the diagonal, energy is exchanged via an interaction that is dominated by a single mode of the large-scale vortex flow arising from the Kelvin-Helmholtz instability. Note that similar nonlinear interactions have been found in other turbulence where a system-size vortex is externally stirred.[155] The coupling in Fig. 10.4 of two small-scale magnetic modes with a large-scale flow is intrinsically nonlocal. However, the energy exchanged tapers off significantly after a decade in wavenumber along the diagonal. This indicates

that an interaction that is intrinsically nonlocal is largely confined within a limited wavenumber range—a phenomenon enforced via energy-removal by the stable modes.

Stable modes vs. Kolmogorov wavenumber and dissipation-range turbulence

The Kolmogorov wavenumber k_d, where the turbulent energy cascade begins getting significantly attenuated because of small-scale energy dissipation, is directly related to the energy injection rate ϵ_f at large scales: $k_d = (\epsilon_f/d^3)^{1/4}$, where d is a coefficient related to small-scale dissipation, such as viscosity or resistivity. As the energy cascade processes do occur in the shear-flow turbulence considered here, k_d approximately delineates the dissipation range from the larger scales of turbulence. The energy injection rate is normally the energy Q_1 that is provided to the fluctuation spectrum by unstable modes. However, when stable modes are significantly excited via nonlinear processes, they act as large-scale turbulent sinks, and thus efficiently remove energy Q_2 from the fluctuation spectrum, steepening the mean-flow gradient. Only the remaining energy $Q_1 - Q_2 \approx \epsilon_f$ is then available to cascade nonlinearly to smaller scales. The energy injection rate for a simulation with $d = \nu = \eta = (1/500)aU_0$ can be determined from Fig. 9.12(b) to be $\epsilon_f \approx 0.5 \times 10^{-3} U_0^3/a$. Taking contributions of stable modes Q_2 into account, the predicted Kolmogorov wavenumber is then $k_d \approx 15.8a^{-1}$. This prediction is confirmed in Fig. 9.7. Neglecting the energetics of stable modes Q_2 yields $k_d \approx 38.8$. The stable modes reduce the energy input rate $\epsilon_f \approx Q_1 - Q_2$ to the small-scale energy cascade channel, and hence the cascade attenuates at a larger length scale.

The exponential fall-off of the MHD energy fluxes in spectral space in Fig. 9.7 also suggests that a simple model of the energy fluxes,[156] may be applicable. To test

such a prospect, we follow the assumption that the spectral energy fluxes, in inertial and dissipative ranges, obey $\Pi(k) = p\,k^{-\beta}\exp\left(-ck^{\alpha}\right)$, where c and p are independent of the wavenumber k; this implies that the energy flux need not be constant, owing to energy absorption by dissipative physics, as opposed to what one would have in a strict inertial range ($\alpha = \beta = 0$).[157–159] Fitting such a profile to the energy fluxes in Fig. 9.7 (with a standard choice $\beta = 0$ to allow a constant energy flux at larger scales), we find that the exponent α for the total magnetic energy flux at smaller scales $k_0 > 10$, $\Pi^{\rm all}_{\mathbf{B}>} = \Pi^{\mathbf{u}<}_{\mathbf{B}>} + \Pi^{\mathbf{u}>}_{\mathbf{B}>} + \Pi^{\mathbf{B}<}_{\mathbf{B}>}$, is very close to $4/3$, which matches with the widely recognized theoretical prediction of Ref. [156]. The exponent α for the total kinetic energy flux $\Pi^{\rm all}_{\mathbf{u}>} = \Pi^{\mathbf{u}<}_{\mathbf{u}>} + \Pi^{\mathbf{B}<}_{\mathbf{u}>} + \Pi^{\mathbf{B}<}_{\mathbf{u}>}$, however, we find, is around $1/2$, which we are unable to explain with such a simple model; it is possible that the nonlinearly excited stable modes have some impact on this exponent.

The effect of stable modes on Kolmogorov dissipation length scale is substantiated also by Figs. 5.14 and 5.15. There, the stable-mode-decoupled simulation shows orders of magnitude of enhancement in the turbulent energy fluxes, which fall off only at much larger wavenumber than the fluxes do in the standard simulation. This result is consequential. Because the small-scale energy fluxes are very large when the stable modes are absent, traditional Kolmogorov-like scaling arguments of energy cascade are expected to fail, as, there, the energy injection rate to the nonlinear cascade is equated to the rate of energy withdrawl by the unstable modes from the mean shear-flow. Incorporating the energy reversal by the stable modes can make the scaling arguments succeed.

Thermodynamic irreversibility and stable modes

It is not unreasonable to assume that the wavenumber of the fastest-growing mode corresponds to the peak of the fluctuation spectrum. However, in gyrokinetic simulations of drift-wave turbulence, a shift of the spectrum peak to lower wavenumber is commonly observed, and is not fully understood. In Figs. 10.2(a) and 9.9, we find that the wavenumber $k_x = 0.4$ where the perturbations linearly grow the fastest depletes energy from the fluctuation spectrum and deposits in the mean background gradients—a finding that is counter intuitive, at first. Further examination in Fig. 9.9 reveals that the stable-mode amplitude exceeds the unstable-mode amplitude at $k_x = 0.4$. This does not violate the laws of thermodynamics, because the energy transfer summed over all wavenumbers is directed from the mean gradient to the fluctuation spectrum, in accordance with the breakdown of time-reversal symmetry due to visco-resistive effects. This forward flow of energy from the mean gradient to the fluctuation spectrum is evident at $k_x = 0.2$, where the spectrum peaks.

5.8 Conclusions

This paper has systematically examined energy transfer processes in MHD turbulence driven by shear-flow instability, quantifying the effect of linearly stable roots of the dispersion relation [113], which are nonlinearly excited to a significant level, thus modifying the landscape of fluctuation source and sink at large scales. The role of nonlinearly excited stable modes as a fluctuation energy sink has been extensively examined for fusion-relevant microinstability, where the prompt loss of energy at the largest scales allows the formulation of saturation balances that exclude extended scale ranges of cascaded energy [32, 95]. In this paper, we have examined the effect of stable modes on the energy cascades, quantifying energy transfer rates under an

eigenmode decomposition that tracks energy transfer between finite-amplitude-induced eigenmodes. The canonical direct cascade of kinetic and magnetic energies [25] remains in force despite the presence of stable eigenmodes. However, the energy carried in the cascade is dramatically reduced compared to the energy fed into the fluctuation spectrum by the unstable modes, with most of that unstable-mode energy returned to the mean flow by the stable modes. This fraction of energy return ranges from around 75% to 97%, depending on the strength of the imposed magnetic field and on the magnetic Prandtl number. The cascading energy flux to small scales does dissipate at small visco-resistive scales, although such energy flux exponentially attenuates at small scales, dictated by the amplitudes of the stable modes at large scales, as such modes directly control the energy input rate into the small-scale cascade.

The energy nonlinearly transferred from the unstable modes and deposited almost in its entirety into the stable modes has two distinct and dominant channels. These arise from the nonlinear interactions, first, among the fluctuations composed of the discrete modes $T_{j\mathrm{dd}}$ and, second, the nonlinear interactions between the fluctuations of the discrete and the continuum modes $T_{j\mathrm{dc}}$. The discrete modes are the unstable $j = 1$ and conjugate-stable $j = 2$ eigenmodes of the ideal linear operator of the Kelvin-Helmholtz instability. The continuum modes are marginally stable and occur across a continuum of frequencies and across all scales, even beyond the instability scale. The strength of the interaction among the fluctuations of the continuum modes $T_{j\mathrm{cc}}$, which in principle affects the evolution of the unstable and stable modes, is found to be negligibly small, ranging from 2% to 23% of $T_{j\mathrm{dd}}$ or $T_{j\mathrm{dc}}$. The interaction term $T_{j\mathrm{dd}}$ is found to always take energy away from the unstable modes and channel it away almost in its entirety to the stable modes. On the other hand, the nonlinear transfer $T_{j\mathrm{dc}}$ always takes energy from the stable modes and provides it nonlinearly to the unstable modes. Nevertheless, $T_{j\mathrm{dd}}$ is always larger than $T_{j\mathrm{dc}}$ in magnitude. Thus

the nonlinearity transfers a net positive energy from unstable to stable modes.

Based upon the strength of the nonlinear interactions between the fluctuations classified in the eigenmode basis, a reduced-order model for the subgrid-scale turbulence generated by the Kelvin-Helmholtz instability may be possible. A self-consistent subgrid-scale model could involve ignoring the eddy-eddy nonlinearity beyond a prescribed cutoff wavenumber.[126] This cutoff wavenumber could be chosen as low as the inverse of the shear-width of the mean profile, which is where the instability ceases to exist (i.e., $|k_x| \sim 1$).

For the first time, we have built and tested a general quasilinear model of Kelvin-Helmholtz-instability-driven turbulence, motivated by prevailing hypothesis of instability saturation[26–29, 38]. We have discovered that even a model where all scales of turbulence are solved exactly, including all eigenmodes—both unstable and continuum modes—but removing just their coupling to the stable modes, fails to reproduce even the primary features of the Kelvin-Helmholtz turbulence. For instance, the usual large-scale vortex merger events in 2D are missed, and instead an explosive separation of large-scale vortices is seen, in addition to a rapid spreading of turbulence away from the shear layer. Such a dramatic difference in the structures and levels of turbulence, along with enhanced turbulent energy fluxes, when the couplings to the stable modes are analytically removed, confirm that the stable modes act as a large-scale energy sink, and thus tame the turbulence near the narrow region of the shear layer. This finding has consequences in modeling efforts of shear-flow turbulence in fusion plasmas when the zonal flows and streamers go unstable.

It has not escaped our understanding that, given the critical role of stable modes with respect to the structures and energetics of the Kelvin-Helmholtz turbulence, studies of MHD turbulence in reconnection-driven sheared outflows[62] may benefit from the investigation of stable modes in such settings, and simpler models of scaling

and cascade rates may be informed from such analyses. Although the stable modes considered in this paper are of the shear-flow instability, other instabilites too have stable modes, for instance, the tearing instability,[159] which can co-exist with the Kelvin-Helmholtz instability. The stable modes, as here in shear-flow turbulence, may deplete the fluctuation energy there as well, thus potentially lowering the small-scale energy cascade rate and affecting the spectral index of the fluctuation power spectrum. More work needs to be carried out in the future to assess the impact of stable modes on, for example, MHD energy fluxes and the breaking of energy cascade.[153]

Appendix: Anti-symmetric S-transfer-function

The anti-symmetry property of the wavenumber-to-wavenumber (S-) transfer function

$$S^{\mathbf{C}}_{\mathbf{A}}(k_x|k''_x) = -S^{\mathbf{A}}_{\mathbf{C}}(k''_x|k_x), \tag{A1}$$

will be proved here.

To begin, take Eq. (5.10)

$$S^{\mathbf{C}}_{\mathbf{A}}(k_x|k''_x) = \mathbb{R}\mathrm{e}\left\{\left\langle \mathbf{A}(-k_x)\cdot\left[\mathbf{B}(k'_x)\cdot\nabla''\mathbf{C}(k''_x)\right]\right\rangle_z\right\}. \tag{A2}$$

where the triadic interaction involves $\mathbf{A}, \mathbf{B}$, and $\mathbf{C}$ at wavenumbers k_x, k'_x, and k''_x such that $-k_x + k'_x + k''_x = 0$. Following the analogy with Eq. (A2), we compose the

expression for $S^{\mathbf{A}}_{\mathbf{C}}(k_x''|k_x)$, with the constraint $-k_x + k_x' + k_x'' = 0$ still applied, as

$$\begin{aligned} S^{\mathbf{A}}_{\mathbf{C}}(k_x''|k_x) &= \mathbb{R}\mathrm{e}\left\{\left\langle \mathbf{C}(-k_x'') \cdot \Big[\mathbf{B}(-k_x') \cdot \nabla \mathbf{A}(k_x)\Big]\right\rangle_z\right\} \\ &= \mathbb{R}\mathrm{e}\left\{\left\langle \mathbf{C}(k_x'') \cdot \Big[\mathbf{B}(k_x') \cdot \nabla \mathbf{A}(-k_x)\Big]\right\rangle_z\right\} \\ &= S^{\mathbf{A}}_{\mathbf{C}}(-k_x''|-k_x), \end{aligned} \tag{A3}$$

which simply means that the energy transfer from k_x to k_x'' is same as the energy transfer from $-k_x$ to $-k_x''$, i.e., conjugate symmetry, as was shown also for the net energy transfer in Eq. (5.6).

With the expressions for $S^{\mathbf{C}}_{\mathbf{A}}(k_x|k_x'')$ and $S^{\mathbf{A}}_{\mathbf{C}}(k_x''|k_x)$ at hand, we now show that they hold an antisymmetry property: $S^{\mathbf{C}}_{\mathbf{A}}(k_x|k_x'') = -S^{\mathbf{A}}_{\mathbf{C}}(k_x''|k_x)$. To prove such, let us evaluate $S^{\mathbf{C}}_{\mathbf{A}}(k_x|k_x'') + S^{\mathbf{A}}_{\mathbf{C}}(k_x''|k_x)$ below

$$\begin{aligned} S^{\mathbf{C}}_{\mathbf{A}}(k_x|k_x'') + S^{\mathbf{A}}_{\mathbf{C}}(k_x''|k_x) = \mathbb{R}\mathrm{e}\left\langle \mathbf{A}^*(k_x) \cdot \Big[\mathbf{B}(k_x') \cdot \nabla \mathbf{C}(k_x'')\Big]\right\rangle_z \\ + \mathbb{R}\mathrm{e}\left\langle \mathbf{C}^*(k_x'') \cdot \Big[\mathbf{B}^*(k_x') \cdot \nabla \mathbf{A}(k_x)\Big]\right\rangle_z \end{aligned} \tag{A4}$$

The first term on the right-hand side of Eq. (A4) is

$$\mathbb{R}\mathrm{e}\left\langle \mathbf{A}^*(k_x) \cdot \Big[\mathbf{B}(k_x') \cdot \nabla \mathbf{C}(k_x'')\Big]\right\rangle_z = \mathbb{R}\mathrm{e}\left\langle \mathbf{A}^* \cdot (B_x' i k_x'' + B_z' \partial_z)\mathbf{C}''\right\rangle_z, \tag{A5}$$

and the second term on the right-hand side of Eq. (A4) is

$$\begin{aligned} \mathbb{R}\mathrm{e}\left\langle \mathbf{C}^*(k_x'') \cdot \Big[\mathbf{B}^*(k_x') \cdot \nabla \mathbf{A}(k_x)\Big]\right\rangle_z &= \mathbb{R}\mathrm{e}\left\langle \mathbf{C}''^* \cdot (B_x'^* i k_x + B_z'^* \partial_z)\mathbf{A}\right\rangle_z \\ &= \mathbb{R}\mathrm{e}\left\langle \mathbf{C}'' \cdot (-B_x' i k_x + B_z' \partial_z)\mathbf{A}^*\right\rangle_z. \end{aligned} \tag{A6}$$

Substituting the expressions from Eqs. (A5) and (A6) in Eq. (A4),

$$
\begin{aligned}
&S^{\mathbf{C}}_{\mathbf{A}}(k_x|k''_x) + S^{\mathbf{A}}_{\mathbf{C}}(k''_x|k_x) \\
&= \mathbb{R}\mathrm{e}\left\langle \mathbf{A}^* \cdot (B'_x i k''_x + B'_z \partial_z)\mathbf{C}'' \right\rangle_z + \mathbb{R}\mathrm{e}\left\langle \mathbf{C}'' \cdot (-B'_x i k_x + B'_z \partial_z)\mathbf{A}^* \right\rangle_z \\
&= \mathbb{R}\mathrm{e}\left\langle B'_x i(k''_x - k_x)\mathbf{A}^* \cdot \mathbf{C}'' \right\rangle_z + \mathbb{R}\mathrm{e}\left\langle B'_z \mathbf{A}^* \cdot \partial_z \mathbf{C}'' + B'_z \mathbf{C}'' \cdot \partial_z \mathbf{A}^* \right\rangle_z \\
&= -\mathbb{R}\mathrm{e}\left\langle i k'_x B'_x \mathbf{A}^* \cdot \mathbf{C}'' \right\rangle_z + \mathbb{R}\mathrm{e}\left\langle B'_z \partial_z (\mathbf{A}^* \cdot \mathbf{C}'') \right\rangle_z \\
&= -\mathbb{R}\mathrm{e}\left\langle i k'_x B'_x \mathbf{A}^* \cdot \mathbf{C}'' \right\rangle_z - \mathbb{R}\mathrm{e}\left\langle (\partial_z B'_z)\mathbf{A}^* \cdot \mathbf{C}'' \right\rangle_z \\
&= -\mathbb{R}\mathrm{e}\left\langle (i k'_x B'_x + \partial_z B'_z)\mathbf{A}^* \cdot \mathbf{C}'' \right\rangle_z \\
&= -\mathbb{R}\mathrm{e}\left\langle [\nabla' \cdot \mathbf{B}(k'_x)]\mathbf{A}^* \cdot \mathbf{C}'' \right\rangle_z \\
&= 0.
\end{aligned}
\tag{A7}
$$

In the second last line of Eq. (A7), it can be seen that divergence of the vector field B appears. Since all the vectors fields—velocity and magnetic fields—are divergenceless in this study, we obtain null at the end. Thus the anti-symmetry property of the wavenumber-to-wavenumber (S-) transfer function

$$
S^{\mathbf{C}}_{\mathbf{A}}(k_x|k''_x) = -S^{\mathbf{A}}_{\mathbf{C}}(k''_x|k_x), \tag{A8}
$$

is proved. It can be a fruitful exercise for the reader to repeat this proof in a fully periodic system,[145] where the proof requires only a couple of lines of equation.

Part II

Instability-Induced Zonal Jets

6 **PAPER D**: THREE-DIMENSIONAL SHEAR-FLOW INSTABILITY SATURATION VIA STABLE MODES

A version of this chapter was published in Phys. Fluids 35, 105151 (2023), in a joint special issue by Phys. Fluids and Phys. Plasmas.

ABSTRACT

Turbulence in three dimensions (3D) supports vortex stretching that has long been known to accomplish energy transfer to small scales. Moreover, net energy transfer from large-scale, forced, unstable flow-gradients to smaller scales is achieved by gradient-flattening instability. Despite such enforcement of energy transfer to small scales, it is shown here not only that the shear-flow-instability-supplied 3D-fluctuation energy is largely inverse-transferred from the fluctuation to the mean-flow gradient, but that such inverse transfer is more efficient for turbulent fluctuations in 3D than in two dimensions (2D). The transfer is due to linearly stable eigenmodes that are excited nonlinearly. The stable modes, thus, reduce both the nonlinear energy cascade to small scales and the viscous dissipation rate. The vortex-tube stretching is also suppressed. Up-gradient momentum transport by the stable modes counters the instability-driven down-gradient transport, which also is more effective in 3D than in 2D ($\approx$70% vs. $\approx$50%). From unstable modes, these stable modes nonlinearly receive energy via zero-frequency fluctuations that vary only in the direction orthogonal to the plane of 2D shear flow. The more widely occurring 3D turbulence is thus inherently different from the commonly studied 2D turbulence, despite both saturating via stable modes.

6.1 Introduction

The directionality of turbulent energy transfer has long been a topic of interest.[160] Early on, energy transfer to small scales was posited in Navier-Stokes inertial-range turbulence, as part of the scale-invariant property of the nonlinearity.[14, 161] Later, inviscid dynamical invariants were shown to govern energy transfer directions in two-dimensional (2D) turbulence.[162, 163] In 2D, because the vortex tubes cannot be stretched, two positively signed invariants exist and demand oppositely directed cascades: enstrophy to small and energy to large scales.[162, 163] Nonlinear energy transfer is also affected by global symmetry breaking processes like rotation,[164–166] stratification,[167] a mean shear flow,[168–173] or an external magnetic field via anisotropic linear physics.[174–177] The important effects observed are spectral condensation at large scales and anisotropic turbulent structures that coincide with the anisotropic linear physics.[178, 179] The mechanism involves the correlation time of nonlinear interactions, which depends on anisotropic frequencies of linear waves.[164–166, 176] Thus, anisotropy is endowed to, otherwise isotropic, nonlinear energy transfer. It is by this mechanism that the inverse energy cascades can be explained in 3D rotating turbulence,[164–166] and similar arguments apply in the creation of large-scale zonal flows[176] in fusion plasmas where the mean magnetic field breaks the symmetry. This understanding, however, must account for the physics of the linear instability, when it drives the turbulence.

If the instability operates at large scales,[110] the tendency of instability to relax its driving gradient implies energy transfer to smaller scales. This traditional argument anticipates that instability-driven turbulence will feature forward energy transfer. While true, the linear-instability-supplied fluctuation energy need not necessarily, in its entirety, be available to a nonlinear energy cascade to other scales. A discrepancy

can arise because the nonlinearity can excite stable-mode solutions of the operator of the linear stability analysis.[15, 32, 88, 89, 91, 93, 95, 97, 98, 110, 111, 140, 141, 143, 144, 180] Stable-mode excitation has also been observed in laboratory experiment.[181] When excited to large amplitudes, the stable modes directly transfer turbulent energy from the instability-scale fluctuations to the driving mean gradient,[180] a process that can be interpreted as an inverse transfer of energy. Such direct fluctuation-to-mean transfer is distinct from the nonlinear energy cascade. However, the former can drastically reduce the latter,[88, 180] a phenomenon that has come to light in turbulence theory in recent years.[15, 176]

All the effects described above can arise in shear flow-driven hydrodynamic turbulence. Our chief concerns in this paper relate to energy transfer directionality, spatial dimensionality, and instability saturation mechanism. We investigate the turbulence driven by a forced, unstable shear flow in three dimensions, specifically the Kelvin-Helmholtz (KH) instability. The KH instability is an inviscid instability[113] whose eigenspectrum is composed of: (i) discrete eigenfrequencies that are purely imaginary and that appear in complex-conjugate pairs, and (ii) a theoretically infinite number of eigenmodes that form a continuum in real frequency.[144] In this study, the discrete modes are an unstable mode and a damped (conjugate-stable) mode. The former extracts energy from the unstable flow-gradient and the latter reverses it.[110, 144] Being a conjugate-stable mode, its mode structure is conceptually similar to that of the unstable mode.[111] Because of the similarity in mode structures and complex eigenfrequencies,[15] the conjugate-stable modes can strongly nonlinearly couple to the unstable modes, and thus get excited to large amplitudes.

In 2D hydrodynamic[110] and magnetized shear flows,[111, 143, 144] the conjugate-stable modes have been shown to be significantly excited in saturation. The modes sequester energy at large scales, reduce the nonlinear energy cascade, and lower the

small-scale dissipation rate.[143] Driving up-gradient momentum transport, the stable modes counter the instability-driven down-gradient transport.[111, 144]

In 3D fluid turbulence, the strong excitation of conjugate-stable modes remains to be confirmed. Possible reasons for a lack of such a mechanism relate to the added degree of freedom in 3D, which may result in an inefficient stable-unstable mode coupling, thus allowing the majority of energy to cascade to small scales. However, with the additional dimension, the number of new unstable and conjugate-stable modes (hereafter interchangeably called stable modes) also increases.[113] Since the turbulence is inherently a multi-scale nonlinear phenomenon, with complexity further enhanced by the presence of large-scale energy sources and sinks in the form of unstable modes and stable modes, reliable understanding can only be gained with quantitative assessment. A detailed analysis of the energetics of 3D turbulence is, thus, crucially needed.

Instability saturation can also be influenced by the anisotropic dispersion relation of the 3D KH instability, where the anisotropy arises because the perturbations that vary only in the spanwise direction (orthogonal to the direction of the mean flow and the direction of shear) are distinct from the perturbations that vary only in the direction of the mean flow. When the spanwise perturbations are analyzed in terms of an eigenspectrum, one finds neither the KH instability nor the waves forming a continuum in frequency: all eigenfrequencies of the inviscid linear operator collapse to zero.[113] One might, thus, assume that these spanwise fluctuations play no role in the saturation of the KH instability, as the instability is largely caused by the fastest-growing two-dimensional streamwise perturbations.[113] However, nonlinear mode couplings can strongly drive the zero-frequency, purely spanwise fluctuations, making the 3D turbulence different from its 2D counterpart in essential regards. For example, the spanwise fluctuations, due to their zero frequencies, can catalyze near-

resonant[164–166, 176] energy transfer between two waves of similarly high frequencies, as such a triad maximizes the turbulent interaction time[32, 88]; in the context of the inviscid-instability-driven dissipative turbulence, this translates to energy transfer between eigenmodes of similar but opposite growth rates.[32, 88, 95, 141] Hence, this new channel involving spanwise fluctuation can participate in the nonlinear saturation of the instability in 3D. However, whether the participation becomes dominant is *a priori* unknown.

Even in linear stability analysis, the 2D and 3D KH instabilities are different, as shown already in 1933 by Squire, stating[182] that 2D perturbations are the least stable. Technically valid only for linear analysis, the theorem is relied upon in insightful nonlinear studies of 2D turbulence, ignoring the possibility that the 3D KH-unstable modes may compete nonlinearly with the 2D KH-unstable modes, and even dominate. A part of the reason is the (computational) cost-effectiveness of the 2D analysis. Such studies commonly appeal to nonlinearly[165, 166] two-dimensionalizing effects such as a strong rotation, although the rotation can introduce new waves.[183] There have, however, been illuminating studies on 3D KH-instability-driven turbulence, where fully 3D fluctuations are connected to the secondary and tertiary instabilities of the fluctuations generated by the primary 2D KH instability (see, e.g, Refs. [119, 184–189]). While such 3D higher-order instability analyses offer a unique perspective on the development of the 3D turbulence and characterize the "zoo" of secondary and tertiary 3D structures, it can be difficult to extract the importance of the 3D primary KH mode evolution because such slowly growing KH modes can take a longer time to rise to appreciable levels. Before those are reached, the mean shear flow can decay, causing a premature demise of the 3D KH modes The issue is, therefore, not just 3D, but the time scale that the 3D primary KH-unstable modes need to be allowed to evolve self-consistently without disadvantaging them by preventing the loss of

the instability. A continuously active free energy source for instability can arise in natural and laboratory flows, including those in galaxies, stars, protoplanetary disks, atmospheres, oceans, at the mouths of rivers and estuaries, and nuclear fusion devices, where flow-shear is supplied externally; see, e.g., Refs. [29, 118, 119, 190–194] In such cases, how the instability saturates nonlinearly is not understood.

Momentum transport by the KH instability is countered by the stable modes:[97, 110] the stable modes steepen the mean flow gradient that the KH instability attempts to flatten. Understanding the efficiency of these competing processes allows to construct reduced and truncated models of turbulent transport.[88, 111, 144] If the unstable and stable modes primarily contribute to momentum transport in the 3D KH-instability-driven turbulence, accurate transport models may be achieved. Exploring such possibilities, therefore, benefits geo- and astrophysical communities (see, e.g., Refs. [82, 195]) who wish to understand the turbulence and predict the momentum and particle transport rates due to the 3D KH instability in nature.

One of the principal findings of this paper is that the 3D KH instability nonlinearly excites zero-frequency, spanwise fluctuations that near-resonantly transfer energy to the conjugate-stable modes at KH-unstable wavenumbers. These stable modes then return the turbulent energy to the mean flow. Such stable modes inhibit the energy cascade to small scales, viscous dissipation rate, momentum transport across the shear layer, and vortex stretching—a purely 3D phenomenon.

This paper is organized as follows. Section 7.2 presents the model of shear-flow turbulence and simulation details. In Sec. 6.3, a complete eigenmode basis is derived using an inviscid linear operator. Stable-mode excitation is demonstrated in Sec. 6.4. Section 6.5 shows significant counter-gradient momentum transport by stable modes and presents a reduced transport model. Inverse transfer of energy by the stable modes from the fluctuations to the mean flow is investigated in Sec. 6.6. How such

stable modes receive energy in the nonlinear phase is explored in Sec. 6.7. The stable modes are shown in Sec. 6.8 to retard 3D vortex stretching and subdue small-scale dissipation. Section 6.9 presents broader issues and implications of the results, before conclusions in Sec. 9.7.

6.2 Model and simulation setup

An incompressible hydrodynamic fluid evolves[113] according to

$$\partial_t \mathbf{u} + \mathbf{u} \cdot \nabla \mathbf{u} = -\nabla p + \nu \nabla^2 \mathbf{u} + \mathbf{f}, \tag{6.1a}$$

$$\nabla \cdot \mathbf{u} = 0, \tag{6.1b}$$

where $\mathbf{u}$ is the fluid velocity, ν the kinematic viscosity, and $\mathbf{f}$ the forcing, or externally supplied acceleration. The pressure (per unit density) p imposes the incompressibility constraint Eq. (6.1b) on the flow.

Background flow and forcing

We consider an initial flow profile $\mathbf{u}(x, y, z, t{=}0) = U_0 \tanh(z/a)\hat{\mathbf{e}}_x$, which is well-known to be unstable.[113] The flow amplitude U_0 and half-width a of the flow-shear are the initial characteristic speed and length scale that are used to non-dimensionalize all the variables henceforth. Thus, time is measured in units of a/U_0 and energy (per unit mass) in terms of U_0^2. The initial mean flow thus becomes $\mathbf{u}(x, y, z, t{=}0) = \tanh(z)\hat{\mathbf{e}}_x$. The viscosity is non-dimensionally measured via the Reynolds number $Re{=}U_0 a/\nu$.

In natural systems, the unstable mean shear flow can evolve in at least two different qualitative ways: first, when the mean shear flow is allowed to freely evolve following the response from the shear flow-driven turbulence, the unstable shear flow relaxes

to a stable configuration. Second, when the mean shear flow is allowed to evolve in the presence of the external drive that brings the shear flow in existence in the first place, the resulting turbulence can be of quasi-stationary nature. Admittedly, the form of the external drives can vary from system to system; avoiding such a system-specific requirement, we use a general form of external forcing that replenishes the initial, unstable equilibrium. Such type of restoring force have previously been used to model external forces in natural environments,[117–119, 190, 196] e.g., jets in stars, driven flows in geo-and astrophysics, which can be related to various forms of external drives,[118, 119, 190–193] for example, fingering convection that ceaselessly seeds secondary instability with shear flow,[29, 194] and, in general, the gravitational force that generates shear layers in accretion disks and stellar interiors. We thus externally drive the mean flow using $\mathbf{f} = f(k_x{=}0, k_y{=}0, z, t)\hat{\mathbf{e}}_x$, where k_x and k_y are the wavenumbers along the x- and y-axes, respectively, with

$$f = \frac{1}{t_{\text{forcing}}} \left[U_{\text{ref}}(z) - \langle u_x(x, y, z, t) \rangle_{x,y} \right] + F_0, \tag{6.2}$$

where $U_{\text{ref}}(z){=}\tanh(z)$ is the initial mean flow; $\langle u_x(x, y, z, t) \rangle_{x,y}$ is the (x, y)-averaged instantaneous flow, directed along the x-axis; and $1/t_{\text{forcing}}$, with units of U_0/a, is the rate at which the mean flow is forced toward the initial equilibrium profile.[118, 119, 144] A time-independent forcing F_0 helps to realize a true equilibrium of the initial mean flow: $Re^{-1}\nabla^2 U_{\text{ref}}(z) + F_0 = 0$, allowing a formal linear analysis.

On this equilibrium system, small-amplitude initial noise is seeded for the present simulation studies.

Initial perturbations, boundary conditions, and simulation parameters

To ensure incompressiblity $\nabla \cdot \mathbf{u}$=0 of the flow in the initial random perturbations, careful steps are taken by first writing $\mathbf{u}$=$\nabla \times \mathbf{C}$, where $\mathbf{C}$=$\sum_{\mu=\{x,y,z\}} C_\mu \hat{\mathbf{e}}_\mu$ is a 3-dimensional vector field, with each component given as

$$C_\mu(x,y,z) = \sum_{\substack{0<|k_x|<k_x^{\max} \\ 0<|k_y|<k_y^{\max}}} \mathrm{e}^{ik_x x}\mathrm{e}^{ik_y y}\hat{C}_\mu(k_x,k_y,z). \tag{6.3}$$

Initial perturbations are excited up to $k_x = k_x^{\max}$ and $k_y = k_y^{\max}$. The Fourier components of such perturbations are

$$\hat{C}_\mu(k_x,k_y,z) = \hat{\mathbf{e}}_\mu A\,\mathrm{e}^{-\frac{z^2}{\sigma^2}}\left(|k_x|^\alpha \mathrm{e}^{i\theta_\mu(k_x)}\delta_{k_y,0} + |k_y|^\alpha \mathrm{e}^{i\theta_\mu(k_y)}\delta_{k_x,0} + |k_x k_y|^\beta \mathrm{e}^{i\theta_\mu(k_x,k_y)}\right), \tag{6.4}$$

where A is an overall amplitude of the perturbation (measured non-dimensionally with respect to the initial mean-flow amplitude U_0); σ is the width (measured non-dimensionally with respect to the half-width of the flow-shear a) along the z-axis of the Gaussian envelope that scales the initial perturbations; α and β are the spectral slopes of the perturbations in the wavenumber space k_x and k_y, respectively; each component of $\mathbf{C}$ is randomized in phase at every wavenumber via random phase functions $\theta_\mu(k_x), \theta_\mu(k_y)$, and $\theta_\mu(k_x,k_y)$. On the right-hand side of Eq. (6.4), the first term inside the brackets excites the k_y=0 Fourier modes, which are the purely 2D perturbations; the second term corresponds to the fluctuations that vary only on the (y,z)-plane, orthogonal to the streamwise direction; and the third term excites perturbations that vary in all directions.

Motivated by earlier studies of 2D shear-flow turbulence,[111, 143, 144, 180] we use

a small-amplitude perturbation, with A=10^{-3}, to allow an unambigious and decades-long linear evolution of the instability, before it gets nonlinearly modified. The 2D studies employed only the first term inside the brackets on the right-hand side of Eq. (6.4). The initially excited perturbations, up to $k_x^{\max} = 128$ and $k_y^{\max} = 128$, have a near-flat spectrum of energy over the (k_x, k_y)-plane, which we achieve by choosing α=-1 and β=$-1/2$ in Eq. (6.4). The perturbations peak at z=0 and have a Gaussian width of σ=2.

To make the initial perturbations fully free of $\mathbf{u}$-divergences, the pressure p is obtained using p=$\nabla^{-2}\nabla\cdot[-(\mathbf{u}\cdot\nabla)\mathbf{u}]$ where ∇^{-2} stands for inversion of the Laplacian operator.

Boundary conditions along the x- and y-axes are periodic, whereas, along the z-axis, we impose no-slip, co-moving (with the initial flow) walls at the top and bottom boundaries z=$\pm\, L_z/2$.

While we have studied the current system with varying forms of initial condition, box size, spectral resolution, and the Reynolds number, we present in this paper results using a box size of L_x=L_y=L_z=10π, resolving a large number of linearly KH-unstable wavenumbers, and using a spectral resolution of 512^3: Fourier modes on the (x, y)-plane and Chebyshev polynomials along the z-axis. To avoid aliasing errors, we dealias the quadratic nonlinearities of the governing equation via the 3/2-rule in all directions. Motivated by earlier studies,[143, 144, 180] t_{forcing}=0.5 is chosen throughout this study (the instability-growth time is $\sim$ 6 and the box-crossing time of the mean flow is 10π). Such a choice adequately replenishes the initial mean flow, thereby preventing the loss of the KH instability. We use the pseudospectral solver Dedalus,[121] with third-order, four-stage implicit-explicit Runge-Kutta time-integrator to advance the system. At the cost of $\sim$10 million CPU-hours, long time-integrated 3D simulations are studied for $Re = 300, 1500$, and 5000, in addition to an ensemble of 10 different

three-dimensional numerical simulation continuations (in Sec. 6.8).

6.3 Complete eigenmode basis

Before analyzing the nonlinear state of the shear-flow instability, we find the inviscid eigenmodes by linearizing Eqs. (9.1a) and (6.1b), dropping the viscous term, and Fourier-transforming the equations,

$$\partial_t \hat{\mathbf{u}} + \mathbf{u}_0 \cdot \nabla \hat{\mathbf{u}} + \hat{\mathbf{u}} \cdot \nabla \mathbf{u}_0 = -\nabla \hat{p}, \tag{6.5a}$$

$$\nabla \cdot \hat{\mathbf{u}} = 0, \tag{6.5b}$$

where $\mathbf{u}$ is decomposed into its mean (k_x=k_y=0) mode $\mathbf{u}_0$ and fluctuation spectrum $\hat{\mathbf{u}}$ at (k_x, k_y); likewise for the pressure $\hat{p}$; the derivative operator ∇ can be expressed as $ik_x\hat{\mathbf{e}}_x + ik_y\hat{\mathbf{e}}_y + \hat{\mathbf{e}}_z\partial_z$.

With $\mathbf{u}_0$=$U_{\rm ref}(z)\hat{\mathbf{e}}_x$, a complete eigenspectrum can be found at any given wavenumber. When k_y=0, one obtains an eigenspectrum corresponding to 2D perturbations:[144] (i) unstable and conjugate-stable eigenmodes at $|k_x| \lesssim 1$, frequencies of which are complex-conjugates, and (ii) a large (theoretically infinite) number of eigenmodes that form a continuum in real frequency and that exist at all k_x≠0. This set of eigenmodes also exists for 3D perturbations. To obtain the eigenmodes, we discretize Eqs. (6.5a) and (6.5b) using 1024 Chebyshev polynomials for each variable $(\hat{u}_x, \hat{u}_y, \hat{u}_z, \hat{p})$ along the z-axis, and form a 4096×4096-sized matrix eigenvalue problem at each wavenumber, and then diagonalize the matrix to find the complete eigenspectrum. The 3D unstable and stable eigenmodes are visually very similar as can be seen, for example, when examining their z-components of velocity at the first Fourier mode numbers along the x- and y-axes in Fig. 10.1. The similarity

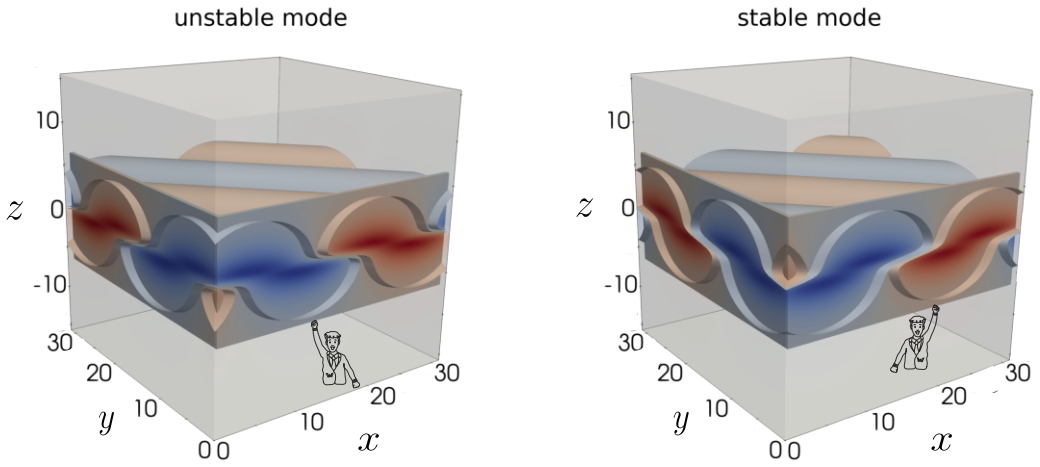

Figure 6.1: For an unstable mean flow $\mathbf{u}_0 = \tanh(z)\hat{\mathbf{e}}_x$, physical structures of perturbed $\hat{u}_z$ of 3D unstable and conjugate-stable modes are shown; the colors represent the magnitude of the $\hat{u}_z$ (in arbitrary units). The isocontours and the surface rendering highlight a symmetry that is illustrated with a cartoon.

appears because, in wavenumber space, they exhibit a special complex-conjugate symmetry: $(\hat{u}_x, \hat{u}_y, \hat{u}_z, p)_{\text{stable mode}} = (\hat{u}_x^*, \hat{u}_y^*, -\hat{u}_z^*, p^*)_{\text{unstable mode}}$, where * denotes the complex-conjugation operation.

A growth rate spectrum of the unstable mode on the (k_x, k_y)-plane is shown in Fig. 10.2. At every wavenumber for which the unstable mode of the inviscid linear operator exists, the conjugate-stable mode must necessarily, as well exist—meaning that Fig. 10.2 also serves as a damping rate spectrum of the conjugate-stable mode. For the special case of k_x=0, the entire eigenspectrum becomes infinitely degenerate, i.e., all eigenvalues collapse to zero on the complex-frequency plane. In that case, the dropped viscous term becomes singularly important, and is the sole active term that damps the fluctuation spectrum.

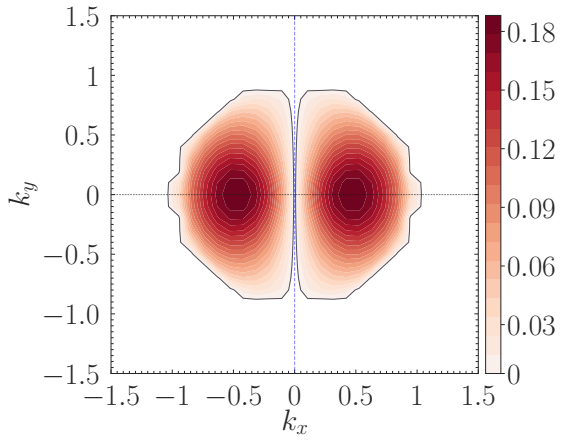

Figure 6.2: Growth-rate spectrum of 3D KH instability, showing an anisotropic dispersion relation. The 2D modes, k_y=0, have the largest growth rates. All wavenumbers with k_x=0, shown with a vertical blue dashed line, are linearly stable. The wavenumber $(0, 0)$ corresponds to the mean flow. As the Kelvin-Helmholtz instability is a large-scale instability, the wavenumbers shown in white, whose boundary is approximated by the black bounding curve, are linearly stable.

6.4 Nonlinear excitation of stable modes

Turning now to the nonlinear saturation of the instability, at any wavenumber $\mathbf{k}$=(k_x, k_y), where discrete linear eigenfrequencies in this system exist, an arbitrary Fourier-transformed state vector $\hat{\chi}$=$(\hat{u}_x, \hat{u}_y, \hat{u}_z, \hat{p})$ can be decomposed in the basis spanned by the complete set of eigenmodes in the manner of $\hat{\chi}$=$\sum_j \beta_j \hat{\chi}_j$, where β_j is the complex-valued amplitude of the jth eigenmode $\hat{\chi}_j$. Since the eigenmodes at hand are non-orthogonal, the mode-amplitudes β_j in the turbulent state cannot be determined simply by taking a Hermitian inner product between the eigenmodes. However, this is merely a technical challenge; the β_j can be uniquely determined by employing the biorthogonal basis, found by solving an adjoint of Eqs. (6.5a) and (6.5b), which produces the same eigenspectrum but a different set of eigenmodes, usually known as left eigenmodes or adjoint solutions. To gain machine-precision accuracy,[144, 197] we use adjoint solutions of discretized equations rather than that

of the analytical equations.

As the unstable modes grow exponentially in the linear phase, they attain large amplitudes. Then the unstable modes, via nonlinear process, excite eigenmodes that are linearly stable (i.e., decaying in the absence of nonlinearity), as shown with the orange curves in Figs. 10.3(a) and 10.3(c). The nonlinear interaction quickly involves multiple eigenmodes and multiple wavenumbers, and, in the fully nonlinear phase, in Figs. 10.3(b) and 10.3(d), the conjugate-stable mode attains an amplitude nearly identical to that of the unstable mode. These figures show that the stable modes are excited even in 3D. Their excitation is universal, as long as the viscosity is not enormously large to lead to a laminar flow. In support of this, we find, for $Re = 1500$ and other lower Re cases (not shown), large excitation of stable modes.

6.5 Efficient 3D counter-gradient momentum transport

We inquire if momentum is transported differently across the mean shear layer due to the stable-mode-rich turbulence. Prior studies have shown counter-gradient momentum transport due to stable modes, but only in 2D systems,[111, 125, 144] leaving the question open whether such a result is generalizable to 3D systems. To address this issue, we measure the Reynolds stress by decomposing the turbulent fluctuations at each KH-unstable wavenumber into eigenmodes and by evaluating stress contribution from each eigenmode. Since the momentum is transported maximally at the middle of the shear layer z=0, because of the strongest shear there, we compare the transport rates at z=0 from individual eigenmodes, along with the total transport from mode-undecomposed fluctuations at z=0.

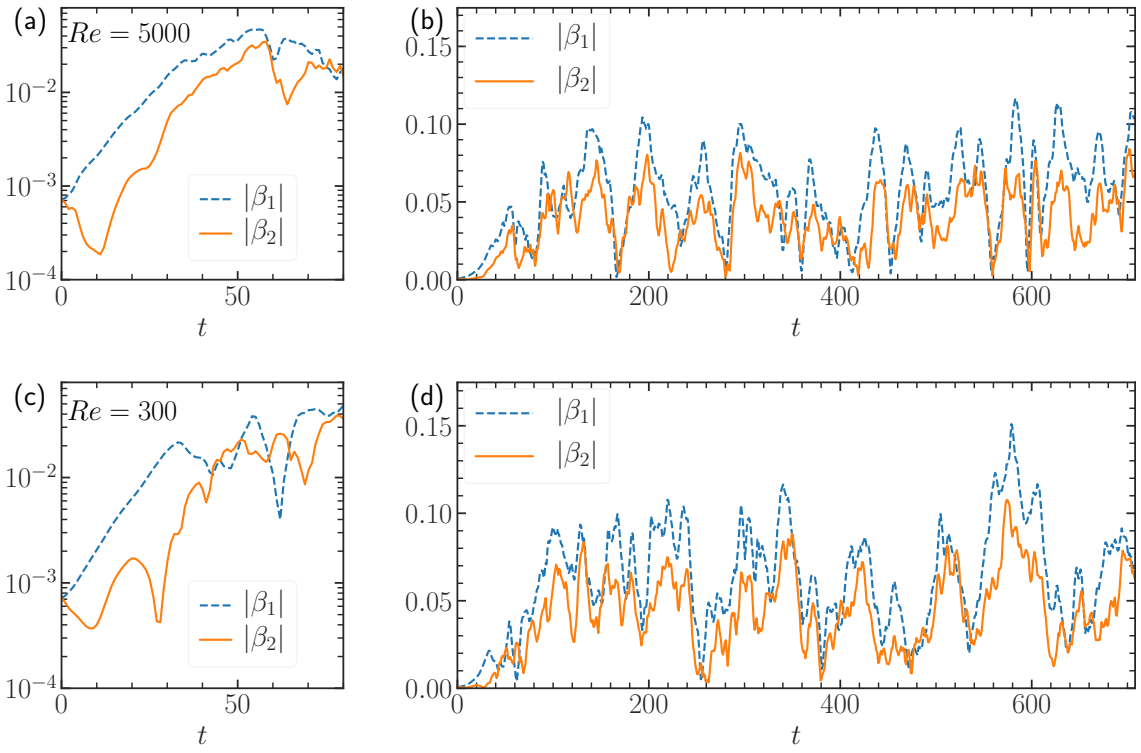

Figure 6.3: Amplitude evolution of unstable ($|\beta_1|$) and conjugate-stable ($|\beta_2|$) modes at k_x=k_y=0.2. In (a) and (b), Re=5000 is used in the initial value simulation; and in (c) and (d), Re=300 is used. In each case, the left panel shows the early evolution using a logarithmic vertical scale, whereas the right panel displays the full time evolution using linear scales on both axes. Stable modes are nonlinearly excited much before the saturation of the unstable mode.

The time-averaged spectrum of the Reynolds stress is shown in Fig. 6.4: in blue, the stress from an unstable mode; in orange, the stress from a stable mode; and in black, the total stress without performing the eigenmode decomposition. The total stress $\tau_{\text{all}}(z{=}0)$ is large (the black bars are taller) for low wavenumbers. Mode-decomposition shows that transport from 3D unstable modes is large, and correspondingly large is that from the 3D stable modes. This immediately challenges a prediction of transport based on unstable modes only.[26–29, 38] A correct transport level, however, can be found by simply adding the contribution of stable modes.

To separate the 2D and 3D modes, we apply a wavenumber-summation to Fig. 6.4

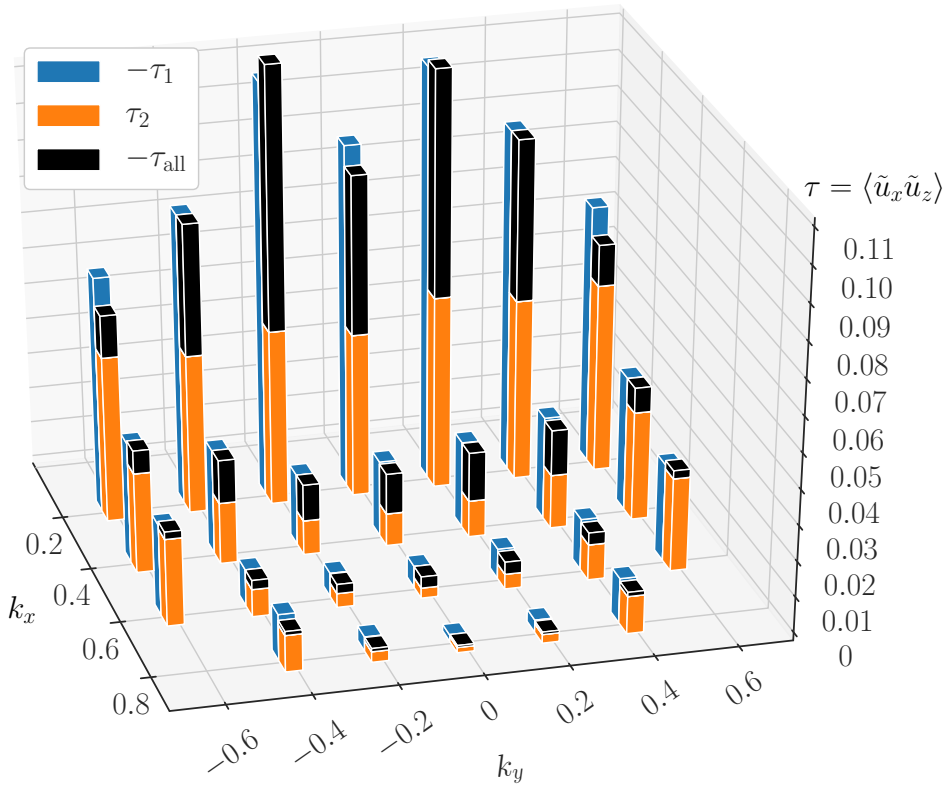

Figure 6.4: Time-averaged spectrum of Reynolds stress due to: the unstable mode τ_1, stable mode τ_2, and mode-undecomposed full fluctuations τ_{all}. Where the peaks of the blue and black bars are at similar heights, $\tau_1 + \tau_2$ is a good approximation to τ_{all}. The difference between $\tau_1 + \tau_2$ and τ_{all} is small, and arises from the contribution of the continuum modes to the total stress τ_{all}. All stresses are averaged over t=200–708 for Re=5000.

and obtain a 2D−3D comparison in Fig. 6.5. It is clear that the total stress, shown in black, is higher for the 3D modes than for the 2D modes. This is easily explained with the aid of Fig. 6.4 where many 3D modes have comparable stress contribution to that of the 2D modes, in addition to the higher density of states of the 3D modes, i.e., number of wavenumbers k_y per k_x.

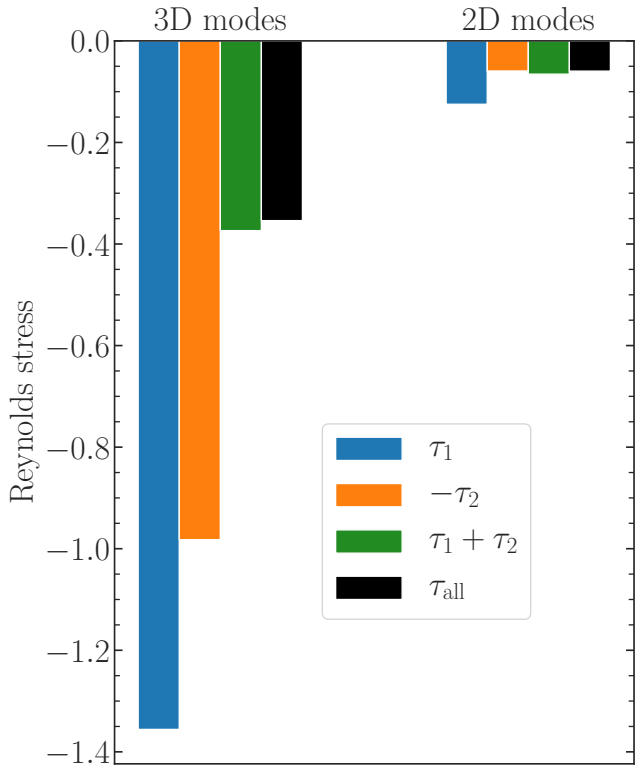

Figure 6.5: Comparison of time-averaged Reynolds stresses at z=0 for all KH-unstable 3D vs. 2D modes. Further decomposition shows contributions from the unstable mode τ_1; stable mode τ_2; the two added together, $\tau_1 + \tau_2$; and the mode-undecomposed full fluctuations τ_{all}. The difference between τ_{all} and $\tau_1 + \tau_2$ arises from the stress due to the continuum modes. Stresses are averaged over t=200–708 for Re=5000.

6.6 Inverse transfer of energy in 3D

We now analyze the energy transfer rate $Q_1(\mathbf{k})$ from the mean flow to the fluctuations at $\mathbf{k}$ by the unstable mode, and the rate of inverse energy transfer $Q_2(\mathbf{k})$ from the fluctuation $\mathbf{k}$ to the mean flow by the stable mode. Both of these are linear processes, as one of the involved wavenumbers is the mean flow—the reservoir of the free energy for the instability and thus turbulence. Two additional linear processes, however, exist: first, because the mean flow also evolves, the instantaneous deviation of the mean from the initial profile can induce a (typically small) linear coupling between the inviscid eigenmodes of the initial profile, thus reducing Q_j by an amount R_j. Second, the

viscous term introduces energy dissipation D_j. However, since the unstable and stable eigenmodes that are analyzed here exist only at large scales ($|k| \lesssim 1$), the dissipative effect at such scales is small, compared to Q_j. This remains true as long as the viscosity is not enormously large to stabilize completely the inviscid Kelvin-Helmholtz (KH) instability; such a case, however, is irrelevant to the scenario we are interested in, where the KH instability drives the turbulence.

To quantify the energy transfer rates described in the previous paragraph, we Fourier-transform Eqs. (9.1a) and (6.1b), and project the equation onto an eigenmode of interest, say the jth eigenmode, by multiplying the Fourier-transformed equation with the jth modified left eigenmode $\hat{Z}_j$; see Appendix A of Ref. [144] for a general overview of modified left eigenmodes. To illustrate this here, Eqs. (9.1a) and (6.1b) can be structurally written, at $\mathbf{k}\neq(0,0)$, as

$$\partial_t M\hat{\chi} = L\hat{\chi} + \sum_{\mathbf{k}',\mathbf{k}'':\mathbf{k}'+\mathbf{k}''=\mathbf{k}} N(\hat{\chi}',\hat{\chi}''), \tag{6.6}$$

where the matrix M of size 4×4 has the form $[[\mathbb{I}_{3\times 3},0],[0,0]]$, with $\mathbb{I}_{3\times 3}$ as the identity matrix of size 3×3; furthermore, L is a linear operator and N a nonlinear operator, with $\hat{\chi}'$ and $\hat{\chi}''$ representing state vectors at $\mathbf{k}'$ and $\mathbf{k}''$, respectively.

Projecting Eq. (6.6) on the modified left eigenmode $\hat{Z}_j$, we obtain the mode-amplitude evolution equation

$$\partial_t\beta_j(\mathbf{k}) = \gamma_j(\mathbf{k})\beta_j(\mathbf{k}) + \sum_l B_{jl}(\mathbf{k})\beta_l(\mathbf{k}) + \sum_{\substack{\mathbf{k}',\mathbf{k}'':\\ \mathbf{k}'+\mathbf{k}''=\mathbf{k}}} \sum_{m,n} C_{jmn}(\mathbf{k},\mathbf{k}')\beta'_m\beta''_n, \tag{6.7}$$

where we have used the biorthogonality relation between the modified left eigenmode $\hat{Z}_j$ and the right eigenmode $\hat{\chi}_l$ such that $\langle\hat{Z}_j,\hat{\chi}_l\rangle \propto \delta_{j,l}$. In Eq. (6.7), $\gamma_j(\mathbf{k})$ is the complex-valued growth rate of the jth eigenmode at a wavenumber $\mathbf{k}$; the coefficient

$B_{jl}(\mathbf{k})$ measures the linear coupling (between the inviscid eigenmodes at $\mathbf{k}$) induced by the viscous term and by the instantaneous deviation of the mean flow from the initial profile; the coefficient $C_{jmn}(\mathbf{k},\mathbf{k}')$ measures the nonlinear coupling between the eigenmode m at $\mathbf{k}'$ and the eigenmode n at $\mathbf{k}''$, driving the eigenmode j at $\mathbf{k}$; and β'_m and β''_n represent the amplitudes of modes m at $\mathbf{k}'$ and n at $\mathbf{k}''$, respectively. Now, we multiply Eq. (6.7) with β^*_j, and add the complex-conjugate of the resulting equation to obtain the evolution equation for the eigenmode energy, which reads

$$\partial_t|\beta_j(\mathbf{k})|^2 = Q_j + (R_j + D_j) + T_j, \tag{6.8}$$

where

$$Q_j = 2\,\mathbb{R}\mathrm{e}\left[\gamma_j(\mathbf{k})\right]|\beta_j(\mathbf{k})|^2, \tag{6.9a}$$

$$R_j + D_j = 2\,\mathbb{R}\mathrm{e}\Big[\sum_l B_{jl}\beta_l\beta^*_j\Big], \tag{6.9b}$$

$$T_j = \sum_{\substack{\mathbf{k}',\mathbf{k}'':\\ \mathbf{k}'+\mathbf{k}''=\mathbf{k}}}\sum_{m,n} T_{jmn}(\mathbf{k},\mathbf{k}'), \tag{6.9c}$$

$$T_{jmn}(\mathbf{k},\mathbf{k}') = 2\,\mathbb{R}\mathrm{e}[C_{jmn}(\mathbf{k},\mathbf{k}')\beta'_m\beta''_n\beta^*_j]. \tag{6.9d}$$

In Eq. (6.8), Q_j measures the energy transfer rate by the jth eigenmode to the fluctuation scale $\mathbf{k}$ from the initial mean flow; R_j is the energy transfer rate by the jth eigenmode to the fluctuation scale $\mathbf{k}$, the energy source here being the instantaneous deviations of the mean flow from the initial mean flow; D_j is the viscous dissipation rate by the jth eigenmode at the fluctuation scale $\mathbf{k}$; T_j is the nonlinear drive to the jth eigenmode. Since the eigenmodes used for the basis expansion are the inviscid eigenmodes of the initial mean flow, the terms R_j and D_j introduce a linear coupling B_{jl} between those eigenmodes, the effect of which we measure next.

For both the 2D and 3D perturbations that the system generates, the energy transfer rates Q_j and $R_j + D_j$ are shown in Figs. 6.6(a) and 6.6(b) for the energetically dominant wavenumbers. The energy transfer reduction term $R_j + D_j$ is of opposite sign compared to Q_j. This physically means that unstable modes are slightly less efficient in extracting energy from the instantaneous mean flow when compared with their efficiency of energy extraction from the initial mean flow; the same applies to the energy return rate by the stable modes. This particular finding is similar to the results reported for 2D MHD shear-flow turbulence.[180]

At early times $t \lesssim 140$, the 2D mode dominates over the 3D mode; Fig. 6.6(c). However, in the turbulent phase, the slowly growing 3D wavenumber competes with the 2D wavenumber. In all cases, the stable modes are significantly excited, nearly to the levels of the corresponding unstable modes.

We note that, because of the added degree of freedom (the y-coordinate) in the 3D system, there exist more wavenumbers that are 3D KH-unstable than that are 2D KH-unstable; for example, there is only one wavenumber that is 2D KH-unstable at k_x=0.2, i.e., $(0.2, 0)$, whereas there are multiple wavenumbers that are 3D KH-unstable at k_x=0.2, namely, $(0.2, \pm 0.2)$, $(0.2, \pm 0.4)$, etc. We avoid double-counting the Hermitian conjugates $(-k_x, -k_y)$ of these wavenumbers (k_x, k_y), which are already included in the definition of $Q_j(\mathbf{k})$.

Time-averaged energy-transfer rates are compared in Fig. 6.7, where the rates are decomposed by unstable and stable modes. Despite growing slowly, the 3D wavenumbers contribute significantly in the fully nonlinear phase in extracting energy from the mean flow. However, the stable modes at the same wavenumbers, whether 2D or 3D, always efficiently deplete fluctuation energy and transfer energy in the reverse direction: from the fluctuation to the mean flow.

The 3D modes are more efficient than the 2D modes in extracting energy from the

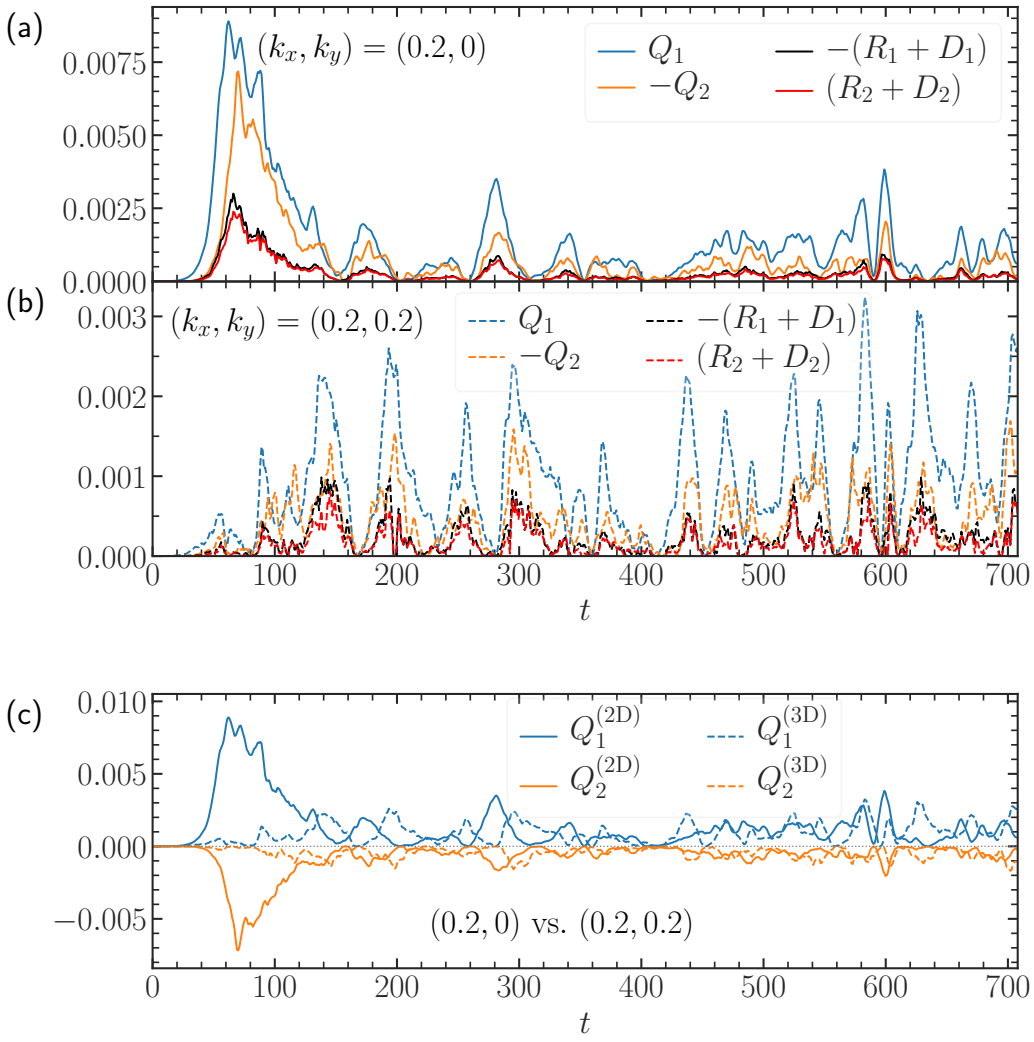

Figure 6.6: Time traces of energy transfer to an unstable, j=1, and a stable, j=2, mode at wavenumbers with (a) 2D and (b) 3D perturbations, in a simulation with Re=5000. The quantity Q_j denotes the energy transfer rate from the initial mean flow to the jth eigenmode at fluctuation scale (k_x, k_y); R_j+D_j collectively represents the effect of time-deviations of the instantaneous mean flow from the initial profile and the effect of viscous dissipation. In (c), 2D and 3D perturbations, decomposed by unstable and stable modes, are compared in terms of the energy transfer rate Q_j; the stable modes reverse the fluctuation energy to the mean flow at all times, once the nonlinearity excites them.

mean flow, as Fig. 6.8 shows. Additionally, the stable-to-unstable mode fraction is higher for 3D modes. The presence of the energy reversal by the stable modes in 3D confirms that the stable modes are not the manifestations of the traditional inverse cascade of 2D turbulence; the former is a direct fluctuation-to-mean transfer of energy, whereas the latter is a fluctuation-to-fluctuation transfer that takes multiple iterations and is a nonlinear process. The quantities measured in Fig. 6.8 are the rates of energy transfer directly between the mean and the fluctuations; we decompose such a linear energy transfer rate into the contributions of the unstable and stable modes, going beyond the simple traditional spectral transfer. The significant direct energy reversal in 3D by the stable modes is a somewhat surprising and important finding of this paper.

6.7 Nonlinear energy transfer to stable modes

Since the stable modes are found to contribute significantly to the energetics and transport, what nonlinear process transfers energy to the stable modes? Established[145, 198] diagnostics of energy transfer in wavenumber space fail here, because they only inform about the energy transfer to a given wavenumber, whereas, at any wavenumber, the total fluctuation is composed of many different eigenmodes, making it desirable to put an eigenmode filter in the transfer analysis.

The total nonlinear energy transfer T_2 from all the fluctuations to a stable mode j=2 at $\mathbf{k}$=$(0.2, 0)$ is shown in Fig. 9.9, using the expressions in Eqs. (6.8) and (6.9c). The overlaid curve is the energy transfer rate $T_{2,\mathrm{Z}}$ based on triad interactions where one of the triad members is a fluctuation with k_x=0, channeling energy to the stable mode. This is found by restricting the summation in Eq. (6.9c) such that either $\mathbf{k}'$=$(0, k_y')$ or $\mathbf{k}''$=$(0, k_y'')$. We note that k_x=0 has zero growth rate and zero frequency.

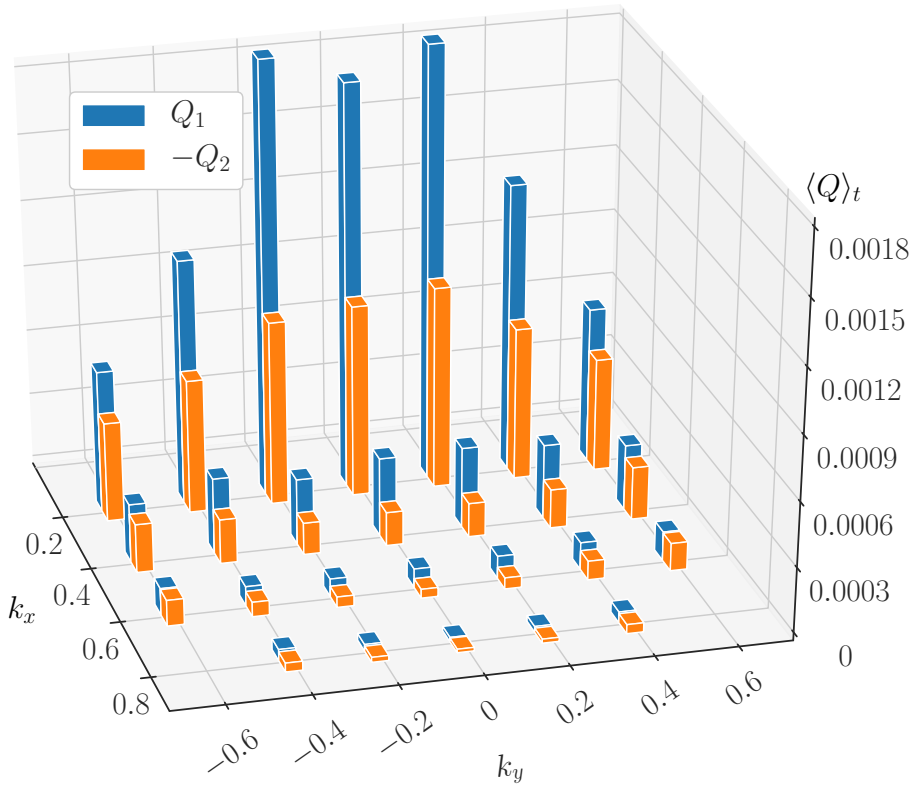

Figure 6.7: Time-averaged rate of energy transfer from initial mean to fluctuation Q_1 by unstable modes, and inverse transfer Q_2 by stable modes, in a simulation with Re=5000; the time-averaging interval is t=200–708. Because of the Hermitian conjugacy in the perturbations over the wavenumbers, only a non-redundant half of the (k_x, k_y)-plane is shown. The linearly fastest growing mode exists at $\mathbf{k}$=$(0.4, 0)$.

This wavenumber, and, in particular, the first Fourier mode number along the y-axis, with k_x=0, is observed to have a large x-component in the turbulent flow, and may be called a zonal mode, analog to secondary instabilities in fusion plasmas.[32, 199, 200] A difference, however, exists: here, these zonal modes contribute to the Reynolds stress, as opposed to those of fusion plasmas, which do not transport momentum and, hence, the contribution of the zonal modes to the stress is null.[88] The main similarity is that both of the systems have qualitatively similar anisotropic dispersion relation and both have zonal modes whose linear frequencies are zeros in the inviscid/ideal

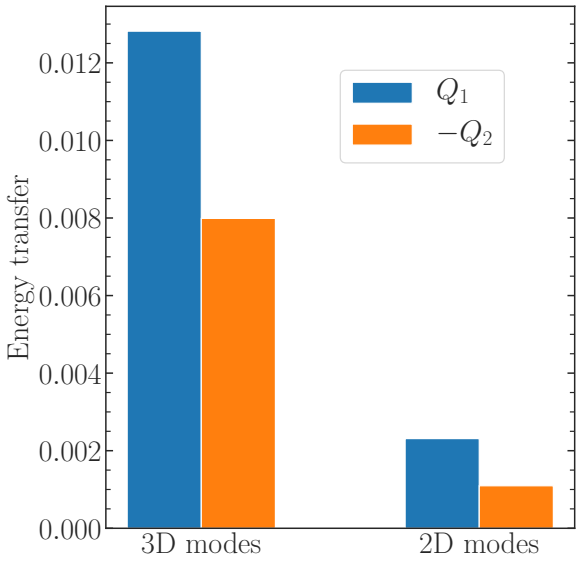

Figure 6.8: Energy transfer rates, classified by 2D and 3D modes, with further decomposition into the unstable and the stable modes. In the simulation with Re=5000, time averaging is taken over t=200–708. The stable-to-unstable mode fraction is larger for 3D modes than for 2D.

limit (when one considers small-scale dissipation coefficient, as well, then the complex frequencies feature damping rates).[32, 88]

We remark that the stable modes are excited in our system primarily via nonlinear interaction with the k_x=0 modes, once the initial transient phase is complete by around t=100 (Fig. 9.9). Since the same triadic interaction continuously feeds energy to the stable mode in the fully saturated phase, one may infer that the process of nonlinear formation of the stable mode is rather coherent, and, to first order, does not involve changing wavevectors; the triad driving the stable mode is largely the same. Such an understanding of stable-mode formation is difficult to obtain in spectral-only representation, as at a given KH-unstable wavenumber, there also exists the stable mode, along with the continuum modes. This does not mean that it is uninsightful to perform traditional diagnostic of energy transfer in wavenumber space by integrating fluctuations along the direction of inhomogeneity. In fact, some recent shear-flow

studies have shown an interesting finding of energy circulation over angles on the wavevector plane, with the magnitude of the wavevector largely unchanged—a process that has been dubbed as “transverse cascade." [168–173] One may investigate the connection between such a cascade and the stable modes to learn if the stable modes favor or impede the transverse cascade. Such a study, however, is beyond the scope of the present paper.

The zero-frequency mode coupling leads to a near-resonant energy transfer to the stable mode,[32, 88, 95, 141] see insets of Fig. 9.9, where both time-steady and slow time-evolution of energy transfers are dominantly zonal-coupled. Such a coupling allows a large amount of energy to be transferred coherently from the unstable mode. This finding is of striking consequence, as it has a direct potential to allow building a reduced, predictive model of saturation levels of unstable and stable modes, as has recently been achieved in the context of fusion microturbulence.[32, 88, 94, 95, 141, 201] The existence of zero-frequency mode coupling and near-resonant energy transfer in 3D hydrodynamic turbulence, as found here, is surprising,[174] and may be considered a finding of the foremost importance.

6.8 Vortex stretching, cascade, and viscous dissipation

After quantifying the effect of stable modes in energetics and transport, we now perform an ensemble of numerical experiments.

We randomly select five snapshots in the turbulent phase of the standard simulation to construct an ensemble. In this ensemble, we project the state vector at each of those times onto the stable eigenmodes at wavenumbers $\mathbf{k}=(0.2, 0)$ and $\mathbf{k}=(0.2, \pm 0.2)$,

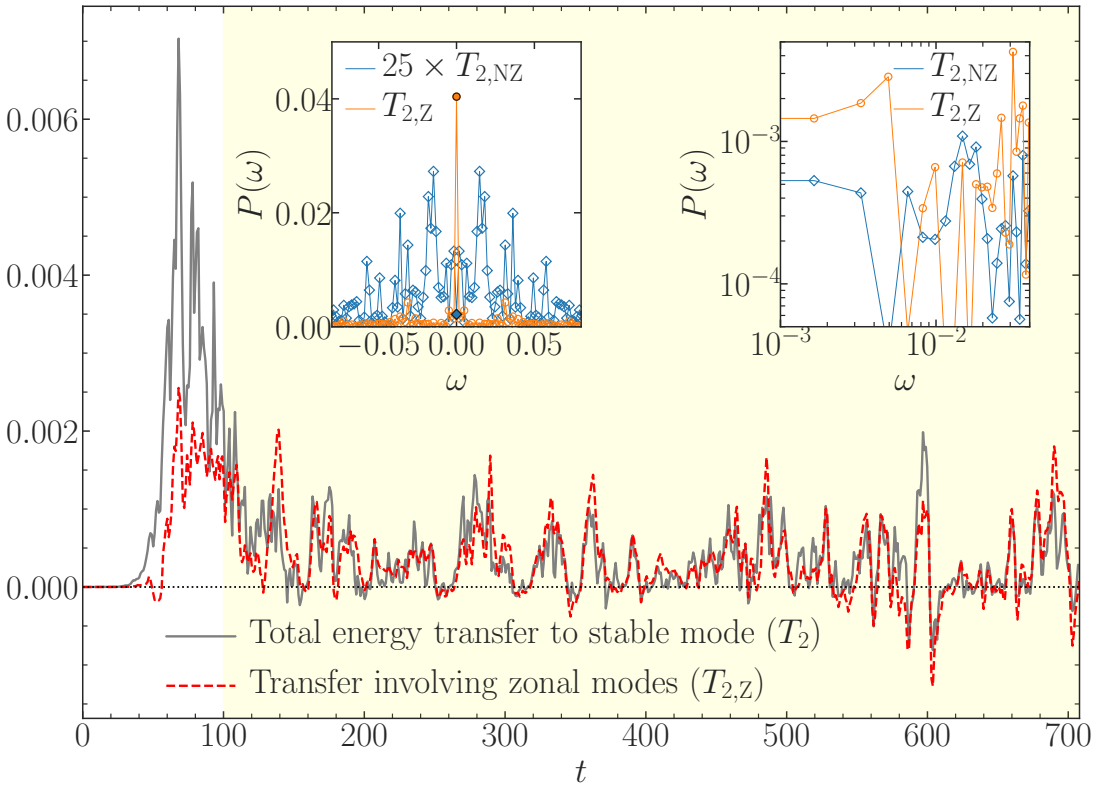

Figure 6.9: Nonlinear energy transfer T_2 to the stable mode, largely channeled via spanwise-only (zero-frequency) fluctuation $T_{2,Z}$, which becomes dominant after $t \gtrsim 100$, shown in the yellow-shaded region. The coupling to zero-frequency modes, labeled zonal modes, is further probed using a power spectrum $P(\omega)$ of energy transfer in frequency ω, shown in the insets, with linear scales (left) and with logarithmic scales (right), where $T_{2,NZ}$=T_2−$T_{2,Z}$ represents a purely non-zonal transfer. At ω=0, filled markers are used. Zonal-coupling dominates at $|\omega|\approx 0$, implying that nonlinear interactions feeding energy to stable modes are primarily coherent.

as these wavenumbers dominate energetically (Fig. 6.7). Then, we delete these stable modes from the chosen state vector, and use the resulting modified state vector as an initial condition to start a new simulation. The restarted simulations, therefore, produce responses to an impulsive zeroing of the stable-mode amplitudes. For a second ensemble, we repeat this process, projecting out this time the unstable modes from the same wavenumbers at the same five snapshots. In both ensembles, the five responses of each impulsive zeroing procedure are then averaged to produce two ensemble-averaged

responses, one from zeroing the stable modes and another from zeroing the unstable modes.

We then evaluate the viscous dissipation rate, computed at wavenumbers other than $(0.2, 0)$ and $(0.2, \pm 0.2)$ so that the initial dissipation rates in the mode-removed and standard simulations are identical. The time-evolution of the dissipation rate $\Delta\epsilon_\nu$ is compared in Fig. 9.10 between the two ensembles. Larger small-scale dissipation rates are observed when stable modes are impulsively removed, similar to a recent finding in 2D turbulence.[143] Although removing the unstable modes initially causes a minor positive change in dissipation rate, the real impact of the unstable-mode removal is quickly seen as a reduced dissipation rate—lower than in the standard simulation. This result is straightforward to explain: first, when an eigenmode of significant amplitude is removed, the resulting large-scale flow structure for a brief moment nonlinearly strains the other scales of the flow. Second, *nota bene*, the linear interaction of the unstable modes (energy source) or stable modes (energy sink) with the mean flow is impulsively impaired, which immediately results in either a depletion of fluctuation energy or a surplus. This second process dominates over the first one after $\Delta t \approx 3$. Soon after $\Delta t \approx 5$, we observe different behaviors in the dissipation rate—a set of curves lying in the positive $\Delta\epsilon_\nu$ region, and the other set lying in the negative. The negative is because the stable modes efficiently return the fluctuation energy to the mean flow; the positive change is due to the enhanced forward cascade of energy that is extracted from the mean flow by the unstable modes, which are not countered by the stable modes here. Around Δt=5, it is observed that the stable-mode removed simulations, on average, feature the highest dissipation rate, whereas the unstable-mode removed simulations, on average, show a change in the dissipation rate that is nearly null.

After quantitative analysis of dissipation rates, we show visualizations of squared

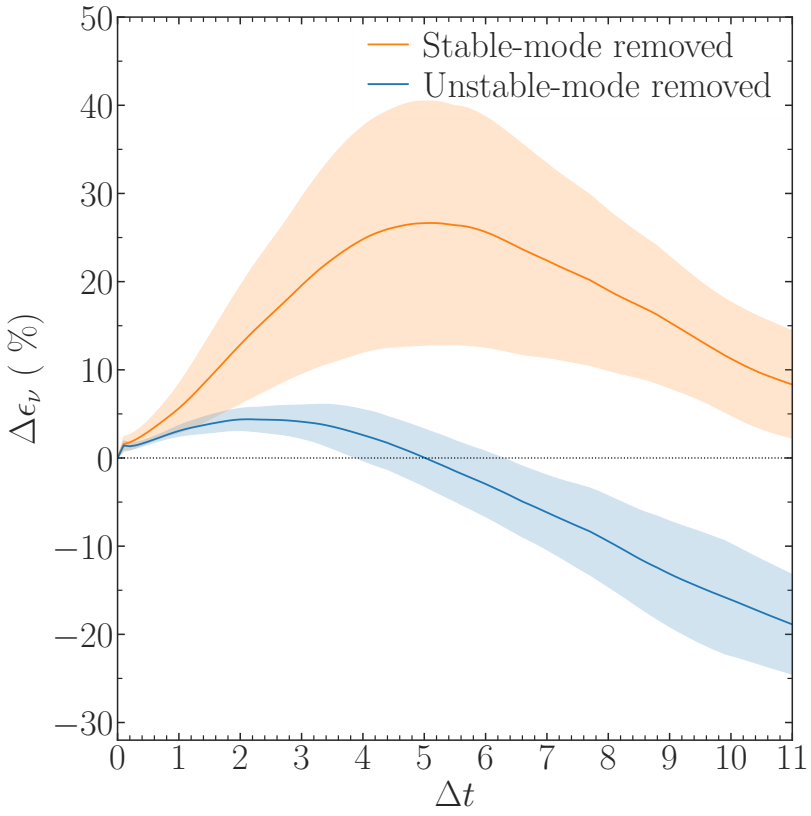

Figure 6.10: Percentage changes in small-scale viscous dissipation rates. The mean (solid curve) and one standard deviation (shaded) is found by simulating an ensemble of 10 different 3D simulations, where either stable or unstable modes are deleted instantaneously at a randomly selected time, and the simulation resumed to measure the effect on the nonlinear cascade via the small-scale dissipation rate. For all Δt shown, stable-mode-removed simulations (orange) show higher dissipation rates than that in a standard simulation, corresponding to a positive $\Delta\epsilon_\nu$; lower dissipation rates are observed after an initial impulsive transient in unstable-mode-removed simulations (blue). All simulations were performed with Re=300.

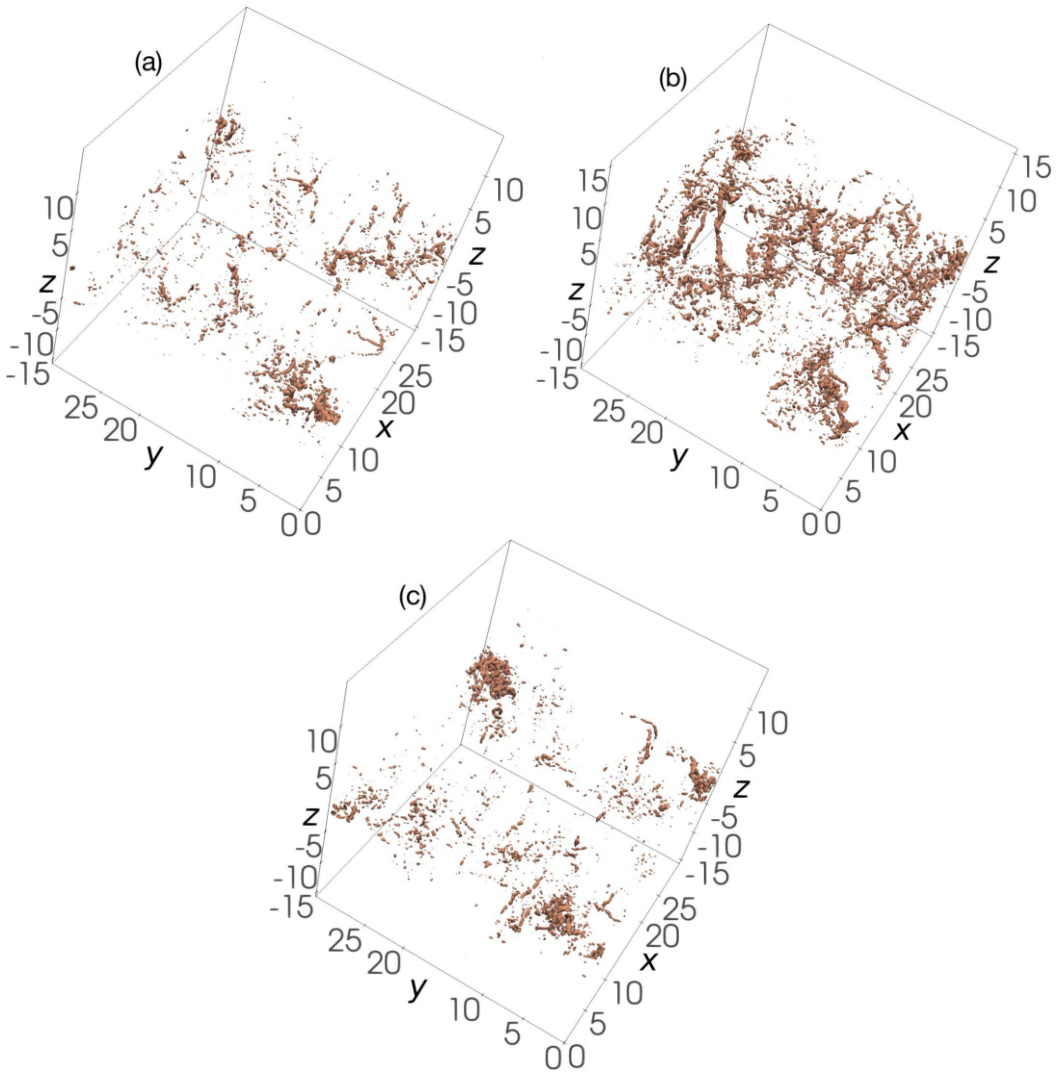

Figure 6.11: Isocontours of squared vorticity in simulations at a time when the viscous dissipation rate peaks. The same isocontour level is chosen in all panels. In the standard simulation in (a), vortex stretching is suppressed compared to a stable-mode-removed simulation in (b), where thin and elongated filamentary vortices are prominent. In an unstable-mode-removed simulation in (c), the long filamentary structures are not as pronounced as in (b). The unstable modes, in the absence of stable modes, rapidly stretch and thin out the vortex tubes; in contrast, the stable modes, in the absence of unstable modes, deplete the fluctuation energy.

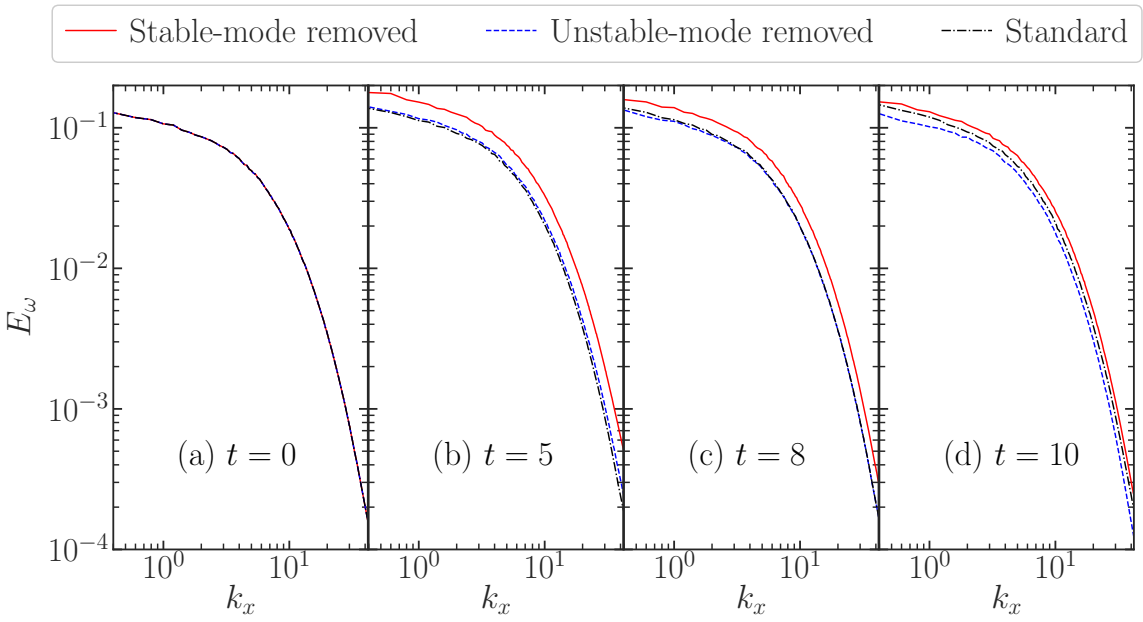

Figure 6.12: Time evolution of enstrophy $E_\omega = \langle|\hat{\omega}|^2\rangle_{y,z}$ spectra in three simulation-continuations: stable-mode removed, unstable-mode removed, and standard. (a) All simulations are restarted with an identical initial condition, except for the removed mode. The mentioned-modes are removed only from the wavenumbers $k_x = 0.2$ and $k_y = \{0, \pm 0.2\}$. The spectra are, therefore, shown for $k_x > 0.2$. (b)–(d) Impulsive responses to the mode-removal are most pronounced when the unstable modes are removed, leading to enhanced turbulence at all scales. The k_y-spectra of (x, z)-averaged enstrophy are similar (not shown).

vorticity (whose volume integral is proportional to the dissipation rate) and compare the physical structures of turbulence across the simulated responses. At the time when the dissipation rate is maximal, the isocontours of squared vorticity show, in a stable-mode impulsively-zeroed simulation, an uninhibited stretching of vortex tubes by the unstable modes, compare Fig. 9.11(b) with Fig. 9.11(a). In the unstable-mode impulsively-zeroed simulation in Fig. 9.11(c), a large-scale structure tends to develop instead of vortex stretching that forms prominent small scales. We note that the vortex-tube stretching is a purely 3D phenomenon, and is associated with the forward cascade of energy in 3D hydrodynamic turbulence. A movie, found in the online supplemental material of this paper, shows several snapshots of stable-mode-removed

simulations, where we observe prominent episodes of vortex stretching.

To quantify the changes in vortex dynamics at smaller scales in response to the large-scale-eigenmode removal, we measure enstrophy spectra in three simulation-continuations, and show a comparison of their time evolution in Fig. 9.12. Although started with an identical initial condition, the simulation with stable-mode-removal rapidly evolves, as a nonlinear response to the mode-deletion, to feature increased level of enstrophy at all scales. The unstable-mode removed simulation also evolves; however, the increment in the small-scale activity, early on, is relatively small, and, at later times, the simulation, in fact, shows decreased enstrophy.

One may interpret the findings of the simulation experiments—increased filamentary vortex structures due to the unstable modes, and reduced filamentary vortex structures due to the stable modes—as the competing effects of forward transfer of energy from the mean flow to the fluctuation by the unstable mode and inverse transfer of energy by the stable mode in reversed direction. The nonlinear process then responds to this linear physics.

6.9 Discussion

Some broader implications and interpretations of the results of this work shall now be provided.

Cascades, Couplings, and Competitions

We have shown with various quantitative measures that only a fraction of unstable-mode energy is cascaded to small scales. A majority, near or greater than 70%, of the instability-extracted energy from the mean flow to the large-scale fluctuations is, in reality, nonlinearly transferred to the conjugate-stable modes. This nonlinear mode-

coupling at the instability-scale controls the rate of the small-scale energy cascade right at its inception.

It remains true that larger Reynolds numbers push the Kolmogorov dissipation length scale to smaller scales, thus allowing more scales to be dynamically relevant in the turbulence. The small-scale turbulence is indeed affected by the Reynolds number; however, the measures of interest, such as the energy injection rate in the cascade channel where it is formed and the momentum transport rate, are under the territorial jurisdiction of the fluctuations at the instability scale. At such a large scale, the conjugate-stable modes are excited, first via a parametric drive from the unstable modes through the mode-coupling coefficient $C_{211}(\mathbf{k},\mathbf{k}')$ in the stable-mode evolution equation

$$\partial_t \beta_2(\mathbf{k}) = -\gamma(\mathbf{k})\beta_2(\mathbf{k}) + \sum_l B_{2l}(\mathbf{k})\beta_l(\mathbf{k}) + \sum_{\mathbf{k}',\mathbf{k}'':\mathbf{k}'+\mathbf{k}''=\mathbf{k}} C_{211}(\mathbf{k},\mathbf{k}')\beta_1'\beta_1'' + \ldots, \quad (6.10)$$

where $C_{211}(\mathbf{k},\mathbf{k}')$ is independent of viscosity, and, therefore, favors excitation of stable modes. Whether this excitation becomes significant or not depends on the relative magnitudes of γ, B_{2l}, and $C_{211}(\mathbf{k},\mathbf{k}')$.[15]

At the large instability scale, with decreasing viscosity, B_{2l} naturally becomes smaller; this is different from the singular limit of small-scale dissipation that does not vanish with decreasing viscosity. Therefore, the large-scale-stable-mode excitation is only weakly impacted once the viscosity is sufficiently low, as we have found in Fig. 10.3. In addition, the small-scale dissipation rate, as well as the scales where intense viscous dissipation occurs, are both controlled by the energy extracted from the mean flow-gradient; the extraction rate, however, depends on the excitation levels of the large-scale stable modes, as shown in Figs. 9.10 and 9.11. Thus, the Reynolds number, although it spawns more small scales, only asymptotically and weakly impacts

the large-scale-stable-mode physics, as the stable modes are coupled to the unstable modes via a nonlinear mode-coupling coefficient whose origin lies in the overlap of the eigenmodes of an instability that is entirely inviscid. Although a competition exists between small-scale cascades and nonlinear coupling among the roots of the inviscid instability, the latter dominates over the former as long as the Reynolds number is not so small that the flow becomes near-laminar, strongly breaking the symmetry between the unstable and stable modes—this latter case does not appear in high-Reynolds-number turbulent flows in natural systems.

Dimensionality, Density of states, Drives, and Dynamics

For a system with n spatial dimensions (physical coordinate axes), we conjecture that the number of KH-unstable wavenumbers grows following an approximate power law $(k/k_0)^{n-1}$, where k is the magnitude of the wavevector, and $k_0{=}2\pi/L$ is the lowest wavenumber in the domain of size L. The increment in the number of KH-unstable wavenumbers follows from the density-of-states effect, associated with each dimension (Fig. 10.2); one of the axes is not counted because that axis represents the direction of inhomogeneity of the mean shear flow.

Such increased number of the KH-unstable wavenumbers put the mean shear-flow under additional stress, all demanding energy and momentum redistribution. Turbulence with increased spatial dimensions, hence, extracts more energy from the mean flow and transports more momentum across the shear layer—i.e., the turbulence features increased energy drive and dynamics. In decaying turbulence, the slowly growing wavenumbers of higher spatial dimension (greater than two) may not get an opportunity to attain high amplitudes in comparison to the 2D-mode amplitudes. However, for a sufficiently forced mean-flow, such a discriminatory scenario is precluded;

as evidenced in Figs. 6.5 and 6.8, the larger density of states of 3D modes manifests in increased levels of momentum transport and energy transfer.

The dynamics of shear-flow turbulence can be substantially different depending on the linear process driving the turbulence. We shall remark here on two important processes: the exponential instability growth and the transient non-modal growth. When the Kelvin-Helmholtz instability is present, as in this paper, the instability rapidly grows exponentially [Figs. 10.3(a) and (c), blue curves]. Such a rapid exponential growth over longer times supersedes the here-inconsequential transient growth due to non-modal effects.[202, 203] The latter are crucial in modally stable non-normal flows,[204–206] e.g., shear flows with no inflection point. With the fluctuations dominated by the unstable modes, they nonlinearly excite conjugate-stable modes, with nearly twice[15] the instability-growth rate [Figs. 10.3(a) and (c), orange curves]. Such stable modes, which are excited by the nonlinearity, are fundamentally different from the linear, transient growth of fluctuations. We also note that the conjugate-stable modes here continuously transfer energy from the fluctuations to the mean flow, as seen in Fig. 6.6(c). This continuous process differs from the transient non-modal growth.

6.10 Conclusions

The ubiquitous Kelvin-Helmholtz instability is traditionally assumed to saturate nonlinearly by cascading to small scales the unstable-mode energy, in its entirety. Recently, a majority of the unstable-mode energy has been reported to be returned to the mean flow from the fluctuation by the linearly stable eigenmodes that are nonlinearly excited in two-dimensional turbulence.[110, 143, 180] Whether such a consequential process exists in 3D fluid turbulence, as well, is the central question

addressed in this work. Here, the linearly stable 3D modes, excited to significant amplitudes, are shown to exhibit similarities with the reports of 2D turbulence, as well as new signatures that are fundamentally 3D. The energy transfer path to stable modes in 3D is wholly different: in the turbulent phase, the transfer occurs via modes, we label as zonal flows, that vary only in the direction orthogonal to the 2D shear flow. Such perturbations have zero linear frequencies due to the anisotropic dispersion relation of the inviscid 3D Kelvin-Helmholtz instability. However, because of their zero frequencies, they allow near-resonant energy transfer from unstable to conjugate-stable modes, saturating the instability in 3D.

The transfer of energy by the stable modes is directly from the instability-scale fluctuation to the mean flow-gradient, which may be interpreted as an *inverse transfer of energy*. This inversion is a linear process, different from the traditional nonlinear energy cascade to small scales. We have shown here not only the existence of such inverse transfer of energy in 3D, but that they are more efficient for the 3D perturbations than for the 2D perturbations.

Vortex-tube stretching, an inherently 3D process, is suppressed by the stable modes. This has been demonstrated through a series of numerical experiments, where we impulsively zeroed either stable or unstable modes in a nonlinear simulation, at randomly selected times, and resumed the simulations to obtain statistical responses in the small-scale activity. The viscous dissipation rates and spectral amplitudes of enstrophy increase with stable-mode removal, and decrease with unstable-mode removal. Further, 3D visualizations of vortex dynamics revealed that, in the absence of the stable modes, the vortex tubes are significantly stretched and continuously thinned out; the stable modes counter this mechanism and remove the thin filamentary structures, attempting to form large-scale structures.

Transporting up-gradient momentum in 3D, the stable modes counteract the

instability-driven down-gradient momentum transport more effectively than they do in 2D (≈70% vs. ≈50%). This competition occurs continuously in time and can occasionally reverse the net transport direction, bearing important implications for shear-flow turbulence in geo- and astrophysical environments.

For future work, this study raises important questions regarding the impact of stable modes in other three-dimensional problems such as 3D MHD shear flows, where, analogous to the vortex stretching, there exists magnetic field amplification, which, at small scales, can be inhibited by the stable modes, favoring large-scale magnetic field generation[42]; 3D stratified shear flows, where the stable modes may serve as a zookeeper, managing a zoo of instabilities[185, 189, 207]; the ideal, magneto-rotational instability (MRI),[208] where it is possible that the transport measured in numerical simulations of MRI-driven turbulence (see, e.g., Ref. [27]) has an unaccounted contribution from the stable modes, and there is an opportunity to build accurate transport models for astrophysical problems, magnetized[209, 210] or not.

7 **PAPER E**: PREDICTING THE SLOWING OF STELLAR DIFFERENTIAL ROTATION BY INSTABILITY-DRIVEN TURBULENCE

A version of this chapter was published in Astrophys. J. 966, 195 (2024).

ABSTRACT

Differentially rotating stars and planets transport angular momentum internally due to turbulence at rates that have long been a challenge to predict reliably. We develop a self-consistent saturation theory, using a statistical closure approximation, for hydrodynamic turbulence driven by the axisymmetric Goldreich–Schubert–Fricke (GSF) instability at the stellar equator with radial differential rotation. This instability arises when fast thermal diffusion eliminates the stabilizing effects of buoyancy forces in a system where a stabilizing entropy gradient dominates over the destabilizing angular momentum gradient. Our turbulence closure invokes a dominant three-wave coupling between pairs of linearly unstable eigenmodes and a near-zero frequency, viscously damped eigenmode that features latitudinal jets. We derive turbulent transport rates of momentum and heat, and provide them in analytic forms. Such formulae, free of tunable model parameters, are tested against direct numerical simulations; the comparison shows good agreement. They improve upon prior quasi-linear or "parasitic" saturation models containing a free parameter. Given model correspondences, we also extend this theory to heat and compositional transport for axisymmetric thermohaline instability-driven turbulence in certain regimes.

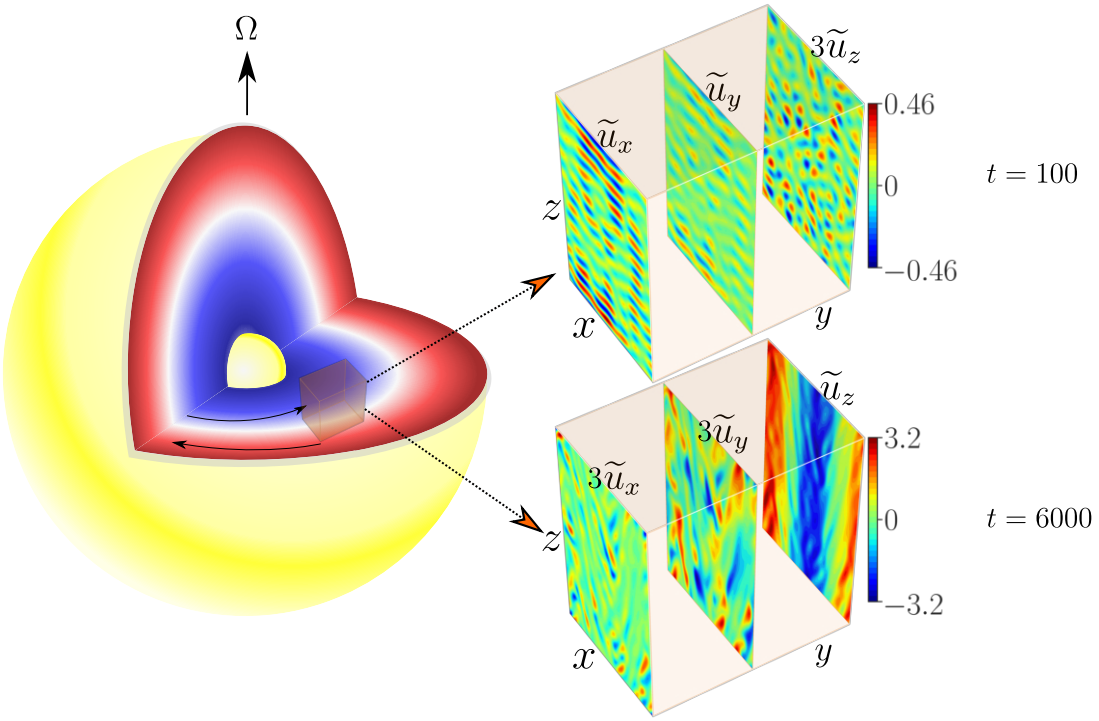

Figure 7.1: (Left) A schematic diagram of a differentially rotating star with a radial shear, gravity, and stable stratification. Such a system subject to the GSF instability is studied using a local Cartesian model. (Right) Snapshots of velocity components $\widetilde{u}_x(x,z)$, $\widetilde{u}_y(x,z)$, and $\widetilde{u}_z(x,z)$ from the axisymmetric GSF instability-driven turbulence; x, y, and z represent the local radial, azimuthal, and latitudinal directions. Though finger-like horizontal structures (as shown by, e.g., $\widetilde{u}_x$) grow the fastest in the linear phase (t=100), strong latitudinal jets $\widetilde{u}_z$ are generated nonlinearly (t=6000). The color bar for t=100 is shared by $\widetilde{u}_x$, $\widetilde{u}_y$, and $3\widetilde{u}_z$; the color bar for t=6000 is shared by $3\widetilde{u}_x$, $3\widetilde{u}_y$, and $\widetilde{u}_z$. The turbulent transport of angular momentum, e.g., $\langle \widetilde{u}_x \widetilde{u}_y \rangle$, is predicted in this paper using a jet-coupled turbulence closure.

7.1 Introduction

Instability-driven turbulence is thought to play a major role in the transport of angular momentum (AM), heat and composition in stellar and planetary interiors [see, e.g., 26, 211–213], as well as in astrophysical disks [e.g., 214, 215]. Unfortunately, rates of turbulent transport are very challenging to predict theoretically, and the lack of reliable theories has hampered our understanding of the evolution of stellar and planetary

internal rotations and structures. For example, the AM redistribution in red giant stars is currently poorly understood, and their core-envelope differential rotations inferred from asteroseismology have not been adequately explained [e.g., 212, 216, 217]. The nearly solid-body rotation observed in the solar radiative interior also lacks a robust explanation [e.g., 218, 219].

Differential rotation is known to drive a variety of hydrodynamic (and hydromagnetic) instabilities. In this paper, we focus on modeling hydrodynamic instabilities of differential rotation in stellar and planetary radiative zones, and in particular on the Goldreich–Schubert–Fricke (GSF) instability[1][36, 37]. This is a double-diffusive centrifugal instability in which rapid thermal diffusion (relative to viscous momentum diffusion) enables instability by tempering the otherwise stabilising effects of buoyancy forces. Prior work has studied the linear and nonlinear properties of the instability, and the turbulence it drives [38, 226–231], but a reliable theory for the resulting turbulent transport is lacking. This means that the effects of the GSF instability on stellar rotational and chemical evolution have not been modeled in a self-consistent manner. Instead, one typically invokes unexplained “additional viscosities" or models that contain free parameters. Such tunable parameters are intended to describe the effects of turbulence on AM transport for which adequate knowledge is lacking.

A fully analytic model containing no free parameters is derived here for the GSF instability-driven turbulence in 2.5 dimensions (2.5-D), i.e., with all three components of velocity but varying spatially only in two dimensions. The predictions of our analytical model are in broad agreement with detailed numerical simulations of turbulence, driven by the axisymmetric (2.5-D) GSF instability at the equator of a star with radial differential rotation. Such model of the instability is, for certain

[1]It has also been referred to as the “Vertical Shear Instability" (VSI) in accretion disks [220–223] and as “inertial instability" enabled by thermal diffusion in stellar interiors [224, 225].

diffusivity ratios and in 2.5-D, formally and nonlinearly equivalent to the thermohaline, or salt-finger, instability that transports heat and chemical elements [38, 227]; thus, the turbulent transport arising from axisymmetric fingering convection is also described by our theory.

The structure of this paper is as follows. In § 7.2, we present our model and methods of analysis. Nonlinear mode coupling and saturation diagnostics of the instability appear in § 7.3. Informed by such diagnostics, we present analytical formulae, without any free parameters, to model the turbulence and its transport properties in § 7.4. We discuss the astrophysical implications and conclude in § 7.5. Details of the closure model are provided in the Appendices.

7.2 The GSF instability and inertial-gravity waves

To study a basic mechanism of angular momentum transport in a differentially rotating star, we consider a local region inside the star near its equator, where the rotation can be split into a uniform or mean part—$\mathbf{\Omega}$=$\Omega\hat{\mathbf{e}}_z$, aligning with the local latitudinal axis z—and a non-uniform part due to the radial differential rotation. The latter is represented by a background linear shear flow $\boldsymbol{U}_0(x)$= $-\mathcal{S}x\hat{\mathbf{e}}_y$ where x is the radial coordinate, y is the azimuthal coordinate, and $\mathcal{S} = -d\Omega_{\rm Shell}(x)/d\ln x$ is the local radial-shear rate, with $\Omega_{\rm Shell}(x)$ representing the "Shellular" rotation of the simplified star. A uniform gravity field with $\boldsymbol{g} = -g\hat{\mathbf{e}}_x$ is directed radially inward (Fig. 7.1). A background radial temperature gradient ∇T_0 then stratifies the fluid density radially, with a thermal expansion coefficient α. In such a background state, any perturbations

in velocity $\boldsymbol{u}$ and scaled temperature $\theta{=}\alpha g T$ evolve [38] as

$$D\boldsymbol{u} + \boldsymbol{u}\cdot\nabla\boldsymbol{U}_0 + 2\boldsymbol{\Omega}\times\boldsymbol{u} = -\nabla p + \theta\hat{\mathbf{e}}_x + \nu\nabla^2\boldsymbol{u}, \tag{7.1a}$$

$$D\theta + \boldsymbol{u}\cdot\nabla\Theta_0 = \kappa\nabla^2\theta, \tag{7.1b}$$

$$\nabla\cdot\boldsymbol{u} = 0, \tag{7.1c}$$

$$D \equiv \partial_t + (\boldsymbol{u}+\boldsymbol{U}_0)\cdot\nabla, \tag{7.1d}$$

where the variables p, ν, and κ are the fluid pressure (per unit density), the kinematic viscosity, and the thermal diffusivity, respectively. We also define the Prandtl number $\mathrm{Pr}{=}\nu/\kappa$. Because the GSF instability operates at length scales much smaller than a pressure scale height in stars, the local approximation is valid; in such a case, when the turbulence drives subsonic flows, the Boussinesq approximation is also appropriate [232]. Assuming a uniform temperature gradient, a fluid element perturbed radially oscillates with a constant Brunt-Väisälä (buoyancy) frequency $\mathcal{N}$, where $\mathcal{N}^2\hat{\mathbf{e}}_x{=}\nabla\Theta_0{=}\alpha g\nabla T_0$.

Henceforth, we non-dimensionalize all variables using the characteristic rotation time scale Ω^{-1} and length scale d, with $d{=}(\nu\kappa/\mathcal{N}^2)^{1/4}$, which is typically similar to the wavelengths of fastest-growing modes. Thus, $N{=}\mathcal{N}/\Omega$ is the dimensionless buoyancy frequency and $S{=}\mathcal{S}/\Omega$ the dimensionless shear rate (Rossby number). The GSF instability occurs in low-Pr fluids whenever $r \in [0,1]$, where $r = \mathrm{Pr}(1{+}N^2\kappa_{\mathrm{ep}}^{-2})/(\mathrm{Pr}{-}1)$, with $\kappa_{\mathrm{ep}}{=}\sqrt{2(2-S)}$ representing the dimensionless epicyclic frequency [38].

Eigenmode analysis

A linear analysis of Eqs. (9.1a)–(7.1b) for axisymmetric (uniform-in-y) perturbations yields a simple matrix equation, which upon Fourier-transforming becomes $\boldsymbol{L}\hat{\boldsymbol{X}}{=}\gamma\hat{\boldsymbol{X}}$, where $\hat{\boldsymbol{X}}{=}[\hat{u}_x, \hat{u}_y, \hat{u}_z, \hat{\theta}]^{\mathrm{T}}$, with $^{\mathrm{T}}$ as the transpose operation, is the state vector of

spatially Fourier-transformed components at wavevector $\mathbf{k}=(k_x, k_z)$; the matrix $\boldsymbol{L}$ is a linear operator, whose eigenvalues are the complex-valued growth rates γ. The size of $\boldsymbol{L}$ demands four linearly independent eigenvectors. Because of the additional constraint $\nabla\cdot\boldsymbol{u}=0$, the system has only three degrees of freedom at any given wavenumber—two components of velocity, and $\hat{\theta}$. Hence, one eigenvector among the four eigenvectors does not satisfy $\nabla\cdot\boldsymbol{u}=0$ and is rejected. We confirm that this eigenvector is not excited within our incompressible Boussinesq simulations. One among the remaining three eigenvectors at a given wavevector becomes GSF-unstable [$\mathrm{Re}\,(\gamma) > 0$, where Re denotes the real part], whenever $r \in [0, 1)$. The remaining two eigenvectors are always stable, and their eigenvalues are complex conjugates of each other whenever they satisfy $\mathrm{Im}\,(\gamma) \neq 0$, where Im denotes the imaginary part; $\mathrm{Im}\,(\gamma)$ corresponds to the frequency of inertial-gravity, or gravito-inertial, waves (IGWs), modified by the shear flow and damped by viscous and thermal diffusion.

The GSF instability grows dominantly via axisymmetric ($\partial_y \equiv 0$) perturbations, therefore we focus upon the (x, z)-variations of the 3-component velocity and temperature fields. The dispersion relation then is a simple cubic polynomial in γ [36] as

$$\gamma_\nu^2\gamma_\kappa + \frac{\kappa_{\mathrm{ep}}^2 k_z^2}{k^2}\gamma_\kappa + \frac{N^2 k_z^2}{k^2}\gamma_\nu = 0, \tag{7.2}$$

where $\gamma_\nu = \gamma + \nu k^2$ and $\gamma_\kappa = \gamma + \kappa k^2$. Equation (7.2) shows that, on the (k_x, k_z)-plane, the growth rate exhibits strong anisotropy: fluctuations with k_x=0 ("elevator modes") grow the fastest, whereas those with k_z=0 are linearly stable. This observation is critical for the nonlinear saturation of the GSF instability because the anisotropy of the linear physics, in particular the k_z=0 fluctuation, can impose its anisotropy on the nonlinear energy transfer, which is otherwise isotropic; such consequential effects have been found in various systems such as 3-D Kelvin-Helmholtz instability [233],

rotating [164, 165] and stably stratified turbulence [167], turbulence with an external magnetic field in astrophysical [175, 177] and fusion plasmas [174, 176].

Using the complete basis provided by the eigenvectors of the linear operator $\boldsymbol{L}$, we can decompose arbitrary incompressible fluctuation $\hat{\boldsymbol{X}}_{\rm arb}$ with $k_z{\neq}0$ as $\hat{\boldsymbol{X}}_{\rm arb}{=}\sum_{j=1}^{3}\beta_j\hat{X}_j$, where β_j is the amplitude of the $j^{\rm th}$ eigenvector $\hat{X}_j$; we reserve $j{=}1$ for the GSF-unstable modes, and $j{=}2,3$ for the IGWs that are always linearly stable in this study. More compactly, $\hat{\boldsymbol{X}}_{\rm arb}{=}\boldsymbol{E}\boldsymbol{\beta}$, where $\boldsymbol{\beta}$ is a (column-)vector of mode amplitudes and $\boldsymbol{E}$ is an eigenvector matrix, whose $j^{\rm th}$ column is $\hat{X}_j$. Thus, $\boldsymbol{\beta}{=}\boldsymbol{E}^{-1}\hat{\boldsymbol{X}}_{\rm arb}$.

For the $k_z{=}0$ modes, $\boldsymbol{E}$ turns out to be an identity matrix, meaning that the three components of velocity, and the temperature, individually form eigenvectors. In what follows, we therefore decompose an arbitrary fluctuation with $k_z{=}0$ into $\hat{\boldsymbol{X}}^{\rm T}_{\rm arb}=\mathcal{X}[1,0,0,0]+\mathcal{Y}[0,1,0,0]+\mathcal{Z}[0,0,1,0]+\Theta[0,0,0,1]$, where the amplitudes of the eigenvectors are denoted by $\mathcal{X},\mathcal{Y},\mathcal{Z}$, and Θ. We reserve the $\boldsymbol{\beta}$-notation above for the amplitudes of eigenvectors with $k_z{\neq}0$.

Initial value problem

We perform an ensemble of direct numerical simulations of Eqs. (9.1a) and (7.1b), by seeding a low-amplitude solenoidal random noise to $\boldsymbol{u}$, in a box of size $(L_x,L_z){=}(100,100)$. To obtain numerically converged results, a spatial resolution of up to 512^2 grid points is used in the pseudo-spectral solver SNOOPY [38, 234].

To determine the contribution of each eigenmode in, for example, the turbulent momentum transport, we decompose the turbulent stress as:

$$\langle\widetilde{u}_x\widetilde{u}_y\rangle{=}\sum_{k_x,k_z}\sum_{m,n}2{\rm Re}\left[\beta_m\hat{u}_{x,m}\beta_n^*\hat{u}_{y,n}^*\right], \tag{7.3}$$

where $\langle\cdot\rangle$ is an (x,z)-averaging operation; m and n are summed from 1 to 3, corre-

sponding to three excited eigenmodes at every wavenumber $\boldsymbol{k}$; the amplitude β_m and the x-component of the velocity $\hat{u}_{x,m}$ correspond to the m^{th} eigenvector at $\boldsymbol{k}$; and likewise for β_n and $\hat{u}_{y,n}$; the operation * denotes complex conjugation. Using such a decomposition, we obtain the contribution of an unstable mode at $\boldsymbol{k}$ to the momentum transport rate, which is $2|\beta_1|^2\text{Re}\left[\hat{u}_{x,1}\hat{u}^*_{y,1}\right]$. This decomposition is performed for every wavenumber, hence allowing us to trace evolution of transport contributions due to individual unstable modes [see Fig. 10.1(a)].

The summed contributions of all eigenvectors from all wavenumbers reproduce, to machine precision, the total transport rates found in the simulation before performing mode decomposition, as we show in Fig. 10.1(b). The contributions of the unstable modes are also compared across different wavenumber sums. Almost identical results are found for heat transport (not shown). The unstable modes from the linearly fastest-growing wavenumber branch k_x=0 transport significantly less momentum than the other wavenumbers with $k_x\neq0$. This is our first surprising result, and it challenges predictions of turbulent transport that rely on an unstable mode at the fastest-growing wavenumber alone [e.g., 38, 235, 236]. This finding also instructs us to investigate nonlinear couplings between eigenmodes to understand the instability-saturation mechanism.

7.3 Nonlinear saturation by coupling to latitudinal flow

Mode-amplitude evolution

To analyze nonlinear mode couplings, Eqs. (9.1a)–(7.1b) are first spatially Fourier-transformed: $\partial_t\hat{\boldsymbol{X}} = \boldsymbol{L}\hat{\boldsymbol{X}}+\sum_{\boldsymbol{k}',\boldsymbol{k}''}\boldsymbol{N}(\hat{\boldsymbol{X}}',\hat{\boldsymbol{X}}'')$, where $\hat{\boldsymbol{X}}$, $\hat{\boldsymbol{X}}'$, and $\hat{\boldsymbol{X}}''$ are state vectors

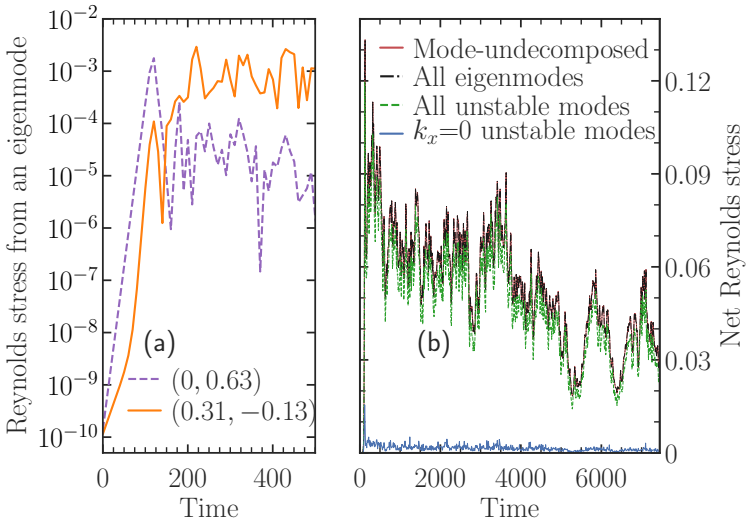

Figure 7.2: (a) Comparison of momentum transport (Reynolds Stress=$2|\beta_1|^2\mathrm{Re}\left[\hat{u}_{x,1}\hat{u}^*_{y,1}\right]$) driven by an unstable mode at the linearly fastest-growing wavenumber $\mathbf{k} = (0, 0.63)$, and by an unstable mode at $\mathbf{k} = (0.31, -0.13)$, the wavenumber that has the largest contribution to the momentum transport in the nonlinear phase. (b) Eigenmode decomposition of net Reynolds stress $\langle\widetilde{u}_x\widetilde{u}_y\rangle$ in nonlinear simulation of the GSF instability-driven turbulence, showing that the transport due to mode-undecomposed fluctuations (red curve) and mode-decomposed all eigenmodes (black curve) agree to machine precision. Transport is almost entirely (88%) due to the unstable modes (green curve); the sum of fastest-growing unstable modes at k_x=0, however, contributes negligibly (3%) to the transport (blue curve). Simulation parameters used are S=2.1, N^2=10 and Pr=0.01.

at $\boldsymbol{k}, \boldsymbol{k}'$, and $\boldsymbol{k}''$, respectively, satisfying $\boldsymbol{k} = \boldsymbol{k}' + \boldsymbol{k}''$. Then, following Sec. 7.2 we substitute $\hat{\boldsymbol{X}}$=$\boldsymbol{E\beta}$, and likewise for $\hat{\boldsymbol{X}}'$ and $\hat{\boldsymbol{X}}''$. We multiply the obtained equation with $\boldsymbol{E}^{-1}$ and take the j^{th} row of the resulting equation. This process yields an evolution equation for the j^{th} eigenmode at $\boldsymbol{k}$. Such an evolution equation for mode amplitude β_j for k_z≠0 is different from that of the mode amplitude $F \in \{\mathcal{X}, \mathcal{Y}, \mathcal{Z}, \Theta\}$

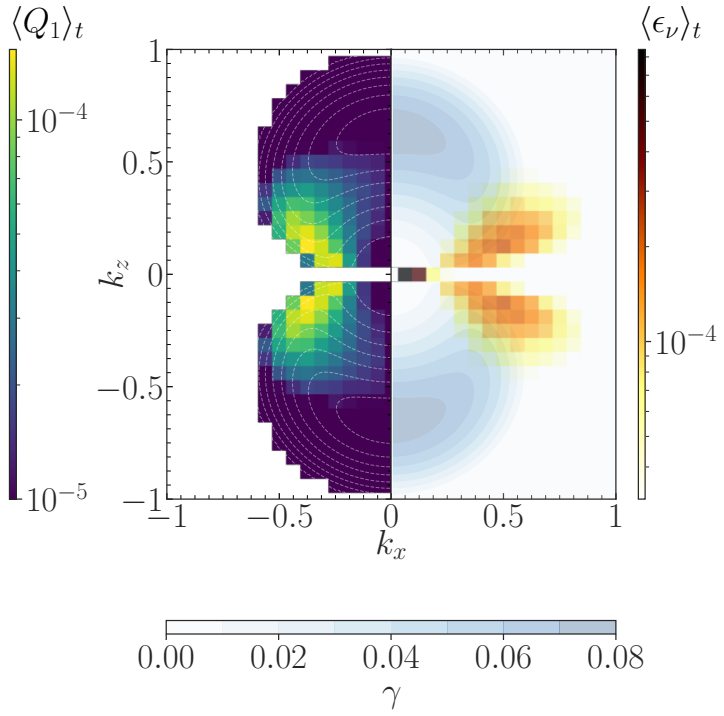

Figure 7.3: Spectra of linear and nonlinear-saturation properties of the GSF instability. On the negative-k_x domain, the colored square boxes (yellow-green-purple) display time-averaged energy extraction rates $\langle Q_1 \rangle_t$ by unstable modes from the mean gradients in a nonlinear simulation. On the positive-k_x domain, colored square boxes (black-red-yellow) show the time-averaged viscous dissipation rates, which are pronounced at low k_z. Over the entire (k_x, k_z)-plane, the non-square filled and line contours show the growth rates γ of unstable modes, with white dashed contour lines on the negative-k_x domain and with bluish filled contours on the positive-k_x domain. The fastest-growing mode resides at around $\mathbf{k} = (0, 0.63)$. The simulation parameters are S=2.1, N^2=10 and Pr=0.01.

for k_z=0, although both are coupled and nonlinear:

$$\partial_t \beta_j = \gamma_j \beta_j + \sum_{\boldsymbol{k}',m,n} C_{jmn}^{(\boldsymbol{k},\boldsymbol{k}')} \beta'_m \beta''_n + \sum_{\substack{\boldsymbol{k}',F,n:k'_z=0 \\ F\in\{\mathcal{X},\mathcal{Y},\mathcal{Z},\Theta\}}} \left[C_{jFn}^{(\boldsymbol{k},\boldsymbol{k}')} + C_{jnF}^{(\boldsymbol{k},\boldsymbol{k}'')} \right] F' \beta''_n, \tag{7.4a}$$

$$\partial_t F = -\gamma_F F + \sum_{\boldsymbol{k}',m,n:k_z=0} C_{Fmn}^{(\boldsymbol{k},\boldsymbol{k}')} \beta'_m \beta''_n, \tag{7.4b}$$

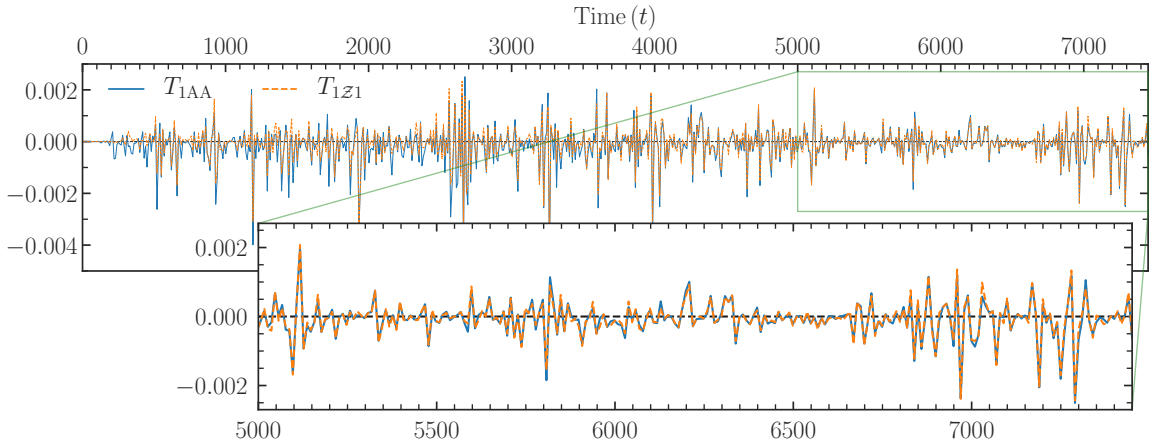

Figure 7.4: Time evolution of the total nonlinear energy transfer $T_{1\mathrm{AA}}$ to an unstable eigenmode at a wavenumber where the spectrum of $\langle \tilde{u}_x \tilde{u}_y \rangle$ peaks. $T_{1\mathcal{Z}1}$ is the energy transfer to the same unstable mode via interactions between the z-component of velocity ($\mathcal{Z}$) with wavenumbers k_z=0, and the other unstable modes. Comparison of two transfer functions reveals that the dominant triad involves a latitudinal flow and two unstable modes. The simulation parameters are S=2.1, N^2=10 and Pr=0.01.

where γ_j is the complex-valued growth rate for the j^{th} eigenmode with $k_z \neq 0$; the real-valued damping rate γ_F is $\gamma_{\mathcal{X}}$ when F is replaced with $\mathcal{X}$ in Eq. (7.4b); likewise for the replacement of F with $\mathcal{Y}, \mathcal{Z}$, and Θ; we note that $\gamma_{\mathcal{X}} = \gamma_{\mathcal{Y}} = \gamma_{\mathcal{Z}} = \nu k_x^2$, and $\gamma_\Theta = \kappa k_x^2$. The nonlinear-coupling coefficient, for example, $C_{jmn}^{(\boldsymbol{k},\boldsymbol{k}')}$ measures the overlap of eigenmodes m with $\boldsymbol{k}'$, n with $\boldsymbol{k}''$, and j with $\boldsymbol{k}$. Such a mode coupling coefficient is found by applying $\boldsymbol{E}^{-1}$ to the (column) vector of $\boldsymbol{N}(\hat{\boldsymbol{X}}'_m, \hat{\boldsymbol{X}}''_n)$, a process that incorporates all the nonlinearities of the system, thus making $C_{jmn}^{(\boldsymbol{k},\boldsymbol{k}')}$ ideal for a comprehensive instability-saturation analysis.

On the right-hand side of Eq. (7.4a), the second term is the nonlinear coupling between eigenmodes with $k'_z \neq 0$ and $k''_z \neq 0$ (hence the two βs), and the third term, with an F and a β, is the nonlinear coupling between eigenmodes with k'_z=0 and $k''_z \neq 0$ (see the last paragraph of Sec. 7.2). Equations (7.4a) and (7.4b) have the same number of degrees of freedom as the original nonlinear equations in physical space, Eqs. (9.1a)–(7.1b). These systems are completely equivalent, but one represents

dynamics in physical space and another in eigenmode space.

Mode-energy evolution

The energy evolution equation for each eigenmode can now be derived by multiplying Eq. (7.4a) by β_j^* and adding the complex conjugate of the resulting equation to arrive at

$$\partial_t|\beta_j|^2 = Q_j + T_{j\mathrm{AA}}, \tag{7.5}$$

where Q_j=2Re $\gamma_j|\beta_j|^2$ is the linear energy transfer rate to $\boldsymbol{k}$ from the mean gradients, and $T_{j\mathrm{AA}}$ is the total nonlinear energy transfer to the j^{th} eigenmode from *all* possible nonlinear interactions; Eq. (A10). We now show the spectrum of time-averaged Q_1, along with that of the growth rate and time-averaged viscous dissipation rate ϵ_ν in Fig. 10.2.

From $T_{j\mathrm{AA}}$ in Eq. (7.5), we separate out the nonlinear transfer $T_{1\mathcal{Z}1}$ in a triad that involves a latitudinal flow $\mathcal{Z}$ at k_z'=0 and two GSF-unstable modes (j=1) at $k_z'\neq$0:

$$T_{1\mathcal{Z}1} = \sum_{\boldsymbol{k}':k_z'=0} 2\mathrm{Re}\left\{ \left[C_{1\mathcal{Z}1}^{(\boldsymbol{k},\boldsymbol{k}')} + C_{11\mathcal{Z}}^{(\boldsymbol{k},\boldsymbol{k}'')}\right] \mathcal{Z}'\beta_1''\beta_1^* \right\}. \tag{7.6}$$

We now compare $T_{1\mathcal{Z}1}$ with $T_{1\mathrm{AA}}$ in Fig. 10.3, for a GSF-unstable mode with a wavenumber that contributes the largest to the momentum transport. Repeating this transfer analysis at different wavenumbers produces similar results. The two transfers are nearly identical, which confirms the conjecture [38] that, in the fully nonlinear phase, the GSF instability saturates via the formation of strong latitudinal jets or flows. Such flows are z-directed, although with no z-variation, and primarily have a wavenumber k_x=$2\pi/L_x$; see Fig. 7.1, right-column snapshot at t=6000. These flows generalize to meridional circulation in stars, and resemble zonal jets in planetary

atmospheres and fusion systems [30]. Flows with k_z=0 are, however, linearly stable to the GSF instability, and, thus, must necessarily be excited nonlinearly by the interactions between the GSF-unstable modes. This energy received is then viscously damped at k_z=0 and at low k_z, as seen in Fig. 10.2. To sum up, the mean shear flow, destabilized by the thermal diffusion, lends energy to the fluctuations via the GSF-unstable modes, which saturate by exciting k_z=0 latitudinal flows to a significant level. Such flows then viscously dissipate the turbulent energy. This is the saturation mechanism of the axisymmetric GSF instability found here.

7.4 Angular momentum transport model

The findings shown so far are sufficient to build a statistical closure model, with no free parameters, and thus with predictive power.

Equation (7.4a) has a quadratic nonlinearity, hence evolutionary equations for mode energy contain triplet interactions [e.g., Eq. (7.6)]. To determine the evolving triplet interaction terms, one can derive an equation with quadruplet interactions [Eq. (A13)], and so on. To truncate this never-ending hierarchy (the so-called “turbulence closure problem"), we invoke a standard turbulence closure, the Eddy-Damped Quasi-Normal Markovian (EDQNM) approximation (see, e.g., **(author?)** 32, 33, 34, 88, 94, 141, 201), that truncates the hierarchy at fourth-order cumulants of the fluctuations, thereby assuming that the statistics for the mode amplitudes are close to Gaussian. The resulting equation, however, is still nonlinear and daunting. But when a latitudinal flow $\mathcal{Z}$, with k_z=0, dominates the nonlinear coupling, the complexity of the equation is significantly reduced [32].

An outline of the Closure Model

We illustrate here the key steps involved to explain most simply our closure model (by omitting details and treating all variables as real). First, we observe that Eq. (7.4a) has the structure:

$$\partial_t \beta = ...\beta + ...\beta\beta + ...\beta\mathcal{X} + ...\beta\mathcal{Y} + ...\beta\mathcal{Z} + ...\beta\Theta\,, \tag{7.7}$$

where the mode amplitudes are explicitly shown, and the dots (...) represent terms such as the linear growth rate and the nonlinear coupling coefficients. One can then obtain evolution equation for second-order correlator as $\partial_t(\beta\beta) = ...\beta\beta + ...\beta\mathcal{Z}\beta$, where the other nonlinear terms, e.g., $\beta\beta\beta$ and $\beta\beta\mathcal{X}$, have been dropped because the nonlinear energy transfer is almost entirely dominated by $\beta\mathcal{Z}\beta$—the latitudinal-flow coupling (Fig. 10.3). Since $\beta\mathcal{Z}\beta$ also evolves, one can similarly obtain evolution equation for third-order correlator as $\partial_t(\beta\mathcal{Z}\beta) = ...\beta\mathcal{Z}\beta + ...\beta\beta\mathcal{Z}\mathcal{Z}$. The closure solution then yields a relation $\beta\mathcal{Z}\beta = ...\beta\beta\mathcal{Z}\mathcal{Z}$. Although useful later, this relation does not predict the mode amplitude β, needed for the turbulent transport prediction.

To predict the mode amplitude β, we consider the latitudinal-flow evolution equation, $\partial_t\mathcal{Z} = ...\mathcal{Z} + ...\beta\beta$, and derive $\partial_t(\mathcal{Z}\mathcal{Z}) = ...\mathcal{Z}\mathcal{Z} + ...\beta\mathcal{Z}\beta$. Then, $\beta\mathcal{Z}\beta$ can be replaced with a product of four amplitudes using the closure solution in the previous paragraph. One thus obtains $\partial_t(\mathcal{Z}\mathcal{Z}) = ...\mathcal{Z}\mathcal{Z} + ...\beta\beta\mathcal{Z}\mathcal{Z}$. In quasi-stationary turbulence, $\partial_t \sim 0$, and thus $\beta\beta\mathcal{Z}\mathcal{Z} = ...\mathcal{Z}\mathcal{Z}$. The EDQNM closure allows writing a fourth-order correlator $\beta\beta\mathcal{Z}\mathcal{Z}$ as a sum of products of second-order correlators, such as $|\beta|^2|\mathcal{Z}|^2$. Then, cancelling $|\mathcal{Z}|^2$ from both sides of $\beta\beta\mathcal{Z}\mathcal{Z} = ...\mathcal{Z}\mathcal{Z}$, one predicts the saturated mode amplitude (or energy): $\beta\beta = ...$. Using this, one can make predictions for turbulent transport rates as we shall show in the next subsection.

Detailed Closure Model

To make quantitative predictions for transport, we take the EDQNM-closed evolution equation for the latitudinal flow energy [see Appendix B, Eq. (A20)],

$$\begin{aligned}\partial_t|\mathcal{Z}|^2/2 = &-\gamma_{\mathcal{Z}}|\mathcal{Z}|^2 \\ &+|\mathcal{Z}|^2\sum_{\boldsymbol{k}'}|\beta_1'|^2\,\mathrm{Re}\,\left[-\tau_{11\mathcal{Z}}\overleftrightarrow{C}^{(\boldsymbol{k},\boldsymbol{k}')}_{\mathcal{Z}11}\overleftrightarrow{C}^{(\boldsymbol{k}'',\boldsymbol{k})}_{1\mathcal{Z}1}\right],\end{aligned} \tag{7.8}$$

where, on the right-hand side, the second term contains a product of four amplitudes, but notably with $|\mathcal{Z}|^2$ that also appears in the first term of the right-hand side. In Eq. (7.8),

$$\tau_{11\mathcal{Z}} = (\gamma_1' + \gamma_1'' - \gamma_{\mathcal{Z}}^*)^{-1}, \tag{7.9}$$

is the three-wave interaction time found from the EDQNM closure, and $\overleftrightarrow{C}^{(\boldsymbol{p},\boldsymbol{q})}_{lmn} = C^{(\boldsymbol{p},\boldsymbol{q})}_{lmn} + C^{(\boldsymbol{p},\boldsymbol{p}-\boldsymbol{q})}_{lnm}$ is the symmetrized coupling coefficient. In quasi-stationary turbulence, $\partial_t \sim 0$, and thus the linear and nonlinear terms must balance. First, for simplicity, we consider a latitudinal flow at $(k_x, 0)$ that is driven by two unstable modes at (k_x', k_z') and $(k_x - k_x', -k_z')$; then, using (7.8), $|\beta_1'|^2 = \gamma_{\mathcal{Z}}\left(\mathrm{Re}\,[-\tau_{11\mathcal{Z}}\overleftrightarrow{C}^{(\boldsymbol{k},\boldsymbol{k}')}_{\mathcal{Z}11}\overleftrightarrow{C}^{(\boldsymbol{k}'',\boldsymbol{k})}_{1\mathcal{Z}1}]\right)^{-1}$. A more general expression for $|\beta_1'|^2$ is found by using a standard Markovian assumption [88]: $|\beta_1'|^2$ is more weakly dependent on wavenumbers than the other factors in Eq. (7.8) arising from the coupling coefficients and $\tau_{11\mathcal{Z}}$. Such a consideration provides an expression for nonlinearly saturated squared-mode-amplitude

$$|\beta'|^2 = \gamma_{\mathcal{Z}} \times \left(\frac{\gamma}{k^2}\right)_{\text{Closure}}, \tag{7.10}$$

with

$$\left(\frac{\gamma}{k^2}\right)_{\text{Closure}} = \frac{1}{|\sum_{\boldsymbol{k}'}\tau_{11\mathcal{Z}}\,\mathrm{Re}\,[-\overleftrightarrow{C}^{(\boldsymbol{k},\boldsymbol{k}')}_{\mathcal{Z}11}\overleftrightarrow{C}^{(\boldsymbol{k}'',\boldsymbol{k})}_{1\mathcal{Z}1}]|}, \tag{7.11}$$

where we note that the coupling coefficients scale linearly with wavenumbers, and $\tau_{11\mathcal{Z}}$ is the inverse of the sum of three growth rates of eigenmodes in a triad.

The growth rates in $\tau_{11\mathcal{Z}}$ should, in principle, also have amplitude-dependent eddy-damping rates as they become non-negligible, for example, in homogeneous isotropic fluid turbulence; however, when waves or instabilities exist, and when the turbulent transport spectrum is dominated by low wavenumbers, as in this study, $\tau_{11\mathcal{Z}}$ is approximated by using the linear growth rates [32, 88]. Using such, one identifies that the triplet interaction time $\tau_{11\mathcal{Z}}$ is maximal when the triad involves a latitudinal flow ($\mathcal{Z}$) and two GSF-unstable modes (j=1). Shorter triplet interaction times $\tau_{12\mathcal{Z}}$ are expected for triads with, for example, the latitudinal flow, an unstable mode, and a strongly damped IGW (j=2), as such an interaction lowers $\tau_{12\mathcal{Z}}$ via both the frequency and damping rate of the IGW. The largest interaction time τ_{11Z} dominates saturation.

The radial turbulent transport of angular momentum is measured by

$$\langle \tilde{u}_x \tilde{u}_y \rangle \approx \sum_{\boldsymbol{k}'''} \hat{u}'''_{x,1} \hat{u}'''^{*}_{y,1} |\beta'''_1|^2, \tag{7.12}$$

where β'''_1 is the unstable-mode amplitude at $\boldsymbol{k}'''$ over which the summation is applied. Then, using $|\beta'''_1|^2$ from the above paragraph,

$$\langle \tilde{u}_x \tilde{u}_y \rangle_{\text{Closure}} = \left(\frac{\gamma}{k^2} \right)_{\text{Closure}} \times \gamma_{\mathcal{Z}} \sum_{\boldsymbol{k}'''} \hat{u}'''_{x,1} \hat{u}'''^{*}_{y,1}. \tag{7.13}$$

The y-component $\hat{u}'''_{y,1}$ of velocity of the unstable eigenvector can be replaced with, e.g., its temperature perturbation $\hat{\theta}'''_1$ to predict the turbulent heat flux $\langle \tilde{u}_x \tilde{\theta} \rangle$.

In our simulations with radial differential rotation, the latitudinal momentum flux is much lower than the radial flux, and, when time-averaged, it is nearly null.

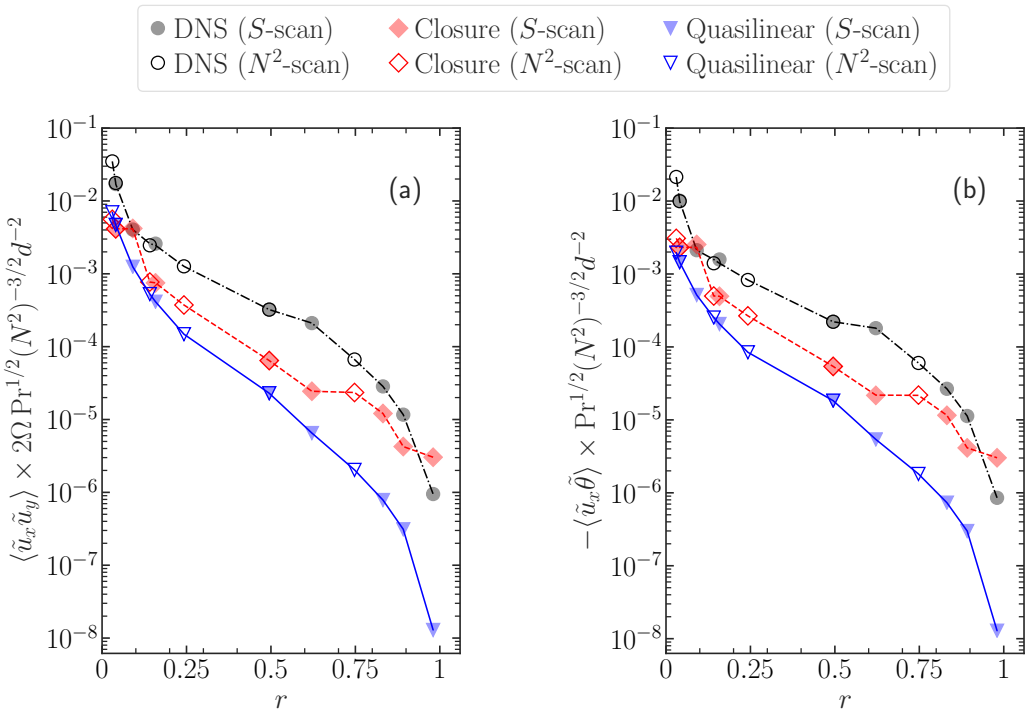

Figure 7.5: Tests of predictions of our closure model (red diamond) and a quasilinear-type, parasitic-saturation model (blue inverted triangle) against direct numerical simulations (DNS, black/gray circle). Variations of momentum transport rates are shown in (a); the filled markers correspond to the cases where the shear parameter S is varied (N^2=10); the unfilled markers correspond to the cases where the squared Brunt-Väisälä frequency N^2 is varied (S=2.1). Both S- and N^2-scan results collapse onto a single master curve, when $\langle \tilde{u}_x \tilde{u}_y \rangle$ is scaled by a factor shown on the y-axis that transforms the governing equations of the GSF instability studied here to depend on only two dimensionless parameters (r, Pr). The GSF instability operates when $r \in [0, 1)$ and Pr<1 (Pr=0.01 is chosen). The shown y-axis is precisely an expression for the chemical transport rate for the thermohaline instability [see Eq. (7.17a)]. Heat transport rates, shown in (b), display nearly identical trends; [see Eq. (7.17b) for the scaling factor]. The closure prediction agrees with full DNS better than the quasilinear prediction over the scanned range of parameters.

Tests of theoretical predictions

A simple quasilinear model of the GSF-instability saturation was recently proposed [38, 230] by assuming that a secondary "parasitic" instability feeds on the primary GSF-unstable mode. Such an assumption, also called "parasitic saturation mechanism" [28,

194, 235–237], is based on a single primary mode at the fastest-growing wavenumber $\mathbf{k}'''$, which predicts the transport rate

$$\langle \widetilde{u}_x \widetilde{u}_y \rangle_{\mathrm{QL}} = \frac{\gamma_1'''^2}{k_z'''^2} \hat{u}_{x,1}''' \hat{u}_{y,1}'''^* f^2(\mathbf{k}'''), \tag{7.14}$$

whose form is made manifestly similar to Eq. (7.13); the factor $f(\mathbf{k}''')$, which is evaluated at $\mathbf{k}'''=(0, k_z''')$, is the normalization factor of eigenmodes. Here, $\gamma_\nu''' = \gamma_1''' + \nu k'''^2$. To find $\langle \widetilde{u}_x \widetilde{\theta} \rangle_{\mathrm{QL}}$, one can replace $\hat{u}_{y,1}'''$ on the right-hand side of Eq. (7.14) with θ_1'''.

Predictions of Eqs. (7.13) and (7.14) are compared against transport rates from direct numerical simulations in Figs. 10.4. Significant improvement in both the momentum and heat transport predictions is observed with the statistical closure model. The orders-of-magnitude variation in transport rates is captured by the closure model.

In Fig. 10.4, for smaller values of r, though the transport rates of the closure and the quasilinear models are similar, we emphasize that this similarity is merely accidental: the physics the two models incorporate is very different. The assumptions of the closure model are supported by detailed numerical evidence (Figs. 10.1 and 10.2), including that of the dominant three-wave coupling between two unstable modes and a latitudinal jet (Fig. 10.3). No jet physics is considered in the quasilinear model. The quasilinear model predicts transport rates based on only one fastest growing wavenumber k_z, with k_x=0, which Fig. 10.1 shows is inadequate. Hence, predictions of the quasilinear model that tend to reproduce the data-validated closure model predictions are at best a fortuitous coincidence, occurring in a very limited parameter regime.

Impact of the new model in astrophysics

Since stellar interiors typically have extreme parameters such as $\mathrm{Pr} \lesssim 10^{-6}$, current and anticipated near-future computational resources are insufficient to permit direct numerical simulations of realistic turbulence in them. In the face of such a challenge, progress can be made by developing analytical theories, informed and tested by numerical simulations at more accessible parameters. Thus, we now employ our analytical theory to extrapolate and make predictions for realistic astrophysical parameters. To achieve this, we derive fully analytic expressions for all elements of the closure model, assuming that the coupling of two GSF-unstable modes with the latitudinal jet remains dominant; see Appendices A and B.

We then compare predictions of the closure model with those of the quasilinear (QL) model, over a wide range of parameters $\mathrm{Pr} \approx 10^{-7}$–1 and $r \approx 10^{-5}$–1 in Fig. 10.5. Noting that $N^2{=}2(S-2)\left[1+r(\mathrm{Pr}^{-1}-1)\right]$, these scans span $N^2 \lesssim 19\times10^6$ (in terms of Ω^2); this ratio is typically around 1 million for the Sun [238]. In Fig. 10.5, with $S{=}3$ (in terms of Ω), the Richardson number is as large as $\approx 2\times10^6$. More extreme parameters can be easily and quickly scanned with the analytic formula we have derived.

Now we predict transport efficiency of the GSF instability in stars. The Reynolds stress is of order $\langle\tilde{u}_x\tilde{u}_y\rangle H^{-1}$, where $H{\equiv}U_0(\partial_x U_0)^{-1}$ is the scale height of the mean flow $U_0{=}-\mathcal{S}x$. The time scale for modifying the flow is $\tau_{\mathrm{turb}} \sim U_0 H/\langle\tilde{u}_x\tilde{u}_y\rangle \sim Sx^2\Omega^{-1}d^{-2}/\langle\tilde{u}_x\tilde{u}_y\rangle_{\mathrm{dimensionless}}$ [see also 38].

Though $\mathrm{Pr} \sim 10^{-6}$, the typical values of r in the solar tachocline and red giant stars are $r \sim 10^{-3}$–1 (varying with radius). Then, using Fig. 10.5 where $\langle\tilde{u}_x\tilde{u}_y\rangle_{\mathrm{dimensionless}}$ is on average 0.5, we predict $\tau_{\mathrm{turb}}\Omega \sim 2S(x/d)^2$. This turbulent transport time scale is sufficiently short to be astrophysically important, depending on the relative length

scale x/d of the mean flow and shear strength S. For example, it can be as short as $\mathcal{O}(10)$ Myr using values of S and x/d for the solar tachocline.

The turbulent transport rate depends sensitively also on the shear parameter S (and latitude and orientation of the shear, i.e., radial or mixed radial-horizontal shear), and orders of magnitude faster turbulent transport is possible. We highlight that, because the turbulent time scale for the GSF instability can be shorter than $\mathcal{O}(10)$ Myr, incorporation of our transport model for the GSF turbulence in stellar evolution codes is warranted (particularly if extended to non-equatorial and 3-D GSF instabilities). Using such, the long-term impact on the evolution of the rotation profile may be assessed, informing us of the effects of the GSF instability in rapidly rotating young stars. In this regard, the transport model built here for the 2.5D equatorial GSF instability (and the thermohaline instability) is significant, as a reliable and reduced numerical treatment of the GSF instability-driven turbulence is now available.

Relation to the thermohaline instability

We emphasize that the equations describing 2.5-D thermohaline and GSF instabilites at the equator are identical, when the compositional diffusivity is equal to the kinematic viscosity—a case often realized in stars. We first write Eqs. (7)–(9) of [236], where they measure distance in units of the characteristic length scales d of the fingers, time in units of the characteristic diffusion time scale $\tau{=}d^2/\kappa$, and scaled temperature T

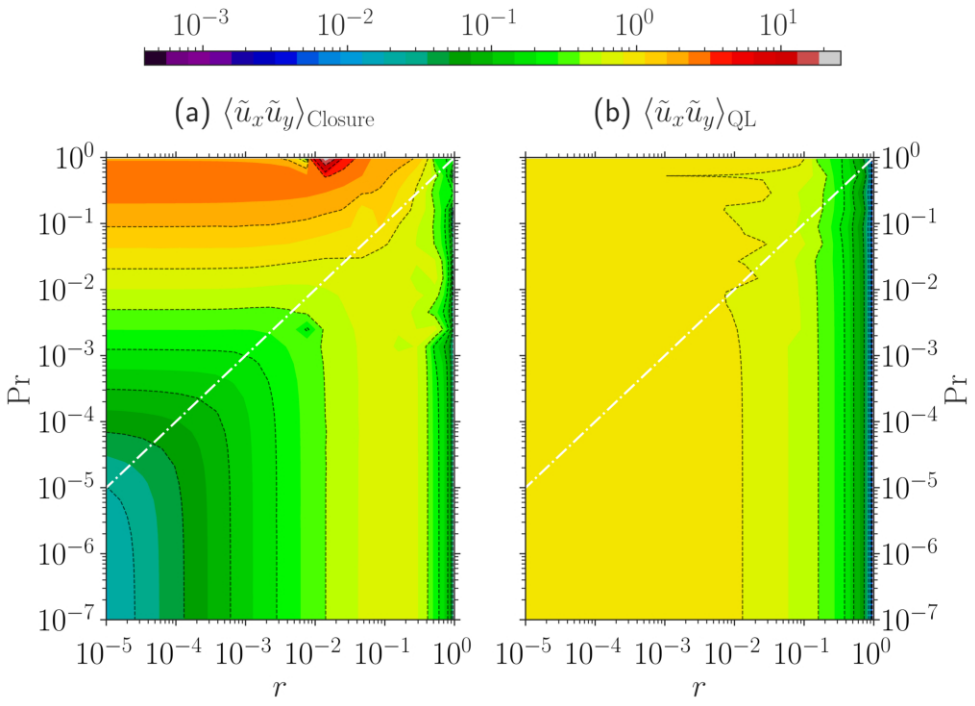

Figure 7.6: Predictions of (a) closure model and (b) quasilinear (QL) model for turbulent momentum transport. The QL model, largely independent of Pr, fails to reproduce the behavior of the closure model. For Pr closer to 1, the closure model predicts that the transport rate increases with decreasing r—until an asymptotically large transport is attained. For $\text{Pr} \ll r$, the transport first increases and then decreases with r, in contrast to the QL prediction. The white dashed-dotted line, with a unit slope, separates distinct regimes of $\text{Pr} < r$ and $\text{Pr} > r$ found in (a).

in units of $N^2 d$ [we label their x-coordinate with our z-coordinate and vice-versa]

$$\text{Pr}^{-1} D u_x^{\text{B}} = -\partial_x p^{\text{B}} + (T^{\text{B}} - \mu^{\text{B}}) + \nabla^2 u_x^{\text{B}}, \tag{7.15a}$$

$$\text{Pr}^{-1} D u_z^{\text{B}} = -\partial_z p^{\text{B}} + \nabla^2 u_z^{\text{B}}, \tag{7.15b}$$

$$D T^{\text{B}} = -u_x^{\text{B}} + \nabla^2 T^{\text{B}}, \tag{7.15c}$$

$$D \mu^{\text{B}} = -\frac{u_x^{\text{B}}}{R_0} + \text{Pr}\, \nabla^2 \mu^{\text{B}}, \tag{7.15d}$$

where the state vector $[u_x^{\text{B}}, u_z^{\text{B}}, T^{\text{B}}, \mu^{\text{B}}, p^{\text{B}}]$ represents Brown-normalized x- and z-velocities, scaled temperature, chemical concentration, and fluid pressure, respectively.

The so-called density ratio $R_0 = -N^2/\kappa_{\rm ep}^2$ may be recast as $R_0 = 1 + r(\mathrm{Pr}^{-1} - 1)$. The solutions of Eqs. (7.15a)–(7.15d) critically depend only on two parameters: Pr and r. Equations (7.15a)–(7.15d) for the thermohaline instability with the state vector $[u_x^{\rm B}, u_z^{\rm B}, T^{\rm B}, \mu^{\rm B}]$ are identical to Eqs. (9.1a) and (7.1b) for the GSF instability with the state vector $[u_x, u_z, \theta, u_y]$, when we note

$$u_x^{\rm B} = \frac{u_x}{d/\tau}, \tag{7.16a}$$

$$u_z^{\rm B} = \frac{u_z}{d/\tau}, \tag{7.16b}$$

$$T^{\rm B} = \frac{\theta}{N^2 d}, \tag{7.16c}$$

$$\mu^{\rm B} = -\frac{2\tau\Omega}{\mathrm{Pr}}\frac{u_y}{d/\tau}. \tag{7.16d}$$

Hence, the transport rates with two kinds of non-dimensionalizations—one using τ and d as the characteristic time scale and length scale, and another using Ω and d as the relevant scales—are related in the manner

$$-\langle \widetilde{u}_x^{\rm B}\widetilde{\mu}^{\rm B}\rangle = \langle \widetilde{u}_x\widetilde{u}_y\rangle \times 2\Omega \mathrm{Pr}^{1/2}(N^2)^{-3/2}d^{-2}, \tag{7.17a}$$

$$\langle \widetilde{u}_x^{\rm B}\widetilde{T}^{\rm B}\rangle = \langle \widetilde{u}_x\widetilde{\theta}\rangle \times \mathrm{Pr}^{1/2}(N^2)^{-3/2}d^{-2}, \tag{7.17b}$$

where the variables with the superscripted 'B' are functions of two essential parameters — r and Pr only, whereas the variables without the superscript are functions defined by the parameters Pr, S, and N^2.

The expressions given in Eqs. (7.17a) and (7.17b) are plotted in Fig. 10.4. Thus our Fig. 10.4 also represents a comparison of chemical and heat transport between direct numerical simulations and analytical models for the thermohaline instability-driven turbulence.

The reduction of the governing equations of the GSF instability to two parameters (r, Pr) is realized only in 2.5-D equatorial case, which is where the analogy of the GSF instability with the thermohaline instability becomes exact.

7.5 Discussion and conclusions

Turbulent transport in stellar interiors is a phenomenon too complex to represent directly in stellar evolution models. It is often parametrized using low-order models, such as mixing-length theories, or models that predict transport rates based on the fastest-growing unstable mode [e.g., 38, 236, 239]. The reliability of such models can be compromised by several factors: first, the instability dispersion relation is often anisotropic, a property that affects the nonlinear energy transfer, thereby driving low-frequency fluctuations (Fig. 10.2). Second, nonlinear mode coupling can strongly excite more weakly growing unstable modes over a wide range of wavenumbers, presenting difficulties to single-mode theory-based predictions. To circumvent such challenges, we build a nonlinear mode-coupling theory, informed by detailed analyses of direct numerical simulations, to arrive at a reliable and analytic transport model, that is free of tunable parameters. We achieve this here for axisymmetric low-Pr turbulence driven by centrifugally unstable differential rotation (the GSF instability) at the equator in a stellar radiative zone.

Although 2.5-D turbulence driven by the GSF instability can differ from fully 3-D cases [38], strong secondary flows or jets have been found in 3-D global systems, also. For example, recent simulations of fully 3-D spherical-shell non-rotating fingering convection have exhibited strong, large-scale jets [240]. Such coherent jets are ubiquitious in various settings such as in geo- and astrophysical observations, numerical simulations of 3-D shear-flow instability-driven turbulence [233], and in laboratory

fusion plasmas [30]. The examples show the large-scale flows can emerge even in global geometry. Hence, the success of our theory offers a future possibility to extend the statistical closure framework, presented here, to the more realistic 3-D simulations of the GSF instability, ideally in a sphere, at a general latitude and for a range of Pr [230, 231, 241]. It is also possible that our closure-model framework can be adapted to magnetized turbulence driven by unstable differential rotation.

Since our formulae are fully analytic, they are quick to implement in stellar evolution codes such as `MESA` [242, 243] to reliably predict axisymmetric GSF instability-driven turbulent transport rates that vary with Pr and r at different spatial grid points in an evolving star. It is straightforward to compute the values of r and Pr at a given spatial grid point in a modeled star, and simply look up transport rates using our Fig. 10.5(a) to prescribe the rates of transport of angular momentum and heat; to access the look up table of transport, see Data Availability. Since we have also provided formulae and frameworks for the turbulent transport of the axisymmetric GSF-analogous thermohaline instability, there now exists a reliable chemical transport model, which employs DNS-confirmed key elements of nonlinear saturation of the instability in stars.

Data Availability

The GitHub repository,
https://github.com/BindeshTripathi/GSF_transport, hosts the data presented in Fig. 10.5(a), and a python script where the closure model is implemented. Other data used in this article will be shared on reasonable request to the corresponding authors.

Appendix A: Nonlinear mode-coupling coefficients of the GSF instability

The j^{th} eigenvector of the linear operator $\mathbf{L}$ of the GSF instability satisfies

$$\hat{u}_{z,j} = -\frac{k_x}{k_z}\hat{u}_{x,j}; \qquad \hat{\theta}_j = -\frac{N^2}{\gamma_{\kappa,j}}\hat{u}_{x,j}; \qquad \hat{u}_{y,j} = -\frac{2\Omega - S}{\gamma_{\nu,j}}\hat{u}_{x,j}, \tag{A1}$$

using which the matrix $\mathbf{E}$ of eigenvectors can be created and inverted as mentioned in the penultimate paragraph of Sec. 7.2. To expedite analytic calculations, one may solve for the adjoint solutions $\mathbf{Y}_j$ of $\mathbf{L}$, which are the eigenvectors of $\mathbf{L}^\dagger$. Such adjoint solutions $\mathbf{Y}_j$ form a biorthogonal basis with the eigenvectors $\mathbf{X}_j$ of $\mathbf{L}$ [111, 143, 233, 244]. That is, $\langle \mathbf{Y}_m, \mathbf{X}_j \rangle = \mathbf{Y}_m^{\mathrm{T}*}\mathbf{X}_j \propto \delta_{j,m}$, where T$*$ is the transpose-conjugation operation; see Appendix A of [144] for a general mathematical proof. It is known that both $\mathbf{L}$ and $\mathbf{L}^\dagger$ have the same eigenvalues. The expedient adjoint technique is equivalent to inverting the matrix $\mathbf{E}$ of size 4×4, and they deliver completely identical results, which we have verified. The j^{th} adjoint solution satisfies

$$\hat{u}_{z,j} = 0; \qquad \hat{\theta}_j = \frac{k_z^2}{k^2\gamma_{\kappa,j}}\hat{u}_{x,j}; \qquad \hat{u}_{y,j} = \frac{2\Omega k_z^2}{k^2\gamma_{\nu,j}}\hat{u}_{x,j}. \tag{A2}$$

Using such, we write the nonlinear mode-coupling coefficient between the two eigenmodes m at wavenumber $\mathbf{k}'$ and n at $\mathbf{k}''$, impacting the eigenmode j at $\mathbf{k}$, as

$$C_{jmn}^{(\mathbf{k},\mathbf{k}')} = \frac{\langle \mathbf{Y}_j(\mathbf{k}), \mathbf{N}(\mathbf{X}'_m, \mathbf{X}''_n) \rangle}{\langle \mathbf{Y}_j(\mathbf{k}), \mathbf{X}_j(\mathbf{k}) \rangle}, \tag{A3}$$

where $\mathbf{N}(\mathbf{X}'_m, \mathbf{X}''_n)$ is the nonlinearity vector; for example, its θ-component is $-\mathbf{u}'_m \cdot \nabla\theta''_n$.

Following this procedure, we have distilled the analytic coupling coefficients for

the GSF instability, and provide below their final expressions:

$$\overleftrightarrow{C}^{(\mathbf{k},\mathbf{k}')}_{\mathcal{Z}11} = \frac{i\left(k_x'^2 - k_x''^2\right)}{k_z' f' f''}, \tag{A4}$$

where f is the eigenmode normalization factor. With inverse dimensions of $\hat{u}_{x,j}$, a suitable mode normalization can be $f'{=}k'/\gamma'$ or $f'{=}k'^2 d/(\gamma'\gamma_\nu'\tau)$ or their variants, with $\tau{=}d^2/\kappa$ as the characteristic diffusion time scale. Equation (A4) is simple as it represents the coupling between two unstable modes that drive the latitudinal flow $\mathcal{Z}$. The second coupling coefficient required in the closure model is

$$\overleftrightarrow{C}^{(\mathbf{k}'',\mathbf{k})}_{1\mathcal{Z}1} = ik_z' \frac{\left[\frac{k''^2}{N^2 k_z''^2}\left(1 - \frac{2k_x k_x''}{k''^2}\right) + \frac{1}{R_0\gamma_\nu'\gamma_\nu''} - \frac{1}{\gamma_\kappa'\gamma_\kappa''}\right] f''}{\left[\frac{k''^2}{N^2 k_z''^2} + \frac{1}{R_0\gamma_\nu''^2} - \frac{1}{\gamma_\kappa''^2}\right] f'}. \tag{A5}$$

We note that the coupling coefficients depend only on wavenumbers and the input parameters such as N^2, Pr, $R_0{=}-N^2/\kappa_{\rm ep}^2$ and the growth rates; the growth rates in turn depend only on wavenumbers and the input parameters [Eq. (7.2)]. Asymptotic approximation to the growth rate in the limit of, e.g., small Pr is possible [236].

Appendix B: Nonlinear mode-coupling coefficients of the Thermohaline instability

Here we provide analytic expressions needed for the closure model applicable to the thermohaline instability.

We find the $j^{\rm th}$ eigenvector of the linear operator $\mathbf{L}$ found from Eqs. (7.15a)–(7.15d) for the thermohaline instability satisfies

$$\hat{u}^{\rm B}_{z,j} = -\frac{k_x}{k_z}\hat{u}^{\rm B}_{x,j}; \qquad \hat{T}^{\rm B}_j = -\frac{1}{\gamma_{\kappa,j}}\hat{u}^{\rm B}_{x,j}; \qquad \hat{\mu}^{\rm B}_j = -\frac{1}{R_0\gamma_{\nu,j}}\hat{u}^{\rm B}_{x,j}. \tag{A6}$$

The $j^{\rm th}$ adjoint solution for the thermohaline instability is

$$\hat{u}^{\rm B}_{z,j} = 0; \qquad \hat{T}^{\rm B}_j = \frac{k_z^2 {\rm Pr}}{k^2 \gamma_{\kappa,j}} \hat{u}^{\rm B}_{x,j}; \qquad \hat{\mu}^{\rm B}_j = -\frac{k_z^2 {\rm Pr}}{k^2 \gamma_{\nu,j}} \hat{u}^{\rm B}_{x,j}. \tag{A7}$$

The coupling coefficients for the thermohaline instability are identically the same as those for the GSF instability; Equations (A4) and (A5) require only a minute modification: N^2 appearing twice in Eq. (A5) should be replaced with Pr. We, conclude that our closure model and predictions are directly applicable to the thermohaline instability, as well. This is significant because the turbulent transport efficiencies of these two instabilites in stars are not known, but are generally thought to be important. With the closure model at hand, we can now make predictions reliably for both instabilities.

Appendix C: Details of Closure Model Calculations

To make the statistical closure model more accessible to a wide range of readers, we provide below detailed, step-by-step derivations.

C1. Amplitude evolution equation

The mode-amplitude β_j evolution equation, given in Eq. (7.4a), for a wavenumber $\mathbf{k} = (k_x, k_z{\neq}0)$, with $j = 1, 2,$ or 3, is

$$\partial_t \beta_j = \gamma_j \beta_j + \sum_{\boldsymbol{k}',m,n} C_{jmn}^{(\boldsymbol{k},\boldsymbol{k}')} \beta'_m \beta''_n + \sum_{\boldsymbol{k}',n} \Bigg\{ \left[C_{j\mathcal{Y}n}^{(\boldsymbol{k},\boldsymbol{k}')} + C_{jn\mathcal{Y}}^{(\boldsymbol{k},\boldsymbol{k}'')} \right] \mathcal{Y}' \beta''_n + \left[C_{j\mathcal{Z}n}^{(\boldsymbol{k},\boldsymbol{k}')} + C_{jn\mathcal{Z}}^{(\boldsymbol{k},\boldsymbol{k}'')} \right] \mathcal{Z}' \beta''_n + \left[C_{j\Theta n}^{(\boldsymbol{k},\boldsymbol{k}')} + C_{jn\Theta}^{(\boldsymbol{k},\boldsymbol{k}'')} \right] \Theta' \beta''_n \Bigg\}, \tag{A8}$$

whereas, at $\mathbf{k} = (k_x, k_z{=}0)$, one finds that the fluctuation amplitude evolves according to Eq. (7.4b), which is expanded below

$$\partial_t \mathcal{Y} = -\gamma_{\mathcal{Y}} \mathcal{Y} + \sum_{\boldsymbol{k}',m,n:k_z=0} C_{\mathcal{Y}mn}^{(\boldsymbol{k},\boldsymbol{k}')} \beta'_m \beta''_n, \tag{A9a}$$

$$\partial_t \mathcal{Z} = -\gamma_{\mathcal{Z}} \mathcal{Z} + \sum_{\boldsymbol{k}',m,n:k_z=0} C_{\mathcal{Z}mn}^{(\boldsymbol{k},\boldsymbol{k}')} \beta'_m \beta''_n, \tag{A9b}$$

$$\partial_t \Theta = -\gamma_{\Theta} \Theta + \sum_{\boldsymbol{k}',m,n:k_z=0} C_{\Theta mn}^{(\boldsymbol{k},\boldsymbol{k}')} \beta'_m \beta''_n, \tag{A9c}$$

where $\gamma_{\mathcal{Y}} = \gamma_{\mathcal{Z}} = \nu k^2$ and $\gamma_{\Theta} = \kappa k^2$ are the damping rates.

C2. Eigenmode-energy evolution

To derive an evolution equation for energy in the j^{th} eigenmode at $\mathbf{k} = (k_x, k_z{\neq}0)$, we multiply Eq. (A8) with β_j^* and add a complex conjugate of the resulting equation to

arrive at

$$\partial_t|\beta_j|^2 = 2\mathrm{Re}\,\gamma_j|\beta_j|^2 + \sum_{\boldsymbol{k}',m,n} 2\mathrm{Re}\,\left[C_{jmn}^{(\boldsymbol{k},\boldsymbol{k}')}\langle\beta'_m\beta''_n\beta_j^*\rangle\right] + \sum_{\boldsymbol{k}'} 2\mathrm{Re}\left\{\left[C_{j\mathcal{Y}j}^{(\boldsymbol{k},\boldsymbol{k}')}\langle\mathcal{Y}'\beta''_j\beta_j^*\rangle + C_{j\mathcal{Z}j}^{(\boldsymbol{k},\boldsymbol{k}')}\langle\mathcal{Z}'\beta''_j\beta_j^*\rangle + C_{j\Theta j}^{(\boldsymbol{k},\boldsymbol{k}')}\langle\Theta'\beta''_j\beta_j^*\rangle\right]\Big|_{k'_z=0} + \left[C_{jj\mathcal{Y}}^{(\boldsymbol{k},\boldsymbol{k}')}\langle\beta'_j\mathcal{Y}''\beta_j^*\rangle + C_{jj\mathcal{Z}}^{(\boldsymbol{k},\boldsymbol{k}')}\langle\beta'_j\mathcal{Z}''\beta_j^*\rangle + C_{jj\Theta}^{(\boldsymbol{k},\boldsymbol{k}')}\langle\beta'_j\Theta''\beta_j^*\rangle\right]\Big|_{k'_z=k_z}\right\}. \tag{A10}$$

Similar equations can be derived for fluctuation energy at GSF-stable wavenumbers $\mathbf{k} = (k_x, k_z{=}0)$ using Eqs. (A9a)–(A9c):

$$\partial_t|\mathcal{Y}|^2 = -2\mathrm{Re}\,\gamma_{\mathcal{Y}}|\mathcal{Y}|^2 + \sum_{\boldsymbol{k}',m} 2\mathrm{Re}\,\left[C_{\mathcal{Y}mm}^{(\boldsymbol{k},\boldsymbol{k}')}\langle\beta'_m\beta''_m\mathcal{Y}^*\rangle\right]\Big|_{k_z=0}, \tag{A11a}$$

$$\partial_t|\mathcal{Z}|^2 = -2\mathrm{Re}\,\gamma_{\mathcal{Z}}|\mathcal{Z}|^2 + \sum_{\boldsymbol{k}',m} 2\mathrm{Re}\,\left[C_{\mathcal{Z}mm}^{(\boldsymbol{k},\boldsymbol{k}')}\langle\beta'_m\beta''_m\mathcal{Z}^*\rangle\right]\Big|_{k_z=0}, \tag{A11b}$$

$$\partial_t|\Theta|^2 = -2\mathrm{Re}\,\gamma_{\Theta}|\Theta|^2 + \sum_{\boldsymbol{k}',m} 2\mathrm{Re}\,\left[C_{\Theta mm}^{(\boldsymbol{k},\boldsymbol{k}')}\langle\beta'_m\beta''_m\Theta^*\rangle\right]\Big|_{k_z=0}. \tag{A11c}$$

Since numerical simulations inform us that the triplets with a latitudinal flow at $(k_x, 0)$, i.e., $\mathcal{Z}$, dominates the nonlinear energy transfer, we may drop nonlinear terms on the right-hand side of Eq. (A10) that do not involve $\mathcal{Z}$. In the resulting equation, because $\mathcal{Y}$ and Θ do not appear, Eqs. (A11a) and (A11c) can also be removed, which allows us to write the following set of equations:

$$\partial_t|\beta_j|^2 = 2\mathrm{Re}\,\gamma_j|\beta_j|^2 + \sum_{\boldsymbol{k}'} 2\mathrm{Re}\left\{\left[C_{j\mathcal{Z}j}^{(\boldsymbol{k},\boldsymbol{k}')}\langle\mathcal{Z}'\beta''_j\beta_j^*\rangle\right]\Big|_{k'_z=0} + \left[C_{jj\mathcal{Z}}^{(\boldsymbol{k},\boldsymbol{k}')}\langle\beta'_j\mathcal{Z}''\beta_j^*\rangle\right]\Big|_{k'_z=k_z}\right\}, \tag{A12a}$$

$$\partial_t|\mathcal{Z}|^2 = -2\mathrm{Re}\,\gamma_{\mathcal{Z}}|\mathcal{Z}|^2 + \sum_{\boldsymbol{k}',m} 2\mathrm{Re}\,\left[C_{\mathcal{Z}mm}^{(\boldsymbol{k},\boldsymbol{k}')}\langle\beta'_m\beta''_m\mathcal{Z}^*\rangle\right]\Big|_{k_z=0}. \tag{A12b}$$

C3. Triplet correlation evolution

To obtain evolution equations for the terms on the right-hand side of Eqs. (A12a) and (A12b), we multiply Eq. (7.4a) with two amplitudes. For example, to determine the evolution of $\langle \mathcal{Z}'\beta_j''\beta_j^*\rangle$, first, we multiply Eq. (A8) for β_j with $\mathcal{Z}'\beta_j''$; second, we multiply another equation, similar to Eq. (A8), but for β_j'' with $\mathcal{Z}'\beta_j^*$; and, finally, we multiply Eq. (A9b), for $\mathcal{Z}'$, with $\beta_j''\beta_j^*$, and add them all together. Using this, we provide below an example evolution equation for triplet correlations:

$$
\begin{aligned}
\left[\partial_t - \left(-\gamma_{\mathcal{Z}}' + \gamma_j'' + \gamma_j^*\right)\right]\langle \mathcal{Z}'\beta_j''\beta_j^*\rangle|_{k_z'=0} = \Bigg\{ & \sum_{\boldsymbol{k}''',m} \left[C_{\mathcal{Z}mm}^{(\boldsymbol{k}',\boldsymbol{k}''')} \langle \beta_m'''\beta_m(\boldsymbol{k}'-\boldsymbol{k}''')\beta_j''\beta_j^*\rangle \right] \\
& + \sum_{k_x'''} \Big[C_{j\mathcal{Y}j}^{(\boldsymbol{k}-\boldsymbol{k}',\boldsymbol{k}''')} \langle \mathcal{Y}'''\beta_j(\boldsymbol{k}-\boldsymbol{k}'-\boldsymbol{k}''')\mathcal{Z}'\beta_j^*\rangle|_{k_z'''=0} \\
& \quad + C_{j\mathcal{Z}j}^{(\boldsymbol{k}-\boldsymbol{k}',\boldsymbol{k}''')} \langle \mathcal{Z}'''\beta_j(\boldsymbol{k}-\boldsymbol{k}'-\boldsymbol{k}''')\mathcal{Z}'\beta_j^*\rangle|_{k_z'''=0} \\
& \quad + C_{j\Theta j}^{(\boldsymbol{k}-\boldsymbol{k}',\boldsymbol{k}''')} \langle \Theta'''\beta_j(\boldsymbol{k}-\boldsymbol{k}'-\boldsymbol{k}''')\mathcal{Z}'\beta_j^*\rangle|_{k_z'''=0} \\
& \quad + C_{jj\mathcal{Y}}^{(\boldsymbol{k}-\boldsymbol{k}',\boldsymbol{k}''')} \langle \beta_j'''\mathcal{Y}(\boldsymbol{k}-\boldsymbol{k}'-\boldsymbol{k}''')\mathcal{Z}'\beta_j^*\rangle|_{k_z'''=k_z} \\
& \quad + C_{jj\mathcal{Z}}^{(\boldsymbol{k}-\boldsymbol{k}',\boldsymbol{k}''')} \langle \beta_j'''\mathcal{Z}(\boldsymbol{k}-\boldsymbol{k}'-\boldsymbol{k}''')\mathcal{Z}'\beta_j^*\rangle|_{k_z'''=k_z} \\
& \quad + C_{jj\Theta}^{(\boldsymbol{k}-\boldsymbol{k}',\boldsymbol{k}''')} \langle \beta_j'''\Theta(\boldsymbol{k}-\boldsymbol{k}'-\boldsymbol{k}''')\mathcal{Z}'\beta_j^*\rangle|_{k_z'''=k_z} \Big] \\
& + \sum_{k_x'''} \Big[C_{j\mathcal{Y}j}^{(\boldsymbol{k},\boldsymbol{k}''')*} \langle \mathcal{Y}'''^*\beta_j^*(\boldsymbol{k}-\boldsymbol{k}''')\mathcal{Z}'\beta_j''\rangle|_{k_z'''=0} \\
& \quad + C_{j\mathcal{Z}j}^{(\boldsymbol{k},\boldsymbol{k}''')*} \langle \mathcal{Z}'''^*\beta_j^*(\boldsymbol{k}-\boldsymbol{k}''')\mathcal{Z}'\beta_j''\rangle|_{k_z'''=0} \\
& \quad + C_{j\Theta j}^{(\boldsymbol{k},\boldsymbol{k}''')*} \langle \Theta'''^*\beta_j^*(\boldsymbol{k}-\boldsymbol{k}''')\mathcal{Z}'\beta_j''\rangle|_{k_z'''=0} \\
& \quad + C_{jj\mathcal{Y}}^{(\boldsymbol{k},\boldsymbol{k}''')*} \langle \beta_j'''^*\mathcal{Y}^*(\boldsymbol{k}-\boldsymbol{k}''')\mathcal{Z}'\beta_j''\rangle|_{k_z'''=k_z} \\
& \quad + C_{jj\mathcal{Z}}^{(\boldsymbol{k},\boldsymbol{k}''')*} \langle \beta_j'''^*\mathcal{Z}^*(\boldsymbol{k}-\boldsymbol{k}''')\mathcal{Z}'\beta_j''\rangle|_{k_z'''=k_z} \\
& \quad + C_{jj\Theta}^{(\boldsymbol{k},\boldsymbol{k}''')*} \langle \beta_j'''^*\Theta^*(\boldsymbol{k}-\boldsymbol{k}''')\mathcal{Z}'\beta_j''\rangle|_{k_z'''=k_z} \Big] \Bigg\}\Bigg|_{k_z'=0} .
\end{aligned}
\tag{A13}
$$

Since the numerical simulations show dominant coupling between the latitudinal flow $\mathcal{Z}$ and two unstable modes in a bath of turbulent interactions, the interactions involving unstable modes only can be excluded. This immediately implies that the first term on the right-hand side of Eq. (A13) can be dropped in the face of remaining dominant terms. Among the remaining terms, the fourth-order correlations that have different components of velocity, e.g., the terms where $\mathcal{Y}$ and $\mathcal{Z}$ appear together on the right-hand side of Eq. (A13), do not form terms that appear in the definition of energy. Guided by numerical simulations where nonlinear coupling to $\mathcal{Y}$ and Θ are unimportant, only the energy(-like) terms with $\mathcal{Z}$ will be kept henceforth. The resulting equation then reads

$$\begin{aligned}
&\left[\partial_t - \left(-\gamma'_{\mathcal{Z}} + \gamma''_j + \gamma^*_j\right)\right]\langle \mathcal{Z}'\beta''_j\beta^*_j\rangle|_{k'_z=0} \\
&\qquad = \Bigg\{ \sum_{k'''_x} \Big[C_{j\mathcal{Z}j}^{(\boldsymbol{k}-\boldsymbol{k}',\boldsymbol{k}''')}\langle \mathcal{Z}'''\beta_j(\boldsymbol{k}-\boldsymbol{k}'-\boldsymbol{k}''')\mathcal{Z}'\beta^*_j\rangle|_{k'''_z=0} \\
&\qquad\quad + C_{jj\mathcal{Z}}^{(\boldsymbol{k}-\boldsymbol{k}',\boldsymbol{k}''')}\langle \beta'''_j\mathcal{Z}(\boldsymbol{k}-\boldsymbol{k}'-\boldsymbol{k}''')\mathcal{Z}'\beta^*_j\rangle|_{k'''_z=k_z} \\
&\qquad\quad + C_{j\mathcal{Z}j}^{(\boldsymbol{k},\boldsymbol{k}''')*}\langle \mathcal{Z}'''^*\beta^*_j(\boldsymbol{k}-\boldsymbol{k}''')\mathcal{Z}'\beta''_j\rangle|_{k'''_z=0} \\
&\qquad\quad + C_{jj\mathcal{Z}}^{(\boldsymbol{k},\boldsymbol{k}''')*}\langle \beta'''^*_j\mathcal{Z}^*(\boldsymbol{k}-\boldsymbol{k}''')\mathcal{Z}'\beta''_j\rangle|_{k'''_z=k_z} \Big] \Bigg\}\Bigg|_{k'_z=0}.
\end{aligned} \tag{A14}$$

The same procedure is then repeated to find evolution equations for the other two triplet correlations that appear in Eqs. (A12a) and (A12b).

C4: Quadruplet correlations and Statistical closure approximation

Equation (A14) can be solved using the technique of Green's function inversion and Markovianization, a standard step in EDQNM closure [although, here, we do not

modify the growth rate γ with the amplitude-dependent nonlinear frequency, an approximation justifiable for the low-wavenumber regime; for more details, see Terry *et al.* 2018 [32]]. Such a solution yields

$$\begin{aligned}
&\langle \mathcal{Z}' \beta_j'' \beta_j^* \rangle|_{k_z'=0} \\
&= -\Bigg\{ \left(-\gamma_{\mathcal{Z}}' + \gamma_j'' + \gamma_j^*\right)^{-1} |\mathcal{Z}'|^2 \\
&\left[\left(C_{j\mathcal{Z}j}^{(\boldsymbol{k}'',-\boldsymbol{k}')} + C_{jj\mathcal{Z}}^{(\boldsymbol{k}'',\boldsymbol{k})} \right) |\beta_j|^2 + \left(C_{j\mathcal{Z}j}^{(\boldsymbol{k},\boldsymbol{k}')*} + C_{jj\mathcal{Z}}^{(\boldsymbol{k},\boldsymbol{k}'')*} \right) |\beta_j''|^2 \right] \Bigg\} \Bigg|_{k_z'=0}.
\end{aligned} \tag{A15}$$

Similarly, the other two triplet correlations that appear in Eqs. (A12a) and (A12b) can also be solved to obtain

$$\begin{aligned}
&\langle \beta_j' \mathcal{Z}'' \beta_j^* \rangle|_{k_z'=k_z} \\
&= -\Bigg\{ \left(\gamma_j' - \gamma_{\mathcal{Z}}'' + \gamma_j^*\right)^{-1} |\mathcal{Z}''|^2 \\
&\left[\left(C_{j\mathcal{Z}j}^{(\boldsymbol{k}',-\boldsymbol{k}'')} + C_{jj\mathcal{Z}}^{(\boldsymbol{k}',\boldsymbol{k})} \right) |\beta_j|^2 + \left(C_{j\mathcal{Z}j}^{(\boldsymbol{k},\boldsymbol{k}'')*} + C_{jj\mathcal{Z}}^{(\boldsymbol{k},\boldsymbol{k}')*} \right) |\beta_j'|^2 \right] \Bigg\} \Bigg|_{k_z'=k_z},
\end{aligned} \tag{A16}$$

and

$$\begin{aligned}
&\langle \beta_j' \beta_j'' \mathcal{Z}^* \rangle|_{k_z=0} \\
&= -\Bigg\{ \left(\gamma_j' + \gamma_j'' - \gamma_{\mathcal{Z}}^*\right)^{-1} |\mathcal{Z}|^2 \\
&\left[\left(C_{j\mathcal{Z}j}^{(\boldsymbol{k}',\boldsymbol{k})} + C_{jj\mathcal{Z}}^{(\boldsymbol{k}',-\boldsymbol{k}'')} \right) |\beta_j''|^2 + \left(C_{j\mathcal{Z}j}^{(\boldsymbol{k}'',\boldsymbol{k})} + C_{jj\mathcal{Z}}^{(\boldsymbol{k}'',-\boldsymbol{k}')} \right) |\beta_j'|^2 \right] \Bigg\} \Bigg|_{k_z=0}.
\end{aligned} \tag{A17}$$

C5: A set of EDQNM-closed energy evolution equations

Solutions of the triplet correlations from Eqs. (A15)–(A17) are now substituted into Eqs. (A12a) and (A12b), which results in the following set of closed equations:

$$\partial_t|\beta_j|^2 = 2\mathrm{Re}\,\gamma_j|\beta_j|^2 - \sum_{\boldsymbol{k}'} 2\mathrm{Re}\left[\frac{C^{(\boldsymbol{k},\boldsymbol{k}')}_{j\mathcal{Z}j}|\mathcal{Z}'|^2}{\left(-\gamma'_{\mathcal{Z}}+\gamma''_j+\gamma^*_j\right)}\left\{\overleftrightarrow{C}^{(\boldsymbol{k}'',-\boldsymbol{k}')}_{j\mathcal{Z}j}|\beta_j|^2+\overleftrightarrow{C}^{(\boldsymbol{k},\boldsymbol{k}')*}_{j\mathcal{Z}j}|\beta''_j|^2\right\}\right]\Bigg|_{k'_z=0}$$
$$-\sum_{\boldsymbol{k}'} 2\mathrm{Re}\left[\frac{C^{(\boldsymbol{k},\boldsymbol{k}')}_{jj\mathcal{Z}}|\mathcal{Z}''|^2}{\left(\gamma'_j-\gamma''_{\mathcal{Z}}+\gamma^*_j\right)}\left\{\overleftrightarrow{C}^{(\boldsymbol{k}',-\boldsymbol{k}'')}_{j\mathcal{Z}j}|\beta_j|^2+\overleftrightarrow{C}^{(\boldsymbol{k},\boldsymbol{k}'')*}_{j\mathcal{Z}j}|\beta'_j|^2\right\}\right]\Bigg|_{k'_z=k_z}, \tag{A18}$$

$$\partial_t|\mathcal{Z}|^2 = -2\mathrm{Re}\,\gamma_{\mathcal{Z}}|\mathcal{Z}|^2$$
$$-|\mathcal{Z}|^2\sum_{\boldsymbol{k}'}\sum_{j=1}^{3} 2\mathrm{Re}\left[\frac{C^{(\boldsymbol{k},\boldsymbol{k}')}_{\mathcal{Z}jj}}{\left(\gamma'_j+\gamma''_j-\gamma^*_{\mathcal{Z}}\right)}\left\{\overleftrightarrow{C}^{(\boldsymbol{k}',\boldsymbol{k})}_{j\mathcal{Z}j}|\beta''_j|^2+\overleftrightarrow{C}^{(\boldsymbol{k}'',\boldsymbol{k})}_{j\mathcal{Z}j}|\beta'_j|^2\right\}\right]\Bigg|_{k_z=0}, \tag{A19}$$

where $\overleftrightarrow{C}^{(\boldsymbol{p},\boldsymbol{q})}_{lmn} = C^{(\boldsymbol{p},\boldsymbol{q})}_{lmn} + C^{(\boldsymbol{p},\boldsymbol{p}-\boldsymbol{q})}_{lnm}$ is the symmetrized coupling coefficient.

Equation (A19) can be simplified by considering that it is the pairs of unstable modes ($j=1$) that excite the latitudinal flow $\mathcal{Z}$:

$$\partial_t|\mathcal{Z}|^2/2 = -\gamma_{\mathcal{Z}}|\mathcal{Z}|^2 + |\mathcal{Z}|^2\sum_{\boldsymbol{k}'}|\beta'_1|^2\,\mathrm{Re}\left[\frac{-\overleftrightarrow{C}^{(\boldsymbol{k},\boldsymbol{k}')}_{\mathcal{Z}11}\overleftrightarrow{C}^{(\boldsymbol{k}'',\boldsymbol{k})}_{1\mathcal{Z}1}}{\gamma'_1+\gamma''_1-\gamma^*_{\mathcal{Z}}}\right], \tag{A20}$$

where the term inside the wavenumber-summation in Eq. (A19) has been symmetrized.

Part III

Jet-Driven Shear-Flow Dynamos

8 **PAPER F**: LARGE-SCALE DYNAMOS DRIVEN BY SHEAR-FLOW-INDUCED JETS

A version of this chapter has been accepted for publication in Nature.

8.1 Abstract

At every scale they occupy, magnetic fields affect various phenomena, including star formation, cosmic ray transport, charged particle acceleration, space weather, transport in planetary atmospheres, and laboratory plasmas. These fields are often generated and sustained by turbulent flows in a process called the dynamo. In 1955, E. N. Parker parameterized the effects of small-scale turbulence to propose a mean-field dynamo theory[1]. The widely used theory reproduces observed large-scale fields but suffers from difficulty in tuning parameters as they are not justified from first principles: Studies of turbulent flows show tangled magnetic fields, which are folded and fragmented into small-scale structures due to shear-flow straining[2,3]. Here, considering a shear flow that is unstable and driven, we develop analytic theory and perform three-dimensional (3D), advanced computer simulations of turbulence with up to $4096 \times 4096 \times 8192$ grid points, showing *ab initio* generation of quasi-periodic, large-scale magnetic fields. The generation occurs via the mean-vorticity effect—an additional mean-field dynamo process postulated[4] in 1990. Crucial to this dynamo is the prior generation of large-scale 3D jets, robustly produced as topologically protected and exact nonlinear solutions of the magnetohydrodynamic equations. The jet-driven dynamo applies to shear-driven laboratory and astrophysical systems. These include binary neutron star mergers[5,6], where the reported dynamo likely operates on microsecond timescales to produce in milliseconds some of the strongest magnetic fields in the Universe[7], providing signals for multi-messenger astronomy[8].

8.2 Article

Flows with gradients are very common in nature; they are often unstable, drive turbulence, and appear with magnetic fields. Examples are found in laboratory experiments, planetary atmospheres and interiors, the meridional circulation and near-surface shear layers of the Sun, stellar interiors, accretion disks and jets, binary neutron star mergers, galaxy clusters, and galactic rotation curves[5,9–18]. Shear flows abet small-scale structures[2,3], especially when the flow is unstable, as the cascade of the flow-energy originating at large scale generates disordered small-scale turbulent fluctuations. A long-standing challenge has been to explain how the *large-scale*, smooth magnetic fields—observed in magnetized planets, the solar cycle, stars, galaxies, and cosmic voids—can arise in the presence of destructive turbulent motions[9,19–23].

Traditional dynamos constrained by magnetic helicity generally fail to generate large-scale fields unless they meet certain strict requirements[1,20,24–27]. Even then, those dynamos have not proved robust because of effects like Alfvénization—a fundamental magnetohydrodynamic (MHD) process via which velocity and magnetic fluctuations becomes equipartitioned and aligned. Because of this alignment, the traditional dynamos are almost completely suppressed[28]. To help explain observations, we investigate here a fundamentally different dynamo mechanism where Alfvénization *enables* the generation of large-scale magnetic fields. This postulated mechanism linked to large-scale vortical structures[4] has remained hypothetical. We find that this hypothetical mechanism develops from the self-organization of large-scale jets. We answer here whether this dynamo can arise naturally in astrophysical environments[5,9–16], by what mechanisms it operates, and how robust it is. Because large-scale self-organized jets are often present in vortex-dominated systems[29], we also address the relationship of the former to the latter, and how they work together to generate large-scale fields.

We analytically and numerically demonstrate a robust non-traditional dynamo effect. The dynamo ensues regardless of whether the domain considered is non-periodic or periodic, and whether an initial large-scale external field is present or absent. We consider a 3D domain with a large-scale flow

$$\mathbf{u}_0 = U_x(z)\hat{\mathbf{e}}_x, \qquad (1)$$

where $\hat{\mathbf{e}}_x$ represents the unit vector along x, and $U_x(z)$ is a z-varying profile. We define the (x,y)-averaged profile as the mean. When the mean shear flow is unstable [Kelvin–Helmholtz (KH) instability[10]], it drives turbulence across a range of scales, including small scales. The small scales saturate over some multiple of the instability growth time $\tau_{\rm grow} \approx 5\, a/U_0$, for $U_x(z) = U_0 \tanh(z/a)$, where a is the half-width of the shear flow with amplitude U_0. The evolution of a large-scale dynamo, however, requires longer times and hence demands substantial computational effort. On the other hand, since turbulence depletes the large-scale flow gradient over time, dynamo eventually becomes inactive. Hence, we maintain the large-scale flow $U_x(z)$ externally[30], mimicking persistent astrophysical shear flows (Methods Sec. V); and we simulate three-dimensional (3D) incompressible MHD turbulence by extending most simulations to $\approx 350\ \tau_{\rm grow}$ and one simulation to $2{,}400\ \tau_{\rm grow}$ (see Methods Sec. I).

Figure 1 displays the temporal evolution of the (x,y)-averaged mean field, turbulent fields, and turbulent flows. The initial horizontal field $\mathbf{b}_0$ in this simulation is weak and uniform throughout the domain [$U_0/|\mathbf{b}_0| = 30$; $\measuredangle(\mathbf{u}_0, \mathbf{b}_0) = 30^{\rm o}$]. The mean field generated by the turbulence, however, is drastically different: the mean-field energy is amplified by 3 orders of magnitude; the mean field is almost entirely (anti-)aligned to the mean flow; and the mean field is reversed across z. The reversed mean field changes its polarity quasi-periodically in Fig. 1**a**, which is reminiscent of the solar magnetic cycles[31]. The generation of the x-directed, z-reversed mean field is unexpected, because here the mean magnetic field cannot be directly generated by the mean flow. This is revealed in the electromotive force (EMF, $\boldsymbol{\mathcal{E}}$)

$$\langle \boldsymbol{\mathcal{E}} \rangle_{x,y} = \underbrace{\langle \mathbf{U} \rangle_{x,y} \times \langle \mathbf{B} \rangle_{x,y}}_{\text{zero } \Omega\text{−effect}} + \underbrace{\langle \tilde{\mathbf{u}} \times \tilde{\mathbf{b}} \rangle_{x,y}}_{\text{dominant } \Upsilon\text{−effect}}, \qquad (2)$$

where the angular brackets $\langle \cdot \rangle_{x,y}$ average fluctuations in the (x,y)-plane; $\mathbf{U}$ and $\mathbf{B}$ respectively represent the (x,y)-averaged mean flow and mean magnetic fields; $\tilde{\mathbf{u}}$ and $\tilde{\mathbf{b}}$ respectively represent turbulent flow and turbulent magnetic fields; thus, $\mathbf{U}+\tilde{\mathbf{u}}$ and $\mathbf{B}+\tilde{\mathbf{b}}$ represent the

total velocity and total magnetic field. In the curl of Eq. (2), the second term produces straining of mean field by mean flow (the so-called dynamo Ω-effect[32]), which is zero here. That is, $\mathbf{B}\cdot\nabla U_x = (B_x\partial_x + B_y\partial_y)U_x = 0$ [for the (x,y)-averaged mean flow and fields, $\nabla\cdot\mathbf{B} = \partial_z B_z = 0$ and $\partial_z U_z = 0$; the mean vertical field B_z and flow U_z are absent in the present simulations]. Thus, the (x,y)-averaged mean field *must* be generated by turbulent effects via the third term of Eq. (2).

The dominant turbulent flows are jet-like because they are directed along x and do not vary along x (similar to axisymmetric azimuthal flows in planetary atmospheres); see the red-blue 3D streamlines of $\tilde{u}_x$ in Figs. 1**c**,**d**. This jet-like flow $\tilde{u}_x$ exhibits even-parity symmetry along z. Since $\partial_z\tilde{u}_x$ changes sign along z, the field-line-stretching $\tilde{\mathbf{b}}\cdot\nabla\tilde{u}_x$ by turbulent jets generates a z-reversed mean field. This is further explained by a semi-local analytic theory (Methods Sec. VIII). The origin of the jets is non-trivial, as perturbations with the wavenumber $k_x = 0$ are linearly stable (Extended data Fig. 1). The jets are formed when the mean flow horizontally stretches a seed fluctuation flow $\tilde{u}_z$ (Methods Sec. VII). The seed fluctuation flow is excited by the KH instability nonlinearly. The jets and seed fluctuation flow have magnetic counterparts.

The large-scale jets $\tilde{u}_x$ are robust to variations in fluid Reynolds number Re ($\propto$ 1/viscosity) and magnetic Reynolds number Rm ($\propto$ 1/resistivity); see Fig. 2**a**. These x-directed, x-invariant jets are exact solutions to the *nonlinear* ideal MHD equations—akin to the Elsässer fields[33] and zonal flows[13]. These structures render all MHD nonlinearities zero. The spatial topology of the jets protects them from being destroyed because the gradients of perturbed fluid pressure and magnetic pressure are zero.

The jets operate on the seed fluctuation magnetic field $\tilde{b}_z$ to induce a dynamo (Methods Sec. VIII). Both of these vary in the (y,z)-plane, but not in x. (In Fig. 2**a**, $\tilde{b}_z$ is evaluated for $k_x = 0$, $k_y = 2\pi/L_y$, with $L_y = 10\pi$.) The amplitude (square root of energy) of the dynamo-generated mean field B_x has weak sensitivity to variations in Pm—the ratio of viscosity to resistivity;

see Fig. 2**b**. This behavior is due to the robust jets $\tilde{u}_x$, as the jets operate on $\tilde{b}_z$ via $\langle\tilde{\mathbf{b}}\cdot\nabla\tilde{u}_x\rangle_{x,y}=\partial_z\langle\tilde{b}_z\tilde{u}_x\rangle_{x,y}$ to generate the mean field B_x.

Traditional mean-field dynamo theory expresses the turbulent EMF $\boldsymbol{\mathcal{E}}$ in terms of the mean magnetic field **B**, by removing a uniform mean flow via Galilean transformation[24]. In the presence of an inhomogeneous mean flow **U**, which cannot be removed, traditional mean-field theory needs to be generalized[4]. The essential elements of this generalization are reproduced by our quasilinear EMF model (Methods Sec. VI). This generalized theory predicts $\boldsymbol{\mathcal{E}}=\alpha\mathbf{B}-\beta\nabla\times\mathbf{B}+\Upsilon\nabla\times\mathbf{U}$, where α captures kinetic helicity $\langle\tilde{\mathbf{u}}\cdot\nabla\times\tilde{\mathbf{u}}\rangle_{x,y}$ and current helicity $\langle\tilde{\mathbf{b}}\cdot\nabla\times\tilde{\mathbf{b}}\rangle_{x,y}$; here, β measures turbulent energy; and the Upsilon Υ stands for the Yoshizawa's postulated mean-vorticity effect[4] related to the cross-helicity $\langle\tilde{\mathbf{u}}\cdot\tilde{\mathbf{b}}\rangle_{x,y}$. The Υ-effect is robust to variations in *Pm* (Fig. 2**c**; Methods Sec. VI). Similar trend of Υ shown during field-growth is found in the saturated phase. In addition to the multidimensional spatial regression[27] used in Fig. 2**c**, we have employed temporal regression[34] to recover the dominance of the Υ-effect.

We develop a physical understanding of the Υ-effect in Fig. 3**a**. This effect has a strong analogy with the α-effect[1]. A visual representation of the α-effect ($\alpha\mathbf{B}\propto\mathbf{B}\langle\tilde{\mathbf{u}}\cdot\nabla\times\tilde{\mathbf{u}}\rangle$) involves three elements: magnetic field (**B**), velocity ($\tilde{\mathbf{u}}$), and vorticity ($\nabla\times\tilde{\mathbf{u}}$). Following that order, an initial straight mean field **B** is bent and rotated[1], thus creating a mean field orthogonal to **B**. To similarly visualize the Υ-effect ($\Upsilon\nabla\times\mathbf{U}\propto\nabla\times\mathbf{U}\langle\tilde{\mathbf{u}}\cdot\tilde{\mathbf{b}}\rangle$), we reverse the order of the previous three elements: vorticity ($\nabla\times\mathbf{U}$), velocity ($\tilde{\mathbf{u}}$), and magnetic field ($\tilde{\mathbf{b}}$). Following thar order, an initial straight mean vortex line is bent, inducing jets (Fig. 3**a**). The jets are 3D as they vary along the *y*-direction. The jets then operate on $\tilde{\mathbf{b}}$ to produce a mean field.

Our proposed dynamo mechanism is confirmed in Fig. 3**b** using a computer simulation of an (x,y,z)-domain with $4096\times4096\times8192$ grid points. The equilibrium flow here is a double shear layer[35] (Methods Secs. II, III). This calculation is, to our knowledge, the highest-resolution Kelvin–Helmholtz spectral dynamo simulation to date (Methods Sec. IV). In the

beginning of this simulation, only the mean flow is present—and *the mean magnetic field is zero*. We add perturbations in velocity and magnetic field with energy 10^{-18} times the mean-flow energy. The physical mechanism presented in Fig. 3 dominantly generates mean magnetic field in all simulations where the mean flow is maintained (Methods Sec. XII).

Figure 4**a** shows vorticity and electric current density, which are aligned because velocity and magnetic fields are aligned, as measured in Fig. 4**b**. Unlike energies, helicities can have different signs at different scales[36]. The dynamo features a cascade of energy from large scales to small scales (Extended data Fig. 2; Methods Sec. IX). Small scales take energy away from the mean field; the large-scale jets give energy to the mean field (Extended data Fig. 3).

The first direct laboratory measurement of a turbulent EMF in the Madison Dynamo Experiment (MDE) presented a finding[37] that challenged traditional theories: The magnetic field and the EMF in the experiment were nearly orthogonal (Extended data Fig. 4), showing that the α-effect fails to explain their dynamo. Their measurement is consistent with the Υ-effect if one considers the observed large-scale radial vorticity[38], which drives the observed radial EMF. In both MDE and our simulations, large-scale vortical motions are replenished by external forces. Both systems host turbulently generated seed fluctuation flows and jets. Both systems exhibit the same alignment of different components of EMF. This work suggests that the large-scale jet-driven dynamos are present in the laboratory and nature[39] (Methods Sec. X).

The classical relaxed states of MHD turbulence are force-free[40]; these states in α-dynamos have $\alpha\mathbf{B} - \beta\nabla\times\mathbf{B} = 0$. However, KH-dynamo simulations show that $\mathbf{B}$ and $\nabla\times\mathbf{B}$ are orthogonal, as the mean magnetic field $\mathbf{B}$ is reversed along z and directed dominantly along x. The relaxed KH-dynamo states feature $\mathbf{B}$ (anti-)parallel to $\mathbf{U}$ because the inductive term takes the form $\nabla\times(\Upsilon\nabla\times\mathbf{U})$. The sign of Υ determines the polarity of $\mathbf{B}$.

Binary neutron stars (BNS), as they approach each other, produce in the merger interface a KH-unstable velocity gradient[5,7], where a non-relativistic treatment captures the essential physics. In the KH-unstable system, the field grows due to the ϒ-dynamo—as seen in simulations—at a typical rate of 0.04 U_0/a, where a is the half-width of the shear flow with an amplitude U_0. Estimates inferred from general-relativistic MHD simulations of BNS mergers show that the flows in the thin merger interface[5,6] have a~10–15 m (likely even smaller[11]) and U_0~0.1c, with c representing the speed of light. Hence, we predict the e-folding time of the ϒ-dynamo in BNS mergers to be ~8 μs (variations depend on the model, but this timescale is likely even shorter). The BNS merger takes milliseconds[5], during which the shear layer persists between the approaching BNS. Thus, the ϒ-dynamo can create large-scale magnetic fields even from zero initial large-scale field and rapidly amplify them to energies similar to the bulk kinetic energy[7]. These fields, possibly[41] of 10^{16}–10^{17} G, impact the merger and post-merger dynamics, and change the gravitational waveforms by increasing their frequencies[8] by 200–300 Hz. These changes are in principle detectable by the LIGO-Virgo-KAGRA Collaboration in upcoming runs[42] and will be measured by the Einstein telescope[43]. Strong magnetic fields affect electron acceleration and synchrotron radiation, thereby impacting the electromagnetic signals[41]. High-resolution space observations and global merger simulations[5,6] can capture the rapid generation of magnetic fields via the ϒ-effect (Methods Sec. XI). Sub-grid models[44] should be able to reproduce the ϒ-dynamo driven by large-scale jets. The ϒ-dynamo also has implications for merging galaxy clusters[17], where large-scale unstable shear flows exist and large-scale magnetic fields have been reported[9,18].

The jet-driven vorticity-related dynamo has bearing for the generation of magnetic fields in the Sun. The solar meridional flow—a key player in flux transport dynamos[14]—has vorticity directed in the azimuthal direction[15]. This vorticity is bound to drive the azimuthal component of the turbulent electromotive force, generating poloidal magnetic fields. The large vorticity of solar subsurface flows[45] is also expected to generate magnetic fields. Simulations show large cross-helicity in the near-surface shear layers, which have poloidal vorticity[46]. Relatedly, zonal jets and torsional oscillations in the outer parts of the solar

interior are precursors of the solar magnetic cycles[29,45,47]. Simpler models of the ϒ-dynamo are useful to explain stellar magnetic cycles[48]. The jet-driven dynamo is expected to generate magnetic fields in planets and galaxies, as well, which host vortical structures[16]. Since common MHD turbulence theories apply only in the case of zero global cross-helicity, this work motivates the understanding of MHD turbulence theories for non-zero global cross-helicity[49] (Extended data Fig. 5).

This article has outlined the salient features of the jet-driven ϒ-dynamo arising in turbulence generated by shear flows, with potential applications in laboratory dynamo experiments, the Sun, main-sequence stars, planets, accretion flows around compact objects, and binary neutron star mergers. The robust nonlinear jets are shown here to be the physical mechanism behind the previously postulated ϒ-effect[4], which this work confirms.

1. Parker, E.N. Hydromagnetic dynamo models. *Astrophys. J.* **122**, 293 (1955).

2. Batchelor, G. K. & Proudman, I. The effects of rapid distortion of a fluid in turbulent motion. *Q. J. Mech. Appl. Math.* **7**, 83 (1954).

3. Terry, P. W. Suppression of turbulence and transport by sheared flow. *Rev. Mod. Phys*. **72**, 109 (2000).

4. Yoshizawa, A. Self-consistent turbulent dynamo modeling of reversed field pinches and planetary magnetic fields. *Phys. Fluids B*. **2**, 1589 (1990).

5. Kiuchi, K., Cerdá-Durán, P., Kyutoku, K., Sekiguchi, Y. & Shibata M. Efficient magnetic-field amplification due to the Kelvin-Helmholtz instability in binary neutron star mergers. *Phys. Rev. D* **92**, 124034 (2015).

6. Kiuchi, K., Reboul-Salze, A., Shibata, M. & Sekiguchi Y. A large-scale magnetic field produced by a solar-like dynamo in binary neutron star mergers. *Nat. Astron.* **8**, 298 (2024).

7. Price, D. J. & Rosswog, S. Producing ultrastrong magnetic fields in neutron star mergers. *Science*. **312**, 5774 (2006).

8. Tsokaros, A., Bamber, J., Ruiz, M. & Shapiro, S. L. Masking the Equation-of-State Effects in Binary Neutron Star Mergers. *Phys. Rev. Lett.* **134**, 121401 (2025).

9. Basu, A. et al. Detection of an ~20 kpc coherent magnetic field in the outskirt of merging spirals: the Antennae galaxies. *Mon. Not. R. Astron. Soc.* **464**, 1003 (2017).

10. Chandrasekhar, S. *Hydrodynamic and Hydromagnetic Stability*. (Clarendon Press, Oxford 1961).

11. Palenzuela, C. et al. Turbulent magnetic field amplification in binary neutron star mergers. *Phys. Rev. D*. **106**, 023013 (2022).

12. Vasil, G. M. et al. The solar dynamo begins near the surface. *Nature*. **629**, 769 (2024).

13. Terry, P. W. *Zonal Flows in Magnetically Confined Plasmas: Theory*, in Zonal Jets, Boris Galperin and Peter L. Read, editors, p. 181-193 (Cambridge University Press, London 2019).

14. Hazra, G., Nandy, D., Kitchatinov, L. & Choudhuri, A. R. Mean Field Models of Flux Transport Dynamo and Meridional Circulation in the Sun and Stars. Space Sci. Rev. **219**, 39 (2023).

15. Gizon L. et al. Meridional flow in the Sun's convection zone is a single cell in each hemisphere. *Science*. **368**, 1469 (2020).

16. Abramowicz, M. A., Lanza, A., Spiegel, E.A. & Szuszkiewicz, E. Vortices on accretion disks. *Nature*. **356**, 41 (1992).

17. Chadayammuri, U. et al. Constraining Merging Galaxy Clusters with X-ray and Lensing Simulations and Observations: The case of Abell 2146. *Mon. Not. R. Astron. Soc.* **509**, 1201 (2021).

18. Chadayammuri, U., ZuHone, J., Nulsen, P., Nagai, D. & Russell, H. Turbulent magnetic fields in merging clusters: a case study of Abell 2146. *Mon. Not. R. Astron. Soc.* **512**, 2157 (2022).

19. Neronov, A. & Vovk, I. Evidence for strong extragalactic magnetic fields from Fermi observations of TeV blazars. *Science*. **328**, 73 (2010).

20. Brandenburg, A. & Subramanian, K. Astrophysical magnetic fields and nonlinear dynamo theory. *Phys. Rep.* **417**, 1 (2005).

21. Kulsrud, R. M. & Zweibel, E. G. On the origin of cosmic magnetic fields. *Rep. Prog. Phys.* **71**, 046901 (2008).

22. Tobias, S. M. & Cattaneo, F. Shear-driven dynamo waves at high magnetic Reynolds number. *Nature*. **497**, 463 (2013).

23. Squire, J. & Bhattacharjee, A. Generation of large-scale magnetic fields by small-scale dynamo in shear flows. *Phys. Rev. Lett.* **115**, 175003 (2015).

24. Steenbeck, M., Krause, F. & Radler, K. -H. *Z. Naturforsch.* **21a**, 369 (1966).

25. Cattaneo, F. & Hughes, D. W. Nonlinear saturation of the turbulent α effect. *Phys. Rev. E* **54**, R4532 (1996).

26. Vainshtein, S. & Cattaneo, F. Nonlinear Restrictions on Dynamo Action. *Astrophys. J.* **393**, 165 (1992).

27. Brandenburg, A., Elstner, D., Masada, Y. & Pipin, V. Turbulent processes and mean-field dynamo. *Space Sci. Rev.* **219**, 55 (2023).

28. Pouquet, A., Frisch, U. & Leorat, J. Strong MHD helical turbulence and the nonlinear dynamo effect. *J. Fluid Mech.* **77**, 321 (1976).

29. Howe, R., Chaplin, W. J., Christensen-Dalsgaard, J., Elsworth, Y. P. & Schou, J. Update on Global Helioseismic Observations of the Solar Torsional Oscillation. *Res. Notes AAS*. **6**, 261 (2022).

30. Smith, K. M., Caulfield, C. P. & Taylor, J. R. Turbulence in forced stratified shear flows. *J. Fluid Mech*. **910**, A42 (2021).

31. Hathaway, D. H. The Solar Cycle. *Living Rev. Sol. Phys.* **39**, 227 (2015).

32. Ebrahimi, F. & Blackman, E. G. Radially dependent large-scale dynamos in global cylindrical shear flows and the local cartesian limit. *Mon. Not. R. Astron. Soc.* **459**, 1422 (2016).

33. Elsässer, W. M. The Hydromagnetic Equations. *Physical Review*. **79**, 183 (1950).

34. Bendre, A. B., Subramanian, K., Elstner, D. & Gressel, O. Turbulent transport coefficients in galactic dynamo simulations using singular value decomposition. *Mon. Not. R. Astron. Soc.* **491**, 3870 (2020).

35. Lecoanet, D. et al. A validated non-linear Kelvin-Helmholtz benchmark for numerical hydrodynamics. *Mon. Not. R. Astron. Soc.* **455**, 4274 (2016).

36. Zhang, H. & Brandenburg, A. Solar Kinetic Energy and Cross Helicity Spectra. *Astrophys. J. Lett.* **862**, L17 (2018).

37. Rahbarnia, K. et al. Direct observation of the turbulent EMF and transport of magnetic field in a liquid sodium experiment. Astrophys. J. **759**, 80 (2012).

38. Kaplan, E. J. et al. Reducing Global Turbulent Resistivity by Eliminating Large Eddies in a Spherical Liquid-Sodium Experiment. *Phys. Rev. Lett.* **106**, 254502 (2011).

39. Mondal, T. & Bhat, P. Unified treatment of mean-field dynamo and angular-momentum transport in magnetorotational instability-driven turbulence. *Phys. Rev. E.* **108**, 065201 (2023).

40. Taylor, J. B. Relaxation of toroidal plasma and generation of reverse magnetic fields. *Phys. Rev. Lett.* **33**, 1139 (1974).

41. Zrake J. & MacFadyen, A. I. Magnetic energy production by turbulence in binary neutron star mergers. *Astrophys J. Lett.* **769**, 29 (2013).

42. Kunnumkai, K. et al. Detecting electromagnetic counterparts to LIGO/Virgo/KAGRA gravitational wave events with DECam: Neutron Star Mergers. *arXiv preprint arXiv:2411.13673* (2024).

43. Maggiore, M. et al. Science Case for the Einstein Telescope. *J. Cosmol. Astropart. Phys.* **03**, 050 (2020).

44. Radice, D. General-relativistic Large-eddy Simulations of Binary Neutron Star Mergers. *Astrophys. J. Lett.* **838**, L2 (2017).

45. Mandal, K., Kosovichev, A. G. & Pipin, V. V. Helioseismic Properties of Dynamo Waves in the Variation of Solar Differential Rotation. *Astrophys J.* **973**, 36 (2024).

46. Yokoi, N. Unappreciated cross-helicity effects in plasma physics: anti-diffusion effects in dynamo and momentum transport. *Rev. Mod. Plasma Phys.* **7**, e33 (2023).

47. Chakraborty, S., Choudhuri, A. R. & Chatterjee, P. Why Does the Sun's Torsional Oscillation Begin before the Sunspot Cycle? *Phys. Rev. Lett.* **102**, 041102 (2009).

48. Yokoi, N., Schmitt, D., Pipin, V. & Hamba, F. A new simple dynamo model for stellar activity cycle. *Astrophys. J.* **824**, 67 (2016).

49. Pecora, F. et al. Relaxation of the turbulent magnetosheath. *Mon. Not. R. Astron. Soc.* **525**, 67 (2023).

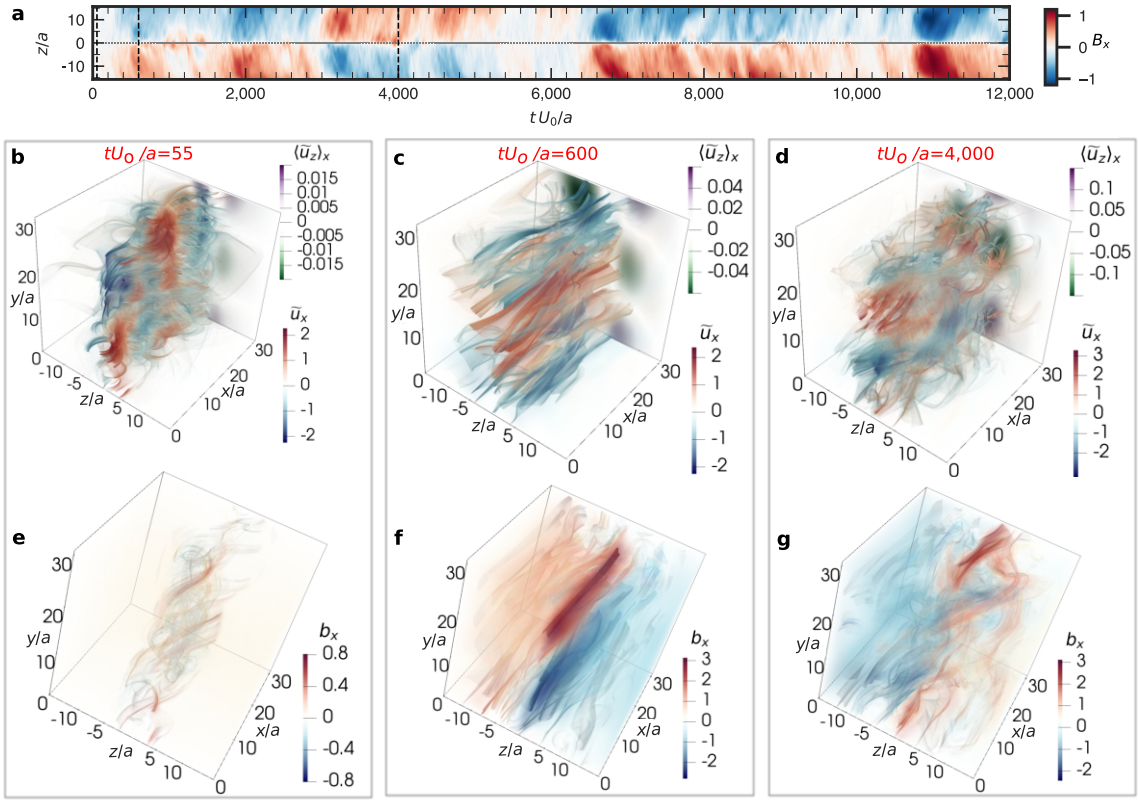

Figure 8.1: **Long-time evolution of the MHD-KH dynamo, displaying phases of turbulent generation of flows and magnetic fields. a**, The (x,y)-averaged mean field B_x quasi-cyclically reverses ($t \approx 3{,}000$; 5,300; 6,000; 6,350). **b**–**d**, 3D streamlines in red-blue show turbulent velocity [the mean flow $U_x(z)$ is not shown]. Colors correspond to $\tilde{u}_x$, at times indicated by vertical dashed lines in **a**. The back-plane at $x=10\pi$ displays vertical velocity $\langle\tilde{u}_z\rangle_x$, which is Fourier-filtered to obtain a fluctuation that is invariant in x and fundamental harmonic in y. At $t=55$ in **b**, the two-dimensional KH eddies appear as cylinders, with almost no variation along y, but they have transformed into x-invariant jets in **c** and **d**. These jets are anchored on the (y,z)-plane at $x=10\pi$, where $\langle\tilde{u}_z\rangle_x$ is large, shown with a purple-green color bar. **e**–**g**, Streamlines of magnetic fields are overlaid on top of volume-rendered volume-filling fields. The polarities of the mean fields flip between **f** and **g**.

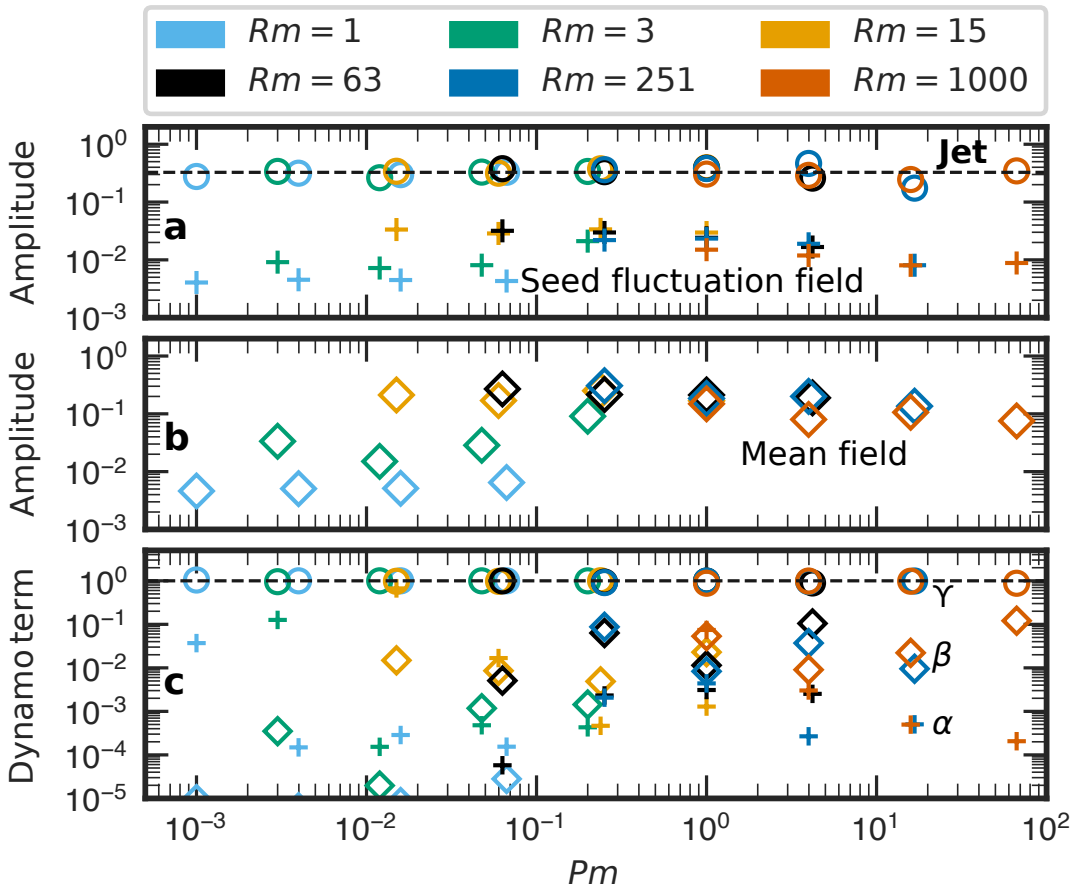

Figure 8.2: **Properties of the KH instability-induced jets and dynamo. a**, Amplitudes of the 3D jets (shown with circles) remain unchanged over variations in magnetic Prandtl number *Pm*. Reynolds numbers *Re* and *Rm* are measured using length a and speed U_0 of the mean flow. Above the threshold Rm_c between 3 and 15, the seed fluctuation field (plus sign) induced by the KH instability does not have drastic variation. For every *Rm*, we show four cases: *Re*=15, 63, 251, and 1000, which are indicated by four circles and four pluses of same color. Thus, amplitudes are observed to be independent of *Re*. **b**, The dynamo-generated mean field B_x does not have strong sensitivity to visco-resistive properties above Rm_c. This is a consequence of the results shown in panel **a**. **c**, The mean turbulent EMF is driven by the Υ-effect. Circles, diamonds, and pluses represent the time-averaged contributions of the Υ-, β-, and α-effects to the mean EMF, quantified by $|\Upsilon(\nabla\times\mathbf{U})_y/\mathcal{E}_y|$, $|\beta(\nabla\times\mathbf{B})_y/\mathcal{E}_y|$, and $|\alpha B_y/\mathcal{E}_y|$, respectively. Similar dominant Υ-effect is found using different time windows. The EMF is the largest where the mean flow reverses.

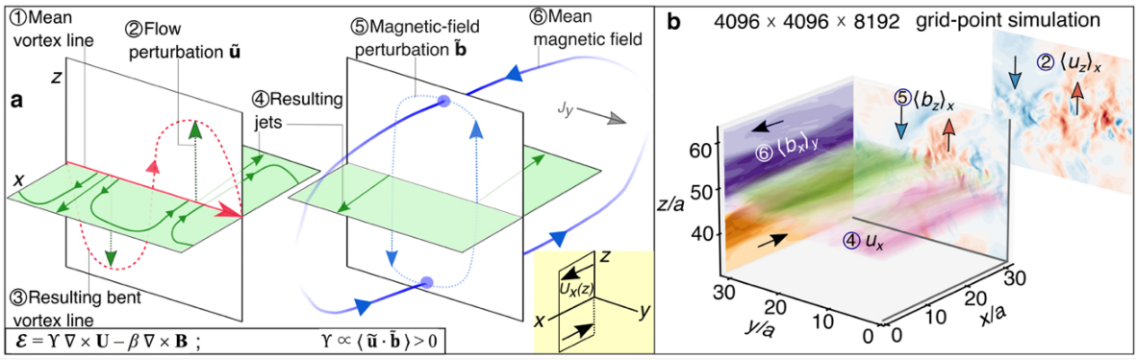

Figure 8.3: **Mechanism of the *jet-driven* ϒ-dynamo. a**, Red, green, and blue represent vorticity, velocity, and magnetic field, respectively. Step ① shows a y-directed mean vortex-line, corresponding to a mean shear flow $U_x(z)$ in the (x,z)-plane, shown at the bottom right of panel **a**. In step ②, the KH instability excites a flow perturbation $\tilde{\mathbf{u}}$, with a sinusoidal variation in y, representing a purely 3D process. This flow perturbation bends the mean vortex line in step ③. Where the vortex line points upward, eddy-like flows are induced around it; these are shown with solid green curves in step ④. This hydrodynamic process generates jets, which have no variation along x but are directed along x. Step ⑤ is the magnetic counterpart of step ②; the alignment between $\tilde{\mathbf{u}}$ and $\tilde{\mathbf{b}}$ represents here the case of positive ϒ (an Alfvénic state). The y-varying jets of step ④ stretch the y-varying magnetic-field perturbation of step ⑤, thereby creating a mean magnetic field (invariant in x and y) in step ⑥. The mean field aligns with the mean flow. **b,** All quantities are plotted using red (pink) for positive and blue (green) for negative, where the color map spans $[-M,M]$, with M representing the absolute maximum of each quantity. A half of the symmetric double shear layer[35] is shown. Since flow and fields in steps ② and ⑤ (in panel **a)** do not vary along x, they are x-averaged and displayed on the (y,z)-plane at arbitrary x-coordinates for visual clarity. Multiple (x,y)-slices of jets u_x are plotted near a shear layer interface where jets are the strongest. The x-directed magnetic field is averaged in y, and $\langle b_x \rangle_y$ shown on the (x,z)-plane. The mean flow is shown with the black arrows.

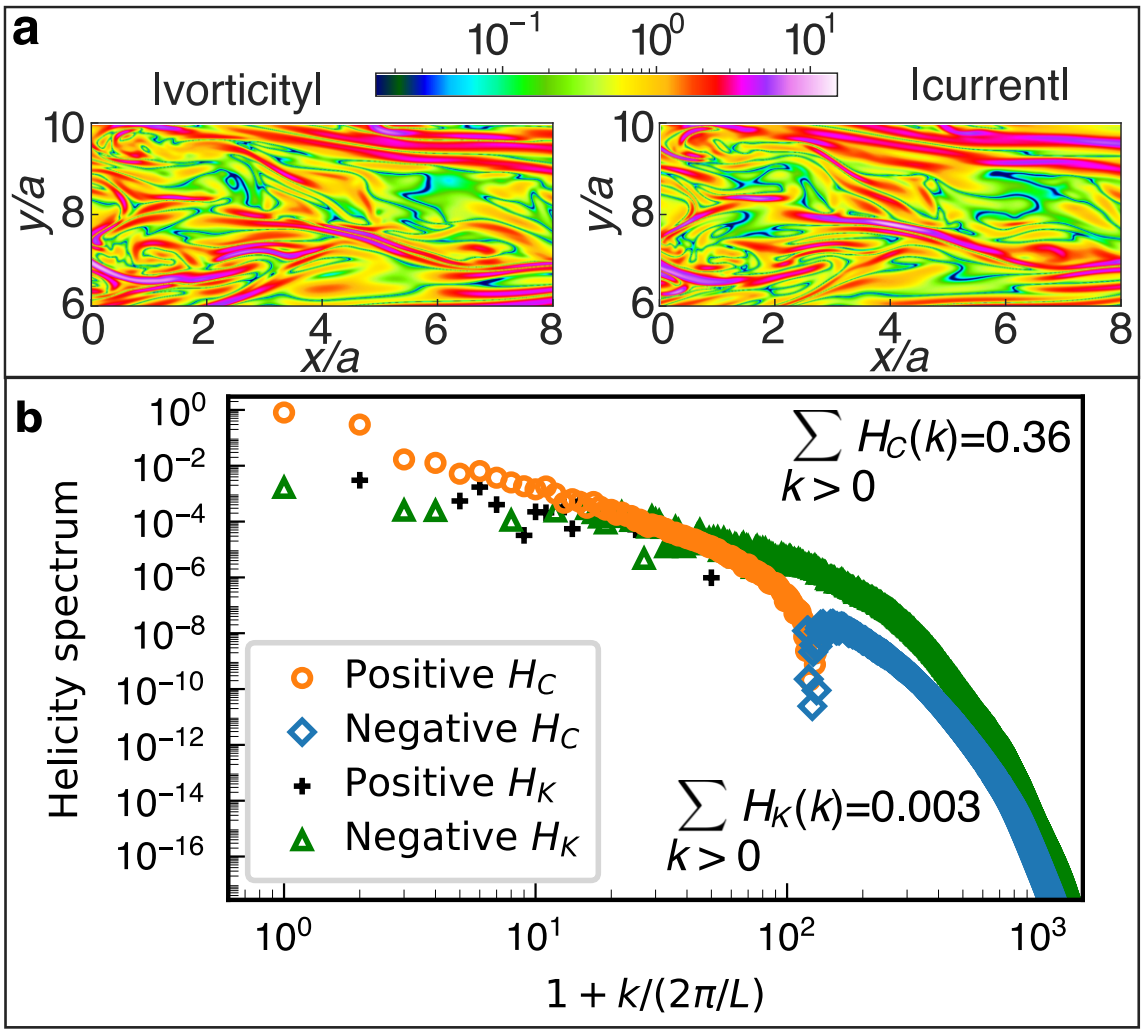

Figure 8.4: **Dominance of cross-helicity. a**, Vorticity $|\omega_z|/\omega_z^{\rm rms}$ and electric current density $|j_z|/j_z^{\rm rms}$ are similar; rms stands for root mean square. A typical slice is shown at a shear-layer interface (z=3L_z/4); the full simulation domain is [0,10π)×[0,10π)×[0,20π). **b**, The total turbulent cross-helicity H_C (= $\tilde{\mathbf{u}} \cdot \tilde{\mathbf{b}}$) is two orders of magnitude larger than the total turbulent kinetic helicity H_K (= $\tilde{\mathbf{u}} \cdot \nabla\times\tilde{\mathbf{u}}$). Cross-helicity dominates at larger scales of fluctuations.

Methods

I. Model and computational considerations.

Using 90 million Central Processing Unit (CPU) hours, we performed more than 90 KH dynamo simulations. We analyzed 0.25 petabytes of turbulence data generated by evolving velocity **u** and magnetic field **b** according to the 3D incompressible MHD equations

$$\partial_t \mathbf{u} - \nu\nabla^2\mathbf{u} + \nabla \mathrm{P} = -\mathbf{u}\cdot\nabla\mathbf{u} + \frac{(\nabla\times\mathbf{b})\times\mathbf{b}}{\mu_0\rho} + \mathbf{f}, \qquad \text{(S1a)}$$

$$\partial_t \mathbf{A} - \eta\nabla^2\mathbf{A} + \nabla\Psi = \mathbf{u}\times\mathbf{b}, \qquad \text{(S1b)}$$

$$\mathbf{b} = \nabla\times\mathbf{A}, \qquad \text{(S1c)}$$

$$\nabla\cdot\mathbf{u} = 0, \qquad \text{(S1d)}$$

$$\nabla\cdot\mathbf{A} = 0, \qquad \text{(S1e)}$$

where **A** is the magnetic vector potential; ν is the kinematic viscosity; η is the electric resistivity; μ_0 is the vacuum magnetic permeability; P is the fluid pressure; Ψ is a scalar function; and **f** represents external acceleration applied on a fluid of density ρ (here, $\mu_0\rho$=1). Equation (S1c) ensures $\nabla\cdot\mathbf{b}$=0. We consider non-periodic and periodic domains. We simulate turbulence with and without an external mean magnetic field.

II. Background profiles and non-dimensionalization.

In non-periodic domains, we consider a single shear layer[10]

$$U_x(z) = U_0 \tanh\left(\frac{z}{a}\right), \qquad \text{(S2)}$$

in a volume $[0,L)\times[0,L)\times[-L/2,L/2]$. In periodic domains, we consider a double shear layer[35]

$$U_x(z) = U_0\left[\tanh\left(\frac{z-z_1}{a}\right) - \tanh\left(\frac{z-z_2}{a}\right) - 1\right], \qquad \text{(S3)}$$

in a volume $[0,L)\times[0,L)\times[0,2L)$. Here, $z_1=L/4$ and $z_2=3L/4$, with $L=10\pi$. Speed and length scales are measured using U_0 and a throughout this work. Fluid and magnetic Reynolds numbers are $Re=U_0a/\nu$ and $Rm=U_0a/\eta$, respectively.

When a weak, uniform, external mean magnetic field $\mathbf{B}_0$ is initially imposed, $\mathbf{B}_0=(\hat{\mathbf{e}}_x\cos\theta+\hat{\mathbf{e}}_y\sin\theta)/M_A$, where M_A is the Alfvénic Mach number, and θ is the angle between the initial mean field and the mean flow. Dynamo saturation properties remain largely unimpacted by variations in M_A until M_A approaches the KH-instability threshold. Variations in θ are found to not affect dynamo saturation.

We seed instability by adding broadband, phase-randomized, divergence-free perturbations[50] to **u** and **A**. The jet-driven dynamo emerges from general random perturbations. We solve Eqs. (S1a)–(S1e) using two disparate pseudospectral solvers: Dedalus (non-periodic and periodic domains) and GHOST (periodic domains).

III. Dynamos in non-periodic and periodic domains.

For non-periodic domains, we choose physical boundaries that confine the plasma within perfectly conducting ($j_x=j_y=b_z=0$), no-slip walls, represented by $u_z=u_y=A_x=A_y=\Psi=0$ and $u_x=\pm U_0$ at $z=\pm L/2$. When a uniform horizontal mean field $\mathbf{B}_0$ is present in the initial condition, we isolate that mean field from the remaining fields; the latter are subjected to the above magnetic boundary conditions.

The dynamo does not depend on the nature of the domain because it is enabled by large-scale jets, which are strongest near the shear layer. Both jets and shear layer lie maximally far away from the boundaries; see Sec. VIII for an analytic calculation. In some dynamos, one injects helicity fluxes through open, manipulated boundaries, hoping to achieve a large-scale dynamo. Here, the shear layer is a minimal and sufficient ingredient for exciting a dynamo. Our simulations with extended vertical domain reproduce the results reported here.

IV. Benchmarks and major code optimizations.

Dedalus simulations: Using Dedalus[51] (an open-source, general code written primarily in python), we employ MPI-parallelization along the periodic directions x and y. We use pseudospectral τ-method[35,51], RK443 and SBDF2 mixed implicit-explicit time-steppers[52,53], and the 3/2 dealiasing for nonlinearities[51]. For non-periodic domains, we use Fourier–Fourier–Chebyshev bases, whose harmonics range from $128^2\times512$ to $1{,}024^3$.

GHOST simulations: Using GHOST[54,55] (an open-source code written primarily in Fortran 90/95 to efficiently solve triply periodic systems), we parallelize with MPI in z and openMP in y. For efficient computations, we place OpenMP threads next to each other within a NUMA node and bind OpenMP threads to an MPI task. The nonlinear terms are solved using the second-order explicit Runge–Kutta scheme. We have benchmarked GHOST against Dedalus, using identical initial conditions[56]. We find the dynamo-enabling jets appear in all test and production simulations, whose resolutions we vary from $32^2\times512$ to $4096^2\times8192$. The high z-resolution captures the mean shear flow.

The public GHOST code solves the visco-resistive terms using an explicit method, which is not ideal to capture small-scale fluctuations. These fluctuations, if not resolved, can lead to numerical instability. We have implemented a new time-integrator, i.e., an exact integrating factor technique, which produces exact solutions corresponding to the visco-resistive terms. We have also implemented a forcing function, which maintains the mean flow.

V. External mean-flow forcing.

We externally force only the mean flow $u_x(k_x=0, k_y=0)$. The magnetic fields evolve freely. This allows us to focus on KH instability, which excites fluctuations at various scales via its nonlinear coupling. The forcing $\mathbf{f}=f_x(z)\hat{\mathbf{e}}_x$ in Eq. (S1a) is[57–62]

$$f_x(z) = \frac{\langle u_x(t=0)\rangle_{x,y} - \langle u_x(t)\rangle_{x,y}}{\tau_f} + F_0, \qquad \text{(S5)}$$

where τ_f is the forcing time scale; F_0 is added to merely remove the viscous relaxation of the mean shear flow at t=0, ensuring that the initial mean flow is a true MHD equilibrium, $F_0+\nu\nabla^2\langle u_x(t=0)\rangle_{x,y}=0$.

We vary τ_f from 0 (frozen mean flow) to infinity (decaying mean flow). We reproduce essentially the same results except when τ_f is very large. In the latter case, the gradient of the mean shear flow quickly flattens because its energy is extracted by the KH instability at a rate faster than the rate of energy injection to the mean flow by the external forcing.

VI. Analytic quasilinear EMF model.

Consider an (x,y)-averaged mean magnetic field **B**=(B_x, B_y, 0) and mean flow **U**=(U_x, U_y, 0). We introduce external perturbations in flow **u**'=(0,0,u_z') and fields **b**'=(0,0,b_z') with wavenumber **k**=(0,k_y); primed quantities in this subsection represent perturbations. This wavenumber dominantly generates mean magnetic field (Extended Data Fig. 3). In a quasilinear model, u_z' and b_z' interact with the mean flow and mean field to self-consistently generate other perturbations, e.g., u_x' and b_x'. These, together with the initial perturbations, compose a mean turbulent electromotive force, which causes the mean magnetic field to evolve.

The (x,y)-averaged mean magnetic field B_x evolves according to $(\partial_t-\eta\partial_z^2)B_x=-\partial_z\mathcal{E}_y$, where

$$\mathcal{E}_y=-b_z'^{*}u_x'+u_z'^{*}b_x'+c.c., \qquad \text{(S6)}$$

where *c.c.* represents complex conjugation of the preceding terms.

To derive expressions for u_x' and b_x' in terms of the initial small-amplitude perturbations u_z' and b_z', we write

$$\left(\partial_t-\nu\nabla^2+U_y ik_y\right)u_x'=-u_z'\,\partial_z U_x+b_z'\,\partial_z B_x+B_y ik_y b_x', \qquad \text{(S7)}$$

and

$$\left(\partial_t - \eta\nabla^2 + U_y i k_y\right) b_x' = -u_z' \, \partial_z B_x + b_z' \, \partial_z U_x + B_y i k_y u_x'. \qquad \text{(S8)}$$

The solutions to u_x' and b_x' are approximately written as

$$u_x' = \tau_{\mathrm{ZF}}\left[-u_z' \, \partial_z U_x + b_z' \, \partial_z B_x + B_y i k_y b_x'\right], \qquad \text{(S9)}$$

and

$$b_x' = \tau_{\mathrm{ZM}}\left[-u_z' \, \partial_z B_x + b_z' \, \partial_z U_x + B_y i k_y u_x'\right], \qquad \text{(S10)}$$

where τ_{ZF} and τ_{ZM} are the coherent-straining times of the zonal jet u_x' and zonal magnetic field b_x'. Here, the word *zonal* refers to *x-averaged fluctuations.* When the effects of the nonlinear turbulent interactions are considered, τ_{ZF} and τ_{ZM} are replaced by nonlinearly modified times, which allows the calculations to be more generally applicable than merely in the small-amplitude limit.

Substituting the solutions for the zonal jet [Eq. (S9)] and zonal field [Eq. (S10)] in Eq. (S6),

$$\mathcal{E}_y = \Upsilon(\nabla \times \mathbf{U})_y - \beta(\nabla \times \mathbf{B})_y + \alpha B_y, \qquad \text{(S11)}$$

where

$$\Upsilon = \underbrace{\tau_{\mathrm{ZM}}\langle u_z' b_z'\rangle_{x,y}}_{\text{kinematic}} + \underbrace{\tau_{\mathrm{ZF}}\langle u_z' b_z'\rangle_{x,y}}_{\text{non-kinematic}}, \qquad \text{(S12a)}$$

$$\beta = \underbrace{\tau_{\mathrm{ZM}}\langle u_z'^2\rangle_{x,y}}_{\text{kinematic}} + \underbrace{\tau_{\mathrm{ZF}}\langle b_z'^2\rangle_{x,y}}_{\text{non-kinematic}}, \qquad \text{(S12b)}$$

$$\alpha = \underbrace{-\tau_{ZM}\langle u_z' \omega_z' \rangle_{x,y}}_{\text{kinematic}} + \underbrace{\tau_{ZF}\langle b_z' j_z' \rangle_{x,y}}_{\text{non-kinematic}}. \qquad \text{(S12c)}$$

Equations (S11) and (S12a)–(S12c) were first derived in analogous forms using a turbulence closure[4] (see also Sec. 2 of Ref. 46).

The non-kinematic terms appearing with τ_{ZF} in Eq. (S12a)–(S12c) arise from the time-evolution of velocity fluctuation in Eqs. (S7) and (S9). Generally, $\tau_{ZF} = \tau_{ZM}$. Thus, for pure Alfvénic states (**u**||±**b**), α reduces to zero[28,63], whereas β and Υ become maximally non-zero.

VII. Zonal jets in the KH dynamo.

Energetically dominant, large-scale jets are generated when fluid motion $u_z(k_x=0,k_y)$ is stretched by the mean flow (Fig. 3**a**). The motion $u_z(k_x=0,k_y)$ is *nonlinearly* generated by the KH instability, as the vertical mean flow and vertical mean field are absent; the KH instability exists only at $k_x \neq 0$ (Extended Data Fig. 1).

The motion $u_z(k_x \neq 0,k_y)$, on the other hand, is sheared by the mean flow on the (x,z)-plane, thus progressively being shortened in its vertical scale until it is broken into multiple fragments[64]; see Fig. 1 of Ref. 3. However, this two-dimensional fragmentation does not apply to the three-dimensional *x-invariant* fluctuation, which can be shown using rapid distortion theory[65]. The mean flow maintains the z-spatial scale of $u_z(k_x=0,k_y)$ and produces strong jets $u_x(k_x=0,k_y)$. The jets are minimally impacted by the Lorentz feedback because the forces on them from the gradients of fluid pressure and magnetic pressure are zero. The jets are robust (Fig. 2**a**).

VIII. Analytic semi-local dynamo characterization.

To characterize the generation of the mean magnetic field that is reversed across the shear layer $z=0$, we expand around $z=0$ the mean flow $u_x^{0,0}$ [the superscript represents the horizontal wavenumber (k_x,k_y)]

$$u_x^{0,0} = \tanh(z) = z \quad \underbrace{-z^3/3 + \cdots}_{\text{KH dynamo source}} , \qquad \text{(S13)}$$

where the terms nonlinear in z are nonlocal. We focus on z^3 in the semi-local analysis below.

Energy transfer analysis informs us that jets are formed when the mean flow stretches u_z^{0,k_y}. Hence, we write

$$\partial_t u_x^{0,k_y} = -\mathbf{u}^{0,k_y} \cdot \nabla u_x^{0,0} + \cdots = -u_z^{0,k_y} \partial_z u_x^{0,0} + \cdots = -u_z^{0,k_y}(1 - z^2 + \cdots) + \cdots, \qquad \text{(S14)}$$

where … represents terms not relevant here. The solution of Eq. (S14) is approximately written as

$$u_x^{0,k_y} = -\tau_c u_z^{0,k_y} \left(1 - \underbrace{z^2 + \cdots}_{\text{jets symmetric in } z} \right) + \cdots, \qquad \text{(S15)}$$

where τ_c is a time scale of flow-straining that generates u_x^{0,k_y}. Equation (S15) shows that the jet amplitude u_x^{0,k_y} is the strongest at the shear-layer interface z=0 and decreases symmetrically with increasing $|z|$. This can be seen in Figs. 1**c** and 1**d**.

Jets $u_x(k_x=0,k_y)$ generate the mean field (Extended Data Fig. 3) via the field-line stretching term $\mathbf{b}^{0,-k_y} \cdot \nabla u_x^{0,k_y} = \nabla_j (b_j^{0,-k_y} u_x^{0,k_y})$, where the repeated index j follows the Einstein's summation convention. We simplify this term by using Eq. (S15) to find

$$\partial_t b_x^{0,0} = \partial_z \left(b_z^{0,-k_y} u_x^{0,k_y} \right) + \cdots = -\tau_c b_z^{0,-k_y} u_z^{0,k_y} \partial_z [1 - z^2 + \cdots] + \cdots$$

$$= \underbrace{2z}_{\text{mean field reversed in } z} \times \tau_c u_z^{0,k_y} b_z^{0,-k_y} \ldots + \cdots, \qquad \text{(S16)}$$

where … represents terms not relevant here.

The linear term z in Eq. (S16) emerges from $\partial_z^2 u_x^{0,0}$ and makes the mean magnetic field $b_x^{0,0}$ reversed across z=0 (Fig. 1**a**). The polarity of the mean field flips over time due to the phase difference between u_z^{0,k_y} and $b_z^{0,-k_y}$. This correlation measures the turbulent cross-helicity ϒ. Equation (S16) suggests

$$b_x{}^{0,0} \propto \hat{\mathbf{e}}_{\boldsymbol{x}} \cdot [\nabla \times (\Upsilon \nabla \times \mathbf{u}^{0,0})]. \qquad \text{(S17)}$$

The foregoing analyses reveal that the Yoshizawa's postulated generic ϒ-effect[4] operates specifically via the formation of 3D jets (see also Fig. 3).

IX. Spectral energy-flux computations.

The KH turbulence is strongly anisotropic and localized around the shear layer. So, for post-processing, it is not ideal to use spherical wavenumber shells. We employ cylindrical shells in the (k_x,k_y)-plane with the axis of the cylinder along z.

The u-to-u energy flux $\Pi_{uu}(k_0)$ passing through the wavenumber k_0 is[66]

$$\Pi_{uu}(k_0) = \frac{1}{L_x L_y L_z} \int_x \int_y \int_z \mathbf{u}^{>} \cdot [-(\mathbf{u} \cdot \nabla)\mathbf{u}] dx dy dz, \qquad \text{(S18)}$$

where **u** represents the entire velocity in the system. The velocity $\mathbf{u}^{>}$ is[66]

$$\mathbf{u}^{>} = \sum_{k_x, k_y : \left(k_x^2 + k_y^2\right)^{1/2} > k_0} \hat{\mathbf{u}}\left(k_x, k_y, z\right) \mathrm{e}^{i k_x x + i k_y y}, \qquad \text{(S19)}$$

where $\hat{\mathbf{u}}(k_x, k_y, z)$ is the Fourier amplitude of the velocity with wavenumber (k_x, k_y).

Similarly, we define the b-to-b energy flux $\Pi_{bb}(k_0)$ passing through the wavenumber k_0 using[66]

$$\Pi_{bb}(k_0) = \frac{1}{L_x L_y L_z} \int_x \int_y \int_z \mathbf{b}^{>} \cdot [-(\mathbf{u} \cdot \nabla)\mathbf{b}] dx dy dz, \qquad \text{(S20)}$$

where **b** represents the entire magnetic field in the system. The magnetic field $\mathbf{b}^{>}$ is defined similar to $\mathbf{u}^{>}$ in Eq. (S19). Computations of these energy fluxes show cascades of kinetic and magnetic energies from large to small physical scales (Extended Data Fig. 2).

X. Relevance of the ϒ-dynamo to laboratory plasmas.

In addition to the fifth-to-last paragraph in the main article and Extended Data Fig. 4, we provide here details comparing the ϒ-dynamo with the Madison Dynamo Experiment[37] (MDE). While there are some differences between the present system and the MDE (such as spherical vs. Cartesian geometry), there are also similarities:

1. Both systems exhibit large-scale vortical flows and jets. The radial vorticity in the MDE is considerably large[38], consistent with the dominant radial EMF (Extended Data Fig. 4**b**).
2. The large-scale flows in both systems are externally maintained: in MDE by rotating impellers and in our simulations by the mean-flow forcing.
3. Both systems exhibit identical alignment of the EMF components. The angle between the mean magnetic field and EMF[37] is ~90°, confirming the α-effect is virtually zero.
4. Both systems show orientations of the EMF components do not depend on microphysical dissipation properties[37].
5. Both systems find the dynamo is driven by large-scale energy-containing flows. Thus, the dynamo growth rate, as measured in simulations of the laboratory MDE[67],

is asymptotically independent of the magnetic Reynolds number Rm. Compare this with a dynamo driven by near-viscous-scale motions, where the growth rate scales as $Rm^{1/2}$.

These findings suggest that the jet-driven dynamos are present in laboratory and nature.

XI. Relevance of the ϒ-dynamo to astrophysical plasmas and BNS mergers.

We address here whether the reported dynamo mechanism is relevant in astrophysical plasmas. The shear-flow-driven dynamo exists in a wide variety of astrophysical systems. We shall therefore present only two specific cases.

Binary Neutron Star (BNS) Mergers: Global GRMHD simulations of BNS mergers show the shear flow profile at the merger interface is similar to the flow profile this work considers. The shear layer half-width is estimated[5] to be $a \approx 10$–15 m (the estimate depends on the grid resolution, and a physically converged width has yet to be established). Since this shear layer appears at small scales of global simulations, the flow velocity is generally $U_0 \lesssim 0.1c$. Within the shear layer, the speed is even smaller. While the spacetime curvature effects are important at the global scale, they are very weak and are amenable to being transformed away in this extremely thin shear layer. This was exploited by Price and Rosswog[7], who used Newtonian KH simulations of BNS mergers. While compressibility introduces adjustments to the KH growth rates, studies of compressible KH systems have shown similar dynamics of the instability as observed in incompressible systems[7,68]. These justify the incompressible model for the first study of the reported new dynamo mechanism.

Major current challenges of BNS merger simulations include the use of unrealistically large-amplitude initial magnetic field and the choice of initial field topology (dipolar fields of $\sim 10^{13}$–10^{15} G are often considered)[6,7,69,70]. However, neither the amplitude nor the topology is supported by astrophysical observations. Observations of Gyr-old neutron stars[71,72] show that their initial total magnetic fields are on the order of $<10^{8}$–10^{10} G. Initial topology of

realistic BNS magnetic fields is multipolar and complex. There are some debates on whether realistic magnetic fields that are initially weak can actually be amplified to magnetar-strength fields. Global relativistic simulations do not capture all KH-unstable wavenumbers appearing at smaller scales in their resolution-limited simulations[5]. They produce increasingly strong magnetic fields with increased grid-resolution.

It is in the context of the preceding paragraph that the results of this work find significance. The results show that, even when the initial large-scale magnetic field is zero, the KH instability generates strong large-scale fields in milliseconds from infinitesimal magnetic fluctuations. Such strong fields are then advected outward to cover the surface of the remnant, impacting observables such as electromagnetic emissions, detected by the LIGO-Virgo-KAGRA collaboration[42]. A proper modeling of BNS merger requires a detailed understanding of the KH dynamo, as the generated magnetic fields can significantly impact the merger time and radiated gravitational waves[8,73]. These fields are potentially responsible for the post-merger evolution of the resultant compact object via efficient transport of angular momentum by turbulence. Other observable consequences include the formation of extraordinarily powerful jets, which depend on the topology and strength of the magnetic fields formed during the BNS mergers. This work provides a foundational framework that can be used to capture the dynamo effects of unresolved KH fluctuations in global simulations[44,74].

The Solar Magnetism: The large-scale poloidal field generation mechanism in the Sun is modeled using ad-hoc, fine-tuned profile of the α-coefficient[75]. The present work suggests a solar dynamo model where the α-effect is replaced with the Υ-effect arising from the azimuthal vorticity of the large-scale solar meridional circulation[14,15]. This azimuthal vorticity contributes to the azimuthal EMF ($\boldsymbol{\mathcal{E}} \propto \Upsilon \nabla \times \mathbf{U}$), which should generate poloidal magnetic fields. Additionally, helioseismology informs that solar sub-surface flows and near-surface shear layers possess substantial vorticity. Cross helicity has been measured at the solar surface using the data from the Hinode satellite and the Swedish 1-m Solar Telescope[76]. Numerical simulations indicate that the normalized cross-helicity is closer to

unity near the solar surface[46]. Thus, the near-surface shear layers[12,77] are the potential sites for the generation of magnetic fields via the vorticity-induced ϒ-dynamo.

XII. How does the jet-driven ϒ-dynamo differ from the classical and other dynamos?

Perhaps the most popular dynamo is the α^2-dynamo[20]. A large-scale magnetic field B_x evolves as $(\partial_t-\eta\nabla^2)B_x=\hat{\mathbf{e}}_x\cdot(\nabla\times\boldsymbol{\mathcal{E}})$. The mean turbulent EMF $\boldsymbol{\mathcal{E}}$ is $\boldsymbol{\mathcal{E}}=\alpha\mathbf{B}-\beta\nabla\times\mathbf{B}$ for helical turbulence[24]. Since B_x couples to another component B_y (or B_z) of the large-scale magnetic field, a way to close the dynamo loop is to write $(\partial_t-\eta\nabla^2)B_y=\hat{\mathbf{e}}_y\cdot(\nabla\times\boldsymbol{\mathcal{E}})$ and assume, again, $\boldsymbol{\mathcal{E}}=\alpha\mathbf{B}-\beta\nabla\times\mathbf{B}$. One of the two steps of the α^2-dynamo is replaced by the Ω-effect if there exists a large-scale flow whose gradient (magnitude given by Ω) points in the direction of the mean magnetic field. This $\alpha\Omega$-dynamo has been numerically observed to be replaced by an $A\Omega$-dynamo in a case of a linear shear flow, where A is to-this-date an unconfirmed mechanism existing in their simulation[78]. A variant of this dynamo is where A is replaced with an anisotropic[23] turbulent diffusion β_{ij}. These and other dynamos share a common feature: The two steps of the dynamo couple two components of large-scale magnetic fields, because all these dynamo processes assume that $\boldsymbol{\mathcal{E}}$ depends on $\mathbf{B}$ and its spatial properties.

We highlight how the jet-driven ϒ-dynamo is fundamentally different from the classical and other dynamos. When a large-scale shear flow $\mathbf{U}$ is present, the postulated generalized mean EMF[4] is $\boldsymbol{\mathcal{E}}=\Upsilon\nabla\times\mathbf{U}-\beta\nabla\times\mathbf{B}$, where $\Upsilon\propto\langle\tilde{\mathbf{u}}\cdot\tilde{\mathbf{b}}\rangle$ measures the alignment between turbulent flow $\tilde{\mathbf{u}}$ and turbulent magnetic field $\tilde{\mathbf{b}}$. Hence, the mean magnetic field B_x along the direction of the mean flow U_x evolves as

$$[\partial_t - (\eta+\beta)\nabla^2]B_x=\hat{\mathbf{e}}_x\cdot[\nabla\times(\Upsilon\nabla\times U_x)]. \qquad \text{(S28)}$$

It is *not* necessary to write the evolution equation of the passive components B_y (or B_z) because Eq. (S28) couples only to U_x, β, and ϒ. Since the traditional mean-field kinematic dynamo coefficients (e.g., α, β, A, β_{ij}) are justifiably constants in time, it is tempting to assume that ϒ is also a constant. This suggests B_x grows only linearly in time[79,80]. Upon

inspection, we realize that β (similar to α) depends on turbulent flow only, but Υ depends also on the magnetic field fluctuations. Since the mean and fluctuations of magnetic fields are inevitably coupled, and both grow at the same rate in the kinematic phase—as we have observed in simulations—Υ grows exponentially in time.

To obtain the correct growth of B_x in Eq. (S28), we analytically derive a self-consistent evolution equation for Υ, which measures cross-helicity in fluctuations. We find that the volume-averaged turbulent cross-helicity Υ evolves as

$$(\partial_t + c)\Upsilon = f(B_x), \qquad \text{(S29)}$$

where c is a constant, and $f(B_x)$ is a linear operator that integrates over volume the mean field B_x with a weight factor, which depends on the mean flow U_x. Thus, Eqs. (S28) and (S29) are linearly coupled equations and produce exponential solutions. Because of the inhomogeneity in the mean flow, the solutions require calculations in Fourier space. Since the calculations are lengthy and technical, we will report the details of the calculations in a forthcoming publication.

This work also presents an interpretation, visualization, and comparison of the non-traditional Υ-dynamo with the traditional dynamo; see Fig. 3**a**. We expect the Υ-effect to drive the dynamo of Ref. 81. The Υ-effect may exist in the dynamo of Ref. 82, as well.

Differences between the Υ- and Ω-effects: The Υ-effect arises in a mean-field theory where the interactions between turbulent fluctuations are averaged. The Ω-effect does not require a mean-field theory and simply represents the straining of the large-scale magnetic field **B** by the large-scale flow **U**. The large-scale field **B**, in general, evolves as

$$\partial_t \mathbf{B} = \nabla \times [(\mathbf{U} \times \mathbf{B}) + \boldsymbol{\mathcal{E}}] + \eta \nabla^2 \mathbf{B}, \qquad \text{(S30)}$$

where $\boldsymbol{\mathcal{E}}=\langle\tilde{\mathbf{u}}\times\tilde{\mathbf{b}}\rangle$ is the turbulent electromotive force averaged suitably over some scales. Using a generalized mean-field theory $\boldsymbol{\mathcal{E}}=\alpha\mathbf{B}-\beta\nabla\times\mathbf{B}+\Upsilon\nabla\times\mathbf{U}$, we simplify Eq. (S30) to

$$\partial_t\mathbf{B}=\underbrace{-\Upsilon\nabla^2\mathbf{U}}_{\substack{\Upsilon\text{-effect}\\(\text{source})}}+\underbrace{\beta\nabla^2\mathbf{B}}_{\substack{\beta\text{-effect}\\(\text{sink})}}+\underbrace{\alpha\nabla\times\mathbf{B}}_{\substack{\alpha\text{-effect}\\(\approx 0)}}+\underbrace{\mathbf{B}\cdot\nabla\mathbf{U}}_{\substack{\Omega\text{-effect}\\=0}}+\cdots, \qquad \text{(S31)}$$

where … represents terms not relevant here. How the KH dynamo operates is indicated by the text below each term.

The jet-driven Υ-dynamo presented in this work is radically different from the classical and other dynamos in many fundamental ways as summarized above.

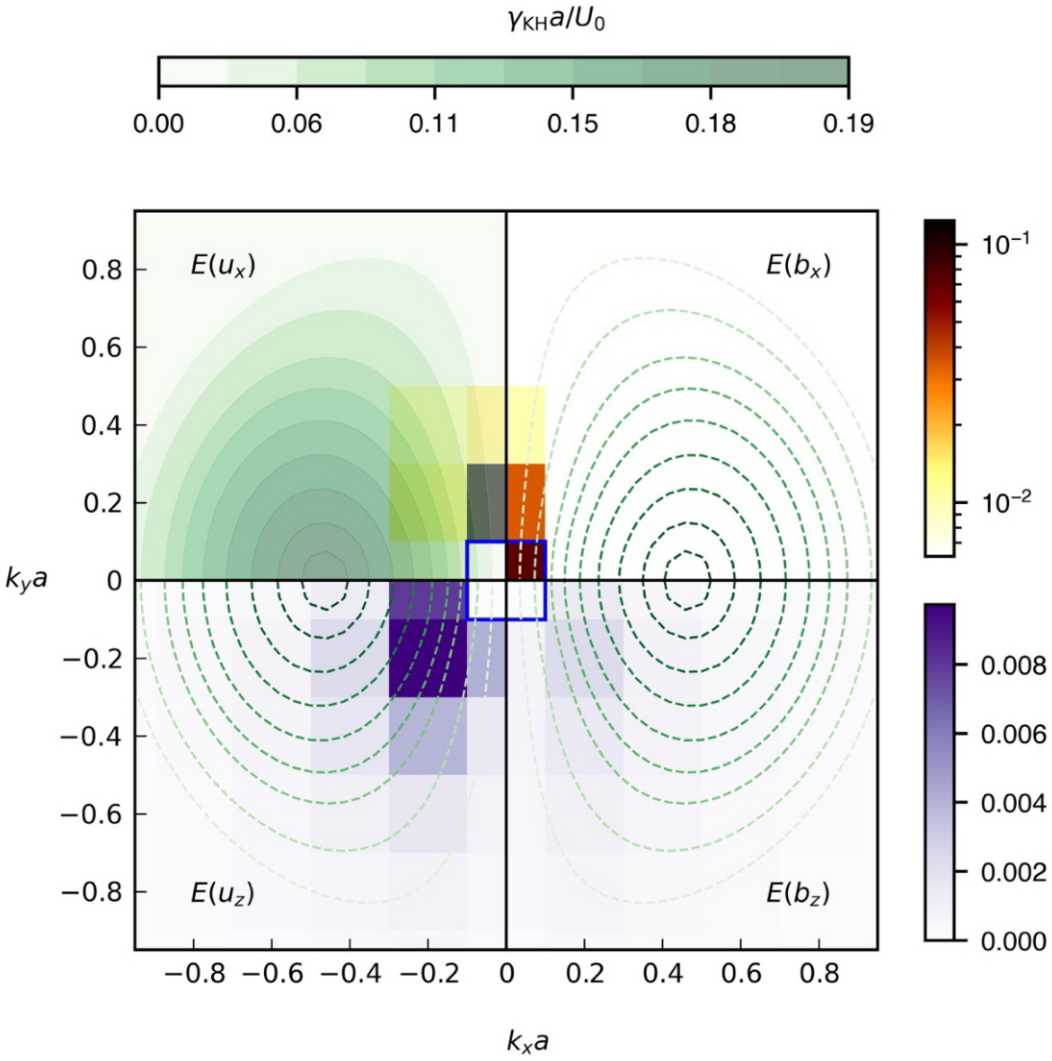

Figure 8.5: **Anisotropic growth rate spectrum of the KH instability, along with the spectra of energies.** The mean flow is directed along x and varies along z. The spectrum of the linear growth rate γ_{KH} of the KH instability is anisotropic. The growth rate is the largest around $\mathbf{k}=(\pm 0.5, 0)$, which represents the 2D KH instability. The growth rate is zero for $k_x=0$ and $k_y\neq 0$. The square boxes in the upper half of the figure show time-averaged spectra of energies in horizontal field $E(b_x)$ and horizontal flow $E(u_x)$ (the contribution of the initial mean flow is removed). These spectra share the upper right-hand logarithmic color bar, extending from yellow to black. The square boxes in the lower half of the figure show time-averaged spectra of energies in vertical field $E(b_z)$ and vertical flow $E(u_z)$. These share the lower right-hand linear color bar, extending from white to blue. The center of each square box represents the wavenumber resolved in the nonlinear simulation (only a small part of the wavenumber range is shown, as the KH instability exists at large scales $|ka|\lesssim 1$). The special square box centered at $\mathbf{k}=\mathbf{0}$ is shared by four quadrants. All quantities are measured using a and U_0.

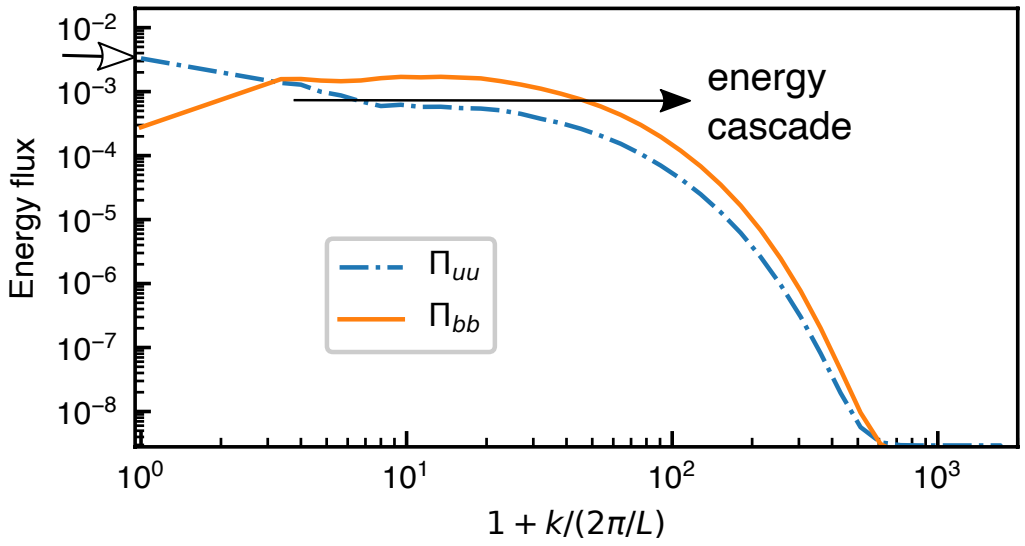

Figure 8.6: **Cascade of kinetic and magnetic energies from large scales to small scales.** Nonlinear energy flux through spectral space is measured in a simulation with 4096 × 4096 × 8192 grid points. Here, $k=(k_x^2+k_y^2)^{1/2}$. The energy flux is integrated over the z-axis. A constant energy flux in k-space indicates an inertial range. Energy injected externally to the mean flow (shown with a white-headed arrow on the left margin) is cascaded to small scales, as shown by Π_{uu}, which measures energy flux due to transfer of energy between two velocity fluctuations. Magnetic-to-magnetic energy flux Π_{bb} shows a prominent small-scale cascade over two decades of inertial range. This analysis shows that the ϒ-dynamo arising in KH-unstable shear flow is *not* due to inverse cascade of energy. The ϒ-dynamo is due to energy transfer from large-scale jets to the mean field, as demonstrated in Extended data Fig. 3.

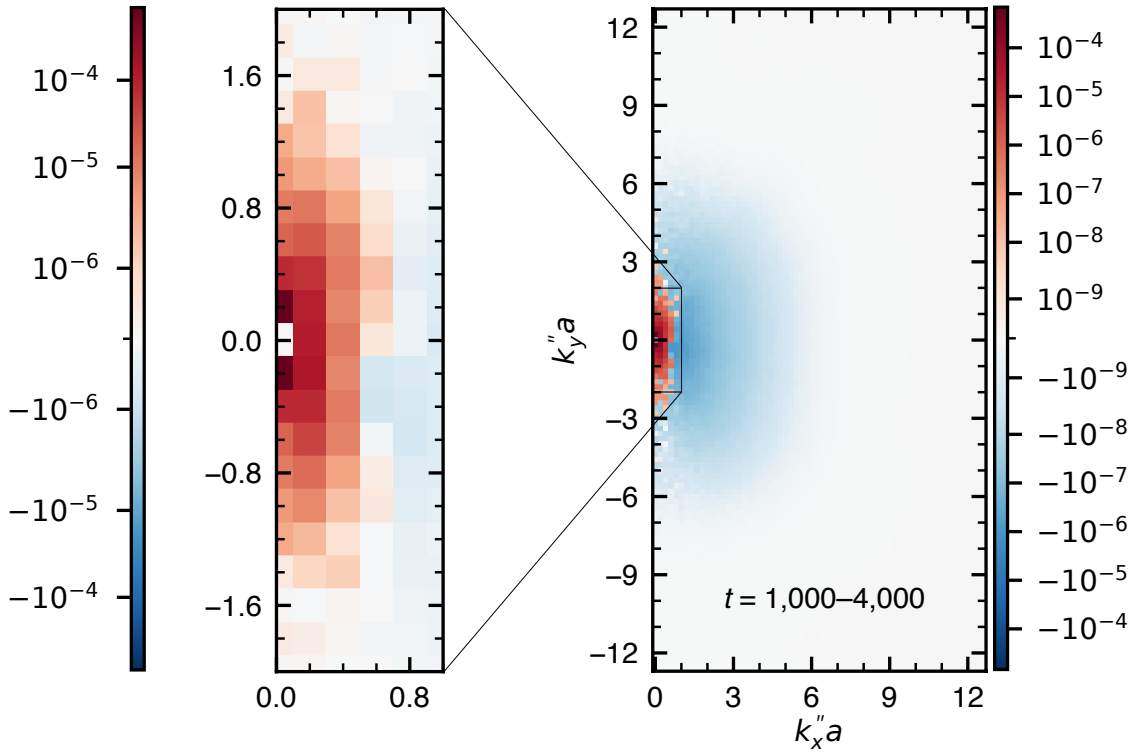

Figure 8.7: **Spectrum of nonlinear energy transfer to the mean magnetic field via turbulent field-line stretching.** This figure confirms that the large-scale velocity fluctuations give energy to the mean magnetic field (red)—and that the small-scale velocity fluctuations receive energy from the mean magnetic field (blue). The shown quantity is $T(\mathbf{k}'')$, which represents the rate of nonlinear energy transfer to the mean field $\hat{b}_x(k_x=0, k_y=0)$. Mathematically, $T(\mathbf{k}'') = \langle \hat{b}_x^*(0,0)[\hat{\mathbf{b}}(\mathbf{k}')\cdot\nabla\hat{u}_x(\mathbf{k}'')]\rangle_z$, where $\mathbf{k}''=(k_x'',k_y'')$ is the horizontal wavenumber of the velocity $\mathbf{u}$ and $\mathbf{k}'=(k_x',k_y')$ is the horizontal wavenumber of the magnetic field $\mathbf{b}$; the wavenumber-triad constraint imposes $(0,0) = \mathbf{k}' + \mathbf{k}''$. The quantities $\hat{\mathbf{b}}(\mathbf{k}')$ and $\hat{u}_x(\mathbf{k}'')$ represent the horizontally Fourier-transformed coefficients of magnetic fields and velocity with wavenumbers $\mathbf{k}'$ and $\mathbf{k}''$, respectively; these quantities are retained in the physical domain z before integrating the transfer function along z. The quantity $\hat{b}_x^*(0,0)$ is the horizontally-Fourier-transformed, complex-conjugated, x-directed mean magnetic field, whose energy is around two orders of magnitude larger than the y-directed mean field in the nonlinear phase. The mean field $\hat{b}_x(0,0)$ is inhomogeneous in z (as is the mean flow); the operation $\langle\cdot\rangle_z$ averages the nonlinear transfer function in z. The transfer function is time-averaged over the saturated phase (t = 1000–4000). Of particular note is the extraordinary contribution of the large-scale jets, especially with wavenumber $(k_x'',k_y'')=(0,0.2)$, which contribute the largest in the mean-field generation. This is consistent with Fig. 3. The square box at $k_x''=k_y''=0$ is white because the mean flow does not directly couple to the mean field in this system (the so-called Ω-effect[32] is zero).

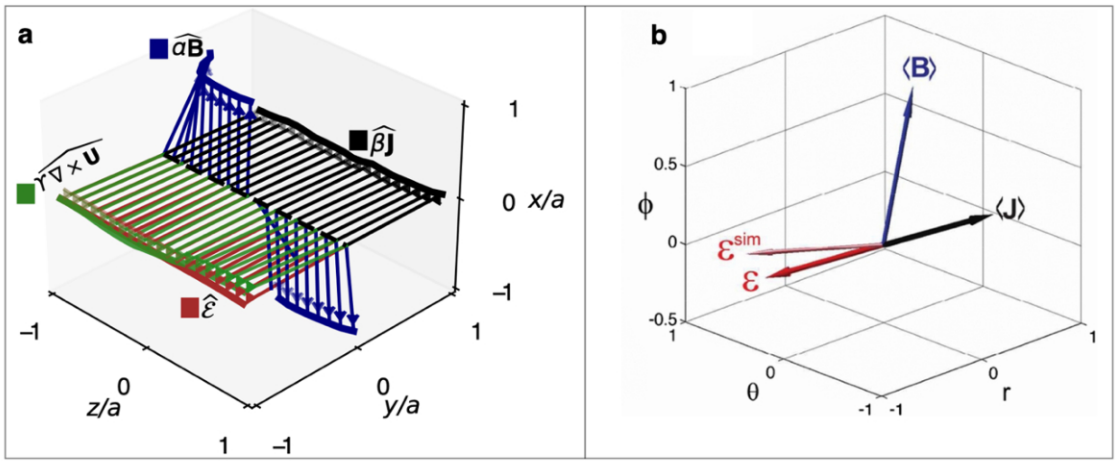

Figure 8.8: **Comparison of three-dimensional unit vectors (shown with carets) of different components of the mean turbulent EMF $\mathcal{E}$ from a KH-instability-driven dynamo simulation in a and from the Madison Dynamo Laboratory Experiment[37] in b.** With respect to $\mathcal{E}$, the β-diffusion term is anti-aligned, and the α-term is orthogonal (indicating the non-helical nature of dynamo). A near-identical orthogonal orientation of the α-term was measured in the Madison Dynamo Experiment[37] in panel **b**. In the Madison Dynamo Experiment, the vorticity is considerably large in the radial direction[38]. This is consistent with the dominance of the observed radial EMF, suggesting the important role of the large-scale vorticity-effect[4] in turbulent EMF. Similarly, the Υ-term in panel **a** is perfectly co-aligned with the mean EMF $\mathcal{E}$. Here, the novel jet-driven Υ-dynamo, arising from the large-scale vorticity, is confirmed to be the source of the dynamo. Diagram in **b** reproduced with permission of the AAS from figure 3 in ref. 37.

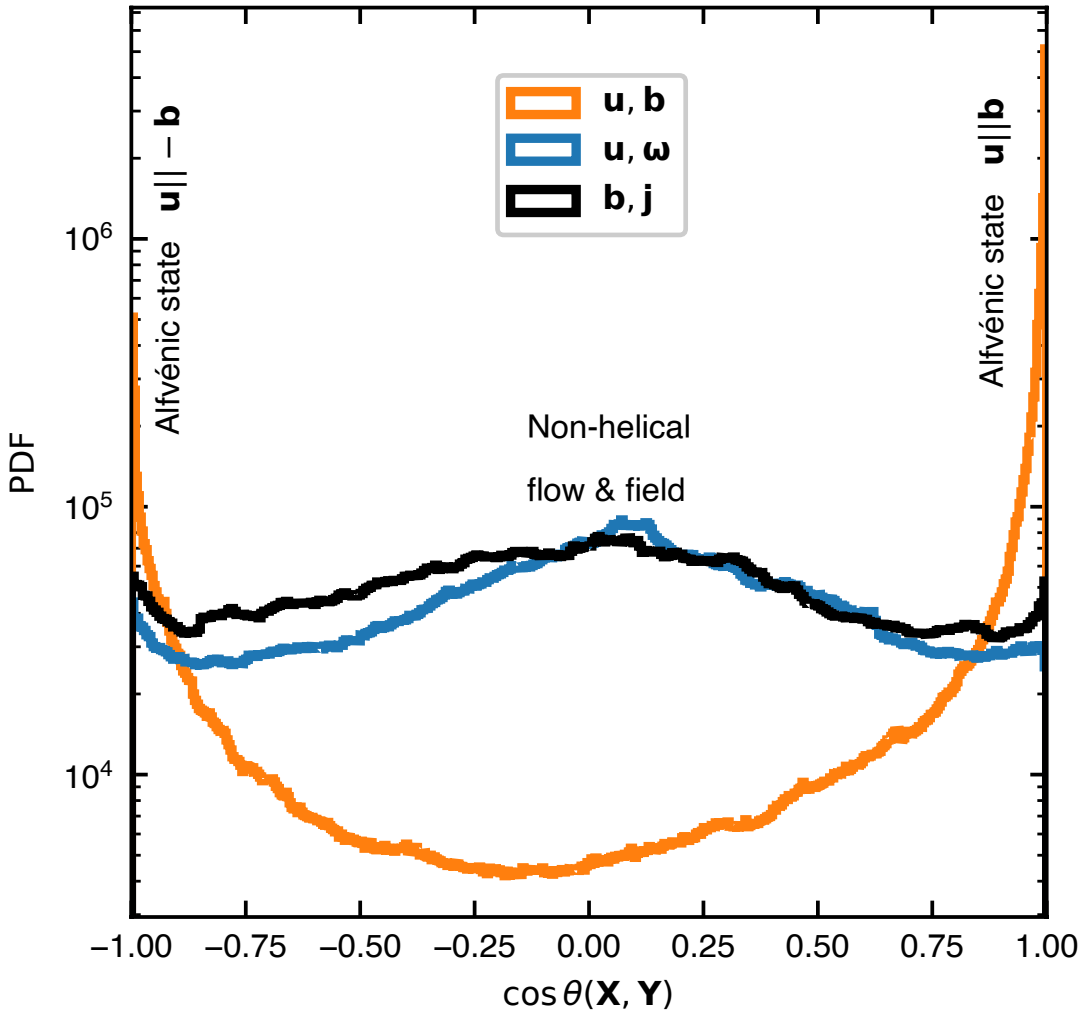

Figure 8.9: **PDF of cosine of angle between u, b, ω(=∇×u), and j(=∇×b), in a simulation with 4096 × 4096 × 8192 grid points.** The turbulent flow and fields measured at the shear layer are non-helical and close to pure Alfvénic states (orange curve), which explains why the ϒ-effect dominates in the mean EMF. For the pure Alfvénic states, α is zero; β and ϒ are similar and are not impacted by the non-kinematic (flow-evolution) effect in the same manner as the α is (see Methods Sec. VI). A large-scale steady shear flow induces an "imbalanced" MHD turbulence (asymmetry of the orange curve) and thus drives the dynamo via the non-zero ϒ-coefficient. Similar PDFs of dominant cross-helicity and non-helical flows were recently detected in the magnetosheath turbulence observed by the Magnetospheric Multiscale Spacecraft[49].

Table 8.1: A list of commonly used symbols and meanings.

Symbols	Meanings
$\langle\cdot\rangle_{x,y}$	(x,y)-average, also called *mean*
$\langle\cdot\rangle_{x}$	x-average, also called *zonal*
$\langle\cdot\rangle_{y}$	y-average
$\mathbf{u}_0$	Initial mean flow
$\mathbf{b}_0$	Initial mean magnetic field
$\mathbf{U}$	Instantaneous mean flow
$\mathbf{B}$	Instantaneous mean magnetic field
$\tilde{\mathbf{u}}$	Flow fluctuations (i.e., without the mean)
$\tilde{\mathbf{b}}$	Magnetic-field fluctuations (i.e., without the mean)
U_0	Amplitude of the mean flow
a	Half-width of the mean flow (shear layer)
τ_{grow}	One e-folding time of the KH instability
Re	Fluid Reynolds number ($Re=U_0a/\nu$)
Rm	Magnetic Reynolds number ($Rm=U_0a/\eta$)
Pm	Magnetic Prandtl number ($Pm=Rm/Re$)
$\mathbf{u}^{k_x,k_y}$	Flow with wavenumber (k_x,k_y)
$\mathbf{b}^{k_x,k_y}$	Magnetic field with wavenumber (k_x,k_y)
$\boldsymbol{u}_{\boldsymbol{x}}^{\mathbf{0},k_y}$	Zonal jets with wavenumber (k_x=0, k_y)
$\boldsymbol{\mathcal{E}}$	Electromotive force (EMF)
α	Parker's alpha-effect
β	Turbulent (beta-) diffusion
Υ	Upsilon dynamo source (a measure of turbulent cross-helicity $\tilde{\mathbf{u}}\cdot\tilde{\mathbf{b}}$)
Ω	A measure of omega-effect $\mathbf{B}\cdot\nabla\mathbf{U}$, which is zero in this work

References for Methods

50. Tripathi, B., Terry, P. W., Fraser, A. E., Zweibel, E. G. & Pueschel, M. J. Three-dimensional shear-flow instability saturation via stable modes. *Phys. Fluids*. **35**, 105151 (2023).

51. Burns, K. J., Vasil, G. M., Oishi, J. S., Lecoanet, D. & Brown, B. P. Dedalus: A flexible framework for numerical simulations with spectral methods. *Phys. Rev. Research*. **2**, 023068 (2020).

52. Ascher, U. M., Ruuth, S. J. & Spiteri, R. J. Implicit-explicit Runge-Kutta methods for time-dependent partial differential equations. *Appl. Numer. Math.* **25**, 151 (1997).

53. Wang, D. & Ruuth, S. J. Variable step-size implicit-explicit linear multistep methods for time-dependent partial differential equations. *J. Comput. Math.* **26**, 838 (2008).

54. Mininni, P. D., Alexakis, A. & Pouquet, A. Shell-to-shell energy transfer in magnetohydrodynamics II. Kinematic dynamo. *Phys. Rev. E.* **72**, 046302 (2005).

55. Alexakis, A., Mininni, P. D. & Pouquet, A. Shell-to-shell energy transfer in magnetohydrodynamics. I. Steady state turbulence. *Phys. Rev. E*. **72**, 046301 (2005).

56. Tripathi, B., Fraser, A. E., Terry, P. W., Zweibel, E. G., Pueschel, M. J. & Fan, R. Codes, Data, and Additional Materials for "Large-Scale Dynamos Driven by Shear-Flow-Induced Jets". *Zenodo*. (2025). https://doi.org/10.5281/zenodo.17162239

57. Tripathi, B., Terry, P. W., Fraser, A. E., Zweibel, E. G. & Pueschel, M. J. Mechanism for sequestering magnetic energy at large scales in shear-flow turbulence. *Phys. Plasmas.* **29**, 070701 (2022).

58. Smith, K. M., Caulfield, C. P. & Taylor J. R. Turbulence in forced stratified shear flows. *J. Fluid Mech.* **910**, A42 (2021).

59. Marston, J. B., Conover, E. & Schneider, T. Statistics of an Unstable Barotropic Jet from a Cumulant Expansion. *J. Atmos. Sci.* **65**, 1955 (2008).

60. Cope, L., Garaud, P. & Caulfield, C. The dynamics of stratified horizontal shear flows at low Péclet number. *J. Fluid Mech.* **903**, A1 (2020).

61. Pueschel, M. J., Jenko, F., Told, D. & Büchner, J. Gyrokinetic simulations of magnetic reconnection. *Phys. Plasmas*. **18**, 112102 (2011).

62. Pueschel, M. J., Told, D., Terry, P. W., Jenko, F., Zweibel, E. G., Zhdankin, V. & Lesch, H. Magnetic reconnection turbulence in strong guide fields: Basic properties and application to coronal heating. *Astrophys. J. Suppl. Ser.* **213**, 30 (2014).

63. Gruzinov, A. V. & Diamond, P. H. Self-consistent mean field electrodynamics of turbulent dynamos. *Phys. Plasmas*. **2**, 1941 (1976).

64. Biglari, H., Diamond, P. H. & Terry, P. W. *Phys. Fluids B*. **2**, 1 (1990).

65. Townsend, A. A. *The Structure of Turbulent Shear Flow*. 2nd Ed. (Cambridge University Press, Cambridge, 1976).

66. Verma, M. K. *Energy Transfers in Fluid Flows: Multiscale and Spectral Perspectives.* (Cambridge University Press, Cambridge 2019).

67. Reuter, K., Jenko, F. & Forest, C. B. Turbulent magnetohydrodynamic dynamo action in a spherically bounded von Kármán flow at small magnetic Prandtl numbers. *New J. Phys.* **13**, 073019 (2011).

68. Baiotti, L., Giacomazzo, B. & Rezzolla, L. Accurate evolutions of inspiralling neutron-star binaries: Prompt and delayed collapse to a black hole. *Phys. Rev. D*. **78**, 084033 (2008).

69. Most, E. R. & Quataert, E. Flares, Jets, and Quasiperiodic Outbursts from Neutron Star Merger Remnants. *Astrophys. J. Lett.* **947**, L15 (2023).

70. Combi, L. and Siegel, D. M. Jets from Neutron-Star Merger Remnants and Massive Blue Kilonovae. *Phys. Rev. Lett.* **131**, 231402 (2023).

71. Olausen, S. A. & Kaspi, V. M. The McGill Magnetar Catalog. *Astrophys. J. Suppl. Ser.* **212**, 6 (2014).

72. Bahramian, A. & Degenaar, N. *Low-Mass X-ray Binaries*. (Springer Nature, Singapore, 2022).

73. Anderson, M. et al. Magnetized Neutron-Star Mergers and Gravitational-Wave Signals. *Phys. Rev. Lett.* **191101**, 100 (2008).

74. Aguilera-Miret, R., Viganò, D. & Palenzuela, C. Universality of the Turbulent Magnetic Field in Hypermassive Neutron Stars Produced by Binary Mergers. *Astrophys. J. Lett.* **926**, L31 (2022).

75. Charbonneau, P. Dynamo models of the solar cycle. *Living Rev. Sol. Phys.* **17**, 4 (2020)

76. Rüdiger, G., Küker, M. & Schnerr, R. S. Cross helicity at the solar surface by simulations and observations. *Astron. and Astrophys.* **546**, 23 (2012).

77. Brandenburg, A. The Case for a Distributed Solar Dynamo Shaped by Near-Surface Shear. *Astrophys. J.* **625**, 539 (2005).

78. Yousef, T. A. et al. Generation of Magnetic Field by Combined Action of Turbulence and Shear. *Phys. Rev. Lett.* **100**, 184501 (2008).

79. Blackman, E. G. Mean Magnetic Field Generation in Sheared Rotators. *Astrophys. J.* **529**, 138 (2000).

80. Brandenburg A. & Urpin, V. Magnetic fields in young galaxies due to the cross-helicity effect. *Astron. and Astrophys.* **332**, 41 (1998).

81. Elias-López, A., Del Sordo, F. & Viganò, D. Vorticity and magnetic dynamo from subsonic expansion waves. *Astron. and Astrophys.* **677**, 46 (2023).

82. Hughes, D. W. & Proctor, M. R. E. Large-scale Dynamo Action Driven by Velocity Shear and Rotating Convection. *Phys. Rev. Lett.* **102**, 044501 (2008).

9 **PAPER G**: THE LIFE-CYCLE OF THE JET-DRIVEN SHEAR-FLOW DYNAMO

A version of this chapter is under review for publication in Phys. Plasmas.

ABSTRACT

Shear flows can generate and sustain large-scale, quasi-cyclic, self-organized magnetic fields in three dimensions via a process called the dynamo. Here, the essential steps of a dynamo process are identified and confirmed using energy transfer analyses of turbulence driven by the Kelvin–Helmholtz (KH) instability. The dynamo cycle begins with an (x, y)-averaged mean horizontal shear-flow $U_x(z)$, which is maintained externally. The KH instability of this flow nonlinearly excites KH-stable, x-invariant, y-varying vertical flows and magnetic fields—labeled **u**-rolls and **b**-rolls. These vertical perturbations are strained by the mean shear flow to generate horizontal x-invariant, y-varying flows and magnetic fields. These are labeled zonal jets and zonal magnetic fields. The zonal jets then stretch the **b**-rolls, creating an (x, y)-averaged mean horizontal magnetic field. The z-gradient of the mean magnetic field saturates when the **u**-rolls advect the mean magnetic field vertically. The zonal jets are sustained by energy transfer from the primary KH instability of the mean shear flow. These processes are robust under key parameter variations. This dynamo cycle explains the operation mechanism of a mean-field dynamo theory—the mean-vorticity effect—applicable in a host of plasmas.

9.1 Introduction

Dynamo action—the generation of magnetic fields and their sustenance against resistive dissipation in magnetofluids and plasmas—is a long-standing research topic [8, 9, 39–43, 51, 52, 74, 134, 245–252], and is traditionally thought to be driven by helical turbulent fluid motions acting on an imposed large-scale field [4, 8, 9, 51, 52, 245]. However, a recent study [253] reported dynamo action even in the absence of an initial large-scale field via a non-traditional mean-field theory—the mean-vorticity effect [66]. This study presented a surprising finding that the dynamo-generated large-scale field is nearly identical in spatial profile to that of the large-scale shear flow. The primary objective of this work is to identify the mechanisms via which the large-scale flow generates the large-scale field, and the mechanisms via which the large-scale field saturates. There exist three broad issues: identification of the chain of steps involved in the dynamo, understanding of the role of the Kelvin–Helmholtz (KH) instability arising from the large-scale shear flow [10], and classification of the steps of the dynamo as they relate to either hydrodynamics or magnetic fields. Since the chain of these complex turbulent processes is not evident in a simple mean-field theory [9], a thorough analysis is required to identify the chain of steps by which the energy in the large-scale shear flow accumulates in the large-scale field.

To understand the chain of steps in a dynamo that generates large-scale field, one needs to analyze the nonlinear energy transfer channels by which the large-scale field receives energy from certain entities and returns it to other entities. The ultimate energy source for the large-scale-vorticity-driven dynamo [66] is the large-scale shear flow, which then becomes linked to a large-scale field. This chain of links connecting the large-scale flow and large-scale field can in principle involve a large number of nonlinear interactions, although in practice the number is often small. Identification

of these interactions requires detailed analyses of magnitude and direction of nonlinear energy transfers.

The linear instability of a shear flow deposits energy in large-scale fluctuations [10], which may directly induce a dynamo—or, the linear instability may nonlinearly excite fluctuations at other scales, which may then induce a dynamo. Usually, the large-scale instability-related fluctuations break down into small scales, when the unstable shear flow relaxes toward a stable configuration due to continual energy extraction from the freely-evolving shear flow [82]. Under such a scenario, large-scale shear flow rapidly generates [21, 70, 71, 127] velocity and magnetic fields at small scales—until the turbulence has decayed and the dynamo action has stopped. By this time, the slowly-evolving large-scale magnetic fields may not have been generated. However, when the large-scale shear flow is forced so as to maintain its initial unstable equilibrium — a natural scenario in various astrophysical environments [117–119, 143, 190, 196] — turbulent eddies exist at large instability scales as well as at small scales. The large-scale eddies continuously extract energy from the large-scale shear flow, nonlinearly distribute energy to other scales, and thus sustain quasi-stationary turbulence with a possible continuous dynamo action, allowing the slow emergence of large-scale magnetic fields. Addressing whether these large-scale magnetic fields are a direct product of large-scale instability-generated fluctuations or a byproduct of small-scale turbulence requires an understanding of turbulent energy transfers.

The operation of the dynamo driven by the KH instability involves a chain of steps, some of which are purely hydrodynamic and others involve magnetic fields. The linear instability of the large-scale shear flow can nonlinearly excite other scales of flow and magnetic fields, in particular both small and large. For example, a recent three-dimensional *hydrodynamic* KH-driven turbulence study [1] showed the emergence of large-scale nonlinear fluctuations that do not vary in the direction of the large-scale

shear flow but vary in the direction orthogonal to the two-dimensional shear-flow plane. These inherently three-dimensional fluctuations are linearly stable but are nonlinearly excited by the instability to large amplitudes [1]. These nonlinear, hydrodynamic, anisotropic, large-scale fluctuations appear in the form of jets [1, 254] — similar to zonal flows in fusion plasmas and planetary atmospheres [176, 255, 256]. The large-scale jets have intrinsically different properties from those of the nonlinear fluctuations at small, dissipative scales. Among these properties, the following critically impact the dynamo: First, the energy-containing jets at large-scales strongly stretch fluctuation fields compared to that by the inertial-range eddies, which are less-energetic (in the presence of large-scale coherent structures, the turbulence spectrum falls off very rapidly compared to the slow Kolmogorov spectrum limited to a homogeneous turbulence). Second, alignment between flow and fields—in addition to their amplitudes—is crucial for a dynamo action: The large-scale jets stretch fluctuation fields coherently [257], whereas the small-scale turbulent flows stretch fields randomly [115, 133]. Third, the jets directed along the mean flow are exact solutions to the nonlinear (magneto-)hydrodynamic equations, similar to the ElsÃ¤sser fields [31, 253]. This exact-soluble property makes these jets resilient to perturbations. While these features of the jets are favorable for large-scale dynamo, the magnetic fields may back-react on the jets via the Lorentz force. Hence, if the shear-flow dynamo is to be better-understood, an analysis of the interaction between the jets and magnetic fields is crucial.

To address the foregoing issues, we perform an ensemble of high-resolution three-dimensional instability-driven magnetohydrodynamic (MHD) turbulence simulations using spectral methods [121]. We conduct comprehensive energy transfer analyses to track the magnitude and direction of energy transfer in wavenumber-triad interactions [145].

The chief finding of this work is the identification of nonlinear interactions of

turbulent flow and magnetic fields that take energy away from the large-scale shear flow and ultimately deposit it in the large-scale magnetic field; the latter two are not directly coupled but are indirectly coupled via turbulence. The steps for this indirect coupling operate in the following way: The large-scale shear flow—which we maintain externally and continuously—excites the KH instability; the KH instability induces hydrodynamic jets; the jets create large-scale magnetic fields via turbulent field-line stretching; and the large-scale fields saturate when the horizontal jets create large-scale fields at a rate that is balanced approximately by the rate at which the large-scale fields are turbulently transported by fluctuating vertical flows. That is, the rate of field-gradient steepening by jets balances the rate of field-gradient flattening by turbulence. This series of steps produces a dynamically-evolving dynamo. Because the jets are nonlinearly driven, this process is observed to develop in the turbulent phase over very long time scales relative to the short linear KH growth time. When the large-scale flow is not maintained, turbulence decays quickly before the reported dynamo emerges.

This article is organized in the following way. Section 9.2 describes the system setup. Section 9.3 presents an overview of the dynamo cycle. Detailed confirmation of the dynamo cycle is presented in Sec. 9.4. In Sec. 9.5, the different elements of the dynamo are measured by varying control parameters. Broader implications of this work are discussed in Sec. 9.6 before concluding in Sec. 9.7.

9.2 MHD-KH dynamo setup

Throughout this article, we label the (x, y)-averaged flow as the *mean* (large-scale) flow. Similarly, we label the (x, y)-averaged magnetic field as the *mean* (large-scale) field.

Governing equations

We evolve the flow $\mathbf{u}$ and magnetic field $\mathbf{b}$ by solving three-dimensional (3D) incompressible MHD equations [25]

$$\partial_t \mathbf{u} - \nu \nabla^2 \mathbf{u} + \nabla P - \frac{\mathbf{j} \times \mathbf{B}_0}{\rho} = -\mathbf{u} \cdot \nabla \mathbf{u} + \frac{\mathbf{j} \times \mathbf{b}_{\rm rem}}{\rho} + \mathbf{f}, \tag{9.1a}$$

$$\partial_t \mathbf{A}_{\rm rem} - \eta \nabla^2 \mathbf{A}_{\rm rem} + \nabla \Psi - \mathbf{u} \times \mathbf{B}_0 = \mathbf{u} \times \mathbf{b}_{\rm rem}, \tag{9.1b}$$

$$\nabla \cdot \mathbf{u} = 0, \tag{9.1c}$$

$$\nabla \cdot \mathbf{A}_{\rm rem} = 0, \tag{9.1d}$$

$$\mathbf{b}_{\rm rem} = \nabla \times \mathbf{A}_{\rm rem}, \tag{9.1e}$$

$$\mathbf{j}_{\rm rem} = \frac{\nabla \times \mathbf{b}_{\rm rem}}{\mu_0}, \tag{9.1f}$$

where ∂_t and ∇ represent differentiation with respect to time and 3D space, respectively; ν and η are kinematic viscosity and electric resistivity, respectively; P is the fluid pressure per unit density ρ; and μ_0 is the vacuum permeability. Following a standard procedure [258], we have separated the total magnetic field into the initial uniform mean field $\mathbf{B}_0$ and the remaining time-evolving field $\mathbf{b}_{\rm rem}$; the total magnetic field in the system is, therefore, $\mathbf{b} = \mathbf{B}_0 + \mathbf{b}_{\rm rem}$. This decomposition separates the *initial* and *time-evolving* fields. The decomposition does not separate spatial spectral modes. So, $\mathbf{b}_{\rm rem}$ includes both *mean and fluctuation* fields.

We write $\mathbf{b}_{\rm rem}$ in terms of the vector potential $\mathbf{A}_{\rm rem}$. This decomposition (9.1e) ensures that the magnetic field $\mathbf{b}_{\rm rem}$ is always divergence-free; the uniform field $\mathbf{B}_0$ is divergence-free. Equation (9.1d) is the Coulomb gauge. The electric current density $\mathbf{j}_{\rm rem}$ is given by Ampere's law (9.1f). The externally applied force per unit mass of the fluid is given by $\mathbf{f}$. Forcing in the magnetic induction equation is avoided [245].

Flow profiles and non-dimensionalization

To investigate the dynamo driven by the KH instability, we consider a mean unstable shear-flow [10] $\mathbf{U}_0$=$U_0 \tanh(z/a)\hat{\mathrm{e}}_x$, where $\hat{\mathrm{e}}_x$ is the unit vector along x. Here, U_0 is the flow-amplitude of the mean shear layer, whose half-width is a.

Throughout this paper, U_0 and a are used to non-dimensionalize parameters, e.g., the fluid Reynolds number is Re=aU_0/ν, and the magnetic Reynolds number is Rm=aU_0/η; the magnetic Prandtl number is Pr=Rm/Re. Time is measured in terms of a/U_0. Energy is measured in terms of U_0^2.

Spectral bases, initial perturbations, boundary conditions, and forcing

The simulation domain size $L_x \times L_y \times L_z$ is measured in units of a; compared to a, a large domain $L_x = L_y = L_z = 10\pi$ is used [82]. Since z is the direction of inhomogeneity (due to the mean shear flow), we expand the state vector corresponding to flow and magnetic fields in z in Chebyshev polynomials.

We seed small-amplitude, multi-mode, divergence-free perturbations in flow and fields, and we randomize the phases of the perturbations at every wavenumber (k_x, k_y). To create these general initial perturbations free of divergences, we first express perturbations in the flow as $\mathbf{u} = \nabla \times \mathbf{C}^u$, and then prescribe a perturbation in the vector $\mathbf{C}^u$, whose j-th component is

$$C_j^u = \hat{\mathrm{e}}_j \, D \, \mathrm{e}^{-\frac{z^2}{\sigma^2}} \Bigg(\sum_{0<|k_x|<k_x^*} \mathrm{e}^{ik_x x} |k_x|^\alpha \mathrm{e}^{i\theta_j(k_x)} \delta_{k_y,0} + \sum_{0<|k_y|<k_y^*} \mathrm{e}^{ik_y y} |k_y|^\alpha \mathrm{e}^{i\theta_j(k_y)} \delta_{k_x,0} + \sum_{\substack{0<|k_x|<k_x^* \\ 0<|k_y|<k_y^*}} \mathrm{e}^{ik_x x} \mathrm{e}^{ik_y y} |k_x|^\beta |k_y|^\beta \mathrm{e}^{i\theta_j(k_x)} \mathrm{e}^{i\theta_j(k_y)} \Bigg), \tag{9.2}$$

where D is the amplitude of the perturbation C_j^u. To create magnetic perturbations $\mathbf{B} = \nabla \times (\nabla \times \mathbf{C}^b)$, we prescribe a similar profile for the vector $\mathbf{C}^b$.

Motivated by our earlier studies on two-dimensional MHD [17, 143, 144] and three-dimensional hydrodynamic shear-flow turbulence [1], we choose a small-amplitude perturbation with $D = 10^{-3}$ to allow a discernible linear evolution of the instability, before it gets nonlinearly modified. To avoid preferential excitation of certain wavenumbers, we require the initial perturbations to have a near-flat spectrum of energy: we take $\alpha = -1$ and $\beta = -1/2$ for the perturbed velocity $\nabla \times \mathbf{C}^u$; we take $\alpha = -2$ and $\beta = -1$ for the magnetic field $\mathbf{B} = \nabla \times (\nabla \times \mathbf{C}^b)$. We use different random phases θ_j for flow and fields at different wavenumbers. The cut-off wavenumbers $k_x^* = k_y^*$ for the initial perturbations are $16k_{\rm min}$, where $k_{\rm min} = 2\pi/L$. The properties of saturated turbulence, however, are independent of these initial choices: We have reproduced statistically the same results using other choices of initial conditions. Here, we choose $\sigma = 2$ (in terms of a). To make the initial perturbations free of divergences in $\mathbf{u}$ and $\mathbf{A}$, we prepare the initial pressure P and initial scalar function Ψ using the respective constraints $P = \nabla^{-2}\nabla\cdot\mathbf{N}_P$ and $\Psi = \nabla^{-2}\nabla\cdot\mathbf{N}_\Psi$, where $\mathbf{N}_P = -(\mathbf{u}\cdot\nabla)\mathbf{u}+(\nabla\times\mathbf{B})\times\mathbf{B}$ and $\mathbf{N}_\Psi = \mathbf{u}\times\mathbf{B}$.

Periodic boundary conditions are applied for x and y. Along the z-axis, where the mean flow is reversed, we use physical boundary conditions: perfectly conducting, no-slip walls that co-move with the flow at the top and bottom $z = \pm L_z/2$. That is, at the boundaries, $A_x = A_y = \Psi = 0$ (equivalently, $j_x = j_y = b_z = 0$), $u_y = u_z = 0$, and $u_x = \pm 1$ (in units of the amplitude U_0). We have performed simulations with extended domains in z and have reproduced similar results of magnetic field evolution.

To focus on the KH-driven dynamo, we maintain the unstable mean flow—by continuously forcing the instantaneous x-directed mean flow toward its initial unstable

profile with the force $\mathbf{f} = f_x \hat{\mathrm{e}}_x$, which has the form

$$f_x = \frac{\langle u_x(t) \rangle_{x,y} - \langle u_x(t{=}0) \rangle_{x,y}}{t_{\mathrm{forcing}}} + F_0, \tag{9.3}$$

where $\langle u_x(t) \rangle_{x,y}$ represents instantaneous x-directed flow that is averaged in x and y. The term F_0 in Eq. (9.3) is insignificant and merely removes the viscous relaxation of the mean shear flow at $t = 0$; this removal helps to attain a true initial MHD equilibrium, with $F_0 + \nu \nabla^2 \langle u_x(t{=}0) \rangle_{x,y} = 0$. The forcing time-scale t_{forcing} is chosen to be adequately short so that the mean flow is continuously replenished before the instability depletes it. The depletion otherwise causes the turbulence to decay and the dynamo to become inactive. The e-folding time of the instability is ≈ 5 (in units of U_0/a); we choose $t_{\mathrm{forcing}} = 0.5$. While the considered forcing may not be fully representative of external drives in every natural system, the chosen forcing profile is general and does maintain large-scale flows that are commonly encountered in various astrophysical environments. These include gravity and convection that continuously generate shear layers in stellar interiors, planetary atmospheres where large-scale shear flows are persistent, the merging of binary neutron stars (BNS) that continuously creates shear layers in between the approaching BNS for an extended time until they fully merge, and secondary KH-unstable shear layers in stars and planets [29, 73, 74, 118, 119, 143, 190, 259]. Equation (9.3) represents a standard forcing that is routinely used in plasma physics and in fluid dynamics as a relaxation operator [117, 118, 196].

To solve Eqs. (9.1a)–(9.1f), we use the pseudospectral τ-method in Dedalus [121], with the standard 3/2 de-aliasing factor to control aliasing errors while computing nonlinearities. We solve linear terms implicitly and nonlinear terms explicitly, using a mixed method, by employing the RK443 [260] and SBDF2 [261] time-stepping schemes.

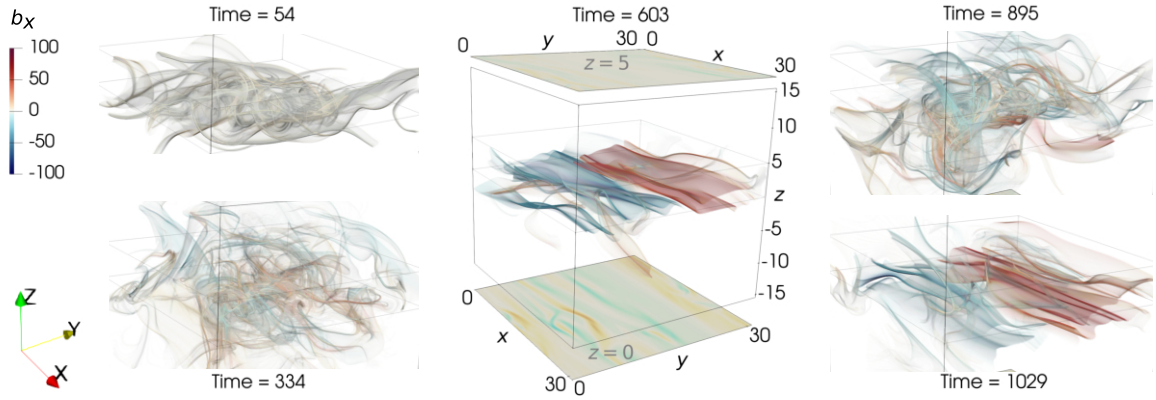

Figure 9.1: Evolution of magnetic fields in a KH-instability-driven dynamo simulation, displaying spontaneous transitions between ordered and disordered phases. The field component b_x is shown only in the region of interest, around z=0, where the gradient of the (x, y)-averaged mean flow is the largest. The first panel (time=54, measured in units of a/U_0) shows an early phase, when the KH instability rapidly folds the magnetic field into small-scale structures. The folding of the field continues (time=334), until the large-scale dipolar-in-y fields emerge (time=603). The (x, y)-averaged mean field is reversed in z throughout the nonlinear phase (not seen in these renderings around z=0 where the mean field is close to zero). Over time, the large-scale field and current sheets are disrupted; the system becomes disordered and turbulent, again (time=895). The large-scale field is self-organized and re-generated (time=1029). This quasi-cyclic transition between ordered and disordered phases continues throughout the simulation evolved up to time=12,000. All times are measured in units of a/U_0, where a is the half-width of the shear layer with amplitude U_0. The parameters used are $M_{\rm A} = 30$, $t_{\rm forcing} = 0.5$, $Re = Rm = 50$, and $\theta = 30^\circ$ (angle between the initial mean flow and the initial mean field).

Simulations show that 128 Fourier modes in x and in y achieve converged dissipation rates for our typical input parameters. Viscous dissipation rates are converged even with lower resolution. We vary the number of modes of Fourier–Fourier–Chebyshev bases from $128^2\times512$ to 1024^3 depending on the Reynolds numbers and other simulation parameters. We have reproduced essentially the same results in triply periodic domains, as well, where we used up to $4096\times4096\times8192$ grid points [253]. In this article, we expressly deal with non-periodic flows only, which are more challenging to simulate than the periodic cases, because the linear operators acting on the Chebyshev polynomials produce many non-diagonal terms, requiring more computational memory, resources,

and efforts to invert the linear operator [121]. All simulations are three-dimensional and are run typically for several hundreds of instability e-folding time. One simulation is run up to 2400 e-folding times.

9.3 An overview of the dynamo cycle

We present here a summary of detailed turbulent processes that cause the magnetic fields to self-organize into ordered phases, disassemble into chaotic disordered phases, and then reassemble, in a quasi-cyclic manner. These phases are shown in Fig. 10.1.

After performing comprehensive analyses of an ensemble of 3D MHD KH-driven dynamo simulations, we have identified a dynamo cycle, whose essential steps are summarized in ten elemental steps in Fig. 10.2. This figure summarizes the principal result of the present article. Each step of the dynamo cycle is briefly explained below. Numerical confirmation of each step is detailed in Sec. 9.4.

The word "steps" is chosen over the word "components," although both may be used interchangeably. In the fully saturated phase, dynamo features all ten steps, which operate with different time scales. However, examining from $t = 0$, the latter steps cannot operate until the former has occurred. For example, the KH instability must grow exponentially before the jets can form and before mean magnetic fields can be created. It is in this sense (examining from $t = 0$), we prefer to use "steps," because one step must happen first before the occurrence of the next until the dynamo saturates.

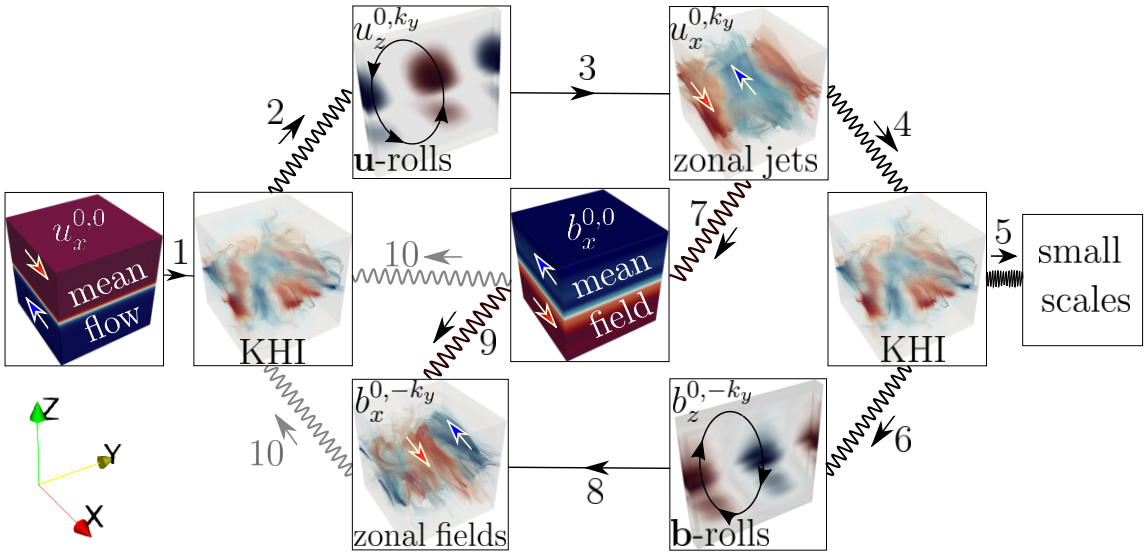

Figure 9.2: The life-cycle of the jet-driven shear-flow dynamo using 10 dominant steps. Solid lines represent linear couplings; oscillating curves represent nonlinear couplings. Arrows outside the boxes indicate causality or energy-flow directions. Arrows inside the boxes indicate the direction of flow or field; this direction is indicated by subscripts, e.g, $u_x^{0,0}$. The superscripts represent the horizontal wavenumber k_x, k_y of a given flow or field. All visualizations are shown at the same time in a simulation. Red (blue) represents positive (negative) values. The essential steps of the dynamo cycle are: **1**—The mean shear flow $u_x^{0,0}$ feeds the Kelvin–Helmholtz instability (KHI). **2**—The KHI nonlinearly generates the x-invariant (KH-stable), y-varying vertical flows u_z^{0,k_y}, labeled **u**-rolls and shown in the (y,z)-plane. **3**—The **u**-rolls are stretched by the mean shear flow to form the x-invariant (KH-stable), y-varying horizontal flows u_x^{0,k_y}, labeled zonal jets. The jets are prominent in the 3D rendering of the total turbulent flow. **4**—The zonal jets saturate via nonlinear excitation of turbulent fluctuations in the KH-unstable wavenumber range ($0 < |k_x| \lesssim 1$). **5**—The KHI launches a small-scale energy cascade. Steps **6** and **8** are magnetic analogues of steps **2** and **3**, involving **b**-rolls in place of **u**-rolls. **7**—The zonal jets create a reversed mean field $b_x^{0,0}$ and steepen the mean-field gradient. **9**—The mean field is advected along z by the **u**-rolls, thus flattening the mean-field gradient. **10**—Magnetic fields couple to the KH instability, thus providing saturation of the dynamo. For more details, see Sec. 9.3.

Step 1: The KHI

The mean flow $u_x^{0,0}$ is KH-unstable. Thus, perturbations with wavenumber $0 < |k_x| \lesssim 1$ grow exponentially. Note that perturbations with $k_x = 0$ are linearly stable to the KH instability. The time scale of the KH instability is very short compared to that of other steps.

Step 2: Generation of x-invariant, y-varying vertical flows (u-rolls)

The KH instability driven by the (x, y)-averaged mean shear flow requires fluctuations to vary along the mean-flow direction, i.e., $k_x \neq 0$. Since the vertical flows $u_z^{k_x=0,k_y}$ do not vary in x but vary in y, they require a purely nonlinear mechanism for their excitation. These x-averaged vertical flows are sliced and shown on the (y, z)-plane in Fig. 10.2. In the absence of nonlinear drive from the KH-scale fluctuations, the vertical flows decay viscously. These vertical flows are referred to as **u**-rolls here, borrowing a nomenclature from studies of wall-bounded KH-*stable* shear flow [262]. The label *rolls* is appropriate because their spatial structures appear in the form of cylindrical rolls—the axis of the cylinder is along the x-axis. The flows lie on the (y, z)-plane, taking the shape of a roll or an eddy with velocity $(u_y^{k_x=0,k_y}, u_z^{k_x=0,k_y})$. The y-component of the flow is not independent and is related to the z component via the incompressibility condition.

Step 3: Generation of x-invariant, y-varying horizontal flows (zonal jets)

The KH-induced **u**-rolls are stretched by the mean shear flow $u_x^{0,0}$ via the hydrodynamic advection term $u_z^{0,k_y}\partial_z u_x^{0,0}$. This stretching process is coherent and is thus able to generate strong zonal jets u_x^{0,k_y}, which are clearly discernible in the streamlines of the *total* turbulent flow in Fig. 10.2. The streamlines are colored by their horizontal velocity. Here, *zonal* fluctuations are defined as those fluctuations that do not vary along x (similar to zonal flows in planetary atmospheres [256], where x corresponds to the azimuthal direction). The time scale of zonal-jet generation is significantly longer than the time scale of the KH instability.

Step 4: Jet saturation via coupling to the KH instability

The zonal jets saturate via nonlinear coupling to the turbulent fluctuations in the KH-unstable wavenumber range.

Step 5: Energy cascade to small scales

The KH-scale fluctuations release a fraction of its energy for small-scale cascade. The small scales do *not* drive the large-scale dynamo here. This fact is likely related to a recent finding in a hydrodynamic context where the small-scale cascade was shown to be significantly reduced by the nonlinear transfer of energy from zonal jets to the stable eigenmodes in the KH-unstable wavenumber range [1]. These stable eigenmodes then transfer energy from fluctuations to the mean shear flow and thus inhibit cascade of energy to small scales [1, 17, 111, 143].

Step 6: Generation of x-invariant, y-varying vertical fields (b-rolls)

This step is identical to step 2, except that this step applies to magnetic fields instead of flow. The **b**-rolls decay resistively in the absence of nonlinearity. Isomorphic to the **u**-rolls, the **b**-rolls are nonlinearly driven by the KH instability.

Step 7: Generation of mean magnetic field by zonal jets

The **b**-rolls $b_z^{0,-k_y}$ of step 6 are stretched by the phase-locked zonal jets u_x^{0,k_y}, via the field-line stretching term $b_z^{0,-k_y}\partial_z u_x^{0,k_y}$. This process continuously generates the mean field $b_x^{0,0}$, which is reversed in z. Consequently, the gradient of the mean field is continuously steepened. The time scale of the mean-field generation is the longest among all the other steps.

Step 8: Generation of x-invariant, y-varying horizontal fields (zonal fields)

The KH-induced **b**-rolls are stretched by the mean shear flow $u_x^{0,0}$ via the field-line stretching term $b_z^{0,k_y}\partial_z u_x^{0,0}$. This stretching process is coherent and thus generates strong zonal fields b_x^{0,k_y}, which are clearly discernible in the streamlines of the *total* turbulent field in Fig. 10.2. The streamlines are colored by their strength of the horizontal field, which is the strongest among the three components. The time scale of zonal-field generation is similar to that of zonal-jet generation.

Step 9: Vertical advection of horizontal magnetic fields

The mean horizontal field is advected vertically by the **u**-rolls, thus depleting the mean field and transforming it into a zonal field. Equivalently, this transport of field due to turbulent advection $\langle -\mathbf{u}\cdot\nabla b_x^{0,-k_y}\rangle_{x,y} = -\partial_z(u_z^{0,k_y} b_x^{0,-k_y})$ attempts to flatten the mean-field gradient. In a self-consistent nonlinear regime after kinematic phase, this gradient-flattening transport effect becomes effective—although this effect is found to be generally slightly weaker than the gradient-steepening, field-stretching effect of step 7. Thus, with small remaining nonlinear coupling and resistive dissipation, a quasi-stationary mean field is successfully maintained dynamically.

Step 10: Field saturation via coupling to the KH instability

When horizontal fields — namely, zonal field $b_x^{0,-k_y}$ and mean field $b_x^{0,0}$ — become strong, they resist vertical motions of turbulent flow, thus preventing unphysical growth of magnetic fields without bound. This Lorentz feedback then impacts steps 2 and 6, and thus self-regulates the amplitude of the horizontal fields and induces temporal dynamics in the quasi-stationary oscillatory phase. In this step, energy of the horizontal magnetic fields is also transferred to energy of magnetic fluctuations at the KH-instability scale. Step 10 thus represents the coupling of magnetic fields to the KH instability.

It is to be emphasized that all ten steps of the dynamo cycle do not operate at their full efficiency at the same time. Time delays are inherently introduced by the wide separation of time scales among the very rapid KHI, slowly evolving zonal jets and fields, and yet more slowly evolving mean field. These time lags in linked dynamical systems produce an inertia that can lead to limit-cycle oscillations [263], which are clearly seen in, for example, time-delay solar dynamo models [3, 264].

9.4 Numerical confirmation of the dynamo cycle

Each step of the dynamo cycle (Fig. 10.2) is confirmed below using detailed numerical analyses.

Step 1: The KHI

The (x, y)-averaged mean shear flow is KH-unstable, as seen in Fig. 10.3, where we show the finite-amplitude-modified growth rate $\gamma_{\rm nl}$. The rate $\gamma_{\rm nl}$ — which is mathematically defined in the subsequent paragraph — measures the rate at which energy is transferred from the mean flow to fluctuations during the nonlinear phase. At early times (see the Fig. 10.3 inset), $\gamma_{\rm nl}$, as found from the initial value solver (direct numerical simulation), agrees with the linear growth rate obtained from the eigenvalue solver; the latter yields a complete eigenspectrum, of which one eigenmode at a given wavenumber (k_x, k_y) is KH-unstable, and the others are either stable or marginally stable [1, 144].

We define the rate $\gamma_{\rm nl}$ using a straightforward procedure. First, we take the momentum equation

$$\partial_t \mathbf{u}(\mathbf{k}) = L + N, \tag{9.4}$$

with L and N representing linear and nonlinear operators, respectively. The evolution equation for kinetic energy associated with the wavenumber $\mathbf{k} = (k_x, k_y)$ is then

$$\partial_t \langle |\mathbf{u}(\mathbf{k})|^2 \rangle_z / 2 = \mathrm{Re}\langle \mathbf{u}^*(\mathbf{k}) \cdot L \rangle_z + \mathrm{Re}\langle \mathbf{u}^*(\mathbf{k}) \cdot N \rangle_z, \tag{9.5}$$

where the angular brackets $\langle \cdot \rangle_z$ represent a z-averaging operation (recall that the mean shear flow is inhomogeneous and non-periodic in z). The first term on the right-hand

side of the energy evolution equation is then manipulated to arrive at

$$\partial_t \langle |\mathbf{u}(\mathbf{k})|^2 \rangle_z / 2 = \gamma_{\rm nl} \langle |\mathbf{u}(\mathbf{k})|^2 \rangle_z / 2 + {\rm Re} \langle \mathbf{u}^*(\mathbf{k}) \cdot N \rangle_z, \tag{9.6}$$

where the finite-amplitude-modified growth rate $\gamma_{\rm nl}$ is defined as

$$\gamma_{\rm nl}(\mathbf{k}) = \frac{{\rm Re} \langle \mathbf{u}^*(\mathbf{k}) \cdot L(\mathbf{u}(\mathbf{k})) \rangle_z}{\langle |\mathbf{u}(\mathbf{k})|^2 \rangle_z / 2}. \tag{9.7}$$

In Eq. (9.7), when $\mathbf{u}(\mathbf{k})$ is replaced with flow fluctuations of the unstable eigenmode at wavenumber $\mathbf{k}$, the rate $\gamma_{\rm nl}$ is exactly the same as the linear growth rate $\gamma_{\rm lin}$ of the KH instability at that wavenumber. When flow fluctuations become nonlinear and turbulent, $\gamma_{\rm nl}$ gets modified—in general, the real part of $\gamma_{\rm nl}$ is smaller than $\gamma_{\rm lin}$. The decrement can be dramatic, ranging from a few tens of percent to as much as 99%, depending on the properties of turbulent fluctuations [1, 17].

The smaller $\gamma_{\rm nl}$ for $\mathbf{k} = (0, 0.2)$ explains why zonal jets u_x (whose $\gamma_{\rm lin}$ is zero) take a long time to evolve, compared to the very rapid KH instability (see Fig. 10.3).

Step 2: Generation of the x-invariant, y-varying, vertical flows (u-rolls)

The **u**-rolls u_z^{0,k_y} with $k_y \neq 0$ are a seed for the formation of the zonal jets u_x^{0,k_y}. Here, we first analyze what nonlinear mechanism generates the **u**-rolls.

The mean flow and the mean fields do not have vertical components ($\nabla \cdot \mathbf{B} = \partial_z B_z = 0$ for the (x, y)-averaged mean field, and $B_z = 0$ is taken due to the perfectly conducting walls). Moreover, there is no KH instability for $k_x = 0$, meaning that vertical motions of the KH instability do not exist for fluctuations with $k_x = 0$. Thus, the **u**-rolls u_z^{0,k_y} with $k_x = 0$ must be generated purely by nonlinear interactions. Via

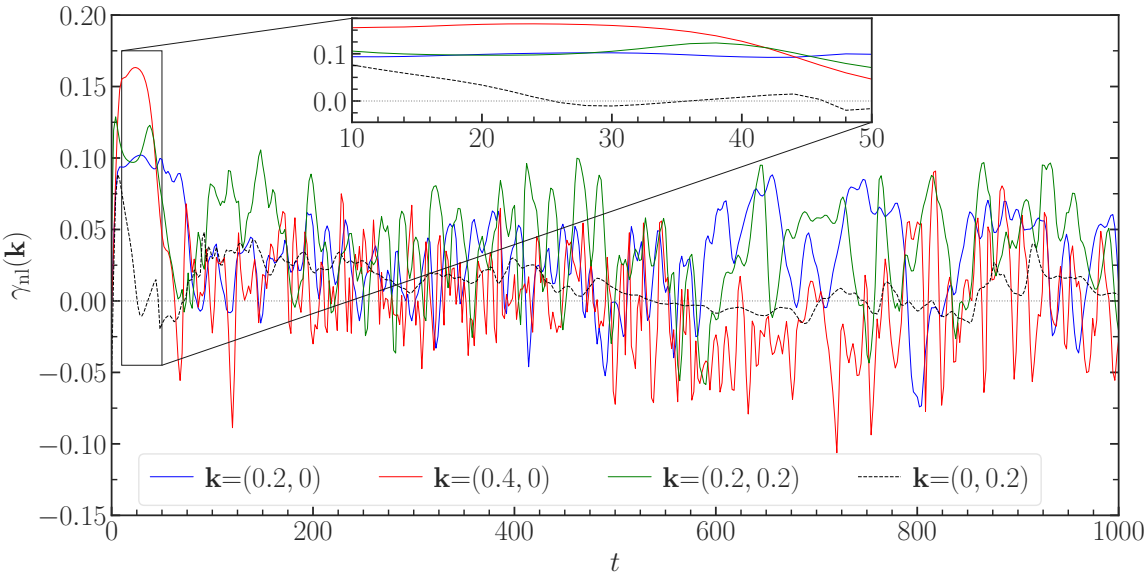

Figure 9.3: Finite-amplitude-modified growth rates $\gamma_{\rm nl}$ are obtained by feeding fluctuations with a wavenumber $\mathbf{k} = (k_x, k_y)$ into the linear operator of the flow; see Eq. (9.7). The rate $\gamma_{\rm nl}$ is constant in time in the early phase of evolution after initial transients have disappeared in the inset. In the nonlinear, quasi-stationary phase, $\gamma_{\rm nl}$ for wavenumbers $k_x{\neq}0$ exhibits fast oscillations. Their time-averaged $\gamma_{\rm nl}$ is larger than the slowly-evolving $\gamma_{\rm nl}$ for $\mathbf{k}$=$(0, 0.2)$. The rate $\gamma_{\rm nl}$ for $\mathbf{k}$=$(0, 0.2)$ is found to be almost entirely due to the fluid advection term (with negligible contribution from the Lorentz force). The parameters used are $M_{\rm A} = 30$, $t_{\rm forcing} = 0.5$, $Re = Rm = 50$, and $\theta = 30\,{\rm deg}$.

the nonlinearity, energy is transferred to (from) u_z^{0,k_y} with a wavenumber $\mathbf{k} = (0, k_y{\neq}0)$ from (to) a vertical fluctuation with a wavenumber $\mathbf{k}''$ if the energy transfer rate

$$T(u_z^{\mathbf{k}};\mathbf{k}'') = {\rm Re}\left\langle u_z^{-\mathbf{k}}\left(-\mathbf{u}'\cdot\nabla u_z'' + \mathbf{b}'\cdot\nabla b_z''\right)\right\rangle_z , \tag{9.8}$$

is positive (negative). In Eq. (9.8), fluctuations with single and double primes are evaluated at wavenumber $\mathbf{k}'$ and $\mathbf{k}''$, respectively, where $\mathbf{k}' = \mathbf{k} - \mathbf{k}''$.

The top panel of Fig. 10.4 shows that $T(u_z^{\mathbf{k}};\mathbf{k}'')$ is predominantly positive at low wavenumbers, indicating that u_z^{0,k_y} is generated by energy transfer from large-scale fluctuations. Small scales act as an energy sink—as expected.

To quantify the relative importance of different turbulent scales, we sum the absolute value of $T(u_z^{\mathbf{k}};\mathbf{k}'')$ over different scales $\mathbf{k}''$ and normalize this sum to unity. As shown in the bottom panel of Fig. 10.4, this procedure reveals that 81% of the energy transfer occurs in the range $0<|\mathbf{k}''|\leq 1$ where the KH instability resides; 11% occurs in the remaining large-scale fluctuations $1<|\mathbf{k}''|\leq 2$; and merely 8% occurs at small scales $|\mathbf{k}''|>2$. Thus, Fig. 10.4 (bottom) confirms that the generation of the **u**-rolls is due to the KH-scale fluctuations.

Step 3: Generation of the x-invariant, y-varying horizontal flows (zonal jets)

To understand the generation of zonal jets, we analyze its energy evolution equation

$$\partial_t \left\langle |u_x^{0,k_y}|^2 \right\rangle_z /2 - \epsilon_\nu = T(u_x^{\mathbf{k}};\mathbf{k}''), \tag{9.9}$$

where ϵ_ν is the viscous dissipation rate of large-scale zonal jets and

$$T(u_x^{\mathbf{k}};\mathbf{k}'') = T_{\mathrm{Adv}}(u_x^{\mathbf{k}};\mathbf{k}'') + T_{\mathrm{Lor}}(u_x^{\mathbf{k}};\mathbf{k}''), \tag{9.10}$$

with energy transfer via the hydrodynamic advective term given by

$$T_{\mathrm{Adv}}(u_x^{\mathbf{k}};\mathbf{k}'') = \mathrm{Re}\left\langle u_x^{-\mathbf{k}}\left(-\mathbf{u}'\cdot\nabla u_x''\right)\right\rangle_z, \tag{9.11}$$

and the energy transfer via the Lorentz force given by

$$T_{\mathrm{Lor}}(u_x^{\mathbf{k}};\mathbf{k}'') = \mathrm{Re}\left\langle u_x^{-\mathbf{k}}\left(-\mathbf{b}'\cdot\nabla b_x''\right)\right\rangle_z. \tag{9.12}$$

The spectrum of hydrodynamic energy transfer rate $T_{\mathrm{Adv}}(u_x^{\mathbf{k}};\mathbf{k}'')$ is shown in the

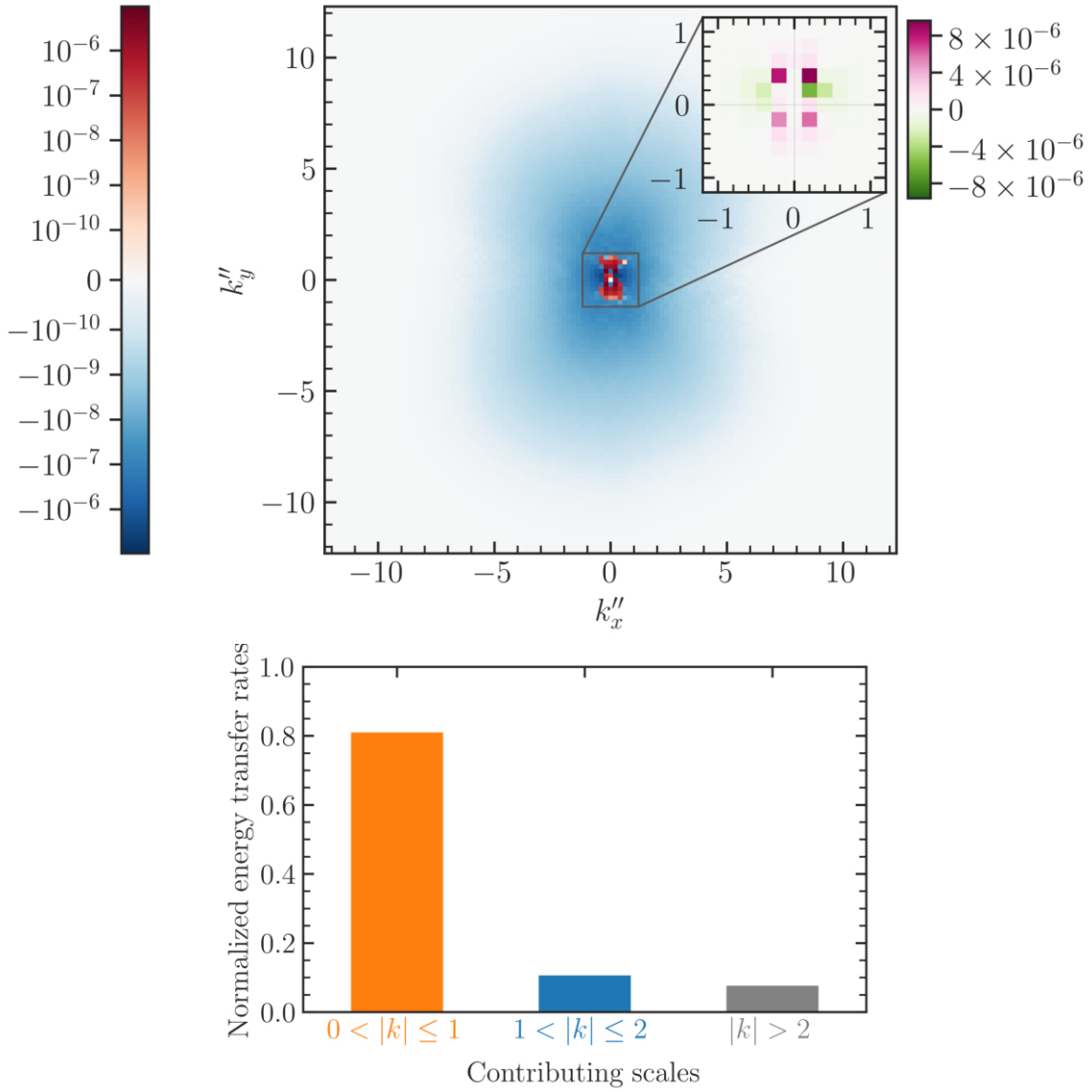

Figure 9.4: (Top) Time-averaged rates of energy transfer $T(u_z^{\mathbf{k}}; \mathbf{k}'')$ to u_z^{0,k_y} from various scales $\mathbf{k}''$ via $-\mathbf{u}' \cdot \nabla \mathbf{u}'' + \mathbf{b}' \cdot \nabla \mathbf{b}''$; see Eq. (9.8). The inset zooms into the central region and highlights the dominant scales with its own color bar using a linear scale, shown on the top right. (Bottom) 81% of the normalized energy transfer is due to the range $0 < |\mathbf{k}''| \leq 1$ where the KH instability resides, 11% is due to the remaining large-scale fluctuations $1 < |\mathbf{k}''| \leq 2$, and merely 8% is due to small scales ($|\mathbf{k}''| > 2$).

top panel of Fig. 10.5, whereas its bottom panel shows the spectrum of total energy transfer $T(u_x^{\mathbf{k}};\mathbf{k}'') = T_{\rm Adv}(u_x^{\mathbf{k}};\mathbf{k}'') + T_{\rm Lor}(u_x^{\mathbf{k}};\mathbf{k}'')$. Energy is transferred to (from) zonal jets u_x^{0,k_y} with wavenumber $\mathbf{k}=(0,k_y)$ from (to) a fluctuation with wavenumber $\mathbf{k}''$ if the energy transfer rate $T(u_x^{\mathbf{k}};\mathbf{k}'')$ is positive (negative).

It is a simple exercise to show using Eq. (9.11) that the advective energy transfer is zero if $\mathbf{k}''$=$\mathbf{k}$ (i.e., $\mathbf{k}'$=$\mathbf{0}$). However, if $\mathbf{k}''$=$\mathbf{0}$ (i.e., $\mathbf{k}'$=$\mathbf{k}$), then energy transfer from the mean shear flow to the jets is non-zero, via the term $-u_z^{0,k_y}\partial_z u_x^{0,0}$

We recall that the **u**-rolls u_z^{0,k_y} cannot be generated by the mean flow or the mean fields fields. Thus, the jets are sustained by a *nonlinear* mechanism.

When the **u**-rolls are nonlinearly sustained, the zonal jets receive energy from the mean flow $\mathbf{k}$=$(0,0)$, via the advective term $-u_z^{0,k_y}\partial_z u_x^{0,0}$. This transfer is shown in the top panel of Fig. 10.5. This term represents the physical process of coherent straining of the nonlinearly-generated **u**-rolls by the mean shear flow $u_x^{0,0}$. The straining process generates zonal jets u_x^{0,k_y}.

A difference between the straining by a mean shear flow in 3D and in 2D is illustrated in Appendix.

Step 4: Jet saturation via coupling to the KH instability

The zonal jets saturate by nonlinearly coupling to the turbulent fluctuations in the KH-unstable wavenumber range. This is shown in Fig. 9.6 where linear and nonlinear energy transfer rates are computed. The linear energy transfer rates are decomposed into multiple contributions: $Q_{u(0,0)}$ is the transfer from the mean flow to the zonal jets; $Q_{b(0,0)}$ is the transfer from the mean field to the zonal jets; and $Q_{\rm ZM}$ is the transfer from the zonal magnetic fields b_x^{0,k_y} to the jets. The nonlinear energy transfer rates are decomposed into $T_{\rm ss}$ and $T_{\rm KH}$. The term $T_{\rm ss}$, when negative, represents the rate

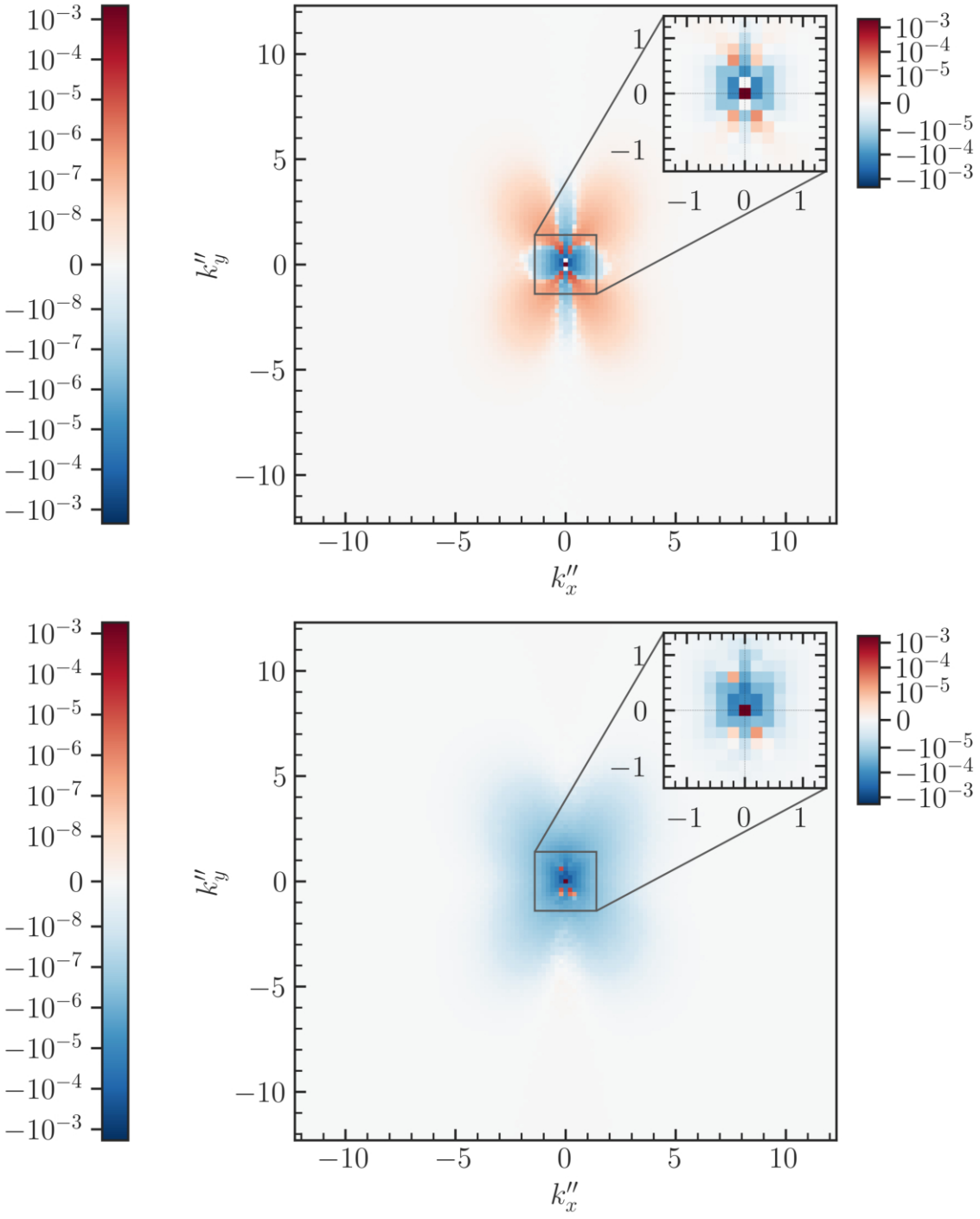

Figure 9.5: Time-averaged rates of energy transfer to u_x^{0,k_y} from various scales $\mathbf{k}''$ via hydrodynamic advection $T_{\mathrm{Adv}}(u_x^{\mathbf{k}};\mathbf{k}'')$ (top) and via magnetohydrodynamic interaction $T(u_x^{\mathbf{k}};\mathbf{k}'') = T_{\mathrm{Adv}}(u_x^{\mathbf{k}};\mathbf{k}'') + T_{\mathrm{Lor}}(u_x^{\mathbf{k}};\mathbf{k}'')$ (bottom). See Eqs. (9.10)–(9.12). The insets magnify the central region and highlight the dominant scales with their own color bars, shown on the top right of either panel.

of energy transfer from the zonal jets to small scales. The term T_{KH}, when negative, represents the rate of energy transfer from the zonal jets to the turbulent fluctuations in the KH-unstable wavenumber range. The large transfer T_{KH} is further decomposed into transfer via the fluid-advective nonlinearity (shown as the blue bar) and transfer via the magnetic nonlinearity (shown as the green bar).

The equation for the evolution of energy E_{ZF} in the zonal jets is

$$\partial_t E_{\mathrm{ZF}} = \epsilon_\nu + Q_{u(0,0)} + Q_{b(0,0)} + Q_{\mathrm{ZM}} + T_{\mathrm{KH}} + T_{\mathrm{ss}}, \tag{9.13}$$

where ϵ_ν is the viscous dissipation of large-scale zonal jets, and the remaining terms are described in the preceding paragraph. These terms are computed using

$$E_{\mathrm{ZF}} = \left\langle |u_x^{0,k_y}|^2 \right\rangle_z /2, \tag{9.14a}$$

$$\epsilon_\nu = \nu \left\langle u_x^{0,-k_y} \nabla^2 u_x^{0,k_y} \right\rangle_z, \tag{9.14b}$$

$$Q_{u(0,0)} = -\left\langle u_x^{0,-k_y} (\mathbf{u}^{0,k_y} \cdot \nabla u_x^{0,0}) \right\rangle_z, \tag{9.14c}$$

$$Q_{b(0,0)} = \left\langle u_x^{0,-k_y} (\mathbf{b}^{0,k_y} \cdot \nabla b_x^{0,0}) \right\rangle_z, \tag{9.14d}$$

$$Q_{\mathrm{ZM}} = \left\langle u_x^{0,-k_y} (\mathbf{b}^{0,0} \cdot \nabla b_x^{0,k_y}) \right\rangle_z, \tag{9.14e}$$

$$T_{\mathrm{KH}} = \sum_{\mathbf{k}',\mathbf{k}'' \in \text{ KH-unstable}} \left\langle u_x^{0,-k_y} (-\mathbf{u}' \cdot \nabla u_x'' + \mathbf{b}' \cdot \nabla b_x'') \right\rangle_z, \tag{9.14f}$$

$$T_{\mathrm{ss}} = \sum_{\mathbf{k}',\mathbf{k}'' \in \text{ small scales}} \left\langle u_x^{0,-k_y} (-\mathbf{u}' \cdot \nabla u_x'' + \mathbf{b}' \cdot \nabla b_x'') \right\rangle_z. \tag{9.14g}$$

Here, T_{ss} captures the nonlinear transfer of energy through scales that are not captured by the other terms of Eq. (9.13).

Jet saturation is shown in the dynamo cycle as Step 4.

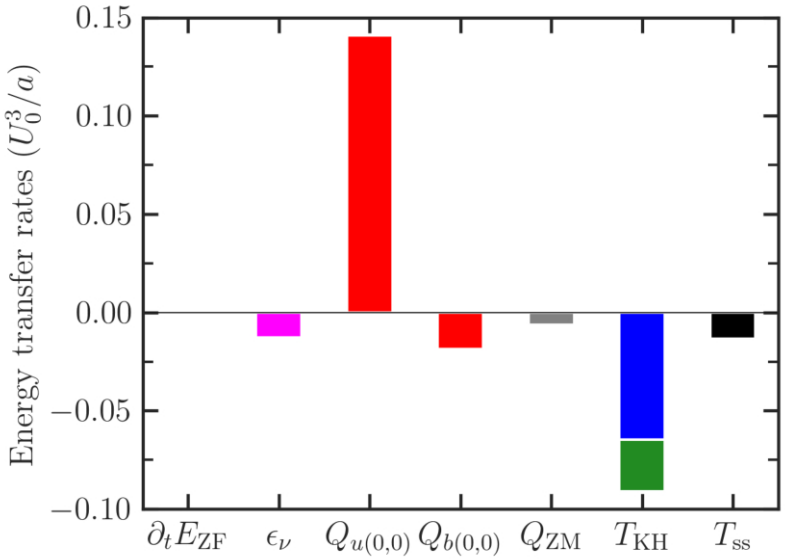

Figure 9.6: Zonal-jet energy-transfer mechanisms and saturation balance in a turbulent steady state. The term $\partial_t E_{ZF}$ represents the rate of time-variations of energy of the zonal flow (ZF). This rate of the saturated zonal flow approaches zero upon long time-averaging. The equation $\partial_t E_{\rm ZF} = \epsilon_\nu + Q_{u(0,0)} + Q_{b(0,0)} + Q_{\rm ZM} + T_{\rm KH} + T_{\rm ss}$ represents the energy budget of the zonal flow, where ϵ_ν is the viscous dissipation rate; the other terms represent rates at which the zonal flow receives energy from the mean flow $Q_{u(0,0)}$, the mean field $Q_{b(0,0)}$, the zonal field $Q_{\rm ZM}$, nonlinear fluctuations in theKH-unstable wavenumber range $T_{\rm KH}$, and the remainder of the scales (i.e., small scales) $T_{\rm ss}$. Positive (negative) values of energy transfer rates represent gain (loss) for the zonal flow. The term $T_{\rm KH}$ is further decomposed into flow fluctuations (blue) and field fluctuations (green).

Step 5: Small-scale energy cascade

The free energy from the mean shear flow is tapped by the KH instability, and a fraction of the KH instability energy is released to small scales. The forward energy cascade has recently been quantified in the context of KH turbulence [253].

Step 6: Generation of x-invariant, y-varying vertical fields (b-rolls)

The **b**-rolls b_z^{0,k_y} are a seed for the formation of zonal magnetic fields b_x^{0,k_y}. Here, we analyze what nonlinear mechanism generates the **b**-rolls.

Since the mean flow and mean fields do not have vertical components and since the k_x=0 perturbations have no KH instability, the fluctuation b_z^{0,k_y} is generated purely by nonlinear interactions. Via the nonlinearity, energy is transferred to (from) the **b**-rolls b_z^{0,k_y} with a wavenumber $\mathbf{k} = (0, k_y{\neq}0)$ from (to) a vertical fluctuation with wavenumber $\mathbf{k}''$, if the energy transfer rate

$$T(b_z^{\mathbf{k}}; \mathbf{k}'') = \mathrm{Re}\left\langle b_z^{-\mathbf{k}} \left(-\mathbf{u}' \cdot \nabla b_z'' + \mathbf{b}' \cdot \nabla u_z''\right)\right\rangle_z , \tag{9.15}$$

is positive (negative). The spectrum of $T(b_z^{\mathbf{k}}; \mathbf{k}'')$ is shown in Figure 9.7.

To quantify the relative importance of different turbulent scales, we sum the absolute value of $T(b_z^{\mathbf{k}}; \mathbf{k}'')$ over different scales and normalize this sum to unity. This procedure shows that 91% of the energy transfer occurs in the range $0 < |\mathbf{k}''| \leq 1$ where KH instability resides; 6% occurs in the remaining large-scale fluctuations $1 < |\mathbf{k}''| \leq 2$; and barely 3% occurs in small scales $|\mathbf{k}''| > 2$. Thus, Fig. 9.7 (bottom) confirms that the generation of the **b**-rolls is due to the KH-scale fluctuations.

Step 7: Generation of mean magnetic field by zonal jets

The mean field in the system we consider cannot be generated directly by the mean flow, because the mean vertical field and the mean vertical flow are both zero ($\nabla \cdot \mathbf{B} = \partial_z B_z = 0$ for the (x, y)-averaged mean field, and $B_z = 0$ is prescribed due to the conducting walls). Therefore, the mean field must be generated entirely by nonlinear

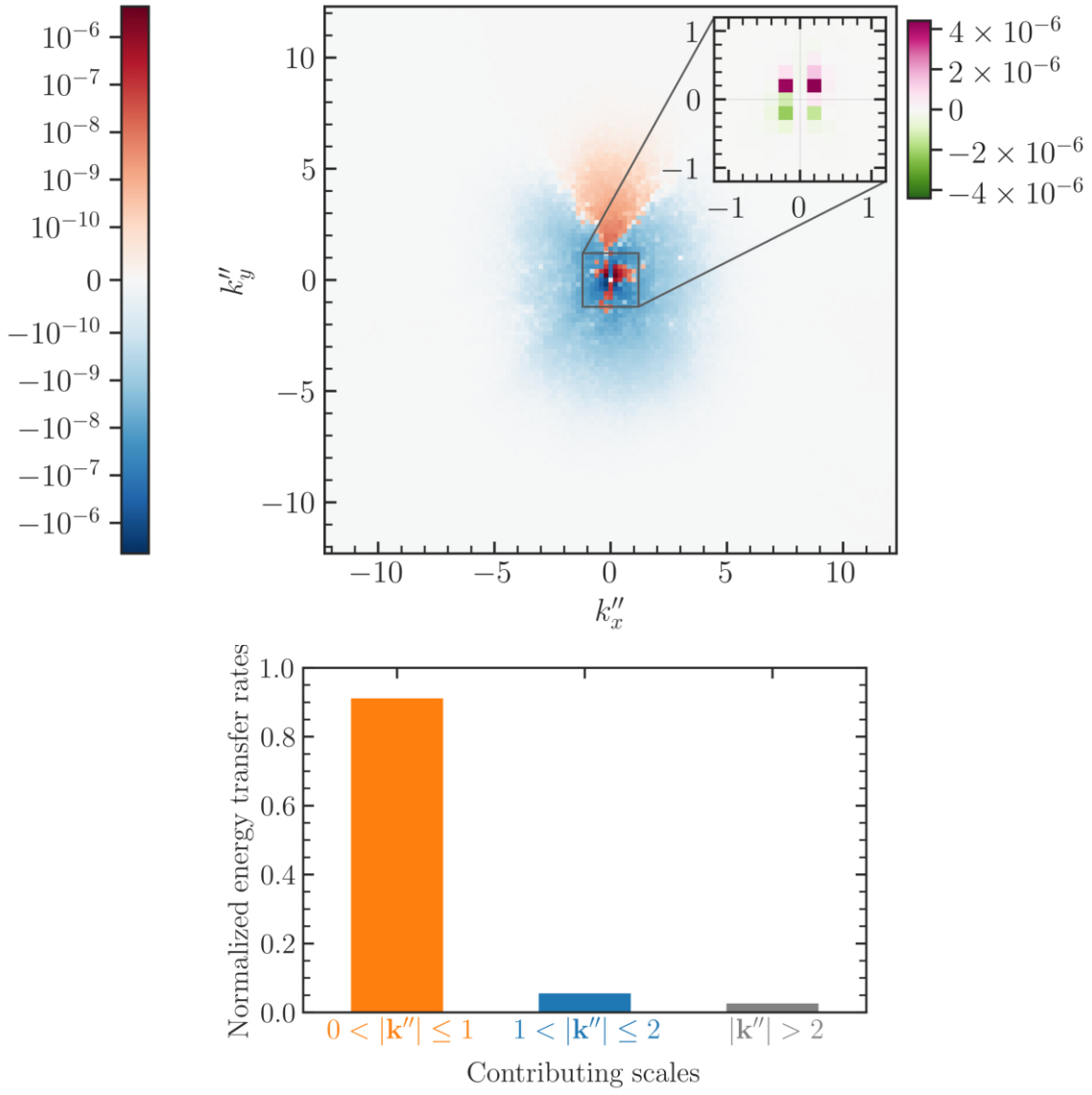

Figure 9.7: (Top) Time-averaged rates of energy transfer $T(b_z^{\mathbf{k}}; \mathrm{k}'')$ to b_z^{0,k_y} from various scales $\mathbf{k}''$ via $-\mathbf{u}' \cdot \nabla \mathbf{b}'' + \mathbf{b}' \cdot \nabla \mathbf{u}''$. The inset magnifies the central region and highlights the dominant scales with its own color bar using a linear scale, shown on the top right. (Bottom) 91% of the normalized energy transfer is due to the range $0 < |\mathbf{k}''| \leq 1$ where KH instability resides, 6% is due to $1 < |\mathbf{k}''| \leq 2$, and merely 3% is due to small scales ($|\mathbf{k}''| > 2$).

interactions. We decompose the nonlinear energy transfer to or from the mean field into three contributions: transfer from large-scale zonal fluctuations is $T_{\rm zonal}$, corresponding to fluctuations with $k_x = 0$ and $0 < |k_y| \leq 1$; transfer from the KH-scale fluctuations is $T_{\rm KH}$, corresponding to fluctuations with $0 < |k_x| \leq 1$ and $|k_y| \leq 1$; and transfer from the remainder of the fluctuations $T_{\rm residual}$, which is obtained from the mean-field energy evolution equation $T_{\rm residual} = (\partial_t E_b(0,0) - \epsilon_\eta) - (T_{\rm zonal} + T_{\rm KH})$. In this expression, $E_b(0,0)$ is the mean-field energy, and ϵ_η is the rate of resistive dissipation of the mean field. A time history of these transfers is presented in Fig. 9.8(a). The zonal transfer is the largest and almost completely reproduces the total nonlinear energy transfer to the mean field; compare $T_{\rm zonal}$ with $\partial_t E_b(0,0) - \epsilon_\eta$ in Fig. 9.8(a).

We further decompose $T_{\rm zonal}$ into two elements: zonal-flow stretching $T(\mathbf{b}\cdot\nabla\mathbf{u}_x^{\rm ZF})$, which transfers energy from the zonal flow (jets) to the mean field; and zonal-magnetic-field advection $T(-\mathbf{u}\cdot\nabla\mathbf{b}_x^{\rm ZM})$, which transfers energy from the zonal magnetic fields to the mean field. On average, zonal-flow stretching transfers energy to the mean field, and zonal-magnetic-field advection takes energy away from the mean field. These are demonstrated in Fig. 9.8(b). These effects do not depend on the polarity of the mean field at any given time. Because these two effects occur concurrently and because the field-stretching effect is typically slightly stronger, the mean field takes a longer time to evolve. See Fig. 9.8(a), where the solid blue curve shows a suitably normalized mean field energy $E_b(0,0)/80$, which evidently evolves slowly (the choice of the proportionality constant, 80, is merely to contain all the curves within the shown y-axis extent, and does not bear any physical meaning).

A simple way to visualize the zonal-flow stretching is to consider the $\mathbf{b}$-rolls $b_z^{0,-k_y}$ that are strained by the zonal flow u_x^{0,k_y} — not the mean flow $u_x^{0,0}$. This mechanism steepens the mean-field gradient.

The field-line stretching by zonal jets (Step 7) continuously generates the mean

field. The zonal jets vary in the y direction and hence do not exist in 2D KH turbulence on the (x, z)-plane. Thus, the dynamo-enabling jets appear only in 3D KH turbulence.

Step 8: Generation of x-invariant, y-varying horizontal fields (zonal fields)

To understand the generation of zonal magnetic fields, we derive the expression for the evolution of energy in zonal magnetic fields

$$\partial_t \left\langle |b_x^{0,k_y}|^2 \right\rangle_z /2 - \epsilon_\eta^{0,k_y} = T(b_x^{\mathbf{k}}; \mathbf{k}''), \tag{9.16}$$

where ϵ_η^{0,k_y} is the rate of resistive dissipation of large-scale zonal magnetic fields, and $T(b_x^{\mathbf{k}}; \mathbf{k}'')$ is the rate of energy transfer to the zonal magnetic fields from wavenumber $\mathbf{k}''$, which is mathematically given by

$$T(b_x^{\mathbf{k}}; \mathbf{k}'') = \mathrm{Re} \left\langle b_x^{-\mathbf{k}} \left(-\mathbf{u}' \cdot \nabla b_x'' + \mathbf{b}' \cdot \nabla u_x'' \right) \right\rangle_z . \tag{9.17}$$

The spectrum of $T(b_x^{\mathbf{k}}; \mathbf{k}'')$ is shown in Fig. 9.9.

To quantify the relative importance of different turbulent scales, we sum the absolute value of $T(b_x^{\mathbf{k}}; \mathbf{k}'')$ over different scales and normalize this sum to unity. This analysis shows that 96% of the energy transfer occurs in the range $0 < |\mathbf{k}''| \leq 1$ where the KH instability resides; 3% occurs in the remaining large-scale fluctuations $1 < |\mathbf{k}''| \leq 2$; and barely 1% occurs at small scales $|\mathbf{k}''| > 2$.

Step 9: Vertical advection of horizontal magnetic fields

The vertical overturning motion of the **u**-rolls generates zonal fields from the mean field. While this mean-to-zonal process can occasionally operate in the reverse direction, the

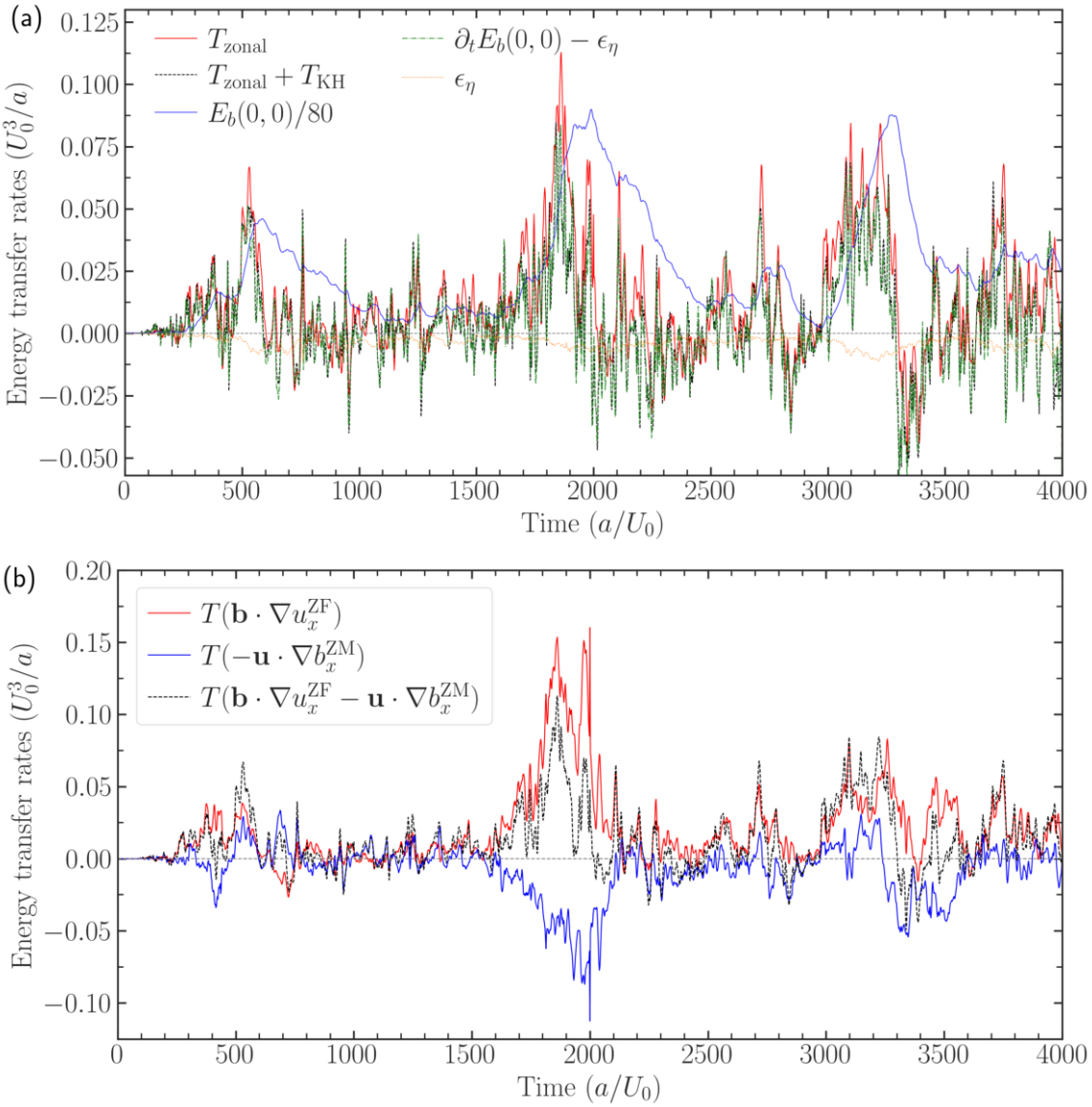

Figure 9.8: Rates of energy transfer to and from the mean magnetic field. (a) Energy in the mean field $b_x^{0,0}$ (proportional to the solid blue curve) is shown together with the rates of nonlinear energy transfer to the mean field. The rate at which the mean field receives energy from the zonal ($k_x = 0$) fluctuations is $T_{\rm zonal}$ and that from the Kelvin–Helmholtz instability is $T_{\rm KH}$. The remainder of the nonlinear energy transfer is given by the difference between the dashed-dotted green curve $\partial_t E_b(0,0) - \epsilon_\eta$ and the dashed black curve $T_{\rm zonal} + T_{\rm KH}$. The resistive dissipation of the mean field is ϵ_η. (b) The zonal energy transfer $T_{\rm zonal}$ is further decomposed into the advective and field-line stretching terms: The former (solid blue), on average, takes energy away from the mean field, while the latter (solid red) gives energy to the mean field.

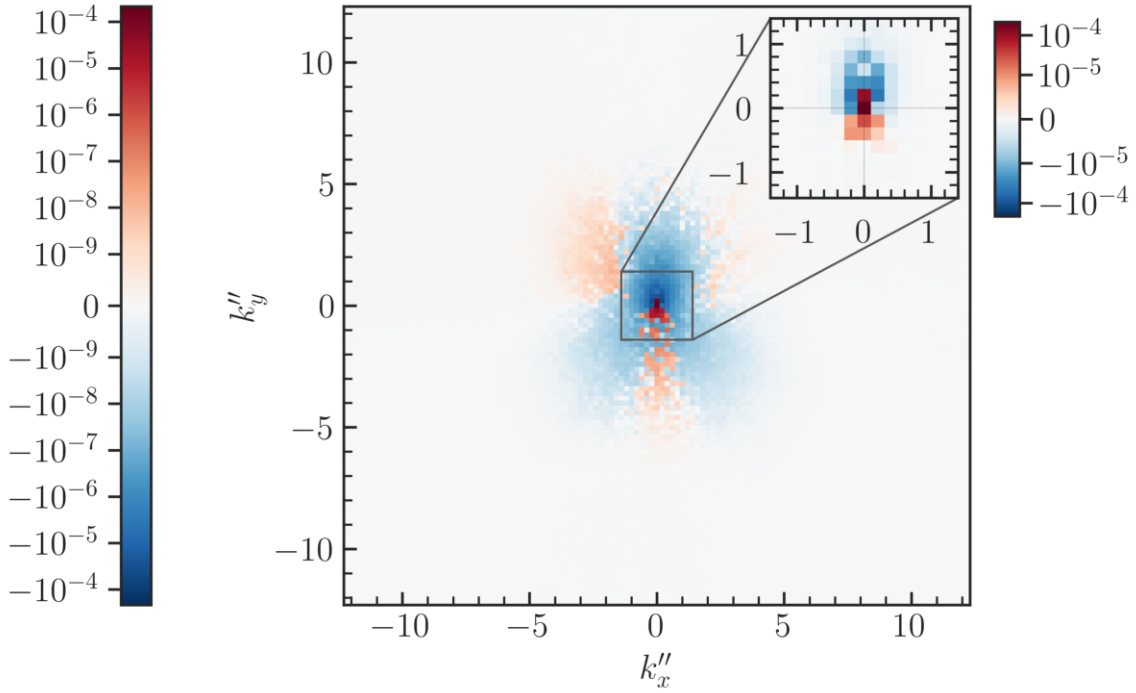

Figure 9.9: Time-averaged rates of energy transfer $T(b_x^{\mathbf{k}};\mathrm{k}'')$ to b_x^{0,k_y} from various scales $\mathbf{k}''$ via $-\mathbf{u}'\cdot\nabla\mathbf{b}''+\mathbf{b}'\cdot\nabla\mathbf{u}''$. See Eq. (9.15). 96% of the normalized energy transfer is due to the range $0<|\mathbf{k}''|\leq 1$ where the KH instability resides, 3% is due to the range $1<|\mathbf{k}''|\leq 2$, and barely 1% is due to small scales ($|\mathbf{k}''|>2$). The inset magnifies the central region and highlights the dominant scales with its own color bar, shown on the top right.

forward process is in general robust and dominant when averaged over a long time. Zonal-magnetic-field advection takes energy away from the mean field. See Fig. 9.8(b).

To visualize zonal-magnetic-field advection, consider a zonal magnetic field b_x^{0,k_y} that is advected vertically in z by the $\mathbf{u}$-rolls u_z^{0,k_y}. Recall that the $\mathbf{u}$-rolls vary in y, with their vertical motion going up and down at different y-locations. This overturning advective motion reduces the existing mean field (Step 9 in Fig. 10.2) by converting the mean field into fluctuation fields, namely, the zonal field. This mechanism works to flatten the mean-field gradient, competing with Step 7, and thus counters the rapid steepening of the mean-field gradient.

Step 10: Field saturation via coupling to the KH instability

In the kinematic phase when the mean field grows steadily, we time-average the energy transfer rates to the mean field. See Fig. 9.10(a). The term $\partial_t E_{b_x(0,0)}$ is non-zero during this growth phase. Zonal fluctuations contribute a majority of the energy transfer T_{zonal} to the mean field $b_x(0,0)$; the x-direction is the most energetic component of the mean field.

In the saturated dynamo phase ($\partial_t \approx 0$), we time-average the scale-decomposed rates of energy transfer to the mean field. See Fig. 9.10(b). The large-scale zonal flows (jets with $k_x = 0, 0 < |k_y| \leq 1$) deposit energy T_{ZF} in the mean field. The mean field then saturates by releasing its energy to the large-scale zonal magnetic fields T_{ZM}. The remaining energy is released to the KH-scale fluctuations T_{KH}. The small-scale transfer T_{ss} is largely decoupled from the mean field.

In this step, the horizontal zonal magnetic fields and mean magnetic fields also have a tendency to inhibit vertical motions associated with the KH instability. This effect is related to the field-line-bending magnetic tension force. To sum up, magnetic fields, when strong, couple back to the KH-scale fluctuations, thus providing a natural mechanism to limit unphysical growth of magnetic fields to unbounded levels. We have found that the turbulent kinetic energy is approximately equal to the mean-flow energy; similarly, the energy in the magnetic fields is approximately equal to the mean-flow energy. This finding of relative levels of energies and mechanisms via which they grow in the kinematic phase will be reported in a forthcoming paper, which details the effect of turbulent stresses and electromotive force and their roles in dynamo action.

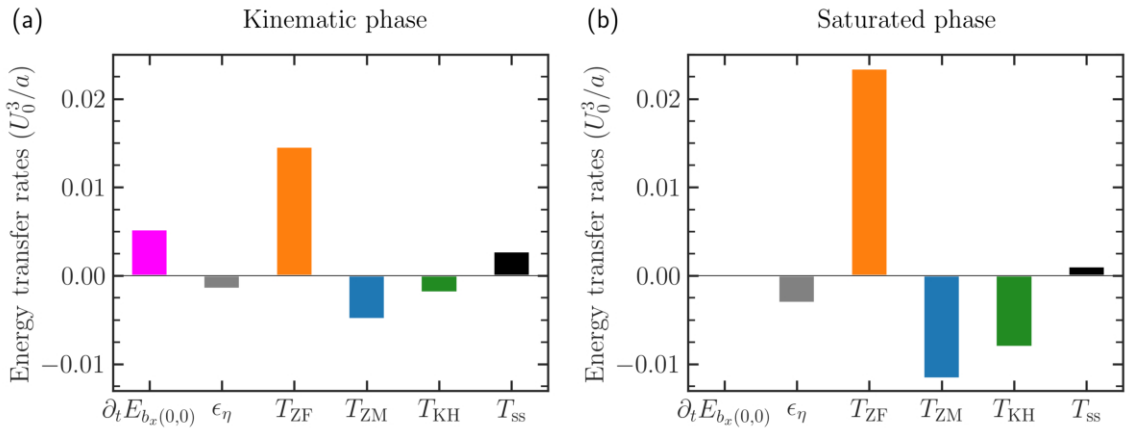

Figure 9.10: Time-averaged rates of energy transfer to the mean field during the mean-field growth phase (a) and saturated phase (b). The shown terms satisfy the relation $\partial_t E_{b_x(0,0)} = \epsilon_\eta + T_{\rm ZF} + T_{\rm ZM} + T_{\rm KH} + T_{\rm ss}$, where $T_{\rm ZF}$ is the rate of energy transfer to the mean field from the zonal flow ($k_x = 0, k_y \neq 0$); $T_{\rm ZM}$ is the transfer from the zonal magnetic fields; $T_{\rm KH}$ is the transfer from the KH-scale fluctuations; $T_{\rm ss}$ is the transfer from the remainder of the (small) scales; ϵ_η is the microphysical resistive dissipation of the mean field. Even in the saturated phase, magnetic fields are continuously generated and continuously depleted, thus maintaining a dynamic equilibrium, instead of a static equilibrium.

9.5 Impact of the initial field on the dynamo

We assess here the impact of the strength and orientation of the initial magnetic field on the dynamo.

Presence of an initial externally-imposed mean field

Variation of field strength

Since the large-scale dynamo involves only the KH-scale fluctuations as critical agents, the only control parameters that impact the dynamo are anticipated to be parameters that impact the KH instability. We recall that the KH instability is impacted by the presence of an initial externally-imposed mean magnetic field, which introduces a line-bending stabilization effect due to magnetic tension force. When this field is

very strong (close to equipartition with the mean flow), the growth rate of the KH instability is substantially reduced. At a critical initial field strength, the growth rate becomes zero. For moderate to weaker fields, the growth-rate reduction is minimal and practically negligible. Since the dynamo is driven by zonal jets stretching the magnetic-field fluctuations (namely, the **b**-rolls), the orientation θ of the initially weak mean field is expected to have a minimal impact on the dynamo. These theoretical expectations are confirmed in Fig. 9.11. In panels (a)–(c), the root-mean-square amplitudes are shown for the zonal jets $u_x^{0,0.2}$, the **u**-rolls $u_z^{0,0.2}$, and the mean field $b_x^{0,0}$, which all exhibit a similar trend. This trend agrees with the trend of the KH-instability growth rate, which decreases with increasing strength of the initial mean field (i.e., smaller Alfvénic Mach number $M_{\rm A} \propto U_0/B_0$, where B_0 and U_0 are the amplitudes of the mean field and mean flow, respectively).

Variation of field orientation

Dynamo elements are robust to variations in θ, as shown in Fig. 9.9 (d)–(f). The saturated nonlinear phase is essentially the same for all cases of θ. Minor amplitude variations are within the statistical variance of the turbulent fluctuations.

The case of θ=90° is potentially the most relevant one for the merging of binary neutron stars (BNS), as the magnetic fields in the interface between the BNS when they first come in contact is more likely to be orthogonal to the shear-flow plane. This orientation is expected because the dipolar magnetic fields of each neutron star is orthogonal to the shear-flow plane, located near the equator of the neutron stars The shear-flow plane features the azimuthal flow (directed along ϕ) of the spinning BNS; this azimuthal flow has a strong radial gradient (along r) at the merger interface. The dipolar (axial) magnetic fields of the BNS threads the shear-flow (r, ϕ)-plane that lies between the BNS. Astronomical observations [265, 266] of Gyr-old neutron

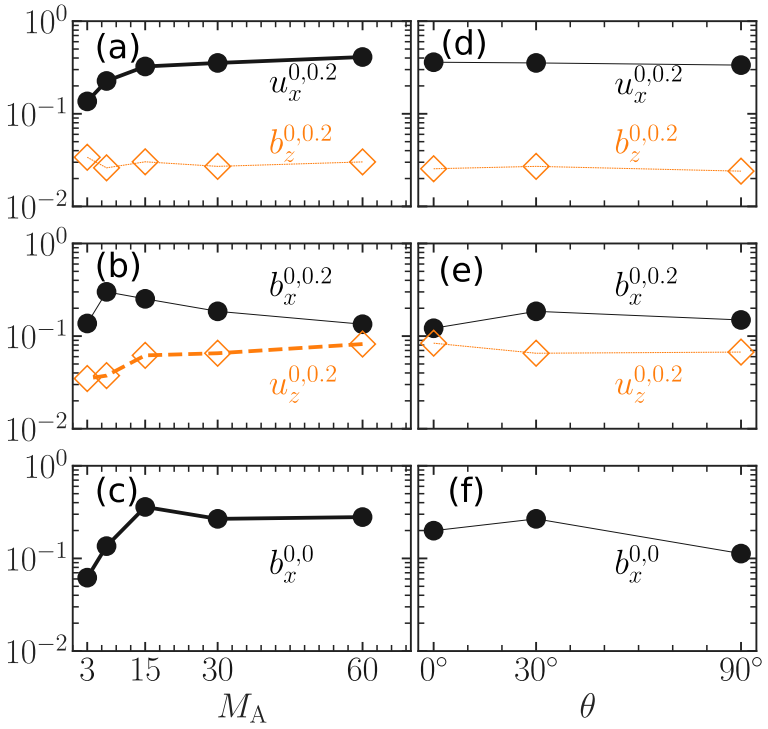

Figure 9.11: Impact of initial mean field strength (quantified by the Alfvénic Mach number $M_A \propto U_0/B_0$) and orientation θ on the root-mean-square (rms) amplitudes of different dynamo elements. The parameter θ measures the angle between the initial mean flow with amplitude U_0 and the initial mean field with amplitude B_0. The rms amplitude $u_x^{0,0.2}$, for example, is the square root of the energy in the zonal jets, $\sqrt{E(u_x^{0,0.2})}$. The superscript represents the wavenumber (k_x, k_y). (a)–(c) A stronger magnetic field (lower M_A) reduces the growth rate of the KH instability, thus reducing the generation of vertical flow-fluctuations $u_z^{0,0.2}$ in panel (b) and of jets $u_x^{0,0.2}$ in panel (a). The trend of these two elements (shown with thicker lines) is replicated by the mean-field amplitude $b_x^{0,0}$ in panel (c). (d)–(f) Saturated amplitudes of dynamo elements do not depend on the initial-field orientation θ. The minor amplitude variations in panels (d)—(f) are within the statistical variance of the turbulent fluctuations.

stars reveal that their total magnetic fields are around $10^8 - -10^{10}$ G, corresponding to an energy that is many orders of magnitude lower than that of the mean shear flow in between the BNS approaching to merge [73]. Thus, the initial Alfvénic Mach number for the KH instability at the start of the BNS merger is too large for the KH instability growth rates to be impacted by the presence of this very weak mean field. Instead, the dynamo cycle presented in Fig. 10.2 generates the magnetic fields via the formation of zonal jets.

Absence of an initial mean field

We have observed that the KH-instability-driven large-scale dynamo operates even in the absence of the initial mean field [253]. Details of this process will be reported in a separate publication, where the growth rates of the dynamo from direct numerical simulations are compared with detailed analytical work we have performed for jet-driven dynamos in both periodic and non-periodic domains.

The essential elements of the large-scale dynamo are robust to variations in small-scale visco-resistive properties, e.g., the fluid and magnetic Reynolds number, which was confirmed by varying the magnetic Prandtl number across 5 orders of magnitude [253].

9.6 Discussions on nonlinear self-organization

Here we discuss how the self-organization of magnetohydrodynamic 3D KH turbulence differs from or shares similarities with that of hydrodynamic turbulence with local or non-local shear flow. In Sec. 9.6, we remark on the differences between the hydrodynamic and magnetohydrodynamic systems. In Sec. 9.6, we offer a general principle of spectral condensation in 3D anisotropic systems; this condensation is

different from that observed in isotropic 2D turbulence. Finally, in Sec. 9.6, we highlight key differences between turbulence with local and non-local shear flows. The former is readily realized in wall-bounded systems with shear flows (e.g., flows in pipes), whereas the latter is general and excites the KH instability.

Comparison of hydrodynamic vs. magnetohydrodynamic 3D KH-instability-driven turbulence

Here, we compare hydrodynamic KH turbulence with magnetohydrodynamic KH turbulence. Steps 1 to 5 of Fig. 10.2 operate in 3D (magneto)hydrodynamic KH turbulence. Steps 6 to 10 appear only in magnetohydrodynamic turbulence. Steps 6, 8, and 10 are magnetic analogues of the hydrodynamic Steps 2, 3, and 4, respectively.

The zonal jets formed in Step 3 require three dimensions in the system; this process can operate in any general (magneto)hydrodynamic system with a shear flow. Although the zonal jets $u_x(k_x{=}0, k_y{\neq}0)$ are formed when the mean shear flow $u_x(k_x{=}0, k_y{=}0)$ strains the **u**-rolls $u_z(k_x{=}0, k_y{\neq}0)$, the **u**-rolls are generated and sustained by nonlinear interactions. If the nonlinearity is removed in a hydrodynamic system, the **u**-rolls cannot be sustained against viscous dissipation. Recall that the KH instability of the mean flow $u_x(k_x{=}0, k_y{=}0)$ requires fluctuations to have variations along the direction of the mean flow, i.e., $k_x \neq 0$. The fluctuations with $k_x{=}0$ are KH-stable. Since the **u**-rolls have $k_x{=}0$, these rolls require nonlinearity to excite them. The requirement that the **u**-rolls $u_z(k_x{=}0, k_y)$ must couple nonlinearly to the KH-scale fluctuations with $k_x \neq 0$ is evident in

$$\partial_t u_z(k_x{=}0, k_y) = \nu\nabla^2 u_z(k_x{=}0, k_y) - \sum_{\substack{k'_x, k''_x: \\ k'_x + k''_x = 0}} \sum_{\substack{k'_y, k''_y: \\ k'_y + k''_y = k_y}} \mathbf{u}(k'_x, k'_y) \cdot \nabla u_z(k''_x, k''_y) + \dots , \tag{9.18}$$

where the ellipsis ... represents the terms irrelevant for the analysis here. These latter terms include, for example, the pressure, which can be recast in terms of the nonlinearity in an incompressible system. Thus, linear physics cannot generate the **u**-rolls.

Similarly, the zonal fields formed in Step 8 require three dimensions in the system; this process can operate in any general magnetohydrodynamic system with a shear flow. Although the zonal fields $b_x(k_x{=}0, k_y{\neq}0)$ are formed when the mean shear flow $u_x(k_x{=}0, k_y{=}0)$ strains the **b**-rolls $b_z(k_x{=}0, k_y{\neq}0)$, the **b**-rolls are generated and sustained by nonlinear interactions. If the nonlinearity is removed in a magnetohydrodynamic system, the **b**-rolls cannot be sustained against resistive dissipation. The requirement that the **b**-rolls $b_z(k_x{=}0, k_y)$ must couple nonlinearly to the KH-scale fluctuations with $k_x \neq 0$ is evident in

$$\partial_t b_z(k_x{=}0, k_y) = \eta\nabla^2 b_z(k_x{=}0, k_y) + \sum_{\substack{k'_x, k''_x: \\ k'_x + k''_x = 0}} \sum_{\substack{k'_y, k''_y: \\ k'_y + k''_y = k_y}} \left[-\mathbf{u}(k'_x, k'_y)\cdot\nabla b_z(k''_x, k''_y) + \mathbf{b}(k'_x, k'_y)\cdot\nabla u_z(k''_x, k''_y)\right]. \tag{9.19}$$

One may consider a system which features — on top of a mean shear flow $u_x(k_x{=}0, k_y{=}0)$ and a mean field $b_x(k_x{=}0, k_y{=}0)$ — additional components of turbulence-generated flow $u_y(k_x{=}0, k_y{=}0)$ and field $b_y(k_x{=}0, k_y{=}0)$. In our nonlinear simulations, the energies in these components are confirmed to be at least two orders of magnitude smaller than the x-directed mean flow and fields. Even in the more general case, $b_z(k_x{=}0, k_y)$ cannot be perpetually sustained against resistive dissipation *without a nonlinearity*. The **b**-rolls $b_z(k_x{=}0, k_y)$ decay away resistively following a wave-like damped solution. The explanation is straightforward: For sustained dynamo action with the magnetic field $b_z(k_x{=}0, k_y)$ varying in two dimensions (y and z), the flow

must vary in all 3 dimensions—a requirement imposed by the Cowling's theorem [46]. Hence, there must be nonlinear couplings among the 3D fluctuations. The linear couplings between the mean flow and the x-invariant fluctuations (k_x=0, $k_y \neq 0$) alone cannot *sustain* generation of magnetic fields (it is recalled that transient growth of magnetic fields occurs in 2D, as well, where the dynamo does not exist).

The foregoing discussions highlight some comparison between the 3D hydrodynamic and 3D MHD systems. The prominent similarity between the two systems is the existence of robust zonal jets [1, 253].

The jets are the central engine in the operation of the dynamo driven by the mean-vorticity effect [66]. We have performed numerical experiments where we scrambled the phases of the zonal jets (making them incoherent), and we observe that the dynamo is inactive. Since the zonal jets are direct products of the **u**-rolls, we have performed additional experiments where we scrambled the phases of the **u**-rolls, and we find that the zonal jets are not prominent—and thus, there too, the dynamo is inactive. In these experiments, where the system is forced to eliminate the zonal jets, we observe that the turbulence is dominated largely by 2D KH-scale fluctuations throughout the nonlinear phase; the transition from 2D to 3D motions in our standard setup is severely impacted. This lack of 2D-to-3D transition is simple to explain if one recalls that the zonal jets are efficient channels for coupling 2D and 3D fluctuations. To illustrate further, consider a triad interaction between the three wavenumbers: the zonal jets with a wavenumber $\mathbf{k}$=$(0, k_y)$, the 2D KH instability with $\mathbf{k}$=$(k'_x, 0)$, and the 3D KH instability with $\mathbf{k}$=(k''_x, k''_y), where k''_x=$-\,k_x$ and k''_y=$k_y - k'_y$. In this wavenumber triad, if the zonal wavenumber is forcefully suppressed manually, the nonlinear channel that couples the 2D and 3D KH-scale fluctuations is significantly impacted. Thus, the 2D and 3D KH-fluctuations are not able to interact as much. When the 2D KH-scale fluctuations dominate the turbulence, the dynamo is ineffective

(by Cowling's theorem [46]).

Spectral condensation and wave-anisotropy principle in 3D turbulence

Here, we present a general principle of spectral condensation and saturation physics in 3D systems where symmetry is broken, making the system anisotropic.

Due to the presence of an inhomogeneous mean shear flow, the system we consider is anisotropic. Whenever a system is anisotropic, it is expected that large-scale coherent structures will emerge in the nonlinear phase. We refer this expectation as the wave-anisotropy principle. This general principle applies to any system where anisotropy is introduced by an external physics, e.g., rotation, a mean (guide) magnetic field, a large-scale shear flow, stratification, etc. In such an anisotropic system, the linear waves—whether stable or unstable—feature an anisotropic spectrum of wave-frequency or growth rate over a wavenumber plane, say $\mathbf{k} = (k_\perp, k_{||})$. Here, $k_{||}$ and $k_\perp$ are defined with respect to the direction of anisotropy arising from the external physics, e.g., rotation, a mean (guide) magnetic field, a large-scale shear flow, stratification, etc.. Because of the anisotropy, the growth rate or frequency of a linear wave is zero or nearly zero along one of the axes, say $k_\perp$. Conversely, along the parallel direction $k_{||}$, the growth rate (frequency) is non-zero and different for different $k_{||}$.

To illustrate, consider Alfvén waves (or Rossby waves), whose frequencies ω in the small-wavenumber limit are proportional to $k_{||}$: $\omega \propto k_{||}$, where $k_{||}$ the component of the wavenumber along the direction parallel to the external magnetic field (or the equatorial direction for Rossby waves in a beta plane). In such a case, there exists a wavenumber $\mathbf{k} = (\mathbf{k}_\perp, k_{||}{=}0)$ that is expected to feature a zero-frequency (or a very-low-frequency) coherent structure. The nature of this coherent structure can be predicted

a priori: Consider the nonlinearity, e.g., $\mathbf{u}\cdot\nabla\mathbf{u}$, and examine the property of $\mathbf{u}$ to predict the nature of the coherent structure. The component of the coherent structure $u_{||}(\mathbf{k}_\perp, k_{||}{=}0)$ pointed along the parallel direction reduces the nonlinearity to exactly zero. For the wavenumber $\mathbf{k} = (\mathbf{k}_\perp, k_{||}{=}0)$, the gradient operator becomes $\nabla = i\mathbf{k}_\perp$. That is, $\mathbf{u}\cdot\nabla\mathbf{u} = \mathbf{u}_\perp i\mathbf{k}_\perp(u_{||}\hat{\mathbf{e}}_{||} + \mathbf{u}_\perp\hat{\mathbf{e}}_\perp)$. Thus, if a system has only a coherent structure $u_{||}(k_\perp, k_{||}{=}0)$, no matter how large its amplitude is, the nonlinearity is always exactly zero. Hence, $u_{||}(\mathbf{k}_\perp, k_{||}{=}0)$ is an exact *nonlinear* solution to the ideal equations of motion. This nature is similar to that of the ElsÃ¤sser fields, which are exact nonlinear solutions to the ideal MHD equations [31]. In a general turbulent system, however, there inevitably exist other kinds of fluctuations $\mathbf{u}(\mathbf{k}_\perp, k_{||} \neq 0)$—although the coherent flow $u_{||}(\mathbf{k}_\perp, k_{||}{=}0)$ tends to dominate over the remainder of the fluctuations. This property explains the origin of jets in the present KH-instability-driven system in 3D, and the origin of jets in the Goldreich–Schubert–Fricke-instability-driven turbulence [35], among others [164–167, 174–177].

The wave-anisotropy principle applies to a wide variety of systems, such as quasi-geostrophic turbulence, Hasegawa-Wakatani turbulence, Hasegawa-Mima turbulence, rotating 3D turbulence, magnetized 3D turbulence, etc., all of which lead to the formation of large-scale anisotropic, coherent fluctuations [164–167, 174–177]. Here, the wave-anisotropy principle has been shown to be a key ingredient of the mean-vorticity dynamo [66].

Secondary instability vs. primary instability in self-sustaining of jets

Here, we remark on key differences between turbulence with local and non-local shear flows, and measure efficiencies of primary and secondary instabilities.

When a mean shear flow varies linearly along a spatial dimension (say, z), the mean flow is stable to the Kelvin–Helmholtz instability; the instability requires a non-zero second derivative in the flow profile. Considering a mean flow with a linear profile, past studies (see, e.g., Refs. [43, 267, 268]) have shown that straining by the mean shear flow is robust, leading to the formation of zonal jets $u_x(k_x{=}0, k_y \neq 0)$; see Step 3 in Fig. 9.12(a). However, to sustain the generation of zonal jets, Step 2—a nonlinear mechanism—is required; otherwise, zonal jets are formed only transiently before they decay and disappear completely. If the mean flow $U_x(z)$ lacks an inflection point ($\partial_z^2 U_x = 0$), the primary KH instability of Step 1 cannot operate. In that case, it has been suggested that the nonlinear zonal jets $U_x(y, z)$—pointing along x and varying sinusoidally along y—may become KH-unstable secondarily, thus generating fluctuations that vary in all three dimensions. This process of jets feeding back on jets is sometimes called the self-sustaining jet-formation mechanism (SSJFM) in studies of wall-bounded shear flow $U_x(z)$ that is linearly stable to the KH instability [267].

Based on the consideration in the foregoing paragraph [267] which is limited to a KH-stable mean flow (e.g., a linear shear flow), it has been speculated that the same SSJFM holds true for an arbitrary shear flow. However, this speculation ignores an important reality: If the mean shear flow has a non-zero second derivative (flow curvature), the mean flow can itself drive a primary instability that can rapidly generate 3D fluctuations. See Step 1 in Fig. 9.12(a). This primary mechanism can easily dominate over any secondary SSJFM.

To test the efficiencies of the primary and secondary instabilities in their ability to generate 3D fluctuations, we compare the energy transfer rates to 3D fluctuations from the mean flow (see Fig. 9.12(b)) against that from the zonal jets (see Fig. 9.12(c)), using Eq. (9.20). The former is found to be an order-of-magnitude larger than the latter. This finding demonstrates that the primary KH instability of the mean shear

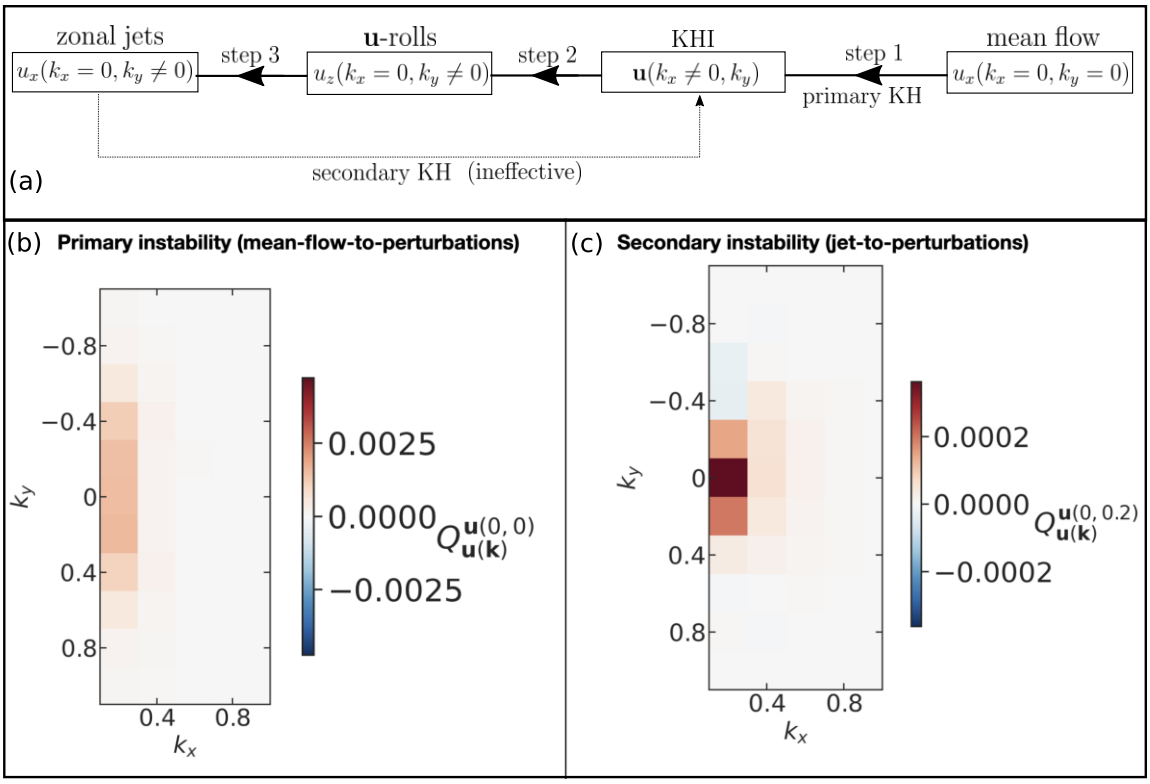

Figure 9.12: The primary instability of the mean shear flow dominates over the secondary instability of the zonal jets by supplying an order of magnitude more energy to 3D KH-unstable fluctuations. (a) Step 1 represents the primary KH instability of the mean flow; Step 2 represents a nonlinear mechanism, namely, the advective nonlinearity $-(\mathbf{u}\cdot\nabla)\mathbf{u}$; Step 3 represents straining by the mean flow. These three steps are described in Fig. 10.2 with the same numbering convention. If the mean shear flow $u_x(k_x{=}0, k_y{=}0)$ is KH-stable, Step 1 is absent. Panels (b) and (c) show the rates of energy transfer to different wavenumbers $\mathbf{u}(\mathbf{k})$ from the mean shear flow and from the zonal jets, respectively. As these data show, the understanding based on KH-stable linear shear flow is inapplicable when the turbulence is driven by a KH-unstable flow. Specifically, turbulence with a KH-*stable* mean shear-flow operates via a less-energetic secondary instability (i.e., the mechanism where the KH instability of zonal jets generates 3D fluctuations, namely those with $k_x \neq 0$; these 3D fluctuations are required to power zonal jets). However, turbulence with a KH-*unstable* mean shear-flow operates via a more-energetic primary instability (i.e., the mechanism where the KH instability of the mean shear flow directly generates 3D fluctuations, thus sustaining the generation of strong zonal jets).

flow generates 3D fluctuations overwhelmingly: The secondary KH instability of the zonal jets generates 3D fluctuations at a rate that is insignificant.

The primary mechanism operates even in the absence of a nonlinearity, whereas the secondary mechanism can only become active in the nonlinear phase. The rates of energy transfer via primary and secondary mechanisms are computed using

$$\partial_t \langle \mathbf{u}_i(-\mathbf{k})\mathbf{u}_i(\mathbf{k})\rangle_z = \underbrace{-2\mathrm{Re}\langle u_i(-\mathbf{k})u_j(\mathbf{k})\partial_j u_i(0,0) + u_i(-\mathbf{k})u_j(0,0)\partial_j u_i(\mathbf{k})\rangle_z}_{\text{KH of mean flow (primary instability)}} + \underbrace{-2\mathrm{Re}\langle u_i(-\mathbf{k})u_j(\mathbf{k}')\partial_j u_i(0,k_y) + u_i(-\mathbf{k})u_j(0,k_y)\partial_j u_i(\mathbf{k}')\rangle_z}_{\text{KH of zonal jets (secondary instability)}} + ..., \tag{9.20}$$

where the ellipsis ... represents the terms not relevant for discussion here. The first term on the right-hand side of Eq. (9.20) measures the rate of energy transfer to the fluctuation with wavenumber $\mathbf{k}$ from the mean flow $u_i(0,0)$. This energy transfer rate can be converted into the growth rate by dividing the first term on the right-hand with the energy $\langle \mathbf{u}_i(-\mathbf{k})\mathbf{u}_i(\mathbf{k})\rangle_z$; this growth rate corresponds to the finite-amplitude-modified growth rate of the KH instability of the mean shear flow in the nonlinear phase (see Fig. 10.3). The second term on the right-hand side of Eq. (9.20) measures the rate of energy transfer to fluctuations with wavenumber $\mathbf{k}$ from the zonal jets $u_i(0,k_y)$. The second term of Eq. (9.20) is an order of magnitude smaller that the first term.

9.7 Conclusions

This work has unveiled an essential nonlinear network of dynamic interactions between flow and magnetic fields in a dynamo cycle driven by the Kelvin–Helmholtz (KH) instability of a maintained mean shear flow. The network detailed in Fig. 10.2 explains

a recent and novel finding that the profile of mean magnetic field generated by the KH instability is nearly identical that of the mean shear flow. It is noted that the mean field $B_x(z)$ and the mean flow $U_x(z)$ do not directly couple, i.e., the field-line stretching term $\mathbf{B} \cdot \nabla_z U_x(z)$ is zero. This fact is due to the absence of the mean vertical field B_z in the direction z: $\nabla \cdot \mathbf{B} = \partial_z B_z = 0$ for the (x, y)-averaged mean field, and B_z is zero for perfectly conducting boundaries. Thus, the mean horizontal field is generated by a sequence of nonlinear interactions between fluctuations. Using nonlinear energy transfer analyses, this work has shown that the mean field and the mean flow are linked by 4 steps in a chain of magnetohydrodynamic interactions: In the first step, the mean shear flow $U_x(z)$ linearly excites the 2D and 3D KH instability fluctuations, which have $k_x \neq 0$. In the second step, KH-unstable fluctuations nonlinearly generate x-invariant, y-varying vertical flow (fields), which are labeled **u**-rolls (**b**-rolls), borrowing nomenclature from the studies of wall-bounded, KH-*stable* shear flows. In the third step, the **u**-rolls (**b**-rolls) are strained by the mean horizontal shear flow $U_x(z)$, thus transforming the rolls into x-invariant, y-varying horizontal flows (fields), labeled zonal jets (zonal fields). Hence, the jets acquire a vertical profile similar to the gradient of the horizontal mean flow $\nabla U_x(z)$. The sustained generation of the jets requires nonlinear KH instability motions varying in all three dimensions. (The foregoing three steps are hydrodynamic in nature.) In the final step, the zonal jets stretch the **b**-rolls, thus creating mean magnetic fields. Since this field-line-stretching process involves the spatial gradient of the jets, the mean magnetic fields display a spatial profile similar to the second derivative of the mean shear flow $\nabla^2 U_x(z)$—the first derivative arises in the jet-creation process, the second in the mean-field creation process.

Additional steps of the dynamo cycle relate to the saturation of the mean fields. The spatial gradient of the mean field is steepened by the shear-flow-induced jets (Step 7 in Fig. 10.2). The steepened mean-field gradient is flattened by turbulent

advection of mean fields along the direction of mean-field gradient (step 9 in Fig. 10.2). This flattening is similar to the turbulent advection of the mean momentum that flattens the mean shear layer. When the mean fields are advected (overturned) by the **u**-rolls vertically, the mean fields get depleted, as the mean fields transform into zonal magnetic fields. Zonal fields are additionally generated (Step 8 in Fig. 10.2) when the mean shear flow strains the **b**-rolls. These **b**-rolls are created by the KH instability (Step 6 in Fig. 10.2). Zonal fields, when strong, tend to inhibit vertical KH instability motion, thus arresting the unbounded growth of the magnetic fields and leading to saturation (Step 10 in Fig. 10.2). These various steps operate on their own characteristic timescales—very rapid KH instability, slow zonal jets and zonal fields, and even slower mean field. This separation of time scales naturally endows the dynamo cycle with inertia, self-organization, and the tendency for cyclic behavior, which is consistent with the observed astrophysical magnetic fields.

Inherently three-dimensional zonal jets develop as a spectral condensate. This condensate is sustained by the KH instability. The instability is found to not directly generate mean field but rather act as a crucial enabler of the dynamo. The KH instability of the mean shear flow sustains the nonlinear generation of the **u**-rolls, which are then strained by the mean shear flow to produce the zonal jets. These jets then create the mean field. The jets are exact nonlinear solutions to the 3D magnetohydrodynamic equations, hence they are resilient to occasional large-amplitude perturbations. Additionally, because the jets are directed along the x axis and do not vary along the x axis, the x-gradients of the fluid pressure and the magnetic pressure are exactly zero, thus leading to minimal impact of the Lorentz feedback on the jets. This topological protection of the jets against strong Lorentz feedback makes the jets robust. The jets are the central engine of the dynamo cycle uncovered in this work.

The jets are robust to variations in key magnetohydrodynamic parameters such as

the strength of the initial mean magnetic field superimposed on the KH instability. The orientation of the initial mean field has no impact on the nonlinear saturation properties of the dynamo. The jet-driven dynamo operates even in the absence of the initial mean field [253], so long as the mean flow is maintained to sustain the interactions of the dynamo. The maintenance of the mean flow is required because the mean-field creation takes a longer time, while the mean shear flow—if not maintained—can quickly deplete due to the momentum transport driven by the fast KH instability. The essential steps of the dynamo cycle are driven primarily by the large-scale fluctuations ($|k|a \lesssim 2$, where k is the horizontal wavenumber and a is the half-width of the shear layer). Smaller physical scales ($|k|a \gtrsim 2$) contribute only 1% to 10% to the energy transfer to zonal jets, zonal fields, and mean field, among others. This finding confirms that, in the large-scale dynamo, energy-containing large-scale eddies are the dynamo source; and the inertial-range eddies merely act as a dynamo sink to dissipate small amounts of waste energy. The small-scale eddies are likely limited by stable eigenmodes existing in the KH-unstable wavenumber range [1, 17, 110, 111, 143, 144]; these stable eigenmodes are excited in the KH turbulence in both 2D [17, 110, 111, 143, 144] and 3D [1], but their overall role in the dynamo cycle is subject to added nuances that are still under study and will be reported elsewhere.

The dynamo cycle helps inform sub-grid models of dynamo and turbulence [269–271], which can be implemented in resolution-limited global simulations of general-relativistic binary neutron star mergers [73, 272]. In these mergers, the KH instability is expected to generate ultra-strong magnetic fields [74, 253], possibly stronger than magnetar fields. The present dynamo cycle also identifies a working mechanism behind a postulated non-traditional mean-field dynamo theory—the mean-vorticity effect [66]. This mean field theory is a simple coarse-grained description of the complex turbulent process detailed in this work.

Appendix: Rapid distortion theory in 2D vs. 3D: Eddy splitting vs. eddy strengthening

Shear flows can distort eddies and split them apart across the axis of the flow-gradient [21]. This eddy splitting, or scale shortening, applies to all 2D and 3D perturbations, except one particular class of perturbations that are topologically protected. This class of perturbations have a topology such that they do not vary along the direction of the mean shear flow.

For the eddy-splitting or scale-shortening to apply, the perturbations must vary along the direction of the mean flow. This result is easily understood if one considers a simple linear shear flow (which may be thought as zooming into the hyperbolic tangent shear layer where the mean flow is close to zero, so the leading-order term is linear in the spatial coordinate, thus making the rapid distortion theory applicable [70]). In that case, the Navier–Stokes equation linearized around a mean flow $U_x(z) = -cz$, where c is a real constant, becomes

$$\frac{\partial u_i}{\partial t} + U_x \frac{\partial u_i}{\partial x} = -u_j \frac{\partial U_x}{\partial x_j} \delta_{i,x} - \partial_i p + \nu \nabla^2 u_i, \tag{9.21}$$

where u_i is the i-th component of the velocity, ν is the kinematic viscosity, p is the fluid pressure (per unit density), and $\delta_{i,x}$ is the Kronecker delta. After Fourier-transforming Eq. (9.21) using $u_i = \sum_{\mathbf{k}} a_i(k,t) \exp(i\mathbf{k} \cdot \mathbf{x})$, the evolution equation for the $\mathbf{k}$-th harmonic becomes

$$\frac{\partial a_i}{\partial t} + c \frac{\partial a_i}{\partial k_z} k_x = c a_z \delta_{i,x} - i k_i p - \nu k_j k_j a_i, \tag{9.22}$$

where the Fourier-transformed p is determined using the incompressibility condition

of the flow.

The amplitude-evolution equation (9.22) is solved using the method of characteristics (a method which reduces a partial differential equation to a family of ordinary differential equations), yielding

$$\frac{da_i}{dt} = ca_z\delta_{i,x} - ik_i p - \nu k_j k_j a_i, \tag{9.23}$$

where

$$\frac{d}{dt} \equiv \frac{\partial}{\partial t} + \frac{\partial k_j}{\partial t}\frac{\partial}{\partial k_j}. \tag{9.24}$$

Comparing Eq. (9.24) with Eqs. (9.22) and (9.23),

$$\frac{\partial k_j}{\partial t}\delta_{j,z} = c\,k_x. \tag{9.25}$$

Equation (9.25) predicts that the wavenumbers k_x and k_y do not change due to straining by the (x, y)-averaged mean shear flow—as expected.

However, since the mean shear flow does vary in z, the vertical scales of perturbations change over time due to the straining by the mean flow. Thus,

$$\frac{\partial k_z}{\partial t} = c\,k_x, \tag{9.26}$$

which explains why all perturbations that vary along the direction of the mean flow (i.e., perturbations with $k_x \neq 0$) are strained by the mean flow, causing them to split apart in z after an appropriate eddy-straining time [21]. However, the x-invariant perturbations are not subjected to the eddy splitting, and thus those eddies are coherently stretched by the mean flow following the amplitude-evolution equation (9.22). This is where the similarity between the simple, local linear mean shear-flow

and the KH-unstable non-local mean shear-flow ends; additional details are given in 9.6 in the main text.

10 **PAPER H**: SPONTANEOUS GENERATION OF MAGNETIC FIELDS VIA TURBULENT CROSS-HELICITY INSTABILITY IN SHEAR FLOWS

A version of this chapter is in preparation for imminent submission to Phys. Rev. Lett.

ABSTRACT

We show analytically that global turbulent cross-helicity — a measure of flow–field alignment, which is conserved in a homogeneous system — grows exponentially in the presence of an inhomogeneous shear flow. This new instability causes magnetic fields to grow exponentially, instead of the previously claimed slow linear growth. The analytic theory is confirmed with three-dimensional numerical simulations of magnetohydrodynamic turbulence. We explain the astrophysical dynamo loop in the mere presence of a shear flow. Alfvénization, instead of suppressing, drives the dynamo.

Magnetic fields are pervasive in astrophysics from Earth's magnetosphere to cosmic voids, yet the origin of these fields remains unresolved [9, 39–43, 52, 134, 245, 249, 250, 254, 273–276]. Although the generation of magnetic fields—called dynamo action—has often been modeled using helical turbulent fluid motions [273], those models have faced serious challenges [4–7], e.g, the requirement of kinetic helicity and an initial large-scale field to generate an amplified large-scale field, and nonlinear dynamo suppression via Alfvénization. The latter is a key magnetohydrodynamic process that tends to create aligned and equipartitioned velocity and magnetic fields [55–57, 59, 60, 277]. However, Alfvénization can be present already in the kinematic growth phase of magnetic fields and may induce a dynamo instead of suppressing it, via the mean-vorticity effect [66]. Nevertheless, previous studies regarding Alfvénization-induced dynamo have claimed, using arguments that lack self-consistency and numerical confirmation, that such a dynamo can generate magnetic fields that grow at best linearly in time [67–69]. Thus, they reported that this mechanism could merely act as a generator of initial large-scale *seed* magnetic fields, and would not be able to achieve exponentially growing astrophysical magnetic fields [67–69].

Here, we challenge previous claims by deriving a self-consistent analytic theory based on constraints of topology and conservation laws to predict that shear flows have a novel effect: Globally averaged alignment between turbulent flow and turbulent field grows exponentially due to the shear flow. Thus, the magnetic fields, coupled to the mean-vorticity effect [66], grow exponentially. This mechanism is general as the only required ingredient is a shear flow with an inflection point, as will be shown below. No additional turbulence-driving or symmetry-breaking mechanism (e.g., rotation) is needed.

To illustrate the foregoing, we start with the magnetic induction equation [273], which is suitably averaged (represented by $\langle\cdot\rangle$) over small scales to derive the evolution

of large-scale (mean) magnetic fields $\mathbf{B}$

$$\partial_t \mathbf{B} = \nabla \times \mathcal{E} + \eta \nabla^2 \mathbf{B}, \tag{10.1}$$

where $\mathcal{E} = \langle \widetilde{\mathbf{u}} \times \widetilde{\mathbf{b}} \rangle$ is the mean electromotive force (EMF). Here, $\widetilde{\mathbf{u}}$ and $\widetilde{\mathbf{b}}$ are fluctuation flow and fluctuation magnetic field. The EMF in the mean-field framework—when a large-scale flow $\mathbf{U}$ is present—is generalized to [66]

$$\mathcal{E} = \Upsilon \nabla \times \mathbf{U} - \beta \nabla \times \mathbf{B}, \tag{10.2}$$

where $\Upsilon \nabla \times \mathbf{U}$ represents the mean-vorticity effect; $\Upsilon = \tau \langle \widetilde{\mathbf{u}} \cdot \widetilde{\mathbf{b}} \rangle / 3$, with $\langle \widetilde{\mathbf{u}} \cdot \widetilde{\mathbf{b}} \rangle$ representing turbulent cross-helicity; $\beta \nabla \times \mathbf{B}$ represents the β-effect; $\beta = \tau \langle \widetilde{\mathbf{u}} \cdot \widetilde{\mathbf{u}} \rangle / 3$ depends on turbulent flow energy; τ is the turbulence correlation time (often measured by the ratio of turbulent kinetic energy and turbulent dissipation rate) [278]. If one assumes Υ to be a constant in the kinematic dynamo phase, similar to the constancy of β and kinetic helicity $\alpha = \tau \langle \widetilde{\mathbf{u}} \cdot (\nabla \times \widetilde{\mathbf{u}}) \rangle / 3$ justified in helical dynamos [52, 273], one concludes that $\mathbf{B}$ grows only linearly in time [67–69]. However, unlike α and β, the coefficient $\Upsilon \propto \langle \widetilde{\mathbf{u}} \cdot \widetilde{\mathbf{b}} \rangle$ depends on the strength of the magnetic-field fluctuations $\widetilde{\mathbf{b}}$, which is inevitably coupled to the evolving mean field $\mathbf{B}$. Thus, Υ *must not* be treated as a constant.

The chief result of this Letter is the derivation of a self-consistent expression for the evolution of Υ [in Eq. (10.6)], which is analytically solved together with Eq. (10.1) to obtain a novel dynamo dispersion relation. The analytic theory is then confirmed using high-resolution numerical simulations of three-dimensional (3D) magnetohydrodynamic (MHD) turbulence. Furthermore, this work explains a mechanism by which Alfvén waves propagating in one direction are generated at an exponentially higher rate than

the waves propagating in the reverse direction, thus giving rise to an exponential dynamo. This wave-selection process is a natural outcome in shear flows, where, via this mechanism, forced turbulence minimizes energy under the constraint of MHD conservation laws.

The evolution equation for an (x, y)-averaged mean shear flow $\mathbf{U}$, varying along z, is [10]

$$\partial_t U_i = -T_i + \nu \nabla^2 U_i + f_i, \tag{10.3}$$

where $i \in \{x, y, z\}$; transport term $T_i = \partial_z \langle u_z u_i - b_z b_i \rangle_{x,y} + \partial_i p_*$ captures the effects related to the mean turbulent stress; $\langle \cdot \rangle_{x,y}$ represents the (x, y)-average; $\langle \cdot \rangle$ is reserved for the volume-average; p_* is the sum of fluid pressure and magnetic pressure; ν is the kinematic viscosity; f_i is an arbitrary external acceleration per unit mass applied to the mean flow only.

To derive the evolution equation of Υ appearing in Eq. (10.2), we first write the evolution equation for the total cross-helicity $\langle \mathbf{u}_{\rm tot} \cdot \mathbf{b}_{\rm tot} \rangle$ in the system, where $\mathbf{u}_{\rm tot}$ and $\mathbf{b}_{\rm tot}$ are total velocity and total magnetic fields, respectively. Then, the cross-helicity in the mean profiles is subtracted. Since MHD three-wave interactions conserve total cross-helicity,

$$\partial_t \langle \mathbf{u}_{\rm tot} \cdot \mathbf{b}_{\rm tot} \rangle = \langle \mathbf{b}_{\rm tot} \cdot \nu \nabla^2 \mathbf{u}_{\rm tot} \rangle + \langle \mathbf{u}_{\rm tot} \cdot \eta \nabla^2 \mathbf{b}_{\rm tot} \rangle + \langle \mathbf{B} \cdot \mathbf{f} \rangle. \tag{10.4}$$

To write the evolution equation for the cross-helicity in the mean profiles $\langle \mathbf{U} \cdot \mathbf{B} \rangle$, we multiply Eq. (10.3) with $\mathbf{B}$ and Eq. (10.1) with $\mathbf{U}$ and then add them to obtain

$$\partial_t \langle \mathbf{U} \cdot \mathbf{B} \rangle = \langle \mathbf{U} \cdot \left\{ \nabla \times \mathcal{E} + \eta \nabla^2 \mathbf{B} \right\} \rangle + \langle \mathbf{B} \cdot \left\{ \nu \nabla^2 \mathbf{U} + \mathbf{f} - \mathbf{T} \right\} \rangle. \tag{10.5}$$

Subtracting Eq. (10.5) from Eq. (10.4), with $\langle \widetilde{\mathbf{u}} \cdot \widetilde{\mathbf{b}} \rangle = 3\Upsilon/\tau$,

$$\frac{3}{\tau}\partial_t \Upsilon = \nu \langle \widetilde{\mathbf{b}} \cdot \nabla^2 \widetilde{\mathbf{u}} \rangle + \eta \langle \widetilde{\mathbf{u}} \cdot \nabla^2 \widetilde{\mathbf{b}} \rangle - \langle \mathbf{U} \cdot \nabla \times \mathcal{E} \rangle + \underbrace{\langle \mathbf{B} \cdot \mathbf{T} \rangle}_{\substack{\text{turbulent transfer} \\ \text{of cross-helicity}}}, \tag{10.6}$$

which is a topologically motivated exact equation. This equation is valid for any incompressible MHD system. Since the mean flow $\mathbf{U}$ is inhomogeneous in z, further calculations require spectral analysis.

We Fourier-transform Eq. (10.1), with $\partial_t \equiv \lambda$, and consider an x-directed mean shear flow $\mathbf{U} = \hat{\mathrm{e}}_x U_x(z)$, which provides the Υ-dynamo source in Eq. (10.2). We find $\widehat{B}_x = \Upsilon k_z^2 \widehat{U}_x/(\lambda + \beta_{\mathrm{T}} k_z^2)$, where carets represent Fourier-transformed variables with a wavenumber k_z, and $\beta_{\mathrm{T}} = \beta + \eta$ is the turbulence-modified magnetic diffusivity.

We analyze Eq. (10.6) term by term, starting from the last. Since the mean flow is directed along x and varies vertically along z, the mean turbulent stress $\mathbf{T}$ transports vertically the x-directed mean momentum. This transport depletes the gradient of the mean shear flow $U_x(z)$. Thus, the transport effect $\mathbf{T} = \hat{\mathbf{e}}_x T_x(z)$ renders $\langle \mathbf{B} \cdot \mathbf{T} \rangle$ of Eq. (10.6) as $\langle B_x T_x \rangle = \sum_{k_z} \widehat{B}_x^*(k_z) \widehat{T}_x(k_z) = \Upsilon \sum_{k_z} [k_z^2 \widehat{U}_x^*(k_z) \widehat{T}_x(k_z)/(\lambda + \beta_{\mathrm{T}} k_z^2)]$, where the result from the preceding paragraph is used. The asterisk denotes the complex-conjugation. The term $\langle \mathbf{U} \cdot \nabla \times \mathcal{E} \rangle$ in Eq. (10.6) is written in spectral space, using Eq. (10.2). Then, $\mathbf{B}$ is expressed in terms of $\mathbf{U}$ in spectral space, using the result from the preceding paragraph. Thus, both the last and second-to-last terms of Eq. (10.6) are linear in Υ, as is the left-hand side. The microphysical dissipative terms in Eq. (10.6) do not *drive* the dynamo and are not necessary for a qualitative understanding. However, we retain those for completeness and apply a numerically supported, standard procedure: $\langle \widetilde{\mathbf{u}} \cdot \nabla^2 \widetilde{\mathbf{b}} \rangle = \langle \widetilde{\mathbf{b}} \cdot \nabla^2 \widetilde{\mathbf{u}} \rangle = -\langle \widetilde{\boldsymbol{\omega}} \cdot \widetilde{\mathbf{j}} \rangle = -\langle \widetilde{\mathbf{u}} \cdot \widetilde{\mathbf{b}} \rangle / l^2$, where l represents the characteristic dissipation scale of cross-helicity. Hereafter, $(\nu + \eta)/l^2$

is labeled $\tau_{\rm diss}^{-1}$, which is the rate of microphysical dissipation of turbulent cross-helicity. These dissipative terms slightly reduce the growth rate λ. Fourier-transforming Eq. (10.6) and manipulating expressions, we derive the dispersion relation of the Υ-dynamo

$$\boxed{\begin{aligned}&\lambda+\tau_{\rm diss}^{-1}+\frac{\tau}{3}\langle(\partial_z U_x)^2\rangle\\&\quad=\frac{\tau}{3}\sum_{k_z}\underbrace{\left[k_z^2\widehat{U}_x^*(k_z)\right]}_{\text{flow-curvature}}\left[\frac{\beta k_z^2\widehat{U}_x(k_z)+\widehat{T}_x(k_z)}{\lambda+\beta_{\rm T}k_z^2}\right],\end{aligned}} \tag{10.7}$$

where $\widehat{U}_x(k_z)$ is the Fourier coefficient of the inhomogeneous shear flow with wavenumber k_z. If the small microphysical damping rate $\tau_{\rm diss}^{-1}$ is discarded for simplicity for now, Eq. (10.7) is an exact dispersion relation for the ideal MHD Υ-dynamo instability. If $k_z^2\widehat{U}_x$=0, the right-hand side of Eq. (10.7) becomes zero, which means that dynamo action is not possible with the mere presence of curvature-less shear flow. Equation (10.7) is valid for an arbitrary shear flow. Due to the summation in k_z, the dispersion relation (10.7) is a polynomial in λ.

We remark that if the conventional α-effect [52, 273] is allowed to co-exist with the Υ-effect in Eq. (10.2), the resulting dispersion relation is almost identical to Eq. (10.7), with the only difference being that β is replaced by β', where β'=$\beta-c$ and $\beta_{\rm T}'$=$\beta_{\rm T}-c$, with $c=\alpha^2/(\lambda+\beta_{\rm T}k_z^2)$. It is trivial to check that this general dispersion relation, in the absence of a mean shear flow, reduces to the conventional dispersion relation for the α^2-dynamo [52, 273]: $\lambda+\beta_{\rm T}'k_z^2=0$, thus yielding $\lambda_{\alpha^2}=\pm\alpha k_z-\beta_{\rm T}k_z^2$. We find that the growth rate λ from the α-included Eq. (10.7) is only slightly changed from the α-excluded Eq. (10.7), when the α-effect (kinetic helicity) is added at the level observed in direct numerical simulations.

Analytic transparency is gained by analyzing a classic shear flow $U_x(z)$=$U_0\sin(Kz)$,

for which Eq. (10.7) reduces to a quadratic equation in λ,

$$\lambda = -D \pm \sqrt{D^2 + \frac{\tau}{3}(U_0 K^2)^2 \left\{ \frac{\mathrm{Im}[-\widehat{T}_x(K)]}{U_0 K^2} - \eta_* \right\}}, \tag{10.8}$$

where $D{=}(\beta_\mathrm{T} K^2 {+} \tau U_0^2 K^2/6 {+} \tau_\mathrm{diss}^{-1})/2 > 0$ is a damping-associated term, and $\eta_*{=}\eta/2 {+} 3\beta_\mathrm{T}/(\tau U_0^2 K^2 \tau_\mathrm{diss})$. Thus, Eq. (10.8) predicts two criteria for when the Υ-effect drives an exponentially growing dynamo:

(i) $U_0 K^2 \neq 0$. That is, the mean flow must have an inflection point. This shear flow thus is unstable to the Kelvin–Helmholtz (KH) instability [10]. It is surprising that, without knowing any details of the KH flow-instability, Eq. (10.8) predicts the growth rate of the magnetic instability, based on the constraints of global topology and MHD conservation laws.

(ii) Imaginary part of $-\widehat{T}_x(K)/(U_0 K^2)$ should be greater than η_*, which may be aproximated as $\mathrm{Im}[-\widehat{T}_x(K)]/(U_0 K^2) \gtrsim \eta/2$, considering negligibly small τ_diss^{-1} (very slow molecular dissipation). This second criterion can be further simplified for the standard gradient-flux transport ($\langle u_x u_z \rangle_{x,y}{=}{-}\mu_\mathrm{T} \nabla_z U_x$) applicable here, which allows us to write $\mathrm{Im}(-\widehat{T}_x(K)){=}\mu_\mathrm{T}(U_0 K^2)/2$, where $\mu_\mathrm{T} = C_\mu \tau E_\mathrm{turb}$ is the turbulent viscosity, $C_\mu{=}0.1$, and $E_\mathrm{turb}{=}\langle \widetilde{u}^2 \rangle/2$ [66, 278]. Thus, for the Υ-dynamo instability, $E_\mathrm{turb} \gtrsim \eta/(C_\mu \tau)$ represents a lower threshold of turbulence generated by the KH instability.

Figure 10.1 shows the ideal-MHD solution for λ using the dispersion relation (10.7) applied to a double shear layer $U_x(z){=}U_0 \{\tanh[(z - z_1)/a] - \tanh[(z - z_2)/a] - 1\}$, where a is the half-width of the shear layers located at $z_1{=}L_z/4$ and $z_2{=}3L_z/4$ (flow-reversal locations) in a z-domain from 0 to L_z [82]. Length and time scales are measured in terms of a and a/U_0, respectively, where U_0 is the flow amplitude. Supplemental data (Fig. 10.6) confirm that behavior similar to Fig. 10.1 is observed

even when microphysical dissipation $\tau_{\rm diss}^{-1}$ is included in Eq. (10.7).

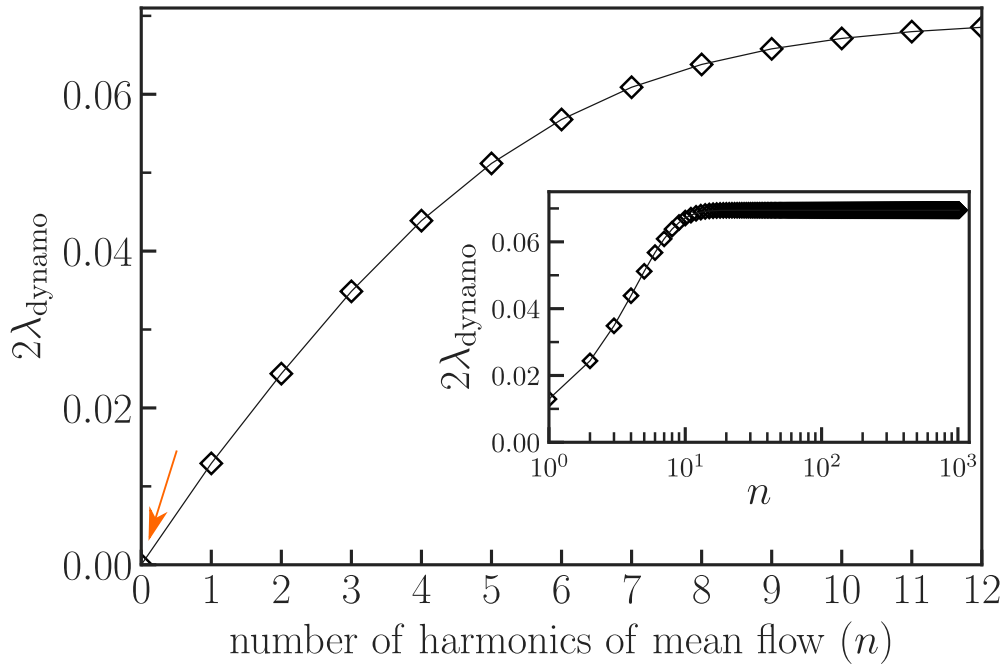

Figure 10.1: The magnetic-energy growth rate ($2\lambda_{\rm dynamo}$) asymptotes as more Fourier harmonics n of the hyperbolic-tangent shear flow $U_x(z)$ are added in the dispersion relation (10.7). The arrow near left-bottom end shows that the cross-helicity instability does not arise when the flow is uniform ($n = 0$).

Informed by the above analytic theory, we perform high-resolution numerical simulations of the 3D MHD dynamo with only one ingredient: the mean shear flow $U_x(z)$. The profile for the mean shear flow is given in the preceding paragraph. The mean magnetic field at t=0 is zero. We then add phase-randomized, broadband, divergence-free noise in velocity and magnetic fluctuations, whose energies compared to that of the mean flow are 10^{-18}. We solve the incompressible 3D MHD equations [10] $\partial_t u_i = -u_j\partial_j u_i + b_j\partial_j b_i - \partial_i(p + b_j b_j/2) + \nu\partial_{jj}u_i + f_i$ and $\partial_t b_i = b_j\partial_j u_i - u_j\partial_j b_i + \eta\partial_{jj}b_i$, with $\partial_i u_i$=0=$\partial_i b_i$, where repeated index represents summation over it; u_i and b_i represent the i-th component of velocity and magnetic fields, respectively; p is the fluid pressure per unit density; ∂_i is the spatial derivative in the i-th direction;

repeated subscripts represent summation over that subscript; f_i=$\hat{\mathbf{e}}_x\, f_x(z,t)\delta_{i,x}$ is as-yet-unspecified external acceleration applied only to the (x,y)-averaged mean flow $U_x(z,t)$. To test the aforementioned analytic theory, which employs a steady mean shear flow $U_x(z)$, we maintain the mean shear flow externally, thus preventing it from getting eroded by its KH instability. No external forcing is applied except to the mean flow. We maintain the mean flow by either freezing it (a standard procedure in dynamo studies [43, 274]) or dynamically driving the instantaneous mean flow $U_x(z,t)$ toward its initial unstable equilibrium $U_x(z,t{=}0)$ using $f_x(z,t){=}[U_x(z,t{=}0) - U_x(z,t)]/\tau_{\rm f}$, where $\tau_{\rm f}$ is the forcing time-scale. This forcing is commonly used in fluid and plasma physics [117–119, 143, 190, 196]. Both methods of forcing—freezing and dynamic driving—produce similar results.

We simulate a large domain (compared to a) of size $L_x \times L_y \times L_z$, with $L_x = L_y = 10\pi$ and $L_z = 20\pi$, using at least $128 \times 128 \times 256$ and as many as $1024 \times 1024 \times 2048$ grid points. We have simulated cases of different domain sizes, initial conditions, and system parameters, and have reproduced essentially the same growth of magnetic fields. For example, L_y is varied in distinct simulations from 10π to $20\pi, 40\pi, 80\pi, 160\pi$, and 320π, with correspondingly large number of grid points. The case of $L_y = 320\pi$ uses 4096 grid points in y. We parallelize a pseudospectral solver GHOST [128, 279] using MPI in z and openMP in y to leverage non-uniform memory-access infrastructure for efficient solution for very large resolutions. We have benchmarked GHOST against another pseudospectral solver, Dedalus [82, 121], reproducing identical results.

Figure 10.2 shows a typical evolution of kinetic and magnetic energies. The kinetic energy grows rapidly due to the KH instability. When the KH instability saturates nonlinearly, it excites 3D fluid motions and large-scale jets with wavenumbers $k_x{=}0$ and $k_y{\neq}0$. Once the turbulence becomes three-dimensional, magnetic fields begin to grow exponentially. This instability is shown here to have a global topological

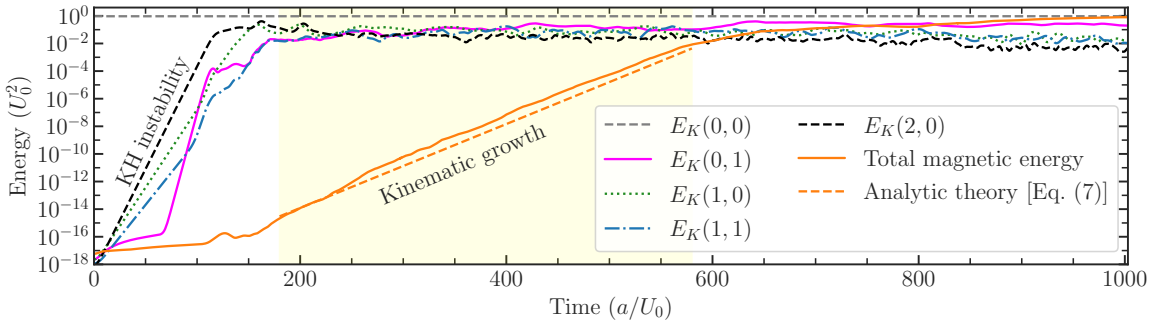

Figure 10.2: A direct numerical simulation showing rapid growth of 2D KH instability, subsequent growth of 3D KH instability and KH-stable perturbations (k_x=0, $k_y\neq$0), and the saturation of turbulent flow. The label $E_K(m,n)$ represents z-integrated kinetic energy associated with the Fourier mode number (m,n) in the (x,y)-plane. After $t\approx$200, a nonlinear instability of magnetic fields ensues. This growth is due to the instability of the turbulent cross-helicity, as predicted analytically in Eq. (10.7). The mean flow is maintained in this self-consistent, non-linear simulation.

constraint: The Υ-instability requires a mean shear flow with a non-zero second derivative in its spatial profile. Both mean and fluctuating fields are found to grow exponentially at the same rate, consistent with the analytic theory that predicts the same growth rate due to coupling between the mean field and the mean of the turbulent cross-helicity via Eqs. (10.1) and (10.6). In the simulation in Fig. 10.2, the mean flow is frozen, thus making it suitable to directly test the presented analytic theory where the the mean flow is steady.

By continuously forcing the mean flow toward its initial unstable equilibrium, the dynamo growth rates are measured in distinct simulations and found to be robust to variations in magnetic Reynolds number Rm=$U_0 a/\eta$, domain size L_y, and mean-flow forcing time-scale $\tau_{\rm f}$, as shown in Fig. 10.3. The cases of smaller $\tau_{\rm f}$ asymptote to the case of $\tau_{\rm f}$=0 (frozen mean-flow), as anticipated. Thus, these confirm our theoretical prediction that an exponentially growing dynamo is possible with a minimal ingredient: the mere presence of a maintained shear flow.

We now provide a physical interpretation of how magnetic fields grow exponentially

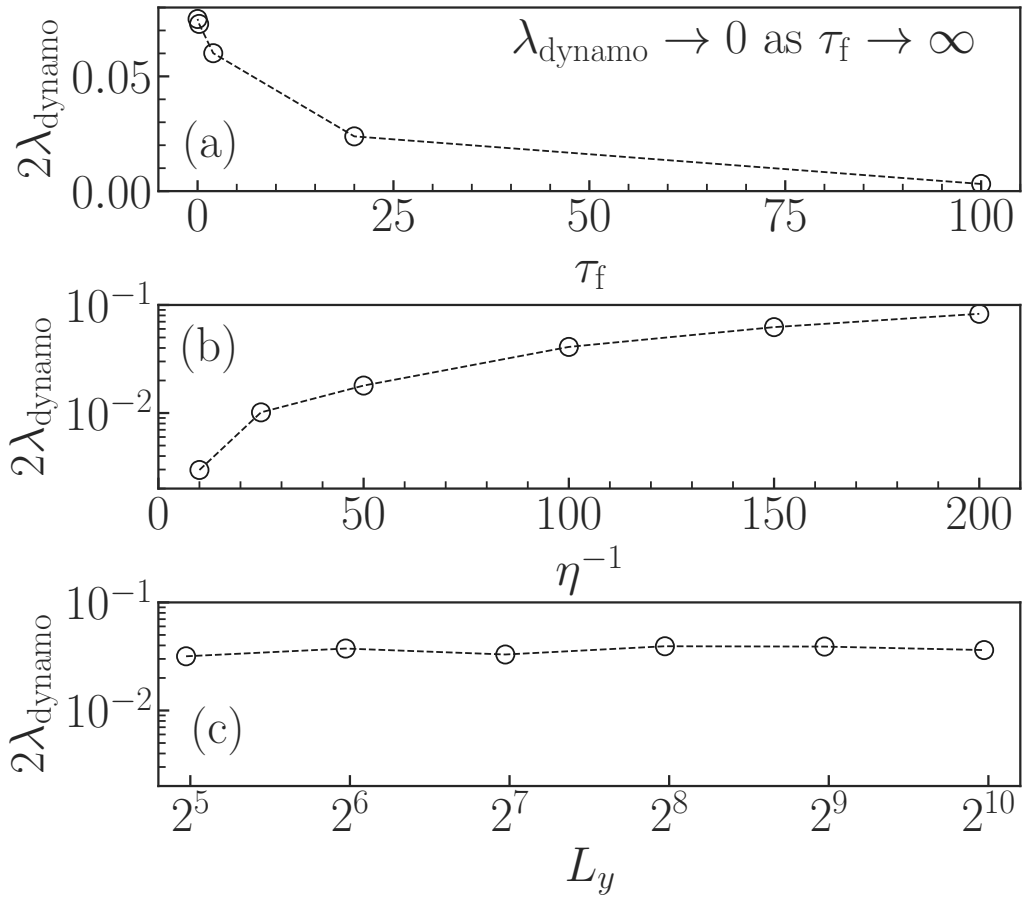

Figure 10.3: Ubiquity of Υ-dynamo. (a) Dynamo growth ($\lambda_{\rm dynamo} > 0$) is observed in cases where mean-flow-forcing time scale $\tau_{\rm f}$ is varied. For the case of $\tau_{\rm f} \to \infty$, where the mean-flow is not forced, turbulence decays quickly before dynamo via the mean-vorticity effect can grow; the dynamo growth rate is thus close to zero. (b) A growing Υ-dynamo is found for various microphysical resistivity η so long as η is small that resistive diffusion does not damp the dynamo. (c) Dynamo—which requires three dimensionality, y-axis here—grows at the same rate when a large domain $L_y/a \gg 1$ is considered.

when all that is present in the system is merely a maintained mean shear flow. For exponential growth in a dynamical system, at least two steps are needed, each feeding on the other in a manner that is cyclic and unstable. For example, in an α^2-dynamo, the generation of a mean-field component induces the generation of another mean-field component, and vice-versa, thus providing an unstable feedback cycle [52, 273]. Here, the dynamo in a shear flow also involves two unstable steps that couple two mean variables, as shown in Fig. 10.4(a):

(i) This step generates mean magnetic field B_x from the *global* mean of turbulent cross-helicity Υ in Eq. (10.1). Here, Υ is not the local turbulent cross-helicity, but its global mean (volume average).

(ii) This step operates when the mean turbulent stress $\mathbf{T}$ transfers cross-helicity of the mean profiles to fluctuations. Hence, the fluctuation-scale magnetic fields $\widetilde{\mathbf{b}}$ become globally more aligned with the fluctuation-scale fluid velocity $\widetilde{\mathbf{u}}$. Thus, the global mean $\langle\widetilde{\mathbf{u}}\cdot\widetilde{\mathbf{b}}\rangle$ of turbulent cross-helicity increases, instigating Step (i). Step (ii) is driven by $\langle\mathbf{B}\cdot\mathbf{T}\rangle$ in Eq. (10.6). This term gives rise to $\mathrm{Im}(-\widehat{T})$ in Eq. (10.8)—the source of the Υ-dynamo instability. Figure 10.4(a) summarizes these two steps.

The first step of the Υ-instability dynamo loop is confirmed in Fig. 10.4(b), where the Υ-effect is shown to dominate in the general expression for the mean turbulent EMF $\mathcal{E} = \alpha\mathbf{B} - \beta\nabla\times\mathbf{B} + \Upsilon\nabla\times\mathbf{U}$. Allowing this general form, we measure the dynamo coefficients using singular-value decomposition applied to a time series of EMF at each z-coordinate [280]. This method has been shown [280] to reproduce results from, and reduce errors compared to, other methods such as the test-field method [281] and simple moment-based regression methods [43, 282]. Additionally, we have obtained consistent results using both quasilinear estimates of the dynamo coefficients and a spatial multi-dimensional regression method [9] applied to each snapshot. Since the magnetic fields grow exponentially in the kinematic phase, the field amplitude

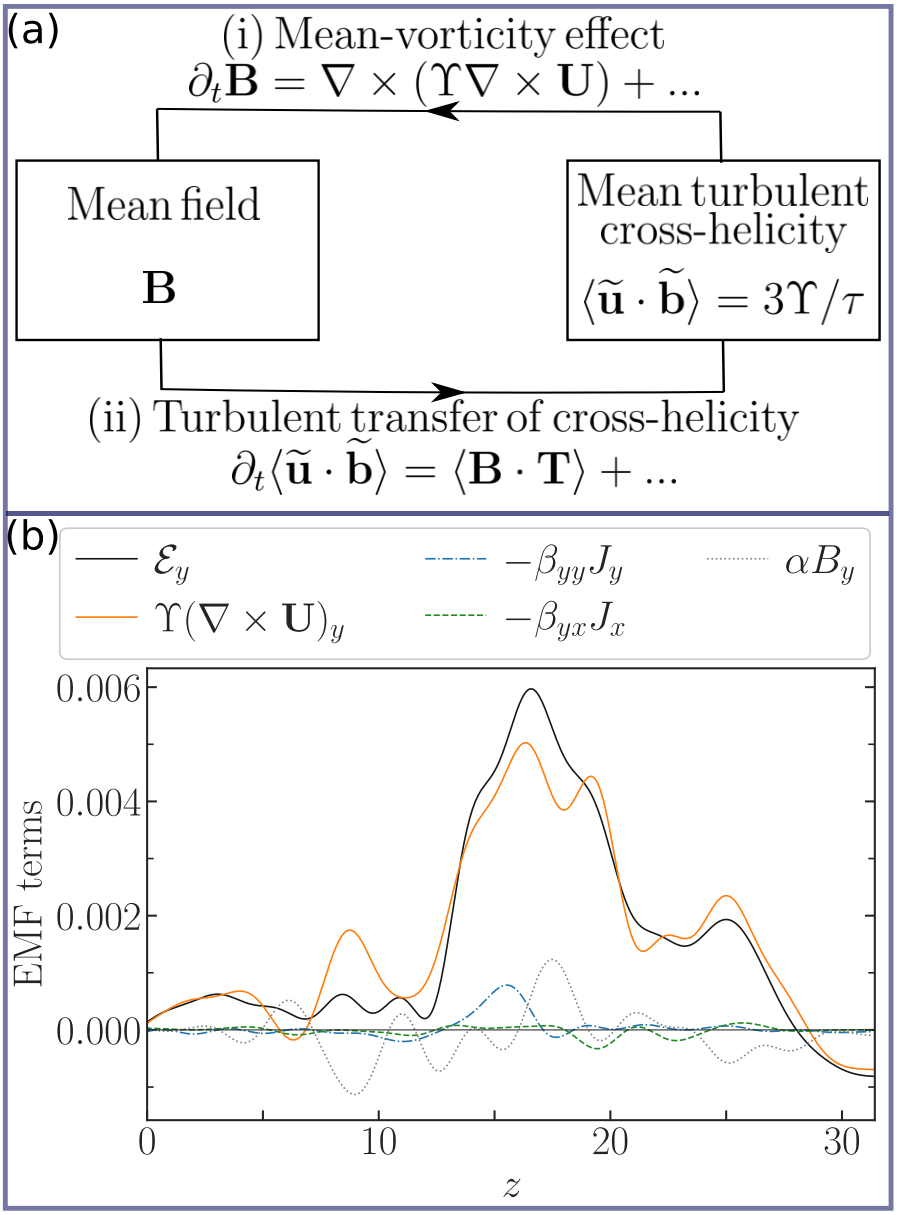

Figure 10.4: (a) The Υ-dynamo loop is identified to operate via coupling between mean field and mean turbulent cross-helicity. The former is generated in Step (i) by the mean-vorticity effect [Eq. (10.1)]; the latter is generated in Step (ii) by the Reynolds stress [Eq. (10.6)]—as the stress transfers cross-helicity from mean to fluctuations in an analogous way as it does momentum and energy from mean to fluctuations. (b) Step (i) is confirmed by decomposing the mean turbulent EMF $\mathcal{E}_y$ into different dynamo components, among which the Υ-related mean-vorticity drives the EMF. The dynamo components are time-averaged over the kinematic phase. Step (ii) is confirmed in Fig. 10.5.

is used to divide each term [280] of the mean EMF $\mathcal{E} = \alpha\mathbf{B} - \beta\nabla \times \mathbf{B} + \Upsilon\nabla \times \mathbf{U}$. Dominance of the Υ-effect is further confirmed by the numerical observation that cross-helicity dominates over kinetic helicity.

The second step of the Υ-instability dynamo loop [Fig. 10.4(a)] is confirmed in Fig. 10.5, where each term of Eq. (10.6) is divided by the exponentially growing field-amplitude to allow a direct comparison of relative importance of each term over time. The transport-related term $\langle \mathbf{B} \cdot \mathbf{T} \rangle$, in particular $\langle B_x T_x \rangle$, drives and modulates the mean turbulent cross-helicity Υ. The term T_x dominates over T_y because the imposed mean flow is directed along x. The remaining terms are non-negligible and, on average, have opposite signs, relative to the signs of Υ and $\langle B_x T_x \rangle$. Thus, the remaining terms act as as a mechanism of dynamo cross-helicity damping—as expected. (The extremely rapid variations of noisy turbulence data are subjected to a standard low-pass filter, which allows us to focus on the long-term trends.) These results are robust across simulations.

The upper-bound on the exponentially growing Υ-coefficient is given by $\Upsilon \leq \tau E_{\rm turb}/6$, where $E_{\rm turb} = \langle \widetilde{\mathbf{u}}^2 + \widetilde{\mathbf{b}}^2 \rangle$ is the volume-averaged turbulent energy. This bound, which agrees reasonably well with numerical simulations, is derived using $(\widetilde{\mathbf{u}} \pm \widetilde{\mathbf{b}})^2 \geq 0$, which upon volume-averaging gives $\langle \widetilde{\mathbf{u}}^2 + \widetilde{\mathbf{b}}^2 \rangle \geq 2\langle \widetilde{\mathbf{u}} \cdot \widetilde{\mathbf{b}} \rangle = 6\Upsilon/\tau$, where $\Upsilon = \tau \langle \widetilde{\mathbf{u}} \cdot \widetilde{\mathbf{b}} \rangle / 3$.

Conclusions.—The foregoing presentation shows how magnetic fields grow exponentially in the mere presence of a maintained shear flow. We have also performed detailed turbulence analyses, which show where in the fluctuation spectrum the dominant mean cross-helicity resides. The fluctuations that drive the Υ-dynamo are those which are directed along x, do not vary in x, but vary in the y-direction orthogonal to the plane of the mean shear flow $U_x(z)$. The wavenumbers $k'_x{=}0$ and $k'_y{\neq}0$ dominate the spectrum of the growth rate of the mean field. These wavenumbers appear only in a

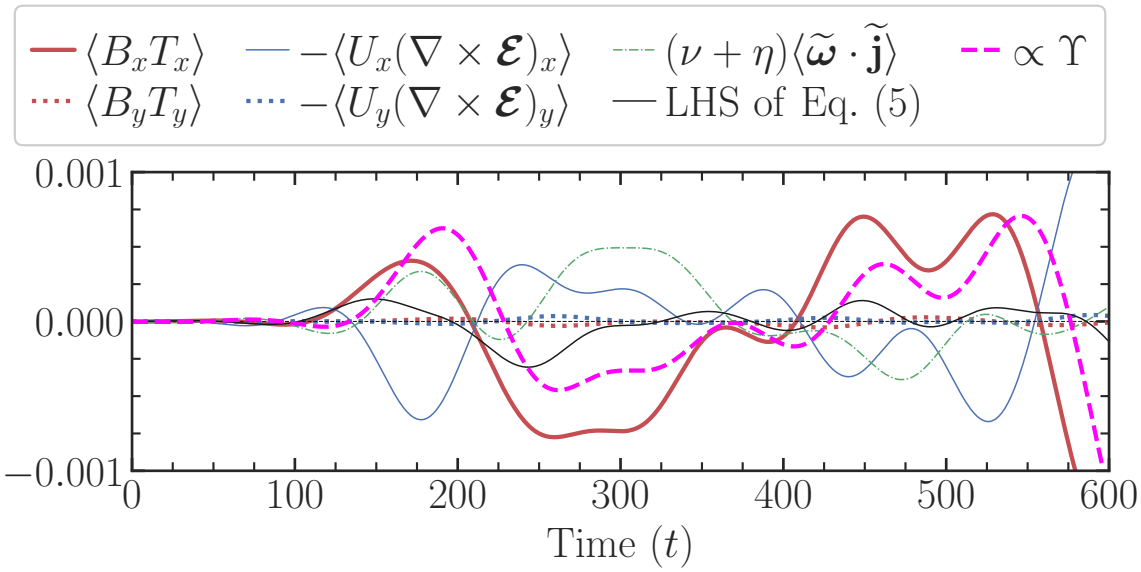

Figure 10.5: Each term in the turbulent cross-helicity evolution equation (10.6) is tracked in the kinematic dynamo phase ($t \approx 200 - -550$) to show: (i) the turbulent cross-helicity ($\langle \widetilde{\mathbf{u}} \cdot \widetilde{\mathbf{b}} \rangle \propto \Upsilon$) follows the transport-related term $\langle B_x T_x \rangle$; (ii) the terms $\langle U_y(\nabla \times \mathcal{E})_y \rangle$ and $\langle B_y T_y \rangle$, which involve y-components, are negligible—as the mean flow U_y and mean turbulent stress T_y are negligible; and (iii) $(\nu+\eta)\langle \widetilde{\boldsymbol{\omega}} \cdot \widetilde{\mathbf{j}} \rangle$, on average, has opposite sign compared to Υ and $\langle B_x T_x \rangle$, meaning that it dissipates cross-helicity.

3D shear flow. The large wavenumbers (along both k_x and k_y), on average, act as a dynamo sink where the waste turbulent energy is dissipated.

This work has shown that—in the presence of a background shear flow—a non-zero global mean of turbulent cross-helicity is generated exponentially more due to the mean Reynolds stress. This stress is, on average, zero in the idealized homogeneous system, and thus the global mean of turbulent cross-helicity is conserved [60, 277]. Since most dynamo studies use homogeneous setup, it may be the reason why the Υ-dynamo instability has not been reported before. This Letter presents a novel and robust mechanism of dynamo instability arising from a flow inhomogeneity.

The rapid generation of Alfvénic states ($\widetilde{\mathbf{u}} || \pm \widetilde{\mathbf{b}}$) at a global scale is an outcome of turbulent relaxation in the presence of a mean shear flow, similar to the rapid generation of local Alfvénic states in the absence of a mean shear flow [59]. The local

Alfvénic states appear as small-scale patchy structures [59], common in homogeneous MHD turbulence (due to dynamic alignment [283]). Here, the global Alfvénic states appear as self-organized, smooth magnetic structures, consistent with commonly observed coherent astrophysical fields [273].

The dynamo instability demonstrated here is general and significant because the mere presence of a maintained shear flow generates exponentially growing magnetic fields. This had been thought impossible, because previous claims were based on inconsistent and inapplicable argument that the dynamo coefficient Υ is a constant in time—similar to the coefficients α and β in the kinematic phase—which led to the claim that the magnetic field can grow, at best, linearly in time [67–69]. This Letter derives an exact expression for the time evolution of the Υ-coefficient, which is then self-consistently coupled to the mean-field evolution equation, to show exponential growth of magnetic fields and mean turbulent cross-helicity. This mechanism is predicted using analytic theory and validated using high-resolution 3D MHD simulations. Additionally, a physical interpretation is given using two cyclic and unstable steps: First, the Υ-effect generates the mean field. Second, the thus-generated mean MHD profiles transfer their cross-helicity to fluctuations via coupling to the mean Reynolds stress—analogous to how the Reynolds stress transfers mean momentum and energy to turbulent fluctuations [1, 10].

Astrophysical systems display large-scale shear flows, e.g., in solar meridional circulation (a key component of flux-transport dynamos), accretion disks, astrophysical jets, the interface between merging galaxy clusters, and the interface between merging binary neutron stars, where some of the strongest magnetic fields are generated [44, 73, 74, 284–289]. These systems are bound to feature the Υ-effect, and depending on the system properties, the effect can be substantial. This effect of cross-helicity in shear flows bears implications for MHD turbulence and magnetic reconnection in the

solar wind where the turbulence features near-maximum cross-helicity [55–57, 277]. The presented mechanism of dynamo growth can provide an explanation for dynamos in other non-local shear flows [254, 275], where dynamo mechanism remains unresolved.

In this Letter, a surprising finding is demonstrated: Alfvénization, instead of suppressing [4, 5, 7], *drives* the dynamo *instability*, when a shear flow is present. This result opens a new path to understanding magnetic-field generation in astrophysical environments, where shear flows appear ubiquitously [10, 73, 284, 286, 287] and potentially so does the reported mechanism of dynamo instability.

Appendix

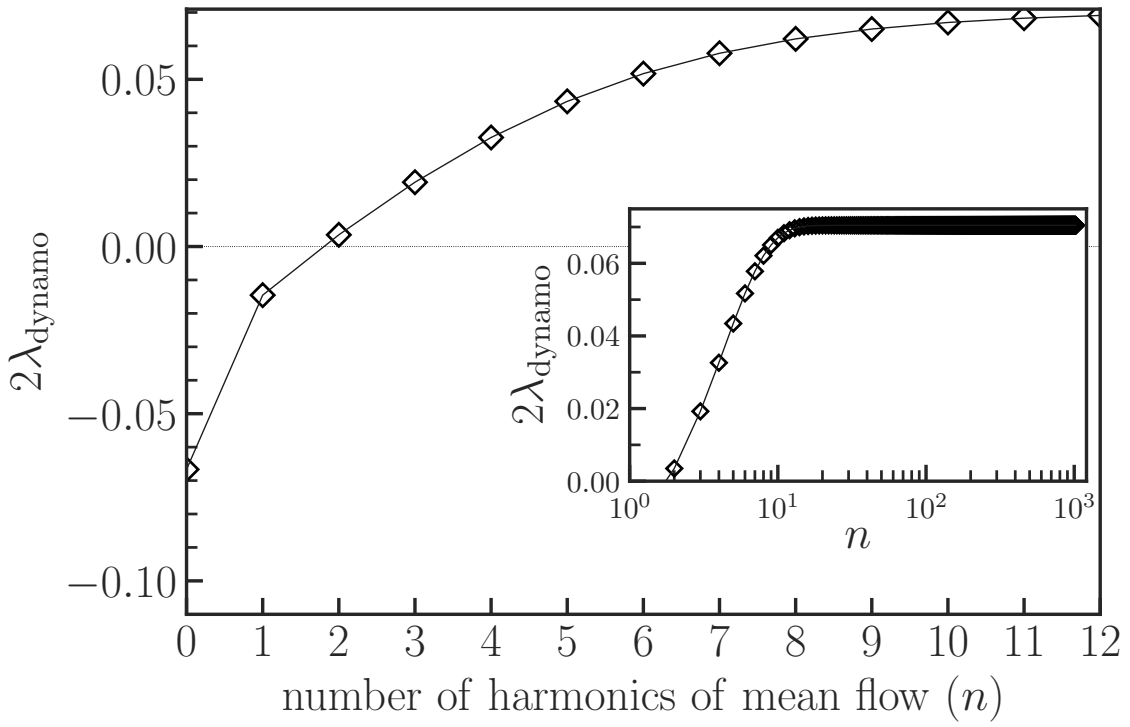

Figure 10.6: Even when visco-resistive dissipation is included in Eq. (10.7), the magnetic-energy growth rate $2\lambda_{\rm dynamo}$ asymptotes to the level observed in numerical simulations as more Fourier harmonics n of the hyperbolic-tangent shear flow $U_x(z)$ are added in the dispersion relation (10.7). The parameter $\tau_{\rm diss}^{-1}$ appears in Eq. (10.6) as $(\partial_t + \tau_{\rm diss}^{-1})\langle \widetilde{\mathbf{u}} \cdot \widetilde{\mathbf{b}} \rangle = \langle \mathbf{B} \cdot \mathbf{T} \rangle - \langle \mathbf{U} \cdot \nabla \times \mathcal{E} \rangle$, where $\tau_{\rm diss}^{-1} = -(\nu + \eta)\langle \widetilde{\omega} \cdot \widetilde{\mathbf{j}} \rangle / \langle \widetilde{\mathbf{u}} \cdot \widetilde{\mathbf{b}} \rangle$. For the simulation in Fig. 10.5, $\tau_{\rm diss} \approx 30$.

11 CONCLUSIONS AND OUTLOOK

This chapter summarizes chief findings of this thesis, their implications, and future work. For expounded technical findings, the reader is suggested to turn to abstracts mentioned in each chapter. Moreover, the reader is guided to Sec. 1.4, where important findings are detailed chapter by chapter, in addition to their inter-relationship and natural development. Hence, those interrelation and chapter-by-chapter summary are not duplicated here. A different approach is taken here, where new findings from various chapters are combined into thematic categories.

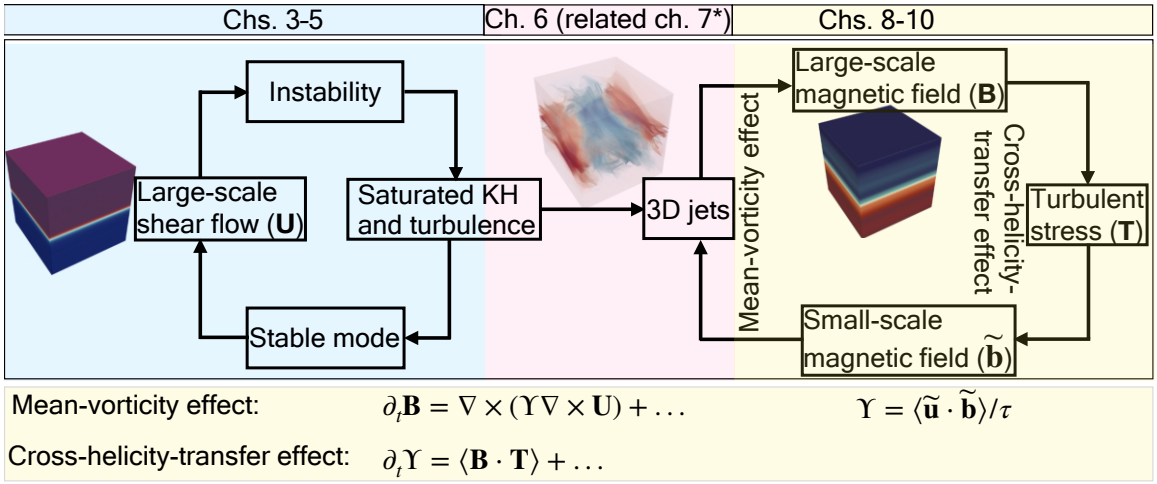

Figure 11.1: Inter-relationship and summary of the three-part thesis: Part I—up to Ch. 5; Part II—Chs. 6 and 7; Part III—Chs. 8–10. Instability grows rapidly and saturates quickly, generating nonlinearly the zonal jets. The 3D jets grow over longer times, and when the jets saturate, they drive the dynamo. The dynamo slowly grows over much longer times. This separation of temporal scales naturally divides the thesis into three parts: instability saturation via stable modes, zonal-jet formation, and jet-driven dynamo.

This thesis is centered around shear flows, with a particular emphasis on the nonlinear saturation of shear-flow instability, the formation of 3D zonal jets, and the subsequent generation of magnetic fields via a novel dynamo mechanism. The interconnection between these three processes are shown in Fig. 11.1, where some of the

chief findings of this thesis are placed in context. Unstable eigenmodes extract energy from the unstable shear flow; most of this energy is transferred to stable eigenmodes via nonlinear mode-coupling. The stable modes then return turbulent energy to the unstable shear flow, thus leaving only a minute part of turbulent energy for cascade to small scales. Turbulence driven by the thus-saturated instability generates 3D zonal jets. The jets then stretch Alfvénized magnetic field fluctuations[1], thus creating large-scale magnetic fields.

Alfvénization, commonly known as a dynamo suppressor, is shown in this thesis to be a dynamo enabler or dynamo stimulant in the presence of a KH-unstable shear flow. This stimulating nature of Alfvénization manifests via the interaction between the zonal jets and Alfvénic magnetic fluctuations, which represents the underlying mechanism behind the postulated mean-vorticity effect [66]. This mechanism is confirmed in Fig. 8.3a. The mean-vorticity effect is the first step of a dynamo loop that exponentiates magnetic fields. The dynamo-generated large-scale magnetic fields are aligned with the large-scale mean flow. The alignment between the large-scale flow and large-scale magnetic field—which represents cross-helicity of large-scale MHD profiles—is then transferred to small scales by the Reynolds stress, analogous to how the stress transfers momentum and energy from large scales to small scales. This transfer constitutes the second step of the dynamo loop that exponentiates magnetic fields. The stress is non-zero for an unstable shear flow, as required by the thermodynamic constraint on free-energy that drives the instability. Hence, this dynamo operates with merely two ingredients: an unstable large-scale shear flow and infinitesimally weak, small-scale MHD fluctuations. No initial large-scale magnetic field is required. The infinitesimally weak velocity fluctuations are exponentiated by the KH instability, which generates inherently 3D zonal jets via hydrodynamic

[1]Alfvénized magnetic fields tend to be aligned with fluid flow.

processes. Then, the infinitesimally weak magnetic fluctuations are exponentiated by the zonal jets due to increasingly more Alfvénization (flow–field-alignment effect). The foregoing dynamo mechanism has been uncovered in this thesis with the help of advanced computer simulations of dynamo by investing nearly 100 million CPU-hours and analyzing 0.25 petabytes of data products.

11.1 Main findings

The main findings are thematically summarized below.

1. **New paradigm of KH-instability saturation and essentiality of three-dimensionality**: Contrary to a widespread belief that an instability necessarily saturates by transferring all of its energy to small scales where dissipation occurs (see, e.g., Refs. [26–29]), this thesis shows that the instability transfers most of its energy to the large-scale conjugate-stable eigenmodes (Chs. 2-6). The latter modes return turbulent energy to the unstable shear flow, thus dramatically reducing the small-scale energy cascade. This new saturation paradigm is shown here to apply to both two and three dimensions, and to both fluids and plasmas. While the KH instability is generally considered to be 2D, this thesis shows that 3D nature is critically important for instability saturation in realistic physical environments.

2. **More effective counter-gradient momentum transport in 3D than in 2D**: Stable eigenmodes turbulently transport momentum in the counter-gradient direction. This transport significantly decreases the down-gradient transport by the instability. The counter-gradient transport is continuous in time, and can occasionally even dominate the down-gradient transport (Ch. 3). This behavior

is sometimes linked, although often incorrectly, to 2D nature of turbulence. Contrastingly, the counter-gradient momentum transport is found here to be more effective for 3D stable eigenmodes than for 2D stable eigenmodes (Ch. 6).

3. **Magnetic-field straining and folding dynamics**: The large-scale stable eigenmodes are demonstrated to inhibit the unstable eigenmodes's ability to strain magnetic fields and flow structures. Hence, when the stable eigenmodes are forcefully deleted in numerical simulations, the unimpeded instability rapidly strains and folds magnetic fields in spiral forms (the classic KH instability). Consequently, small-scale fluctuations become prominent, and visco-resistive dissipation is increased by more than order of magnitude (Ch. 4). This result also illustrates that stable eigenmodes inhibit fluid mixing and field-line stretching by turbulent flow.

4. **Large-scale pattern formation**: When stable modes are significantly excited, structures in velocity and magnetic fields tend to appear at large scales in both 2D and 3D. In 2D, when stable modes are surgically removed from the governing MHD equations, the large-scale KH eddies split apart and ballistically move away from the shear layer, instead of merging; the latter is commonly observed in simulations based on the unmodified equations, where the stable eigenmodes are kept intact (Ch. 5). In 3D, the large-scale jets provide energy to stable eigenmodes, which saturate the instability (Ch. 6).

5. **Energy-cascade direction in instability-driven turbulence**: Stable eigenmodes reduce the rate of energy cascade to small scales. The forward cascade found in both 2D and 3D is because the free-energy for the instability resides at large scales. Moreover, the wavenumber-decomposed traditional energy transfer analysis is extended to include energy transfer among different families of eigen-

modes. This extension reveals the dominant channels that transfer energy to stable modes in 2D (Ch. 5) and 3D (Ch. 6).

6. **Vortex stretching vs. vortex fattening in three dimensions**: Vortex stretching—a purely 3D process—is carried out by the KH instability, which generates increasingly filamentary structures, representing forward cascade of energy [290]. Stable modes, on the other hand, counteract the stretching process (Ch. 6), i.e., the vortices appearing in the form of thin, long cylinders become thick, short cylinders with larger diameter due to the stable modes. Thus, the stable modes effectively act as an agent of vortex fattening, which counters vortex stretching by the instability [1].

7. **Predictive analytic closure models for slowing of stellar spins**: Stars spin down due to turbulent transport of angular momentum, which in this thesis is modeled using an analytic closure model. The model provides a predictive framework where zonal flows, excited nonlinearly, dominate nonlinear mode-couplings. The predicted rates of transport agree with numerical simulations. The parameter regimes — which the simulations cannot probe — are accessed using the analytic closure model. The model in Ch. 7 suggests that the GSF-instability-driven turbulent transport is substantial in the solar tachocline (where the ratio of viscosity to thermal diffusivity is 10^{-6}) and red giant stars, among others.

8. **Jets in astrophysically relevant dynamos**: The linear physics of an instability is generally anisotropic. When such instability drives turbulence, common nonlinear structures are zonal jets. The jets, which are long lived, can significantly generate magnetic fields because the jets coherently stretch magnetic fields for long times, as shown in Chs. 8—10. The jets are exact nonlinear

solutions to the governing equations, and hence they are robust agents that drive astrophysically relevant dynamos (Ch. 8).

9. **Dynamo cycle**: Spontaneous reversals of large-scale magnetic fields are observed in three-dimensional Kelvin-Helmholtz instability-driven magnetohydrodynamic turbulence (Ch. 8). The reversals occur when the cross phase between zonal jets and magnetic fluctuations rapidly slips from 0 to $\pm\pi$. The operation of the dynamo cycle is probed using detailed energy transfer diagnostics. An unstable large-scale shear flow is shown to spontaneously generate various forms of turbulent fluctuations, which via a series of turbulent interactions generates a large-scale magnetic field (Ch. 9). The initial large-scale field is not required for the dynamo, as the dynamo is driven by turbulent effects and not by the turbulent distortion of initial magnetic field. The dynamo here operates by the turbulent distortion of the initial vortex line, related to the large-scale shear flow.

10. **Alfvénization-enabled dynamo loop—Step 1: the mean-vorticity effect**: Alfvénization — a suppressor of the traditional dynamo [4–9] — is shown here to be a dynamo enabler. This novel dynamo-stimulating effect operating in the presence of a large-scale shear flow is thus, in some sense, the *reverse* of dynamo quenching (suppression); the latter has frustrated efforts to understand the α-effect-driven dynamos for several decades [4, 6, 8, 9]. The mean-vorticity effect [66], which is a product of the large-scale vorticity and the turbulent cross-helicity, is only a step of the two involved in the dynamo exponentiation loop (Ch. 10).

11. **Alfvénization-enabled dynamo loop—Step 2: the cross-helicity-transfer effect**: When an initial large-scale magnetic field is zero, Step 1 of the dynamo

(described in the preceding paragraph) generates a weak large-scale magnetic field, which is aligned along the large-scale shear flow. This cross-helicity (flow-field alignment) residing in the large-scale MHD profiles is transferred to small-scale fluctuations by the Reynolds stress, in a way analogous to how the stress transfers momentum and energy of the large-scale flow to small-scale fluctuations. This cross-helicity transfer effect—Step 2 of the dynamo loop—thus increases cross-helicity in the MHD turbulent fluctuations. Due to this increase of turbulent cross-helicity, Step 1 of the dynamo loop is reinforced. Thus, the dynamo loop continues until magnetic fields are amplified to the level comparable to the energy in the flow. Numerical simulation data confirm these two steps of dynamo (Ch. 10).

12. **Analogy between the α- and Υ-effects**: While the α- and Υ-effects are fundamentally different—as are their responses to Alfvénization (α is suppressed; Υ is maximized)—there exists an analogy between the two effects. The α-effect begins with a large-scale magnetic field that is perturbed by velocity fluctuations and rotated by vorticity fluctuations [51]. The Υ-effect, on the other hand, is shown here to begin with a large-scale vortex line (analogous to a magnetic field line) that is perturbed by velocity fluctuations. This process creates a bent vortex line, which induces jet-like fluctuation flows (see Fig. 8.3a). These flows then operate on fluctuation magnetic fields, creating a large-scale magnetic field (Ch. 8).

13. **Effects of boundaries on dynamos**: Boundaries are often a point of contention in dynamo theory [8, 9]. This thesis demonstrates that the jet-driven Alfvénization-enabled dynamo does not depend on the nature of boundaries—whether they are periodic or non-periodic (Ch. 8). The explanation is simple:

The jets are the strongest near the shear layer, which lies maximally far away from the boundaries.

14. **Explanation for confounding measurements in laboratory experiments**: In 2012, the laboratory dynamo experiment directly measured, for the first time, mean turbulent EMF — in addition to the mean magnetic field and mean current density [72]. This observation, however, presented a surprising finding: The mean magnetic field was orthogonal to the mean electromotive force. This experimental finding shows that the dynamo is not driven by the α-effect, as the α-effect requires the EMF and the magnetic field to be parallel, not orthogonal. The novel dynamo presented in this thesis is able to explain the experimental finding using the following: The laboratory experiment reports a large vorticity in the radial direction [291], along which the mean EMF is also directed [72]. Hence, considering the mean-vorticity effect, the mean EMF direction is explained (Ch. 8). Additionally, in the mean-vorticity-driven nonhelical dynamo, the mean magnetic field is orthogonal to the current density — a prediction that agrees with the laboratory experiment .

15. **Implications for astrophysical magnetic field generation**: When binary neutron stars approach each other to merge (the merging can produce another neutron star or a black hole), a large velocity gradient is created in the interface between the stars. This gradient is KH-unstable and drives the dynamo [73, 74]. The growth timescale of the dynamo is predicted in this thesis to be on the order of microseconds, which in milliseconds (the merger timescale) can produce some of the strongest magnetic fields in the Universe, of strength 10^{17} G or larger [292], thus producing strong signals for multi-messenger astronomy (Ch. 8). In the Sun, the meridional circulation has large-scale azimuthal vorticity [284, 285] and

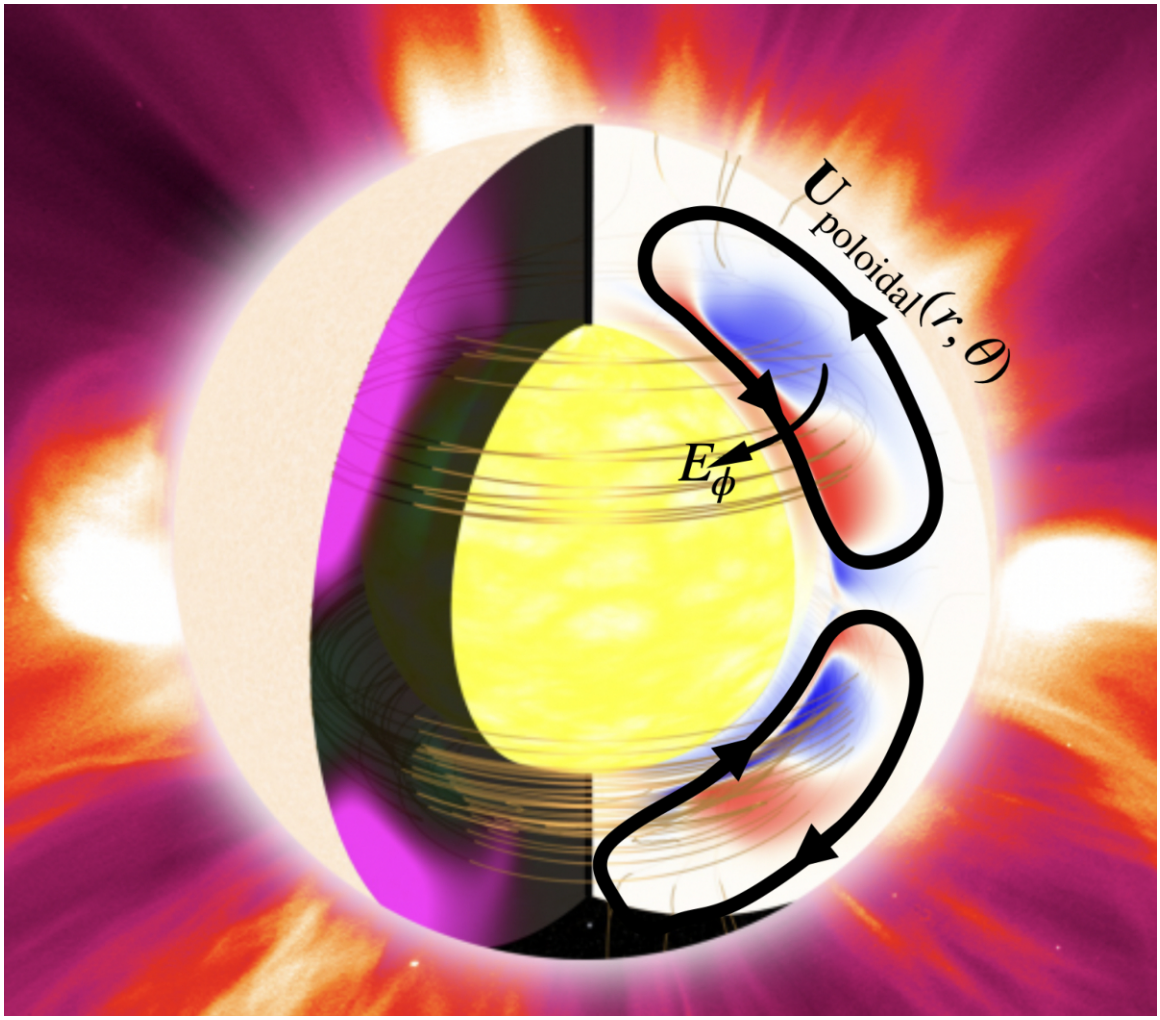

Figure 11.2: A visualization of the spinning Sun from the Royal Astronomical Society, UK, press release on Tripathi *et al.* 2021 [3]. Solar poloidal magnetic fields are created via (the curl of) the azimuthal EMF E_ϕ. The latter is expected to contribute to the azimuthal vorticity of the poloidal flow (called meridional circulation), given by $E_\phi \propto \Upsilon \nabla \times \mathbf{U}_{\text{poloidal}}(r,\theta)$. Here, Υ captures the effects of small-scale Alfvénic fluctuations. Most current solar dynamo models rely on the traditional α-effect, but given that Alfvénic fluctuations dramatically suppress the α-effect [4–9], the Alfvénization-enabled Υ-effect has the potential to provide more robust dynamo models. Image credit: CESSI / IISER Kolkata / NASA-SVS / ESA / SOHO-LASCO.

hence is bound to contribute to the large-scale azimuthal EMF (see Fig. 11.2); the latter generates poloidal magnetic fields. In other stars, galaxies mergers, and planets, the effect of vorticity and jets can be substantial, as well [293].

11.2 Future work

This thesis has addressed a number of fundamental questions that are related to instability saturation, pertinent to fusion devices and astrophysical systems, in addition to the generation of cosmic magnetic fields. As is common to all areas of science, new questions have arisen from these findings. Among various possible research directions, some promising candidates are listed below, categorized into two classes: fundamental questions and applications.

A. Fundamental science research directions

1. **Momentum transport versus visco-resistive properties**: While the dynamo has been found to be robust to variations in microphysical dissipation properties (Chs. 8, 10), the behavior of momentum transport requires further analyses. The Reynolds stress, which transfers cross-helicity from large scales to small scales, is one of the two steps in the dynamo loop. For an unstable shear flow, the thermodynamic constraint demands momentum transport and the Reynolds stress to be non-zero even when the Reynolds numbers approach infinity (the singular limit).

2. **Saturation of the Rayleigh–Taylor instability, magneto-rotational instability, and tearing instability**: Since the Rayleigh–Taylor and magneto-rotational instabilities are ideal instabilities, they preserve parity-time-reversal

symmetry. Thus, the stable eigenmodes that are conjugate to the instability exist. Since these eigenmodes are complex conjugates to each other, three-mode overlap is expected to be significant, similar to the large nonlinear mode-coupling in the KH system. Thus, it would be *unsurprising* if the stable modes played a key role in the saturation of these instabilities. Although the resistive tearing instability is a non-ideal instability, the net sum of the damped eigenmodes can effectively behave as a conjugate to the tearing-unstable eigenmode, as has been shown for resistive interchange instability [294] and gyrokinetic systems [123]. Applying the machinery used in this thesis (e.g., mode-projection and mode-coupling diagnostics), one may be able to better understand the MHD cascades and examine the effect of stable modes in the break-off of spectral slope in the plasmoid-instability-mediated reconnection [153].

3. **Mechanics of the cross-helicity cascade**: Given that the dynamo arising from the KH instability generates substantial cross-helicity in fluctuations (by coupling to the large-scale shear flow)[2], it is instructive to analyze the cascade processes related to the cross-helicity and its dissipation mechanisms.

4. **Three-dimensional magnetic-field straining by stable eigenmodes**: Similar to the three-dimensional vortex stretching ($\omega \cdot \nabla \mathbf{u}$) by instability and vortex fattening by stable modes [1], magnetic-field straining ($\mathbf{b} \cdot \nabla \mathbf{u}$) is also expected to feature such competition. Specifically, instability is expected to create small-scale filamentary and folded magnetic fields, whereas the stable modes counteract the fluid motions related to the instability, thereby preserving magnetic fields at large scales.

[2] In the absence of the large-scale shear flow, the volume-averaged turbulent cross-helicity cannot grow as it is conserved by the nonlinearities.

5. **Vortex dynamics in large domains**: Chapter 5 shows that, when stable modes are removed forcefully from the governing nonlinear equations, the Kelvin-Helmholtz vortices split apart, instead of merging. Although the considered simulation domain is large, it remains to be seen how this behavior manifests when even larger domain is considered. Available data and analyses, however, suggest that the KH vortices should split apart and generate overwhelming small-scale structures in the absence of the stable modes. This expectation can be confirmed by performing stable-mode-removed simulations in very large domains. Coalescence of eddies is also commonly observed in tearing-instability-driven turbulence [25, 295], hence it is conceivable that the stable modes therein also can play a significant role.

6. **Analytic closure model for the jet-driven dynamo**: Similar to the statistical turbulence closure model for the jet-coupled instability saturation [35], it is possible to construct a jet-coupled dynamo closure model. Such a model can provide an alternative way to access extreme parameters that otherwise are not possible using state-of-the-art numerical simulations. Preliminary investigations suggest that such a closure model can explain behavior of dynamo when key parameters are varied.

7. **Effect of domain size on coherent jets**: It is a natural question to investigate whether the dynamo-enabling 3D zonal jets formed via the KH instability will continue when domain size is enlarged indefinitely. Simulations with 2, 4, 8, 16, 32, and 64 times larger domain size, in the y-axis orthogonal to the shear flow plane, show continued dominance of zonal jets (Ch. 10). The y-spectrum of the jet-energy peaks at a characteristic scale $k_y a \sim 0.1$, where a is the shear-layer half-width. However, lower wavenumbers require longer time to evolve and

hence it is not definitively known whether energy will continue to build up at even lower k_y if the system is allowed to evolve indefinitely. This numerical experiment is prohibitively expensive because one must enlarge the box size while increasing grid-resolution, and at the same time one must perform simulation for substantial long times.

8. **Resonances between unstable, stable, and zero-frequency fluctuations**: Similar to resonances found in the ion-temperature-gradient-driven turbulence between three relevant fluctuations [32, 91], it is possible that such resonances are involved in the sustained generation of zonal jets found in this thesis. Zonal jets here have zero-frequency; even with nonlinear corrections, it is shown that the their frequency is substantially small (Ch. 9). Since unstable and stable eigenmodes have oppositely signed growth rates, the sum of three growth rates is close zero for a frequency-triad involving unstable mode, stable mode, and zonal fluctuation. This triad allows (near-)resonant transfer of energy from instability to stable eigenmodes, as confirmed in Ch. 6 in 3D hydrodynamic KH turbulence. Repeating similar diagnostics for the 3D KH dynamo system will provide a deeper physical understanding and natural interpretation for why there exist three temporal scales—fast, intermediate, and slow—for instability, zonal jets, and dynamo fields, respectively.

9. **Roles of stable modes in the KH-driven dynamo**: Stable modes play at least three critical roles in the KH-driven dynamo, shown in Fig. 11.1. First, the stable modes return energy to the unstable shear flow, which reduces energy cascade to small scales and, consequently, suppresses small-scale fluctuations (Chs. 3–6). Second, the stable modes decrease turbulent stress $\mathbf{T}$ (Chs. 4,6), shown on the right end of Fig. 11.1. The stress $\mathbf{T}$ transfer cross-helicity from large

scale to small scale, which constitutes a part of the dynamo loop. Third, the stable modes strongly couple to zonal jets via a three-wave-coupling among an unstable mode, a stable mode, and zonal jets, as confirmed in Ch. 6 in a hydrodynamic context. This near-resonant three-wave-coupling favors sustainment of zonal jets. While the first and third roles of the stable modes help the dynamo process, the second role does not. Hence, although the stable modes sustain the jets that drive the dynamo, the direct effect of stable modes in the KH dynamo is nuanced, requiring future work.

B. Application-focused research directions

1. **Solar model with the vorticity of the meridional circulation as the dynamo source**: As displayed in Fig. 11.2, the large-scale solar meridional circulation — a key player in flux-transport dynamos [285] — has its vorticity directed in the azimuthal axis [284] . This vorticity is thus bound to contribute to the azimuthal EMF. If this contribution is appreciable compared to the presently ad-hoc, fine-tuned α-source for the azimuthal EMF in solar dynamo models, the vorticity-related Alfvénization-enabled dynamo likely has the potential to become the next generation of solar dynamo models to predict magnetic flux and its effect on hazardous space weather.

2. **Compressibility effects in binary neutron star merger and KH dynamo**: To be undertaken by the author via a joint postdoctoral research fellowship at Columbia University and the Canadian Institute for Theoretical Astrophysics under the Simons Collaboration on Extreme Electrodynamics of Compact Sources, a logical next step is to include the effect of compressibility and the pertinent equation of state in neutron stars to model the KH dynamo. This extension of

the model can help predict realistic widths of the shear layer in the interface between binary neutron stars, as they approach each other to merge. These stars are gravitationally bound and forced to collide, which generates a persistent shear layer at the merger interface. Current, resolution-limited global numerical simulations show increasingly thin shear layer widths (down to a few tens of meters) with increasing grid-resolution, and hence the precise width of the shear layer is not known at this time [73, 296].

3. **Dynamos in accretion flows around black holes**: Current simulations of multi-messenger astronomy signals arising from compact objects do not resolve relevant physical scales [73, 272]. This limitation prevents simulations from making accurate predictions regarding the effect of dynamos driven by the Kelvin–Helmholtz, Rayleigh–Tayler, and magneto-rotational instabilities. Instead of self-consistently evolving magnetic fields from weak amplitudes, these simulations use arbitrarily large initial magnetic field [73, 269, 272, 297]. Thus, they do not resolve fast temporal scales in the merger phase when magnetic fields are rapidly created as well as in the accretion flows around compact objects. Magnetic fields, however, play a chief role in launching jets from black holes and generating synchrotron radiations. The vorticity-related magnetic dynamo can critically impact these observables, hence a thorough understanding of field generation is to be sought using the novel dynamo mechanism.

4. **Long-term magnetic-cycle reversal statistics**: Since the large-scale magnetic fields take longer time to evolve (compared to the fast KH instability), collecting statistics of large-scale magnetic-cycle reversals requires integrating the MHD dynamo equations for very long times. While Fig. 8.1a is obtained using a 90-day simulation parallelized on 2048 CPUs (maximally parallelized

in two periodic axes x and y with a moderate grid resolution), only a handful of reversals are captured. Hence, substantially longer simulation is required to statistically and reliably claim the nature of distribution of magnetic-cycle reversals. If one simulates the same problem 10 times longer (compared to Fig. 8.1a), the simulation would take three years to complete — excluding the wait times on large computing facilities. Another approach therefore can be performing the same simulation using fewer grid points; simulations using the latter has been found to reproduce certain critical features of the large-scale dynamo.

5. **GRMHD KH-dynamo simulations for binary neutron star mergers**: While the current thesis uses a Newtonian MHD model to understand the fundamentals of the novel dynamo mechanism, a next step is to implement the vorticity-related Alfvénization-enabled dynamo in General-Relativistic-MHD simulation softwares [298]. This implementation allows to analyze how magnetic fields are generated in binary neutron star mergers and how such magnetic fields affect global dynamics and post-merger evolution. This modeling effort of the new dynamo is being pursued in collaboration with compact object merger experts. These efforts allow direct modeling of multi-messenger astronomy signals currently detected by the LIGO-Virgo-KAGRA Collaboration [299] and to be measured with high precision by the upcoming Einstein Telescope [300].

6. **Better understanding of dynamo saturation at extreme Reynolds numbers**: This thesis has explored the behavior of the dynamo by varying magnetic Prandtl number (the ratio of viscosity to electric resistivity) over 5 orders of magnitude and has reproduced similar dynamo and jets. However, future work is needed to access astrophysically extreme parameters. Alternatives

to such exploration are developing a better analytic understanding of the dynamo and performing direct statistical simulations instead of full-scale direct numerical simulations [42].

7. **Modeling slowing of stellar spins**: A project is currently underway to develop a turbulence closure model for the GSF (diffusive shear flow) instability applicable to stars at a general latitude [230]. Chapter 7 of this thesis built a similar model for the equatorial system. At higher latitudes, the GSF turbulence is more vigorous and hence its impact on stellar angular momentum transport is stronger [230]. Early calculations show promising results on predicting the momentum transport rate using a turbulence closure model in the weak-turbulence limit—where certain triadic interactions dominate over the remaining ones [32].

8. **KH-dynamo-driven particle acceleration**: The KH instability is routinely studied in two dimensions, owing to its computational efficiency [82]. However, this thesis has established that the instability is fundamentally different in 3D compared to 2D, as the former system generates inherently 3D zonal jets and a jet-driven dynamo. The dynamo-generated magnetic fields can accelerate charged particles, causing them to radiate, whose signatures are measurable in astrophysical observations. Such signatures can be theoretically predicted by coupling MHD codes to particle-in-cell (PIC) codes [301, 302] — the latter would then be used to track particle acceleration under the effect of large-scale magnetic fields evolved using the MHD model. Although using this MHD-PIC hybrid modeling framework in two spatial dimensions (for computational efficiency) is a novel and ambitious approach, the predictions using the 2D system with an imposed, external magnetic fields cannot be reliable, as a self-consistent generation of magnetic fields via the dynamo requires three-dimensionality

[46, 47]. In 3D, the KH turbulence naturally creates the dynamo-enabling zonal jets [1, 65], which can thus critically impact the nature of detectable synchrotron radiation emitted from accelerating particles.

BIBLIOGRAPHY

[1] B. Tripathi, P. W. Terry, A. E. Fraser, E. G. Zweibel, and M. J. Pueschel. Three-dimensional shear-flow instability saturation via stable modes. *Phys. Fluids*, 35(10):105151, October 2023.

[2] E. N. Parker. The Generation of Magnetic Fields in Astrophysical Bodies. I. The Dynamo Equations. *Astrophys. J.*, 162:665, November 1970.

[3] B. Tripathi, D. Nandy, and S. Banerjee. Stellar mid-life crisis: subcritical magnetic dynamos of solar-like stars and the breakdown of gyrochronology. *Mon. Not. R. Astron. Soc.*, 506(1):L50–L54, September 2021.

[4] A. Pouquet, U. Frisch, and J. Leorat. Strong MHD helical turbulence and the nonlinear dynamo effect. *J. Fluid Mech.*, 77:321–354, September 1976.

[5] S. I. Vainshtein and F. Cattaneo. Nonlinear Restrictions on Dynamo Action. *Astrophys. J.*, 393:165, July 1992.

[6] A. V. Gruzinov and P. H. Diamond. Self-consistent mean field electrodynamics of turbulent dynamos. *Phys. Plasmas*, 2(6):1941–1946, June 1995.

[7] F. Cattaneo and D. W. Hughes. Nonlinear saturation of the turbulent α effect. *Phys. Rev. E*, 54(5):R4532–R4535, November 1996.

[8] A. Brandenburg and K. Subramanian. Astrophysical magnetic fields and nonlinear dynamo theory. *Phys. Rep.*, 417(1-4):1–209, October 2005.

[9] A. Brandenburg, D. Elstner, Y. Masada, and V. Pipin. Turbulent Processes and Mean-Field Dynamo. *Space Sci. Rev.*, 219(7):55, October 2023.

[10] S. Chandrasekhar. *Hydrodynamic and hydromagnetic stability*. 1961.

[11] H. Tennekes and J. L. Lumley. *First Course in Turbulence*. 1972.

[12] S. B. Pope. *Turbulent Flows*. 2000.

[13] L. D. Landau. On the Problem of Turbulence. *Compt. Rend. Acad. Sci. URSS*, 44, 1944.

[14] A. Kolmogorov. The Local Structure of Turbulence in Incompressible Viscous Fluid for Very Large Reynolds' Numbers. *Akademiia Nauk SSSR Doklady*, 30:301–305, January 1941.

[15] P. W. Terry, D. A. Baver, and S. Gupta. Role of stable eigenmodes in saturated local plasma turbulence. *Phys. Plasmas*, 13(2):022307, February 2006.

[16] Y. Fu and H. Qin. The physics of spontaneous parity-time symmetry breaking in the Kelvin-Helmholtz instability. *New J. Phys.*, 22(8):083040, August 2020.

[17] B. Tripathi, A. E. Fraser, P. W. Terry, E. G. Zweibel, M. J. Pueschel, and E. H. Anders. Nonlinear mode coupling and energetics of driven magnetized shear-flow turbulence. *Phys. Plasmas*, 30(7):072107, July 2023.

[18] B. Tripathi, A. E. Fraser, P. W. Terry, E. G. Zweibel, and M. J. Pueschel. Near-cancellation of up- and down-gradient momentum transport in forced magnetized shear-flow turbulence. *Phys. Plasmas*, 29(9):092301, September 2022.

[19] B. Tripathi, A. E. Fraser, P. W. Terry, E. G. Zweibel, and M. J. Pueschel. Mechanism for sequestering magnetic energy at large scales in shear-flow turbulence. *Phys. Plasmas*, 29(7):070701, July 2022.

[20] M. Polini and A. K. Geim. Viscous electron fluids. *Phys. Today*, 73(6):28–34, June 2020.

[21] P. W. Terry. Suppression of turbulence and transport by sheared flow. *Rev. Mod. Phys.*, 72(1):109–165, January 2000.

[22] J. E. Pringle and A. King. *Astrophysical Flows*. 2003.

[23] U. Chadayammuri, J. ZuHone, P. Nulsen, D. Nagai, and H. Russell. Turbulent magnetic fields in merging clusters: a case study of Abell 2146. *Mon. Not. R. Astron. Soc.*, 512(2):2157–2170, May 2022.

[24] R. H. Levy and R. W. Hockney. Computer Experiments on Low-Density Crossed-Field Electron Beams. *Phys. Fluids*, 11(4):766–771, April 1968.

[25] D. Biskamp. *Magnetohydrodynamic Turbulence*. 2003.

[26] J. Fuller, Anthony L. Piro, and Adam S. Jermyn. Slowing the spins of stellar cores. *Mon. Not. R. Astron. Soc.*, 485(3):3661–3680, May 2019.

[27] M. E. Pessah, C.-K. Chan, and D. Psaltis. The signature of the magnetorotational instability in the Reynolds and Maxwell stress tensors in accretion discs. *Mon. Not. R. Astron. Soc.*, 372(1):183–190, October 2006.

[28] J. Goodman and G. Xu. Parasitic Instabilities in Magnetized, Differentially Rotating Disks. *Astrophys. J.*, 432:213, September 1994.

[29] P. Garaud. Double-Diffusive Convection at Low Prandtl Number. *Ann. Rev. Fluid Mech.*, 50(1):275–298, January 2018.

[30] *Zonal Flows in Magnetically Confined Plasmas*, pages 179–180. Cambridge University Press, 2019.

[31] W. M. Elsasser. The Hydromagnetic Equations. *Phys. Rev.*, 79(1):183–183, July 1950.

[32] P. W. Terry, B. J. Faber, C. C. Hegna, V. V. Mirnov, M. J. Pueschel, and G. G. Whelan. Saturation scalings of toroidal ion temperature gradient turbulence. *Phys. Plasmas*, 25(1):012308, January 2018.

[33] S. A. Orszag. Analytical theories of turbulence. *J. Fluid Mech.*, 41:363–386, January 1970.

[34] C. C. Hegna, P. W. Terry, and B. J. Faber. Theory of itg turbulent saturation in stellarators: Identifying mechanisms to reduce turbulent transport. *Phys. Plasmas*, 25(2):022511, 02 2018.

[35] B. Tripathi, A. J. Barker, A. E. Fraser, P. W. Terry, and E. G. Zweibel. Predicting the Slowing of Stellar Differential Rotation by Instability-driven Turbulence. *Astrophys. J.*, 966(2):195, May 2024.

[36] P. Goldreich and G. Schubert. Differential Rotation in Stars. *Astrophys. J.*, 150:571, November 1967.

[37] K. Fricke. Instabilität stationärer Rotation in Sternen. *Z. Astrophys.*, 68:317, January 1968.

[38] A. J. Barker, C. A. Jones, and S. M. Tobias. Angular momentum transport by the GSF instability: non-linear simulations at the equator. *Mon. Not. R. Astron. Soc.*, 487(2):1777–1794, August 2019.

[39] A. Neronov and I. Vovk. Evidence for Strong Extragalactic Magnetic Fields from Fermi Observations of TeV Blazars. *Science*, 328(5974):73, April 2010.

[40] A. Basu, S. A. Mao, A. A. Kepley, T. Robishaw, E. G. Zweibel, and J. S. Gallagher, III. Detection of an $\sim$20 kpc coherent magnetic field in the outskirt of

merging spirals: the Antennae galaxies. *Mon. Not. R. Astron. Soc.*, 464(1):1003–1017, January 2017.

[41] R. M. Kulsrud and E. G. Zweibel. On the origin of cosmic magnetic fields. *Rep. Prog. Phys.*, 71(4):046901, April 2008.

[42] S. M. Tobias and F. Cattaneo. Shear-driven dynamo waves at high magnetic Reynolds number. *Nature*, 497(7450):463–465, May 2013.

[43] J. Squire and A. Bhattacharjee. Generation of Large-Scale Magnetic Fields by Small-Scale Dynamo in Shear Flows. *Phys. Rev. Lett.*, 115(17):175003, October 2015.

[44] A. Tsokaros, J. Bamber, M. Ruiz, and S. L. Shapiro. Masking the Equation-of-State Effects in Binary Neutron Star Mergers. *Phys. Rev. Lett.*, 134(12):121401, March 2025.

[45] H. K. Moffatt. *Magnetic field generation in electrically conducting fluids*. 1978.

[46] T. G. Cowling. The magnetic field of sunspots. *Mon. Not. R. Astron. Soc.*, 94:39–48, November 1933.

[47] Y. B. Zel'dovich. The magnetic field in the two-dimensional motion of a conducting turbulent liquid. *J. Exp. Theor. Phys.*, 4(3):460–462, 1957. (Also published as Zh. Eksp. Teor. Fiz. 31, 154 (1956)).

[48] A. Herzenberg. Geomagnetic Dynamos. *Philos. Trans. R. Soc. A*, 250(986):543–583, August 1958.

[49] G. Backus. A class of self-sustaining dissipative spherical dynamos. *Ann. Phys.*, 4(4):372–447, August 1958.

[50] A. Gailitis. Self-excitation of a magnetic field by a pair of annular vortices. *Magnetohydrodynamics*, 6:14–17, 1970.

[51] E. N. Parker. Hydromagnetic Dynamo Models. *Astrophys. J.*, 122:293, September 1955.

[52] M. Steenbeck, F. Krause, and K. H. Rädler. Berechnung der mittleren. *Zeitschrift Naturforschung Teil A*, 21:369, April 1966.

[53] H. K. Moffatt and E. Dormy. *Self-Exciting Fluid Dynamos*. 2019.

[54] J. C. Perez and S. Boldyrev. Role of cross-helicity in magnetohydrodynamic turbulence. *Phys. Rev. Lett.*, 102:025003, Jan 2009.

[55] T. N. Parashar, A. Chasapis, R. Bandyopadhyay, R. Chhiber, W. H. Matthaeus, B. Maruca, M. A. Shay, J. L. Burch, T. E. Moore, B. L. Giles, D. J. Gershman, C. J. Pollock, R. B. Torbert, C. T. Russell, R. J. Strangeway, and V. Roytershteyn. Kinetic Range Spectral Features of Cross Helicity Using the Magnetospheric Multiscale Spacecraft. *Phys. Rev. Lett.*, 121(26):265101, December 2018.

[56] L. Yang, J. He, D. Verscharen, Hui Li, T. A. Bowen, S. D. Bale, H. Wu, W. Li, Y. Wang, L. Zhang, X. Feng, and Z. Wu. Energy transfer of imbalanced Alfvénic turbulence in the heliosphere. *Nat. Comm.*, 14:7955, December 2023.

[57] F. Pecora, Y. Yang, A. Chasapis, S. Servidio, M. E. Cuesta, S. Roy, R. Chhiber, R. Bandyopadhyay, D. J. Gershman, B. L. Giles, J. L. Burch, and W. H. Matthaeus. Relaxation of the turbulent magnetosheath. *Mon. Not. R. Astron. Soc.*, 525(1):67–72, October 2023.

[58] H. Alfvén. Existence of Electromagnetic-Hydrodynamic Waves. *Nature*, 150(3805):405–406, October 1942.

[59] W. H. Matthaeus, A. Pouquet, P. D. Mininni, P. Dmitruk, and B. Breech. Rapid Alignment of Velocity and Magnetic Field in Magnetohydrodynamic Turbulence. *Phys. Rev. Lett.*, 100(8):085003, February 2008.

[60] L. Woltjer. On Hydromagnetic Equilibrium. *Proc. Natl. Acad. Sci. U.S.A.*, 44(9):833–841, September 1958.

[61] Federrath C. Klessen R. S. Beattie, J. R. and S. Cielo. The spectrum of magnetized turbulence in the interstellar medium. *Nat. Astron.*, 9:1195–1202, 2025.

[62] A. A. Schekochihin. MHD turbulence: a biased review. *J. Plasma Phys.*, 88(5):155880501, October 2022.

[63] Fraser A. E. Terry P. W. Zweibel E. G. Pueschel M. J. Tripathi, B. and R. Fan. Large-Scale Dynamos Driven by Shear-Flow-Induced Jets. *Accepted for publication in Nature*, 2025.

[64] Fraser A. E. Terry P. W. Zweibel E. G. Tripathi, B. and M. J. Pueschel. Spontaneous Generation of Magnetic Fields via Turbulent Cross-Helicity Instability in Shear Flows. *To be submitted to Phys. Rev. Lett.*

[65] Fraser A. E. Terry P. W. Zweibel E. G. Tripathi, B. and M. J. Pueschel. The Life-Cycle of the Jet-Driven Shear-Flow Dynamo. *Under review in Phys. Plasmas.*

[66] A. Yoshizawa. Self-consistent turbulent dynamo modeling of reversed field pinches and planetary magnetic fields. *Phys. Fluids B*, 2(7):1589–1600, July 1990.

[67] E. G. Blackman and T. Chou. A Vorticity–Magnetic Field Dynamo Instability. *Astrophys. J. Lett.*, 489(1):L95–L98, November 1997.

[68] A. Brandenburg and V. Urpin. Magnetic fields in young galaxies due to the cross-helicity effect. *Astron. Astrophys.*, 332:L41–L44, April 1998.

[69] E. G. Blackman. Mean Magnetic Field Generation in Sheared Rotators. *Astrophys. J.*, 529(1):138–145, January 2000.

[70] G. K. Batchelor and I. Proudman. The effects of rapid distortion of a fluid in turbulent motion. *Q. J. Mech. Appl. Math.*, 7:83–103, 1954.

[71] A. A. Townsend. *The structure of turbulent shear flow /2nd edition/.* 1976.

[72] K. Rahbarnia, B. P. Brown, M. M. Clark, E. J. Kaplan, M. D. Nornberg, A. M. Rasmus, N. Zane Taylor, C. B. Forest, F. Jenko, A. Limone, J.-F. Pinton, N. Plihon, and G. Verhille. Direct Observation of the Turbulent emf and Transport of Magnetic Field in a Liquid Sodium Experiment. *Astrophys. J.*, 759(2):80, November 2012.

[73] K. Kiuchi, P. Cerdá-Durán, K. Kyutoku, Y. Sekiguchi, and M. Shibata. Efficient magnetic-field amplification due to the Kelvin-Helmholtz instability in binary neutron star mergers. *Phys. Rev. D*, 92(12):124034, December 2015.

[74] D. J. Price and S. Rosswog. Producing Ultrastrong Magnetic Fields in Neutron Star Mergers. *Science*, 312(5774):719–722, May 2006.

[75] E. C. Harding, J. F. Hansen, O. A. Hurricane, R. P. Drake, H. F. Robey, C. C. Kuranz, B. A. Remington, M. J. Bono, M. J. Grosskopf, and R. S. Gillespie. Observation of a Kelvin-Helmholtz Instability in a High-Energy-Density Plasma on the Omega Laser. *Phys. Rev. Lett.*, 103:045005, 2009.

[76] H. Hasegawa, M. Fujimoto, T.-D. Phan, H. Rème, A. Balogh, M. W. Dunlop, C. Hashimoto, and R. TanDokoro. Transport of solar wind into Earth's magnetosphere through rolled-up Kelvin-Helmholtz vortices. *Nature*, 430:755, 2004.

[77] D. W. Waugh, A. H. Sobel, and L. M. Polvani. What is the polar vortex and how does it influence weather? *Bull. Am. Meteorol. Soc.*, 98:37, 2017.

[78] P. L. Read, R. M. B. Young, and D. Kennedy. The turbulent dynamics of Jupiter's and Saturn's weather layers: order out of chaos? *Geosci. Lett.*, 7:10, 2020.

[79] J. Alves, C. Zucker, A. A. Goodman, J. S. Speagle, S. Meingast, T. Robitaille, D. P. Finkbeiner, E. F. Schlafly, and G. M. Green. A Galactic-scale gas wave in the solar neighbourhood. *Nature*, 578:237, 2020.

[80] R. Fleck. The 'Radcliffe Wave' as a Kelvin–Helmholtz instability. *Nature*, 583:E24, 2020.

[81] A. Miura. Self-organization in the two-dimensional Kelvin-Helmholtz instability. *Phys. Rev. Lett.*, 83:1586, 1999.

[82] D. Lecoanet, M. McCourt, E. Quataert, K. J. Burns, G. M. Vasil, J. S. Oishi, B. P. Brown, J. M. Stone, and R. M. O'Leary. A validated non-linear Kelvin-Helmholtz benchmark for numerical hydrodynamics. *Mon. Not. R. Astron. Soc.*, 455(4):4274–4288, February 2016.

[83] C. Ho and P. Huerre. Perturbed free shear layers. *Annu. Rev. Fluid Mech.*, 16:365, 1984.

[84] F. K. Browand and C. M. Ho. The mixing layer, an example of quasi two-dimensional turbulence. *J. de Mec. Theor. et Appl.*, 2:99, 1983.

[85] V. P. Starr and N. E. Gaut. Negative viscosity. *Sci. Am.*, 223:72, 1970.

[86] A. Miura and T. Sato. Theory of vortex nutation and amplitude oscillation in an inviscid shear instability. *J. Fluid Mech.*, 86:33, 1978.

[87] W. Horton, T. Tajima, and T. Kamimura. Kelvin–Helmholtz instability and vortices in magnetized plasma. *Phys. Fluids*, 30:3485, 1987.

[88] P. W. Terry, P.-Y. Li, M. J. Pueschel, and G. G. Whelan. Threshold Heat-Flux Reduction by Near-Resonant Energy Transfer. *Phys. Rev. Lett.*, 126:025004, 2021.

[89] G. G. Whelan, M. J. Pueschel, and P. W. Terry. Nonlinear Electromagnetic Stabilization of Plasma Microturbulence. *Phys. Rev. Lett.*, 120:175002, 2018.

[90] M. J. Pueschel, B. J. Faber, J. Citrin, C. C. Hegna, P. W. Terry, and D. R. Hatch. Stellarator Turbulence: Subdominant Eigenmodes and Quasilinear Modeling. *Phys. Rev. Lett.*, 116:085001, 2016.

[91] K. D. Makwana, P. W. Terry, M. J. Pueschel, and D. R. Hatch. Subdominant Modes in Zonal-Flow-Regulated Turbulence. *Phys. Rev. Lett.*, 112(9):095002, March 2014.

[92] D. R. Hatch, F. Jenko, A. B. Navarro, and V. Bratanov. Transition between saturation regimes of gyrokinetic turbulence. *Phys. Rev. Lett.*, 111:175001, 2013.

[93] D. R. Hatch, P. W. Terry, F. Jenko, F. Merz, and W. M. Nevins. Saturation of gyrokinetic turbulence through damped eigenmodes. *Phys. Rev. Lett.*, 106:115003, 2011.

[94] M. J. Pueschel, P.-Y. Li, and P. W. Terry. Predicting the critical gradient of ITG turbulence in fusion plasmas. *Nucl. Fusion*, 61:054003, 2021.

[95] P.-Y. Li and P. W. Terry. Assessing physics of ion temperature gradient turbulence via hierarchical reduced-model representations. *Phys. Plasmas*, 29:042301, 2022.

[96] G. G. Whelan, M. J. Pueschel, P. W. Terry, J. Citrin, I. J. McKinney, W. Guttenfelder, and H. Doerk. Saturation and nonlinear electromagnetic stabilization of ITG turbulence. *Phys. Plasmas*, 26:082302, 2019.

[97] A. E. Fraser, M. J. Pueschel, P. W. Terry, and E. G. Zweibel. Role of stable modes in driven shear-flow turbulence. *Phys. Plasmas*, 25:122303, 2018.

[98] K. D. Makwana, P. W. Terry, J.-H. Kim, and D. R. Hatch. Damped eigenmode saturation in plasma fluid turbulence. *Phys. Plasmas*, 18:012302, 2011.

[99] K. D. Makwana, P. W. Terry, and J.-H. Kim. Role of stable modes in zonal flow regulated turbulence. *Phys. Plasmas*, 19:062310, 2012.

[100] N. J. Zabusky and G. S. Deem. Dynamical Evolution of Two-Dimensional Unstable Shear Flows. *J. Fluid Mech.*, 47:353, 1971.

[101] L.-S. Huang and C.-M. Ho. Small-scale transition in a plane mixing layer. *J. Fluid Mech.*, 210:475, 1990.

[102] R. D. Moser and M. M. Rogers. The three-dimensional evolution of a plane mixing layer: Pairing and transition to turbulence. *J. Fluid Mech.*, 247:275, 1993.

[103] J. J. Riley and R. W. Metcalfe. Direct numerical simulation of a perturbed turbulent mixing layer. In *18th Aerospace Sciences Meeting*, pages AIAA Paper 1980–0274, 1980.

[104] D. Oster and I. Wygnanski. The forced mixing layer between parallel streams. *J. Fluid Mech.*, 123:91, 1982.

[105] Y. Ito, K. Nagata, Y. Sakai, and O. Terashima. Momentum and mass transfer in developing liquid shear mixing layers. *Exp. Therm. Fluid Sci.*, 51:28, 2013.

[106] A. VanDine, H. T. Pham, and S. Sarkar. Turbulent shear layers in a uniformly stratified background: DNS at high Reynolds number. *J. Fluid Mech.*, 916:A42, 2021.

[107] A. López Zazueta and L. Zavala Sansón. Self-oscillations of a two-dimensional shear flow with forcing and dissipation. *Phys. Fluids*, 30:044101, 2018.

[108] A. K. M. F. Hussain and K. B. M. Q. Zaman. An experimental study of organized motions in the turbulent plane mixing layer. *J. Fluid Mech.*, 159:85, 1985.

[109] A. K. M. F. Hussain. Coherent structures and turbulence. *J. Fluid Mech.*, 173:303, 1986.

[110] A. E. Fraser, P. W. Terry, E. G. Zweibel, and M. J. Pueschel. Coupling of damped and growing modes in unstable shear flow. *Phys. Plasmas*, 24:062304, 2017.

[111] A. E. Fraser, P. W. Terry, E. G. Zweibel, M. J. Pueschel, and J. M. Schroeder. The impact of magnetic fields on momentum transport and saturation of shear-flow instability by stable modes. *Phys. Plasmas*, 28:022309, 2021.

[112] B. Tripathi, A. E. Fraser, P. W. Terry, E. G. Zweibel, and M. J. Pueschel. Mechanism for Sequestering Magnetic Energy at Large Scales in Shear-Flow Turbulence. *Phys. Plasmas*, 2022. Submitted to Phys. Plasmas, arXiv:2205.01298.

[113] S. Chandrasekhar. *Hydrodynamic and Hydromagnetic Stability*. Clarendon Press, Oxford, 1961.

[114] J. Mak, S. D. Griffiths, and D. W. Hughes. Vortex disruption by magnetohydrodynamic feedback. *Phys. Rev. Fluids*, 2:113701, 2017.

[115] A. A. Schekochihin, J. L. Maron, S. C. Cowley, and J. C. McWilliams. The Small-Scale Structure of Magnetohydrodynamic Turbulence with Large Magnetic Prandtl Numbers. *Astrophys. J.*, 576:806, 2002.

[116] F. Ebrahimi, S. C. Prager, and D. D. Schnack. Saturation of Magnetorotational Instability Through Magnetic Field Generation. *Astrophys. J.*, 698:233, 2009.

[117] M. J. Pueschel, D. Told, P. W. Terry, F. Jenko, E. G. Zweibel, V. Zhdankin, and H. Lesch. Magnetic Reconnection Turbulence in Strong Guide Fields: Basic Properties and Application to Coronal Heating. *Astrophys. J., Suppl. Ser.*, 213:30, 2014.

[118] J. B. Marston, E. Conover, and T. Schneider. Statistics of an Unstable Barotropic Jet from a Cumulant Expansion. *J. Atmos. Sci.*, 65:1955, 2008.

[119] K. M. Smith, C. P. Caulfield, and J. R. Taylor. Turbulence in forced stratified shear flows. *J. Fluid Mech.*, 910:A42, 2021.

[120] A. Allawala, S. M. Tobias, and J. B. Marston. Dimensional reduction of direct statistical simulation. *J. Fluid Mech.*, 898:A21, 2020.

[121] K. J. Burns, G. M. Vasil, J. S. Oishi, D. Lecoanet, and B. P. Brown. Dedalus: A flexible framework for numerical simulations with spectral methods. *Phys. Rev. Res.*, 2:023068, 2020.

[122] C. M. Bender. *PT symmetry: In quantum and classical physics*. World Scientific Publishing, 2019.

[123] D. R. Hatch, F. Jenko, A. Banon Navarro, V. Bratanov, P. W. Terry, and M. J. Pueschel. Linear signatures in nonlinear gyrokinetics: interpreting turbulence with pseudospectra. *New J. Phys*, 18(7):075018, 2016.

[124] K. M. Case. Stability of Inviscid Plane Couette Flow. *Phys. Fluids*, 3:143, 1960.

[125] P. W. Terry, D. A. Baver, and D. R. Hatch. Reduction of inward momentum flux by damped eigenmodes. *Phys. Plasmas*, 16:122305, 2009.

[126] J. B. Marston, G. P. Chini, and S. M. Tobias. Generalized quasilinear approximation: application to zonal jets. *Phys. Rev. Lett.*, 116:214501, 2016.

[127] G. K. Batchelor. On the spontaneous magnetic field in a conducting liquid in turbulent motion. *Proc. Roy. Soc. London, Ser. A*, 201:405, 1950.

[128] A. Alexakis, P. D. Mininni, and A. Pouquet. *Phys. Rev. E*, 72:046301, 2005.

[129] A. E. Fraser. *Role of stable eigenmodes in shear-flow instability saturation and turbulence*. PhD thesis, University of Wisconsin-Madison, 2020.

[130] K. J. Burns. *Flexible spectral algorithms for simulating astrophysical and geophysical flows*. PhD thesis, Massachusetts Institute of Technology, 2018.

[131] K. Taira, S. L. Brunton, S. T. M. Dawson, C. W. Rowley, T. Colonius, B. J. McKeon, O. T. Schmidt, S. Gordeyev, V. Theofilis, and L. S. Ukeiley. Modal Analysis of Fluid Flows: An Overview. *AIAA J*, 55:4013, 2017.

[132] P. L. Johnson. Energy Transfer from Large to Small Scales in Turbulence by Multiscale Nonlinear Strain and Vorticity Interactions. *Phys. Rev. Lett.*, 124:104501, 2020.

[133] J. Maron, S. Cowley, and J. McWilliams. The nonlinear magnetic cascade. *Astrophys. J.*, 603:569, 2004.

[134] R. M. Kulsrud. A critical review of galactic dynamos. *Annu. Rev. Astron. Astrophys.*, 37:37, 1999.

[135] B. Tripathi, A. E. Fraser, P. W. Terry, E. G. Zweibel, and M. J. Pueschel. Near-cancellation of up- and down-gradient momentum transport in forced magnetized shear-flow turbulence. *Phys. Plasmas*, 2022. Submitted.

[136] A. Ishizawa, Y. Kishimoto, and Y. Nakamura. Multi-scale interactions between turbulence and magnetic islands and parity mixture—a review. *Plasma Phys. Control. Fusion*, 61:054006, 2019.

[137] M. Sato and A. Ishizawa. Nonlinear parity mixtures controlling the propagation of interchange modes. *Phys. Plasmas*, 24:082501, 2017.

[138] B. Tripathi, A. E. Fraser, P. W. Terry, E. G. Zweibel, M. J. Pueschel, and E. H. Anders. Testing quasilinear theories in shear-flow turbulence. 2022. (Unpublished).

[139] K. J. Burns. *Flexible spectral algorithms for simulating astrophysical and geophysical flows*. PhD thesis, Massachusetts Institute of Technology, 2018.

[140] D. R. Hatch, P. W. Terry, F. Jenko, F. Merz, and W. M. Nevins. Saturation of gyrokinetic turbulence through damped eigenmodes. *Phys. Rev. Lett.*, 106:115003, 2011.

[141] P.-Y. Li, P. W. Terry, G. G. Whelan, and M. J. Pueschel. Saturation physics of threshold heat-flux reduction. *Phys. Plasmas*, 28:102507, 2021.

[142] G. Salvesen, K. Beckwith, J. B. Simon, S. M. O'Neill, and M. C. Begelman. Quantifying energetics and dissipation in magnetohydrodynamic turbulence. *Mon. Not. R. Astron. Soc.*, 438:1355, 2014.

[143] B. Tripathi, A. E. Fraser, P. W. Terry, E. G. Zweibel, and M. J. Pueschel. Mechanism for sequestering magnetic energy at large scales in shear-flow turbulence. *Phys. Plasmas*, 29:070701, 2022.

[144] B. Tripathi, A. E. Fraser, P. W. Terry, E. G. Zweibel, and M. J. Pueschel. Near-cancellation of up- and down-gradient momentum transports in magnetized shear flow turbulence due to stable modes. *Phys. Plasmas*, 29:092301, 2022.

[145] M. K. Verma. *Energy Transfers in Fluid Flows: Multiscale and Spectral Perspectives*. Cambridge University Press, Cambridge, 2019.

[146] R. H. Kraichnan. The structure of isotropic turbulence at very high reynolds numbers. *J. Fluid Mech.*, 5:497, 1959.

[147] O. Debliquy, M. K. Verma, and D. Carati. Energy fluxes and shell-to-shell transfers in three-dimensional decaying magnetohydrodynamic turbulence. *Phys. Plasmas*, 12:042309, 2005.

[148] B. Teaca, M. K. Verma, B. Knaepen, and D. Carati. Energy transfer in anisotropic magnetohydrodynamic turbulence. *Phys. Rev. E*, 79:046312, 2008.

[149] B. Teaca, A. B. Navarro, and F. Jenko. The energetic coupling of scales in gyrokinetic plasma turbulence. *Phys. Plasmas*, 21:072308, 2014.

[150] B. Teaca, F. Jenko, and D. Todd. Gyrokinetic turbulence: between idealized estimates and a detailed analysis of nonlinear energy transfers. *New J. Phys.*, 19:045001, 2017.

[151] P. Grete, B. W. O'Shea, K. Beckwith, W. Schmidt, and A. Christlieb. Energy transfer in compressible magnetohydrodynamic turbulence. *Phys. Plasmas*, 24:092311, 2017.

[152] M. K. Verma. Variable energy flux in turbulence. *J. Phys. A: Math. Theor.*, 55:013002, 2021.

[153] C. Dong, L. Wang, Y.-M. Huang, L. Comisso, T. A. Sandstrom, and A. Bhattacharjee. Reconnection-driven energy cascade in magnetohydrodynamic turbulence. *Science Advances*, 8(49):eabn7627, December 2022.

[154] L. Biferale, S. Musacchio, and F. Toschi. Inverse energy cascade in three-dimensional isotropic turbulence. *Phys. Rev. Lett.*, 108:164501, 2012.

[155] A. Alexakis, P. D. Mininni, and A. Pouquet. Imprint of large-scale flows on turbulence. *Phys. Rev. Lett.*, 95:264503, 2005.

[156] Y.-H. Pao. Structure of turbulent velocity and scalar fields at large wavenumbers. *Phys. Fluids*, 8:1063, 1965.

[157] P. W. Terry and V. Tangri. Magnetohydrodynamic dissipation range spectra for isotropic viscosity and resistivity. *Phys. Plasmas*, 16:082305, 2009.

[158] P. W. Terry, A. F. Almagri, G. Fiksel, C. B. Forest, D. R. Hatch, F. Jenko, M. D. Nornberg, S. C. Prager, K. Rahbarnia, Y. Ren, and J. S. Sarff. Dissipation range turbulent cascades in plasmas. *Phys. Plasmas*, 19:055906, 2012.

[159] D. Hu, A. Bhattacharjee, and Y.-M. Huang. Energy spectrum of tearing mode turbulence in sheared background field. *Phys. Plasmas*, 25:062305, 2018.

[160] A. Alexakis and L. Biferale. Cascades and transitions in turbulent flows. *Phys. Rep.*, 767:1, 2018.

[161] U. Frisch. *Turbulence: The Legacy of A. N. Kolmogorov*. Cambridge University Press, Cambridge, England, 1995.

[162] R. H. Kraichnan. Inertial ranges in two-dimensional turbulence. *Phys. Fluids*, 10:1417, 1967.

[163] C. E. Leith. Diffusion approximation for two-dimensional turbulence. *Phys. Fluids*, 11:671, 1968.

[164] F. Waleffe. Inertial transfers in the helical decomposition. *Phys. Fluids A*, 5:677, 1993.

[165] L. M. Smith and F. Waleffe. Transfer of energy to 2d large scales in forced, rotating 3d turbulence. *Phys. Fluids*, 11:1608, 1999.

[166] L. M. Smith and F. Waleffe. Generation of slow, large scales in forced, rotating, stratified turbulence. *J. Fluid Mech.*, 451:145, 2002.

[167] J. J. Riley and M.-P. Lelong. Fluid motions in the presence of strong stable stratification. *Annu. Rev. Fluid Mech.*, 32:613, 2000.

[168] W. Horton, J.-H. Kim, G. D. Chagelishvili, J. C. Bowman, and J. G. Lominadze. Angular redistribution of nonlinear perturbations: A universal feature of nonuniform flows. *Phys. Rev. E*, 81:066304, 2010.

[169] G. R. Mamatsashvili, D. Z. Gogichaishvili, G. D. Chagelishvili, and W. Horton. Nonlinear transverse cascade and two-dimensional magnetohydrodynamic subcritical turbulence in plane shear flows. *Phys. Rev. E*, 89:043101, 2014.

[170] G. Khujadze, G. Chagelishvili, S. Dong, J. Jiménez, and H. Foysi. Dynamics of homogeneous shear turbulence: A key role of the nonlinear transverse cascade in the bypass concept. *Phys. Rev. E*, 94:023111, 2016.

[171] D. Z. Gogichaishvili, G. R. Mamatsashvili, W. Horton, G. D. Chagelishvili, and G. Bodo. Nonlinear transverse cascade and sustenance of MRI turbulence in Keplerian disks with an azimuthal magnetic field. *Astrophys. J.*, 845:70, 2017.

[172] D. Z. Gogichaishvili, G. R. Mamatsashvili, W. Horton, and G. D. Chagelishvili. Active modes and dynamical balances in MRI turbulence of Keplerian disks with a net vertical magnetic field. *Astrophys. J.*, 866:134, 2018.

[173] G. R. Mamatsashvili, G. D. Chagelishvili, M. E. Pessah, F. Stefani, and G. Bodo. Zero net flux MRI turbulence in disks: Sustenance scheme and magnetic Prandtl number dependence. *Astrophys. J.*, 904:47, 2020.

[174] D. Biskamp and A. Zeiler. Nonlinear instability mechanism in 3d collisional drift-wave turbulence. *Phys. Rev. Lett.*, 74:706, 1995.

[175] C. Ng and A. Bhattacharjee. Interaction of shear-Alfven wave packets: Implication for weak magnetohydrodynamic turbulence in astrophysical plasmas. *Astrophys. J.*, 465:845, 1996.

[176] P. W. Terry. Inverse energy transfer by near-resonant interactions with a damped-wave spectrum. *Phys. Rev. Lett.*, 93:235004, 2004.

[177] S. Du, H. Li, X. Fu, and Z. Gan. Anisotropic energy transfer and conversion in magnetized compressible turbulence. *Astrophys. J.*, 948:72, 2023.

[178] A. M. Rubio, K. Julien, E. Knobloch, and J. B. Weiss. Upscale energy transfer in three-dimensional rapidly rotating turbulent convection. *Phys. Rev. Lett.*, 112:144501, 2014.

[179] C. Guervilly, D. Hughes, and C. A. Jones. Large-scale vortices in rapidly rotating Rayleigh-Bénard convection. *J. Fluid Mech.*, 758:407, 2014.

[180] B. Tripathi, A. E. Fraser, P. W. Terry, E. G. Zweibel, M. J. Pueschel, and E. H. Anders. Nonlinear mode coupling and energetics of driven magnetized shear-flow turbulence. *Phys. Plasmas*, 30:072107, 2023.

[181] T. M. Qian and M. E. Mauel. Observation of weakly damped modes using high resolution measurement of turbulence in a dipole confined plasma. *Phys. Plasmas*, 27:014501, 2020.

[182] P. Drazin and W. Reid. *Hydrodynamic Stability.* Cambridge University Press, Cambridge, 2004.

[183] M. Buzzicotti, H. Aluie, L. Biferale, and M. Linkmann. Energy transfer in turbulence under rotation. *Phys. Rev. Fluid*, 3:034802, 2018.

[184] G. P. Klaassen and W. R. Peltier. The onset of turbulence in finite-amplitude Kelvin-Helmholtz billows. *J. Fluid Mech.*, 155:1, 1985.

[185] G. P. Klaassen and W. R. Peltier. The influence of stratification on secondary instability in free shear layers. *J. Fluid Mech.*, 227:71, 1991.

[186] A. Mashayek and W. R. Peltier. The 'zoo' of secondary instabilities precursory to stratified shear flow transition. part 1 shear aligned convection, pairing, and braid instabilities. *J. Fluid Mech.*, 708:5, 2012.

[187] A. Mashayek and W. R. Peltier. The 'zoo' of secondary instabilities precursory to stratified shear flow transition. part 2 the influence of stratification. *J. Fluid Mech.*, 708:45, 2012.

[188] H. Salehipour, W. Peltier, and A. Mashayek. Turbulent diapycnal mixing in stratified shear flows: The influence of Prandtl number on mixing efficiency and transition at high Reynolds number. *J. Fluid Mech.*, 773:178, 2015.

[189] C. Liu, A. Kaminski, and W. Smyth. The butterfly effect and the transition to turbulence in a stratified shear layer. *J. Fluid Mech.*, 953:A43, 2022.

[190] L. Cope, P. Garaud, and C. Caulfield. The dynamics of stratified horizontal shear flows at low Péclet number. *J. Fluid Mech.*, 903:A1, 2020.

[191] P. Garaud and L. Kulenthirarajah. Turbulent transport in a strongly stratified forced shear layer with thermal diffusion. *Astrophys. J.*, 821:49, 2016.

[192] D. Lucas, C. P. Caulfield, and R. R. Kerswell. Layer formation in horizontally forced stratified turbulence: connecting exact coherent structures to linear instabilities. *J. Fluid Mech.*, 832:409, 2017.

[193] C. P. Caulfield. Open questions in turbulent stratified mixing: Do we even know what we do not know? *Phys. Rev. Fluids*, 5:110518, 2020.

[194] A. E. Fraser, S. A. Reifenstein, and P. Garaud. Magnetized fingering convection in stars, 2023.

[195] A. Masson and K. Nykyri. Kelvin-helmholtz instability: Lessons learned and ways forward. *Space Sci. Rev*, 214:71, 2018.

[196] M. J. Pueschel, F. Jenko, D. Told, and J. Büchner. Gyrokinetic simulations of magnetic reconnection. *Phys. Plasmas*, 18:112102, 2011.

[197] E. Paul, I. Abel, M. Landreman, and W. Dorland. An adjoint method for neoclassical stellarator optimization. *J. Plasma Phys.*, 85:795850501, 2019.

[198] S. Gomé, L. Tuckerman, and D. Barkley. Patterns in transitional shear turbulence. part 1. energy transfer and mean-flow interaction. *J. Fluid Mech.*, 964:A16, 2023.

[199] B. N. Rogers, W. Dorland, and M. Kotschenreuther. Generation and stability of zonal flows in ion-temperature-gradient mode turbulence. *Phys. Rev. Lett.*, 85:5336, 2000.

[200] M. J. Pueschel, T. Görler, F. Jenko, D. R. Hatch, and A. J. Cianciara. On secondary and tertiary instability in electromagnetic plasma microturbulence. *Phys. Plasmas*, 20:102308, 2013.

[201] P.-Y. Li, M. J. Pueschel, P. W. Terry, and G. G. Whelan. On the role of mode resonances in regulating zonal-flow-moderated plasma microturbulence. *Nucl. Fusion*, 63:026028, 2023.

[202] C. Arratia, C. P. Caulfield, and J. M. Chomaz. Transient perturbation growth in time-dependent mixing layers. *J. Fluid Mech.*, 717:90, 2013.

[203] A. K. Kaminski, C. P. Caulfield, and J. R. Taylor. Transient growth in strongly stratified shear layers. *J. Fluid Mech.*, 758:R4, 2014.

[204] L. H. Gustavsson. Energy growth of three-dimensional disturbances in plane Poiseuille flow. *J. Fluid Mech.*, 224:241, 1991.

[205] G. D. Chagelishvili, A. G. Tevzadze, G. Bodo, and S. S. Moiseev. Linear mechanism of wave emergence from vortices in smooth shear flows. *Phys. Rev. Lett.*, 79:17, 1997.

[206] G. D. Chagelishvili, J.-P. Zahn, A. G. Tevzadze, and J. G. Lominadze. On hydrodynamic shear turbulence in Keplerian disks: Via transient growth to bypass transition. *Astron. Astrophys.*, 402:401, 2003.

[207] C. P. Caulfield. Layering, instabilities, and mixing in turbulent stratified flows. *Annu. Rev. Fluid Mech.*, 53:113, 2021.

[208] J. S. Oishi, G. M. Vasil, M. Baxter, A. Swan, K. J. Burns, D. Lecoanet, and B. P. Benjamin. The magnetorotational instability prefers three dimensions. *Proc. R. Soc. A.*, 476:20190622, 2020.

[209] S. Ji, J. Fuller, and D. Lecoanet. Magnetohydrodynamic simulations of the Tayler instability in rotating stellar interiors. *Mon. Not. R. Astron. Soc.*, 521:5372, 2022.

[210] R. Blandford and N. Globus. Ergomagnetosphere, ejection disc, magnetopause in M87 - I. Global flow of mass, angular momentum, energy, and current. *Mon. Not. R. Astron. Soc.*, 514:5141, 2022.

[211] P. Garaud. Double-Diffusive Convection at Low Prandtl Number. *Ann. Rev. Fluid Mech.*, 50(1):275–298, January 2018.

[212] Conny Aerts, Stéphane Mathis, and Tamara M. Rogers. Angular Momentum Transport in Stellar Interiors. *Annual Rev. Astron. Astrophys.*, 57:35–78, August 2019.

[213] H. C. Spruit. Dynamo action by differential rotation in a stably stratified stellar interior. *Astron. Astrophys.*, 381:923–932, January 2002.

[214] S. A. Balbus and J. F. Hawley. Instability, turbulence, and enhanced transport in accretion disks. *Rev. Mod. Phys.*, 70:1–53, Jan 1998.

[215] G. Lesur, M. Flock, B. Ercolano, M. Lin, C. Yang, J. A. Barranco, P. Benitez-Llambay, J. Goodman, A. Johansen, H. Klahr, G. Laibe, W. Lyra, P. S. Marcus, R. P. Nelson, J. Squire, J. B. Simon, N. J. Turner, O. M. Umurhan, and A. N. Youdin. Hydro-, Magnetohydro-, and Dust-Gas Dynamics of Protoplanetary Disks. In S. Inutsuka, Y. Aikawa, T. Muto, K. Tomida, and M. Tamura, editors, *Astronomical Society of the Pacific Conference Series*, volume 534 of *Astronomical Society of the Pacific Conference Series*, page 465, July 2023.

[216] Paul G. Beck, Josefina Montalban, Thomas Kallinger, Joris De Ridder, Conny Aerts, Rafael A. García, Saskia Hekker, Marc-Antoine Dupret, Benoit Mosser, Patrick Eggenberger, Dennis Stello, Yvonne Elsworth, Søren Frandsen, Fabien Carrier, Michel Hillen, Michael Gruberbauer, Jørgen Christensen-Dalsgaard, Andrea Miglio, Marica Valentini, Timothy R. Bedding, Hans Kjeldsen, Forrest R. Girouard, Jennifer R. Hall, and Khadeejah A. Ibrahim. Fast core rotation in red-giant stars as revealed by gravity-dominated mixed modes. *Nature*, 481(7379):55–57, January 2012.

[217] P. Eggenberger, J. Montalbán, and A. Miglio. Angular momentum transport

in stellar interiors constrained by rotational splittings of mixed modes in red giants. *Astron. Astrophys.*, 544:L4, August 2012.

[218] P. Garaud and J. D. Garaud. Dynamics of the solar tachocline - II. The stratified case. *Mon. Not. R. Astron. Soc.*, 391(3):1239–1258, December 2008.

[219] Toby S. Wood and Michael E. McIntyre. Polar confinement of the Sun's interior magnetic field by laminar magnetostrophic flow. *J. Fluid Mech.*, 677:445–482, June 2011.

[220] V. Urpin and A. Brandenburg. Magnetic and vertical shear instabilities in accretion discs. *Mon. Not. R. Astron. Soc.*, 294(3):399–406, March 1998.

[221] R. P. Nelson, O. Gressel, and O. M. Umurhan. Linear and non-linear evolution of the vertical shear instability in accretion discs. *Mon. Not. R. Astron. Soc.*, 435(3):2610–2632, November 2013.

[222] A. J. Barker and H. N. Latter. On the vertical-shear instability in astrophysical discs. *Mon. Not. R. Astron. Soc.*, 450(1):21–37, June 2015.

[223] H. N. Latter and J. Papaloizou. Vortices and the saturation of the vertical shear instability in protoplanetary discs. *Mon. Not. R. Astron. Soc.*, 474(3):3110–3124, March 2018.

[224] J. Park, V. Prat, and S. Mathis. Horizontal shear instabilities in rotating stellar radiation zones. I. Inflectional and inertial instabilities and the effects of thermal diffusion. *Astron. Astrophys.*, 635:A133, March 2020.

[225] J. Park, V. Prat, S. Mathis, and L. Bugnet. Horizontal shear instabilities in rotating stellar radiation zones. II. Effects of the full Coriolis acceleration. *Astron. Astrophys.*, 646:A64, February 2021.

[226] E. Knobloch and H. C. Spruit. Stability of differential rotation in stars. *Astron. Astrophys.*, 113(2):261–268, September 1982.

[227] E. Knobloch. Nonlinear diffusive instabilities in differentially rotating stars. *Geophys. Astrophys. Fluid Dyn.*, 22:133, 1982.

[228] D. G. Korycansky. Two-dimensional Hydrodynamic Calculations of the Nonlinear Development of the Goldreich-Schubert-Fricke Instability in a Rotating Annulus. *Astrophys. J.*, 381:515, November 1991.

[229] F. Q. Rashid, C. A. Jones, and S. M. Tobias. Hydrodynamic instabilities in the solar tachocline. *Astron. Astrophys.*, 488(3):819–827, September 2008.

[230] A. J. Barker, C. A. Jones, and S. M. Tobias. Angular momentum transport, layering, and zonal jet formation by the GSF instability: non-linear simulations at a general latitude. *Mon. Not. R. Astron. Soc.*, 495(1):1468–1490, June 2020.

[231] R. W. Dymott, A. J. Barker, C. A. Jones, and S. M. Tobias. Linear and nonlinear properties of the Goldreich-Schubert-Fricke instability in stellar interiors with arbitrary local radial and latitudinal differential rotation. *Mon. Not. R. Astron. Soc.*, July 2023.

[232] E. A. Spiegel and G. Veronis. On the Boussinesq Approximation for a Compressible Fluid. *Astrophys. J.*, 131:442, March 1960.

[233] B. Tripathi, P. W. Terry, A. E. Fraser, E. G. Zweibel, and M. J. Pueschel. Three-dimensional shear-flow instability saturation via stable modes. *Phys. Fluids*, 35(10):105151, October 2023.

[234] G. Lesur and P. Y. Longaretti. On the relevance of subcritical hydrodynamic turbulence to accretion disk transport. *Astron. Astrophys.*, 444(1):25–44, December 2005.

[235] T. Radko and D. P. Smith. Equilibrium transport in double-diffusive convection. *J. Fluid Mech.*, 692:5–27, February 2012.

[236] J. M. Brown, P. Garaud, and S. Stellmach. Chemical Transport and Spontaneous Layer Formation in Fingering Convection in Astrophysics. *Astrophys. J.*, 768(1):34, May 2013.

[237] P. Z. Harrington and P. Garaud. Enhanced Mixing in Magnetized Fingering Convection, and Implications for Red Giant Branch Stars. *Astrophys. J. Lett.*, 870(1):L5, January 2019.

[238] J. Christensen-Dalsgaard, W. Dappen, S. V. Ajukov, E. R. Anderson, H. M. Antia, S. Basu, V. A. Baturin, G. Berthomieu, B. Chaboyer, S. M. Chitre, A. N. Cox, P. Demarque, J. Donatowicz, W. A. Dziembowski, M. Gabriel, D. O. Gough, D. B. Guenther, J. A. Guzik, J. W. Harvey, F. Hill, G. Houdek, C. A. Iglesias, A. G. Kosovichev, J. W. Leibacher, P. Morel, C. R. Proffitt, J. Provost, J. Reiter, Jr. Rhodes, E. J., F. J. Rogers, I. W. Roxburgh, M. J. Thompson, and R. K. Ulrich. The Current State of Solar Modeling. *Science*, 272(5266):1286–1292, May 1996.

[239] Pavel A. Denissenkov. Numerical Simulations of Thermohaline Convection: Implications for Extra-mixing in Low-mass RGB Stars. *Astrophys. J.*, 723(1):563–579, November 2010.

[240] T. Tassin, T. Gastine, and A. Fournier. Fingering convection in a spherical shell. *arXiv e-prints*, page arXiv:2309.01602, September 2023.

[241] P. Garaud and N. Brummell. 2D or Not 2D: The Effect of Dimensionality on the Dynamics of Fingering Convection at Low Prandtl Number. *Astrophys. J.*, 815(1):42, December 2015.

[242] B. Paxton, L. Bildsten, A. Dotter, F. Herwig, P. Lesaffre, and F> Timmes. Modules for Experiments in Stellar Astrophysics (MESA). *Astrophys. J.*, 192(1):3, January 2011.

[243] B. Paxton, R. Smolec, J. Schwab, A. Gautschy, L. Bildsten, M. Cantiello, A. Dotter, R. Farmer, J. A. Goldberg, A. S. Jermyn, S. M. Kanbur, P. Marchant, A. Thoul, R. H. D. Townsend, W. M. Wolf, M. Zhang, and F. X. Timmes. Modules for Experiments in Stellar Astrophysics (MESA): Pulsating Variable Stars, Rotation, Convective Boundaries, and Energy Conservation. *Astrophys. J. Supp.*, 243(1):10, July 2019.

[244] B. Tripathi, A. E. Fraser, P. W. Terry, E. G. Zweibel, M. J. Pueschel, and E. H. Anders. Nonlinear mode coupling and energetics of driven magnetized shear-flow turbulence. *Phys. Plasmas*, 30(7):072107, July 2023.

[245] S. M. Tobias. The turbulent dynamo. *J. Fluid Mech.*, 912:P1, 2021.

[246] K. Cline, N. Brummell, and F. Cattaneo. Dynamo action driven by shear and magnetic buoyancy. *Astrophys. J.*, 599:1449, 2003.

[247] K. Cline, N. Brummell, and F. Cattaneo. On the formation of magnetic structures by the combined action of velocity shear and magnetic buoyancy. *Astrophys. J.*, 588:630, 2003.

[248] G. M. Vasil, D. Lecoanet, K. Augustson, K. J. Burns, J. S. Oishi, B. P. Brown, N. Brummell, and K. Julien. The solar dynamo begins near the surface. *Nature*, 629:769, 2024.

[249] K. Subramanian and A. Brandenburg. Traces of large-scale dynamo action in the kinematic stage. *Mon. Not. R. Astron. Soc.*, 445:2930, 2014.

[250] P. Bhat, K. Subramanian, and A. Brandenburg. A unified large/small-scale dynamo in helical turbulence. *Mon. Not. R. Astron. Soc.*, 461:240, 2016.

[251] P. Bhat, F. Ebrahimi, and E. G. Blackman. Large-scale dynamo action precedes turbulence in shearing box simulations of the magnetorotational instability. *Mon. Not. R. Astron. Soc.*, 462:818, 2016.

[252] P. Bhat. Saturation of large-scale dynamo in anisotropically forced turbulence. *Mon. Not. R. Astron. Soc.*, 509:2249, 2021.

[253] B. Tripathi, A. E. Fraser, P. W. Terry, E. G. Zweibel, M. J. Pueschel, and R. Fan. Large-scale dynamos driven by shear-flow-induced jets. *Nature*, 2025. Accepted for publication.

[254] A. Elias-López, F. D. Sordo, and D. Viganò. Vorticity and magnetic dynamo from subsonic expansion waves. *Astronomy & Astrophysics*, 677:46, 2023.

[255] P. W. Terry. Zonal flows in magnetically confined plasmas: Theory. In Boris Galperin and Peter L. Read, editors, *Zonal Jets*, pages 181–193. Cambridge University Press, London, 2019.

[256] B. Galperin, H. Nakano, H.-P. Huang, and S. Sukoriansky. The ubiquitous zonal jets in the atmospheres of giant planets and Earth's oceans. *Geophys. Res. Lett.*, 31:L12203, 2004.

[257] S. Tobias and F. Cattaneo. Limited role of spectra in dynamo theory: coherent versus random dynamos. *Physical Review Letters*, 101:125003, 2008.

[258] I. G. Cresswell, E. H. Anders, B. P. Brown, J. S. Oishi, and G. M. Vasil. Force balances in strong-field magnetoconvection simulations. *Phys. Rev. Fluids*, 8:093503, 2023.

[259] A. E. Fraser, S. A. Reifenstein, and P. Garaud. Magnetized fingering convection in stars. *Astrophys. J.*, 964:184, 2024.

[260] U. M. Ascher, S. J. Ruuth, and R. J. Spiteri. Implicit-explicit Runge-Kutta methods for time-dependent partial differential equations. *Applied Numerical Mathematics*, 25:151, 1997.

[261] D. Wang and S. J. Ruuth. Variable step-size implicit-explicit linear multistep methods for time-dependent partial differential equations. *Journal of Computational Mathematics*, 26:838, 2008.

[262] B. F. Farrell and P. J. Ioannou. Dynamics of streamwise rolls and streaks in turbulent wall-bounded shear flow. *J. Fluid Mech.*, 708:149, 2012.

[263] P. W. Terry, A. S. Ware, and D. E. Newman. Relaxation oscillations induced by amplitude-dependent frequency in dissipative trapped electron mode turbulence. *Phys. Plasmas*, 1:3974, 1994.

[264] A. L. Wilmot-Smith, D. Nandy, G. Hornig, and P. C. H. Martens. A time delay model for solar and stellar dynamos. *Astrophys. J.*, 652:696, 2006.

[265] S. A. Olausen and V. M. Kaspi. The McGill magnetar catalog. *Astrophys. J. Supplement Series*, 212:6, 2014.

[266] A. Bahramian and N. Degenaar. Low-mass X-ray binaries. In *Handbook of X-ray and Gamma-ray Astrophysics*, pages 1–62. Springer Nature, Singapore, 2022. Published in 2022, but often cited with a later date depending on context.

[267] F. Rincon. Dynamo theories. *Journal of Plasma Physics*, 85:205850401, 2019.

[268] V. Skoutnev, J. Squire, and A. Bhattacharjee. On large-scale dynamos with stable stratification and the application to stellar radiative zones. *Mon. Not. R. Astron. Soc.: Letters*, 517:526, 2022.

[269] E. R. Most and E. Quataert. Flares, Jets, and Quasiperiodic Outbursts from Neutron Star Merger Remnants. *Astrophys. J. Lett.*, 947(1):L15, April 2023.

[270] D. Radice. General-relativistic Large-eddy Simulations of Binary Neutron Star Mergers. *Astrophys. J. Letters*, 838:L2, 2017.

[271] R. Aguilera-Miret, D. Viganò, and C. Palenzuela. Universality of the Turbulent Magnetic Field in Hypermassive Neutron Stars Produced by Binary Mergers. *Astrophys. J. Letters*, 926:L31, 2022.

[272] K. Kiuchi, A. Reboul-Salze, M. Shibata, and Y. Sekiguchi. A large-scale magnetic field produced by a solar-like dynamo in binary neutron star mergers. *Nat. Astron.*, 8:298–307, March 2024.

[273] A. Brandenburg and K. Subramanian. Astrophysical magnetic fields and nonlinear dynamo theory. *Physics Reports*, 417:1, 2005.

[274] T. A. Yousef. Generation of magnetic field by combined action of turbulence and shear. *Physical Review Letters*, 100:184501, 2008.

[275] D. W. Hughes and M. R. E. Proctor. Large-scale dynamo action driven by velocity shear and rotating convection. *Physical Review Letters*, 102:044501, 2008.

[276] F. Ebrahimi and E. G. Blackman. Radially dependent large-scale dynamos in global cylindrical shear flows and the local Cartesian limit. *Mon. Not. R. Astron. Soc.*, 459:1422, 2016.

[277] A. Schekochihin. MHD turbulence: a biased review. *Journal of Plasma Physics*, 88:155880501, 2023.

[278] N. Yokoi. Unappreciated cross-helicity effects in plasma physics: anti-diffusion effects in dynamo and momentum transport. *Reviews of Modern Plasma Physics*, 7:E33, 2023.

[279] P. D. Mininni, A. Alexakis, and A. Pouquet. Shell-to-shell energy transfer in magnetohydrodynamics. II. Kinematic dynamo. *Physical Review E*, 72:046302, 2005.

[280] A. B. Bendre, K. Subramanian, D. Elstner, and O. Gressel. Turbulent transport coefficients in galactic dynamo simulations using singular value decomposition. *Mon. Not. R. Astron. Soc.*, 491:3870, 2020.

[281] A. Brandenburg. Advances in theory and simulations of large-scale dynamos. *Space Science Reviews*, 144:87, 2009.

[282] A. Brandenburg and D. Sokoloff. Local and nonlocal magnetic diffusion and alpha-effect tensors in shear flow turbulence. *Geophysical & Astrophysical Fluid Dynamics*, 96:319, 2002.

[283] S. Boldyrev. Spectrum of Magnetohydrodynamic Turbulence. *Physical Review Letters*, 96:115002, 2006.

[284] L. Gizon, R. H. Cameron, M. Pourabdian, Z.-C. Liang, D. Fournier, A. C. Birch, and C. S. Hanson. Meridional flow in the Sun's convection zone is a single cell in each hemisphere. *Science*, 368(6498):1469–1472, June 2020.

[285] G. Hazra, D. Nandy, L. Kitchatinov, and A.R. Choudhuri. Mean Field Models of Flux Transport Dynamo and Meridional Circulation in the Sun and Stars. *Space Sci. Rev.*, 219(5):39, August 2023.

[286] M. A. Abramowicz, A. Lanza, E. A. Spiegel, and E. Szuszkiewicz. Vortices on accretion disks. *Nature*, 356:41, 1992.

[287] A. M. Fridman, V. L. Afanasiev, S. N. Dodonov, O. V. Khoruzhii, A. V. Moiseev, O. K. Sil'chenko, and A. V. Zasov. The orientation parameters and rotation curves of 15 spiral galaxies. *Astronomy & Astrophysics*, 430:67, 2005.

[288] U. Chadayammuri, J. ZuHone, P. Nulsen, D. Nagai, S. Felix, F. Andrade-Santos, L. King, and H. Russell. Constraining merging galaxy clusters with X-ray and lensing simulations and observations: The case of Abell 2146. *Mon. Not. R. Astron. Soc.*, 509:1201, 2021.

[289] M. Anderson, E. W. Hirschmann, L. Lehner, S. L. Liebling, P. M. Motl, D. Neilsen, C. Palenzuela, and J. E. Tohline. Magnetized neutron-star mergers and gravitational-wave signals. *Physical Review Letters*, 100:191101, 2008.

[290] D. I. Pullin and P. G. Saffman. Vortex Dynamics in Turbulence. *Ann. Rev. Fluid Mech.*, 30:31–51, January 1998.

[291] E. J. Kaplan, M. M. Clark, M. D. Nornberg, K. Rahbarnia, A. M. Rasmus, N. Z. Taylor, C. B. Forest, and E. J. Spence. Reducing Global Turbulent Resistivity by Eliminating Large Eddies in a Spherical Liquid-Sodium Experiment. *Phys. Rev. Lett.*, 106:254502, Jun 2011.

[292] J. Zrake and A. I. MacFadyen. Magnetic Energy Production by Turbulence in Binary Neutron Star Mergers. *Astrophys. J. Lett.*, 769(2):L29, June 2013.

[293] U. Chadayammuri, J. ZuHone, P. Nulsen, D. Nagai, and H. Russell. Turbulent magnetic fields in merging clusters: a case study of Abell 2146. *Mon. Not. R. Astron. Soc.*, 512(2):2157–2170, May 2022.

[294] P. W. Terry. Nonlinear Mechanisms of Mirror-Mode Excitation. In *66th Annual Meeting of the APS Division of Plasma Physics (DPP24)*, Atlanta, Georgia, October 2024. Abstract No. TP12.00013, Session TP12. Conference Abstract.

[295] M. Zhou, P. Bhat, N. F. Loureiro, and D. A. Uzdensky. Magnetic island merger as a mechanism for inverse magnetic energy transfer. *Phys. Rev. Research*, 1(1):012004, August 2019.

[296] C. Palenzuela, R. Aguilera-Miret, F. Carrasco, R. Ciolfi, J. V. Kalinani, W. Kastaun, B. Miñano, and D. Viganò. Turbulent magnetic field amplification in binary neutron star mergers. *Phys. Rev. D*, 106:023013, Jul 2022.

[297] L. Combi and D. M. Siegel. Jets from Neutron-Star Merger Remnants and Massive Blue Kilonovae. *Phys. Rev. Lett.*, 131:231402, Dec 2023.

[298] E. R. Most. Impact of a mean field dynamo on neutron star mergers leading to magnetar remnants. *Phys. Rev. D*, 108(12):123012, December 2023.

[299] K. Kunnumkai, A. Palmese, A. M. Farah, M. Bulla, T. Dietrich, P. T. H. Pang, S. Anand, I. Andreoni, T. Cabrera, and B. O Connor. Detecting electromagnetic counterparts to LIGO/Virgo/KAGRA gravitational wave events with DECam: Neutron Star Mergers. *arXiv e-prints*, page arXiv:2411.13673, November 2024.

[300] M. Maggiore, C. Van Den Broeck, N. Bartolo, E. Belgacem, D. Bertacca, M. A. Bizouard, M. Branchesi, S. Clesse, S. Foffa, J. García-Bellido, S. Grimm, J. Harms, T. Hinderer, S. Matarrese, C. Palomba, M. Peloso, A. Ricciardone, and M. Sakellariadou. Science case for the Einstein telescope. *J. Cosmol. Astropart. Phys.*, 2020(3):050, March 2020.

[301] X.-N. Bai, D. Caprioli, L. Sironi, and A. Spitkovsky. Magnetohydrodynamic-particle-in-cell Method for Coupling Cosmic Rays with a Thermal Plasma: Application to Non-relativistic Shocks. *Astrophys. J.*, 809(1):55, August 2015.

[302] A. J. van Marle. Combining PIC and MHD to model particle acceleration in astrophysical shocks. *arXiv e-prints*, page arXiv:2509.12150, September 2025.